Loss Reduction in Axial Flux Machines using Magnetic Shielding

Nasiru Aliyu

Thesis submitted for the degree of Doctor of Philosophy

School of Engineering

Newcastle University 2021

Abstract– The introduction of compacted insulated iron powder in electrical machines design makes their manufacturing process easy together with high rates of production and the machine parts made from it are stable dimensionally compared to conventional laminated steel. The research work presented in this thesis was carried out with the main aim to improve the overall performance of a three-phase Axial Flux Machine (AFM) using Soft Magnetic Composite (SMC). To realise it, the machine was redesigned in a way to benefit from the unique properties of the material such as low eddy current loss at high frequency, isotropic magnetic properties and simple manufacturing process.

Due to the three-dimensional (3D) nature of the SMC material and AFM structure, 3D Finite Element Analysis (FEA) was carried out for accurate prediction of performance and extensive simulation results were provided. Higher fill factor up to 70% was achieve by compacting the pre-formed coils on a bobbin before sliding onto the tooth for final assembly, which offered a significant improvement in performance. AC winding loss analysis was performed due to open-slot stator winding configuration and the higher frequency of operation resulting in skin-depths of the same order of size as the typical conductor diameters. A method of AC winding loss reduction was introduced using a single steel lamination sheet to shield the windings from stray fields due to the open-slot stator construction which encourage an elevated AC loss at AC operation. Moreover, this approach is easy to implement for this machine topology and does not require the use of more complex twisted and Litz type conductors.

To validate the 3D FEA, a prototype machine was built which ultimately resulted in 6 machines being tested without and with steel lamination sheet during this PhD. The measured result which includes the back EMF, full load voltage, torque, power and losses are thoroughly presented and agreed with the 3D FEA very well. Depending on lamination type, it is shown that the AC winding loss reduced by up to 48.0%, total loss reduced by up to 31.7%, this method has disadvantages of minor reduction of up to 3.5%, 5.8% and 2.8% in the peak back EMF, torque and output power respectively. The efficiency has increased by up to 10.3%.

The research studies signify the viability of designing and producing a highly efficient AFM with SMC and has the potential for mass production, this thesis makes significant contribution by implementing a simple novel method for AC winding loss reduction using steel lamination sheet to shield the stray flux due to open-slot stator winding construction.

Table of Contents

List of Figures

List of Tables

List of Symbols

AFM	Axial Flux Machine	I_{con}	Current in the conductor
SMC	Soft Magnetic Composite	f	Frequency
3D	Three Dimensional	k_w	Winding factor
T	Torque	n	Speed
MMF	Magnemotive Force	p	Number of poles
EMF	Electromotive Force	l_{ag}	Airgap length
AC	Alternating Current	l_m	Magnet thickness
NdFeB	Neodymium Iron Boron	r_o	Outer radius
D_0	Outer Diameter	r_i	Inner radius
K_{af}	Axial Flux Constant	B_{ag}	Airgap flux density
K_{rf}	Radial Flux Constant	B_{cb}	Core-back flux density
L	Radial Length	D_{cb}	Core-back thickness
B_z	Airgap flux in z-direction	B_r	Remanent flux density
FFT	Fast Fourier Transform	F	AC to DC factor
R_{ac}/R_{dc}	AC to DC resistance ratio	P_C	Core loss
FEA	Finite Element Analysis	k_e	Eddy current loss constant
BLDC	Brushless DC Machine	k_h	Hysteresis loss constant
W	Slot Width	P_{cu}	Copper loss
H	Slot height	d	Wire diameter
A_s	Slot area	Vol	Volume of copper
A_{cu}	Copper area	φ	Flux linkage
F_F	Fill factor	V	Terminal voltage
J	Current density	X	Reactance
A_{con}	Conductor area	η	Efficiency
N	Number of turns	P_{out}	Output power
R_{coil}	Coil resistance	P_{in}	Input power
ρ_{cu}	Resistivity of copper	P_W	Windage loss

Dedication

I hereby dedicate this thesis to a father, teacher, mentor, scholar, mediator, community organiser… Sheikh Alhaji Aliyu Usman Babando, who passed away at the middle of my PhD programme. May his gentle soul rest in peace. Amin.

Acknowledgements

I would like to start by thanking my sponsor; The Petroleum Technology Development Fund (PTDF) Nigeria and NASRDA-CBSS. Thanks to my Supervisor, Dr. Glynn Atkinson, for all his support and encouragement throughout the completion of my research work.

I would also like to thank Alhaji Armiya'u Umar Baba of PTDF, Dr. Nick Stannard who has lent his advice and expertise during my time at Newcastle University. I also will like to acknowledge Jamie Washington and the mechanical workshop guys.

Special thanks to my parents, especially my father Sheikh Alhaji Aliyu Usman Babando who would not see the end of this work, my mother Aishatu (Asabe) Garba Muri, my beautiful wife Rashida and my children Gumaisa'u Nasiru and Khuzaima Nasiru for supporting me during these years of PhD study.

Finally, to all the PhD students and technicians within the UG LAB, I say many thanks.

1. Introduction

The present global challenges and growing pressure for innovative solution will demand electrical machines to take a leading role in the lives of everyone in developing countries, especially thousands of machines used in domestic applications. The main aim of this research work is to further knowledge in the development of highly efficient open-slot stator winding axial flux machine (AFM) with soft magnetic composite (SMC). This chapter outlines the background of the research and challenges associated with the open-slot stator winding configuration. It also presents the main objectives, procedures to achieve the design development and principal contributions developed in this research work together with the thesis outline. Details are also provided of the published work.

1.1 Project Background

Since the inception of electrical engineering, the efficient and cost-effective design of electrical machines has been a demand quality for machine designers. Consequently, electrical machines produced have better efficiency. A little enhancement in the machine efficiency can even reduce energy consumption and the cost of production. To develop a highly efficient machine requires correct understanding of the losses in the electrical machines. Therefore, designing more dependable, energy-saving and highly efficient electrical machines is an area of interest for machine designers.

The main sources of losses in electrical machines are the stator winding copper loss and magnetic core iron losses. Regarding the former, concentrated windings pre-wound on a plastic bobbin and slid onto a single tooth, which offers a good usage of copper and can reduce copper losses in the magnetic circuit design. Magnetic core iron loss, on the other hand, is affected by excitation frequency and the speed of the machine. This causes eddy currents in the core which reduces the machine performance. The traditional way to reduce this effect is by the use of laminated steel. Steel lamination sheet has been used for electrical machine core construction for decades [1] and to reduce the effect of eddy current. It has a number of disadvantages; this includes significant iron losses at high speed, material waste in the process of traditional punching and introduction of mechanical strain. The latest method of making steel lamination sheet, such as Hot-roll, extrusion, flame and adhesive has the effect of increasing the cost and decreasing the mechanical strength of steel lamination sheet. Therefore, there is a need of looking at alternative materials in producing the machine core that offer lower losses than the conventional steel lamination sheet at high speed.

A lot of research has been carried out which offers alternative to steel lamination sheets using SMC and the principle of loss reduction is similar to that of steel lamination sheet when the path of flux is reduced [2]. In the recent development of SMC powder each grain is insulated from all of the neighbouring grains which increase the resistivity and they can be compacted into finished shape. Moreover, this material has some drawbacks, including lower magnetic permeability and lower saturation flux density, when compared with steel laminated sheets [3], a company behind much of the development in SMC technology is Höganäs AB of Sweden [3]. A detailed discussion on SMC production and properties will be presented in Chapter 2.

The AFM is well known for 3D structure, high torque and power density, high efficiency and short axial length [4]. The majority of applications require compact electrical machines design with high efficiency and one of the factors that affect efficiency of a machine at high speed is AC winding loss, enhanced skin and proximity effect. It can also be influenced by the size of the conductor and amplitude of the current flowing in a conductor [5]. Recently machine designers have a lot of interest in AFMs as reported in [6] due to their use in a wide variety of applications when high efficiency together with high torque density is required. Fundamental properties such as short axial length and compact design make its suitable for direct drive applications as stated in [7]. Increasing the operating speed of such machines can lead to a reduction in their size, weight and cost. The losses in electrical machines constrain the overall efficiency and the output characteristic of such machines has a significant effect on their selection.

A single-sided open-slot AFM has been designed and developed in Newcastle University as a demonstrator. The stator of the prototype machine is built using SMC developed by Höganäs AB of Sweden. This machine however had a poor overall performance due to the open-slot stator winding configuration which influenced more AC winding loss in the machine as a result of field from the rotation of the permanent magnets on the rotor assembly.

1.2 Challenges of Open-Slot Stator Winding

In open-slots stator, the teeth are straight to allow easy coil placement and replacement but resulting stray flux enters slot (and coil) as shown in Figure 1-1. The changing flux through the coil induces losses which at high frequency can be significant. However, the configuration encourages an elevated winding loss from the PM rotor. The eddy-current losses induced in the stator winding as a result of the time-changing field from the rotation of the PM rotor assembly are the dominant component of the winding loss at the AC operation [8]. This issue of excess AC winding loss in open-slot configuration needs to be address to reduce the losses and improve the overall performance by using different techniques of shielding the coils from stray fields, which are discussed in Chapter 5, 6, 7 and 8.

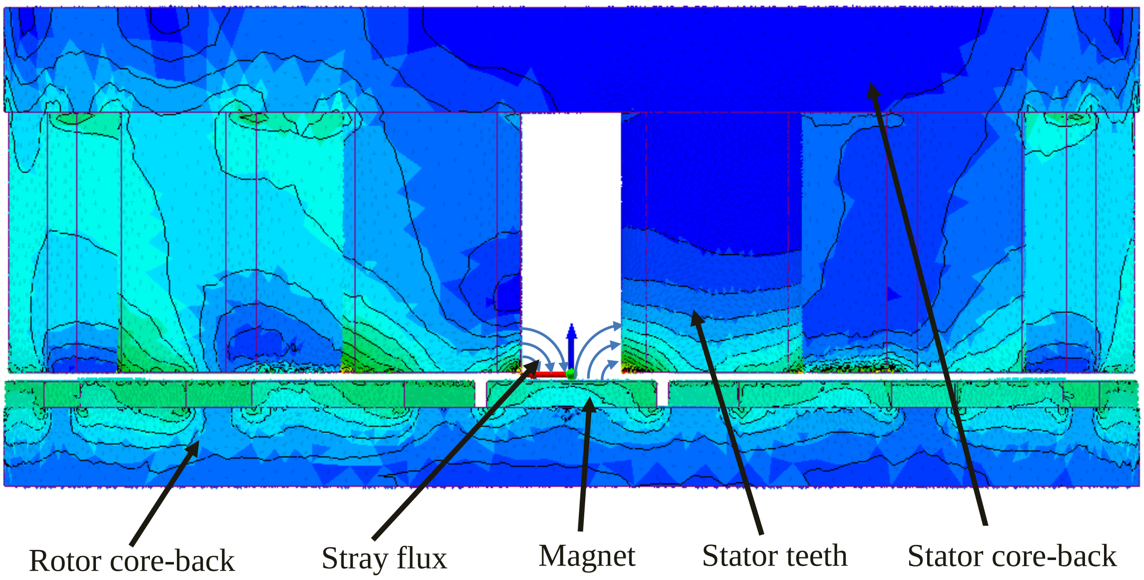

Figure 1-1: Stray flux due to open-slot configuration.

The slot opening distorts the waveform of the airgap flux density which causes increased additional AC winding loss at high speed and torque ripples and reduces efficiency of the machines. The employment of the slot magnetic wedges in the stator or rotor open-slots has proved an efficient technique when dealing with radial flux machines and an effective method to improve the induction motor performances was reported in [9]. Magnetically anisotropy wedge in the stator slots of radial flux machines especially a model rotating machine has proved to be a powerful technique in the reduction of the leakage flux and flux ripple in the airgap compared to isotropic wedge within a given anisotropy range [10].

The utilization of magnetic wedges is a good solution to improve the performances of an electrical machine with open stator slots [11] however it has a little influence on the core losses under no-load condition [12]. The relative permeability of slot wedges material plays a vital role in electrical machines performance improvement with low relative permeability materials improved performance with minor reduction in torque and no-load parameters as reported in [13].

It is clear that the slot wedges have proved to be an efficient method used in high speed radial flux machines to improve the performances, but they cannot be done cheaply using a single steel lamination sheet for all slots as in axial flux machines.

This work will focus on a cheaply technique of AC winding loss reduction in an AFM using a single steel lamination sheet, in a radial flux machine it is hard to imagine a single steel lamination sheet making all the slot wedges. This partially results from wanting to slip the coils onto the tooth. The AFM is design with SMC material together with high-energy magnets like Neodymium Iron Boron (NdFeB), which can be used to improve the overall performance of the machines. This combination has become a good replacement to radial flux machines when the pole number is high and axial length is short [7] [14]. Also, a reduction in the costs of production has made them suitable for low and medium-power motor and generator applications [15].

The problem of open-slot stator winding construction in an AFM was responsible for the poor overall performance of the machine due to excess AC winding loss at high speed. Hence improving the machine’s performance by reducing the magnitude of AC winding loss is important. In this thesis, several methods were proposed, and it is shown that AC winding loss and total loss can all be significantly reduced with a significant effect on the overall performance of the machine and minor effect on the back EMF and overall torque output.

1.3 Objectives of the Thesis

The main objectives of this research work are to:

1. Develop a highly efficient open-slot AFM using SMC material.
2. To make the winding aspect of the design simple by being pre-wound on a former before sliding onto the stator tooth.

3. To improve the overall performance and prevent an increase in slot temperature by introducing a new approach to AC winding loss reduction as a result of open-slot stator winding construction using a single steel lamination sheet.
4. To design, construct and test a prototype machine and validate the 3D FEA results.

In order to achieve the design development and validate the 3D FEA, the thesis proposes the following steps:

1. Carry out a literature and technology review on state of the art on AFM which includes the design and FEA modelling, loss and thermal analysis evaluation, materials and manufacturing, torque and extended speed and review the use of magnetic shielding in the stator slots.
2. Carry out 3D FEA and verification on a baseline machine designed in Newcastle University, to see how the performance can be improved by using a design investigation on different parameters variation and assessing the AC winding loss due to open-slot configuration. Develop a method for AC winding loss reduction with the aid of a single steel lamination sheet to shield the coils from stray fields.
3. Production and testing of a prototype machine to validate the 3D FEA, this construction uses a simple way of winding the coils on a former before sliding onto a tooth for fill factor improvement, easy replacement and full testing scale at different conductor size and operating conditions.
4. Presenting the experimental test results of the prototype machine.

Due to the 3D nature of the SMC and that of AFM, 3D FEA (Infolytica MagNet and JMAG) were used to analyse the machine. Verification of baseline machine was done with Infolytica MagNet software and one-quarter of the machine was used in the analysis to minimise simulation time, furthermore it is used in the design improvement of the machine and half of the machine was utilised in the simulation due to slot and pole number combination. AC winding loss was carried out using JMAG software due to complexity in the coil design and shorter computational time moreover one-twelfth of the machine was used to evaluate AC winding loss and reduction.

The advantages of JMAG over others electromagnetic finite element software to electrical machine analysis have been proven time and again. Even though electrical machines are considered mature products, they still face new demands for higher performance and these demands have increased competition among machine designer to get the most result from a design. It is faster, high productivity, accurate, open interface and has the capabilities of designing and evaluating complex phenomena such as AC loss in an individual stranded conductor in addition to basic characteristics such as induced voltage, torque and inductance.

This PhD used different single steel lamination sheet to reduce the AC winding loss due to open-slot stator winding construction. It is shown that AC winding loss and total loss in the machine can all be significantly reduced with minor effect on the back EMF and overall torque output. Six machine variants were built and tested for AC winding loss reduction and one best machine was chosen that reduced the AC winding loss by 48.0%, total loss by 31.7%, however this method has disadvantages of minor reduction of 3.5%, 5.8% and 2.8% in the peak back EMF, torque and output power respectively. The efficiency has increased by 10.3%.

1.4 Research Contributions to Knowledge Furtherance

The principal contributions developed in this research work are as follows;

1. AC winding loss analysis in which the effect of 3D nature of SMC and AFM were taken into consideration.
2. A novel method to AC winding loss reduction in AFM was explored using different steel lamination sheet. This approach is easy to implement for this machine topology and does not require the use of more complex twisted and Litz type conductors. It is shown that this technique has reduced the AC winding loss by up to 48.0% and total loss by up to 31.7%, the efficiency increased by 10.3%.
3. Constructing and testing of 6 prototype machines without and with different single steel lamination sheet to assess the effect of magnetic shielding.

1.5 Outline of Thesis

This thesis is structured as follows;

Chapter 1 provides the Introduction and project background, challenges of open-slot stator winding construction, objective of the thesis together with procedures to achieve the design development, research contribution to knowledge furtherance, thesis outline and work published from the research work.

Chapter 2 presents the AFM history together with comparison between AFM and radial flux machine, SMC in electrical machines, typical applications area and the state of the art in AFM development which includes; AFM stator winding, design and FEA modelling, loss evaluation and thermal analysis, torque and extended speed, materials and manufacturing. It also presents SMC production and properties, review on the use of magnetic shielding in the stator slots and loss mechanisms in electrical machines. Topologies of AFM that includes; single-sided, double-sided and multi stage configuration. Finally, it reviews the features advantages and disadvantages of AFM.

Chapter 3 gives the 3D FEA and verification of a baseline machine together with machine topology and overall performance simulation, which includes; meshing, cogging torque, axial force between stator disc and rotor disc, losses at full-load current, back EMF and harmonic analysis. Experimental validation of cogging torque and on-load torque of the machine together with the instrument used to conduct the tests measurement are also presented. Moreover, recommend techniques to improve the machine performance.

Chapter 4 investigates the design improvement of AFM with 110 mm outer diameter, this comprises the design methodology and optimisation with respect to sensitivity of average torque on parameter variation such as airgap length, magnet length and span, slot width, inner and outer diameter and core-back of the stator and rotor using 3D FEA. The final topology and dimensions were chosen, and three-dimensional finite element analysis of the machine was conducted and overall performance simulation results of the back EMF, loss, output power and efficiency were presented.

Chapter 5 provides an assessment of AC winding loss in the machine, eddy current loss in stranded conductor, effect of conductor diameter, conductor position within the slot, speed, and mesh size on AC loss calculation and alternative method of calculating AC loss; analytical expression for R_{ac}/R_{dc}. Current density distribution within the conductors and AC to DC ratio factor.

Chapter 6 explores a new technique for AC winding loss reduction, which relies on different single steel lamination sheet together with the principles of slot leakage inductance. It also provides the 3D finite element analysis together with comparison of losses, airgap flux density, cogging torque and axial force and machine efficiency with different steel lamination sheet.

Chapter 7 provides the academic investigation into the mechanism of loss reduction (shielding mechanism) by using idealised materials (high reluctance/zero conductivity and vice versa). These includes, material conductivity and thickness, flux linkage, back EMF and harmonic analysis, no-load and on-load total loss, cogging torque and axial force and on-load torque together with slot designs.

Chapter 8 describes the mechanical design, prototype construction and assembly. Mega Ohm test and Surge test. Block diagram of the experimental tests setup is also presented.

Chapter 9 presents the test rig and equipment set up for the experimental tests together with the results and evaluations of the experimental tests carried out on the optimised prototype machine with 1.4 mm and 3.2 mm conductor diameter. This includes winding resistance, back EMF measurements and harmonic analysis without and with steel lamination sheet, on-load torque, output power and terminal voltage, total loss in the machine, AC winding loss with 3.2 mm conductor diameter, efficiency and coils temperature rise.

Chapter 10 presents the conclusion of the research work and outlines further work that can be done to improve the performance of the machine. Finally, the thesis concludes with appendix and references.

1.6 Published Work

The following publications and conference proceedings have stemmed from this research work;

1. Aliyu, N., Atkinson, G. and Stannard, N., "**Concentrated winding permanent magnet axial flux motor with soft magnetic composite core for domestic application"** 2017 IEEE 3rd International Conference on Electro-Technology for National Development (NIGERCON) pp. 1156-1159. November 2017 IEEE.
2. N. Aliyu, G. Atkinson, N. Stannard "**Assessment of AC Copper Loss in Permanent Magnet Axial Flux Machine with Soft Magnetic Composite Core**" PEMD 2018 held at ACC Liverpool UK.

3. N. Aliyu, G. Atkinson, N. Ahmed, N. Stannard "**AC Winding Loss Reduction in High Speed Axial Flux Permanent Magnet Machine using a Lamination Steel Sheet"** International Electric Machines & Drives Conference (IEMDC 2019) held on May 12-15, 2019 at Westin San Diego, San Diego USA.

2. Literature Review

2.1 Introduction

This chapter presents a literature and technology review of the research work done so far relating to this thesis. It has two main objectives: to ensure that the research work to be carried out is novel. Secondly to give a summary of the work done by other researchers in this field of study and see how to further knowledge in the course of this project.

The research work in this thesis proposes to use soft magnetic composite in the design of single-sided open-slot AFM as a demonstrator. In order to realise a highly efficient machine, magnetic shielding is used to divert the stray flux reaching the windings, it is also important to look at other AFM topologies in the course of reviewing. The review has been approached in by separating it into a number of areas as follows:

1. The history of axial flux machines to give a level of background.
2. Comparison of axial flux machines with radial flux machines in terms of torque production together with a review on SMC in Electrical Machines and typical application areas of axial flux machines.
3. A review of the progress achieved over the years in the design and analysis of AFM, attention would be given to the aspects of stator winding design, FEA modelling, evaluation of loss and thermal analysis, torque and extended speed, materials and manufacturing.
4. A review on soft magnetic composite material that include the production process and properties, particularly the typical prototype SMC Somaloy.
5. A review on magnetic shielding and loss mechanism, attention would be given to the used of magnetic slot wedges for overall machine performance improvement.
6. A review on the AFM topologies these to include; single-sided consists of a single stator and a single rotor, double-sided consists of either two stator and a single rotor or two rotor and a single stator, multistage consists of multi rotor and multi stator.
7. Finally, to review the advantages and disadvantages of axial flux machine features.

2.2 History of Axial Flux Machine

Axial flux machines are highly compact structure together with high torque, power density and high efficiency which can be kept over a wide operating range. The issue of complex mechanical questions can now be eliminating by new techniques in the design and constructions. Typically, AFM's with larger diameter and relatively shorter axial length can be used in many applications which are cost-effective in terms of active electromagnetic material for a given output power ranging for low speed to high speed, high torque to low torque applications, it can also be considered for applications in a wide power range.

This section gives the brief history of axial flux machine design. The first electrical machine in Figure 2-1 built as a disc generator by Faraday in 1831 was based on axial flux idea [16]. It is called homopolar generator or disc dynamo and consists of an electrically conductive disc or cylinder rotating in a planer perpendicular to a uniform static magnetic field. A potential difference was created between the centre of the disc and the ends of the cylinder. The electrical polarity depends on the direction of rotation and field orientation. The output voltage is low, on the order of a few volts.

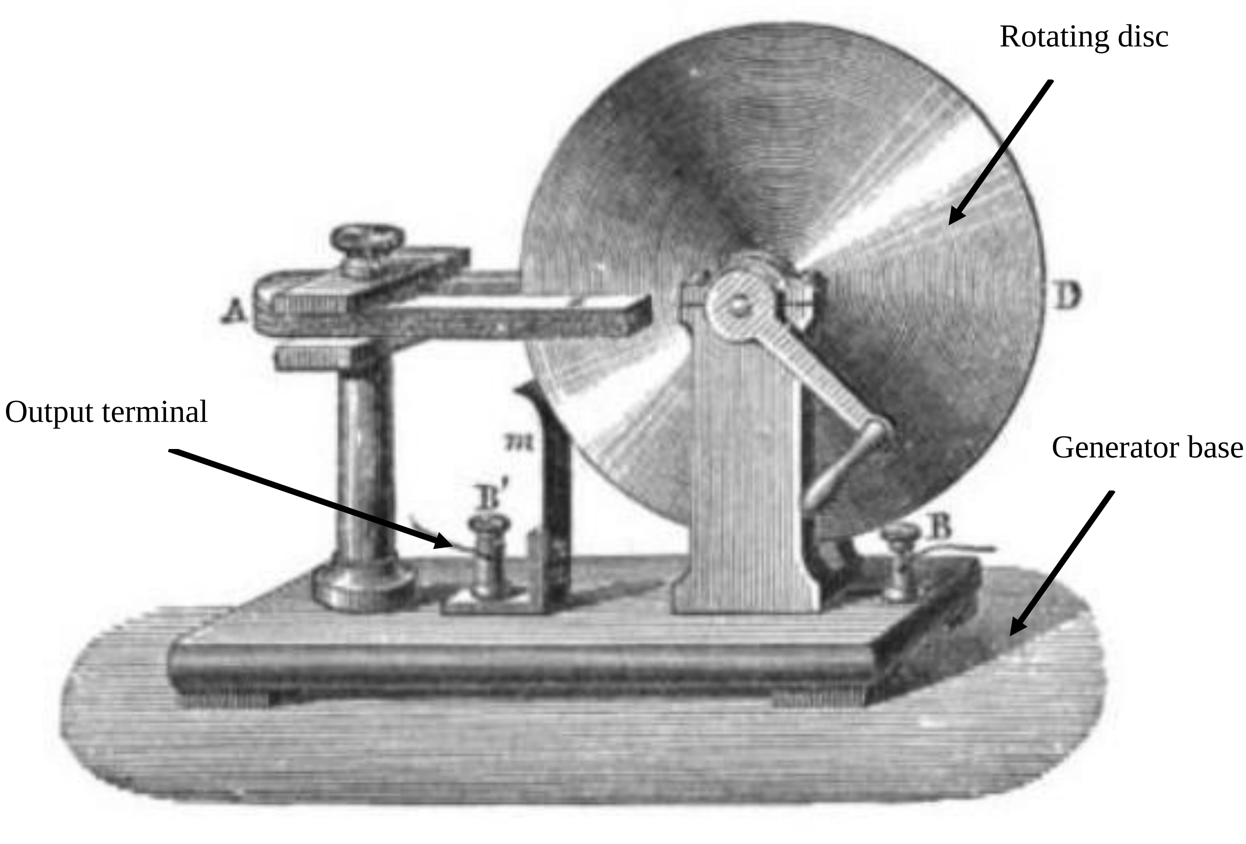

Figure 2-1: Disc generator built by Faraday in 1831 [16].

A machine that used the axial flux concept was patented by Tesla in 1889, as shown in Figure 2-2 [17]. The upper picture shows the frame holding the machine disc, whereas the two lower pictures shows the side view and cross-sectional view of the machine.

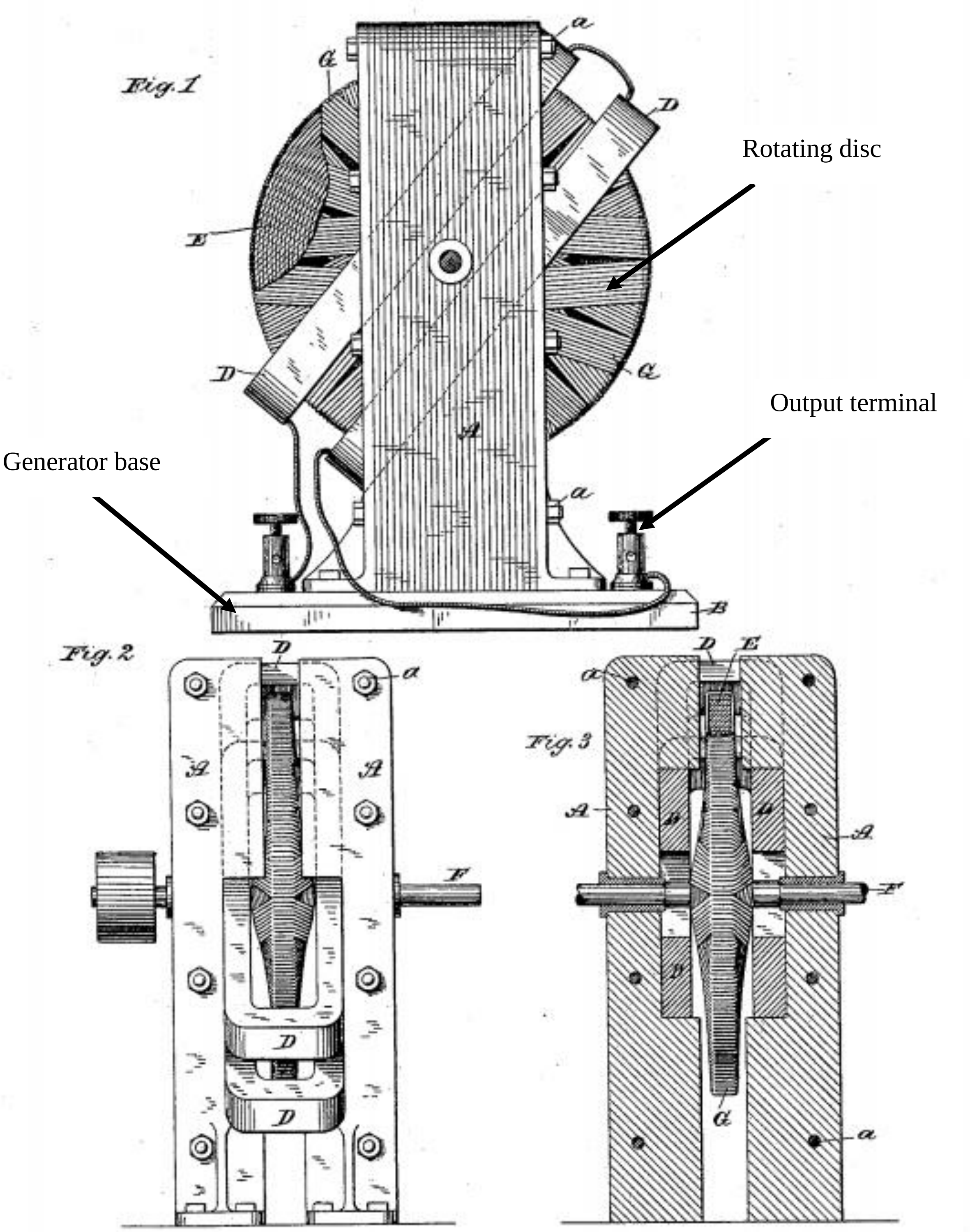

Figure 2-2: Electromagnetic machine with a disc rotor built by Tesla [17]

Torque in the machine is produce due to the angular displacement of the magnetised movable parts by the same currents with respect to one another. Instead of being the result in the difference in the magnetic poles or attractive parts to whatever due, however the best means to achieve these results was related to the armature and field laminations of the magnetic core for the significant magnetic attractions. AFM become dormant after the first radial flux machine was patented in 1937 [18].

Some of the reasons for the displacement of axial flux machines by radial flux machines were the large force of attraction between the stator and rotor, high cost of production and balancing the stator disc and rotor disc together with manufacturing difficulties.

Notwithstanding, of recent years interest in axial flux machines has grown due to the advent of rare earth permanent magnets and invention of new materials such as SMC and technology in manufacturing, hence, the rise for this machine in new applications.

2.3 Comparison of AFM and RFM

The magnetic flux path in an AFM is different from that of the radial flux machine (RFM). In RFM the flux travels radially from the rotor and the stator through the airgap which result in longer flux path and the flux must make a bend that must follow a two-dimensional (2D) path. But, in this machine the flux travels parallel to the axle of the machine and his type of rotor is often referred to as a pancake rotor and can be made much thinner and lighter than other types [19].

The magnets are usually located further away from the central axis, which results in a larger lever on the central axis and for a double rotors configuration, its result in a large surface area in relation to the size of the machine. Figure 2-3 presented a typical representation of AFM and it shows the direction of rotation together with the force and flux density. The inner and outer radius was also shown in the diagram.

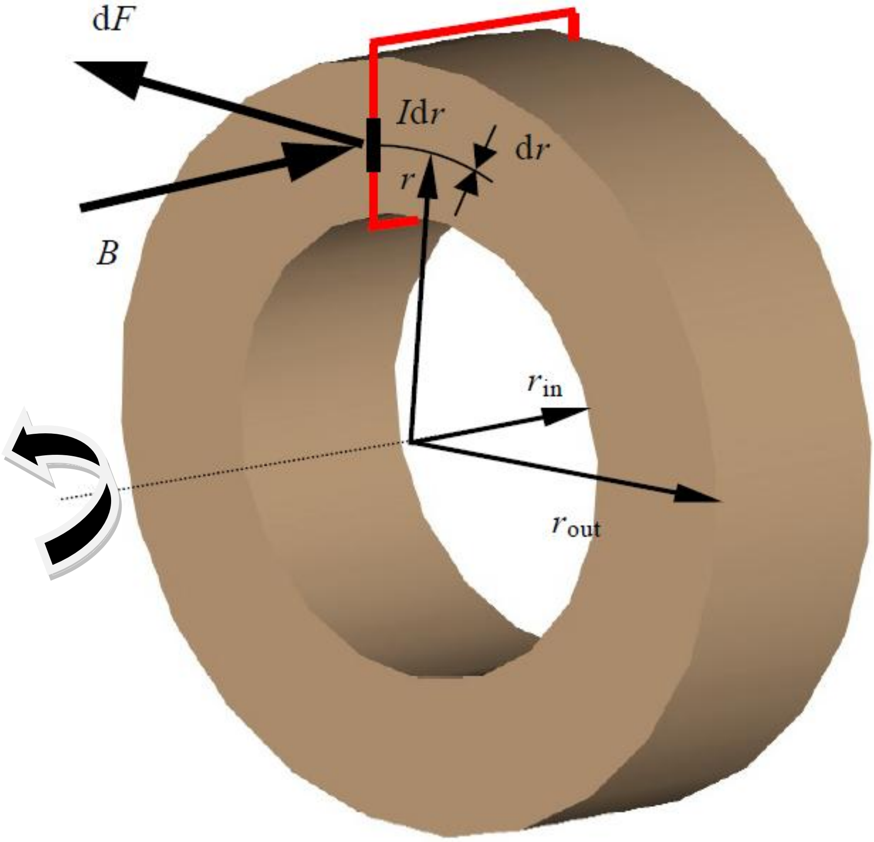

Figure 2-3: Typical representation of AFM

Figure 2-4 shows the axial flux machine in which the torque, T is given by equation (2.1), whereas Figure 2-5 shows the radial flux machine and torque, T is given by equation (2.2).

$$T = K_{af}{D_o}^3 \tag{2.1}$$

$$T = K_{rf}{D_o}^2 L \tag{2.2}$$

where D_o is the outer diameter, L is the length, K_{af} and K_{rf} are axial and radial constants based on the machine dimension.

It can be seen from equation (2.1) that the torque of axial flux machine is proportional to the cube of outer diameter D_o, while it is proportional to the square of outer diameter D_o in the case of radial flux machine as in equation (2.2), which means that the larger the diameter the bigger the torque produce by the machine. The strong axial magnetic forces between the stator and rotor, positioning of the stator, rotor, winding and fabrication difficulties are some of the initial challenges of axial flux machine design as reported in [17].

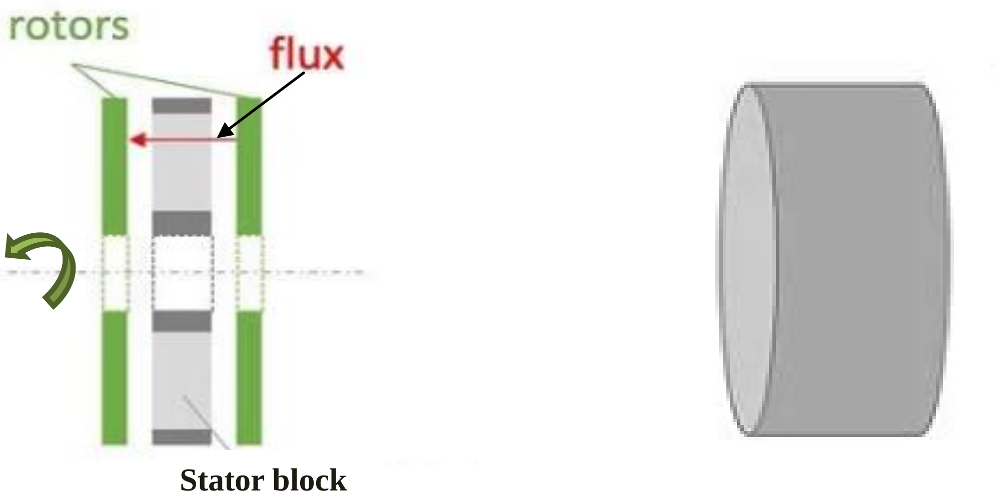

Figure 2-4: Axial Flux Machine

In the electromagnetic perception, AFM has an inherently more efficient topology as compared to RFM. The flux path is shorter, from the first magnet through one core-back to the other magnet. About 50% of the RFM winding is not active, that is the part located outside the stator teeth which is called coil overhang or end winding and results to additional electrical resistance and more heat dissipation. This type of winding is called distributed and results in much worse power to weight ratio compared to AFM which have no coil overhang or end winding when concentrated windings are used where almost 100% of the winding is fully active.

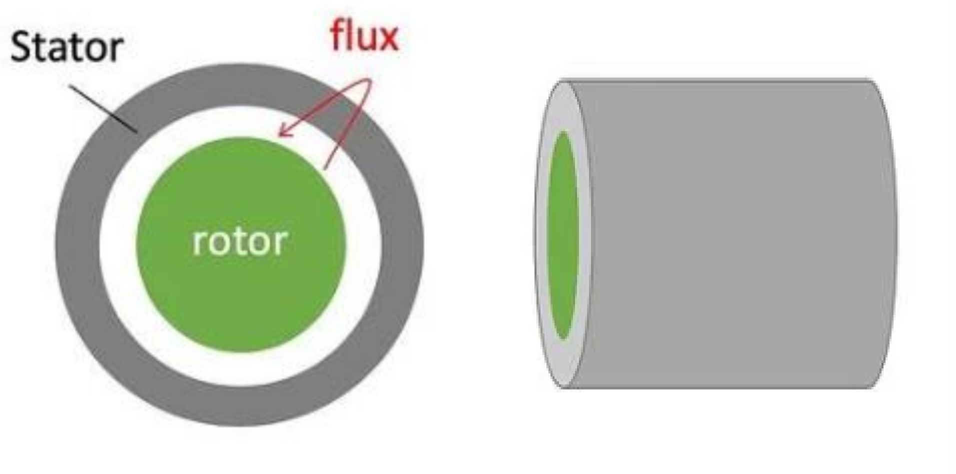

Figure 2-5: Radial Flux Machine

In RFM, heat has to be conveyed through the stator to the outside of the machine. But steel is not a very good heat conductor however the coil overhang or end winding is very difficult to cool, because it has no direct contact with machine casing.

In AFM especially when aluminium casing was used, heat transfer is excellent because the core is directly in contact with the outside casing and aluminium is a very good conductor of heat.

In [20] a comparison between an inside rotor RFM and three different AFM was reported. Their work was based on the sizing equations and the electromagnetic torque, it is found that the AFM has a better performance by a factor of up to 2.4 depending on the type of AFM, however they have not discussed two rotor AFM also known as TORUS NS type. Similarly, a details comparison of double-sided AFM was discussed in [21].

A comparison between the RFM and four (4) different type of AFM were provided in [22] and the analysis were carried out at five power levels ranging from 0.25 kW to 10 kW at rated speed ranging from 1000 rpm to 2000 rpm. The comparison consisted of volume, weight, power loss and inertia. It is found that AFMs have high power density and less weight, the slotted AFM require less material than the RFM, but more magnet than RFM. However, the copper loss is much higher in slotless AFM than that of the slotted RFM.

From a simple thermal point of view, a comparison between AFM and RFM was reported in [23] and the machines were compared in terms of electromagnetic torque and torque density and several design for a range of aspect ratios were carried out and found that at large aspect ratio, the AFM showed a very high specific torque when compared to small aspect ratio.

A detailed study on comparing RFM and AFM together with introduced mechanical constraints was presented in [24] and the analysis has been based on the electric and magnetic loading in the machines and their conclusion in terms of cost were that with 8 poles the design have similar cost, as the poles increased above 8 AFM has lower cost compared to RFM.

Form the above comparison; it is clear that machine designers have demonstrated that at a high pole number together with free or constrained to large aspect ratio, AFM geometries should be earnestly considered.

The three-dimensional nature of the fluxes in AFM makes their construction perhaps very difficult, complex and impractical to some extent with steel lamination sheet. However, the introduction of SMC as core material of electrical machine overcome the limitation of steel lamination sheet and the problem will be solved, because they are isotropic in nature and have 3D flux path and low losses as compared to conventional steel lamination sheet at high frequency. But, they have a low permeability which requires more material and they can be compacted into finished shape which is very difficult to achieve using steel laminations sheet as stated in [25].

2.4 SMC in Electrical Machines

SMC application in electrical machines is not new and there is research effort in the recent years focusing on using SMC due to advancement in the production and its unique properties such as low iron loss and isotropic magnetic properties [26]. Electrical machines with steel laminated sheet core are inherently limited to 2D magnetic flux paths.

AFM fluxes are 3D in nature, designing them with steel lamination sheet is inefficient and complex, although earlier designs used lamination due to lack of other material technology availability. SMC provide the answer to steel lamination sheet limitation and have a reasonable iron loss compared to steel.

The Electrical Power Group at Newcastle University has used SMC in the development of electrical machine using iron powder with refined coating technology from Höganäs AB of Sweden. At the beginning a simple machine was constructed and tested, it compared well with the identical steel laminated design. Furthermore, they extended it to more complex machine that were impossible to be designed using steel lamination sheet as reported in [2].

Similarly, another student developed a modulated pole machine topology exploiting mutual flux paths with SMC for high torque and low speed electric bicycle application [27], this machine exhibits high cogging torque and back EMF harmonic which causes vibrations, however work has also been presented on minimising these effect to enhance the performance as reported in [28].

Some of the research work done on utilising SMC in machine design includes; Transverse field machines with 3D SMC core structures for direct drive application in which high torque and low speed is required and is shown in Figure 2-6. The figure illustrates the magnetically relevant parts of the prototype machine with an SMC stator core. This machine consists of 6 SMC stator and 3 circular coils which offers a potentially reduced manufacturing cost compared to the conventional steel laminated stator motors with distributed windings [29].

The analysis of the machine investigates the benefit of SMC in the design and making small motors with complex geometries and the performance of the machine was reported at 640 W and 1800 rpm.

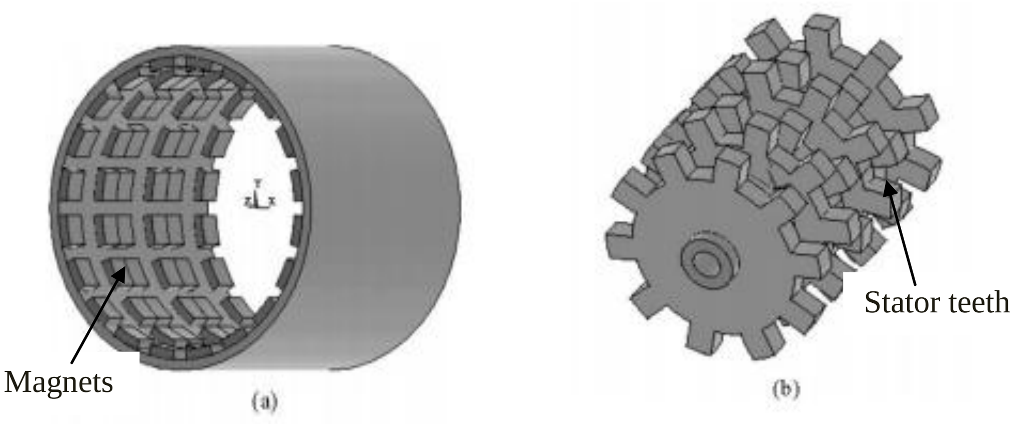

Figure 2-6: Magnetically relevant parts of TFM (a) rotor and (b) stator [29]

Application for linear motion is shown in Figure 2-7 [30]. The authors investigated the influence of three different SMC materials on the performance of a tubular permanent magnet machine to compares the relative advantages of steel lamination sheet and SMC. The prototype machine is equipped with a modular stator winding and employs a quasi-Halbach magnetized moving-magnet armature.

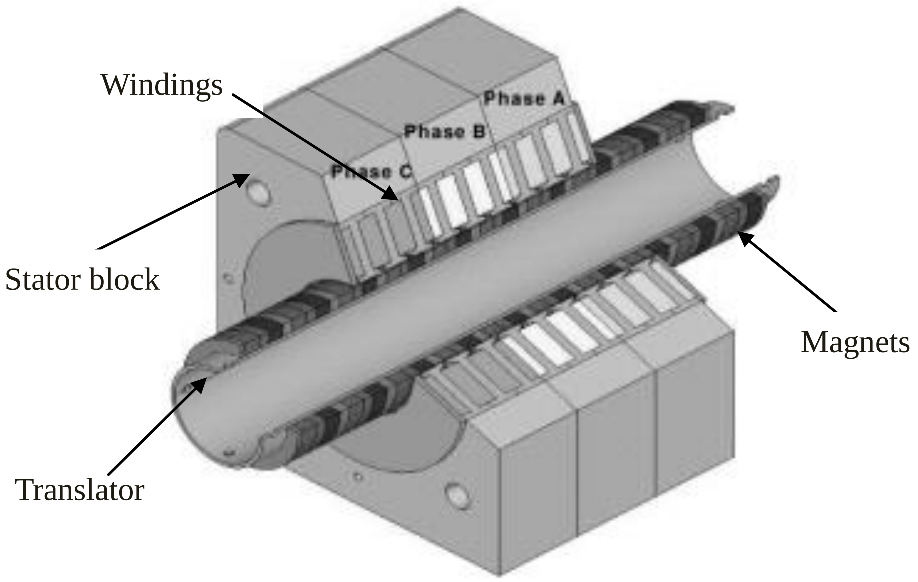

Figure 2-7: Schematic of 9/10 slot/pole tubular modular PM machine [30].

It has been shown that, despite its poorer space utilization, a machine whose stator is fabricated from steel laminations has the highest force capability, efficiency and power factor. A machine with a SMC stator, on the other hand, has potential advantages in terms of ease of manufacture and lower cost. [30].

SMC teeth in conventional flux machines were presented in [31] to evaluate the performance of the machine. The machine characteristics, such as iron loss was measured with the SMC as teeth in the machine and found to have a comparable iron loss and efficiency as low-grade magnetic steel lamination sheet such as M300-35A and M470-50A.

SMC material was used in the design of a low speed wind generator AFM for high torque density applications as stated in [32]. The machine is double-sided with slotted, it was built and tested to demonstrate the advantages of reduced size, weight and cost in the production. It is found that the combination of SMC and AFM can lead to new machine design with improved performance if accurate design measures are taken into consideration. The prototype machine is shown in Figure 2-8.

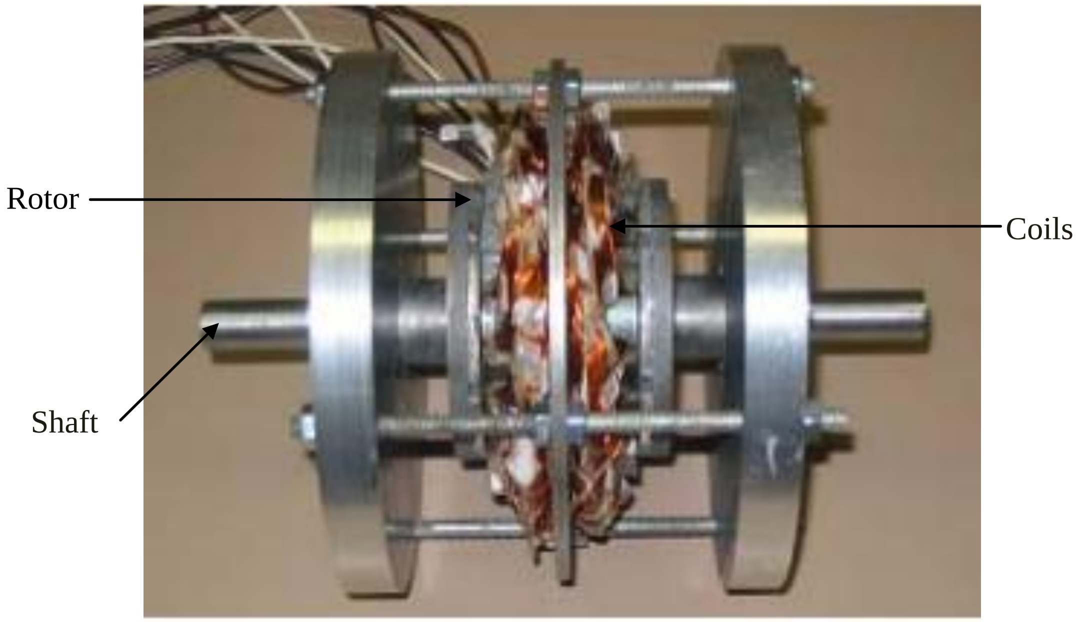

Figure 2-8: Complete assembled double-sided axial flux machine [32].

A comparative study of 3D flux machines with SMC was presented in [33]. The machines are claw pole and transverse flux machine and equivalent electric circuit was used to determine the machine performance and found that the transverse flux machine uses PMs and copper as twice as the claw pole machine and produces more output power at a given rotor speed.

Brushless DC motors for mass advantage in manufacturing for use in automobile application using SMC was presented in [34] it also shows the benefit of having better core shape and winding together with high fill factor.

A novel vertical machine using soft magnetic composites was presented in [35] as shown in Figure 2-9. This machine employs a very different structure when compared to conventional electrical machine.

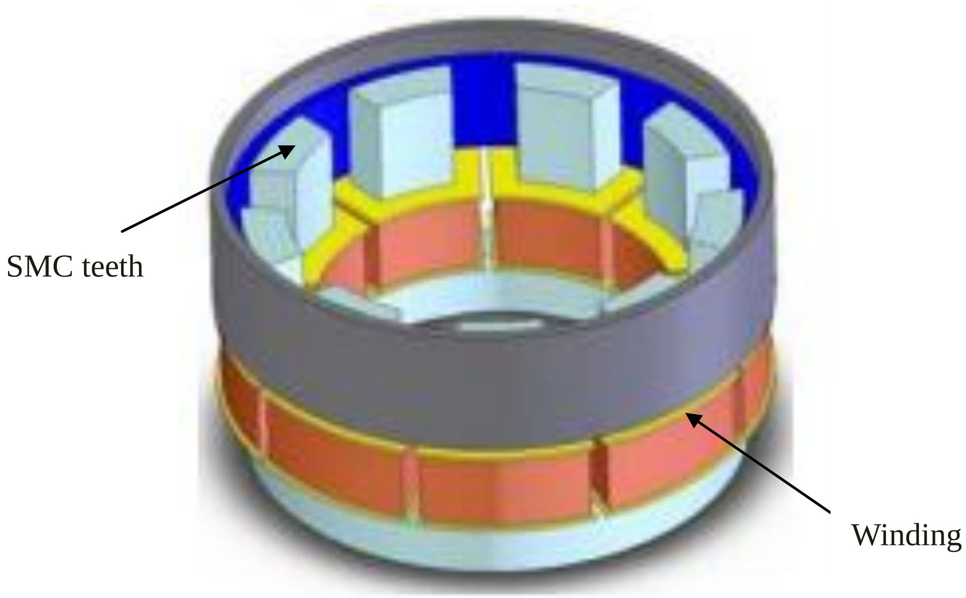

Figure 2-9: Typical vertical machine [35]

The stator of the machine has poles that do not point at the shaft of the machine, but they are parallel to the shaft so that they can interact radially with rotor and magnets. It is found that varying the airgaps and using different SMC materials in the machine results to several improvements including efficiency.

SMC material was used in the design of modular PM machines as presented in [36] furthermore PM Wind generator with SMC cores and performance evaluation was reported in [37] as shown in Figure 2-10. However, the effect of machining SMC was investigated and found that the iron particle regions are smeared on the machined surfaces.

This smeared iron was removed to reduce the eddy current losses using an acid treatment. This process resulted in lower back EMF and the benefits of using acid treatment appear to outweigh the adverse effects introduced by the process.

Figure 2-10: Acid treated stator core fully assembled machine [37].

A dynamic analysis of Reluctance switched motor using SMC was presented in [38]. The 2D model is as shown in Figure 2-11. It is a doubly salient and singly excited machine in which the stator accommodates the winding and the rotor is made of steel lamination sheets.

Three different materials namely: M19 steel, SMC 500 and SMC 1000 were used in the static magnetic analysis through FEA and found that machine with SMC offers reduced torque ripple and total weight in the machine.

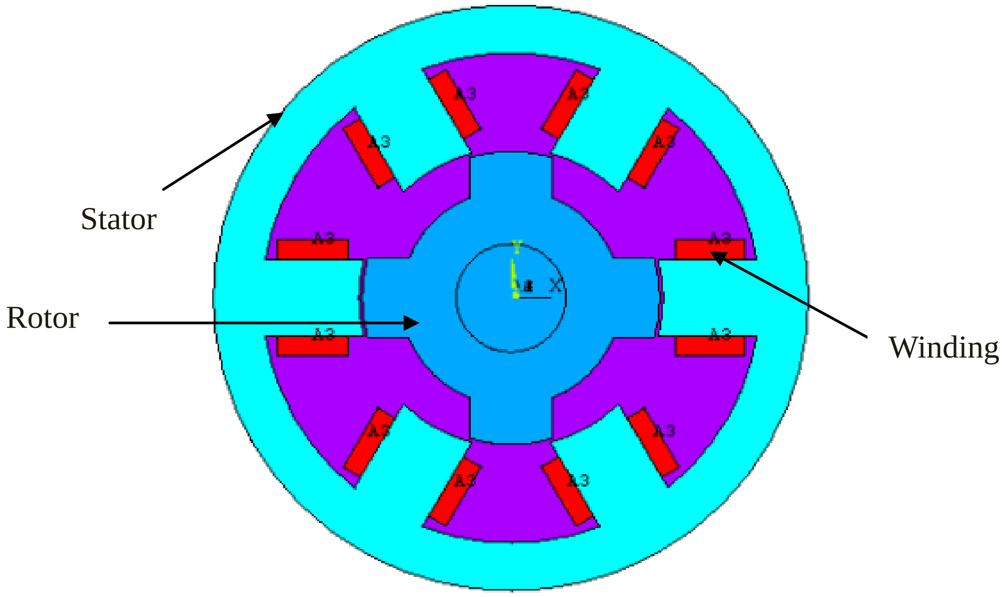

Figure 2-11: CAD model of 6/4, 3-phase SRM [38].

The benefits of using SMC in the design of high speed permanent magnet motor was discussed and reported in [39] and the 2D model of the machine is shown in Figure 2-12.

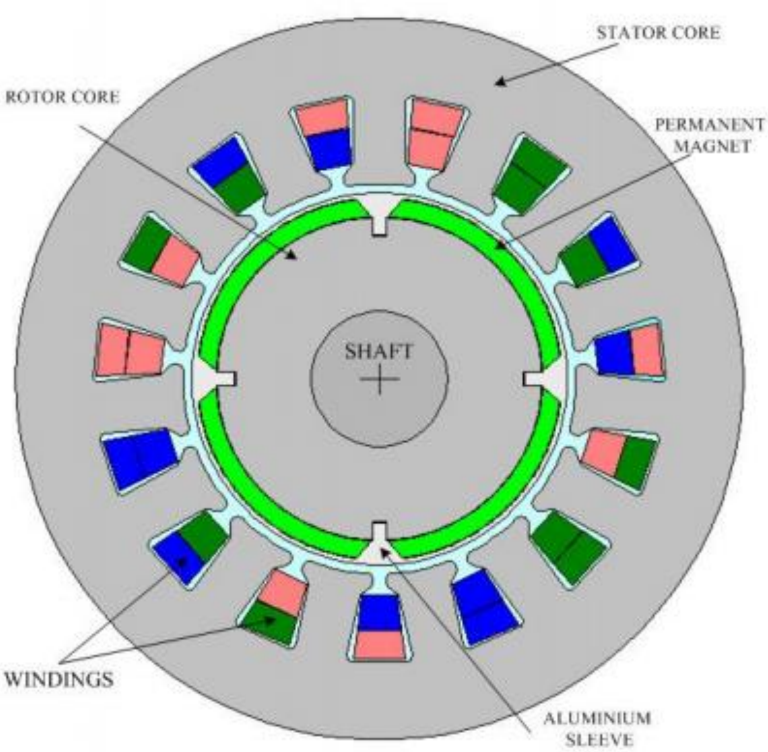

Figure 2-12: 2D view of high-speed PM machine [39].

The machine has 15 stator slots and 4 pole magnets, and the analysis was carried out using edge element method. It is found that at high speed the efficiency of the machine is high and concluded that this SMC material can be an alternative in the design of high-speed machines working at frequency above 400 Hz.

2.5 Typical Applications of AFM

AFM appear in extensive variety of applications where its geometric features are proposing some significant advantages over the conventional radial flux machines. Other alluring features of these machines are lowered losses, high power and high torque density, simple construction and above all high efficiency.

Typical area of applications of AFM includes: wind generator, elevator, mobile drill rigs, power generation, oil beam pumps and electric vehicle as reported in [40]. Application as direct motor in an electric bicycle with SMC has been describe in [41] [42], AFM machines are suitable for application in ship propulsion with two direct driven counter rotating propellers to eliminate the use of gearbox in traditional system as stated in [43]. This system which permits opposite rotation of the rotors is used to recover the loss energy due to the rotational flow of the main propeller.

Slotless AFM can be an appropriate direct drive machine to compute with the conventional induction machine in adjustable-speed pump applications as presented in [44] due to the light weight, high torque density and low cost manufacturing. It can also be use in applications where a very compact machine design is required as mention in [45] and compact wheel direct drive for electric vehicle as reported in [46].

AFM can be a perfect candidate in a flywheel energy storage device to decrease fuel consumption in hybrid electric vehicle as design in [47]. It can also be used in an application which includes: high speed power generation driven by a gas turbine in a hybrid traction system [48], storage devices and computer peripherals [49]. The improvement in AFM fabrication technique and the introduction of compacted insulated iron powder makes them a better candidate in low cost domestic direct drive application [17].

From the above discussion it is clear and interesting that AFM can be utilise in almost all area of electrical machine applications with advantages of high torque density and high power density, light weight, compact design and direct drive application.

2.6 State of the Art in AFM

AFMs are being designed and built for many applications due to their attractive features such as compact design. They can be designed to have a higher power density which can result in less core material. Moreover, the airgaps in the machine can easily be adjusted due to the fact that they are having a surface without bends. The noise and vibration levels are less when compared to the conventional RFM. Also, the direction of the main airgap flux can be varied and many design topologies can be obtained. These benefits present the AFMs with certain advantages over conventional RFMs in various applications as mention in section 2.5 above.

This section reviews the recent progress in the design and analysis of AFM, particular attention would be given to the aspects of stator winding design, design and FEA modelling, evaluation of loss and thermal analysis, materials and manufacturing, torque and extended speed.

2.6.1 AFM Stator Winding

This sub-section discusses the stator winding design of AFM. Generally, the stator windings of any electrical machines can either be distributed or concentrated windings. In distributed windings coils span in more than one slot, while in concentrated windings coils are wound around a single tooth only. They can be wound around each tooth either single layer or double layer concentrated winding. Moreover, concentrated winding offer lower copper loss due to their shorter and compact end windings as reported in [50], simpler winding automation and greater magnetic and electrical isolation between phases, but generally has smaller winding factor and larger winding space harmonics when compared to distributed windings. The shorter end windings can result in shorter total length and lower manufacturing cost.

Concentrated winding permanent magnet machines have attracted strong interest due to their low cogging torque and copper loss, the design, analysis and performance evaluation of such machines was examined in [51] and [52].

The slotted stator AFM is well suited for concentrated windings as demonstrated in [52]. Notwithstanding, eddy current losses in the rotor core-back and surface mounted permanent magnet for concentrated winding designs can be very significant due to sub-harmonics from the slot winding [53], which can significantly reduce the efficiency. The stator windings of AFM can either be connected in parallel or in series.

To avoid the circulating currents, the series connection is generally preferred. A parallel connection allows the machines to operate continuously even if one of the stator winding is disconnected [32]. In this thesis concentrated windings and series connection were used to achieve a high fill factor in the slot and lower copper losses.

2.6.2 Design and FEA Modelling

At the initial stage, analytical electromagnetic models are used in the design, in which quick results are required and for a detailed analysis a fraction of the machine is modelled and analysed using 3D FEA to reduce the simulation time.

Recent development in compacted insulated iron powder and the use of concentrated winding has made AFM the subject of discussion among machine designers due to decreased core losses at high frequency and ease of fabrication for mass production.

In general, AFM design uses the sizing equation, which the standard approach as reported in [54] gives two types of sizing equations; the classical equation and the electromagnetic torque to the principal geometrical, electrical and magnetic parameters of an AFM. In [55] the classical equation for mechanical power was adapted for motor and apparent power [56] for generator.

The standard form of the classical equation in terms of mechanical power is given by equation (2.3) below as reported in [6]:

$$P_m = C_m f {D_o}^2 L_e \tag{2.3}$$

where C_m is the mechanical constant and is mostly expressed as shown in equation (2.4), which however takes into consideration the ability of utilising wound excitation.

$$C_m = \frac{1}{1+K_\phi}\frac{m}{m_1}\frac{\pi}{2}K_e K_i K_L K_p \eta B_g A_{avg}\frac{1}{p}(1-\lambda^2)\frac{1+\lambda}{2} \tag{2.4}$$

Equation (2.3) above is mostly utilised when dealing with power density of the machine and is obtained by either dividing it by the total volume of the machine in W/m^3 or by using the total mass of the active parts of the machine in W/kg.

The most general expression of electromagnetic torque equation which relates to the principal geometrical, electrical and magnetic parameters as mention in [6] is given as:

$$T_{em} = \frac{\pi}{4}B_{ave}A_{in}K_d\lambda(1-\lambda^2)D_0^3 \tag{2.5}$$

This equation (2.5) has been implemented in the design of electrical machines by different electrical research engineer across the globe for several years. To obtain the magnetic shear stress of a machine, equation (2.5) can be used together with the total active rotor surface similarly torque density in a machine can be derived by dividing the equation with the total weight of the active component of the machine.

In [57] an analytical function by 3D FEA to account for the curvature effect was derived, in which the model used 2D analytical solution of the magnetic field and later expanded it to 3D problem based on effective radial dependence modelling of the magnetic field. The projected analytical computation of magnetic field was found to agree with the experimental measured values in the case of a prototype machine with rated power of 22 W moreover the cogging torque of the axial flux machine has been studied.

Similarly, an analytical technique for calculating the magnetic field distribution of a single-sided, axial flux PM synchronous generator without armature core has been presented in [58]. The analysis used a Fourier series method to solve the Laplace's equation in terms of scalar magnetic potential and the model proved to be efficient computationally, which determined the airgap and magnet field components accurately. FEA was used to confirm the validity of the technique as well as experimental results. This technique can be used in optimal design procedure for the given type of axial flux generator.

An analytical algorithm model to calculate the magnetic field in the airgap of a surface mounted slotted AFM using quasi-3D was presented in [59] which results in shorter the computation time compared to FEA models. The model offers a sufficiently accurate result and to improve the correctness of the model, they proposed a thermal lumped-parameter model.

A proposed 3D analytical model that can take both curvature and edge effect into account was given in [60]. Since the AFM airgap magnetic field density depends on the radial coordinate a corrector factor can be utilise to account for the flux density near the inner and outer radii of the machine. This simple factor of correction improved the formulas accuracy of the output properties derived based on 2D.

2.6.3 Evaluation of Loss and Thermal Analysis

This sub-section presents the literature review on the evaluation of loss and thermal analysis carried out on AFM. Losses and temperature have played a vital role on efficiency of a machine hence there is a need to look at the previous research work on these problems. One of the main issues machine designers faced in designing electrical machines is induced eddy current which has a major impact on the overall performance of a machine.

This problem sometimes often identifies as an open-slot stator winding configuration which supports winding loss elevation from the permanent magnet rotor assembly, as well as the skin effect if a single current-carrying conductor or proximity effect if many current-carrying conductors.

In a multi-layer conductor, the skin effect is the tendency of a high frequency alternating current to flow through only the outer layer of a conductor such that the current density near the conductor surface is largest and decreases with greater depths in the conductor. But when the current density of a conductor is caused by the nearby current-carrying conductor the effect is proximity. Both effects result in a non-uniform current density distribution in a conductor.

An analytical computation of the eddy currents for a define number of stranded conductors in a slot together with strands phase relation was reported in [61]. It is found that the main causes of eddy current loss are the magnetic flux entering the slot next to the airgap and proposed that this loss can be reduced by magnetic wedges in the slot.

A method for obtaining the eddy current loss (proximity effect) in round conductor using squared field derivative was presented in [62]. This method can be used for both 2D and 3D field effects in multi-layer windings to calculate the total AC winding loss in a machine. The experimental results show that the method is very correct for round conductors.

Analytical techniques are mainly limited to obtaining the effect on a leakage flux. Besides it an additional eddy current loss can be produced by the main flux entering the slot from the airgap as stated in [61].

The invented of computers leads to introduction of different type of numerical techniques of eddy current calculation due to skin and proximity effects. In [63] a method of determining the skin effect in single and multiple conductors was reported. It used the current density distribution within the conductor to calculate the losses and other electrical parameters.

A technique for computing induced eddy current losses in the stator of round rotor generator based on the airgap flux density waveform was presented in [64]. The experimental results verify that this technique has proved to be a cost-effective design tool.

In [65] a common formulation to accommodate the issue of eddy current diffusion using 2D FEA was presented. The method used three bus bars conductors and is based on conventional circuit analysis which takes into consideration the external circuit connections between conductors.

A cost-effective frequency-domain and time-domain homogenisation methods to examine the skin and proximity effects on multilayer conductors using 2D FEA was utilised in [66]. The authors considered several conductors shape in the analysis and found that in applications it has shown a clear advantage of using homogenisation techniques.

Temperature rise in the stator and rotor of an electrical machine with non-sinusoidal voltage was studied using a time step method to compute the current harmonics in [67]. The losses in the machine are incorporate into heat transfer equation to determine the temperature distribution. From the experimental results, it is found that the temperature was 5% higher due to harmonic current from the supply.

The electromagnetic and thermal design of a 28 poles single-sided machine utilising SMC stator core was performed using 3D FEA together with electromagnetic thermal and fluid-dynamical which offers an approach to magneto thermal analysis and experimental tests prove that the rotor is much hotter than expected as presented in [68]. It is found that the 3.5A rated current was compatible with that of the class of insulation used.

The loss distribution in a 24 slot and 20 pole single layer single-sided axial flux machine was investigated in [69] and found that difficulties encounter was addressed with machine fitted with non-overlapped windings. A lumped parameter model for thermal modelling of AFM was proposed in [70], this model takes account of both conduction and convention heat transfer and results in potential for simple flow pattern.

A comparison between experimental and computational fluid dynamic results in air-cooled AFM was performed using 3D models in [71], in which the research work focus on the stator convective heat transfer and found that losses in stator is lower than losses in rotor.

Form the above literatures; it is clear that the issue of eddy current loss in machines is extremely paramount. In open-slot AFM there is a need for reducing these effects in other to improve its performance.

2.6.4 Torque and Speed

Cogging torque and torque ripple are the main components of pulsating torque in electrical machine and to improve the performance of a machine there is a need to maintain a certain level of these two elements.

A method for multistage AFM for cogging torque reduction with careful selection of magnet pole arcs was proposed in [72]. The results show that this technique can effectively minimises the cogging torque without losing much on the peak torque and pulsation torque component. Double-sided machines with 6 poles were analysed based on pulsating torque in [73] in which magnet skewing, pie shaped winding, magnet pole arc ratio and non-slotted machine have great effect on pulsation torque component reduction.

Several methods for minimising cogging torque have been investigated and reviewed in [74] which show that the effect of skewing, open-slot, slot and pole combination, magnet pole arc to pole pitch ratio and utilizing the double-sided configuration are very effective tools for reducing the cogging torque in axial flux machine. But it is disadvantageous as the back EMF becomes more sinusoidal in waveform which may result in additional torque ripple in brushless DC machines.

Axial flux permanent magnet machine with 8 poles was investigated for cogging torque reduction in [75], in which the impact of magnet shape, stator side displacement to minimise cogging torque were investigated. The results show that magnet shape modification reduced cogging torque by 60% of the original value and finally the data from the analysis were used to produce a 5 kW machine.

In [76] 16 poles AFM starter/generators was presented to achieve wide constant power speed range using technique for flux linkage regulation by displacing the rotors of the machine using a constant voltage and current sources and the results show that the devices have no effect on the torque density and overload capacity of the machine.

Furthermore, in [77] the method of stator shifting was explored using a mechanically flux weakening device and much higher constant power speed range was achieved, this method allows a simplification of the circuitry downstream from the alternator. The only side effect of this method was shift in the stator by electrical actuator used. That is to say mechanical complexity verses electrical complexity.

2.6.5 Materials and Manufacturing

The material commonly used in the design and construction of axial flux machine are the steel lamination sheet and SMC. The former is limited to 2D flux path, while the later has advantages of 3D flux path which take into account the nature of AFM.

The design and construction of a 12 poles AFM with SMC teeth was reported in [25] and resolved the difficulties related to punching in steel lamination sheet and windings in the stator. However, it fixes the issues of stability in mechanical design and offers a high fill factor which increased the overall performance of the machine. The combination of SMC and steel lamination sheet can be applied to other types of machine due to the severe lacking magnetisation given by machines build with SMC only.

A cost effective AFM with SMC/steel lamination sheet core and 14 poles was presented in [78], higher efficiency was obtained in the machine and smear of iron particles was removed on the SMC surface by the means of a chemical process using phosphoric acid solution. A yokeless and segmented armature topology motor with SMC and has 10 poles was designed in [79] and found that the machines have higher torque density of 20% compared with other motors and the iron loss in the stator decreased by 50% and peak efficiency of 96% .

The adoption of SMC wedges to obtain semi-closed and closed slots was investigated in [6], however, an AFM with 10 poles for direct drive application was design and constructed in [80] in which segmented armature torus topology was used and an efficient approximation method was introduced to overcome complexity in the analytical model.

In [81] an efficient improvement technique of AFM for generator applications with concentrated pole windings was examined, in which mass can be decreased with only a small reduction in efficiency. Similarly, the design of a small wind energy generator and performance comparison of the proposed structure with a trapezoidal teeth structure was carried out in [82]. A method of core losses was presented and found that copper losses were most influential and the results shows that the efficiency of the machine was 80%.

A closed-form expression for axial force and optimal torque path of single-sided axial flux machine was derived in [83] together with voltage and current limitation moreover from the analysis field-oriented control can be achieved using operation guidance.

The design of a single-sided AFM with non-overlap concentrated windings for in-wheel traction hub motor drive was optimise using 3D FEA in [84] which results in volume and mass reduction by 35%, is thus a good candidates for in-wheel traction application and has the torque ripple reduction of value 3.3% peak to peak. In addition, the winding issue like length and end of winding were investigated in [85] which lead to better torque performance in non-overlap concentrated windings as compared to the normal overlap windings, less copper mass of almost 15% and less harmonics in the induced voltage waveform.

A new AFM configuration which combines PM and wound coil excitation that can be used for small scale engine driven generator was presented in [86], in which lumped-parameter magnetic equivalent circuit model was used in the machine design. Furthermore, an analytical expression to calculate the structural mass of AFM from both FEA model and data from already existing low speed AFM was derived in [87]. The results show that 60% of the machine total mass was inactive at small scale and 90% at megawatts rating and proposed a multistage design to reduce the mass.

2.7 Soft Magnetic Composite

Steel lamination sheet was early used in the manufacturing of AFM to offer flux linkage to the winding of the machine as stated in [88] however the development of SMC and the 3D design techniques overcome the limitations when using steel lamination sheet. Many impossible and complex shape that cannot be make using lamination punching can now be made using SMC which makes AFM design more efficient, reliable and cost effective.

Internationally, the name Soft Magnetic Composites (SMC) was accepted for pressed and heat-treated metal powder components with 3D magnetic properties. Somaloy is a Höganäs trade name for SMC powders with unique 3D flux properties. They materials are developed for constructing electrical machine component to provide high performance and low losses. They can be used for a cost-effective and efficient volume production. In general, Somaloy can be utilised to provide a compact design with reduction in size and weight that requires less need of machining and low scrap volume.

SMC materials are produced from high purity and compressible iron powders, in which the bonded particles are coated with an organic material, producing high electrical resistivity. The coated powder is then pressed into a die to form a solid magnetic core and finally heat-treated to anneal and cure the bond [89]. Figure 2-13 shows a schematic diagram of the component elements of a powder core [90].

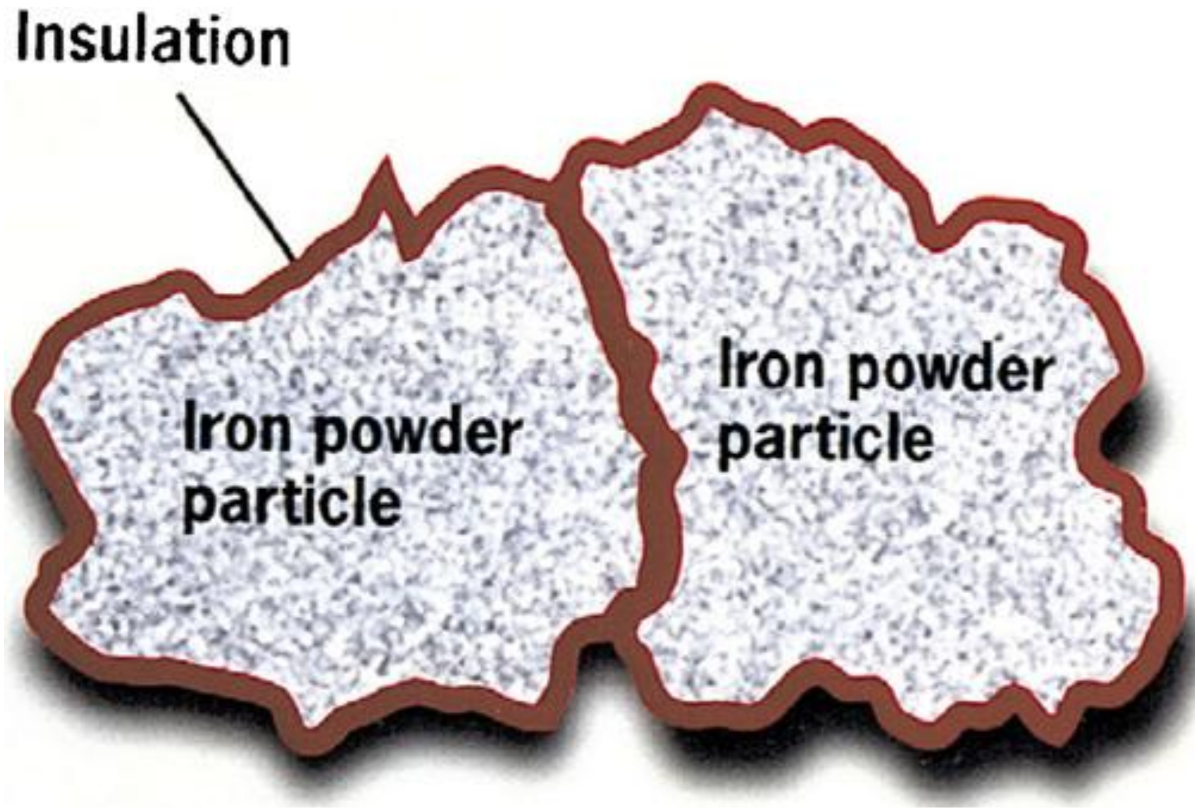

Figure 2-13: Schematic diagram of the component elements of a powder core [90]

A typical iron powder particle has a size of 100 μm and coating thickness of less than 1 μm. The mechanical and electrical properties of SMC are based on the mixture of powder used. Each final component product is based on the mixture for specific requirement needed.

The magnetic properties of each product are attained based on the type of wax containing. Typically, Kenolube is used. On the other hand, the mechanical strength is achieved using a polymer binder.

Typically, properties of SMC as stated in [90] are given as:

1. Somaloy 500+0.5% Kenolube 800 MPa at 500ºC have saturation magnetic flux density of 1.45 T at 5000 A/m and 500Hz.
2. Solid stacking factor.
3. Unsaturated relative permeability of 500.
4. Electric resistivity of 10,000 μΩcm.
5. 7 W/kg specific core losses at 50 Hz and 1 T.
6. 3D magnetic flux paths.

A completed typical data for Somaloy prototyping base material is presented in Appendix C, which included the standard mechanical properties up to 150^{o}C, standard physical and magnetic properties, available blanks size and magnetizing curve for data adjusted for use in Finite Element modeling which is also represented by the B-H curve, the B is the density of the flux and H is the magnetic field strength applied. In this case only the positive side of the B-H curve is used.

The data sheet also provides the core loss of different value of B from 0.5 T to 1.5 T at interval of 0.5 T from 50 Hz up to 2000 Hz based on the measurement according to CEI/IEC 60404-6:2003 on ring sample. Furthermore, it presented the loss model, which is verified up to 1.5 T and 5000 Hz. This model included the hysteresis loss coefficient, in particle eddy current coefficient, smallest cross section of the component in mm, frequency in Hz, Magnetic field strength in Tesla, density and resistivity.

Recently for cost-effective and high-volume manufacturing, Somaloy is well cut by the use of Powder Metallurgy (PM) method. This technique has the advantage of producing a complex net-shape component from and almost waste-less metal powder that reduce the need for future operation. Moreover, to practically attain a best density and efficient rate of production these components made of Somaloy are formed into net-shape at large compaction pressures using a special toolset before heat treatment to improve the performance especially the magnetic property.

The final stage in the process is assembling the individual components for application in magnetic circuit which results in easy manufacturing, assembly and cost-effective when compared to other adjacent components in the same area application. Figure 2-14 presented the three steps used in the compaction process as reported in [91].

The main merits of Somaloy and the SMC technology is in the design of complex machine shape and for high volume production that is complete manufacturing process which come face to face with future demands on efficiency, cost, performance and recyclability. This technology has the potential to unlock a global possibility due to their unique properties offering new solution for electromagnetic applications.

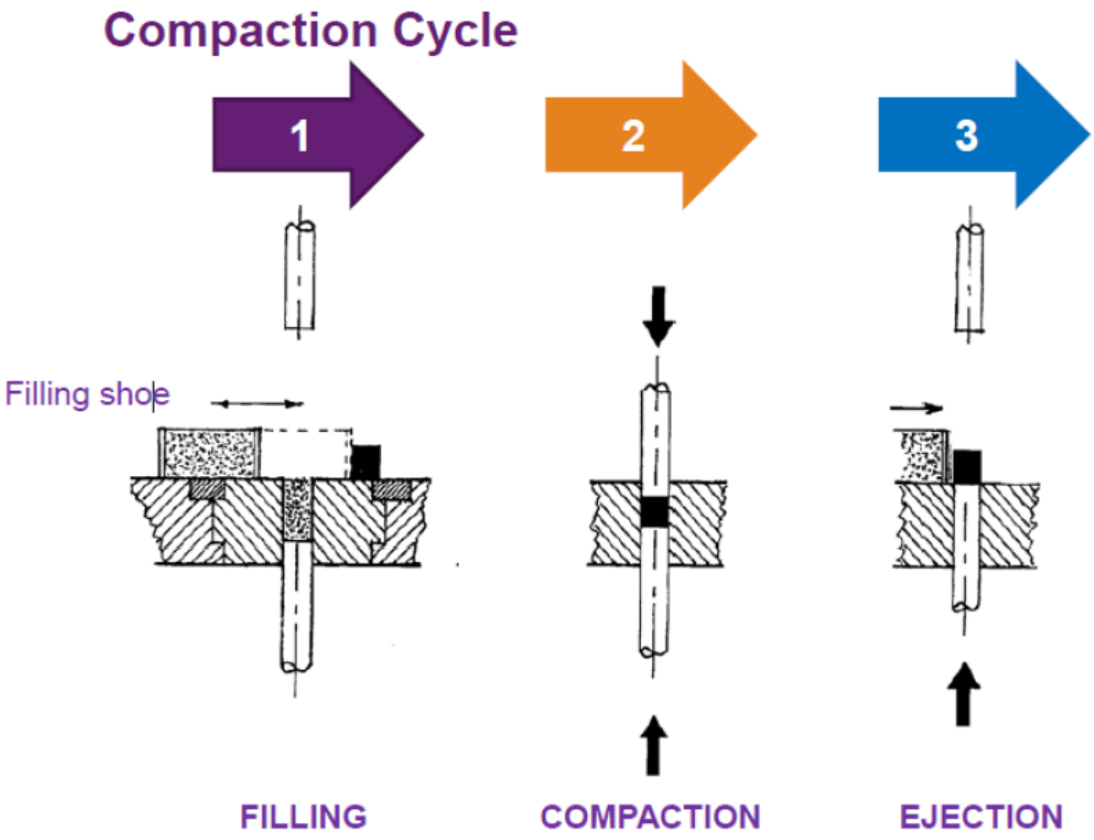

Figure 2-14: The three steps involved in compacting the powder [91]

To obtain a better finished product without losing much of its properties, is to machine the component from the prototype fabricated blank using a traditional machining technique which includes turning, drilling and milling. However, non-conventional machining method such as Electro Discharge Machining (EDM) should be steer clear of due to decaying in the material. Moreover, to be successful with SMC in designing electrical machine components the following five steps need to be taken:

1. The first step involves machining for the design for manufacturing and prototype material.
2. Initial testing of the prototype produced.
3. Evaluating the design component and performance of the material by carry out measurements.
4. Using the available data from the previous evaluation to simulate the final properties of the compacted component.
5. Finally, confirmation and production of compacted component.

These composite materials have several advantages over traditional steel laminated sheet cores in most applications, which the unique features are 3D isotropic ferromagnetic behavior, very low eddy current loss and high electrical resistivity due to insulation between the individual iron particles, relatively low total core loss at medium and high frequencies, possibilities for improved thermal characteristics, flexible machine design and assembly and a prospect for greatly reduced weight, environmentally friendly manufacturing and production costs as reported in [92].

A comparison of magnetization curves of a steel laminated material and an SMC is given in Figure 2-15 [93]. It consist both the linear and saturation characteristic region and from the graph it can be seen that, the permeability of the SMC is much lower compared to that of steel lamination sheet. The porous microstructure of SMC and the resulting lower density of ferromagnetic element iron are some of the reason for lower permeability of SMC.

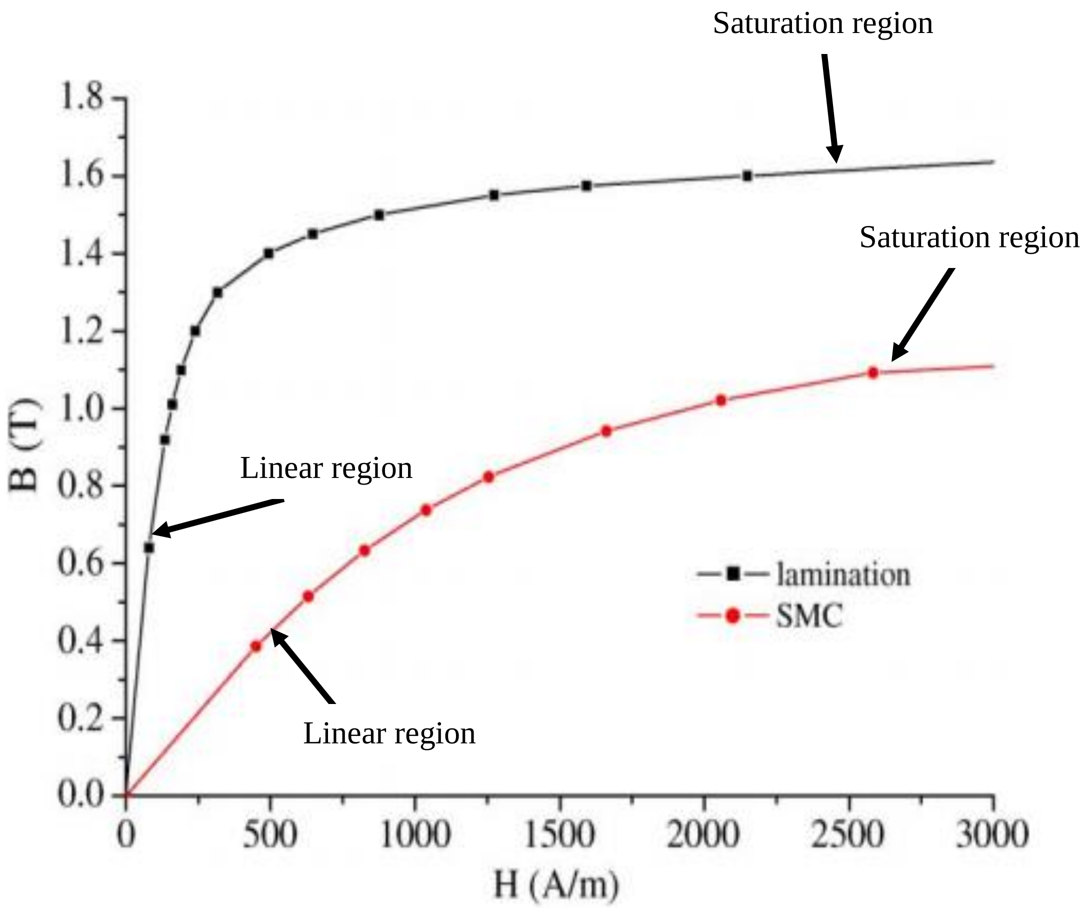

Figure 2-15: Magnetization curves of SMC and lamination steel [93].

2.8 Magnetic Shielding

It is well known that the slots of an electrical machine create disruption in the airgap magnetic field which at high speed generate more losses and reduce the overall performance. The used of magnetic wedges in the stator slots seems to effectively address these unwanted consequences. AFM are really important in almost applications and to make them cheaply they have open-slots. One of the drawbacks of open-slots stator winding configuration is elevation of losses in the machine especially at AC operation.

The techniques of using slot wedges have proved to be an efficient approach to reduce losses in high speed radial flux machines and to improve the performances, but they cannot be done cheaply using a single steel lamination sheet for all slots as in axial flux machines.

The quality of magnetic shielding is seriously affected by the properties of the material used which include permeability, conductivity and frequency. Research shows that the shielding effects of steel can be greatly changed by those properties together with the material dimension if it is implemented in an AC field.

As stated in [94] magnetic shielding is when a material with huge relative permeability such as silicon steel achieves shielding by diverting the stray magnetic flux reaching the machine coils. However a high electrical conductivity material such as copper will performs shielding by providing a medium for eddy currents, whose fields oppose the applied magnetic field as reported in [94], this is called electromagnetic shielding, although the shielding is important for the normal operation of electrical machines and to avoid the local heating. In this thesis only the magnetic shielding is considered as it is impractical to implement the electromagnetic shielding using copper.

In [95] the effects of stator slots wedges of different magnetic material on the behavior of an induction machine was studied. The analysis was carried out using 2D FEA to investigate the influence on the machine performance. It is found that the value of magnetic permeability of the material used as a slot wedges play a vital role on the performance of the machine which lead to increase in the starting torque and decrease in the starting current.

Similarly, a dynamic harmonics field analysis of a cage type induction motor when magnetic slot wedges are applied was investigated in [96] and found that stator slot ripple components of the flux density distribution in the airgap reduced successfully using slot wedge.

The impact of rotor slot wedges on stator currents and stator vibration of an induction machines using transient 2D FEA was carried out in [97]. The analysis was done on an open and closed rotor slots. The former increases the harmonic content in the airgap field and the stator currents, in addition there was increased in the stator vibration level for frequencies higher than 1 kHz. Reduction in the level of the permeance variations due to slot opening can be realised with the use of closed or semi-closed magnetic slot wedges.

The effects of slot closure and magnetic saturation on induction machine behaviour were performed using FEA as reported in [98] and found that the flux density and force waves generated by stator slotting have reduced significantly. In addition, it was discovered that the full load power factor has improved and decrease full load speed in the machine.

To mitigate the level of the harmonic magnetic field pulsation and to enhance the airgap magnetic field in high voltage open-slots machines, magnetic slot wedge should be place in the slot opening.

Investigation and analysis of the influence of magnetic wedges on high voltage motors performance was carried out in [99]. The analysis show that the use of magnetic slot wedge reduces the starting current and iron loss in the motors, but it decreases the locked torque and pull-out torque. The FEA and experimental results agree with the theoretical analysis, which provides a valuable reference for magnetic slot wedges for high voltage motors. Furthermore, 3D FEA was used to determine electromagnetic fields and forces on rotor slot wedges due to the presence negative sequence currents in large synchronous turbo generator as reported in [100].

The evaluation of switched reluctance motor with magnetic slot wedges was presented in [101] and the authors proposed a method to reduce the torque ripple and stator vibration which are inherently in traditional switched reluctance motor. Although, this method decreases the average torque, radial force and the torque ripple.

Magnetic wedges used in the open-slot design of electrical machine can be utilised in energy efficiency improvement of induction motors as reported in [102] and it is found that increase in energy savings and cost-effective operation together with efficiency are main interest of utilising magnetic wedges.

The impact of temperature on magnetic wedges in an induction motors were investigated as stated in [103], it is clear from the analysis that the used of magnetic wedges lower the temperature rise in totally enclosed motors which results an increase in the efficiency.

A soft ferrite magnetic wedges were implemented in squirrel cage induction machine to reduce the harmonic torques as reported in [104] and found that the 17^{th} and 19^{th} harmonics decreased as a result of wedges used but the use of skewed rotor increases the stray loss and leakage reactance as the 5^{th} harmonic remain high.

The influence of semi-magnetic stator wedges on the electromagnetic characteristics and the behaviour of an induction motor were investigated in [105]. The study was done using FEM analysis and found that the airgap space harmonic content decreased by 9% at nominal speed, but with lower output power, power factor and stator current. In general, the overall performance of the motor increased.

AC winding loss in an electrical machine can also be reducing by utilising Litz wire. This type of conductor is too expensive and have bad thermal behaviour and high resistance compared to solid conductor. In addition, it can be reduced by placing the conductors far from the airgap at the expense of much reduced fill factor in the machine.

Another method of AC winding loss reduction is using a shaped pole pieces, but this method can produce more eddy current reaction due to the delay in the portion of flux crossing the airgap however this method is not cost-effective and it also has the disadvantages of slightly smaller PM alignment torque and lower saliency ratio which reduced the reluctance torque in the case of interior permanent magnet machine as stated in [106].

From the above discussion, it shown that to reduce the AC winding loss in an electrical machine, a magnetic shielding using slot wedge has to be utilised. For cost-effective reduction of AC winding loss in an AFM due to an open-slot stator winding configuration, a magnetic slot wedge using single steel lamination sheet must be implemented. Moreover, this technique is easier to utilise in such machine topology.

2.9 Loss Mechanisms in Electrical Machines

2.9.1 Winding Loss

The total loss in any electrical machine is the summation of the resistive loss, core loss and windage loss. To obtain the resistive loss of an electrical machine, the winding resistance must be known. The resistance of a single coil in a slot either single layer or double layer as shown in Figure 2-16 can be calculated using the equation (2.6) as mention in [107].

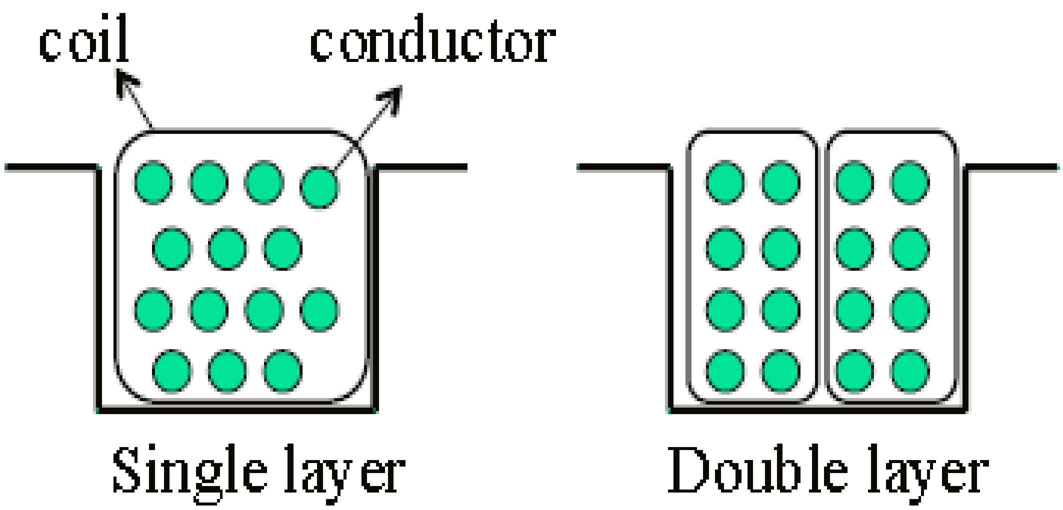

Figure 2-16: Conductors arrangement in slot.

$$R_{coil} = N_{coil} \frac{\rho L}{A_{con}} \tag{2.6}$$

where R_{coil} is the resistance of a coil, N_{coil} is the number of turns per coil, ρ is the resistivity of the conductor usually copper, A_{con} is the cross-sectional area of a single conductor in the coil and L is the length of a single conductor in the coil.

Winding resistance can also be calculated based on the effect of temperature of the conductor, for example if a resistance of a coil R_1 at a particular temperature T_1 (usually at room temperature 20˚C), then the resistance of a coil R_2 at temperature T_2 can be obtained by equation (2.7) below.

$$\frac{R_2}{R_1} = \frac{234.5+T_2}{234.5+T_1} \text{ [C]} \qquad (2.7)$$

It is clear from equation (2.7) that the resistance of an electrical machine winding should be calculated at working temperature. Moreover, the winding power loss of the machine conductors which is usually the main source of heat with in any electrical machine is temperature dependence and can be obtained using equation (2.8) as stated in [108].

$$\rho = \rho_0\big(1 + \alpha(T - T_0)\big) \qquad (2.8)$$

where, ρ_0 is the electrical resistivity of the conductor material at reference temperature $T_0 = 20^{\circ}C$, and α is the temperature coefficient of the electrical resistivity.

In an electrical machine under high speed operation there are additional copper losses. These losses increase significantly mainly because of two effects namely skin and proximity effect.

Skin effect is the tendency of an alternating electric current to become distributed within a conductor such that the current density is largest near the surface of the conductor, and decreases with greater depths in the conductor, while the proximity effect is the influence in one conductor on the current distribution in a nearby conductor with in slot in a machine which result in an increase in the effective resistance of the conductor and it become more under high frequency of operation, it can be reduced by using either Litz wire or transposed wire. A detail on these effects will be presented in Chapter 5.

2.9.2 Core Loss

Core loss in high speed electrical machines is very difficult to be evaluated due to higher excitation frequency, harmonics due to pulse width modulation and influence of machine geometry on the flux density distribution as stated in [109].

The conventional way for estimating the core loss is using the Steinmetz Equation with fixed coefficients and assuming the excitation is sinusoidal and equation (2.9) presented the conventional Steinmetz Equation.

$$P_c = P_h + P_e + P_{ex} = k_h f B^{\propto} + k_e f^2 B^2 + k_{ex} f^{1.5} B^{1.5} \qquad (2.9)$$

where k_h is the hysteresis loss coefficient, k_e is the eddy current loss coefficient, k_{ex} is the excess loss coefficient and $\propto$ is the Steinmetz coefficient.

These coefficients are usually obtained from the magnetic materials data sheet provided by manufacturers of magnetic materials and are fixed values. The conventional core loss method is imprecise for the majority of high speed electrical machine.

For more accurate core loss estimation an improved version of Steinmetz equation to include harmonic contents was presented in [110].

2.9.3 Windage Loss

In any electrical machine windage loss in the rotor becomes significant under high speed rotation, theoretical equation for windage loss calculation for a rotating cylinder with in a concentric cylinder as reported in [111] is given as:

$$P_w = \pi C_d \rho r^4 \omega^3 L \qquad (2.10)$$

where ρ is the density of the fluid in (kg/m^3), r is the radius of rotor in (m), ω is the angular velocity in (rad/s), L is the rotor length in (m) and C_d is the skin friction coefficient.

However, the skin friction coefficient C_d can be obtained using equation (2.11) as mention in [111].

$$\frac{1}{\sqrt{C_d}} = 2.04 + 1.768\, In\left(R_e\sqrt{C_d}\right) \qquad (2.11)$$

where R_e is the Reynolds number and is given by equation (2.12) as stated in [111].

$$R_e = \omega r \frac{\rho}{\mu} \varphi \qquad (2.12)$$

where μ is the dynamic viscosity of the cooling fluid used in the machine in (kg/ms) and φ is the length of the airgap in the machine in (m).

All these theoretical equation for windage loss evaluation exists, but with limited accuracy however it can also be calculated using computational fluid dynamic (CFD) if the machine do not have smooth rotor surface.

2.10 Topologies of AFM

As stated earlier, AFM is a machine in which the direction of flux is axial, or the flux flows axially in the direction parallel with the shaft of the machine. This section introduces the AFM topologies together with the pros and cons, particular attention will be given to single-sided, double rotor single stator, double stator single rotor and multi-stack topologies.

A general classification of AFM topologies as shown in Figure 2-17 [6] can be performed by using a tree diagram with five stage levels. The first stage is structure in which AFM are divided into four main structures: a single-sided machine which is single rotor single stator, double-sided machines which are divided into double stator single rotor and double rotor single stator, and multistage machines which are combination of one or more double-sided machines.

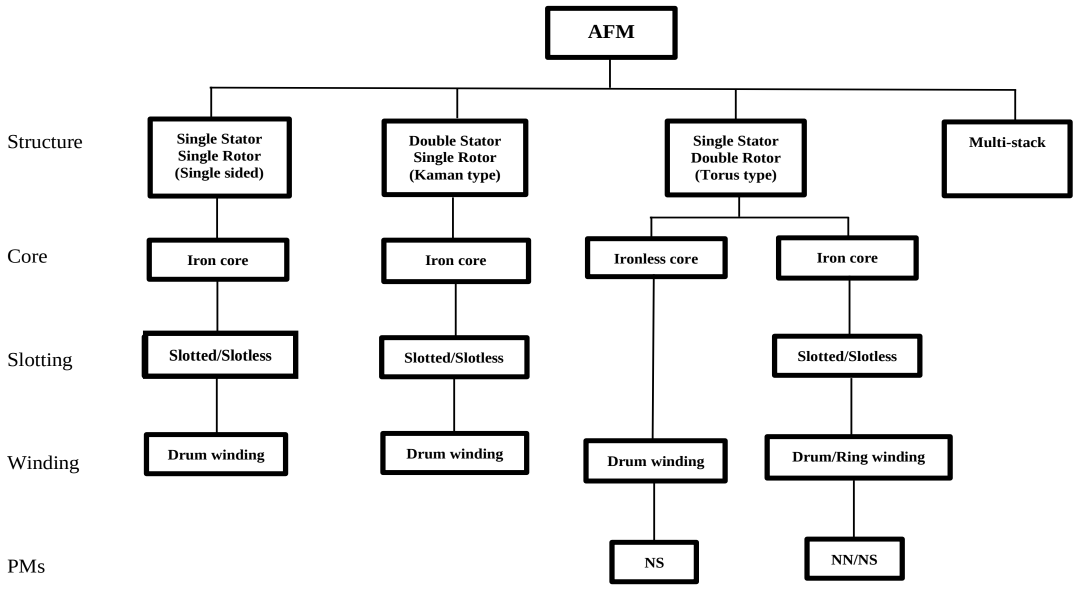

Figure 2-17: AFM topologies [6].

The flexibility in construction makes axial flux machines suitable for different applications. The second stage shows that the core can either be iron core or ironless core depends on the application. The third stage is slotting of core, which can be slotted or slotless. The fourth stage is winding of AFM which may be either drum winding (tooth wound) or ring winding (core wound); in some machine configurations it is possible to have a toroidal winding. In this case, the coils are wound in the stator, which results in a toroidal shape. The last stage is permanent magnet which the single stator double rotor AFM can either be North-North (NN) or North-South (NS).

2.10.1 Single-Sided

A single-sided AFM consists of a single stator and a single rotor. The stator core may be either slotted with drum tooth-wound winding or slotless with drum winding. Figure 2-18 [84] shows a simple single-sided AFM. The main advantages of this topology are simple construction and low cost manufacturing, but the main issue with this configuration is the large axial force exerted on the stator by the rotor. Research has shown that the axial force can be eliminated by using either the single-stator double-rotor structure or the double-stator single-rotor structure.

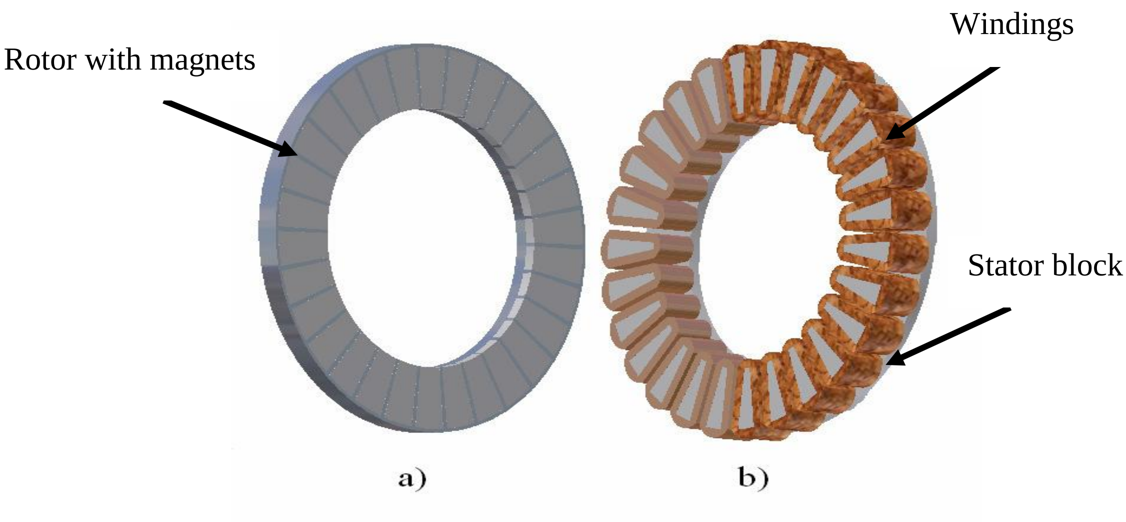

Figure 2-18: Single-Sided AFM a) rotor and b) stator [84].

2.10.2 Double Rotor Single Stator

A double rotor single stator AFM is shown in Figure 2-19 [16]. The machine is composed of toroidally steel laminated iron stator cores positioned between two soft iron rotor discs, rigidly fixed to the machine shaft. In order to produce an axially directed magnetic field in the machine air gaps, permanent magnets are mounted on the surface of each disc, the stator winding is either slotted or slotless configuration [112].

This particular configuration of the machine proves to be the most appropriate structure for lightweight, low volume, low cost and low-speed high-torque applications as compared to double stator single rotor and multistage configuration. The reason for that is fixing of the rotors which may be reasonably easily as stated in [59].

This type of arrangement offers a range of possibilities of stators configuration, the North-North (NN) configuration and North-South (NS) configuration machine. In this case, magnets with the same magnetization direction are placed in front of each other. This machine configuration is particularly considered as advantageous in relation to double stator single rotor and multistage configuration as mention in [17].

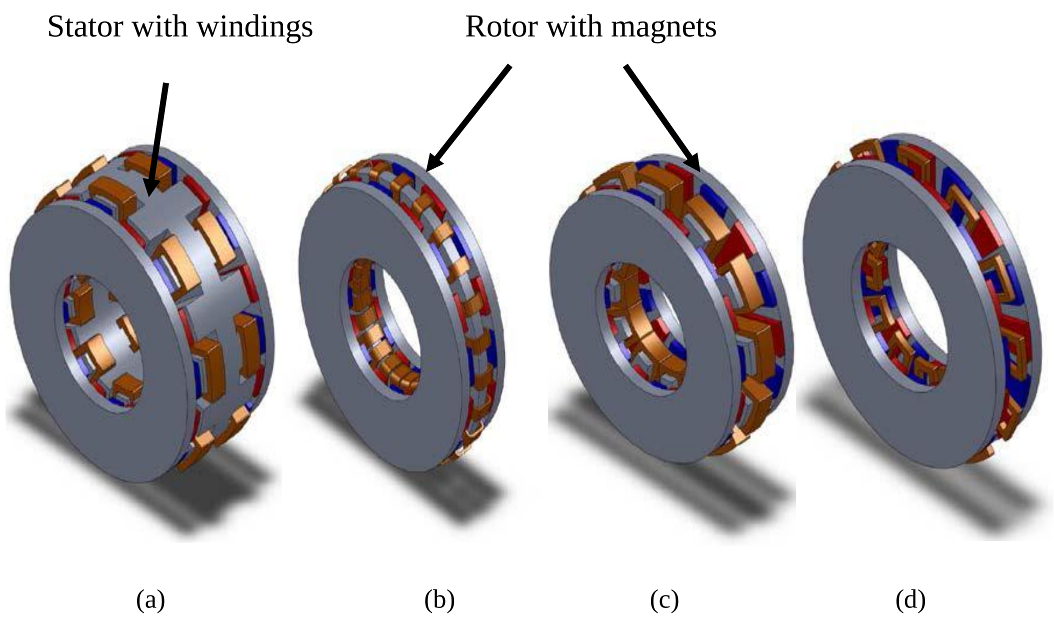

Figure 2-19: (a) Interior slotted stator, (b) Interior slotless stator, (c) Interior ferromagnetic core stator, (d) Interior coreless stator [16].

2.10.3 Single Rotor Double Stator

In Figure 2-20 [4] single rotor double stators structure with ferromagnetic core in the rotor is shown, the permanent magnets may be located on a surface of the rotor disc or inside the rotor disc, with coreless in the rotor. Thereby, the main flux may flow axially through the rotor disc or flow circumferentially along the rotor disc. The slotted stator cores of the machine are realized by a tooth wound winding located in the stator slots [113].

This machine configuration has the advantage of using fewer permanent magnets at the expense of poor winding utilization [17].

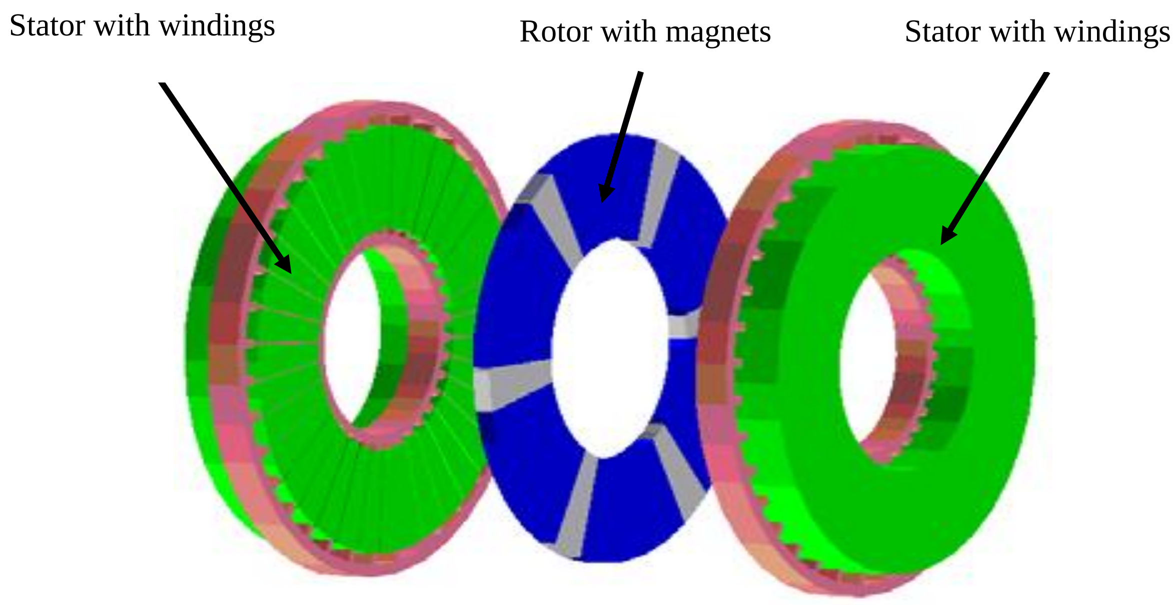

Figure 2-20: Single rotor double stator AFM [4].

2.10.4 Multi Rotor Multi Stator AFM

In this type of AFM, several machines, either single rotor double stators or single stator double rotors, are lined up on the same shaft to form more-complex arrangements, known as multi-stage AFMs [40].

This configuration offers a quite interesting possibility and modularity. Figure 2-21 [40] shows a multistage axial flux machine with two stators and three rotors. The winding connection between different stages could be either in series or parallel.

Furthermore, a connection/disconnection of stages could be done depending on the temporary requirements of the application. This connection may allow fault tolerance as the machine can keep working even if any of the stages is damaged or disconnected.

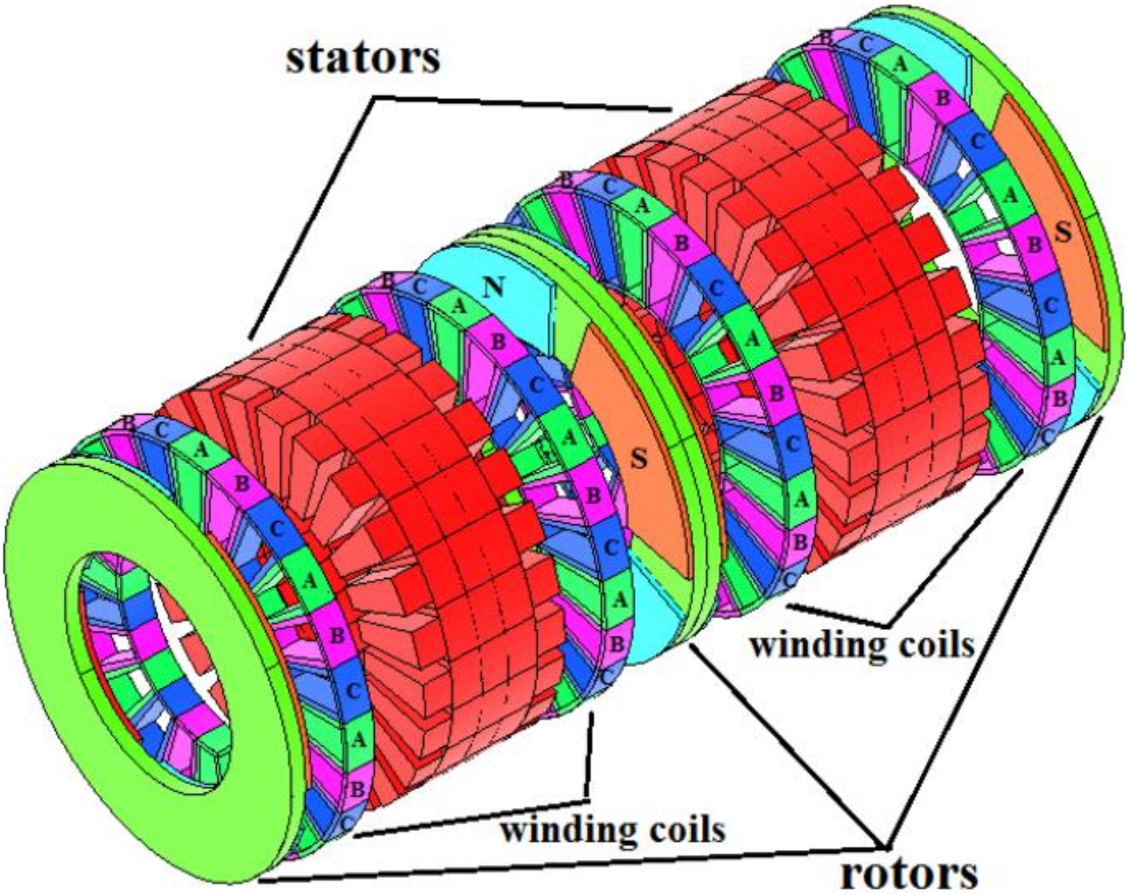

Figure 2-21: Multistage AFM with two stators and three rotors [40].

2.10.5 Pros and Cons Features

In general, AFM have some common features which can be classified as pros and cons that includes, high power density, high torque density and high efficiency, short rotor in axial direction, compact machine construction and short frame.

These features gives rise to the ability of construction without rotor steel, and more robust structure when compare to cylindrical type radial flux machine. With two airgaps in double-sided, the machine is complicated and has high windage losses at high speed application.

Table 2-1 presented the advantages and disadvantage of different axial flux machine topologies.

Table 2-1: Advantages and disadvantages of different AFM topologies

AFM Topologies	**Advantages**	**Disadvantages**
Single sided	1. Simple construction. 2. Low cost.	1. Large axial force between the stator and rotor. 2. Low output power. 3. Low torque.
Double rotor single stator	1. Lightweight, low volume and low cost as compared to double stator single rotor and multistage configuration. 2. High torque. 3. Low axial force between the stator and rotor.	1. High windage losses. 2. Low fill factor.
Double stator single rotor	1. Fewer permanent magnets. 2. High speed application. 3. Low axial force between the stator and rotor.	1. High windage losses. 2. Low fill factor.
Multistage	1. Fault tolerance. 2. Ability of construction without rotor steel.	1. High windage losses. 2. High cost.

2.11 Conclusion

In this chapter a brief history into the literature and technology review of AFM and SMC was presented. Comparisons between AFM and RFM in terms of torque production were discussed. It was shown that early electrical machine such as the one built by Faraday used axial flux concept, however it become dormant due to some problem associated with it. Moreover, the introduction of SMC which harness the 3D nature of flux in AFM and availability of strong permanent magnets have renewed research in AFM, especially in application when high efficiency and high torque density are required.

A brief review on SMC in electrical machines together with the typical AFM area of application was presented. Also, it gives a brief review on state of the art in AFM which discussed the stator windings, design and FEA modelling, loss and thermal analysis, manufacturing and materials, torque and speed. In addition, it reviewed soft magnetic composite that discussed the SMC material's production process and properties such as its isotropic and thermal and its ability to produce 3D flux path that are required for AFM.

Finally, different methods are highlighted in the literature on reducing the AC winding loss using magnetic shielding which is the main aim of this thesis. It also discussed the advantages of using magnetic slot wedges over Litz wire, placing the conductors far from the airgap and shaping the pole pieces to reduce the machine losses. AFM topologies such as single-sided, double-sided and multistage AFM were discussed together with advantages and disadvantages features of AFM.

3. 3D FEA and Verification of Baseline Machine

3.1 Introduction

The permanent magnet axial flux machines (AFM) are well known for their high torque density and high efficiency together with more robust structure than the cylindrical type. In this chapter a baseline machine is presented and analysed, in addition it outlines the specification and the overall performance simulation using 3D FEA. The machine being developed as a demonstrator is single-sided open-slot and designed to operate as a 3 phase Brushless DC machine.

The stator of the prototype machine is constructed from Soft Magnetic Composite (SMC) developed by Höganäs AB of Sweden. Concentrated windings are used and a rotor of NdFeB magnets mounted on a solid carbon steel core-back was utilised. This is an example of a machine of this type, developed at Newcastle University as reported in [114]. In order to verify the design process, the prototype machine is tested, and its performance compared with these 3D FEA and details of some of these experimental measurements are also presented in this chapter.

The major objectives of this chapter are:

1. To examine the benefit of using SMC in the design of a small compact AFM.
2. To use a single-sided open-slot AFM as a demonstrator for easy manufacturing process.
3. To investigate the performance of the machine using 3D FEA, including; back EMF, cogging torque, axial force, loss and on-load torque.
4. In order to validate this 3D FEA, the prototype machine is tested, and its performance compared with these predictions at no-load and on-load condition.

3.2 The Baseline machine

Axial flux machine design procedures are the same as a conventional radial flux machine; which are constrained by some output parameters, such as torque and speed, slot dimension, terminal voltage, phase current and number of turns. The first step in the process is to develop a good estimate of the required dimensions of machine, in particular, the inner and outer diameters of the stator and the rotor, axial length of the machine using the allowable 120 mm outer diameter of the SMC prototype material. This section will cover the machine topology and key dimensions.

3.2.1 Topology

The machine is single-sided open-slot as stated earlier to offer a simple manufacturing process which eliminates the need for the balanced positioning of the rotors and stators in a double-sided AFM configuration; rotor-stator-rotor configuration or stator-rotor-stator configuration. The physical size of this machine shown clearly that at this scale the airgap closing forces are small and not a problem for “off the shelf” steel metal shielded thin bearings.

An exploded diagram of the electromagnetically active components is shown in Figure 3-1. The stator block with twelve teeth, is constructed from Soft Magnetic Composite (SMC) and the stator tooth are trapezoidal in shape. Concentrated windings are placed over the stator teeth. It is envisaged that these would be wound off the machine on a former and slid onto the open, parallel sided stator tooth. This process would ensure a high slot fill factor and copper conductors were used in the simulation.

The rotor consists of NdFeB magnet segments glued to a Cold rolled 1010 solid carbon steel core-back. The Cold rolled carbon steel was utilised due to it 49.8 W/m.ºC thermal conductivity and electric conductivity of 0 S/m at 20ºC and for easy fixing the magnets together with the shaft using screws as it is impractical to use screw on SMC material. An 8-pole design is used with the magnets magnetised in the axial direction.

Based on the required specifications, the key dimensions and operating parameters which were obtained for the baseline machine with a desired speed at 3000 rpm are presented in Table 3-1.

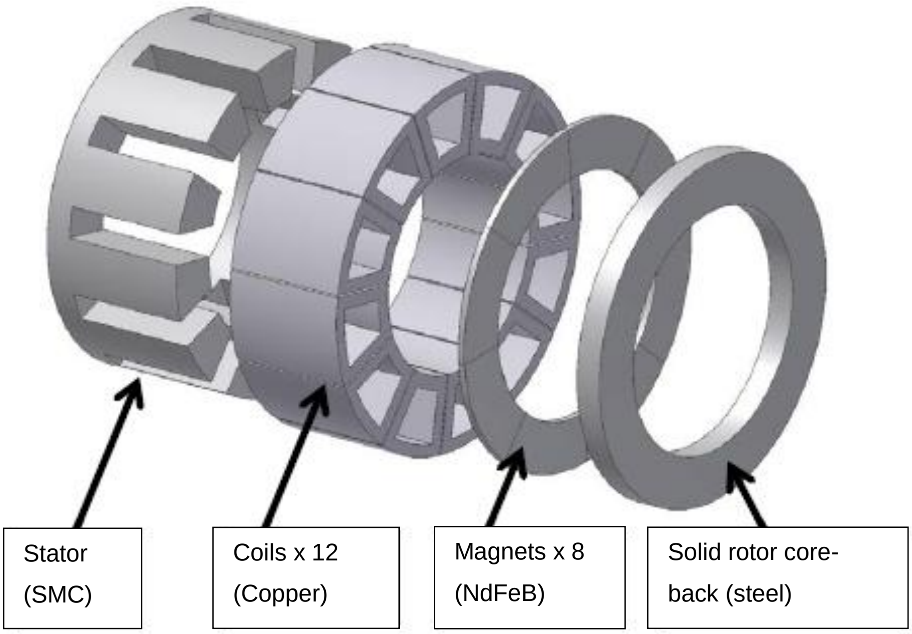

Figure 3-1: Baseline machine exploded diagram of the electromagnetic assembly.

Table 3-1: The key dimensions of the baseline machine

Outer diameter (including coil overhang)	76.2 mm
Inner diameter (including coil overhang)	43.2 mm
Axial length	36.4 mm
Magnetic gap	1 mm
Magnet thickness	1.4 mm
Magnet span	180^{o}(electrical)
Rotor core-back thickness	5 mm
Current density	3.3 A/mm^2
Operating speed	3000 rpm
Slot width	6.2 mm
Slot depth	24 mm
Slot cross section for coil	74.4 mm^2
Fill factor	60%
Total conductor cross sectional area	44.6 mm^2
Turns	336
Conductor diameter	0.4mm (26AWG)

3.3 3D Finite Element Analysis

The machine is modelled and analysed using Infolytica MagNet 3D FEA software as the main design tool due to its availability. To predict the machine's performance, a fully parameterised AFM model was created in which all stator and rotor dimensions and electrical input can be altered. An initial design is generated to see the maximum torque it can offer, and this is then applied to an optimisation routine which alters the parameters automatically and assesses the results according to a set of design parameters.

Although a machine's symmetry can be used to reduce the 3D FEA model size and the simulation time, in this case one quarter of the machine was implemented, since one pole pairs is equal to three stator teeth. The magnetic flux path in the AFM and that of the SMC material are largely in three-dimensions (3D). This section covers the 3D FEA, meshing sensitivity analysis and motion together with simulation results.

3.3.1 Meshing and Flux Density

Based on the specification of the machine as stated in Table 3-1 and optimising for minimal magnet mass, minimal axial length and high efficiency, the 3D FEA mesh in Figure 3-2 was generated. One pole pair section of the machine is shown which takes advantage of the periodical symmetry and reduces computing time. Even periodic and magnetic field normal boundary conditions were used based on the slot and pole number combination.

The airgap has a finer mesh region of maximum element size 0.5 mm and curvature refinement angle of 1 degree to accurately model the region where most energy is stored and field directions changes more rapidly as stated in [115]. Furthermore, the airgap is sub-divided into four sections namely; stator region, stator slip, rotor slip and rotor region, these means that the stator region and rotor region extended to one-quarter of the airgap at both ends. Virtual air was applied as material in the stator and rotor region, while air was utilise as material for the rotor slip and stator slip.

Transient 3D with motion using Newton-Raphson is utilised in solving the model with fixed interval time step method of 0.083 ms, which correspond to 60 steps solution.

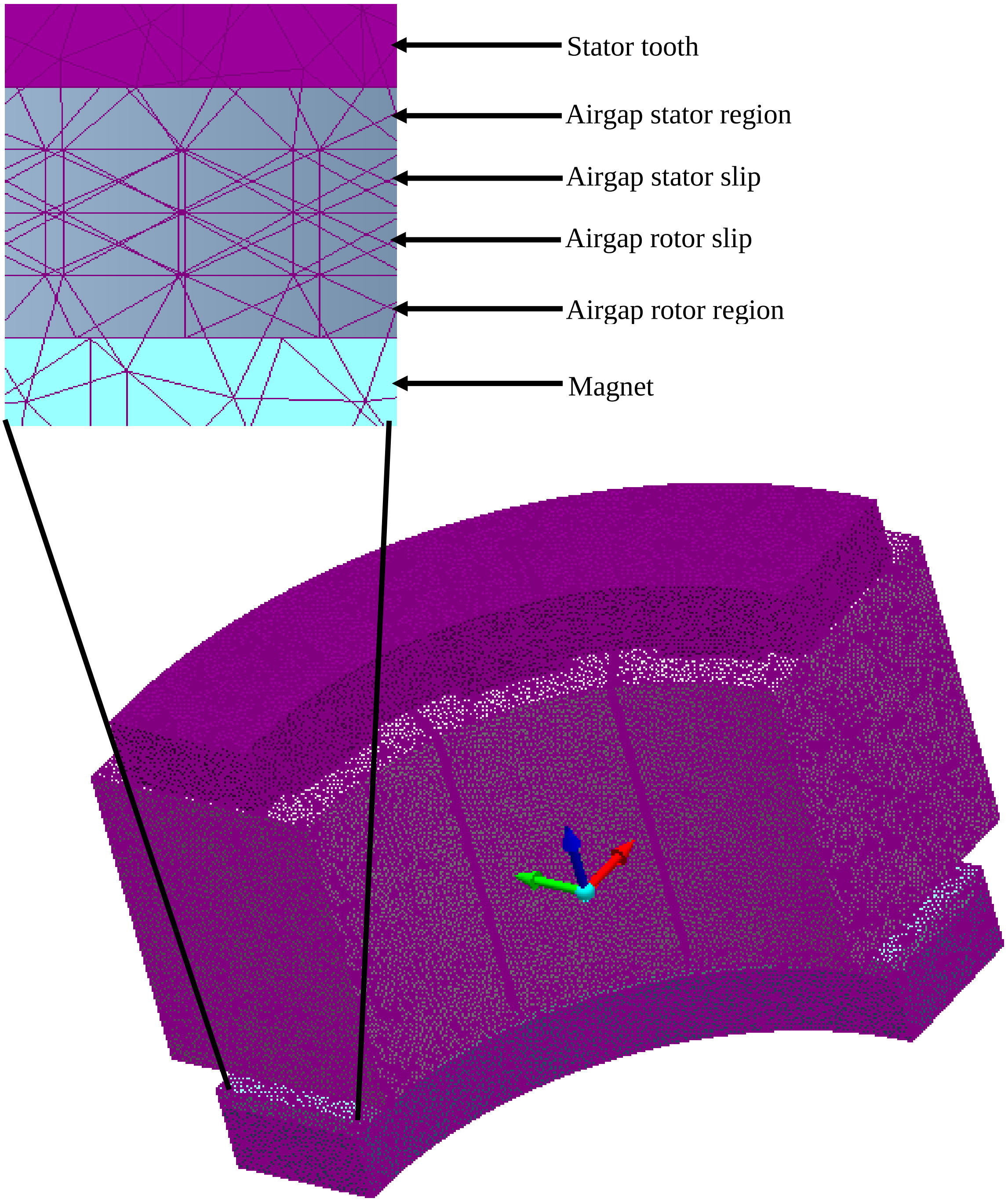

Figure 3-2: 3D FEA mesh of the baseline machine.

Some of the constraint imposed on the software include that the rotary component; rotor slip, rotor airbox, magnets and rotor core-back in the machine were set as the reference paths in motion properties and rotary is used as the motion type in z-direction, this is only applicable and relevant to Infolytica MagNet software. Speed based position was used with initial time of 0 ms and final time of 5 ms at 18000 deg/s speed corresponding to 3000 rpm and 200 Hz

(Electrical). The motion centre was set to zeros in all direction with position and speed at start up.

Figure 3-3 shows the flux density shaded plot and the shaded plot displays the outline of the model and a field. The field values are represented by colors. A color legend is displayed that associates the field values to the colors.

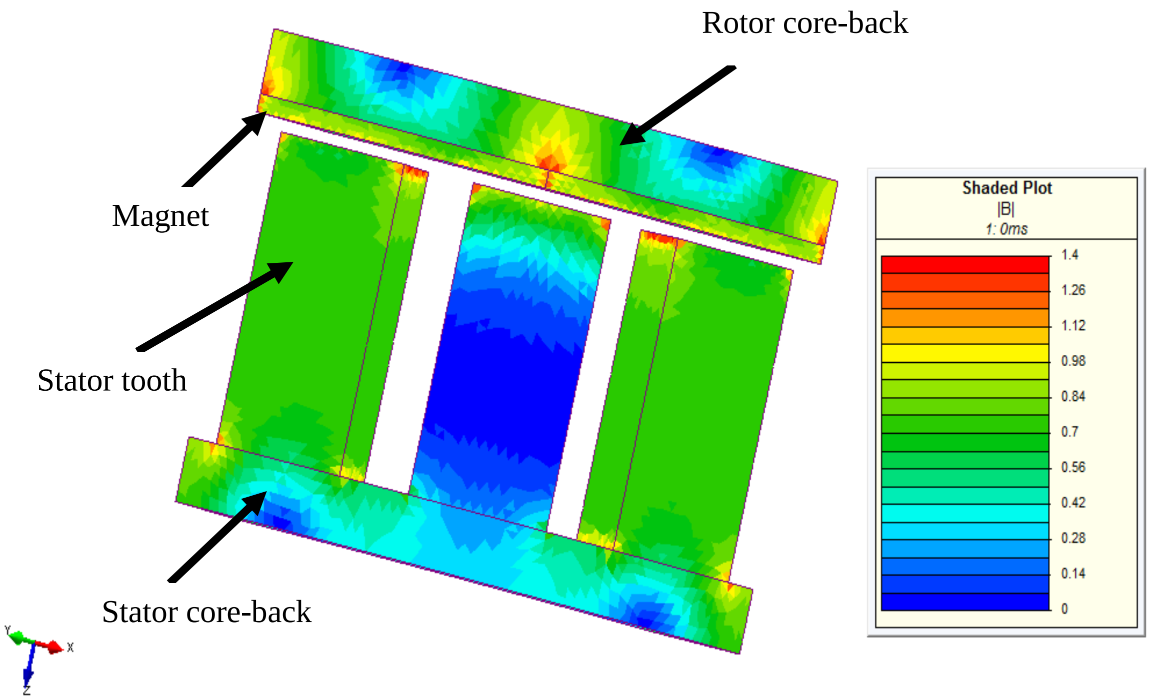

Figure 3-3: 3D FEA flux density shaded plot of the baseline machine.

It is clear from the above figure that the SMC material is not saturated at current density of 3.3 A/mm^2, but tends to only at the edges of teeth and magnets. The material has a flux density of 0.7 T.

3.3.2 Baseline Machine Performance

This sub-section covers the back EMF and harmonic analysis, axial force, loss, cogging torque and on-load torque analysis of the machine. The back EMF is the voltage induced in the stator winding of the machine by the rotor magnets at given rotational speed, it is also proportional to the speed of the machine and phase flux linkage.

To get the back EMF of the coil from the flux linkage, the following expression in equation (3.1) can be used.

$$E = \frac{d\varphi}{dt} \tag{3.1}$$

where $\frac{d\varphi}{dt}$ is the rate of change of flux linkage.

The induced rms voltage can be obtained using the induced voltage equation which is given in [17].

$$E = 4.44 N_{ph} \Phi_{pk} f \tag{3.2}$$

where E: rms induced voltage f: frequency of the supply, Φ_{pk} peak flux in the stator teeth and N_{ph} number of turns per phase.

The back EMF, in this case is obtained at no-load and rated speed. From the FEA software, it can be found either from the coil flux linkage or directly from coil voltage. Figure 3-4 presented the back EMF of the baseline machine.

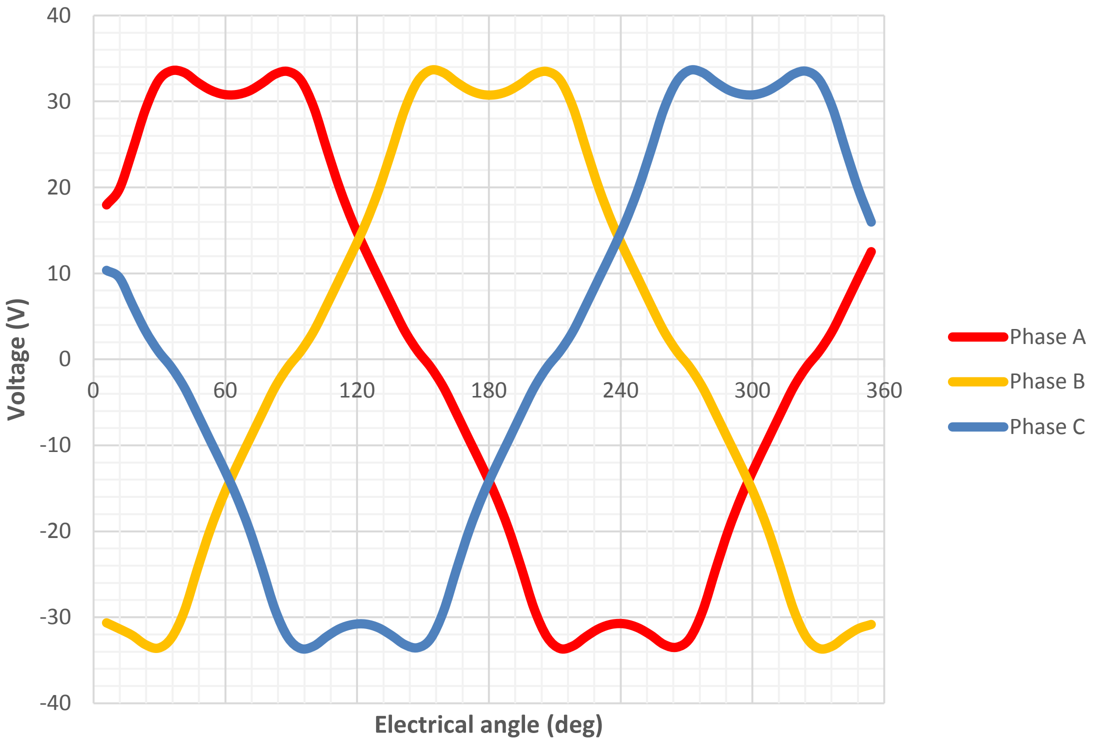

Figure 3-4: 3D FEA Back EMF of the baseline machine

The harmonic analysis was carried out using the Fast Fourier Transform (FFT) as shown in Figure 3-5, to get the maximum amplitude of each harmonics and the accuracy depends on the number of data points used.

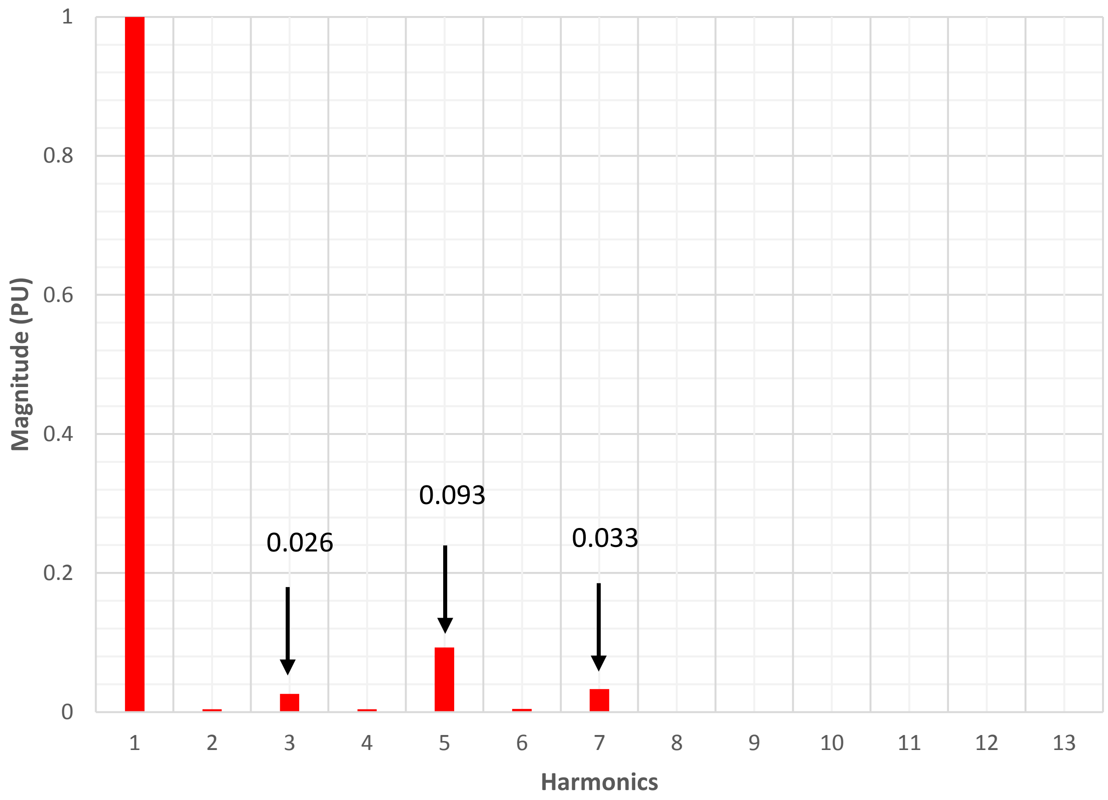

Figure 3-5: Back EMF harmonics of the baseline machine

In this analysis, 60 data point samples were used and from the harmonic analysis spectrum in Figure 3-5, the only significant harmonic beyond the fundamental are the 3rd, 5th and 7th at 2.6%, 9.3% and 3.3% respectively due to the combination of 12 slots and 8 poles in the machine. All other harmonics are less than 1% of the fundamental, these harmonics are undesirable and subsequent work in Chapter 4 will describe a way to reduce them.

Single tooth winding usually utilises a fractional slot winding pattern and a combination of 12 slots as well as 8 poles has a winding factor of 0.866. Winding factor is what makes the rms generated voltages in a three-phase machine become lesser due to the armature winding of each phase in a slot. The induced voltage in each slot is not in phase, and their phasor sum is less than their numerical sum. This reduction is called distribution factor. Another factor that reduced the winding factor is pitch factor and occurs when the slot pitch is less than the pole pitch.

Numerically, winding factor can be obtained from the product of distribution factor and pitch factor. The combination was chosen because of the good experience in designing compact machine.

A large force of attraction between the stator and rotor is one of the problems associated with AFMs and if care is not taken during design, this force of attraction can cause serious damage to the machine which can lead to failure modes. To calculate the axial force of AFM, the 3D FEA software must evaluate the field in the layer of airgap with air elements adjacent to the component and evaluate the field immediately adjacent to sharp corners where there is a potential for error.

This method ensures that the software will calculate the forces and torques with accurate field values. The axial force obtained from 3D FEA, shows an attractive force between the rotor and stator of 184.3 N, which is well within the capability of standard “off the shelf” bearings. A deep groove steel metal shielded thin bearings W 61900-2Z with basic static load rating of 1.3 kN, limiting speed of 36000 rpm and mass of 9.4 g was utilised in the final assembly in which the force of attraction is within the limit.

To determine the overall performance of a machine, the losses within the machine need to be calculated. In this case the losses were found from the 3D FEA software at full-load current. The FEA uses the Steimmetz equation at 20˚C and Figure 3-6 illustrates the approximately percentages of losses in the individual parts of the baseline machine obtained from the 3D FEA using pie chart.

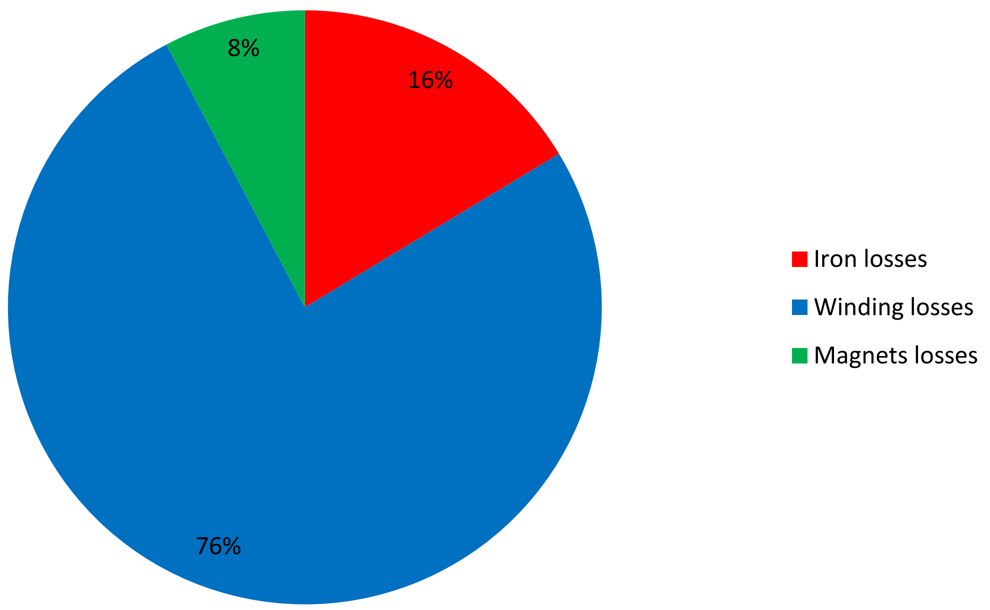

Figure 3-6: 3D FEA losses of the baseline machine

The total iron loss comprises of hysteresis loss and eddy loss, and the iron loss in the baseline machine is found to be 41.8 W which represents 16.4% of the total loss in the machine. The winding loss is 194.1 W representing 75.9% by assuming the copper resistivity to be 6×10^{-4} Ω.m. Losses in the magnets found using the 3D FEA amounted to 19.7 W representing 7.7%. The total loss of the machine is the sum of all the losses and was found to be 255.5 W.

The cogging torque also known as no-current torque is produce due to the interaction between the permanent magnets of the rotor and the stator slots. It depends on the position, number of magnetic poles and the number of teeth on the stator. Machines that operate at lower speed have a high cogging as compared to those at high speed as reported by [74].

From the 3D FEA, the baseline machine exhibits a peak-to-peak cogging torque of 0.36 Nm and this may be considered too high as compared to on-load torque. Cogging torque causes mechanical noise and vibration and it is desirable to minimise. Figure 3-7 illustrates the 3D FEA simulated cogging torque variation with electrical angle.

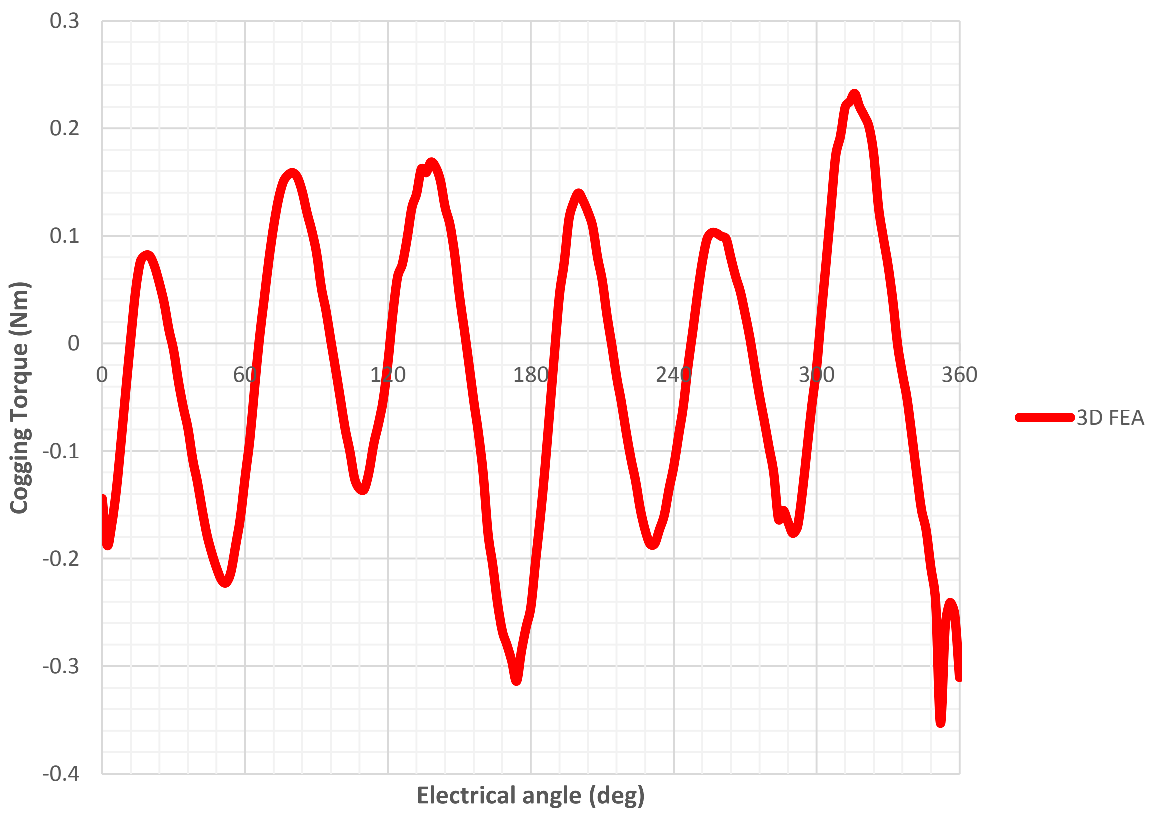

Figure 3-7: Baseline machine 3D FEA simulated cogging torque.

The on-load torque of the machine is obtained by applying a DC current to the model with the rotor advanced through two-poles. The current is passed through two coils of the machine to replicate a switching period for a brushless DC machine, with the positive terminal of the DC supply connected to phase A and negative terminal connected to phase B. Phase C is left unconnected.

The peak torque variation with the applied current is as shown in Figure 3-8 and the maximum achievable peak static torque was attained before entering the saturation zone of the SMC used as core material when the machine is loaded. The machine is tested at rated current of 1.2 A.

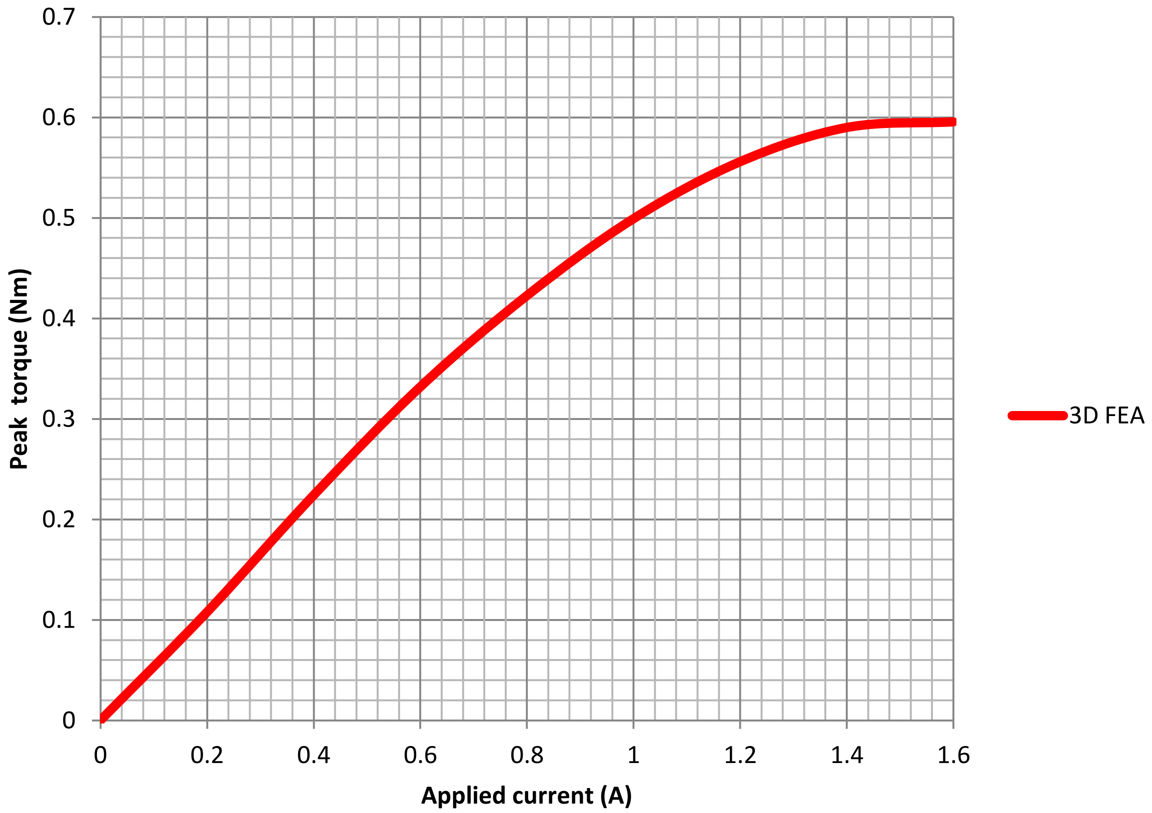

Figure 3-8: Baseline machine 3D FEA simulated on-load torque.

3.4 Mass of Baseline Machine

The active mass of the machine is shown in Figure 3-9, as SMC material is used in the stator block, copper in the coils, Cold rolled 1010 solid steel in the rotor core-back and Neodymium Iron Boron for the magnets. It shows that the machine active mass is 480 g. The stator mass is

284 g, rotor mass is 73.4 g, magnets is 20.0 g and coils are 102.6 g representing 59.0%, 15.0%, 4.0% and 22.0% respectively.

From the pie chart, it can be seen that the stator block has the highest mass in the machine, follow by stator winding coils and rotor however magnets in the baseline machine have the lowest mass when compared to stator block, coils and rotor.

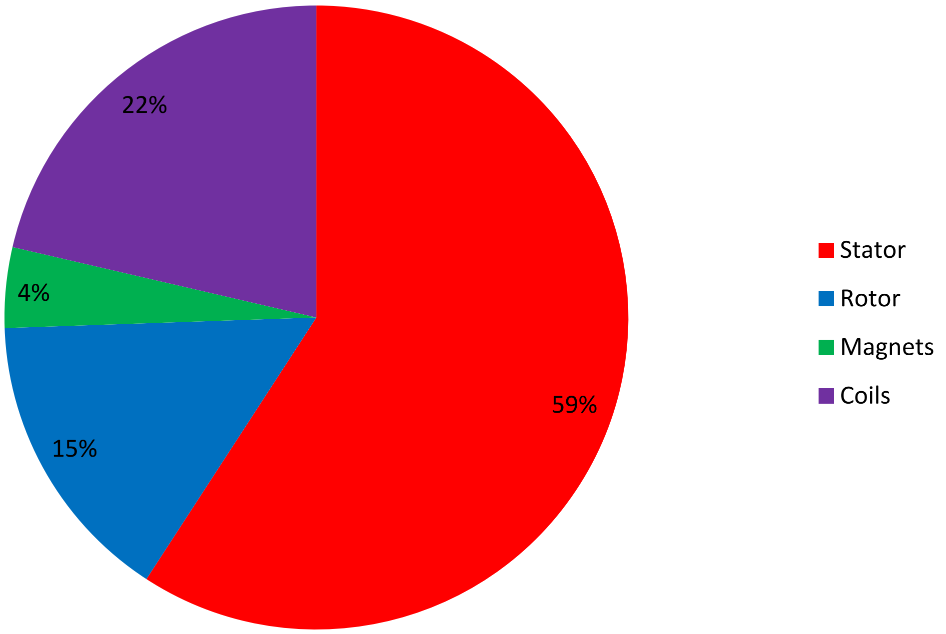

Figure 3-9: Mass of baseline machine component.

3.5 Performance Summary

Table 3-2 summarises the overall 3D FEA performance of the baseline machine with peak torque of 0.59 Nm, axial force of 184.3 N and peak back EMF of 33.7 V. The only significant harmonic apart from the fundamental are the 3rd, 5th and 7th representing 2.6%, 9.3% and 3.3% respectively of the fundamental. This is due to the combination of 12 number of slot and 8 number poles in the baseline machine.

The machine exhibits a peak-to-peak cogging torque of 61% of the on-load torque. The output power of the baseline machine is 486 W and the on-load loss is 255.5 W. The on-load loss represented 52.6% of the machine output power. Based on the 3D FEA the machine has efficiency of 65.5 %.

Table 3-2: 3D FEA Performance Summary

Output parameter	Value
Peak back EMF (V)	33.7
3^{rd} harmonic back EMF (PU)	0.026
5^{th} harmonic back EMF (PU)	0.093
7^{th} harmonic back EMF (PU)	0.033
Peak Torque (Nm)	0.59
Peak-to-peak cogging torque (Nm)	0.36
Axial force (N)	184.3
Output Power (W)	486.0
Full-load loss (W)	255.5
Efficiency (%)	65.5
Total mass (kg)	0.48

3.6 Experimental Verification

After the 3D FEA analyses have been completed on the baseline machine, an experimental verification has been conducted on a prototype baseline machine so that comparisons can be made. A static test rig was used to carry out the measurements and the test results can be split into two categories:

1. Cogging torque tests
2. On-load torque tests.

In these tests two phases have been connected in series and the third phase left open circuit. The no-load test was conducted at open circuit without DC current supply, while the on-load test was carried out when a DC current is then applied replicating a switching period for a brushless DC machine. Figure 3-10 presented the three timing graphs and Figure 3-11 shows the switching period for a brushless DC machine.

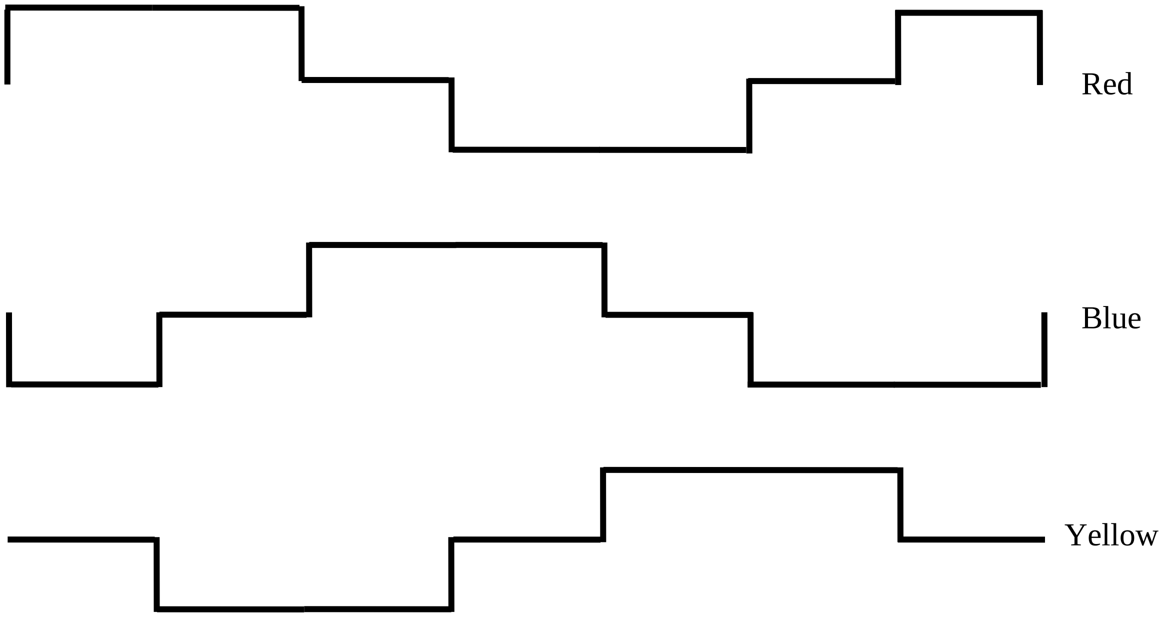

Figure 3-10: The three timing graph of BLDC.

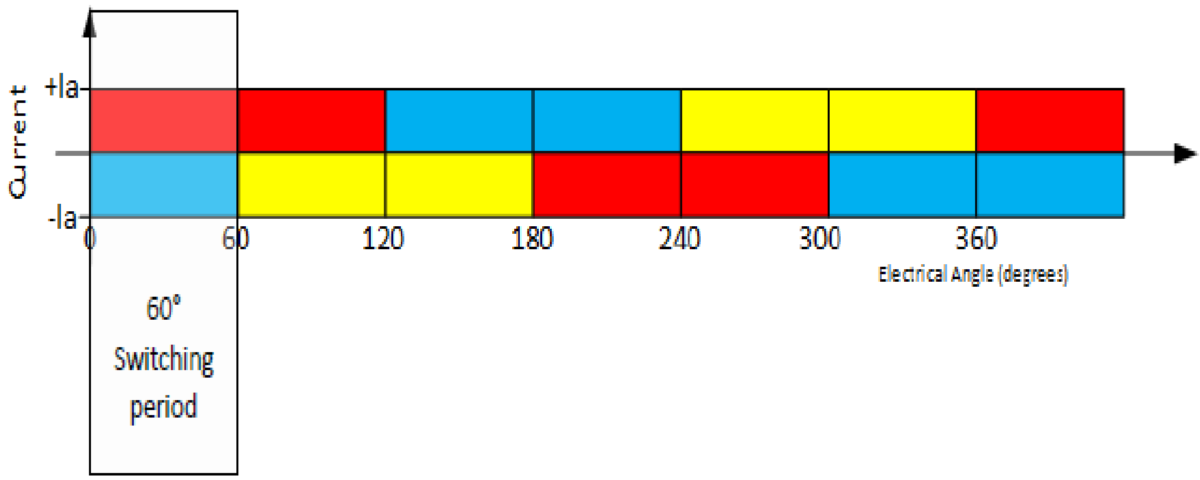

Figure 3-11: BLDC switching sequence.

The twelve teeth stator and core-back were manufactured as a single block, by using two SMC prototype materials. CNC milling machine is used in the workshop to produce the stator block core. The design requires 336 turns per coil, to achieve the required number of turns the coils are pre-wound on a former and then placed over the stator teeth, as shown in Figure 3-12. A winding machine was used, and the winding were wound on a thermal insulation paper to achieve the desired turns and high fill factor in the slot. To obtain the three phase of the machine, four coils are connected in series and the other ends of the coils are connected as star point.

Figure 3-12: Baseline prototype stator block with concentrated windings.

3.6.1 Static Test Rig

Figure 3-13 shows the experimental test rig for a three phase AFM and Figure 3-14 presented the instrument setup to conduct the tests. The test rig bench is equipped with a mechanical dividing head, the torque transducer, coupling and the baseline machine under test. The instruments consist of a DC power supply, torque transducer display and connecting cables from the DC power supply to the terminals of the baseline machine on tests.

The machine is connected to a dividing head via a torque transducer as shown in Figure 3-13. The dividing head can position the shaft with a high angular precision. Torque measurements are taken at 1º intervals. For an 8-pole machine this equates to 4º electrical between each torque measurement. The measurements are taken over a full rotation to ensure the correct BLDC switching window is captured.

General risk assessment was carried out to identify hazards and anything that may cause harm during the experimental measurements. This includes a provision of an emergency stop switch to break or isolate the supply to the baseline machine in case of any fault during the testing. In addition, safety lab coat was wear as protection and signs were display to show that an experimental test is ongoing.

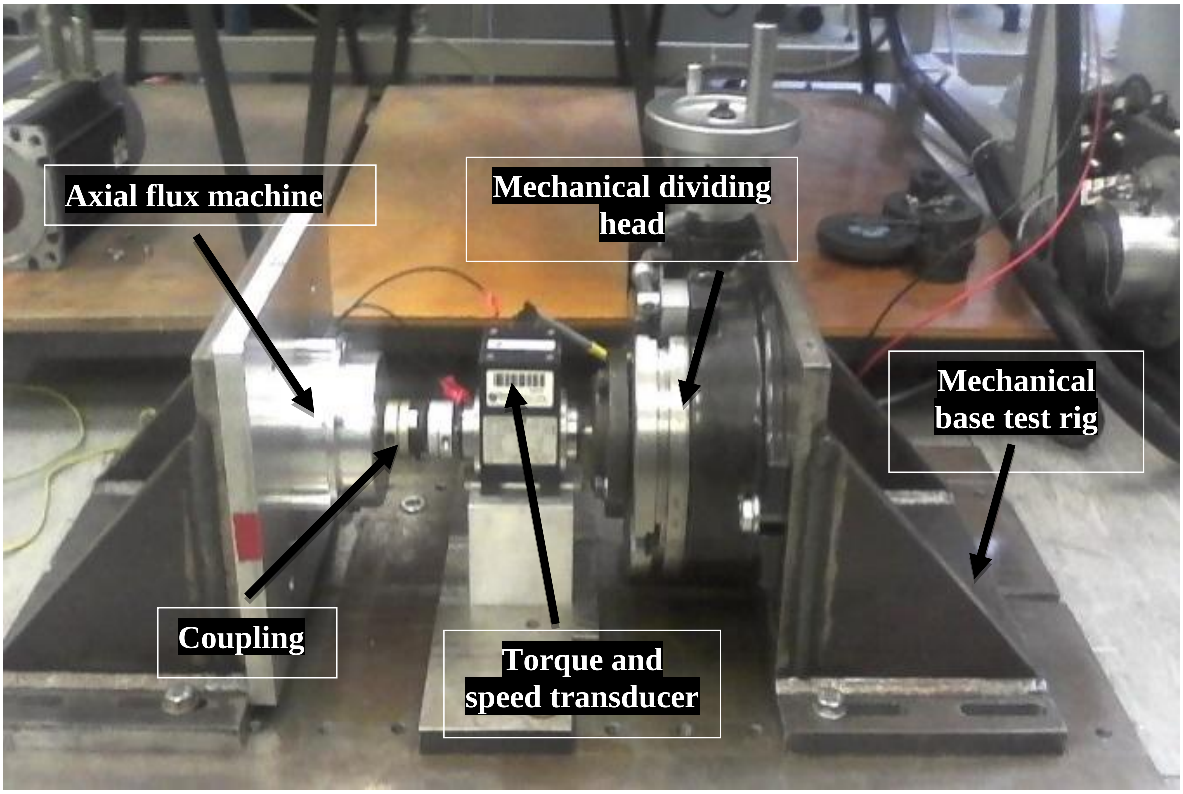

Figure 3-13: Static Test Rig

The static test rig consists of the following components;

1. Mechanical dividing head (INDEXA TSL200 horizontal/vertical rotary table)
2. Torque transducer (MAGTROL TM HS 306/111, Rated torque 5 Nm, Accuracy <0.1 %, Maximum speed 50000 rpm, Torsional stiffness 725 Nm/rad and Moment of inertia 3.08×10^{-5})
3. Coupling (R+W)
4. Machine under test.
5. The mechanical base test rig hosing the entire components.

The torque measurements are with highly sensitive torque transducer TM HS 306/111 with rated torque of 5 Nm and maximum speed of 50000 rpm and the torque readings were captured using a high quality MAGTROL MODEL 3411 torque display. The torque display is designed for use with all Magtrol TM, TMHS, TMB and TF torque transducer; moreover it has addition of high-resolution quadrature encoder enables low RPM applications of position measurements with accuracy of 0.02% pf range ± 10V.

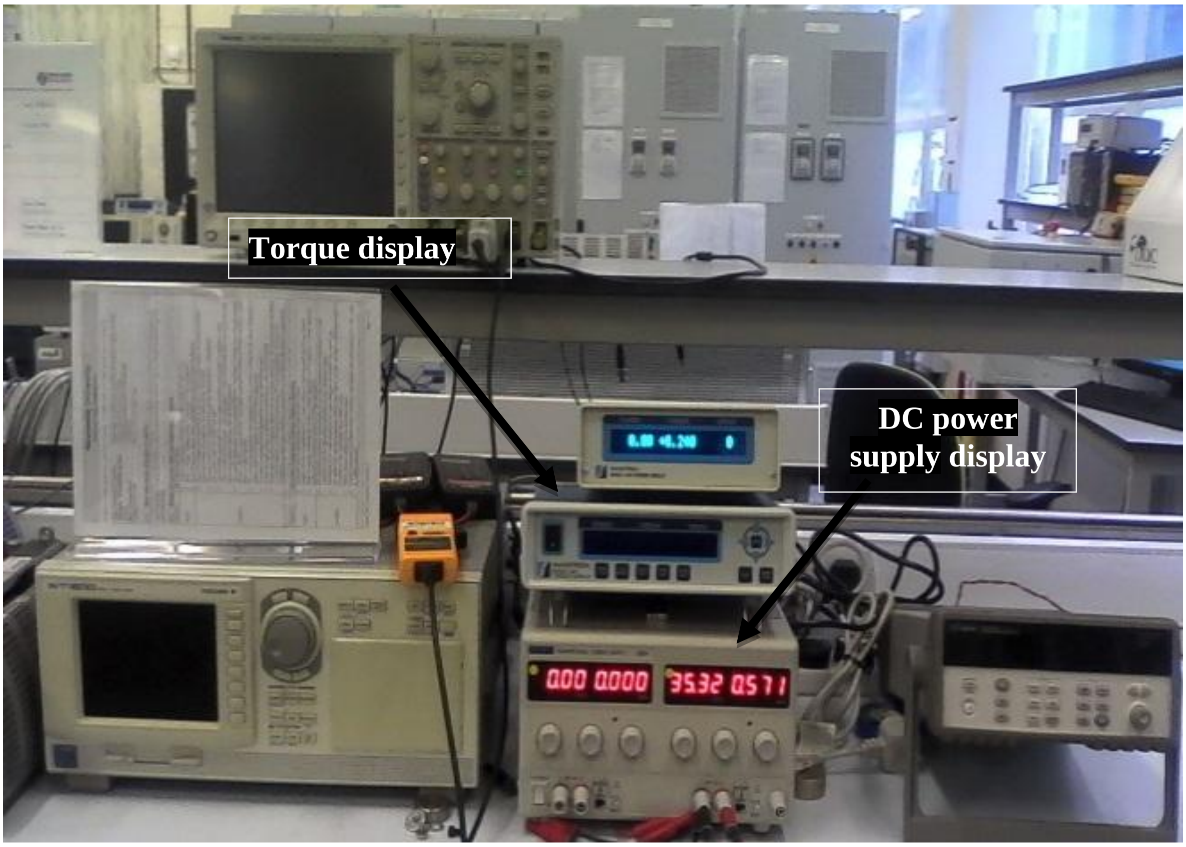

Figure 3-14: Baseline machine equipment set up for the experimental test.

The Instrument rack for the baseline machine tests consist of the following equipment;

1. DC power supply (EX355R compact bench power supply, Mixed-mode regulation, Power rating of 175 W, Switched remote sense terminals, Voltage 0 to 35V, Current 0 to 5A, 4-digit meters on each output)
2. Torque display (MAGTROL MODEL 3411, High Quality, Easy-to-Read Vacuum Fluorescent, Maximum speed 199999 rpm, Input frequency 199999 Hz, Speed accuracy 0.01%, Torque accuracy 0.02% Operating temperature 5ºC to 50ºC, Relative humidity <80%).
3. Connecting cables.

3.6.2 Cogging Torque Tests

The cogging torque test looks at the performance of the baseline machine in terms of its torque characteristic. Measurements were taken of the cogging torque produced over one electrical cycle, in which the rotor was rotated using the mechanical dividing head at angle interval of 1º mechanical (equals to 4º electrical angle) for a 8 pole machine between each torque measurement at no-load ($I_{dc} = 0$) by a torque transducer and display in the torque display metre. The measurements are taken over a 360° rotation to ensure the correct BLDC switching window is captured. Readings were taken in both clockwise and anticlockwise directions to eliminate the effect of hysteresis torque and backlash due to dividing head, and the average of the two measurements calculated.

The dominant cogging torque is produced by the magnets on the rotor wanting to take up an angular position corresponding to minimum reluctance. As the torque is a result of the field from the permanent magnet, it is independent of applied current and hence it is always present in the output torque level. It is for this reason that it must be minimised. Figure 3-15 illustrates the 3D FEA and measured cogging torque over one electrical cycle to caption different switching period.

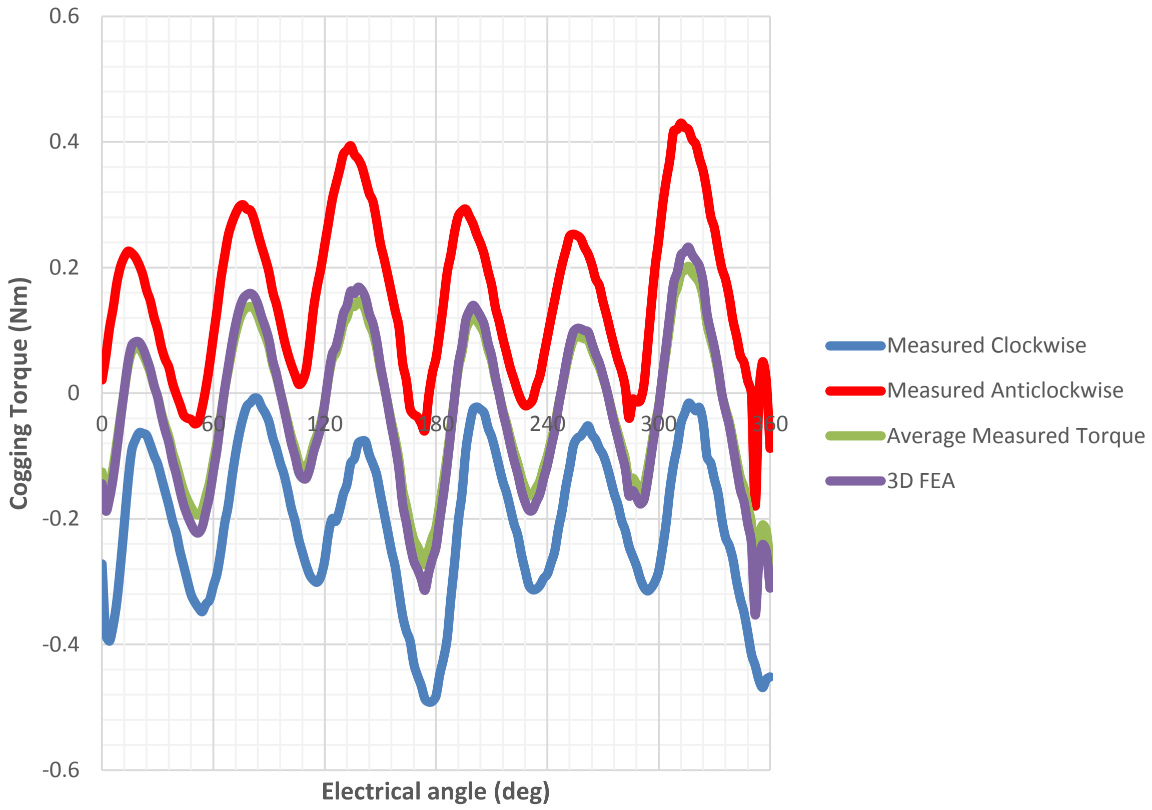

Figure 3-15: 3D FEA and Measured static cogging torque.

The prototype machine has 1.5 stator teeth per pole. Therefore, looking at one pole pair, a magnet is in the aligned position every 60° electrical. This alignment produces a cogging torque, the period and magnitude of each are similar and the machine exhibits measured cogging torque of 39%.

It is clear from the graph of Figure 3-15 that the difference between the lines of the 3D FEA and the measured is due to the dividing head equipment backlash and the effect of hysteresis torque which cannot be eliminated 100%. Since the dividing head was operated manually there is also a mechanical error due to parallax and alignment. Table 3-3 presented the raw data of the 3D FEA, measured clockwise, measured anticlockwise and the average measured cogging torque of the baseline machine together with the mechanical and electrical angle of each raw data.

Table 3-3: Raw data of baseline machine

Mechanical angle	Electrical angle	Measured clockwise	Measured anticlockwise	Average measured	3D FEA
0	0	-0.272	0.021	-0.126	-0.144
0.5	2	-0.384	0.058	-0.163	-0.187
1	4	-0.395	0.103	-0.146	-0.168
1.5	6	-0.37	0.136	-0.117	-0.135
2	8	-0.331	0.176	-0.078	-0.089
2.5	10	-0.273	0.202	-0.036	-0.041
3	12	-0.208	0.217	0.005	0.005
3.5	14	-0.141	0.226	0.043	0.049
4	16	-0.091	0.223	0.066	0.076
4.5	18	-0.074	0.216	0.071	0.082
5	20	-0.063	0.204	0.071	0.081
5.5	22	-0.064	0.188	0.062	0.071
6	24	-0.067	0.164	0.049	0.056
6.5	26	-0.082	0.147	0.033	0.037
7	28	-0.099	0.121	0.011	0.013
7.5	30	-0.113	0.101	-0.006	-0.007
8	32	-0.135	0.073	-0.031	-0.036
8.5	34	-0.157	0.054	-0.052	-0.059
9	36	-0.179	0.041	-0.069	-0.079
9.5	38	-0.204	0.016	-0.094	-0.108
10	40	-0.223	-0.002	-0.113	-0.129
10.5	42	-0.252	-0.018	-0.135	-0.155
11	44	-0.275	-0.035	-0.155	-0.178
11.5	46	-0.299	-0.04	-0.170	-0.195
12	48	-0.321	-0.042	-0.182	-0.209
12.5	50	-0.333	-0.049	-0.191	-0.220
13	52	-0.342	-0.045	-0.194	-0.223
13.5	54	-0.348	-0.022	-0.185	-0.213
14	56	-0.336	0.009	-0.164	-0.188
14.5	58	-0.329	0.047	-0.141	-0.162

15	60	-0.307	0.091	-0.108	-0.124
15.5	62	-0.287	0.133	-0.077	-0.089
16	64	-0.252	0.181	-0.036	-0.041
16.5	66	-0.209	0.217	0.004	0.005
17	68	-0.179	0.251	0.036	0.041
17.5	70	-0.135	0.271	0.068	0.078
18	72	-0.096	0.286	0.095	0.109
18.5	74	-0.064	0.297	0.117	0.134
19	76	-0.039	0.3	0.131	0.150
19.5	78	-0.021	0.293	0.136	0.156
20	80	-0.015	0.291	0.138	0.159
20.5	82	-0.008	0.276	0.134	0.154
21	84	-0.009	0.254	0.123	0.141
21.5	86	-0.022	0.233	0.106	0.121
22	88	-0.032	0.214	0.091	0.105
22.5	90	-0.046	0.192	0.073	0.084
23	92	-0.071	0.161	0.045	0.052
23.5	94	-0.089	0.141	0.026	0.030
24	96	-0.111	0.115	0.002	0.002
24.5	98	-0.129	0.087	-0.021	-0.024
25	100	-0.154	0.064	-0.045	-0.052
25.5	102	-0.183	0.045	-0.069	-0.079
26	104	-0.204	0.029	-0.088	-0.101
26.5	106	-0.233	0.014	-0.110	-0.126
27	108	-0.254	0.019	-0.118	-0.135
27.5	110	-0.274	0.038	-0.118	-0.136
28	112	-0.29	0.082	-0.104	-0.120
28.5	114	-0.298	0.135	-0.082	-0.094
29	116	-0.301	0.171	-0.065	-0.075
29.5	118	-0.291	0.2	-0.046	-0.052
30	120	-0.266	0.236	-0.015	-0.017
30.5	122	-0.224	0.271	0.024	0.027
31	124	-0.2	0.307	0.054	0.062
31.5	126	-0.204	0.332	0.064	0.074
32	128	-0.186	0.355	0.085	0.097
32.5	130	-0.161	0.38	0.110	0.126
33	132	-0.145	0.387	0.121	0.139
33.5	134	-0.112	0.394	0.141	0.162
34	136	-0.104	0.38	0.138	0.159
34.5	138	-0.08	0.373	0.147	0.168
35	140	-0.076	0.361	0.143	0.164
35.5	142	-0.077	0.34	0.132	0.151
36	144	-0.098	0.318	0.110	0.127
36.5	146	-0.113	0.305	0.096	0.110

37	148	-0.13	0.274	0.072	0.083
37.5	150	-0.161	0.238	0.039	0.044
38	152	-0.191	0.214	0.012	0.013
38.5	154	-0.221	0.187	-0.017	-0.020
39	156	-0.252	0.159	-0.047	-0.053
39.5	158	-0.277	0.131	-0.073	-0.084
40	160	-0.317	0.105	-0.106	-0.122
40.5	162	-0.355	0.048	-0.154	-0.177
41	164	-0.379	0.02	-0.180	-0.206
41.5	166	-0.395	-0.025	-0.210	-0.242
42	168	-0.431	-0.034	-0.233	-0.267
42.5	170	-0.45	-0.038	-0.244	-0.281
43	172	-0.466	-0.048	-0.257	-0.296
43.5	174	-0.487	-0.059	-0.273	-0.314
44	176	-0.492	-0.006	-0.249	-0.286
44.5	178	-0.491	0.032	-0.230	-0.264
45	180	-0.482	0.056	-0.213	-0.245
45.5	182	-0.448	0.097	-0.176	-0.202
46	184	-0.423	0.143	-0.140	-0.161
46.5	186	-0.39	0.192	-0.099	-0.114
47	188	-0.326	0.221	-0.053	-0.060
47.5	190	-0.269	0.257	-0.006	-0.007
48	192	-0.204	0.282	0.039	0.045
48.5	194	-0.159	0.29	0.066	0.075
49	196	-0.092	0.293	0.101	0.116
49.5	198	-0.053	0.281	0.114	0.131
50	200	-0.026	0.269	0.122	0.140
50.5	202	-0.022	0.252	0.115	0.132
51	204	-0.026	0.238	0.106	0.122
51.5	206	-0.032	0.22	0.094	0.108
52	208	-0.055	0.194	0.070	0.080
52.5	210	-0.07	0.171	0.051	0.058
53	212	-0.092	0.136	0.022	0.025
53.5	214	-0.117	0.114	-0.002	-0.002
54	216	-0.141	0.087	-0.027	-0.031
54.5	218	-0.159	0.064	-0.048	-0.055
55	220	-0.183	0.04	-0.072	-0.082
55.5	222	-0.208	0.022	-0.093	-0.107
56	224	-0.226	0.003	-0.112	-0.128
56.5	226	-0.257	-0.012	-0.135	-0.155
57	228	-0.282	-0.02	-0.151	-0.174
57.5	230	-0.306	-0.018	-0.162	-0.186
58	232	-0.313	-0.011	-0.162	-0.186
58.5	234	-0.312	0.011	-0.151	-0.173

59	236	-0.306	0.028	-0.139	-0.160
59.5	238	-0.295	0.059	-0.118	-0.136
60	240	-0.288	0.089	-0.100	-0.114
60.5	242	-0.27	0.12	-0.075	-0.086
61	244	-0.251	0.149	-0.051	-0.059
61.5	246	-0.215	0.179	-0.018	-0.021
62	248	-0.186	0.206	0.010	0.012
62.5	250	-0.148	0.228	0.040	0.046
63	252	-0.118	0.25	0.066	0.076
63.5	254	-0.084	0.253	0.085	0.097
64	256	-0.072	0.251	0.090	0.103
64.5	258	-0.068	0.246	0.089	0.102
65	260	-0.059	0.232	0.087	0.099
65.5	262	-0.052	0.221	0.085	0.097
66	264	-0.066	0.204	0.069	0.079
66.5	266	-0.074	0.182	0.054	0.062
67	268	-0.088	0.171	0.042	0.048
67.5	270	-0.098	0.145	0.024	0.027
68	272	-0.115	0.123	0.004	0.005
68.5	274	-0.137	0.098	-0.020	-0.022
69	276	-0.16	0.075	-0.043	-0.049
69.5	278	-0.178	0.053	-0.063	-0.072
70	280	-0.203	0.035	-0.084	-0.097
70.5	282	-0.219	0.009	-0.105	-0.121
71	284	-0.244	-0.04	-0.142	-0.163
71.5	286	-0.26	-0.01	-0.135	-0.155
72	288	-0.275	-0.014	-0.145	-0.166
72.5	290	-0.295	-0.012	-0.154	-0.177
73	292	-0.309	0.013	-0.148	-0.170
73.5	294	-0.315	0.074	-0.121	-0.139
74	296	-0.31	0.14	-0.085	-0.098
74.5	298	-0.3	0.2	-0.050	-0.058
75	300	-0.283	0.244	-0.020	-0.022
75.5	302	-0.248	0.297	0.025	0.028
76	304	-0.207	0.338	0.066	0.075
76.5	306	-0.154	0.372	0.109	0.125
77	308	-0.114	0.417	0.152	0.174
77.5	310	-0.085	0.42	0.168	0.193
78	312	-0.048	0.43	0.191	0.220
78.5	314	-0.032	0.423	0.196	0.225
79	316	-0.016	0.42	0.202	0.232
79.5	318	-0.021	0.404	0.192	0.220
80	320	-0.028	0.396	0.184	0.212
80.5	322	-0.023	0.373	0.175	0.201

81	324	-0.048	0.353	0.153	0.175
81.5	326	-0.101	0.321	0.110	0.127
82	328	-0.111	0.282	0.086	0.098
82.5	330	-0.137	0.263	0.063	0.072
83	332	-0.16	0.229	0.035	0.040
83.5	334	-0.201	0.199	-0.001	-0.001
84	336	-0.23	0.181	-0.025	-0.028
84.5	338	-0.243	0.153	-0.045	-0.052
85	340	-0.265	0.116	-0.075	-0.086
85.5	342	-0.3	0.09	-0.105	-0.121
86	344	-0.328	0.06	-0.134	-0.154
86.5	346	-0.35	0.048	-0.151	-0.174
87	348	-0.382	0.019	-0.182	-0.209
87.5	350	-0.416	-0.002	-0.209	-0.240
88	352	-0.434	-0.18	-0.307	-0.353
88.5	354	-0.457	-0.001	-0.229	-0.263
89	356	-0.469	0.05	-0.210	-0.241
89.5	358	-0.456	0.018	-0.219	-0.252
90	360	-0.452	-0.088	-0.270	-0.311

3.6.3 On-Load Torque Tests

The on-load static torque test looks at the performance when a DC current is applied to the baseline machine. This characteristic is used to show the relationship between the current applied to the machine and the torque it produces. The same procedures are used as in no-load tests, but in this case with applied current. However, during testing no noticeable temperature rise was felt on the outer case. Figure 3-16 compares 3D FEA and measured on-load static torque with applied current over a complete electrical cycle switching period.

The results show that torque increases as the applied current increase and the period of the measured torque is similar to that of the 3D FEA , but the magnitude of the measured peak torque is 0.55 Nm; an 8.5% reduction as compared to 3D FEA. This reduction is due to mechanical error in the assembly of the prototype baseline machine. The net static torque can be obtained by subtracting the measured no-load static torque from the measured on-load static torque tests at the same mechanical and electrical position.

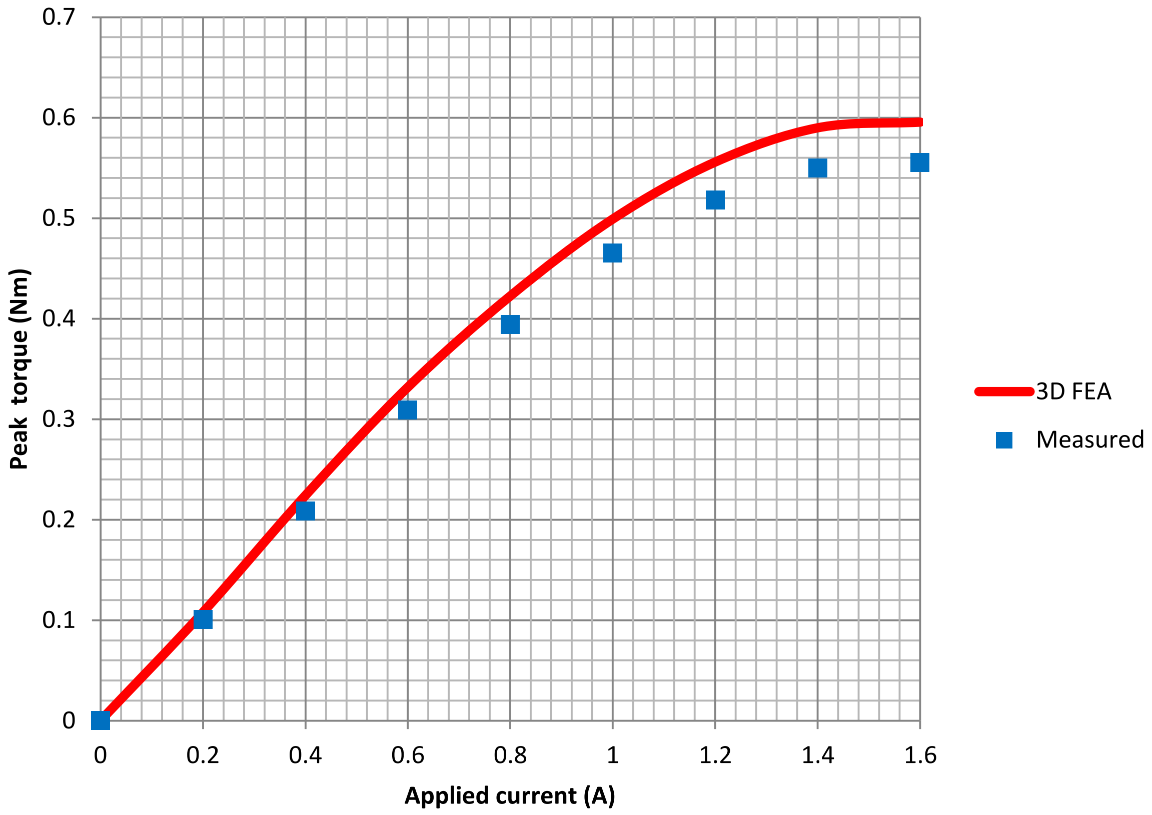

Figure 3-16: 3D FEA and Measured on-load static torque.

3.7 Performance Summary

Table 3-4 summarises the performance of baseline machine based on SMC material and 3000 rpm by comparing the predicted 3D FEA and measured machine static performance. It is noted that the measured peak torque is 0.55 Nm; an 8.50% less than the predicted peak torque and the average no-load ripple of 39% for the measured as compared to the 41% of the 3D FEA. The machine has peak measured net torque of 0.48 Nm, a decrease of 2.05% as compared to the predicted net average torque.

Table 3-4: Performance Summary

Output parameters	3D FEA	Measured	% Change
Peak Torque (Nm)	0.59	0.55	8.50
No-load torque ripple (%)	41	39	4.90
Net peak Torque (Nm)	0.49	0.48	2.05

3.8 Conclusion

In this chapter verification of a baseline machine developed at Newcastle University using 3D FEA and experimental tests were presented. The main problems highlighted were low efficiency due to high losses in the machine as a result of open-slot stator winding configuration, low on-load torque and back EMF harmonics and therefore high torque ripple due to interaction between the MMF and airgap flux harmonics.

The machine produces 8.5% less peak torque than the 3D FEA peak torque. This proximity at an early prototype stage is encouraging. Damage and error during the assembly and construction of the prototype stator may account for the reduction in torque and the accuracy of the torque transducer. However, there is a significant 3^{rd}, 5^{th} and 7^{th} harmonics at 2.6%, 9.3% and 3.3% respectively of the fundamental harmonic in the back EMF, which is too high and need to be reduce. From the 3D FEA analysis the machine exhibits efficiency of 65.5% this is as a result of open-slot stator construction which encourage an elevated AC winding loss at AC operation.

The average flux density attained in the machine SMC core is approximately 0.7 T as shown in Figure 3.3 and it is clear that the material was working hard on a maximum average flux density of 0.7 T.

Higher performance could not be achieve as a results of trapezium shape in the stator tooth, the pre-wound coils require a sharp turn to fit over the teeth and a rounder tooth corner as shown in Figure 3-17 will help with the coil construction, and may allow for an additional layer of turns, thereby allowing for more MMF and torque per amp. Moreover, changing the slot and poles number combination of the baseline machine will also help in reducing the amplitude of the significant harmonics beyond the fundamental.

The double-sided AFM would produce higher specific torque, but in this analysis only single-sided surface-mounted AFM is considered for simple manufacturing process and as a demonstrator to avoid the balancing position problem in the double-sided configuration.

Chapter 4 presents the design improvement of the baseline machine to achieve higher performance by altering the main dimension of the machine described in this chapter based on the available dimension of the SMC prototype material.

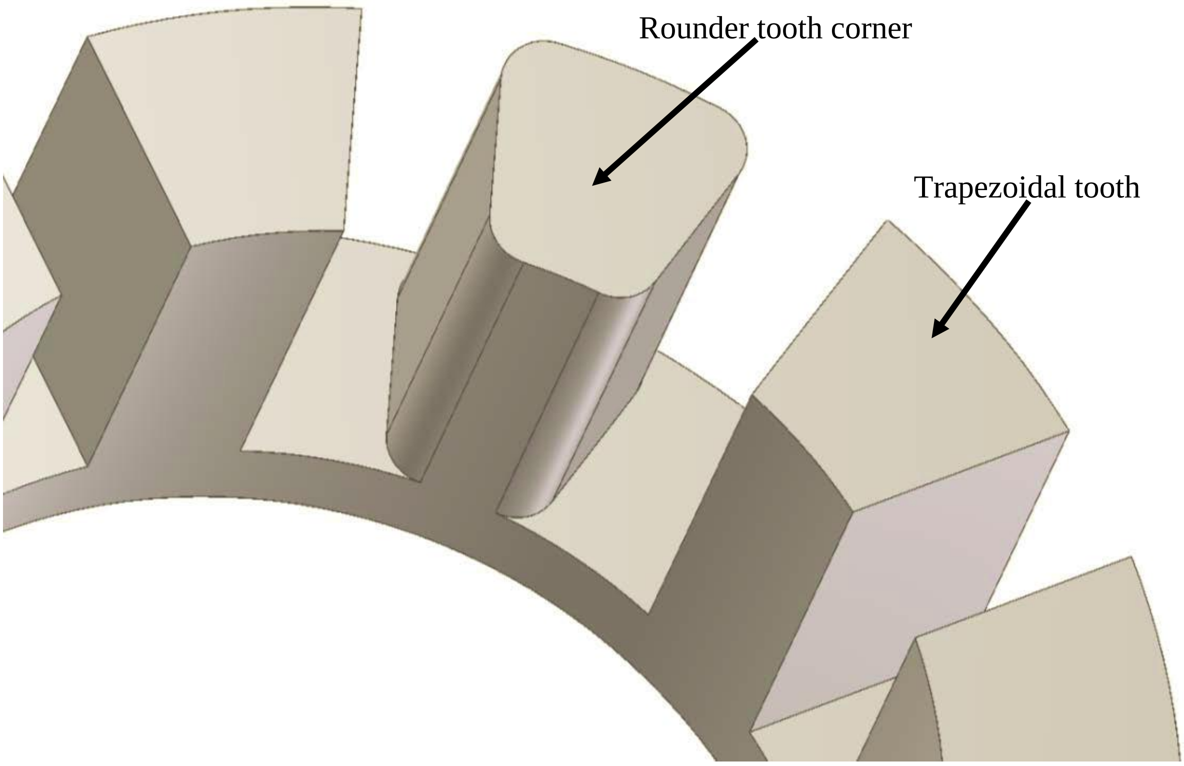

Figure 3-17: **Current and proposed rounded tooth stator.**

4. Design and Investigations

This chapter will present the design improvement and investigation of sensitivity of torque on parameters variation, which includes airgap length, magnet thickness, magnet span, slot width, inner/outer radius and core-back thickness of the stator and rotor. The cogging torque produced by baseline machine describes in Chapter 3 is very high and account for 39% of the machine total torque at rated current due to high torque ripple. Other problems encountered in the machine are the harmonics in the induced back EMF, high losses due to open-slot stator winding configuration and low efficiency.

In this design, we are looking to meet or exceed the performance of the baseline machine reported in Chapter 3 by altering most of the machine specifications that were presented in Table 3-1; moreover we are limiting the size of the new machine due to available SMC prototype material (maximum diameter 120 mm).

A basic analytical model was developed to speed the initial design process followed by 3D finite element electromagnetic simulation software (Infolytica MagNet), in which a fully parameterised AFM model was created, all stator and rotor dimensions and electrical input can be altered.

An initial design is generated to exceed the torque produced by baseline machine in Chapter 3, and this is then applied to an optimisation routine which alters the parameters automatically and assesses the results according to a set of design parameters. Optimisation can be done for minimal magnet mass, axial length and losses and high efficiency.

4.1 Introduction

The torque of AFM depends on the outer diameter and electrical loading; the outer diameter in this case is limited by the available SMC Somaloy prototype material developed by Höganäs AB of Sweden which has a maximum outer diameter of 120 mm. There are several methods as mentioned in Chapter 2, section 2.6.4 [72-75] which can be utilised to reduce cogging torque as well increase the torque of a machine.

In AFM, increasing the outer diameter can have a great effect on the torque since torque is proportional to the cube of outer diameter as stated in Chapter 2, equation (2.1). Increasing the electrical loading (by expanding the slot area) can give rise to increment in torque at the same time increasing the losses. Similarly, the strength of the magnets use in the machine has an impact on the flux in the airgap which determines the cogging torque magnitude.

The slot and pole number combination in a machine has an effect on back EMF harmonics; a good combination would be selected to have low induced EMF harmonics which can improve the torque of the new machine.

SMC will be utilised in both the stator and rotor for lower losses at rated speed and a rounded tooth corner will help with the coil construction as suggested in Chapter 3 as shown in Figure 3-17, and may allow for an additional layer of turns, thereby allowing for more MMF and torque per amp. The machine will be tested as a 3-phase generator feeding a 3-phase resistive load bank at unity power factor using a high-speed test rig.

4.2 Analytical Design Approach

A basic analytical model of the AFM was used in order to speed the initial design process and the following assumptions were made;

1. The airgap flux density is uniform parallel to the stator tooth tips and zero parallel to the slot opening.
2. The maximum outer diameter of stator and rotor disc is 110 mm.
3. The current density is 5A/mm^2 and a 70% fill factor is assumed for high performance.
4. The diameter of the copper wire was based on the number of turns calculated and nearest AWG/SWG.
5. The coil cross sectional area is half of the stator cross sectional area.

The simplified slot layout shown in Figure 4-1 was used to obtain the area of the slot, copper area, coil MMF, conductor area, number of turns and current in the conductor. The area of the slot A_s is given by as the product of the slot width and slot height.

$$A_s = W \times H \tag{4.1}$$

where W is the width of the slot and H is the height of the slot in millimetres.

Copper area A_{cu} is given by the product of the slot area and slot fill factor as in equation (4.2).

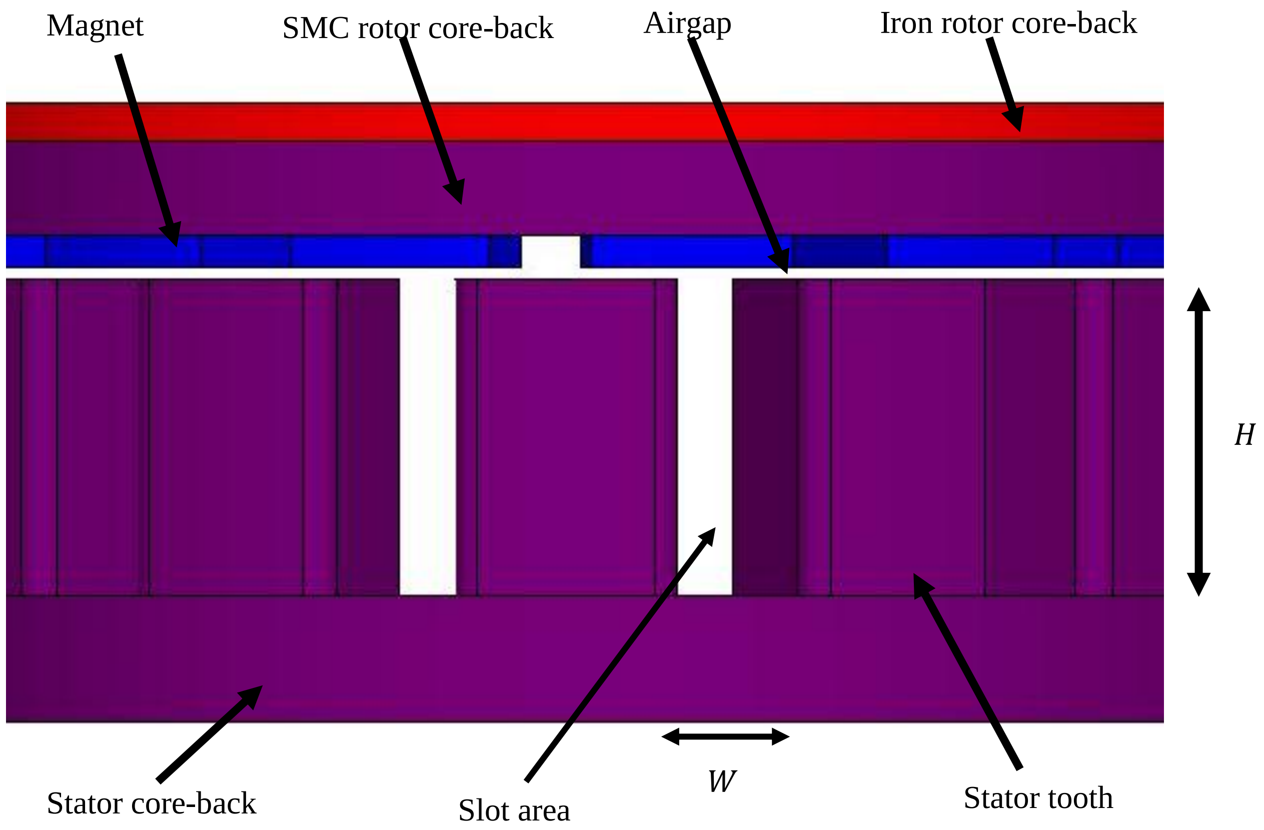

Figure 4-1: Simplified slot layout.

$$A_{cu} = A_s \times F_F \tag{4.2}$$

where A_s is the area of the slot in mm^2 and F_F is the fill factor

The total coil MMF in the slot is obtained as the product of the copper area and current density using equation (4.3) below.

$$MMF = A_{cu} \times J \tag{4.3}$$

where J is the current density in A/mm^2 and assume at 5 A/mm^2

Similarly, the conductor area is given by equation (4.4) below.

$$A_{con} = \pi r^2 \tag{4.4}$$

where r is the radius of the conductor in millimetres and the number of turns N in the slot is obtain by dividing the copper area by conductor area as shown in equation (4.5) below.

$$N = \frac{A_{cu}}{A_{con}} \tag{4.5}$$

Finally, the current in the conductor I_{con} is also obtained by multiplying the conductor area and the current density as presented in equation (4.6) below.

$$I_{con} = A_{con} \times J \tag{4.6}$$

The coil resistance of the stator winding denoted as R_{coil} is calculated based on estimating the total length and cross sectional area of the conductor and is given in equation (4.7) below [116].

$$R_{coil} = \rho_{cu} \frac{N2\pi l_{com}}{A_{con}} \tag{4.7}$$

where l_{con} is the mean radius of armature coil, A_{con} is the cross sectional area of conductor and in this case N is the number of turns/coil and ρ_{cu} is the electrical resistivity of copper.

The main objective of winding design is to achieve a certain level of flux density at the airgap with minimal losses. Slot dimension, turns number, coil diameter, machine speed, skin effect and current density are parameters that play vital roles in the design of coils. For simplicity and to achieve high fill factor, concentrated winding is used and the coil resistance of the stator winding can be obtained from equation (4.7) above.

The winding factor of the fundamental harmonic which is the product of the distribution factor and the pitch factor can be obtained from the induced voltage equation as stated in [19]. In general, it can be found from the phase EMF phasor vector graph as described in [117] and is given as in equation (4.8) below.

$$E = 4.44 N_{ph} \Phi_{pk} k_{w1} f \tag{4.8}$$

where k_{w1} is the winding factor and f is the electrical frequency in Hz.

The analytical ways of determining winding factor are also given in [118] in which transforming the winding from double layer to single layer can increase the winding factor.

4.3 3D FEA Modelling

FEA is a numerical method that can accurately analyse complex electromagnetic fields using Maxwell equations. Due to 3D geometry of AFM and that of SMC material, the machine was modelled using 3D FEA package Infolytica MagNet to predict the performance of the machine.

This section presents the initial analysis of the machine design and results reported include the selection of slot and pole number combination, meshing sensitivity on the total loss and 3D arrow plot, H tangential and shaded plot |B| smoothed field view of the machine at full-load current.

A parameterised machine model was created with an odd periodic boundary condition applied to the half edge of the model and a field normal boundary condition is applied to the shaft position in the model. This reduced the time required to solve the model by half and by reducing the number of elements it contains as running a full model is time consuming.

110 mm outer diameter with 25 mm slot depth, sintered magnets (N35SH), constant current density and round tooth are used as the baseline in this design investigation analysis. The reason for using 110 mm was based on the maximum availability of the prototype material outer diameter of 120 mm and to allow the remaining 10 mm for machining in the process of construction and production of the prototype machine.

The machine has 12 tooth stator and 14 numbers of poles on the rotor which means the structure of the machine has a periodicity of 180 degrees. Hence, half of the machine model was created to reduce the computation time by half as shown in Figure 4-2. Two different materials were utilised in the rotor that is the SMC and a solid stainless steel, the idea of using the stainless steel is to enable screws to be use in attaching the shaft to the rotor as it is not practical to fix the shaft directly on the SMC rotor using screws. Appendix A gives the final main dimension and specification of the machine.

The model was first generated using a 2D model and extruded axially to form a full 3D model and SMC Somaloy 700HR 3P material with electric resistivity of 0.6 kΩm at 20ºC was used. The typical B-H characteristic of the material is shown in Appendix C, and the data of the material was used to input all other information regarding the material in the software which includes;

1. Magnetic permeability.
2. Iron loss.
3. Electric resistivity.
4. Permittivity.
5. Mass density.

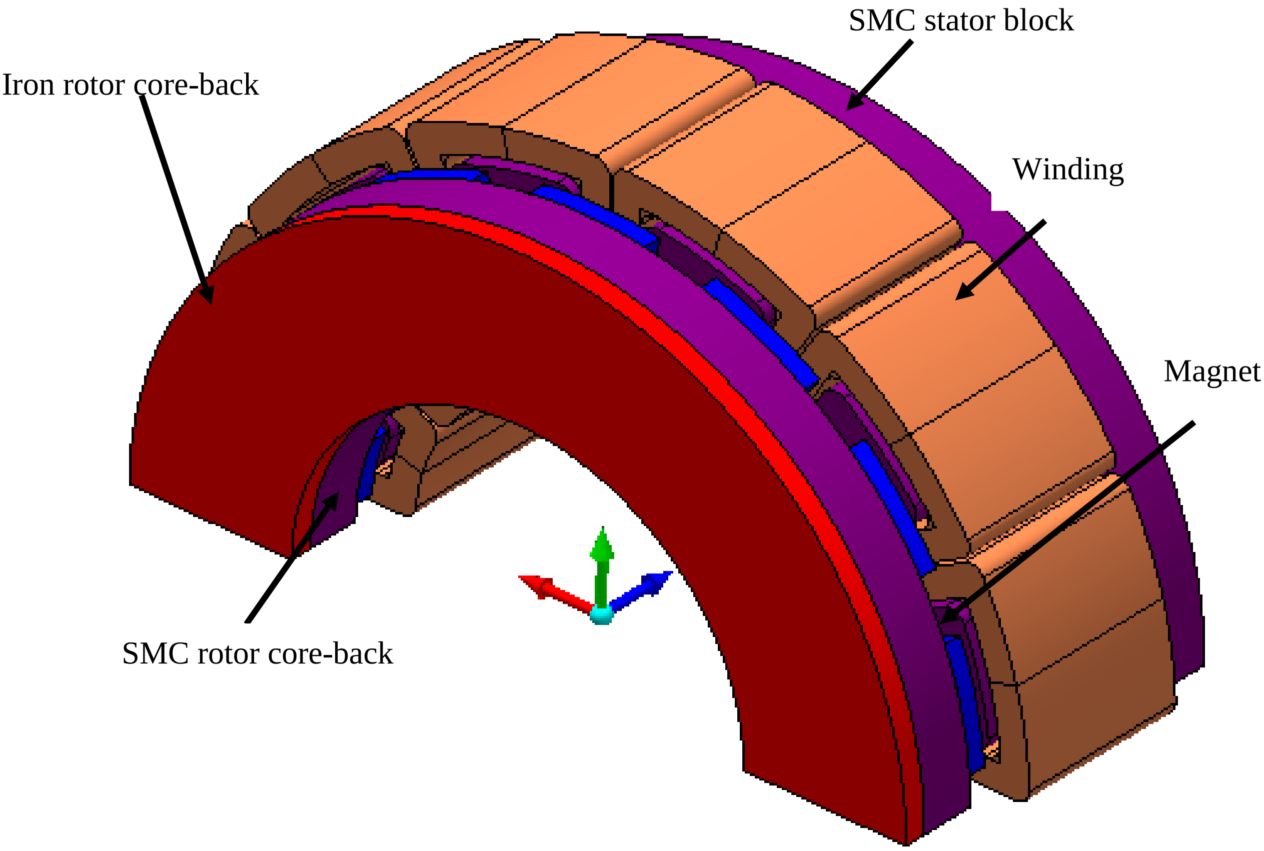

Figure 4-2: 3D FEA half model of the machine.

From the data sheet it is clear that the B-H curve of SMC is sensitive to the compaction process and so varies depending on the method of moulding. Neodymium Iron Boron N35SH magnet and copper with 100% IACS are used as materials in the magnets and conductors respectively.

The machine speed is 6000 rpm, the electrical frequency, mechanical frequency and simulation time steps can be calculated as:

Mechanical frequency f_m is given as:

$$f_m = \frac{rpm}{60} = \frac{6000}{60} = 100\ Hz \tag{4.9}$$

Mechanical angular frequency ω_m can be obtained using equation (4.10) below.

$$\omega_m = 2\pi f_m = 628.4\ rad/sec \tag{4.10}$$

The mechanical revolution time t_m is obtained as in equation (4.11) below.

$$t_m = \frac{1}{f_m} = \frac{1}{100} = 0.01\ sec \tag{4.11}$$

The electrical frequency f_e for 14 pole machine (7 pole pairs) at 6000 rpm is given as:

$$f_e = pole\ pairs \times\ f_m = 7 \times 100 = 700\ Hz \tag{4.12}$$

Electrical angular frequency ω_e can be obtained using equation (4.13) below.

$$\omega_e = pole\ pairs\ \times \omega_m = 7 \times 628.4 = 4398.8\ rad/sec \tag{4.13}$$

The electrical revolution time t_e is obtained as in equation (4.14) below.

$$t_e = \frac{1}{f_e} = \frac{1}{700} = 1.4285\ msec \tag{4.14}$$

The above values were inserted in fixed interval time step method of the transient option in the Infolytica MagNet software and used in the analysis of the machine.

4.3.1 Slot and Pole Combination

In this design, 12 stator tooth and 14 poles rotor (12S14P) is used. The slot depth is chosen to maintain the tooth and core-back flux densities at rated speed. Table 4-1 summarised the possible tooth and pole combination for a three-phase concentrated winding with twelve teeth. The increase in pole number affects the harmonics and allows for a thinner core-back and hence greater slot depth, within the same axial length. In [52], the slot and pole number selection for double-sided AFM that used SMC as stator core was described.

Figure 4-3 presented the variation of airgap flux density with electrical angle in the machine and it is clear that the flux density attained a maximum value of 0.8 T within the machine airgap.

Table 4-1: Possible Tooth/Pole Combination

Pole pairs	Tooth number	Coil span [°]electrical
4	12	120
5	12	150
7	12	210
8	12	240

The slot depth of a machine has effects on the extent of saturation in the teeth which would modify the slot ripple component in the airgap flux density however if the magnitude of slot ripple flux is too significant, it may lead to consequent torque ripple in the machine.

The width of the slot opening varies with different positions on the airgap flux which lead to the main harmonic in the airgap to gradually shift from third harmonic to second harmonic and less affected when the slot width is the same as the gap between two permanent magnets.

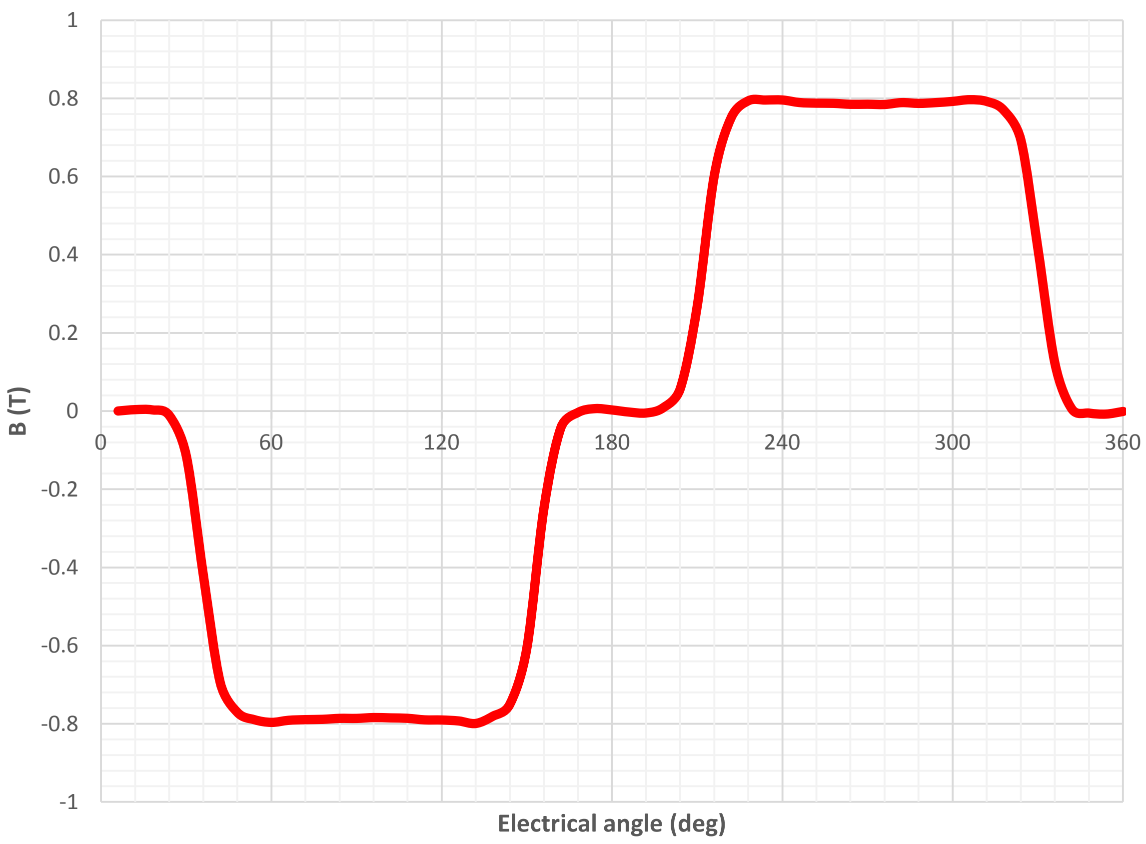

Figure 4-3: Airgap flux density variation with electrical angle in the machine.

Figure 4-4 presented the effect of number of pole pairs on the average torque and total loss in the machine. From 3D FEA the result shows that the lower the number of pole pairs the higher the average torque, 4 pole pairs have the highest torque of 3.12 Nm and 8 pole pairs has the lowest torque of 1.53 Nm. Moreover, the 5 pole pairs and 7 pole pairs have average torque of 2.77 Nm and 2.08 Nm respectively.

This analysis is carried out with the same magnet mass, rotor core-back and overall axial length in the machine. The reason for chosen the 7 pole pairs is based on the total loss associated with each pole pairs.

It can be seen from the bar chart of Figure 4-4 that, 4 pole pairs has the highest total loss, while 7 pole pairs with the lowest total loss. The total loss in 7 pole pairs represents 47%, 29% and 35% decreased as compared to 4 pole pairs, 5 pole pairs and 8 pole pairs respectively.

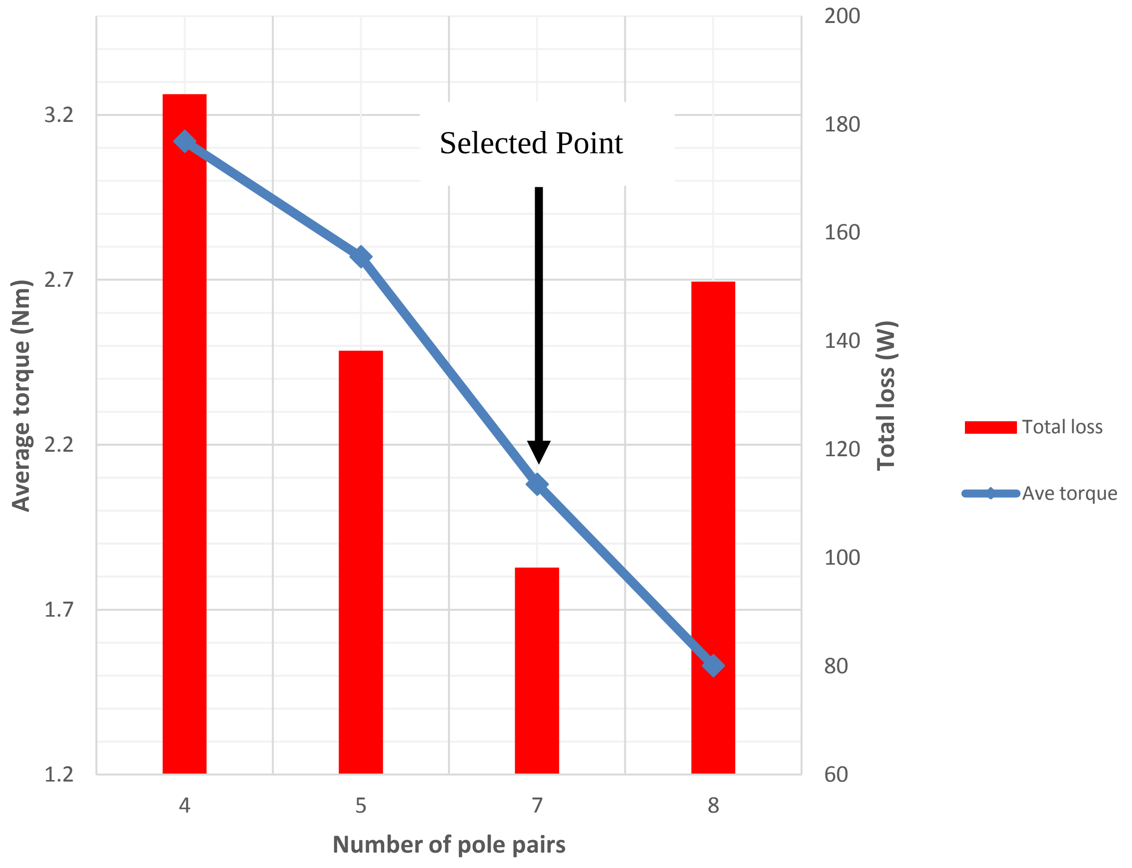

Figure 4-4: Effect of number of pole pairs on average torque and total loss.

4.3.2 Meshing Sensitivity

The level of meshing size used in the machine model determines the time taken for computation and results accuracy, the finer the mesh size the more accurate the numerical results and smoother wave forms. The field inside each element is a set of polynomial functions with unknown coefficient and shape like tetrahedral with four vertices. The most valuable part of the design is to verify the sensitivity of the solution mesh and Figure 4-5 shows the mesh view of the half model together with expanded airgap view.

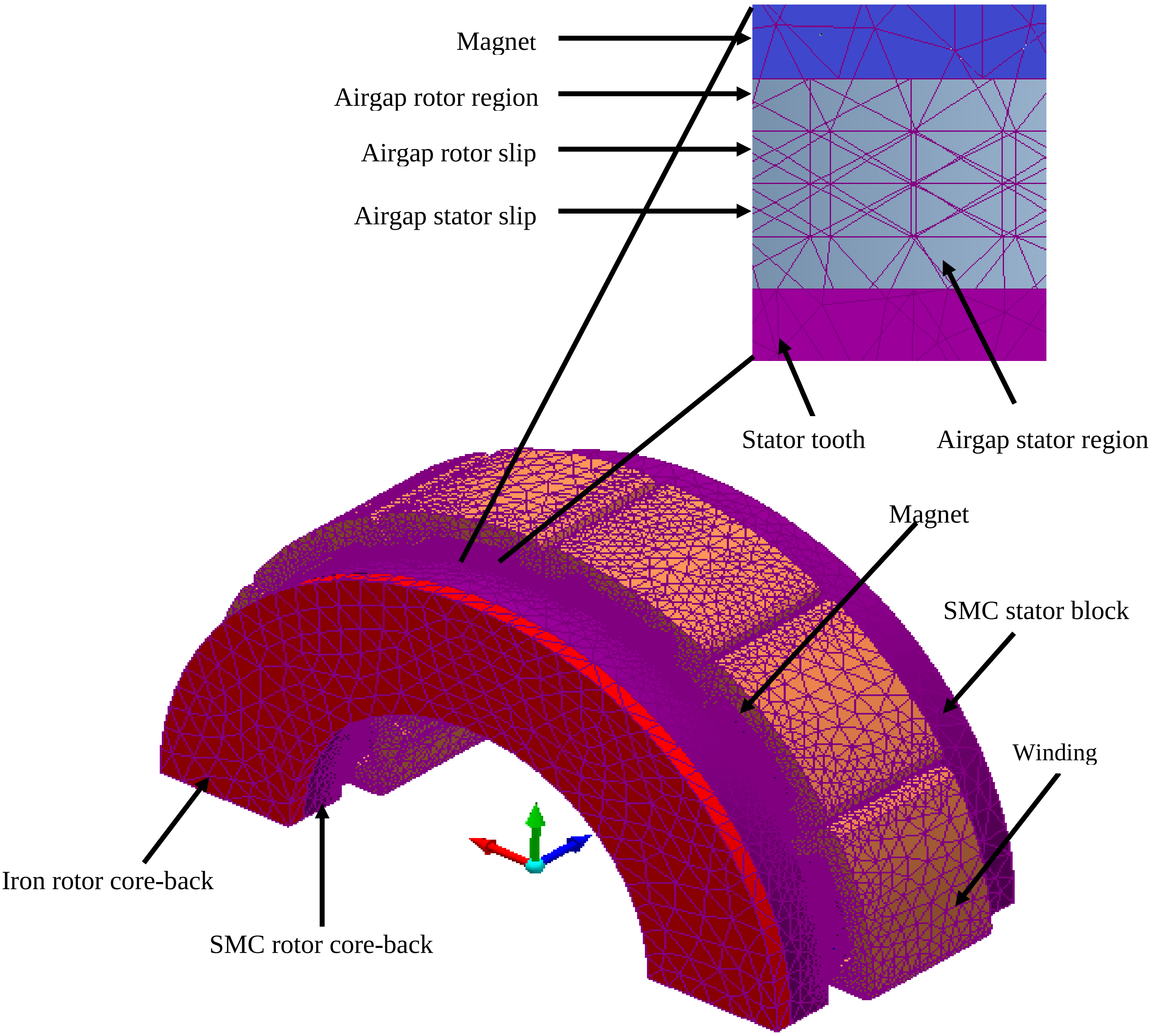

Figure 4-5: 3D FEA mesh of the machine.

The initial analysis is based on 3D Finite Elements solutions, which are highly sensitive to mesh size especially in the airgap region due to changes in the magnetic fields. For reasonable solution the mesh size should be within a practical limit.

The airgap of the machine was divided into four sections as done in the baseline machine analysis described in Chapter 3, namely; stator region, stator slip, rotor slip and rotor region. The stator and rotor air box extend to the airgap by 0.25 mm each on their side and virtual air material was used in that region and in stator slip and rotor slip, air was utilised as material.

The reason for that is to eliminate the possibilities of field’s irregularity in the region, since magnetic field changes direction frequently in those regions. With this set up and mesh size the maximum element in the airgap was over 70,000 elements. The Figure in addition shows a clearly view of the expanded airgap. It can be seen that in the rotor slip and stator slip the meshing is denser compared to rotor airgap region and stator airgap region.

Transient 3D with motion using Newton-Raphson is utilised in solving the model with fixed interval time step method, because in this method each time step is of an equal length, whereas in the adaptive time stepping method, MagNet finds the appropriate time step length for the solution.

The rotary component; rotor slip, rotor airbox, magnets and rotor core-back in the machine were set as the reference paths in motion properties and rotary is used as the motion type in z-direction with velocity driven as the source type. Speed based position was used with initial time of 0 ms and final time of 1.4 ms at 36000 deg/sec, speed corresponding to 6000 rpm. The motion centre was set to zeros in all direction with position and speed at start up. These specification terminologies above are related only to Infolytica MagNet software.

A Larger mesh size was initially used, and the size was reducing until there are little changes in results obtained for both the flux linkages and peak torque. Since half of the machine was modelled, element size of 0.5 mm was applied to the airgap slip and magnet with curvature refinement angle of 1° due to the fact that airgap of the machine is where most energy is stored and field’s direction changes, while the remaining parts element size was kept at 5 mm. in this analysis, the coils element size used was 4 mm, 1 mm and 0.3 mm mesh size. Figure 4-6 presents the side view of the machine half model.

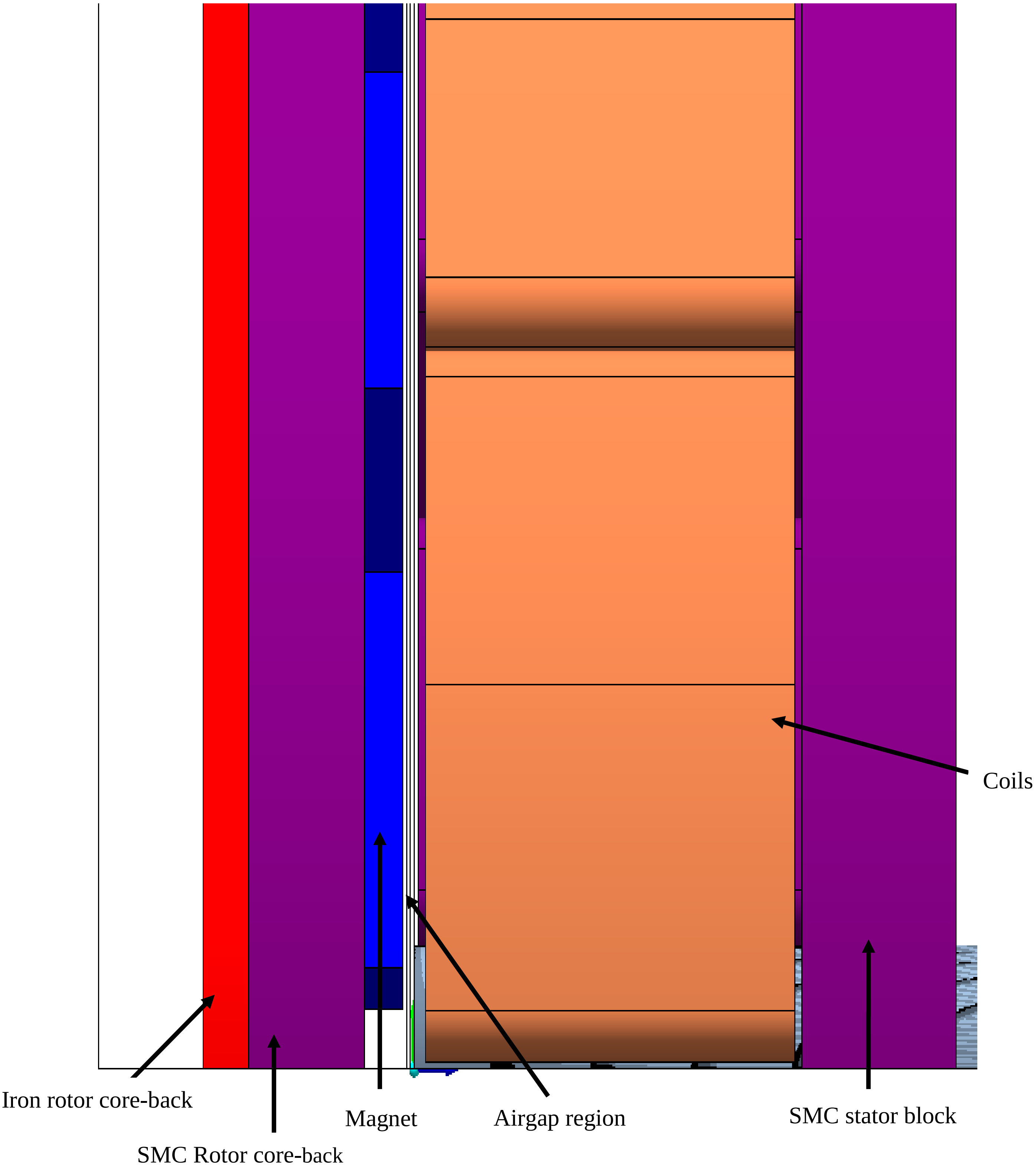

Figure 4-6: Side view of the machine half model.

Figure 4-7 shows the total loss in the machine at different mesh size on the coils. The results show that the smaller the mesh sizes on the coils the higher the loss. The 0.3 mm mesh size total loss is 7.5% higher as compared to 4 mm mesh size due to the fact that larger mesh size underestimates the loss in the conductor layers close to airgap.

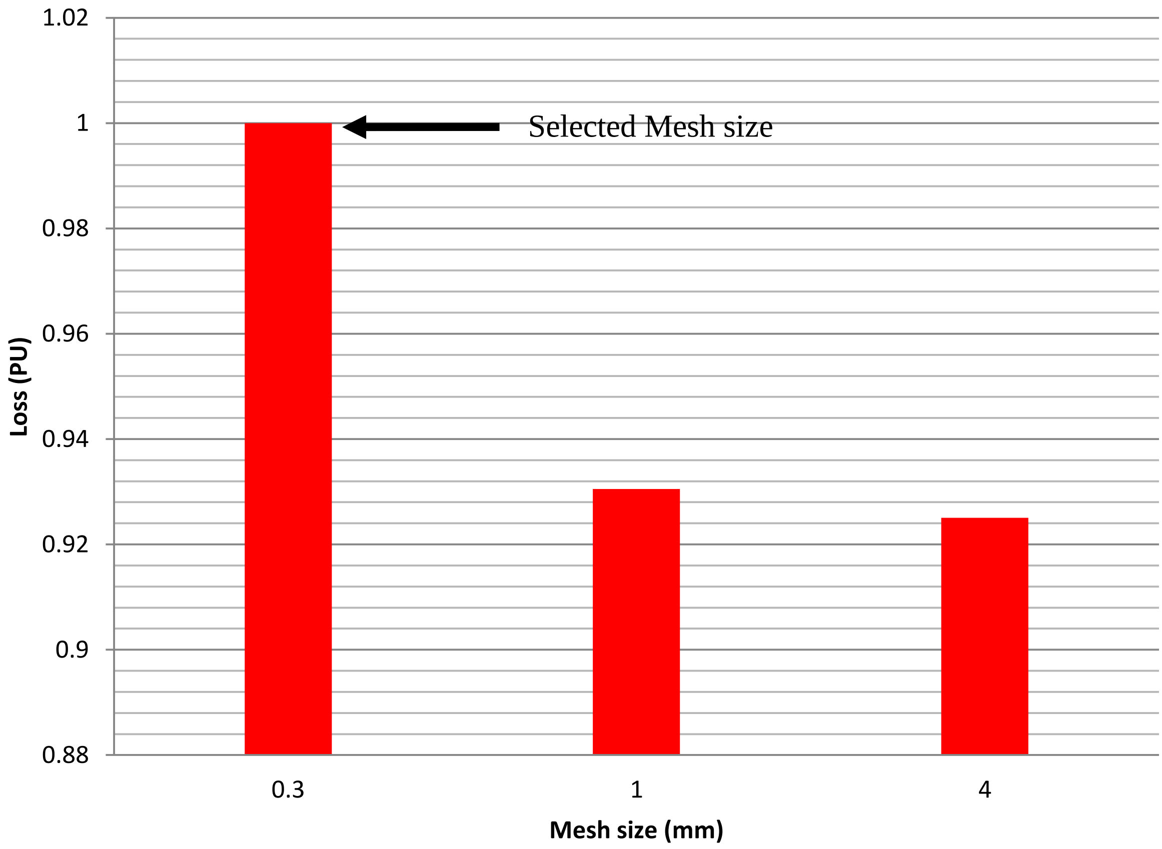

Figure 4-7: Loss variation with mesh size.

Figure 4-8 presented the 3D arrow plot, H tangential and shaded plot |B| smoothed field view of the machine half model at full-load current. From the plot, it is clear that the magnets, SMC core were not saturated when machine is operated at full-load current.

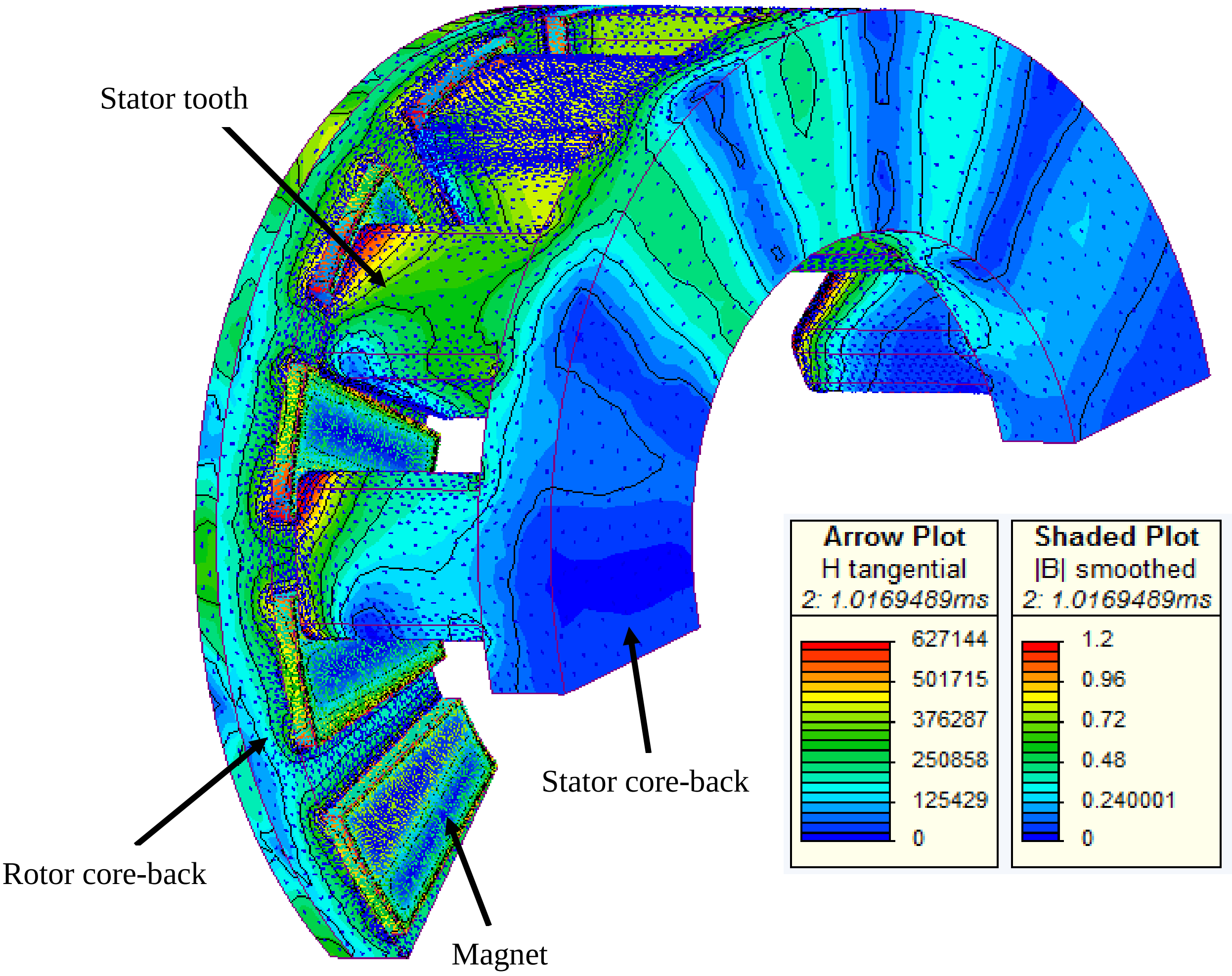

Figure 4-8:3D FEA field view of the machine.

4.4 Parameters Variation Investigation

This section covers investigation on sensitivity of average torque, peak-to-peak cogging torque, power and total loss using 3D FEA on parameters variation, such as airgap length, magnet span and thickness.

4.4.1 Airgap, Magnet Span and Magnet Thickness

The area of applications, the airgap length and magnet size determine the maximum overall axial length of AFM. It is also affected by the large axial force of attraction and mechanical consideration between the stator and the rotor. Large magnet thickness is usually avoided because of the cost involved. Neodymium magnets are popular in almost all permanent magnet machines applications due to its high energy product with suitable magnetic and physical properties. For this design, N35SH sintered neodymium magnets were utilised due to the fact that it can withstand maximum temperature of 150°C with B_r typical of 1.210 T and has electric resistivity of 180 μΩcm. The length of the airgap l_{ag} and the thickness of magnet l_m can be expressed as a function of stator core outer diameter D_o as stated in [19] and are given by the relationship in equation (4.15) and (4.16) below:

$$l_{ag} = 0.0091D_o \tag{4.15}$$

$$l_m = 0.0228D_o \tag{4.16}$$

Figure 4-9 shows the variation of airgap length for optimal average torque and peak-to-peak cogging torque. In this case the magnet thickness and magnet span were kept constant.

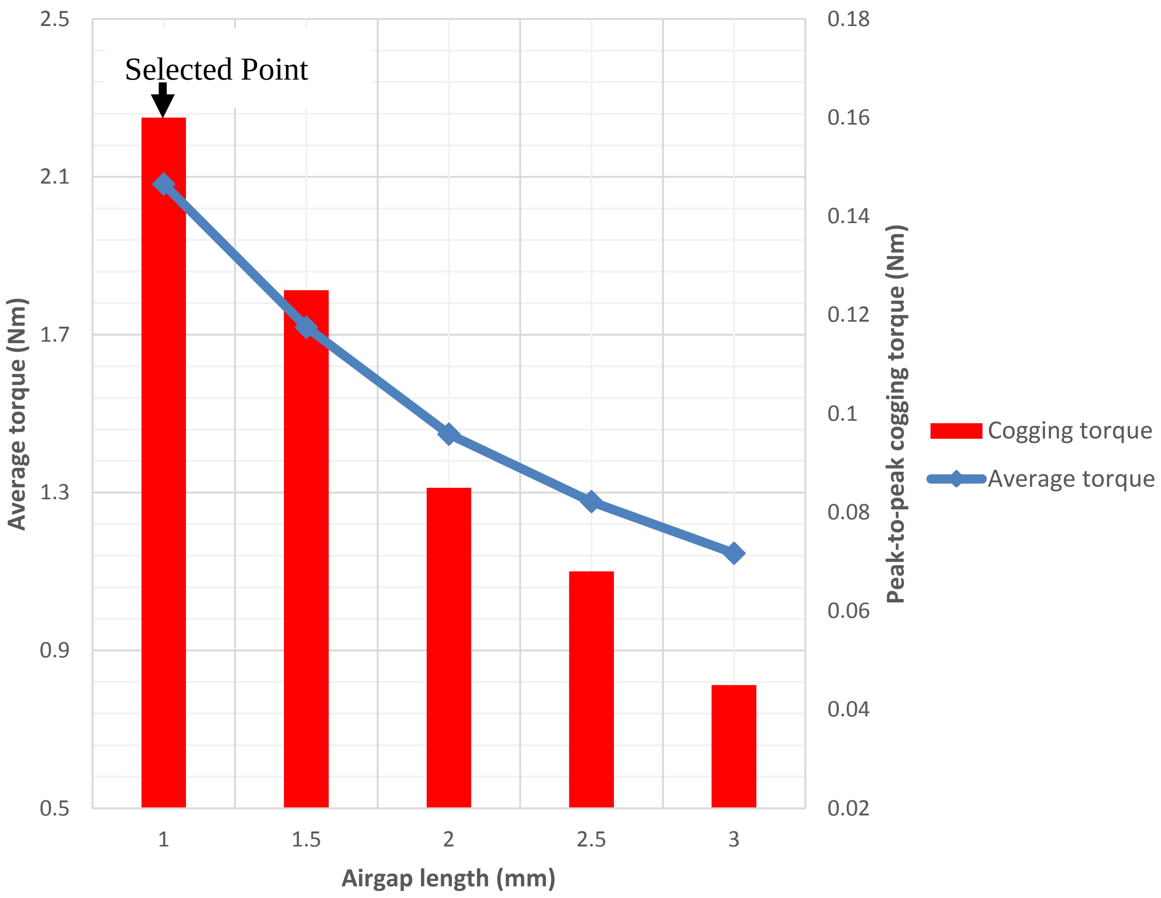

Figure 4-9: Effect of airgap length on average torque and cogging torque.

It can be seen that at 1 mm magnetic airgap the average torque of the machine is 21.1% higher than that at 1.5 mm airgap; moreover it is 43.8%, 63.0% and 81.7% higher at 2 mm, 2.5 mm and 3 mm respectively. The results show that as the magnetic airgap between the stator and rotor increases from 1 mm to 3 mm the average torque of the machine decreases.

Similarly, for different airgap length the results show that the peak-to-peak cogging torque decreases as the magnetic airgap increased, and at 1 mm the peak-to-peak cogging torque is 28%, 88.2%, 135%and 256% higher compared to 1.5 mm, 2 mm, 2.5 mm and 3 mm respectively. Therefore, from the analysis the machine has the maximum average torque and peak-to-peak cogging torque at 1 mm airgap. This configuration was chosen for the final design, since the cogging torque exhibits in the machine is 7.8% of the average torque.

Figure 4-10 shows the average torque, peak-to-peak cogging torque and total loss in the machine when the magnet span was varied at different electrical angles by keeping the magnet thickness constant at 2.5 mm and magnetic airgap at 1 mm. For optimal average torque in AFM the magnet span should range from 120º to 150º as reported in [75].

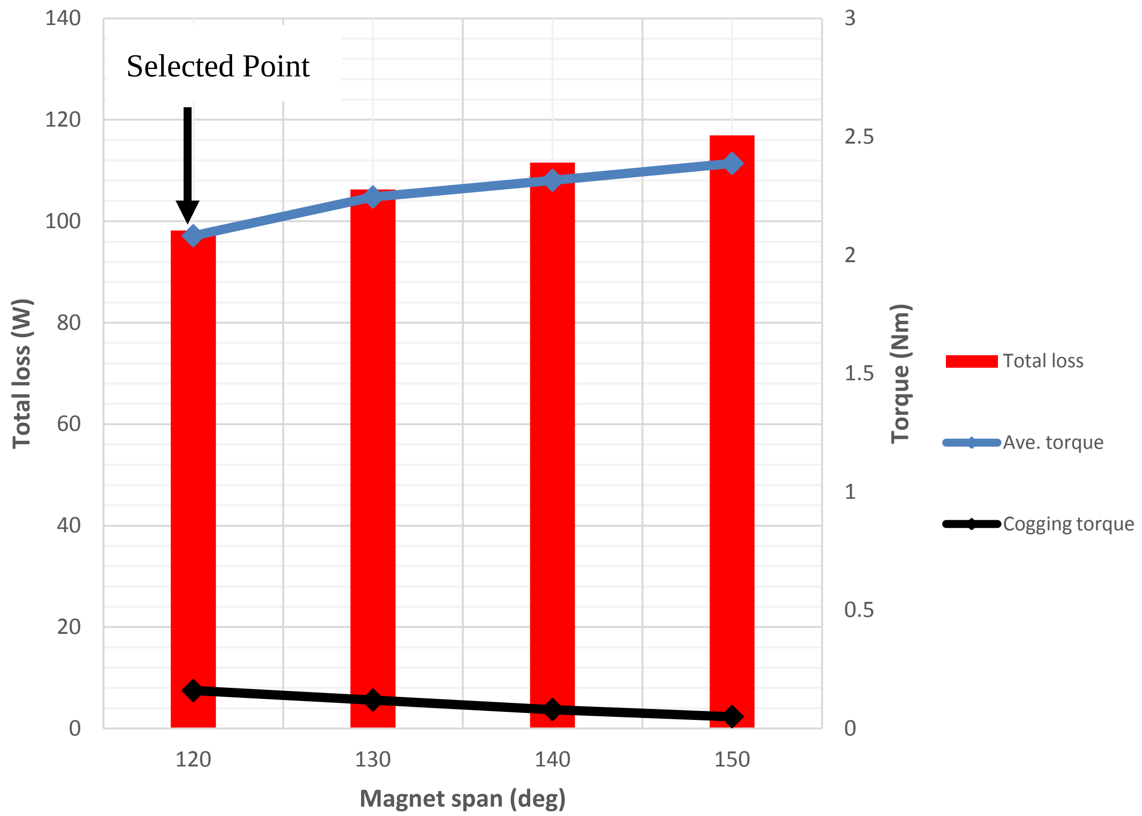

Figure 4-10: Effect of magnet span on average torque, cogging torque and total loss.

When selecting the magnet span stability between the total loss and average torque in machine needs to be formed. It is rational to select a magnet span that gives a lower total loss and average torque but come up with a highly efficient machine than a higher total loss and average torque which can be expensive.

It is very clear that as the magnet span increases the average torque also increases, but the peak-to-peak cogging torque decreases however the losses in the machine also increased. From 120º to 150º magnet span, the average torque increased by 11% and the total loss increased by 19.6%. The result also shows that 120º magnet span has the lowest loss as shown in Figure 4-10.

The 130º magnet span total loss increased by 7.9%, 140º magnet span by 13.6% and 150º magnet span by 19.6% as compared to 120° magnet span respectively. The peak phase back EMF from the FEA shows that the 120° magnet span has the lowest peak back EMF of 113.5 V, and represent a decreased by 3.3%, 5.4% and 7.6% as compared to 130° magnet span, 140º magnet span and 150° magnet span respectively.

The peak total loss for 120º magnet span, 130º magnet span, 140º magnet span and 150º magnet span are 98.18 W, 106.23 W, 111.54 W and 116.96 W respectively. While the peak average torque for 120º magnet span, 130º magnet span, 140º magnet span and 150º magnet span are 2.08 Nm, 2.25 Nm, 2.32 Nm and 2.39 Nm respectively. Furthermore, the peak-to-peak cogging torque for 120º magnet span, 130º magnet span, 140º magnet span and 150º magnet span are 0.16 Nm, 0.12 Nm, 0.08 Nm and 0.05 Nm respectively.

For cost effective and optimal overall performance of the machine, the 120º electrical degree magnet span was chosen for the final design due to low losses associated with it.

Figure 4-11 shows the variations of average torque and torque per active mass of the machine at different magnet thickness, in which the magnet span and magnetic airgap length were kept constant. In this case, the magnet thickness is varied between 2 mm to 4.5 mm and the result shows that the maximum average torque is at 3.5 mm. The machine has the peak average torque at 3.5 mm magnet thickness and lowest at 2 mm magnet thickness, moreover, the torque per active mass of the machine is maximum and minimum at the same magnet thickness as the average torque.

At 2.5 mm thickness the machine exhibits average torque of 2.08 Nm and torque per active mass is 4.5% higher compared to 2 mm magnet thickness and 1.4% 2.5%, 1.92% and 0.5% lower as compared to the 3 mm, 3.5 mm, 4 mm and 4.5 mm magnet thickness respectively. But, 2.5 mm was chosen due to the cost, mechanical issue associated with surface mounted magnets machine and the lower total losses in the machine at that magnet thickness.

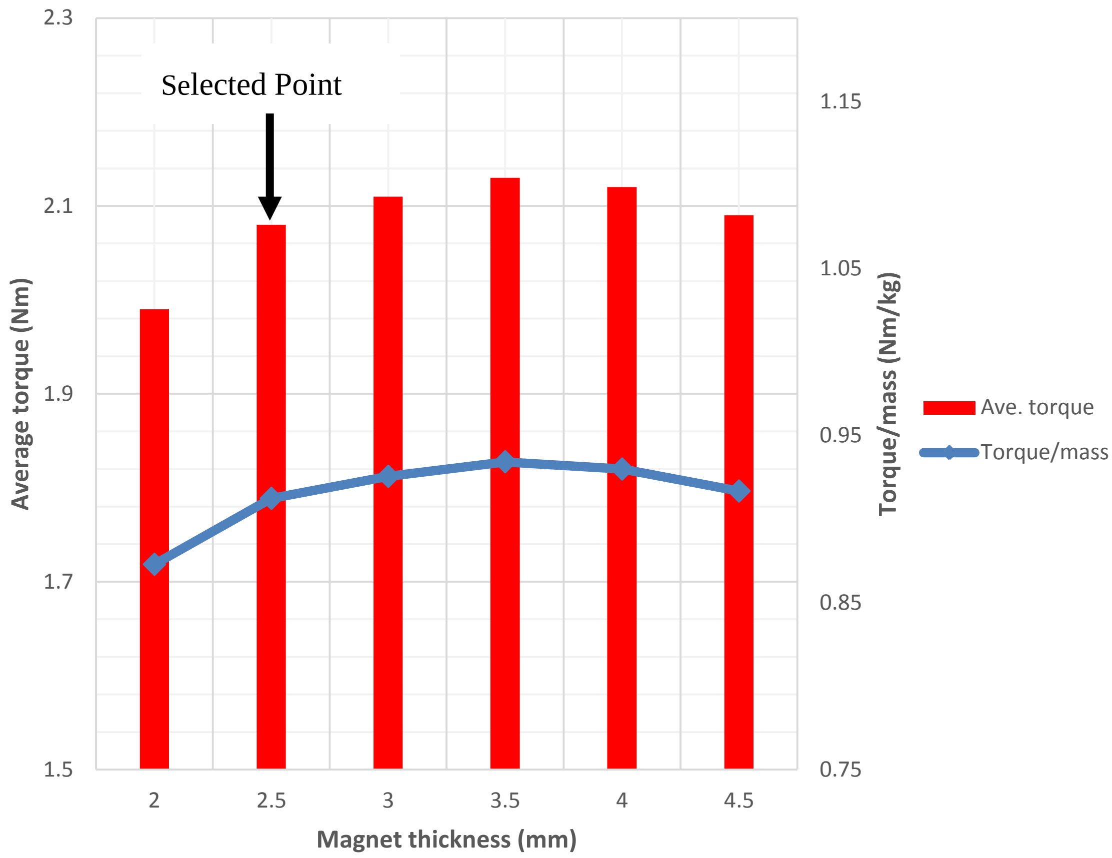

Figure 4-11: Average torque and torque /active mass variation with magnet thickness.

Figure 4-12 shows the total loss comparison with output power in the machine for different magnet span at constant magnetic airgap length and magnet thickness. The result shows that at 120º magnet span the machine has the lowest total loss and output power. This represents a decreased in terms of output power by 7.3%, 10.1% and 12.8% as compared to the 130º, 140º and 150º magnet span respectively.

The machine exhibits efficiency of 92.49%, 92.47%, 92.33% and 92.20% for the 120º, 130º, 140º and 150 º magnet spans respectively. It is clear from the analysis that the machine has the highest efficiency at 120º magnet span due to lower total loss associated with it. Hence 120º magnets span was chosen for the final design.

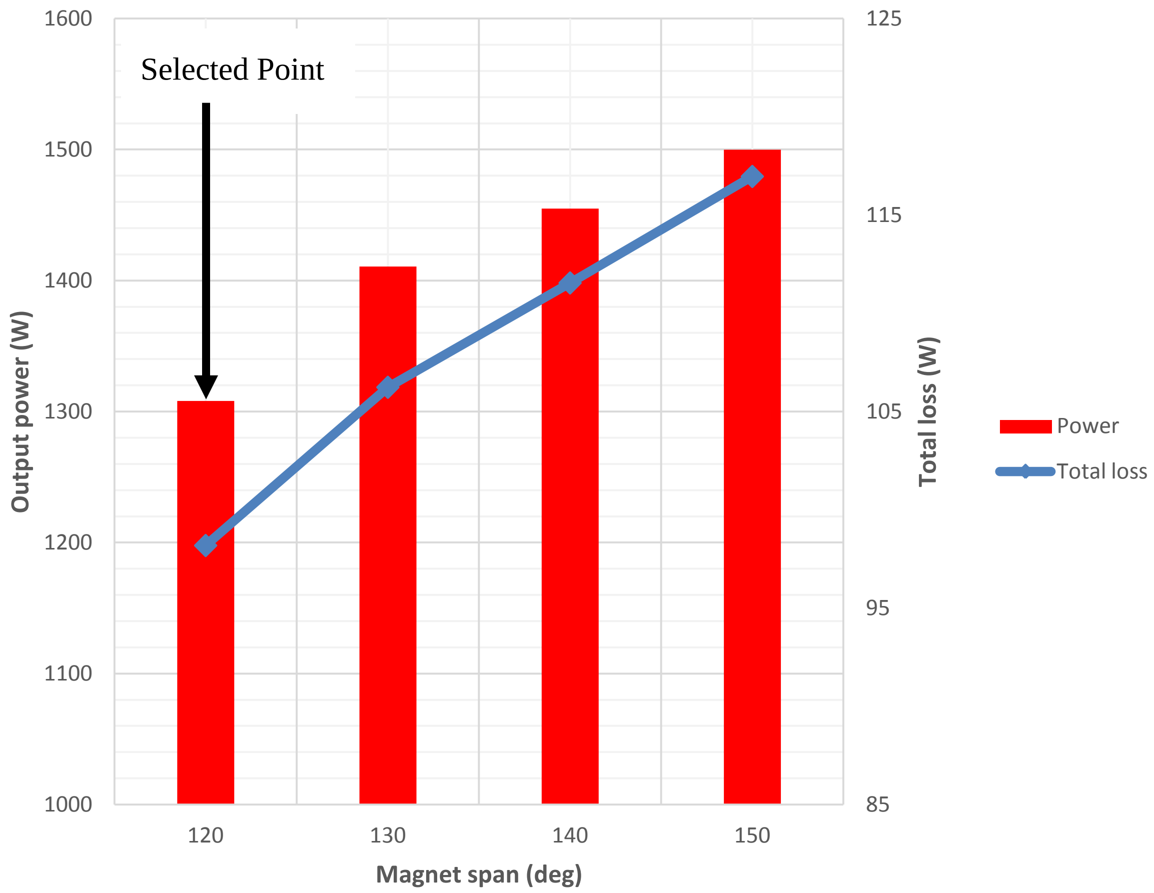

Figure 4-12: Output power and Loss comparison for different magnet span.

4.4.2 Airgap Flux Density

The approximation flux density in the airgap can be obtained based on the magnet remanent flux densityB_r, the magnet thickness l_m and airgap length l_{ag} as stated in [19] and as shown in equation (4.17) below.

$$B_{ag} = \frac{l_m}{l_m + l_{ag}} B_r \qquad (4.17)$$

Similarly, the air gap flux density can be expressed in terms of MMF and permeability as given in equation (4.18).

$$B_{ag} = \frac{MMF}{l_m + l_{ag}} \mu_0 \qquad (4.18)$$

This flux density in the airgap will oppose the magnet remanent flux density and demagnetisation in the magnets will occur if this flux density in the airgap is comparable to that of the magnet remanent flux density. The z-component of the magnetic field in AFM together with the magnetic field distribution and the flux linkage in the machine are obtained based on a model stated in [119].

The investigation of peak airgap flux in z-direction is carried out at different airgap length ranges from 1 mm to 3mm magnetic airgap, the reasons for that are based on the issues of mechanical clearance and maximum axial force of attraction between the stator and rotor. Figure 4-13 presented the B-H curve of SMC extracted from the data sheet in Appendix C.

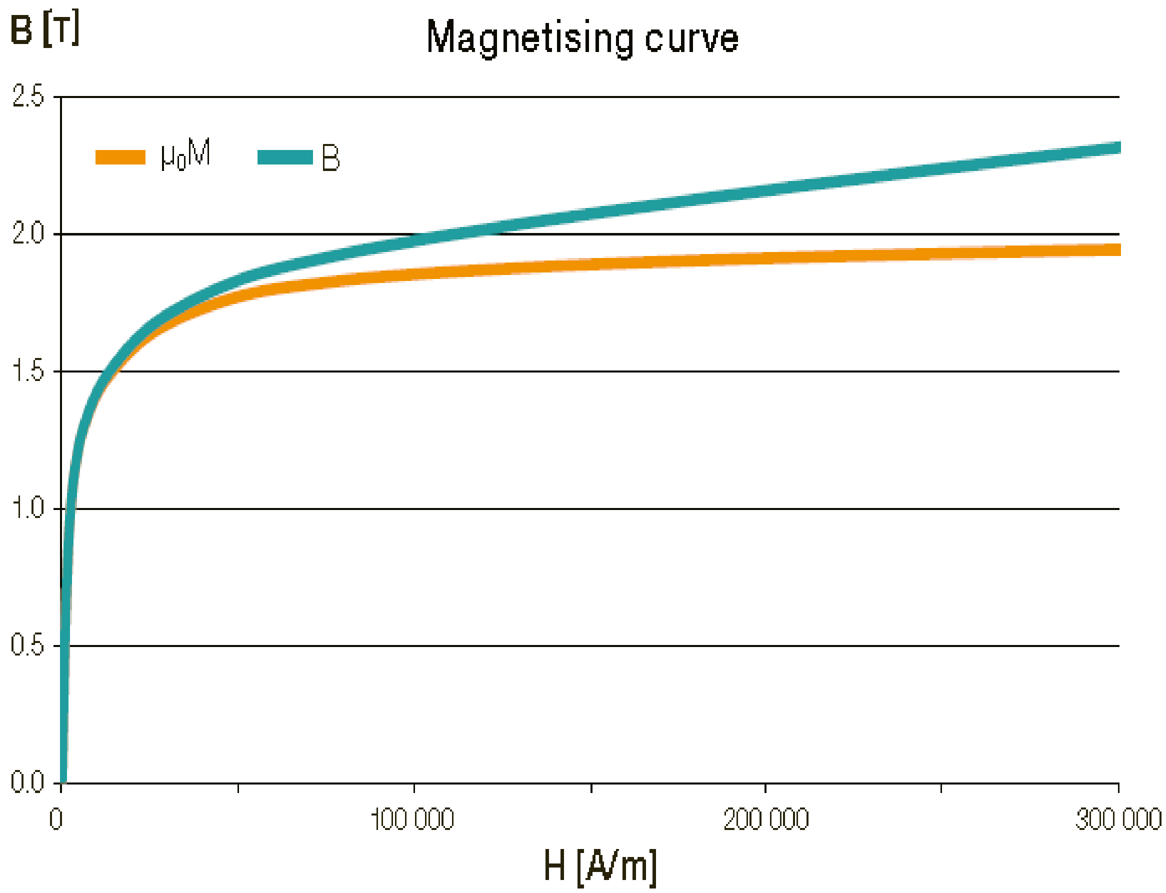

Figure 4-13: B-H curve of SMC prototype material.

Figure 4-14 shows the airgap flux variation for different airgap length. It is clear from the graph that at 1 mm magnetic airgap length, the machine has maximum airgap flux of 0.8 T. This represents an increase by 17.5%, 30%, 38.8% and 45% as compared to 1.5 mm, 2 mm, 2.5 mm, and 3 mm airgap length respectively.

Decreasing the airgap beyond 1 mm will result to increase in the flux and possibly the machine will experience some mechanical issues during assembly and running at rated speed. To avoid that the 1 mm magnetic airgap was used in the final design.

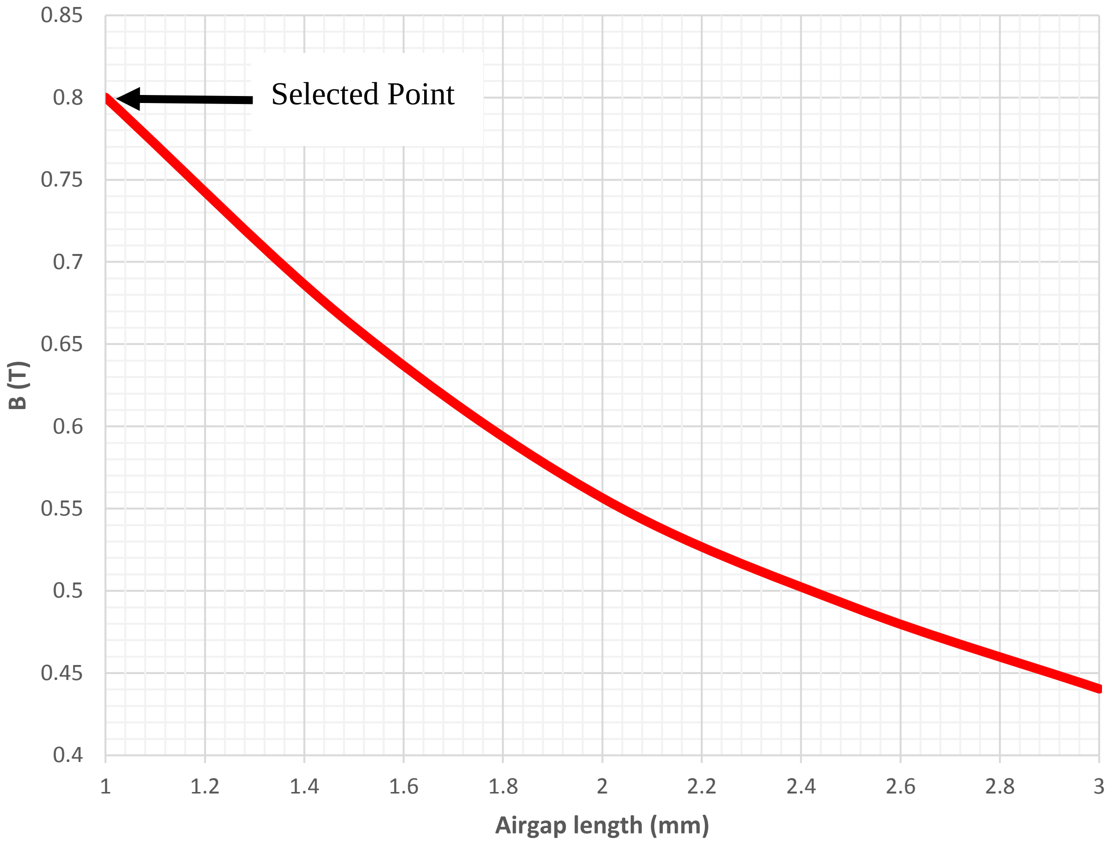

Figure 4-14: Airgap flux density variation with airgap magnetic length.

4.4.3 Operating Point of the Magnet.

From the design investigation of optimum average torque on parameters variation, 2.5 mm magnet thickness, 1 mm magnetic airgap and 120 º electrical magnet spans were chosen for the final design. By using the magnetic circuit, the operating point of the magnet was found to be 0.80 T at 120ºC. 3D FEA software was used to predict the demagnetisation within the magnet at 120ºC. Figure 4-15 shows the demagnetisation of the magnet when the rated full-load current flows through the coils.

It is clear that the magnets were not demagnetised when the full-current is applied as shown in Figure 4-15, because the operating temperature of the magnet is not exceeded, and the magnets are safe throughout the operation, but tends to demagnetised when the rated full-load current is about 1.5 times.

This shows that increasing the current beyond the rated full-load, the magnets edges starts to saturate since the operating temperature of magnets begin to exceed it normal operating condition and the airgap flux density begins to compare with the magnet remanent flux density as shown in Figure 4-16.

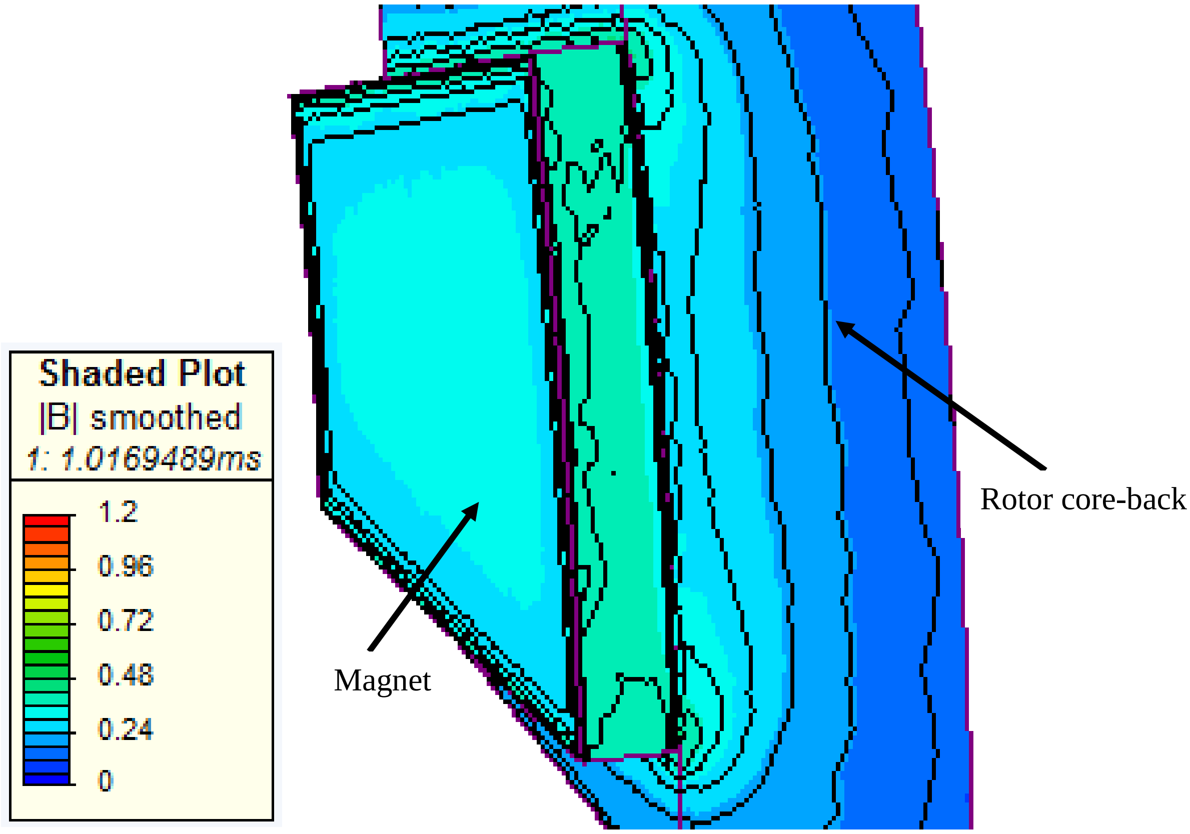

Figure 4-15: Magnet demagnetisation at full-load current.

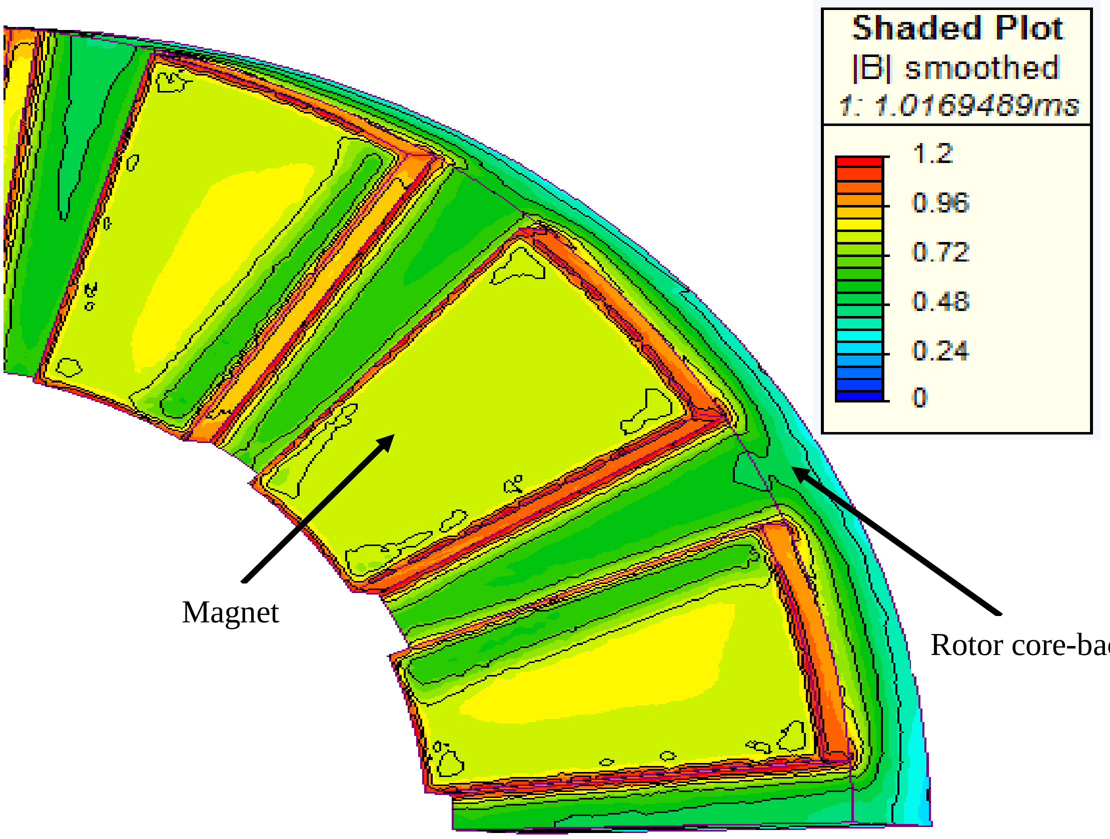

Figure 4-16: Magnet demagnetisation at 1.5 full-load current.

4.4.4 Optimum Inner/Outer Radius

The torque in AFM growth with cube of the outer diameter as stated in [17]. Figure 4-17 shows the stator block of an AFM which must have hole at the centre as it is not possible for magnet or end winding to touch the centre point. The inner radius can either be half the outer radius or as given by equation (4.19) and this relationship is obtained by maximising the expression for armature power in terms of magnetic loading and electrical loading [17].

$$r_o = \sqrt{3} r_i \tag{4.19}$$

This outer radius is constrained by the available outer diameter of the SMC prototype material which has maximum diameter of 120 mm, it is assume that the outer diameter is less than the maximum diameter of 120 mm and the inner radius of the machine is large enough to accommodate the inner end windings as they are not suppose to touch the centre point of the machine. The output torque for AFM machine is given in terms of the outer diameter as mention in Chapter 2, equation (2.1).

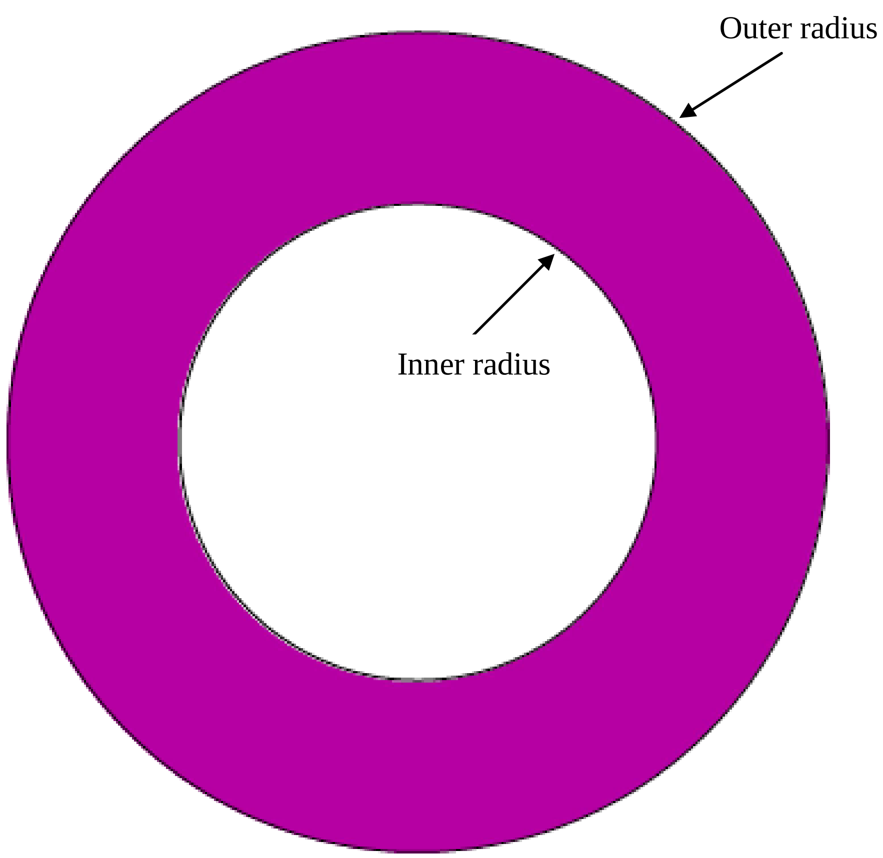

Figure 4-17: AFM stator block.

Figure 4-18 presents the average torque of the machine at fixed outer radius of 55 mm and different inner to outer radius. The inner radius is varied from 22 mm to 38 mm however concentrated winding will not fit onto the stator tooth if the inner radius is beyond 22 mm. In this case the analyses were carried out with constant airgap length, magnet span and thickness.

As depicted in Figure 4-18, the average torque increases as the ratio of inner to outer radius decreases. This allows for more electrical loading in the machine, it is clear from the figure that to achieve high average torque, the ratio of inner radius to outer radius must be low. In this design 32 mm and 55 mm were chosen as the inner radius and outer radius respectively.

This is for easy coils placement and to allow for effective air cooling in the machine during operation at full-load current and rated speed.

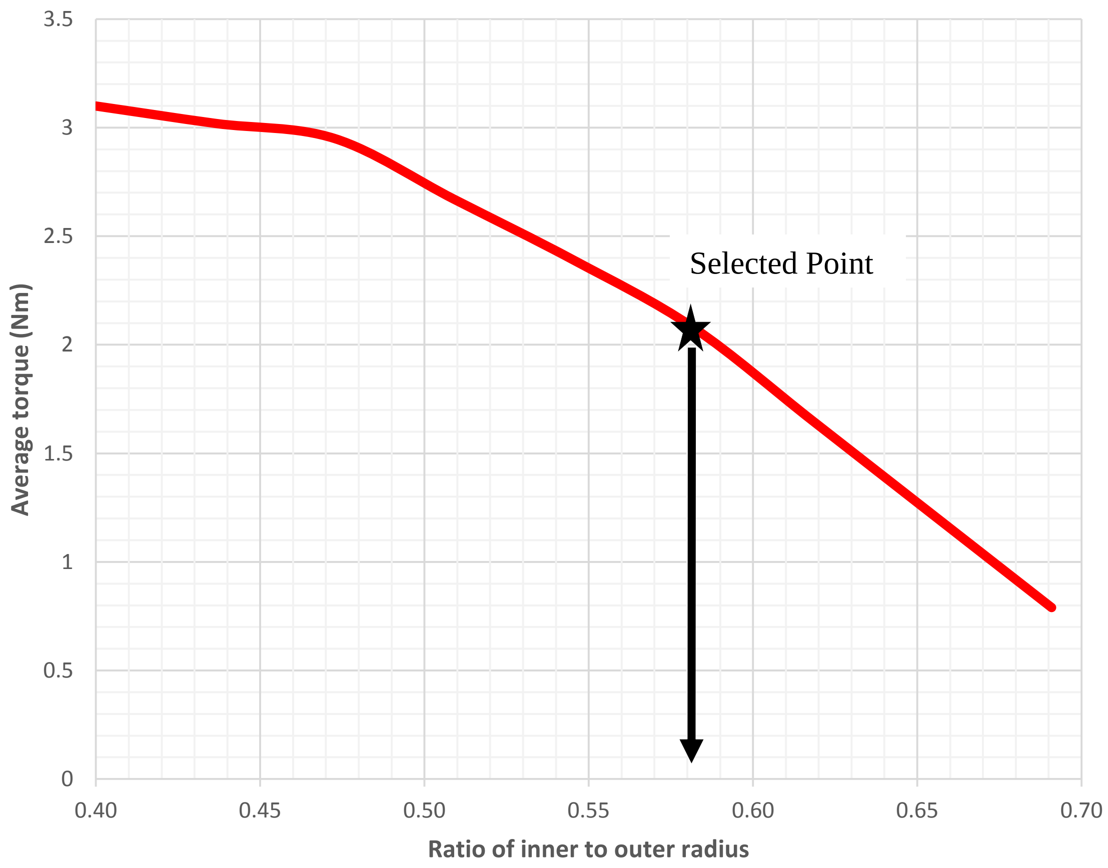

Figure 4-18: Effect of inner to outer radius ration on average torque.

4.4.5 Electric and Magnetic Loading

Electrical and magnetic loading gives an insight on how the design of machine parameters can affect the overall performance, the former is limited by the rise of temperature in the stator winding, while the later by saturation in the magnetic materials. Maximising electrical loading implies increasing the volume of the slot, which increases the MMF. While maximising magnetic loading has to do with decreasing the slot volume, which increases the thickness of the stator yoke.

To obtain optimum average torque a balance is needed between the electrical loading and magnetic loading. Figure 4-19 shows the average torque of the machine as the slot width was varied. The results show that the machine average torque increases as the slot volume is increased and a slot width of 5 mm was chosen for final design due to the average torque and total loss associated with it. The analysis stop at slot width of 5 mm as the target design average torque of 2.08 Nm is reached.

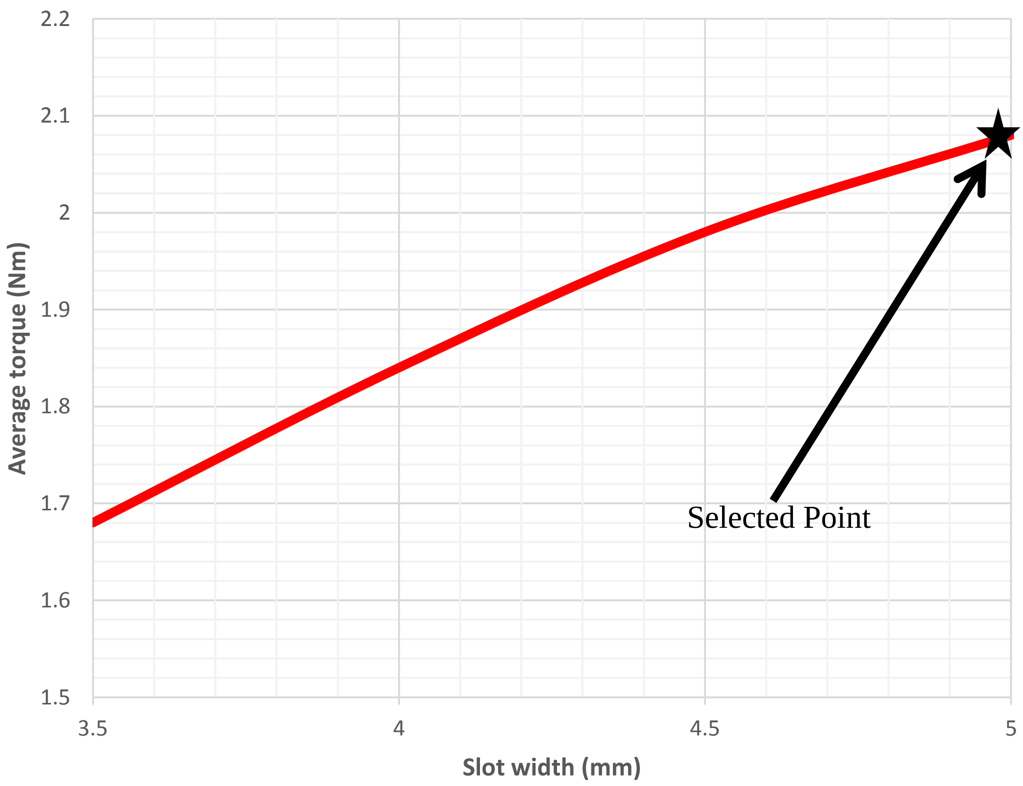

Figure 4-19: Average torque variation with slot width.

The overall machine performance is also affected by the slot geometry, in this analysis two slot designs, the rectangular slot and trapezoidal slot having the same slot MMF were investigated for optimal performance of the machine, Figure 4-20 shows the rectangular slot design and trapezoidal slot design while Figure 4-21 presented the total loss comparison in the machine between rectangular slot design and trapezoidal slot design having the same magnetic airgap length, magnet span and magnet thickness.

The results show that machine with trapezoidal slot has the highest total loss due to increase in the total length of the conductor as compared to rectangular slot design. The total loss in machine with rectangular slot is 17.6% lower as compared to trapezoidal slot. Rectangular slot design will be use in the final machine design.

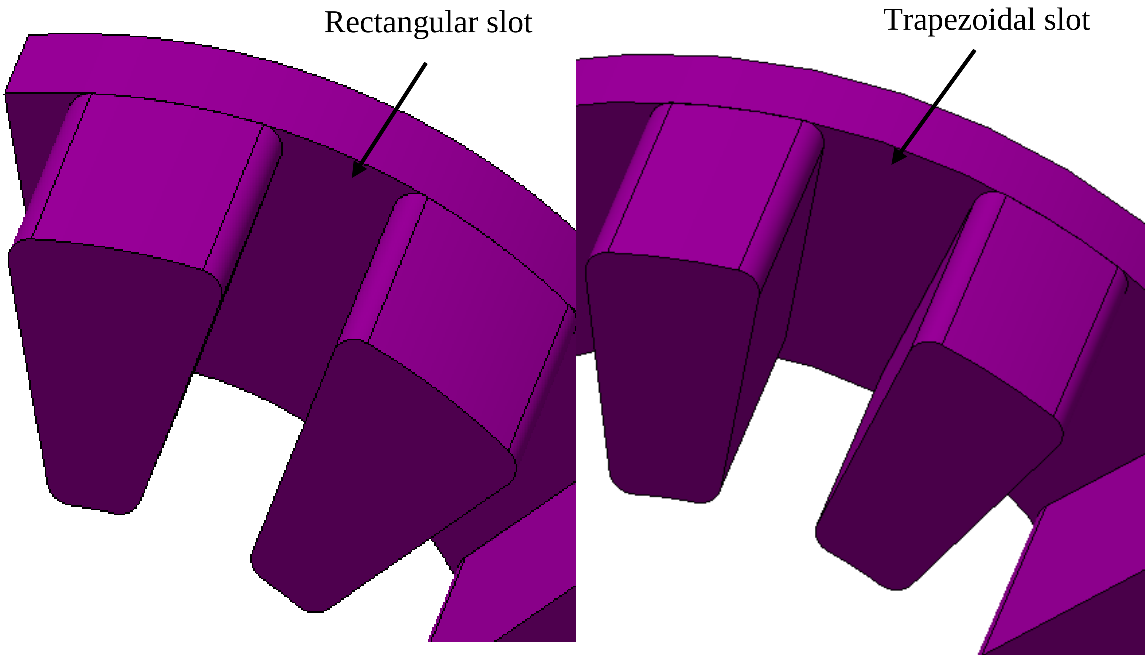

Figure 4-20: Rectangular and Trapezoidal slots.

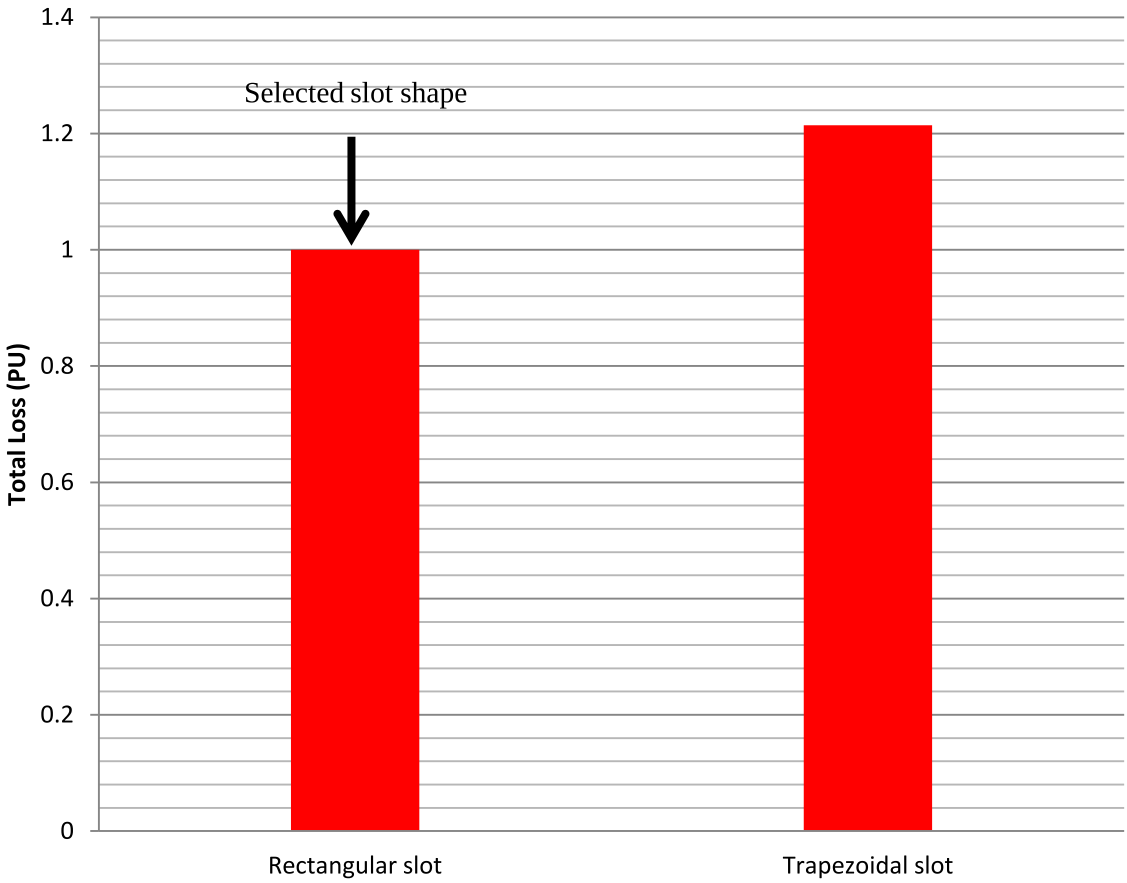

Figure 4-21: Total loss comparison between rectangular slot and trapezoidal slot.

4.4.6 Core-Back Depth

The thickness of core-back D_{cb} is usually defined by the amount of flux it must channel. The flux per pole is flux density by area and can be expressed as stated in [120].

$$D_{cb} = B_{ag} \times \frac{\pi(r_0^2 - r_i^2)}{poles} \tag{4.20}$$

The core-back thickness can be selected based on the desired flux density in the material used and all the magnet flux per pole must be channelled through the core-back and Figure 4-22 shows the average torque at different rotor core-back thickness.

$$B_{ag} \times \ pole\ sweep = \ B_{cb} \times D_{cb} \tag{4.21}$$

where B_{ag} is the airgap flux density, r_o and r_i are the outer and inner radius of the rotor respectively. B_{cb} is the core-back flux and D_{cb} is the thickness of the core-back.

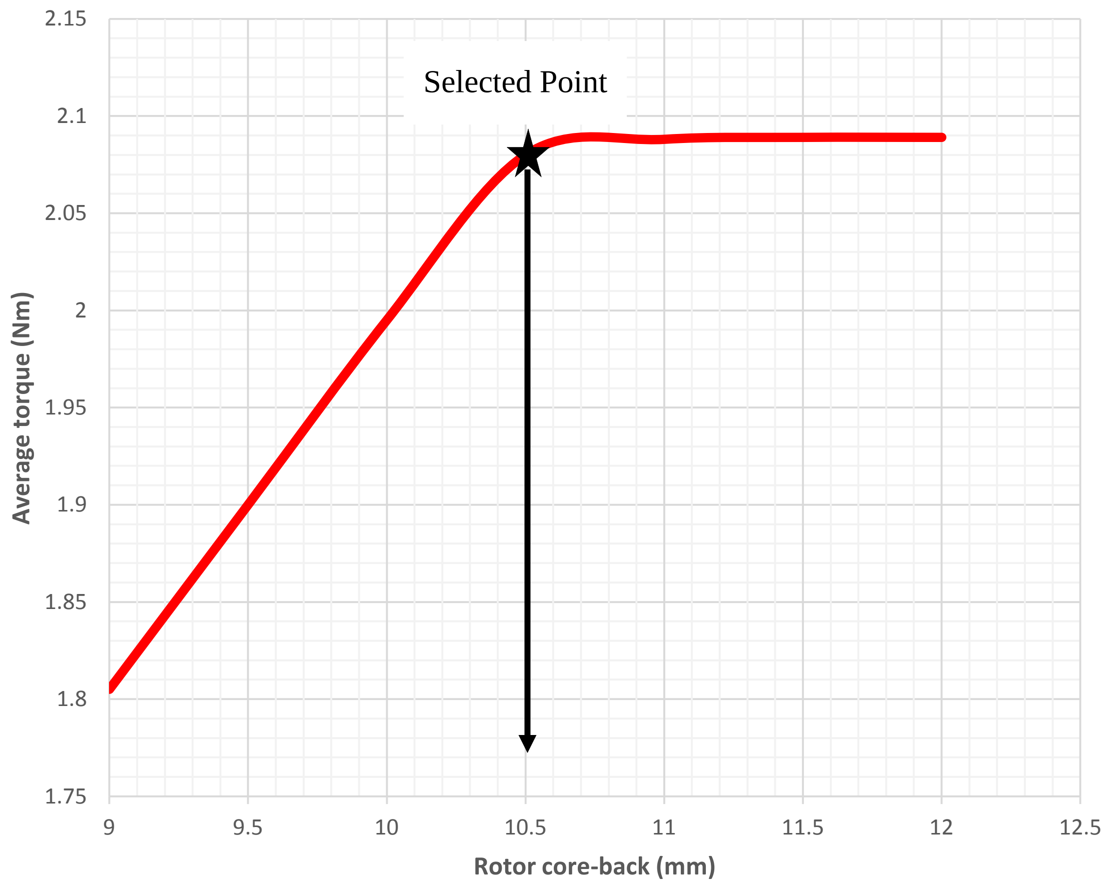

Figure 4-22: Effect of rotor core-back variation on average torque.

It is clear from Figure 4-22 that, the average torque of the machine is approximately constant when the rotor thickness is between 10.5 mm to 12 mm. To reduce the weight and cost of SMC material in the final machine, 10.5 mm was chosen as the rotor core-back of the machine.

The stator core-back thickness variation for optimal average torque is shown in Figure 4-23. It is clear from the graph that the machine has a peak average torque when the stator core-back thickness is 10 mm. At lower stator core-back and full-load current the machine exhibits lower average torque, but as the core-back is increasing the average torque also is increasing until the thickness of the core-back reaches 10 mm.

It is clear from the graph in Figure 4-23 that, beyond 10 mm stator core-back thickness the average torque in the machine is almost constant which slightly decreases by 0.2% of the average torque from 10.5 mm to 12 mm stator core-back thickness.

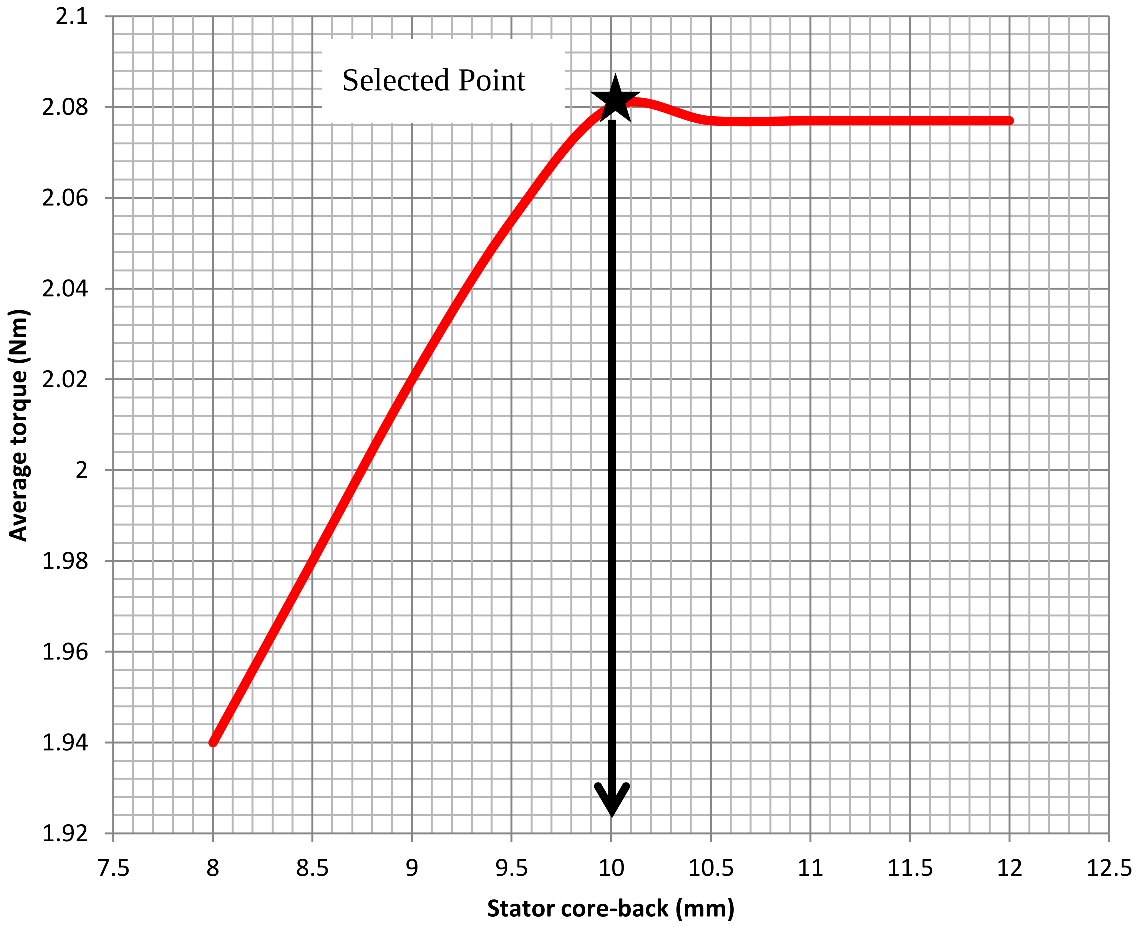

Figure 4-23: Effect of stator core-back variation on average torque.

4.5 Final Design Analysis

This section presents the analysis of the final machine design using 3D FEA and results reported include the cogging torque and axial force, no-load and on-load loss, back EMF and harmonic analysis, on-load torque, terminal voltage, output power, efficiency and temperature in coils.

From the analysis in section 4.3 and 4.4 the machine main dimensions and operating parameters are presented in Appendix A which are used to created a final parameterised machine model.

The machine is single-sided for simplicity as reported in [17] and SMC Somaloy 700HR 3P is used as material to both the stator and rotor. Neodymium Iron Boron N35SH magnet and copper with 100% IACS are used due to their availability as materials in the magnets and conductors respectively.

4.5.1 Cogging Torque and Axial Force

One of the problems in designing AFM at 6000 rpm and above is the axial force of attraction between the stator and rotor, which if care is not taken will lead to the collision of the stator and rotor at high speed which can damage the machine.

For the large radius machines this will require a very large core-back iron structure, because the force is as results of tensile Maxwell stress acting in the same direction as the orientation of the field as reported on [121] and is given by equation (4.22).

$$F = \frac{B_{ag}^2}{2\mu_0} \times A \qquad (4.22)$$

where B_{ag} is the flux density in the airgap and A is the area.

Figure 4-24 gives the FEA cogging torque at rated speed and this was obtained in the simulation by setting torque and electromagnetic force calculation condition, under no-load the torque generated is the cogging torque without excitation and is caused by the tendency of the rotor magnets to line up with the stator teeth where the magnetic circuit has the highest permeance when the machine is operating under no-load condition.

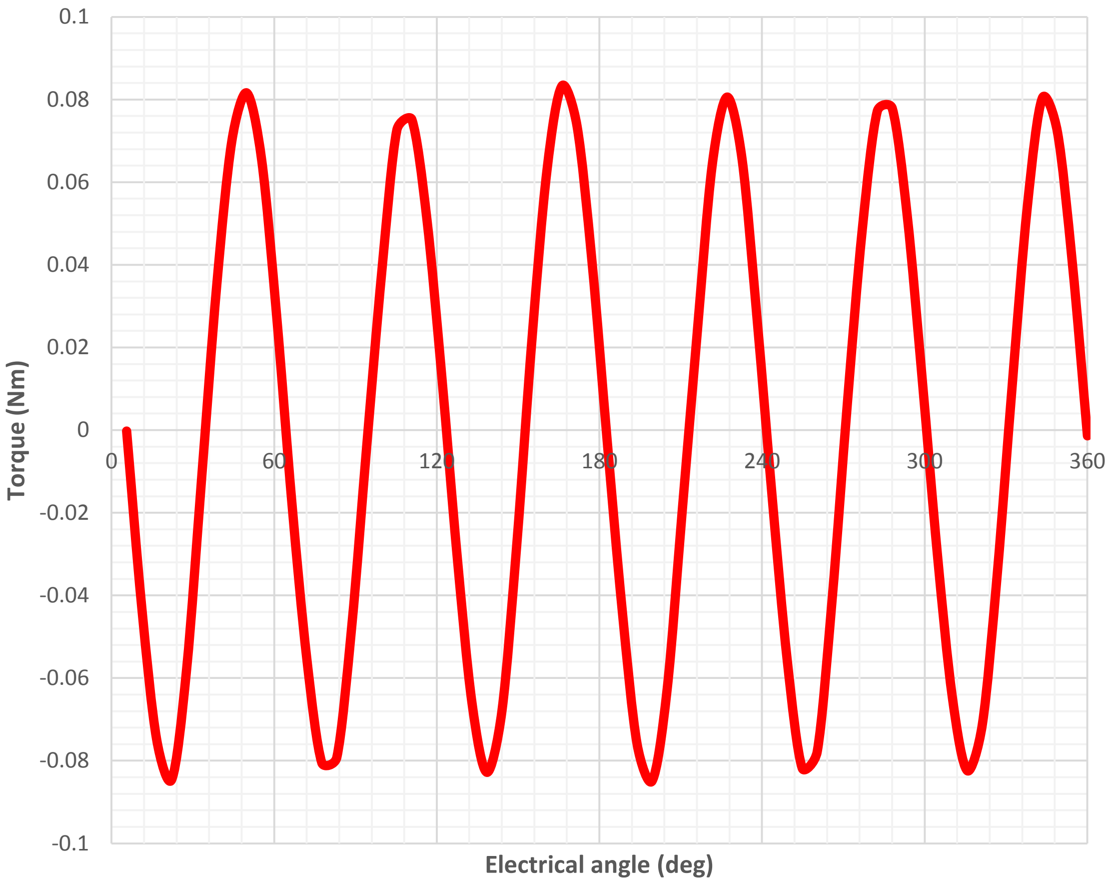

Figure 4-24: Cogging torque variation with electrical angle.

In [4] a method to analyse cogging torque on axial field flux-switching permanent magnet machine for application in wind turbine based on 3D FE model was presented. In this optimised design, cogging torque was small or negligible due to the slot and pole number combination and having rounded tooth. There is a 47% decrease in cogging torque as compared to the baseline machine reported in Chapter 3.

The average axial force of the machine at different airgap length is presented in Figure 4-25. It was obtained from the 3D FEA. It is evident that, from 1 mm to 5 mm magnetic airgap the axial force decreases. Moreover, for 1 mm magnetic airgap length, it represents an increased by 3.8%, 7.1%, 9.6% and 11.9% as compared to 2 mm, 3 mm, 4 mm and 5 mm airgap respectively. At 1 mm airgap the axial force is four times that of the baseline machine described in Chapter 3 and this value is within the range of the available “off the shelf” steel metal shielded thin bearings.

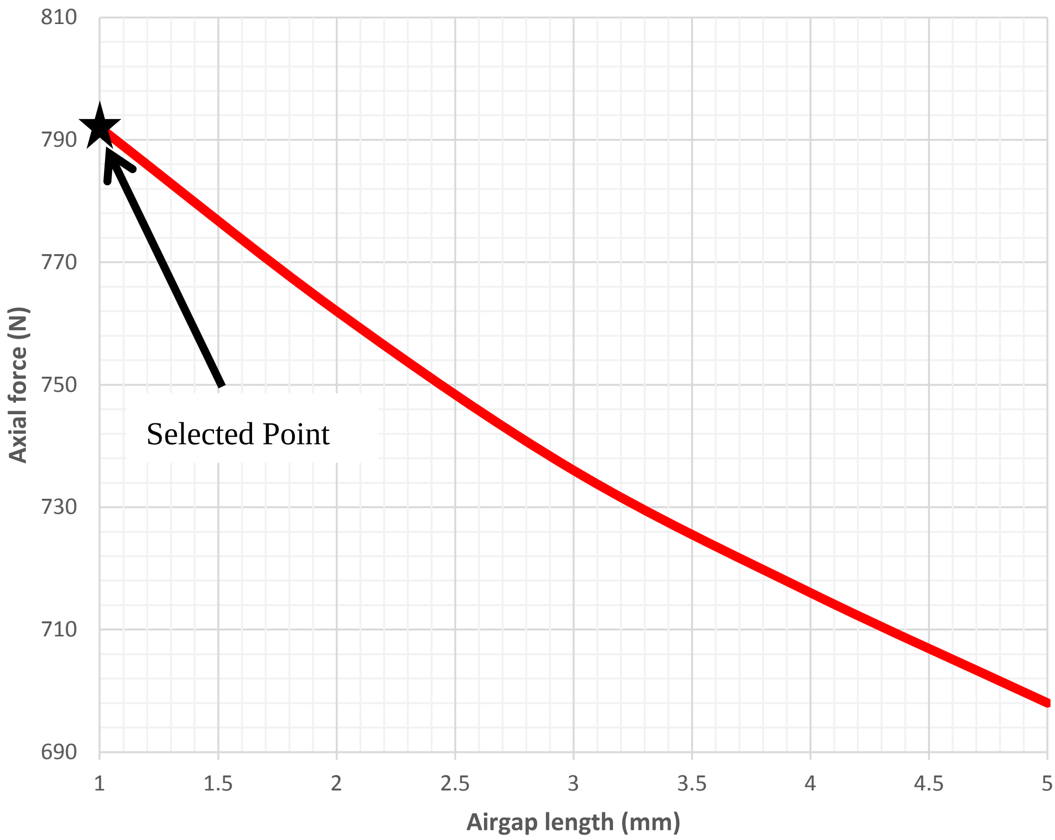

Figure 4-25: Axial force variation with airgap length.

4.5.2 Loss Evaluation

The idea of loss calculation in a machine is to know the efficiency. The total core loss of the machine can be determined from the 3D FEA by using the Steinmetz equation in equation (4.18) as reported in [109].

$$P_C = k_e B^2 f^2 + k_h B^2 f \tag{4.23}$$

where k_e is eddy current loss coefficient, k_h is hysteresis loss coefficient and B is the average flux density.

These constant values are obtained from data sheet of the material as supply by Höganäs AB and were inserted in the 3D FEA simulation to get the core loss of the machine. This data is valid for the frequency and induction range. The Infolytica MagNet software do not have an inbuilt data for SMC Somaloy, the typical data of prototype Somaloy as presented in

Appendix C were inserted into the new user materials to create a new material data for SMC and these includes: Magnetic permeability is nonlinear, isotropic and uses the adjusted data for magnetising curve, loss which uses Steinmetz Equation, resistivity or conductivity, permittivity which is linear – isotropic and real and the mass density of the material. All these information were used at 20˚C temperature. The core loss in the software is divided into two, the hysteresis loss and eddy current loss.

In [8] a modelling for minimum power loss was presented, the research work focus on the winding design together with low cost manufacture and found that from the analysis of different winding design the most promising is the edge wound winding which provides the lowest loss at AC operation. Similarly, power loss analysis in thermal design of permanent magnet machines were review in [108] and found that there are different techniques available for power loss analysis and modelling in electrical machines which include computational method like FEM or CFD however experimental measurement into power loss mechanism is also a vital part of the research on loss derivation method.

For a three-phase machine the stator winding copper loss in the machine can be found using the resistance and current or based on current density as reported in [19] [122] and are given by the equation (4.24) and (4.25) below.

$$P_{ClossR} = 3I_{ph}^2 R_w \qquad (4.24)$$

$$P_{Closs} = J^2 \rho_c Vol \qquad (4.25)$$

where ρ_c is electrical resistivity of copper conductor and Vol is the volume of copper conductor.

Figure 4-26 shows the no-load and on-load loss comparison for the final machine design. In this case AC winding loss was not considered, as eddy current circulation in the coils is turn off in the software and the winding conductor diameter at the operating frequency is less than the skin depth. Since half model was used in the analysis, the results must be multiply by a factor of two to get the total loss.

The loss is divided into stator hysteresis loss, stator eddy loss, stator bulk loss, magnet loss and coils Ohmic loss. It can be seen that, at no-load the dominant loss was stator hysteresis loss.

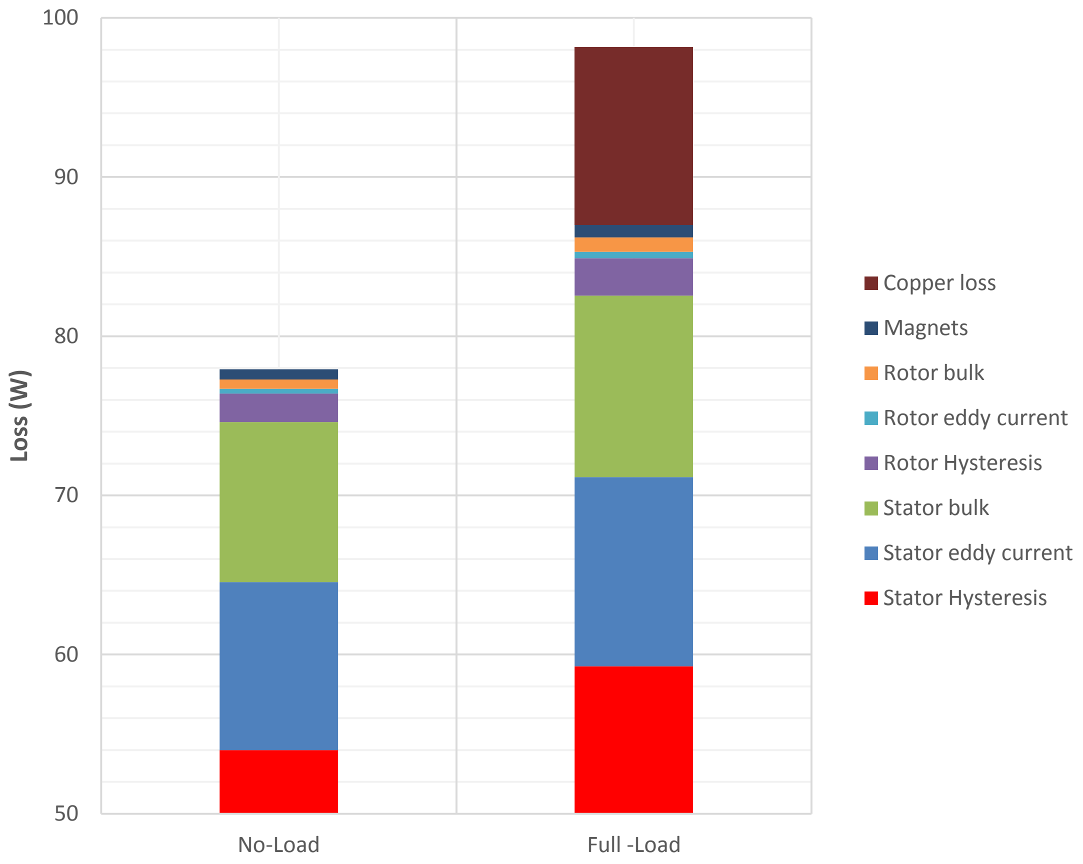

Figure 4-26: No-load and on-load loss comparison.

The on-load losses with copper conductor were obtained when excitation current was applied to the terminal of the machine at rated speed as reported in [123]. In this case only the dominant loss was considered. It can be seen from the graph that, the eddy current losses in the rotors of surface mounted permanent magnet machines are very small when compared to the eddy current losses in the stator.

The main sources of eddy current losses in the rotor are the space harmonics due to the slotting effects, stator winding distribution and stator current time harmonics. A developed model to determine the losses as a result of spatial harmonics was presented in [124].

Figure 4-27 shows the loss variation with speed, in this analysis AC winding loss was not considered due to the fact that the conductor diameter (1.4 mm) used is less than the skin depth (3.03 mm) at the operating frequency of 700 Hz (6000 rpm). The results show that the loss increases with the frequency squared and the on-load loss is higher to no-load loss by 26% at rated speed.

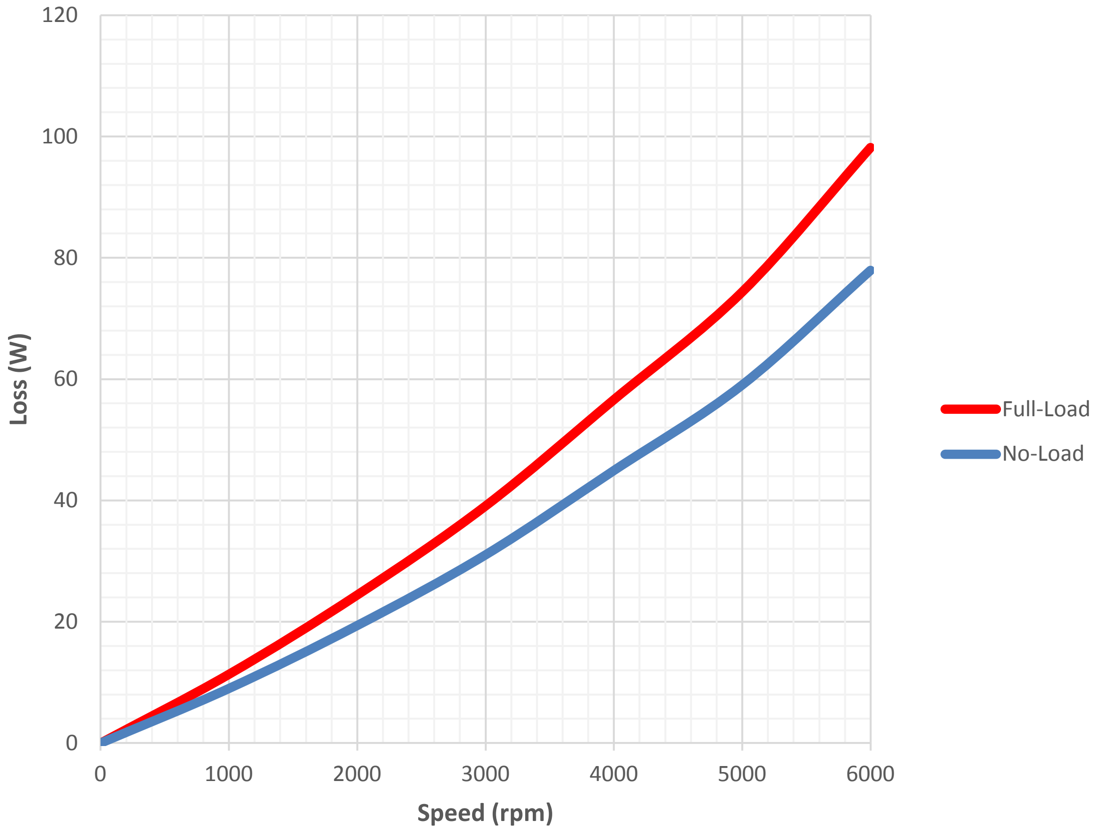

Figure 4-27: Loss variation with speed.

4.5.3 Back EMF and Harmonic Analysis

The back EMF of the machine at different electrical angles was obtained at zero excitation current. Also, it is proportional to the speed of the machine, number of turns and phase flux linkage. From the simulated 3D FEA results, it can be found either from the coil flux linkage or directly from coil voltage. The magnetic field distribution and the back EMF of axial field machine were analysed based on a model as mention in [119]. The back EMF of the coils was obtained from the flux linkage based on equation (3.1), while the induced rms voltage can be obtained using the induced voltage equation (3.2).

Figure 4-28 presented the three-phase induced back EMF of the machine at rated speed. The results show that the phases are separated by 120º electrical which confirm the circumferential tooth displacement between the three phase flux linkages in the machine. Furthermore, the induced EMF is sinusoidal in shape with little or no harmonics as required.

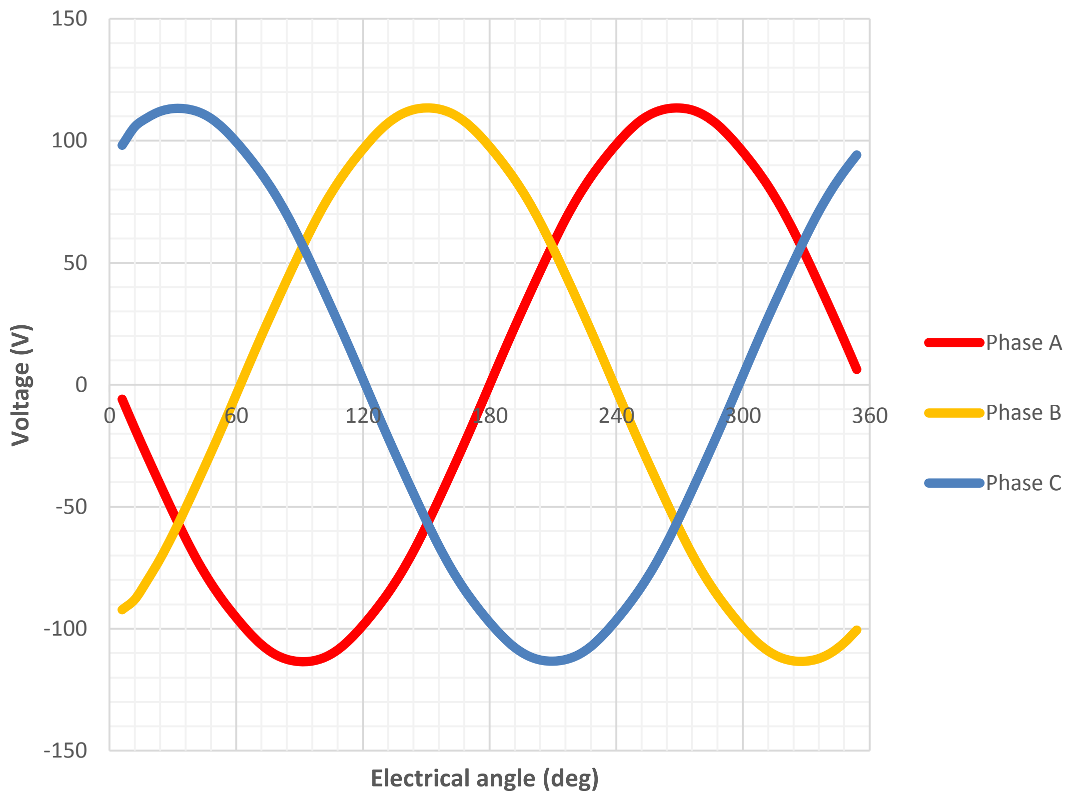

Figure 4-28: 3D FEA Back EMF at 700 Hz.

The harmonic analysis of the back EMF was carried out using the Fast Fourier Transform (FFT) to get the maximum amplitude of each harmonics and the accuracy depends on the number of data point used, in this case 60 data point based on the time steps was used. Figure 4-29 presented the harmonics analysis of back EMF. The combination of 12 slots and 14 poles number have minimised most of the harmonics present in the baseline machine described in Chapter 3 and the significant harmonics besides the fundamental harmonic are the fifth, seven and eleventh harmonic, with almost all the remaining harmonics are less than 0.5% of the fundamental harmonic. The peak back EMF fundamental harmonic is 113.4 V, which is required for the application.

Figure 4-30 presented the percentage comparison of three significant harmonics of the baseline machine and the improved machine, it can seen that the 3rd harmonic of the improved machine reduced by 96.2%, while the 5th and 7th harmonics by 97.8% and 90.9% respectively.

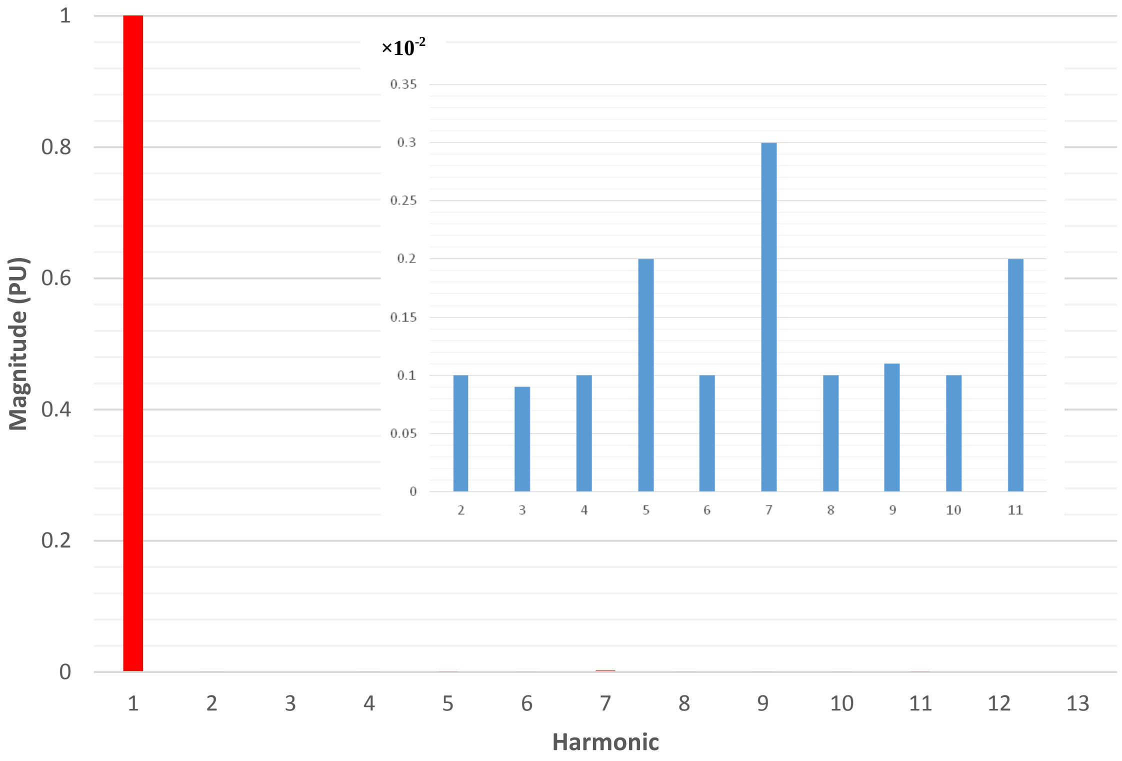

Figure 4-29: First eleven harmonics of Back EMF.

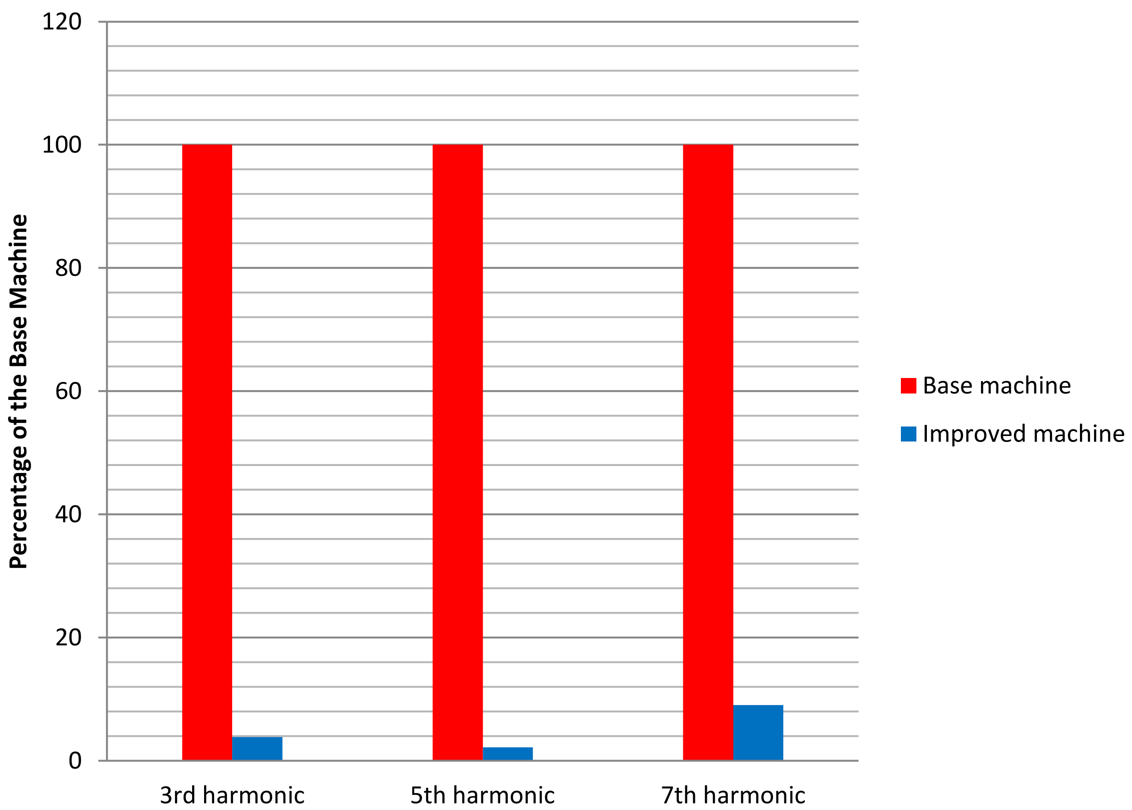

Figure 4-30: Baseline and improved machine harmonics comparison.

4.5.4 On-Load Torque

The torque of a machine is define as a force that tends to cause rotation or is a measure of the force that can cause the rotor of the machine to rotate about an axis. In another word is what causes the rotor to acquire angular acceleration in an electrical machine. The torque T on a conductor wire with radius r in metres is given by equation (4.26).

$$T = Fr \qquad (4.26)$$

where F is the force in Newton (N)

For a machine with slotted core and having N number of turns, the torque is given by:

$$T = B_{ave} IlrN \qquad (4.27)$$

whereas B_{ave} is average airgap flux density.

The machine average torque under loaded condition was obtained from the software. Figure 4-31 shows the average torque at different level of current. The design requires an MMF of 245At with 32 turns per coil.

The average torque was obtained by varying the current from zero to full load current at a step of 1A and the relationships were plotted. It shows that, as the current increased the slot MMF also increased due to the fact that MMF in a machine slot is directly proportional to applied current and the number of turns.

It is clear from the graph that from zero current to about 6A rms the relationship between the average torque and applied current is linear. After the applied current exceed 6A the relationship become non-linear and the onset saturation started.

Figure 4-32 compared the average torque and net torque produced; the machine exhibits an average torque of 2.08 Nm and net torque of 2.05 Nm. In the case of net torque, the cogging torque is subtracted from the on-load torque and is the actual torque exhibits by the machine. This shows that cogging torque in this machine always opposes the main torque. However, cogging torque does not always oppose main torque; it oscillates with a net zero average.

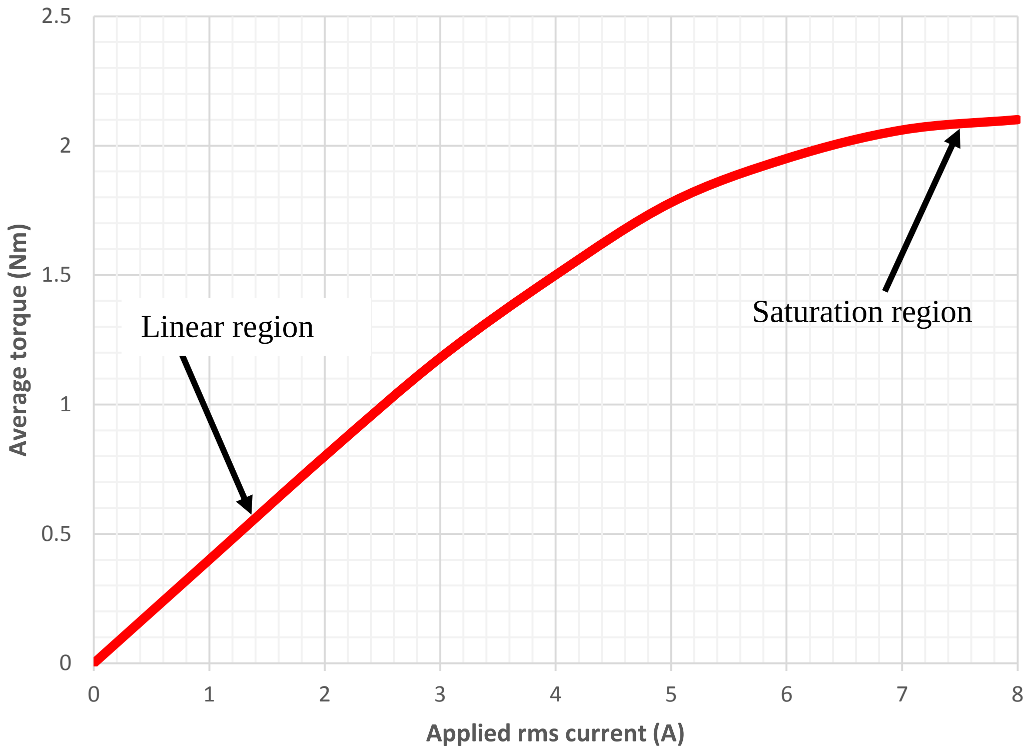

Figure 4-31: Average torque variation with current at 700 Hz.

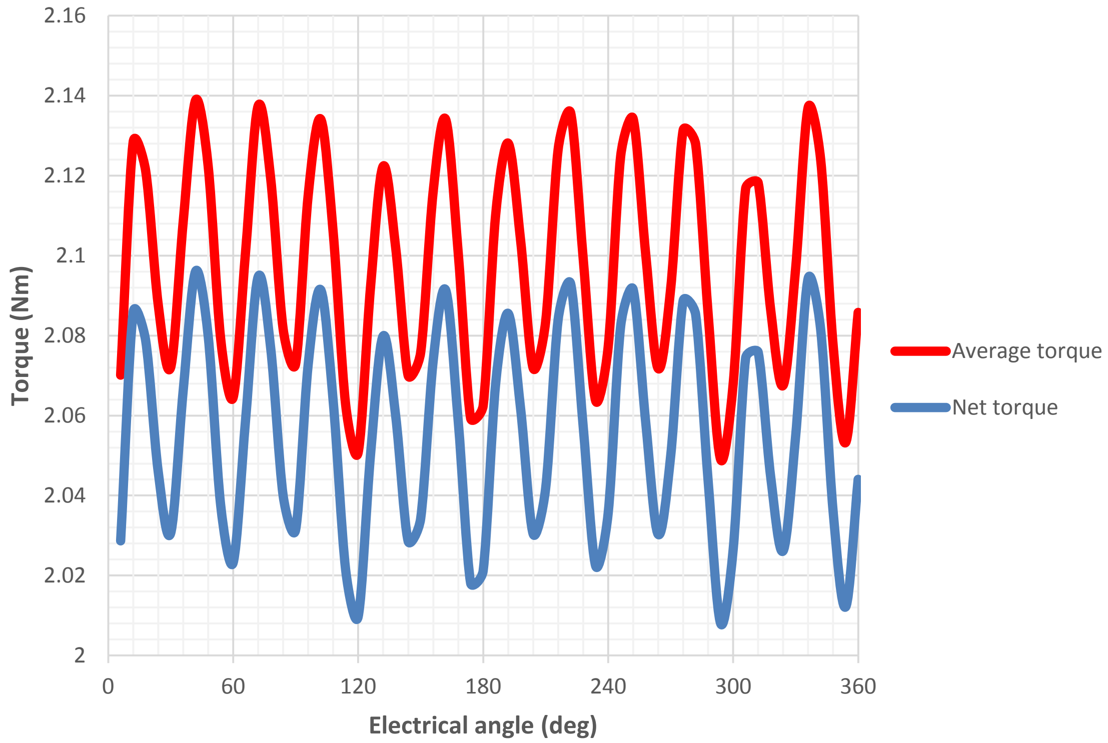

Figure 4-32: Average and Net torque of the machine at 700 Hz.

4.6 Terminal Voltages, Output Power and Efficiency

The machine performance with resistive load can be obtained from the phasor diagram as shown in Figure 4-33, where V is the terminal voltage, I is the current, R is the resistance and X is the reactance.

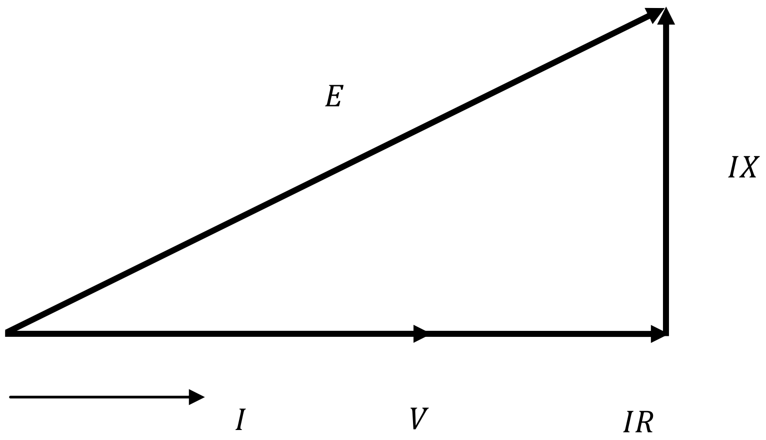

Figure 4-33: Phasor diagram of a resistive load

From the phasor diagram in Figure 4-33, assuming unity power factor, the performance of a machine with resistive load for any defined current can be determined using Pythagoras theorem, the terminal voltage can be expressed as given in equation (4.28), and the phase terminal voltage can also be found from the voltage equation given in [17].

$$V = \sqrt{E^2 - (IX)^2} - IR \tag{4.28}$$

For a three-phase machine the output terminal power is calculated using equation (4.29).

$$P_{out} = 3IV = 1208.9\,W \tag{4.29}$$

The applied mechanical power is obtained as given by equation (4.30).

$$P_{in} = T\omega = 1307.1\,W \tag{4.30}$$

The phase resistance of the machine can also be calculated together with the reactance as mention in [125] and are given by equations (4.31) and (4.32).

$$R = \frac{n_{series}}{n_{pall}} R_{coil} \tag{4.31}$$

$$X = \omega \frac{n_{series}}{n_{pall}} L_{coil} \qquad (4.32)$$

where R_{coil}, L_{coil}, n_{series} and n_{pall} are the resistance of the coil, inductance of the coil, number of series and parallel coils respectively.

The efficiency is a function of load torque of the machine, it should be noted that the efficiency was based on the output torque from the 3D FEA results and the total loss of the machine at rated speed. In this analysis we are looking at the importance of AC loss in relation to the overall performance of the machine.
Efficiency calculation was performed in [17] and it can be obtained using the expression in equation (4.33).

$$\eta = \frac{P_{out}}{P_{in}} \times 100\% \qquad (4.33)$$

4.7 Temperature Rise

From the thermal 3D FEA, the temperature rise in coils at full load current for 5000 seconds is shown in Figure 4-34. The ambient temperature of 20˚C was set as the initial temperature this rises to about 48.9˚C at full load current. This analysis is serves as a benchmark for this demonstrator since we required a low increase in temperature in the coils. The graph shows that, the temperature rise in the machine coils was 28.9˚C.

A thermal model of axial flux PM synchronous machines with SMC stator core through 3D Coupled electromagnetic thermal and fluid-dynamical FEA was given in [68]. The steady state temperature of the machine was obtained giving the typical behaviour of the winding with air as natural cooler and to obtain the temperature rise in the winding, a DC current of 10A was applied to a phase of the machine for about 5000 seconds. It is shown also from the graph that the temperature is constant for the first 15-20 sec, after that the temperature starts to rise gradually until almost 3000 sec and 4000 sec, later the temperature rises stabilised and become constant for the remaining duration.

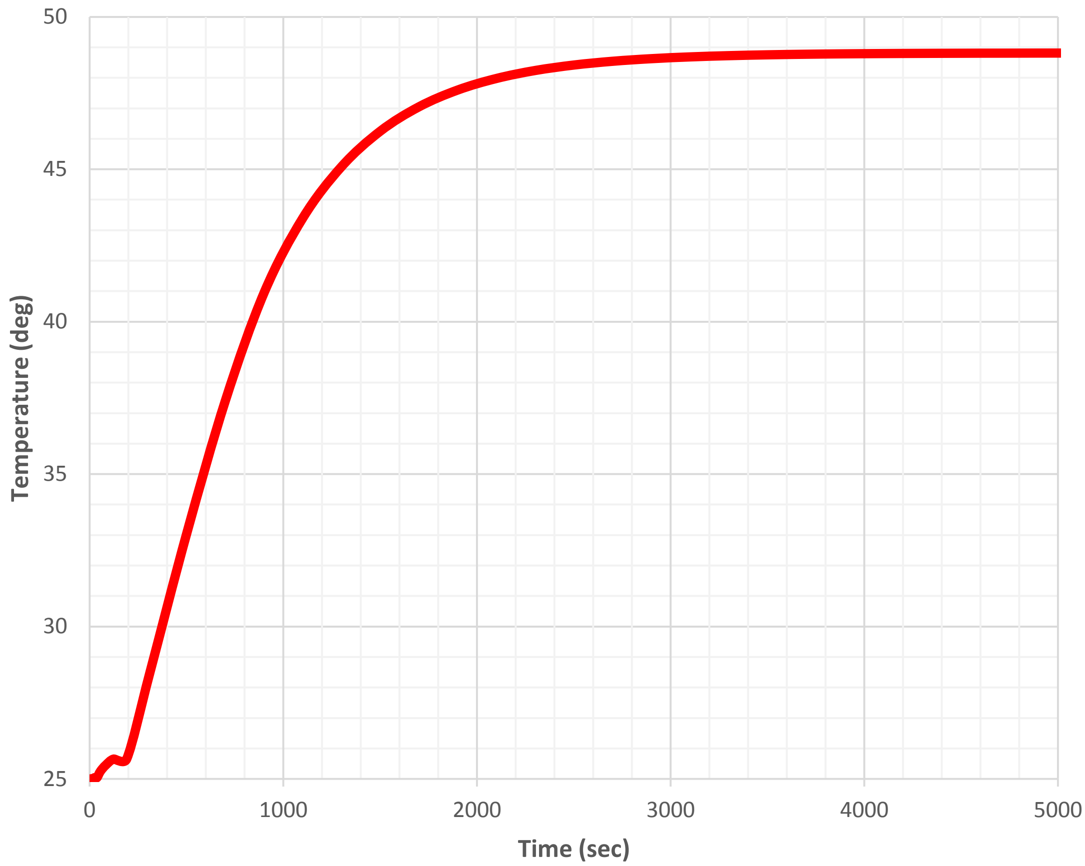

Figure 4-34: Temperature rise in the coils

4.8 Mass and Volume

The mass and volume of each component of the machine are presented in Figure 4-35 and Table 4-2 respectively, it can be seen that SMC account for 55% of the total active mass of the machine and it is 57.8% of the total active volume of the machine.

The machine windings represent 36% and 32.7%, the magnets account for 3% and 2.9% of the total active mass and volume respectively. Rotor iron core-back is 6% of the total active mass and 6.6% of the total active volume.

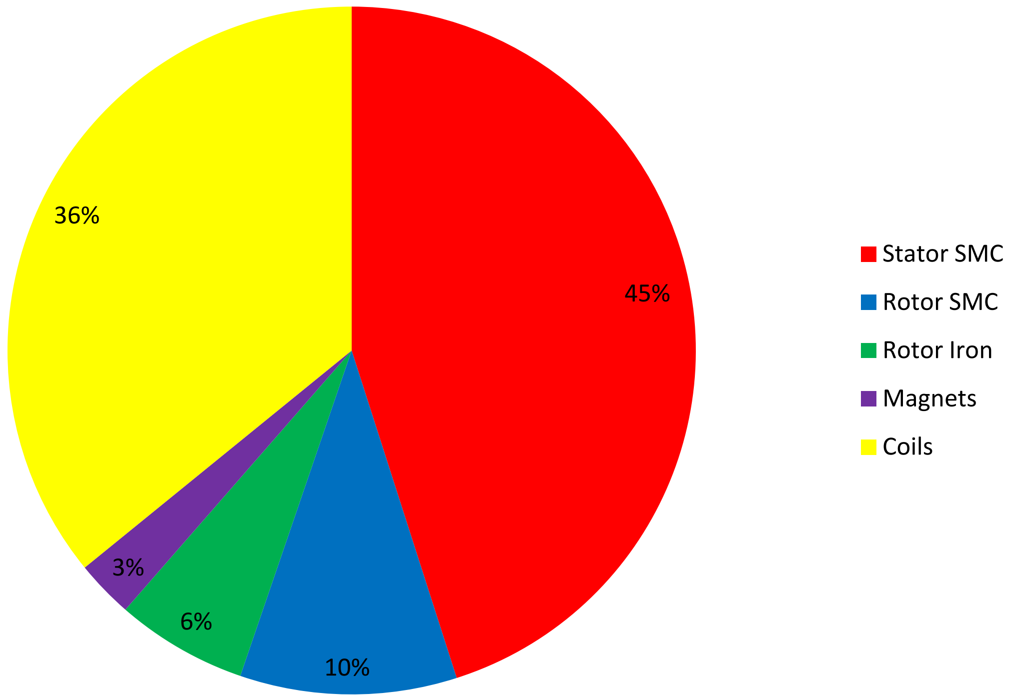

Figure 4-35: Mass percentage of each component

Table 4-2: Volume of Components

Component	Volume (m^3)	Percentage (%)
Stator SMC	133.6E-06	46.8
Rotor SMC	31.4E-06	11.0
Magnets	8.4E-06	2.9
Rotor Iron	18.9E-06	6.6
Coils	93.1E-06	32.7
Total SMC	165.0E-06	57.8
Total active	285.4E-06	100

4.9 Performance Summary

Table 4-3 summarised the key machine parameters obtained from the 3D FEA, which comprises of back EMF, phase resistance, input and output power, average torque, torque ripple, winding temperature rise and densities in terms of torque and power.

Table 4-3: **Performance Summary**

Parameter	**Value**
Peak Back EMF (V)	113.4
Phase Resistance (Ω)	0.1789
Frequency (Hz)	700
Input Power (W)	1307.1
Output Power (W)	1208.9
Phase Current rms (A)	7.7
Total Loss (W)	98.2
Winding Temperature rise (˚C)	28.9
Average Torque (Nm)	2.08
Torque ripple (%)	4.2
Torque/Magnet (Nm/kg)	33.2
Torque/Active mass (Nm/kg)	0.9
Torque/Active volume ripple (kNm/m^3)	4.8
Power/Active mass (kW/kg)	0.5
Power/Active volume (MW/m^3)	2.8

4.10 Conclusion

The sensitivity of average torque on various parameters was investigated using 3D FEA in this chapter and extensive simulation results were presented. It was shown that the combination of 12 slots and 14 poles number reduced the cogging by 47% as shown in Figure 4-24 when compared to baseline machine described in Chapter 3 and harmonics in back EMF by a significant amount as shown in Figure 4-29 and 4-30.

It is seen from the 3D FE studies that the final design has improved the overall performance of the machine by altering the main dimension of the baseline machine described in Chapter 3 which resulted in 375% increase in the mass of the machine compared to the baseline machine moreover the peak back EMF increased by 237%. This improvement above that of the baseline machine is as a result of the increase in slot area which increases the copper area and therefore results in the reduction of loss per unit MMF. This 3D FEA based optimisation offer the opportunity to further improve the performance of any machine demonstrating in particular improvements in average torque.

The AFM with higher number of pole than the slots number may be attractive in terms of torque density; in addition, the combination of low permeability SMC material together with strong rare earth magnets and concentrated windings allows the production of a highly efficient and smaller size machine.

Lastly, this chapter has implemented a conductor diameter less than the skin depth at rated speed however Chapter 5 will discuss the assessment of AC winding loss in the machine with conductor diameter larger than the skin depth at operating frequency.

5. AC Winding Loss Analysis

This chapter presents AC winding loss evaluation for the final machine design described in Chapter 4, in which the machine 3D nature using SMC are taken into consideration. The analysis focused in coils of open-slot configuration with rotor motion for three different conductor sizes. The losses of each coil are calculated separately, basic analytical model and 3D Finite Element methods were used. Sensitivity analysis is then used to assess the losses in individual stranded conductor and in full model to see the effect on conductor size and placing the conductor close to the airgap and far from the airgap within the slot. This is necessary in order to justify the effect on loss of conductor position and to have a more efficient machine.

5.1 Introduction

One of the factors that affect the efficiency of machines at operating speed is AC winding loss this is due to the higher frequency of operation resulting in skin-depths of the same order of size as the typical conductor diameters [5]. Therefore, AC winding loss analysis at operating frequency is very important in determining the overall performance of a machine. At AC operation the open-slot stator winding construction encourages an elevated winding loss from the PM rotor as stated in [8]. This is as a result of coils exposure to more magnetic fields from the rotor magnets.

The losses increase significantly when exposed to a changing magnetic field. This flux variation within the machine windings produces additional eddy current besides the losses in the core, which induced a magnetic field that tends to cancel the applied magnetic field as stated in [122]. If the effect is as a result of the conductor AC current within itself; it is called skin effect, while it is called proximity effect if it is due to a nearby conductor. This effect increases the I^2R losses and reduces the overall machine efficiency as a result of a decrease in the effective conductor area for current flow. These effects together with slot leakage effect in an alternating current environment can seriously impact the performance of the machine.

A method for modelling high frequency losses in the rotor iron of a permanent magnet brushless AC machine is reported in [124] and for magnets is mention in [126]. AC winding losses analysis of the ironless brushless DC motor used in a flywheel energy storage system are presented in [5]. Method for the analysis of circulating current losses in random wound electrical machines is reported in [127]. Similarly, AC losses in coated conductors are presented in [128]-[131]. Transport AC loss are discussed in [132]-[137]. Much literature proposed various methods of AC winding loss analysis which are limited and have not considered 3D nature of the AFM using SMC.

5.1.1 Skin Effect

Skin effect is the tendency of an alternating electric current to become distributed within a conductor so that the current density is largest near the surface of the conductor and decreases with greater depth in the conductor. The current flows mainly at the "skin" of the conductor as shown in Figure 5-1, between the outer surface and a level called the skin depth. The skin effect causes the effective resistance of the conductor to increase at higher frequencies where the skin depth is smaller, thus reducing the effective cross-section of the conductor. The skin effect is due to opposing eddy currents induced by the changing magnetic field resulting from the alternating current.

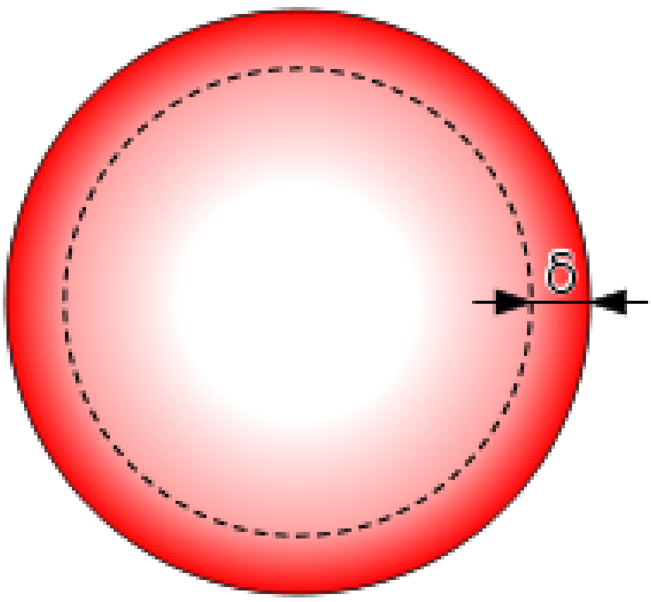

Figure 5-1: The skin depth in a circular conductor.

The skin depth δ depends on the electrical properties of the material, and the frequency f of the current through the conductor [138]. Therefore, the skin depth δ is given by equation (5.1).

$$\delta = \sqrt{\frac{\rho}{\pi . f . \mu_0 \mu_r}} \tag{5.1}$$

where ρ and μ_r are resistivity and relative permeability of the conductor respectively and μ_0 is the permeability of the free space ($4\pi \times 10^{-7}$ H/m). The maximum mechanical speed of the machine is 6000 rpm, the electrical frequency (14 poles) is 700 Hz and the skin depth is 3.03 mm.

5.1.2 Proximity Effect

In a conductor carrying alternating current, if currents are flowing through one or more other nearby conductors, such as within a closely wound coil of wire, the distribution of current within the first conductor will be constrained to smaller regions. The resulting current crowding is termed the proximity effect. Figure 5-2 presented the magnitude of current density in the windings of a slot.

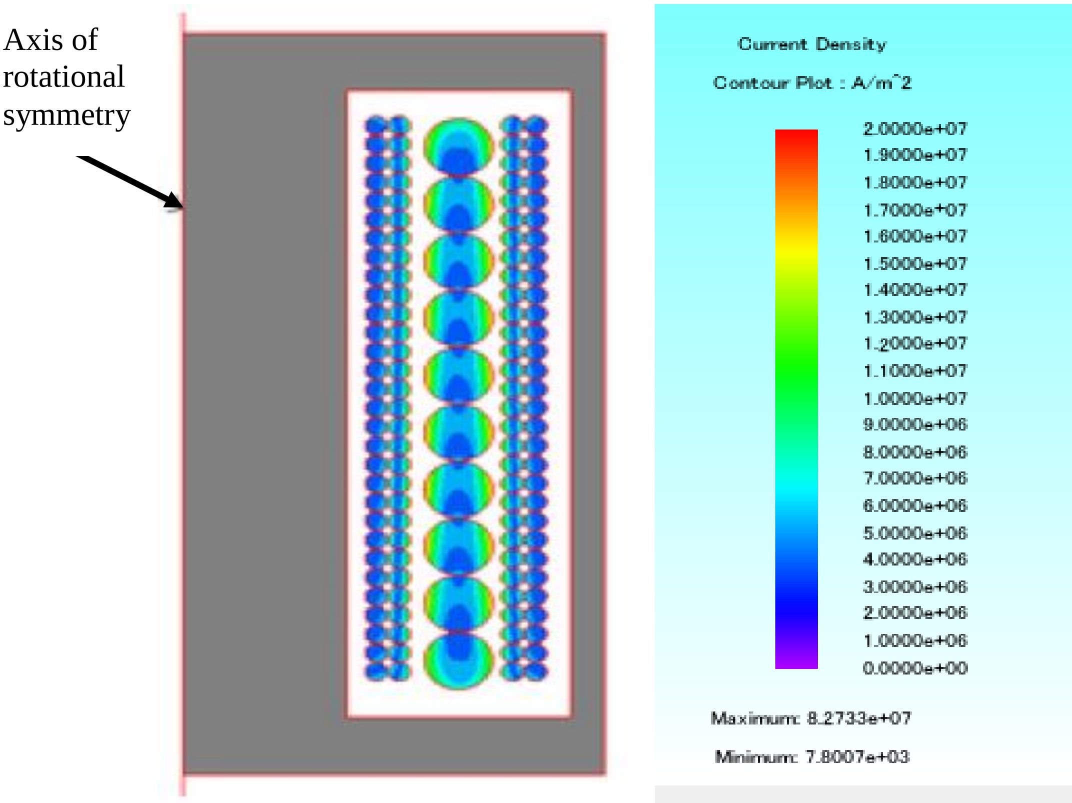

Figure 5-2: Magnitude of current density in the windings of a slot.

This effect results in an increase in the effective resistance of the circuit in which the conductors are placed with increase in the frequency. The alternating flux in a conductor is caused by the current of the other nearby conductor and produces a circulating current or eddy current in the conductor which results an apparent increase in the resistance of the conductor and; thus, more power losses in the windings.

Proximity effect dominates in a multi-layer conductor and is important when larger conductor diameter sizes greater than 100 mm^2 is used [123]. It also depends on the following factors like conductor's material and diameter, frequency of operation and conductor structure. In this analysis only skin effect is taken into consideration, as for the 3.2 mm conductor diameter we have only one layer of conductors in the slot.

5.1.3 Slot Leakage Effect

In an electrical machine, when the main magnetic circuit is saturated the flux in the slot can flow out of the main magnetic path and pass through the conductors causing more power losses in the conductors closer to airgap because of a higher uneven AC resistance created by the higher slot flux leakage and a higher changing magnetic field. Furthermore, the principle of slot leakage inductance will be discussed in Chapter 6.

5.2 Eddy Current Loss in Stranded Conductor

To calculate eddy current loss in a machine, it is advisable to incorporate an easy eddy current loss calculation technique in the design optimisation procedure, such as the analytical solution of the eddy current loss in a single conductor situated in a transverse alternating field [139].

Figure 5-3 presented the coils arrangement to carry out eddy current loss checks on stranded conductors with rotor motion (rotation) and at different position within the slot and the eddy current loss model assumes a stranded conductor of diameter d and radial length L. To model the cross sectional area of the conductor, the eddy current can be assumed to flow in concentric circular paths within this cross section with varying magnetic flux density of peak value B and angular frequency ω.The eddy current loss or joule loss P in single conductor can be calculated from equation (5.2) as stated in [139].

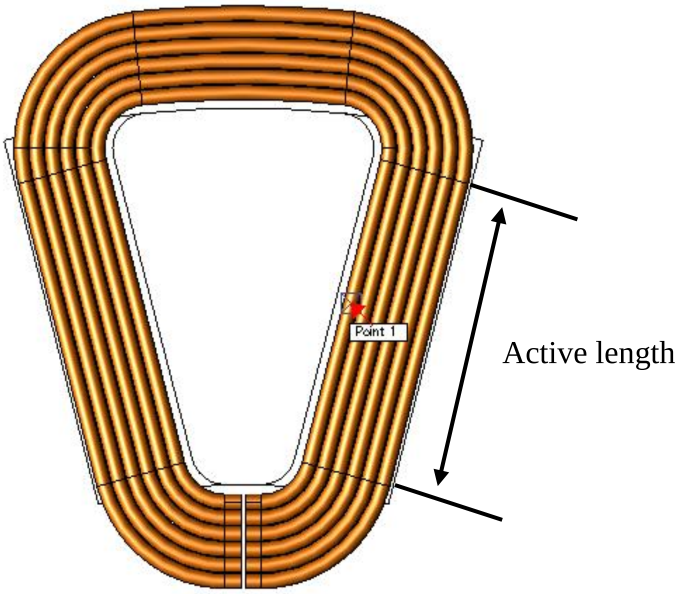

Figure 5-3: Coils arrangement for eddy current loss analysis on stranded conductor.

$$\frac{P}{m^3} = \frac{(\omega B d)^2}{32\rho} \tag{5.2}$$

where d is the conductor diameter, B is the peak flux density, ρ is the resistivity of conductor and m^3 is the conductor volume.

Since:

$$\omega = 2\pi f \tag{5.3}$$

where f is the frequency and conductor volume m^3 is given by equation (5.4).

$$conductor\ volume = m^3 = 2L\left(\frac{\pi d^2}{4}\right) \tag{5.4}$$

where L is the radial conductor length sitting in the field and '2' accounts for each side of the coil.

Substituting equations (5.3) and (5.4) into equation (5.2), then eddy current loss in stranded conductor $P_{Eddy\ loss}$ is obtained as equation (5.5).

$$P_{Eddy\ loss} = \frac{\pi^3 B^2 f^2 d^4 L}{16\rho} \tag{5.5}$$

In a slotted stator AFM, the flux density waveform in the air gap has an appreciable third and fifth special harmonic content [140]. The air-gap magnetic field exhibits a variable 3D nature. It can be seen also from equation (5.5) that the eddy losses are proportional to d^4 and it was also observed that the amplitude of the field varies greatly with airgap position. Eddy current loss in the individual conductors depends upon their positions in the airgap. The conductor nearer the face of the magnet experiences higher flux density, and therefore, has larger induced eddy current loss, since $P_{Eddy\ loss} \propto\ B^2$ [141].

5.2.1 Methodology

3D FEA using JMAG software was used in this analysis due to the complexity in the design of the coils and the advantages it has over Infolytica MagNet software as stated in Chapter 1, section 1.3, page 5 and 6. The peak value of the flux density obtained using the probe feature at the centre of each strand at a mean radius is used in equation (5.5) to get the eddy current loss on individual conductor within the slot analytically.

The rotor effects were considered in the analysis and the study was conducted on a 0.85 mm, 1.4 mm and 3.2 mm conductor diameter. As shown in Figure 5-4, Eddy current loss occurs outside the active region and in this case, a 0.85mm conductor diameter positioned 1.5 mm from the airgap within the slot is used. The radial length of coils within the slot area is considered as the active length of the coils. To simplify the analysis, extra losses from flux leakage and higher harmonics are not considered. Only the top 6 layers of the coils close to airgap at 1.5 mm are shown in the Figure 5-4.

In order for the 3D FEA model to accurately calculate the losses, it must be of a high enough resolution and with elements smaller than one-third skin depth at operating frequency to ensure correct modeling of current distribution near the conductor surface. At the operating frequency, and taking into consideration the material properties, the skin depth is 3.03 mm. For accurate modeling, it requires a mesh with a circumferential resolution of at least twenty nodes per pole.

Due to the periodic nature of the machine, there was no need for a full twelve tooth finite element model; rather a single tooth of the machine with odd boundary condition to minimize simulation time was implemented, since there is provision for conversion in the software to account for the remaining tooth of the machine. Conductors are set as solid to allow eddy current circulation due to skin effect and current was applied to the model with conductor resistivity of 1.9e-08Ωm. The reason for using this type of conductor is their availability in market.

This analysis is based on numerical checked experimented to help explain and separate the proximity to slot and proximity to other conductors AC winding losses. Current was set to zero and then the coils were move back into the slot to isolate the rotor proximity effect. At the moment now it has only the skin effect.

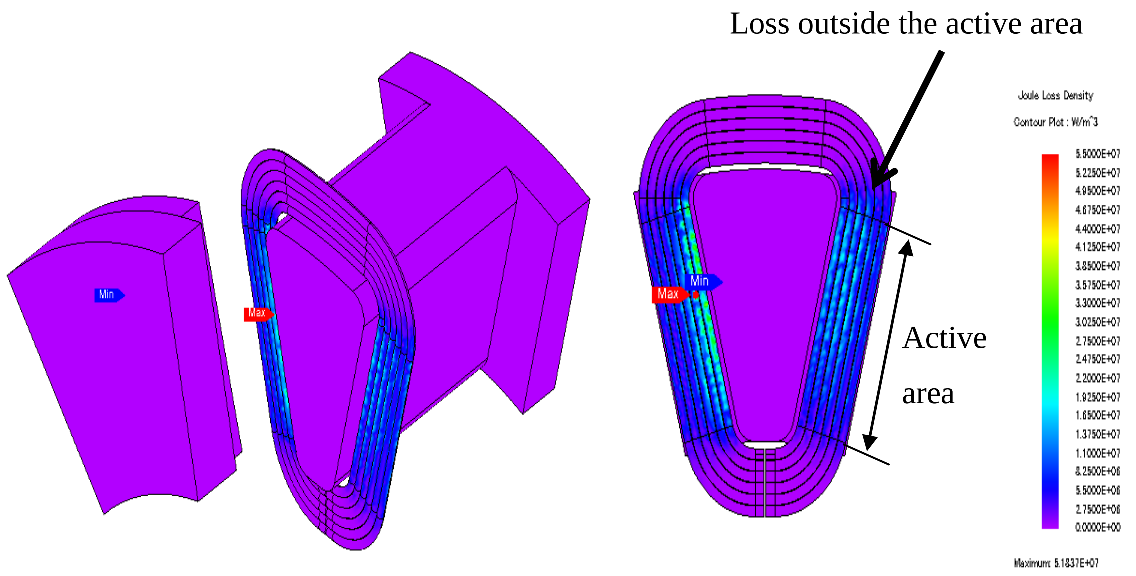

Figure 5-4: Eddy current loss occurs outside the active region at 700 Hz.

5.3 Analysis of Conductor Diameter and Slot Position

In this section, the influence of conductor diameter and frequency on AC winding loss are analysed along with the effect of conductor position within the slot. To consider the effect of diameter, three models with different diameter conductor were used; 6 turns of 0.85 mm diameter conductor, 2 turns of 1.4 mm diameter conductor and a single turn of 3.2 mm diameter conductor positioned at 1.5 mm, 12 mm and 24 mm from the airgap. Analysis was carried out at 700 Hz. In each case of the analysis, all other parameters are kept constants except the conductor position.

The analytical loss is based on equation (5.5) above and the peak value of the flux density used were obtained using probe feature from the 3D FEA, while the FEA loss is based on the results obtained directly from the 3D FEA model. The reason for using 6 turns, 3 turns and a single turn for 0.85 mm, 1.4 mm and 3.2 mm diameter conductor respectively is, in the full model, the machine has six layers of conductors with 0.85 mm diameter conductors, three layers of conductor with 1.4 mm diameter conductor and a single layer of conductor with 3.2 mm diameter conductor.

Figure 5-5, Figure 5.6 and Figure 5-7 presents the bar chart comparison of analytical loss and FEA loss at 1.5 mm, 12 mm and 24 mm from the airgap respectively. The results show that with an increase in the conductor diameter, the loss increases significantly. Moreover, for a 3.2 mm diameter conductor positioned 1.5 mm from the airgap the FEA calculated loss increased by 7.5% as compare to the analytical loss. Similarly, at 12 mm from the airgap, the loss increased by 2.7%.

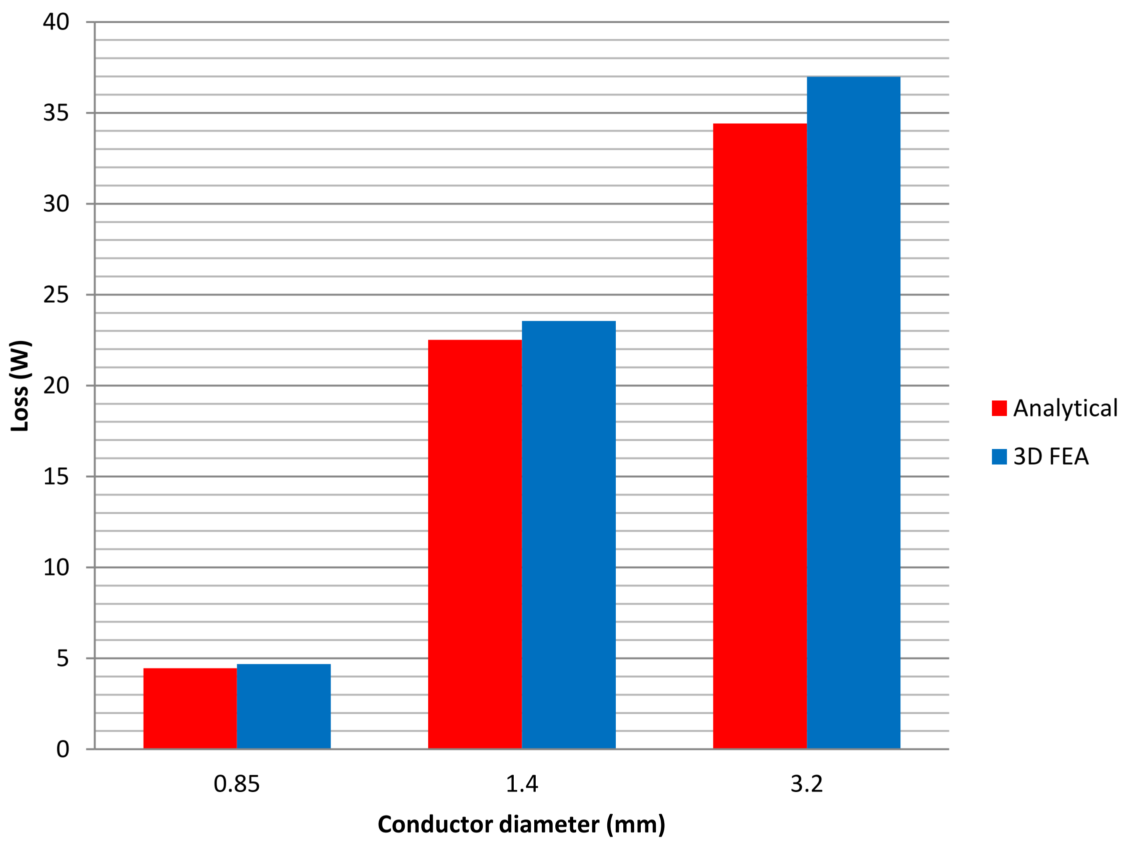

Figure 5-5: Analytical and FEA loss comparison at 1.5 mm from the air gap at 700 Hz.

For 1.4 mm diameter conductor the FEA loss increased by 4.5% and 10.1% at 1.5 mm and 12 mm from airgap respectively. The FEA loss of 0.85 mm diameter conductor increased by 5.5% at 1.5 mm from the airgap and by 1.7% at 12 mm from airgap. This may be due to the fact that in analytical loss analysis extra losses from flux leakage and higher harmonics are not considered and as the diameter increases, the skin-effect become more significant.

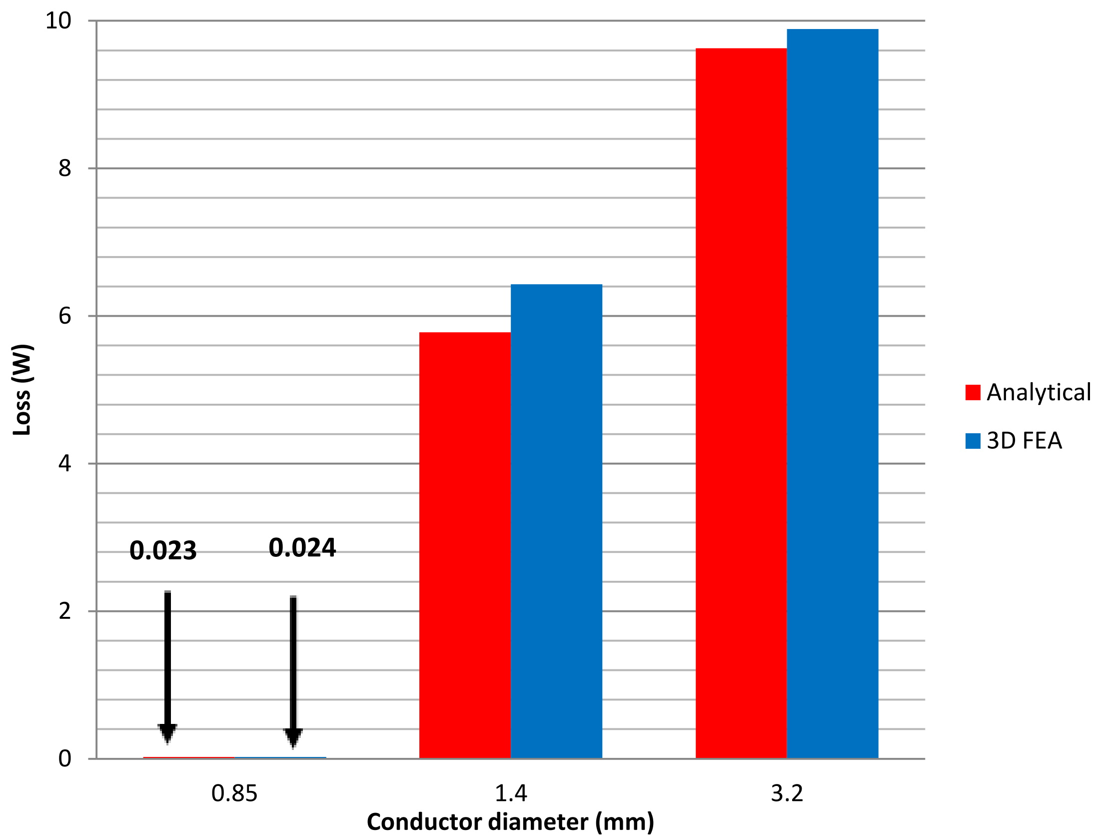

Figure 5-6: Analytical and FEA loss comparison at 12 mm from the air gap at 700 Hz.

The analysis also checks on placing the conductors at the bottom of the slot (far away from the airgap) as shown in Figure 5-7. For the 3.2 mm diameter conductor the peak FEA loss is 156.5 mW, an increase of 9.3% as compared to the analytical loss at 700 Hz. In the case of 1.4 mm and 0.85 mm diameter conductor, the peak FEA loss is 101.8 mW and 23.8 mW; an increase of 9.3% and 1.7% respectively.

From the above analysis and discussion, it is evidence that conductor diameter (size) and position in a slot has effect on the magnitude of the eddy current loss in a machine.

The frequency was doubled to 1400 Hz to see the effect of AC winding loss and Figure 5-8 shows the comparison between the analytical and FEA loss. In this case the coils are positioned only at 1.5 mm from the airgap.

The results shows that the FEA loss for 0.85 mm diameter conductor increased by 4.6% as compared to the analytical loss, while it increased by 7.1% for 1.4 mm diameter conductor and for the 3.2 mm diameter conductor the FEA loss to analtyical loss increased by 8.8%.

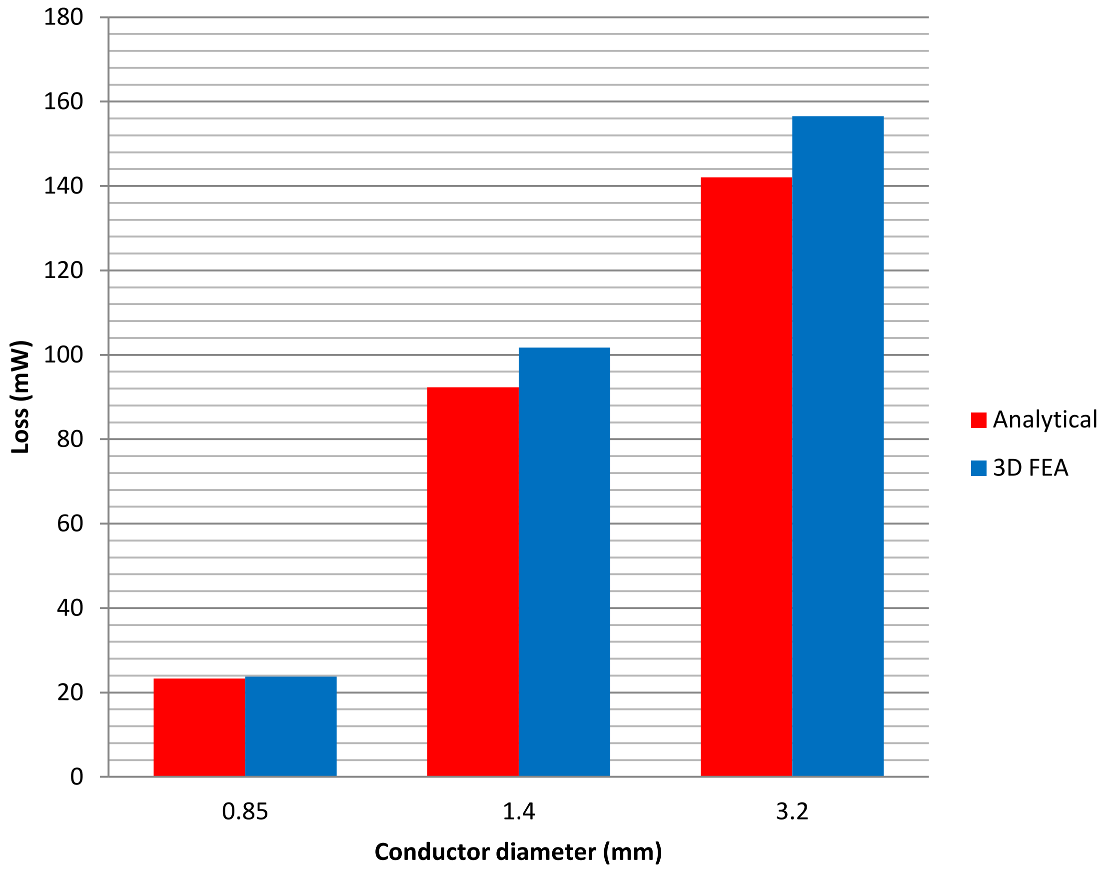

Figure 5-7: Analytical and FEA loss comparison at 24 mm from the airgap at 700 Hz.

It can be seen that frequency of operation in an electrical machine as an effect on the magnitude of eddy current loss, since eddy current loss is directly proportional to the square of frequency as stated in equation (5.5) above.

From the bar charts (Figure 5-5, Figure 5-6, Figure 5-7 and Figure 5-8) it can be seen that the losses increase as the conductor diameter increases. Similarly, as the frequency is doubled for 3.2 mm diameter conductor the losses increased significantly due to skin effect and open-slot stator winding configuration which encourage an elevated AC winding loss at AC operation.

It is also observed that, in the case of using diameter conductor greater than skin depth the current tends to flow toward the surface of the conductor and the inner part of the wire do not actually participate in current conduction. The inner part of the conductor serve as a coolant by absorbing most of the heat generated in the surface of the conductor during operation. As the frequency increase, the conductor effective resistance increases due to the decreased in the effective cross-sectional area for the AC current flow and the power loss also increased.

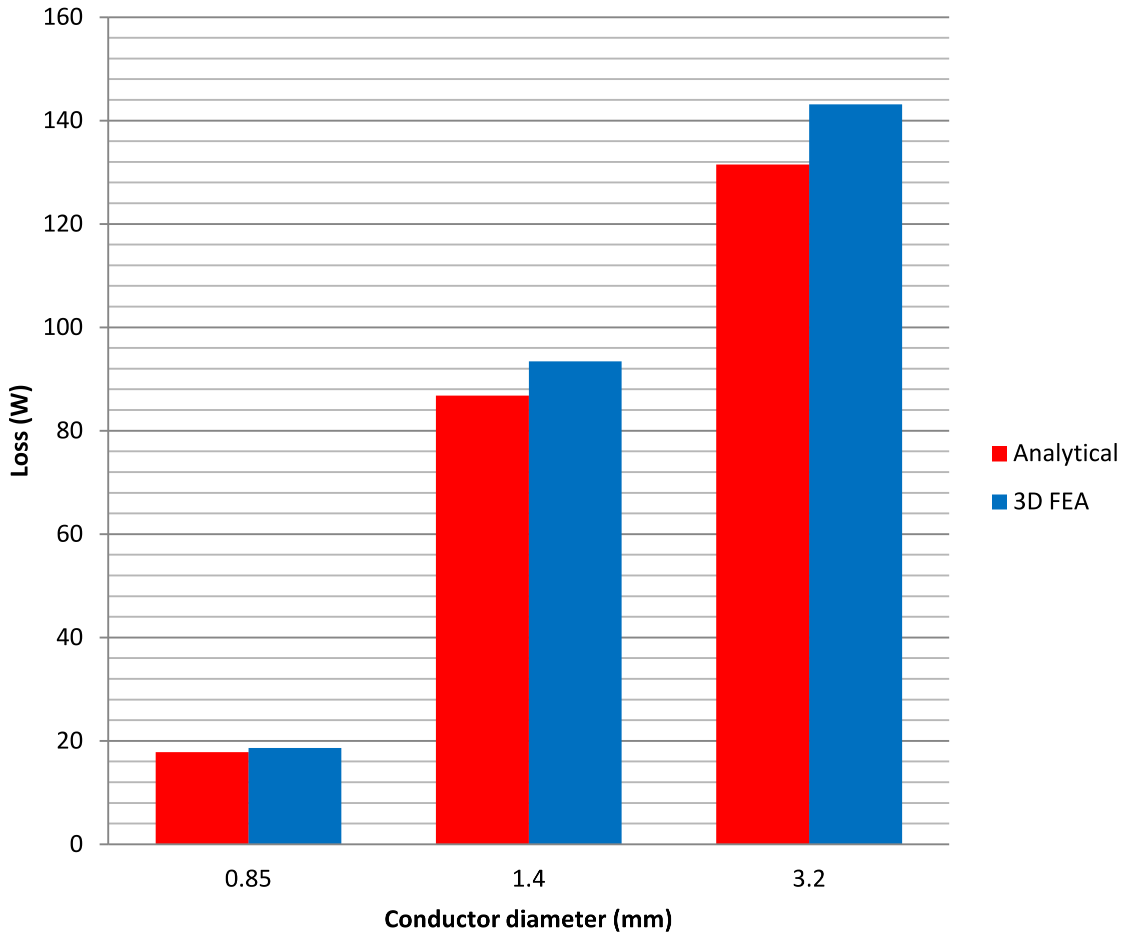

Figure 5-8: Analytical and FEA loss comparison at 1400 Hz and 1.5mm from air gap.

5.4 Alternative Method of Calculating AC Winding Loss; Analytical Expression for R_{ac}/R_{dc}

It is well established that the presence of a magnetic field within a conductor produces eddy current which tends to cancel the applied field [142].

In this section, comparison of R_{ac}/R_{dc} ratio in FEA and analytic model would be presented. According to [142], equation (5.6) is used for thin conductors, while equation (5.7) for thick conductor.

$$\frac{R_{ac}}{R_{dc}} = \left\{1 + \frac{1}{9}\left(\frac{d_s}{\delta}\right)^2 \left(\frac{h}{\delta}\right)^2\right\} \tag{5.6}$$

$$\frac{R_{ac}}{R_{dc}} = \frac{h}{\delta}\left\{1 + \frac{2}{3}\left(\frac{d_s}{h}\right)^2\right\} \tag{5.7}$$

where d_s = slot height, δ = skin depth, h = conductor diameter.

Equation (5.6) and equation (5.7) are valid for this type of machine topology depending if the eddy currents are resistance limited linear relationship or inductance limited which may be non-linear due to the area changing with frequency.

Table 5-1 presented the AC to DC loss ratio based on FEA calculation from the 3D FEA software. It was obtained from the total FEA AC loss and total FEA DC loss, the average turn length of 3.2 mm conductor diameter is 2.3 % and 1.1% higher when compared to 0.85 mm and 1.4 mm conductor diameter respectively.

Table 5-1: FEA calculation based on loss ratio

Conductor diameter (mm)	0.85	1.4	3.2
Average turn length (mm)	87.5	88.5	89.5
Radial conductor length (mm)	23	23	23
Radial length/end-winding ratio	0.49	0.51	0.54
Sum AC and DC (FEA) (W)	79.60	199.23	306.50
Total loss (FEA) (W)	78.49	197.85	304.39
AC/DC loss ratio	1.54	2.53	9.31

Table 5-2 presented the analytical calculation based on equation (5.5). The analytic expression for loss seems to match quite well with the FEA.

Table 5-2: Analytical calculation

Conductor diameter (mm)	0.85	1.4	3.2
Slot depth (mm)	25	25	25
skin depth (mm)	3.03	3.03	3.03
Conductor diameter/skin depth ratio	0.28	0.46	1.06
R_{ac}/R_{dc}	1.59	2.62	9.42

5.5 Full 3D FEA of AC Winding Loss

This section will discuss in detail the full 3D FEA of coils AC loss; attention will be given to the influence of conductor diameter, current and operating frequency on AC winding loss. The same methodology used on stranded conductors within slot is applied on a full coil model and three different size of conductor diameter were utilised in the analysis. The investigation were carried out on 88 number of turn of 0.85 mm conductor diameter, 32 number of turn of 1.4 mm conductor diameter and 6 number of turn of 3.2 mm conductor diameter in addition the rotor effects (rotor motion) were considered in all the analysis. For the 0.85 mm conductor diameter, the machine has 6 layers of coil, 2 layers of coils for 1.4 mm conductor diameter and a single layer for 3.2 mm conductor diameter.

Figure 5-9 shows the model with finer mesh on single tooth coils of 0.85 mm conductor diameter with 88 number of turn and other parts of the machine have larger mesh size.

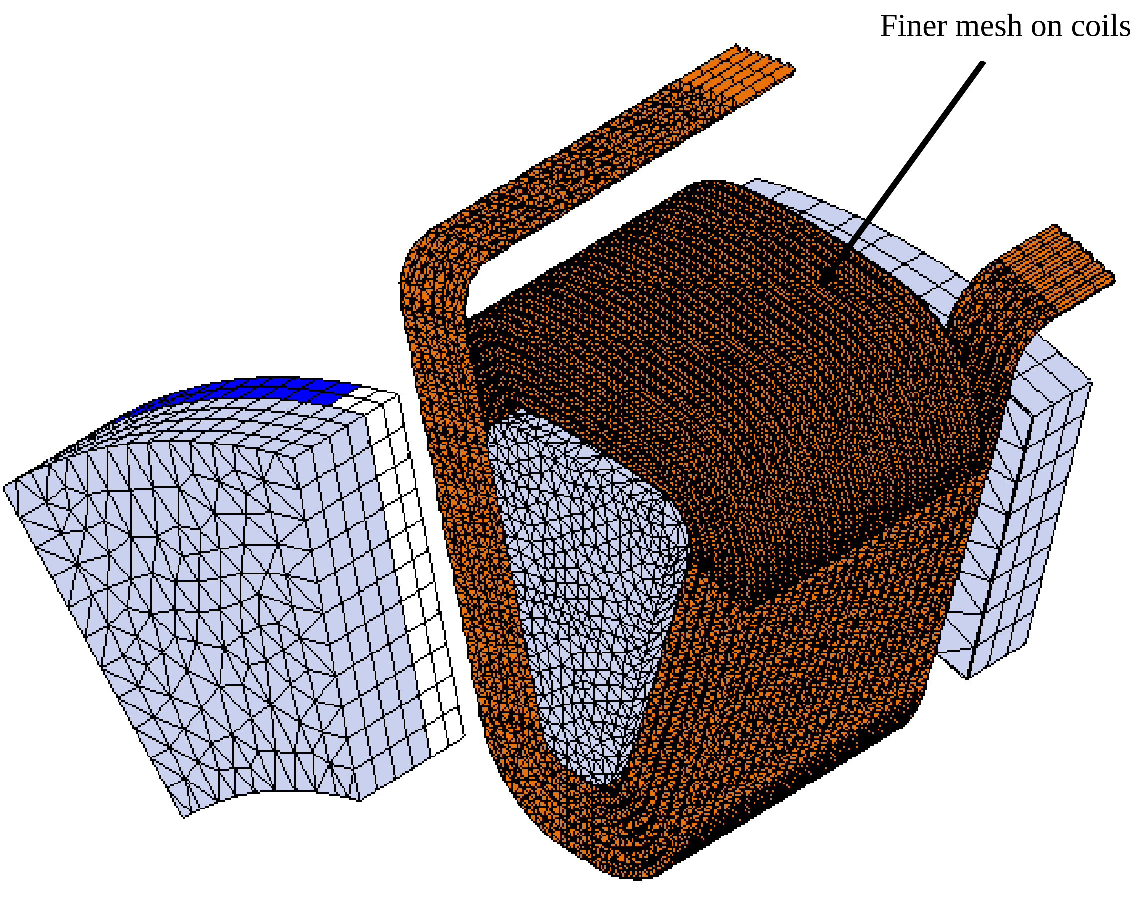

Figure 5-9: Finer mesh on single tooth coil of 88 turn, 0.85 mm conductor at 700 Hz.

Mesh size on coil does affect loss calculation, because larger mesh size underestimates loss in layers near teeth. The mesh size should be in similar order to conductor diameter to accurately model the winding loss.

When having two or more conductor strands in parallel there is a possibility of current recirculation within the parallel conductor. In this analysis the area of conductor with in the slot, the MMF and current density were kept constant and being preserved to be able to carry out comparison among the three different conductor diameter.

Figure 5-10 present the machine windings magnetic field strength contour plot of 0.85 mm conductor diameter with 88 number of turn at operating frequency. It has maximum value of 944.3 kA/m and minimum value of 12.2 A/m. To isolate the rotor proximity effect, the current was set to zero and then the coils were moved back into the slot at the moment it has only the skin effect.

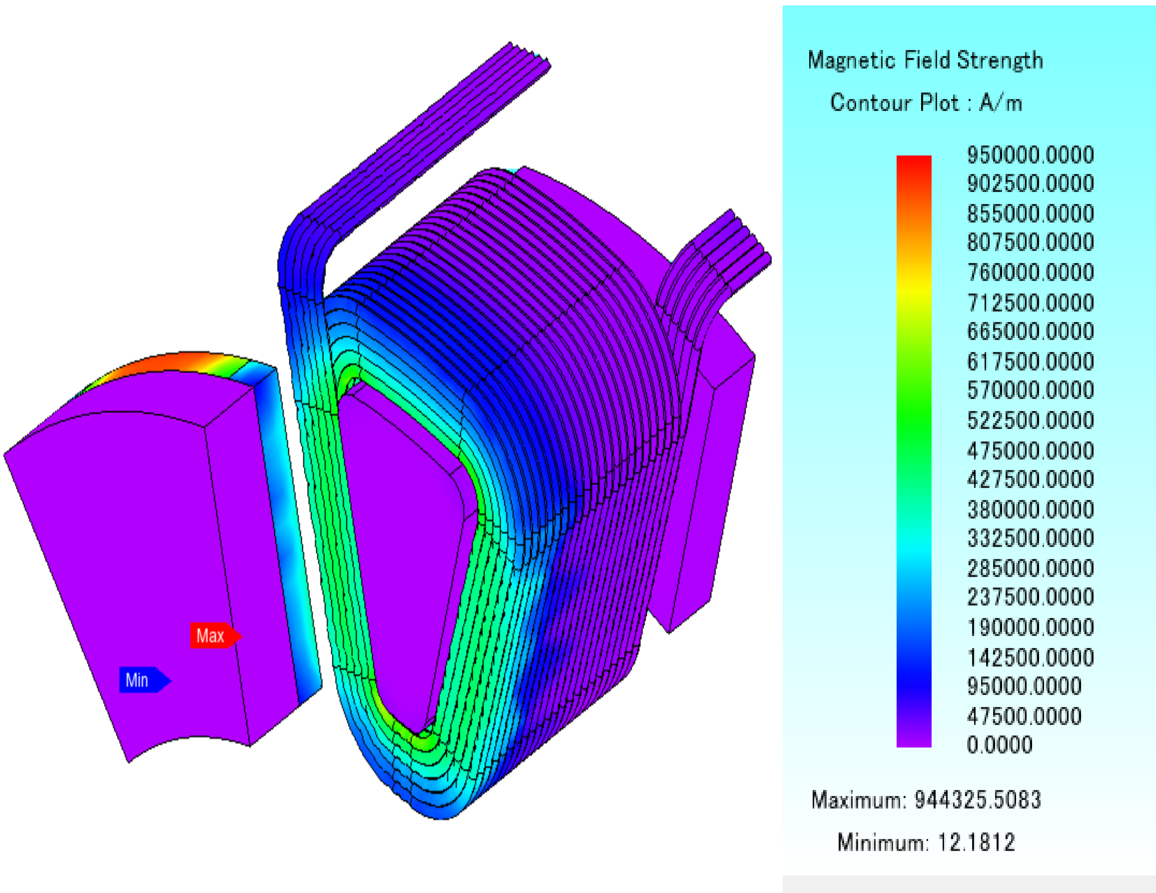

Figure 5-10: Magnetic field strength contour plot of 88 turn, 0.85 mm conductor at 700 Hz.

It can be seen from Figure 5-10 that winding layers close to airgap of the machine are more exposure to strong magnetic field strength compared to those that are far from the airgap. This also shows that, they have more power loss to those at the middle and bottom of the stator slots.

Current density contour plot of the machine windings is given in Figure 5-11, with maximum value of 205 MA/m^2 and minimum value of 34.3 kA/m^2 and from the contour plot, it is clear that the machine windings are not saturated at full-load current. Winding layers close to airgap experience more current density when compared to those winding layers at the middle and bottom of the stator slot.

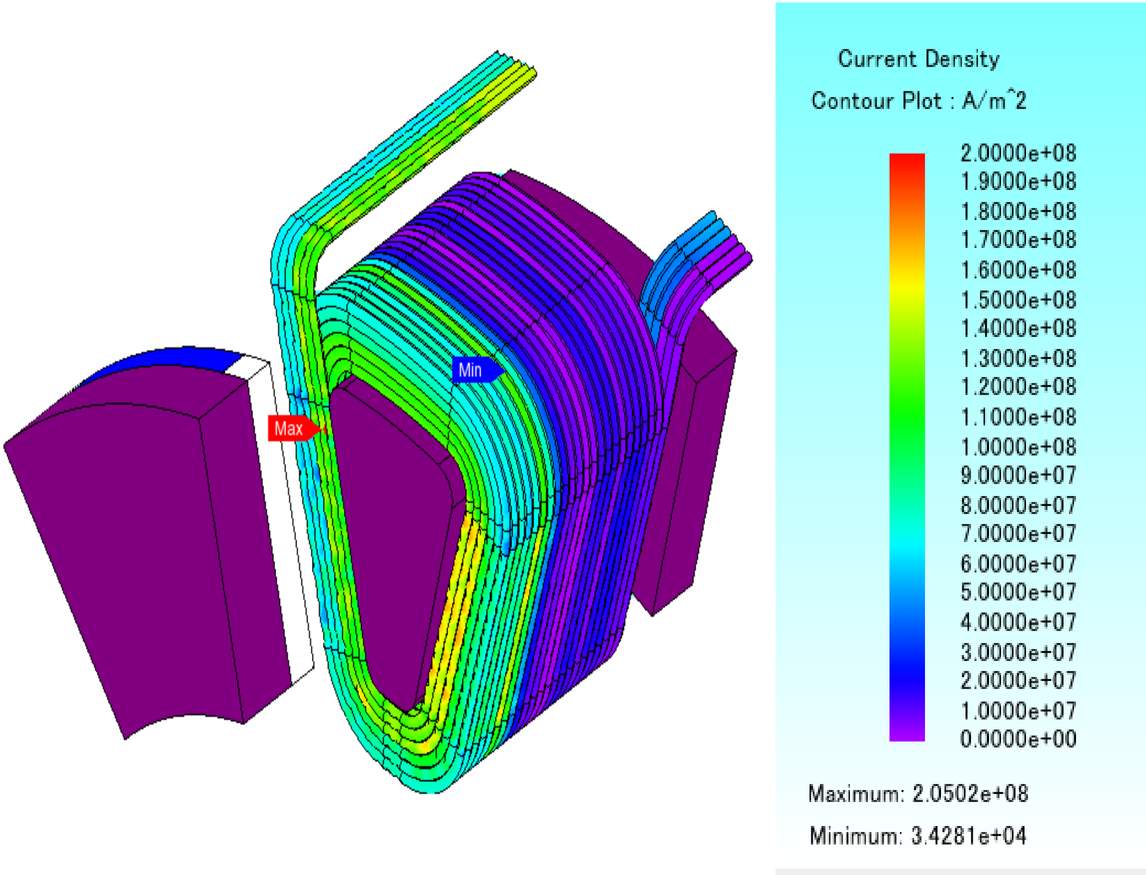

Figure 5-11: **Current density contour plot of 88 turn, 0.85 mm conductor at 700 Hz.**

Figure 5-12 shows the magnetic flux density contour plot of the machine, with maximum and minimum value of 2.0 T and 0.1 mT respectively. It can be seen from the contour plot that the SMC stator tooth edges tends to saturate and any other parts of the machine do not show any sign of saturation. The magnetic flux density is strong in machine windings and layers close to the airgap and decreases in strength as it go down to the middle and bottom of the stator slot.

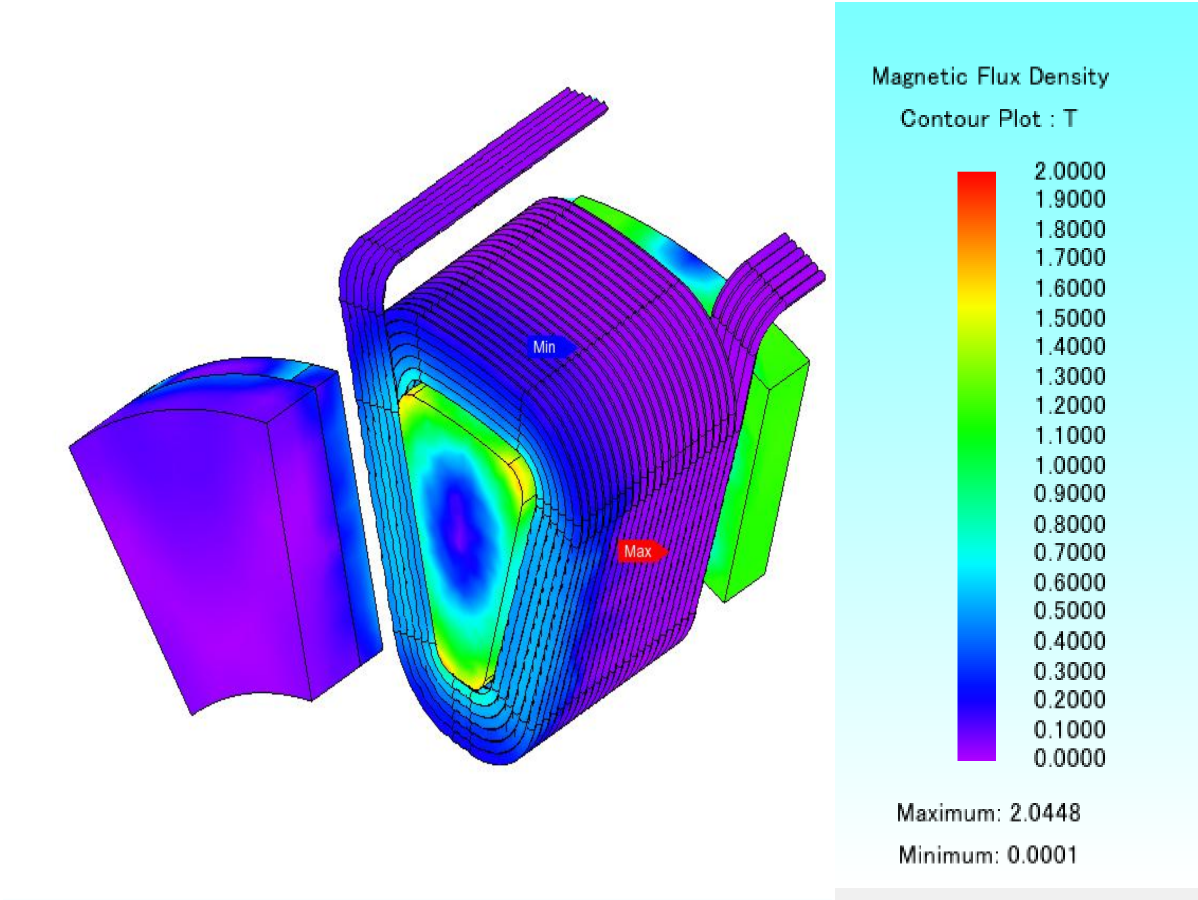

Figure 5-12: Magnetic flux density contour plot of 88 turn, 0.85 mm conductor at 700 Hz.

Figure 5-13 shows the variation of coil loss with different mesh size of 4 mm, 1 mm and 0.3 mm mesh for 0.85 mm diameter conductor. It can be seen from the graph that, the loss decreased from the peak value at layer close to the airgap to almost zero at layer far from the airgap.

The result shows, as expected, that the turns exposed to more airgap leakage do have more AC loss and those further away experience less AC loss. That is to say turns close to airgap experience more flux when compared to those far away from the airgap. It is clear from the analysis that, AC winding loss can be reduced in a machine by placing the conductors further away from the air gap, however at the expense of a much-reduced slot fill factor.

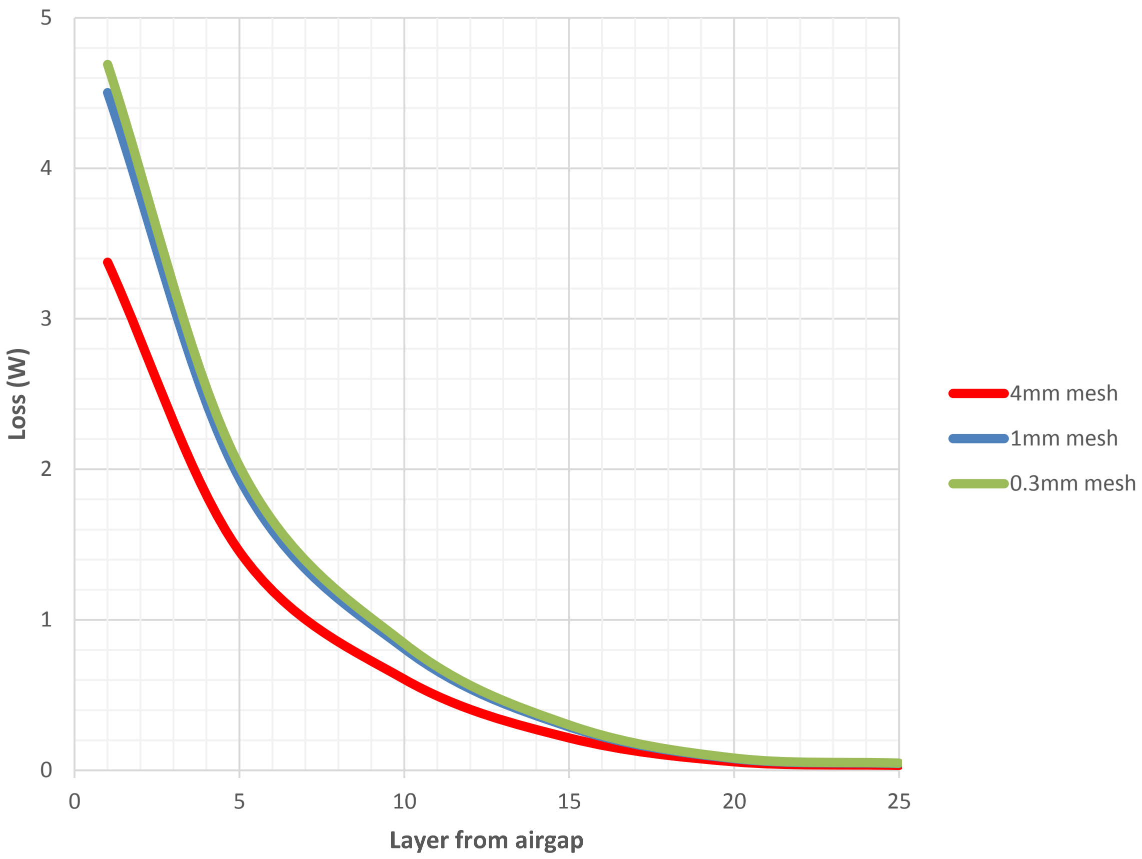

Figure 5-13: Loss variation at different winding layers of 0.85 mm conductor diameter.

All the 3D FEA solution are carried out in transient magnetic on a single tooth with full model conversion set to 12 on periodic boundary based on the number of stator teeth in the machine. Figure 5-14 presented the coils arrangement in the stator slot which shows the first and the second layer of coils wound on the stator tooth, that is those close to the stator tooth, while Figure 5-15 shows the current in the two near coils (the first and the second layer) for 0.85 mm diameter conductor at 5 A/mm^2, series connection and 700 Hz.

Similarly, Figure 5-16presented the coils arrangement in the stator slot which shows the fifth and the sixth layer of coils, that is those two coils far from the stator tooth and Figure 5-17 shows the current in the two far coils (the fifth and the sixth layer) for 0.85 mm diameter conductor at 5 A/mm^2, series connection and 700 Hz.

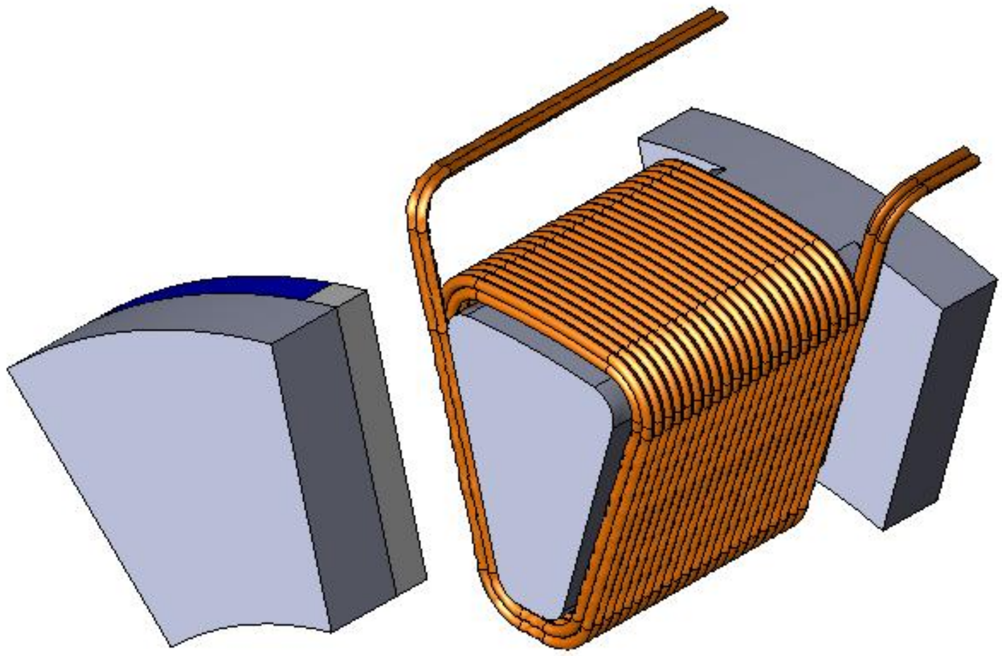

Figure 5-14: The first and second layer of coils of 0.85 mm conductor diameter

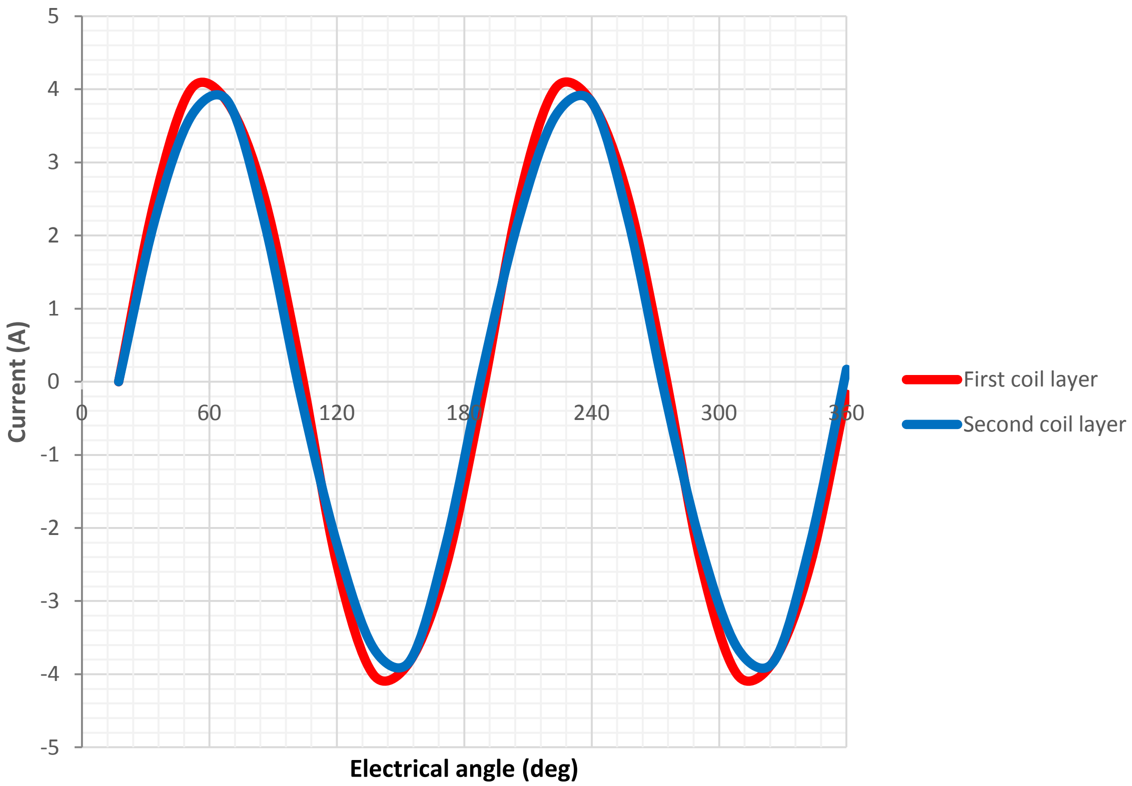

Figure 5-15: Current in the first and second layer of coils.

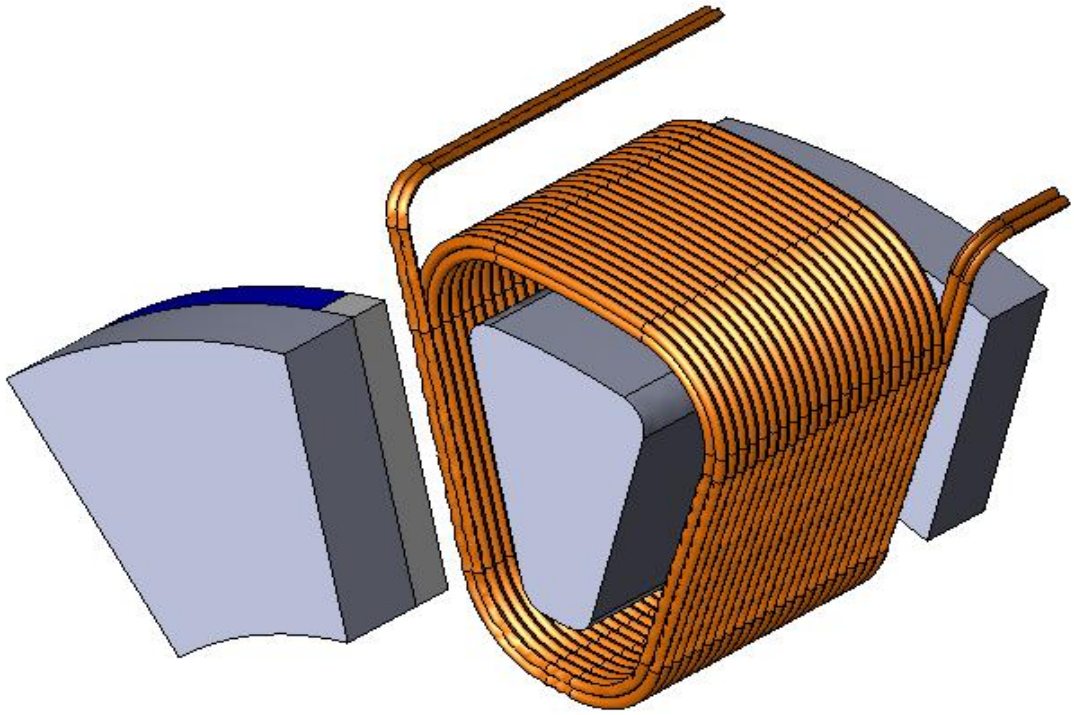

Figure 5-16: The fifth and sixth layer of coils of 0.85 mm conductor diameter.

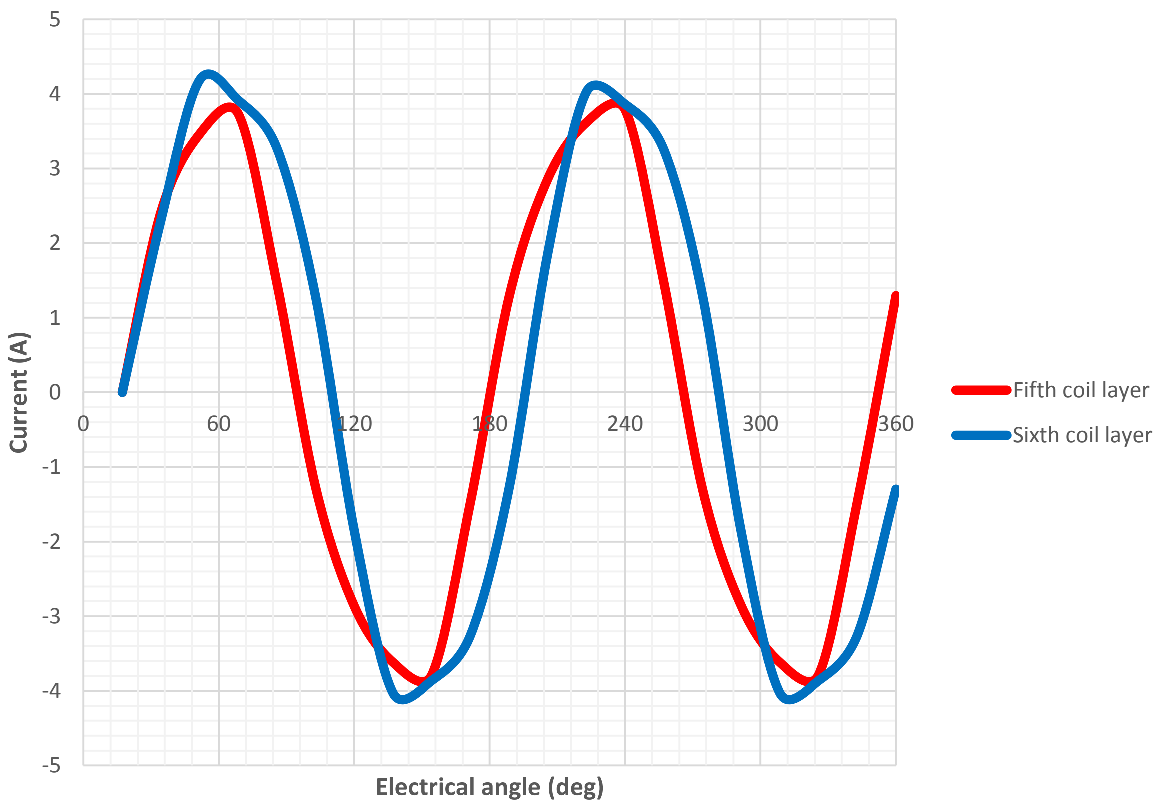

Figure 5-17: Current in the fifth and sixth layer of coils.

It can be seen from the waveform of two near coils (first and second layer) as shown in Figure 5-15 that, the currents have little difference in amplitude between the inner coil and outer coil. But in Figure 5-17, it is clear that the currents have difference in amplitude and the waveform shape between the fifth (inner) coil and sixth (outer) coil.

For 0.85 mm diameter conductor, six concentric layers of coils are modelled and are connected in series to examine the effect of circulating currents within the coil at 700 Hz, 4.02A/strand (rms) (5A/mm^2), copper temp was set to 150ºC to accurately calculate the loss in the model. Similarly, for 3.2 mm and 1.4 mm diameter conductor, a single coil and double coils are modelled.

The result show the difference in loss between the first layer of coils and the second layer of coils which may be due to the high resistivity of the copper conductor at 150ºC which tends to decrease eddy current loss of the second layer of coils. Figure 5-18 and Figure 5-19 presented the joule loss in two near coils (first layer and second layer) and the two far coils (fifth layer and sixth layer) of 0.85 mm diameter conductor. In the former, that is the two near coils close to the stator tooth, the first layer coil has the peak loss of 14.5 W, while the second layer coil has the peak loss of 18.2 W, a difference of 3.7 W between the two coils.

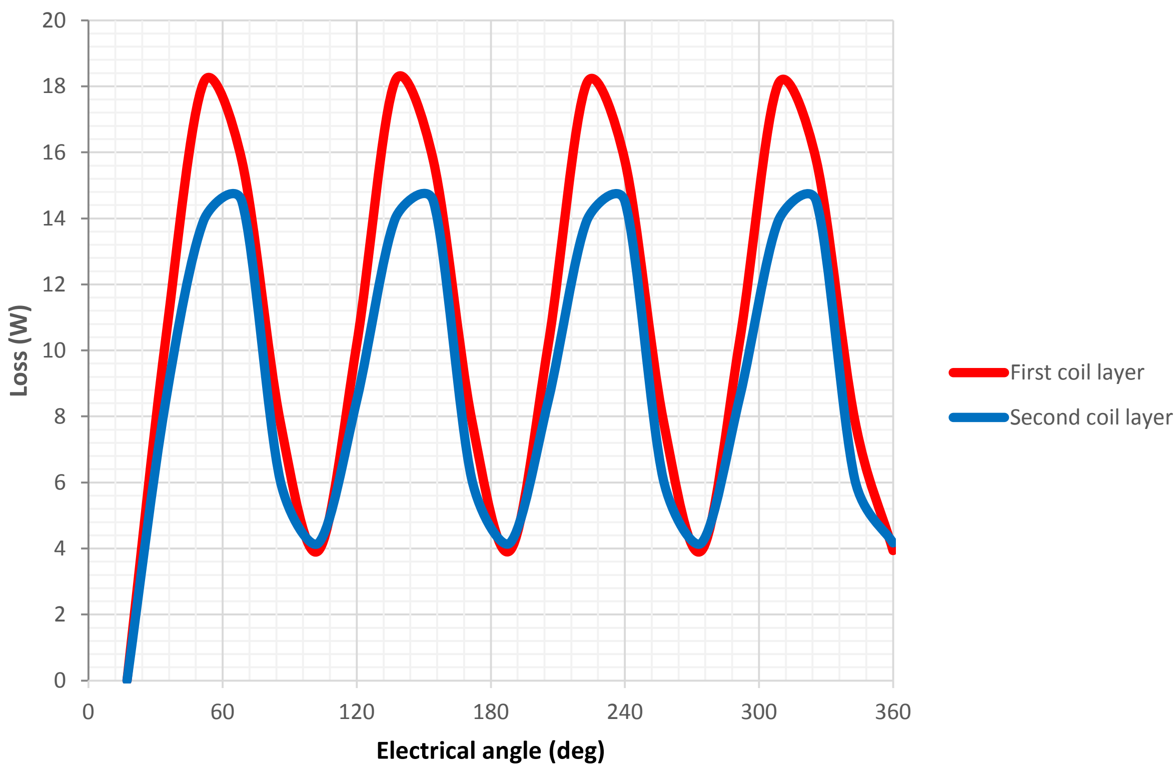

Figure 5-18: Joule loss in the first and second layer of coils.

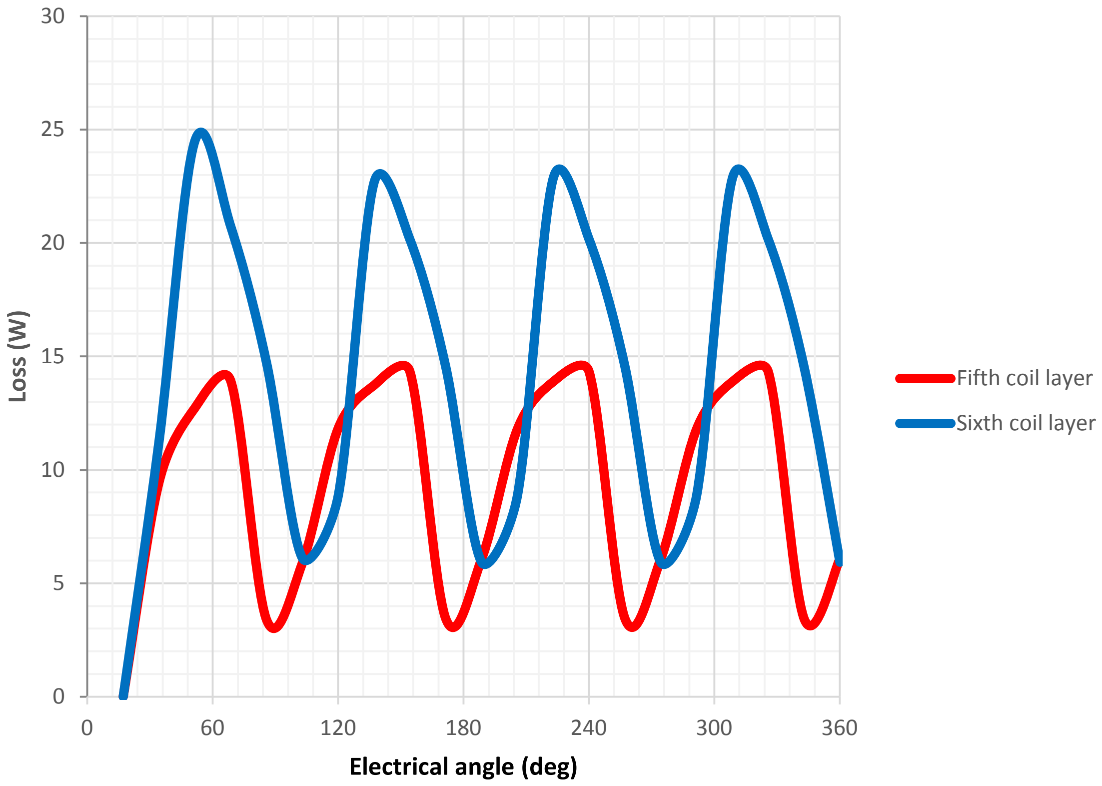

Figure 5-19: Joule loss in the fifth and sixth layer of coils.

In the far coils from the stator tooth, the joule loss from the waveform shows that the fifth layer (inner) and sixth layer (outer) coils have the peak loss of 14.3 W and 24.5 W respectively, a difference of 10.2 W between the coils. Proximity effect is always the most prevalent in the outer most coils of an electrical machine due to their exposure to a greater magnetic field gradient by nearby coils from adjacent stator tooth.

The effect of operating frequency for a full model winding was examined with different conductor diameters and Figure 5-20 shows the AC winding losses of different conductor diameter at different speed. It is shown that as the frequency increase, the AC winding loss increases due to skin effect on the conductor.

From the graph it is clear that as the diameter of conductor increasing, the AC winding loss increases as a result of the losses induced by the excitation field as the power of four based on equation (5.5).

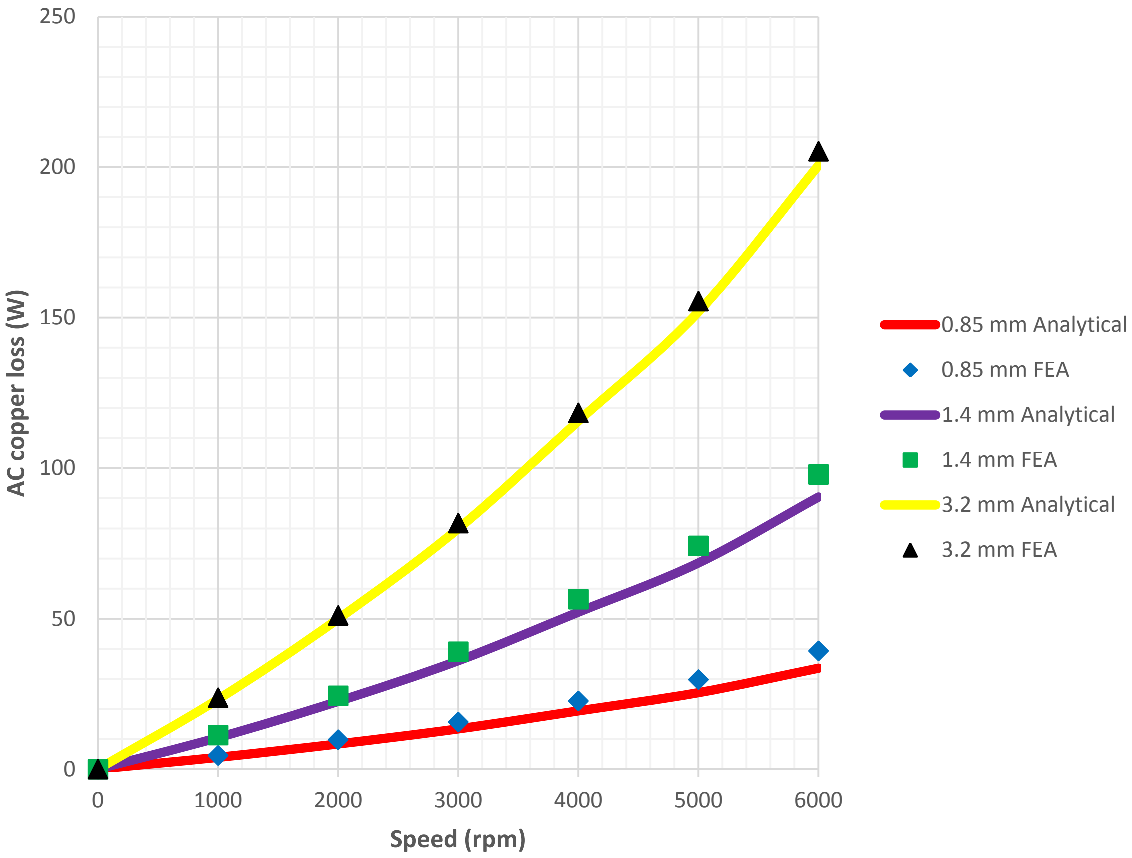

Figure 5-20: Influence of speed on AC winding losses

Figure 5-21 compared the sum of analytical AC and DC loss with the total 3D FEA loss from the detail model, it is clear that the sum of AC loss and DC loss agree with the detailed 3D FEA model with high accuracy.

The result shows that the 3D FEA total loss of 0.85 mm conductor diameter decreased by 1.4% as compared to sum of AC and DC loss. Similarly, for 1.4 mm and 3.2 mm conductor diameter the total FEA loss to sum of AC and DC decreased both by approximately 0.7%.

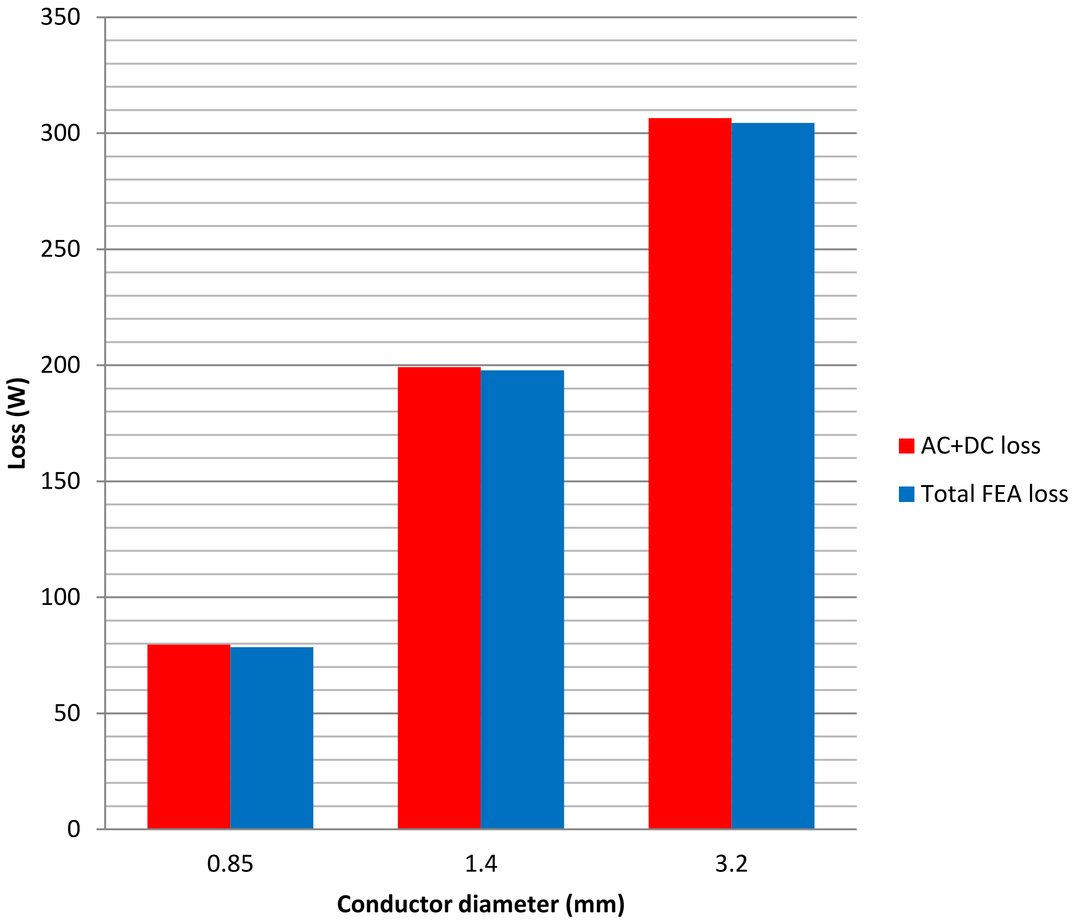

Figure 5-21: Comparison of AC+DC loss and Total 3D FEA loss.

At full load speed, the efficiency of the machine were obtained based on equation (4.33) and decreased when AC winding loss is included. Figure 5-22 compared the efficiency of the machine with different conductor diameter and the results show that as the conductor diameter increase the effect of AC winding loss due to skin effect and open-slot stator winding configuration is significant and the efficiency decrease.

It shows that the efficiency of the machine with larger conductor diameter of 3.2 mm decreased by 10.8% as compared to 0.85 mm diameter conductor and decreased by 6.2% when compared to 1.4 mm diameter conductor.

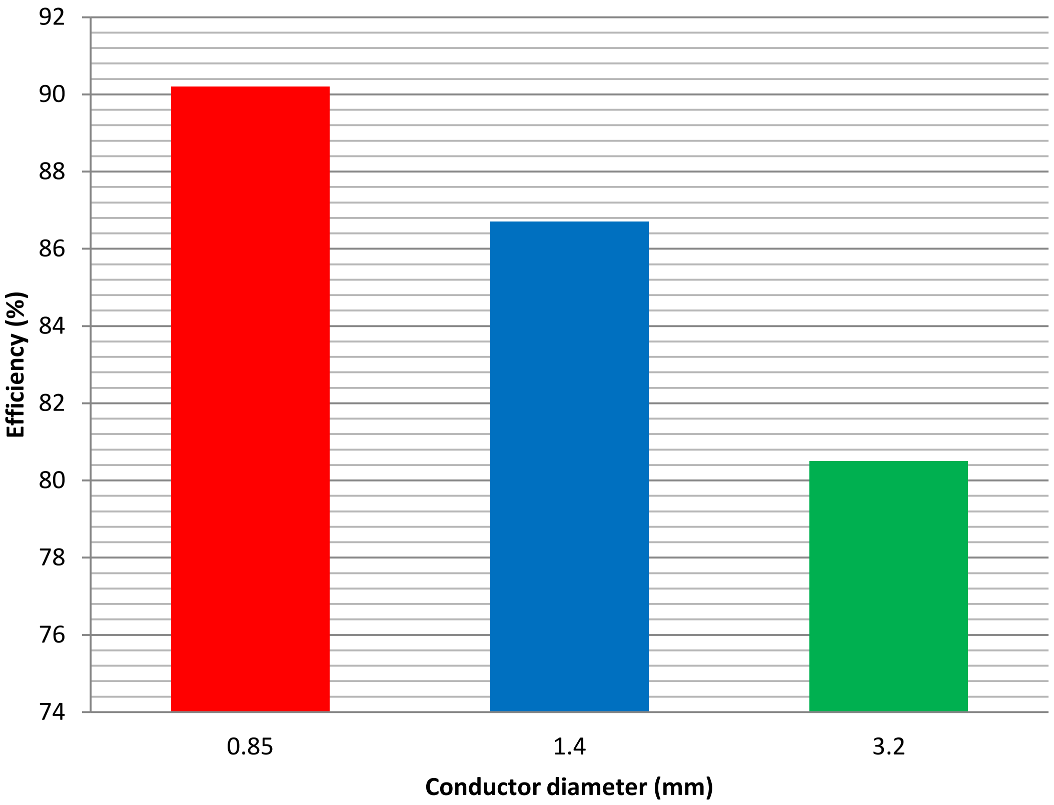

Figure 5-22: Efficiency with AC winding loss.

5.6 Current Density Distribution

The current density distribution of a cross section of winding coils is shown in Figure 5-23. It is clear from the figures that with the diameter increasing, the skin-effect becomes more significant. There is difference in the current in the inner and outer conductors. This is as a result of larger resistance of the outer coil due to the longer circumference. At 700Hz the inner coil current has a peak value of 3.73Arms and 4.78Arms in the outer coil. The contour plot has a maximum value of current density 208 MA/m^2 and minimum value of 56 KA/m^2.

Skin effects is responsible for AC current and cause it to distribute a proportion equal to 66.7% within a layer one skin depth thick around the surface of the conductor [143]. However, in a double arrangement the current distributions are more complex due to proximity effects as a result of adjacent magnetic field and leakage on a turn.

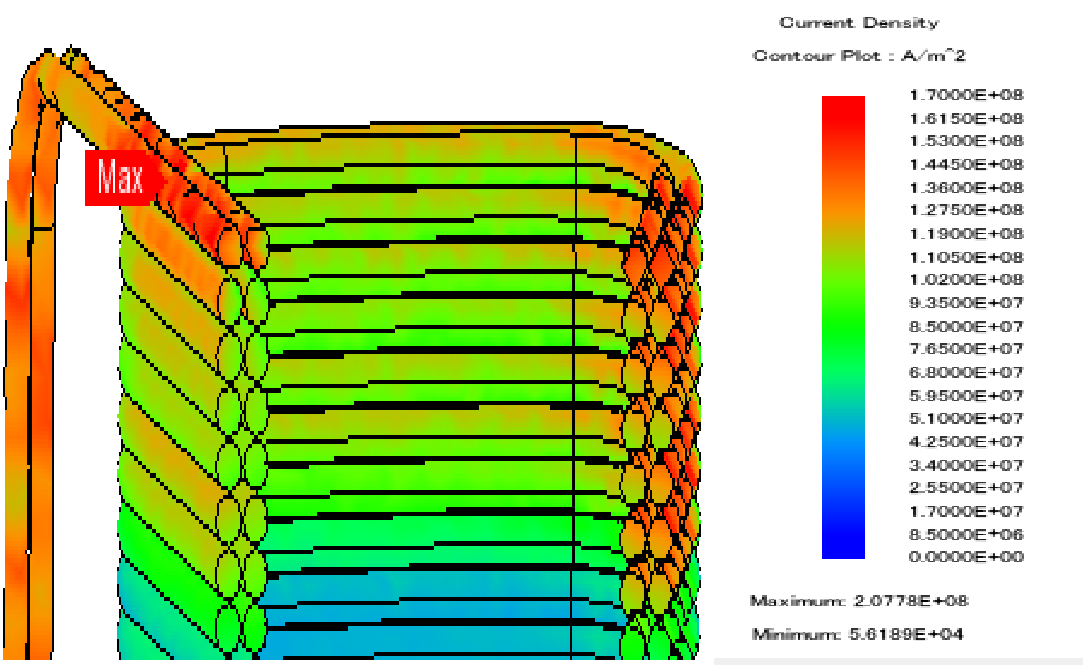

Figure 5-23: Cross sectional view of current distribution within the conductor of 32 turns with 2 layers.

5.7 AC to DC Ratio

When a winding is energised at DC or low frequency, in which the skin depth is larger than the conductor diameter, the current density is uniform. However, when the frequency is high, the current density is not uniform, and the AC winding resistance is higher than the DC resistance due to skin and proximity effects and the ratio of AC to DC power loss is given by equation (5.8) as reported in [123] and assuming $I_{rms}^2 = I_{DC}^2$

$$\frac{P_{AC}}{P_{DC}} = \frac{R_{AC} I_{rms}^2}{R_{DC} I_{DC}^2} = \frac{R_{AC} I_{rms}^2}{R_{DC} I_{rms}^2} = \frac{R_{AC}}{R_{DC}} = F \qquad (5.8)$$

where P_{AC} is the AC power loss, $P_{DC}$is the DC power loss, R_{AC} is the AC resistance, R_{DC} is the DC resistance, I_{rms}^2 is the rms current and I_{DC}^2 is the DC current.

Hence, eddy current increases the AC winding loss over the DC copper loss by a factor of F. At DC the factor F is 1, this rises with increase in frequency and conductor diameter size.

5.8 Conclusion

AC winding loss of open-slotted AFM has been analysed and presented in this chapter. The effect of conductor diameter and position in the slot, operating frequency and element mesh size on coils which relates to solution accuracy only has been discussed. Analytical and 3D FEA method for the AC winding loss were given.

It was examined that the AC winding loss increased with increasing the conductor diameter due to the skin effect. Three conductor diameters were modelled and investigated at operating frequency; it was found that the peak AC winding loss for 3.2 mm conductor diameter was 410% and 110% higher as compared to 0.85 mm conductor diameter and 1.4 mm conductor diameter respectively. The 3D FEA of the machine have shown that the eddy-current losses induced in the stator winding as a result of the time-changing field from the rotation of the PM rotor assembly are the dominant component of the winding loss at the AC operation. This is caused by the open-slot stator winding construction, which encourages an elevated winding loss from the PM rotor.

Eddy current loss is proportional to square of frequency and fourth power of conductor diameter, a property which can be used to simplify further loss analysis. Sensitivity analysis has been used to accurately determine the AC winding loss. The sum of the analytical AC loss and DC loss has been compared to the total 3D FEA loss from the detail model and a close agreement found. The result shows that the 3D FEA total loss of 0.85 mm conductor diameter decreased by 1.4% as compared to sum of analytical AC and DC loss. Similarly, for 3.2 mm conductor diameter and 1.4 mm conductor diameter, the total FEA loss to sum of AC and DC decreased both by 0.7%.

The efficiency of the machine with 3.2 mm conductor diameter decreased by 10.8% and 6.2% as compared to 0.85 mm diameter conductor and 1.4 mm conductor diameter respectively. To implement a bigger conductor diameter in the winding design for easy pre-wound on a former before sliding onto the stator tooth and termination, there is a need for a technique to reduce the AC winding loss at operating frequency. Chapter 6 explores a simple method of AC winding loss reduction in open-slotted AFM that relied on different single steel lamination sheet for shielding stray flux.

6. AC Winding Loss Reduction

The outcome from the AC winding loss analysis carried out in Chapter 5 shows that the efficiency of the machine at rated speed with conductor diameter larger than the skin depth is low; In addition, it demonstrated quantifiably the need for protection against AC losses in this type of machine topology.

This chapter introduces techniques that can be used to improve the overall performance of AFM with open-slotted configuration described and analysed in Chapter 4 and 5 using a single steel lamination sheet, by reducing the eddy-current losses induced in the stator winding as a result of the time-changing field from the rotation of the PM rotor assembly, and the effect of higher frequency of operation resulting in skin-depths of the same order of size as the typical conductor diameters.

This approach is easy to implement for this machine topology with conductor diameter larger than skin depth together with easy termination and does not require the use of more complex twisted and expensive Litz type conductors. The techniques were first simulated using 3D Finite Element methods software; results and comparisons are presented in this chapter.

Ten different steel lamination sheet and two designs segmented and non-segmented were investigated and are described in table 6-1 together with some of the properties of steel lamination sheet used in the analysis which include: thickness, conductivity, loss and relative permeability at 1.5 T, resistivity and the material hardness.

Table 6-1: Steel lamination sheet properties description.

Label	Description	Thickness (mm)	Conductivity (MS/m)	Loss at 1.5T (W/kg)	μ_r at 1.5T	Resistivity (μΩcm)	Hardness HV5
L1	without steel lamination	NA	NA	NA	NA	NA	NA
L2	Segmented M235-35A	0.35	1.70	2.25	610	59	220
L3	Non-segmented M235-35A	0.35	1.70	2.25	610	59	220
L4	Segmented M270-35A	0.35	1.81	2.47	700	52	215
L5	Non-segmented M270-35A	0.35	1.81	2.47	700	52	215
L6	Segmented M300-35A	0.35	2.0	2.62	830	50	185
L7	Non-segmented M300-35A	0.35	2.0	2.62	830	50	185
L8	Segmented N020	0.20	1.9	2.16	530	59	210
L9	Non-segmented N020	0.20	1.9	2.16	530	59	210
L10	Segmented M270-35A, torque as L1	0.35	1.81	2.47	700	52	215

6.1 Introduction

It is seen in Chapter 5 that, AC winding loss analysis with bigger conductor diameter has more losses when compared to smaller conductor diameters and the efficiency of the machine with larger conductor diameter decreases due to enhanced AC winding loss at operating frequency. A method of AC winding loss reduction in a single-sided open-slot AFM using SMC and steel lamination to shield the coils from stray fields will be discuss. AFM is suitable for application where compact design and high efficiency are required as stated in [7] and [14]. A lot of research has been done to minimise AC winding loss in electrical machines.

AC loss reduction in superconducting coils was investigated [144]-[148]. Similarly, AC copper losses reduction of the ironless brushless DC machine was reported in [5]. Litz wires with twisted transposed strands to reduce circulating currents were presented in [149] and [126]. But, Litz wire is too expensive which can increase the cost of production, in addition it has unequal current density distribution, bad thermal behaviour and large DC resistance as compared to a solid conductor.

Skin and proximity effect under high frequency operation will significantly result in more copper loss in an electrical machine. The latter is more complex and difficult to estimate when compared to the former. The majority of literature has not considered the proximity effect; however at high frequency the magnitude of the loss due to proximity effect cannot be disregarded.

This clearly shows that when the excitation frequency increases, the machine winding AC resistance will increase considerably, resulting to a large amount of winding loss. The proximity effect is predominant in a multi-layer wire. Litz wire can be use in order to handle the increased winding loss due to proximity as for skin effect the correct wire gauge should be use for the intended frequency of operation.

Litz wires are usually made for exceptional high frequency applications and are manufactured using hundreds of small diameter twist strands divided into many bundles and the bundles are also transposed along the length. This type of wire is too expensive for most applications. In [150] a cost-effective method to reduce proximity effect using transposed wire bundles was presented and its dissimilarity with Litz wire is the number of transposed strands and bundles is much smaller. The analysis was carried out on Litz wire, transposed and untransposed wire. They conclude that the loss in an untransposed wire increases rapidly as the frequency of operation is becoming higher and the level of transposition also affects the proximity effect.

The shape of the conductors used play a vital role reducing proximity loss in a machine as presented in [126]. They found that an appropriate conductor positioning in the slot and minimising the height of the conductors in radial direction can reduced the proximity loss effectively.

In [151] the performance of untwisted solid strand windings and Litz wire were analysis and compared. The result shows that Litz wire which is more expensive decreased the AC winding loss significantly but has a lower fill factor when compared to solid conductor. They also found that copper loss can be limited to 150% to those of Litz wire by placing the conductors far from the airgap and covering only half of the slot at the expense of low fill factor. Similarly, they proposed alternative approach by using several strands in parallel and this limit the copper loss to 193% of the ideal Litz wire which is more appealing for a better fill factor and lower thermal capacity in a machine.

In actual engineering application, some balance is needed on the selection of conductor type. Litz wire can be utilised to reduce a winding loss due to high frequency, if cost is not a problem. The issue of low fill factor and high thermal resistivity should be in mine when using the Litz wire.

The size of end-winding in machine has an influence on the total power loss at AC operation. In [152] the influence of an end-winding size on proximity losses in a high-speed PM synchronous motor was reported. In the analysis, they investigated the end-winding arrangements in the machine using different conductor profile sizes and shapes and found that the end-winding in this particular machine donates winding loss significantly and equate to an average of 26% for the total winding loss.

An optimal twisting criterion that allows the reduction of the AC winding losses due to parasitic circulating currents in machines having tooth-wound coils was proposed in [153]. This technique was based on a single transposition of the parallel-connected strands and is cost-effective and replacement to Litz wire. However, they found that there is reduction in the machine DC winding loss and increased in the fill factor.

Winding design for minimum power loss in application to fixed-speed PM generator was reported in [8] using an edge wound preformed concentrated winding design which used rectangular copper conductors profiled. Moreover, this type of winding arrangement allows for an automated coil forming process that can lower manufacturing and assembly cost together with the total power loss in the machine as compared to alternative low cost conductor arrangement. But, this type of conductor arrangement cannot be implemented in AFM.

A lot of research has proposed various techniques on offsetting proximity effect in an electrical machine, this could be pole shaping, having deeper slots and utilising Litz wire. All these techniques are limited and too expensive, that is to say they can’t be implemented cheaply as in an AFM using a single steel lamination sheet.

6.2 AC Winding Loss Reduction

In this section, an approach for AC winding loss reduction using different single steel lamination sheet for flux diversion is presented. The steel lamination sheets on trial are M235-35A, M270-35A, M300-35A and N020 with conductivity of 1.70 MS/m [154], 1.81 MS/m [155], 2.0 MS/m [1] and 1.9 MS/m [156] respectively.

The reason for using these types of steel laminations with 0.35 mm and 0.2 mm thicknesses is their availability and they are cost effective. The laminations were cuts based on the inner and outer diameter of the machine with opening for the teeth. It is placed 0.5mm from the top of coil to shield the stray flux.

Two designs were proposed and used in the analysis that is the segmented and the full CAD diagram is as shown in Figure 6-1 and non-segmented steel lamination sheet full diagram is as shown in Figure 6-2.

The segmented design is not a true segmented that is to say, it is not 100% segmented due to mechanical design and to meet a simply mechanical minimum requirement to avoid problems of fixing during the machine assembly. There is no or little leakage eddy current through it when compared to non-segmented design.

The novelty of this research work is that, this technique has not been tried before on AFM and the magnetic shield can be made from a single steel lamination sheet whereas it is hard to imagine a single steel lamination sheet making all the slot wedges in radial flux machines. This partially results from wanting to slip the coils onto the tooth.

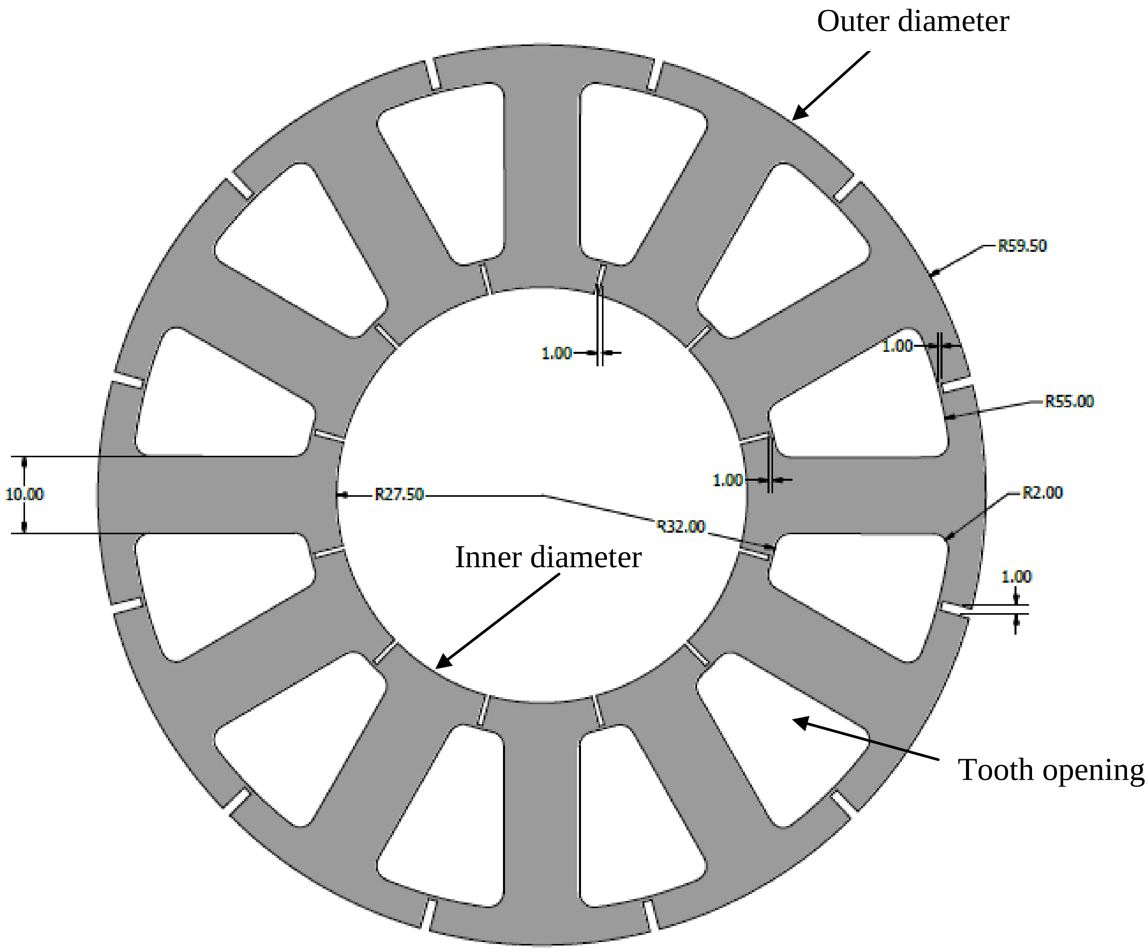

Figure 6-1: CAD diagram of segmented steel lamination sheet.

This steel lamination sheet covers both the coils in the slot openings and end windings to control the machine slot leakage inductance and to achieve less AC winding loss and high efficiency. The idea of using the non-segmented design is to allow eddy current circulation on the steel lamination sheet, while the segmented design is to prevent the circulation of eddy current.

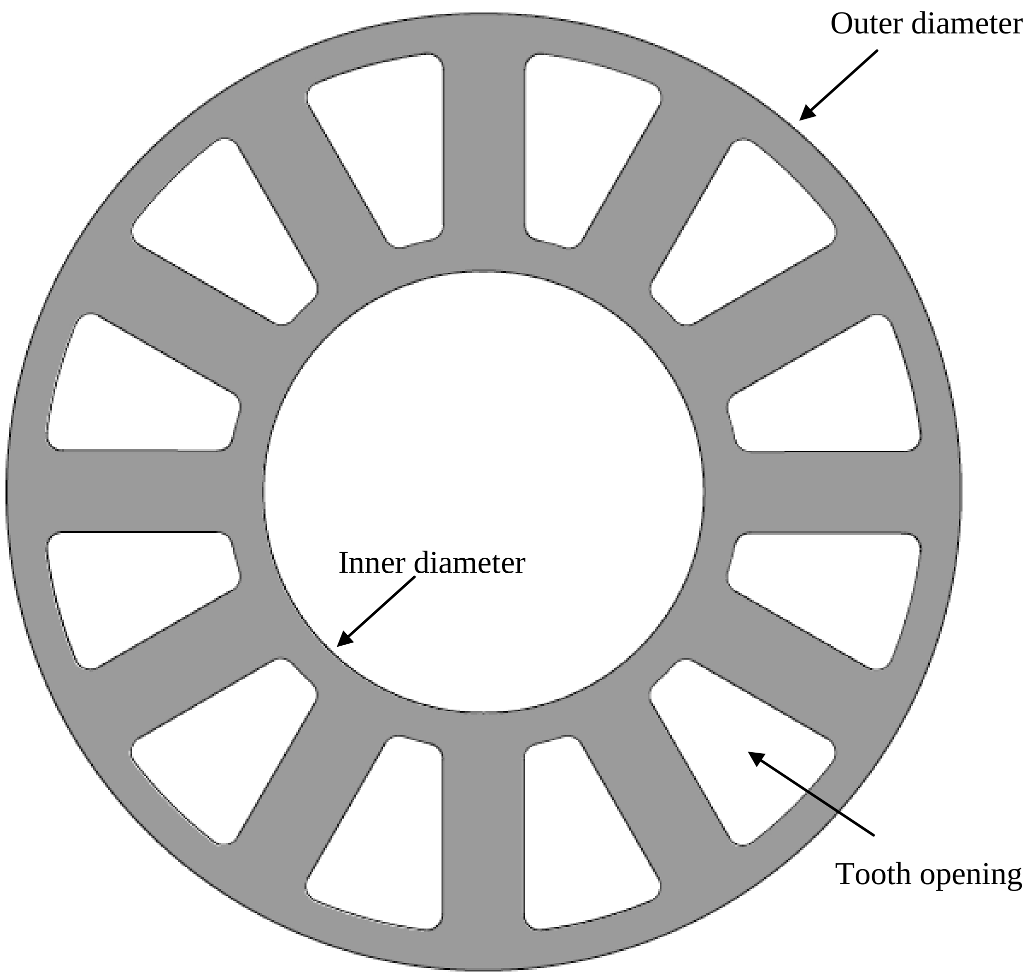

Figure 6-2: CAD diagram of non-segmented steel lamination sheet.

6.3 The Principals of Slot Leakage Inductance

To make the AFM work very well under full load current with steel lamination sheet for AC winding loss reduction, there is a need of a phase inductance design approach by altering the machine inductance created by the real leakage flux. The total current in the slot is obtained by the product of the number of conductors in the slot and the current flowing through them.

The reduction in the AC winding loss, total loss and slightly decrease in average torque and back EMF in the machine due to the introduction of magnetic shielding is as results of changes in the slot leakage inductance of the machine. Hence, there is a need to discuss the slot leakage inductance.

The phase inductance of surface mounted machine comprises of the slot leakage inductance, synchronous inductance, harmonic inductance and end leakage inductance, at higher speeds when the phase resistance is less than the ωL, the characteristic current I_{ch} of the machine is given by equation (6.1) as stated in [157].

$$I_{ch} = \frac{\psi_{pm}}{L} A\, rms \tag{6.1}$$

where ψ_{pm} is the rms magnetic flux linkage of the PMs and L is the inductance.

Assuming the condition for optimal leakage inductance in an SPM machine occurs when the machine.

$$I_{ch} = I_R \tag{6.2}$$

where I_R is the rated current.

The different steel lamination sheet controls the machine inductance and is a design parameter for AC winding loss reduction in the machine. The slot leakage inductance is investigated with the diagram in Figure 6-3.

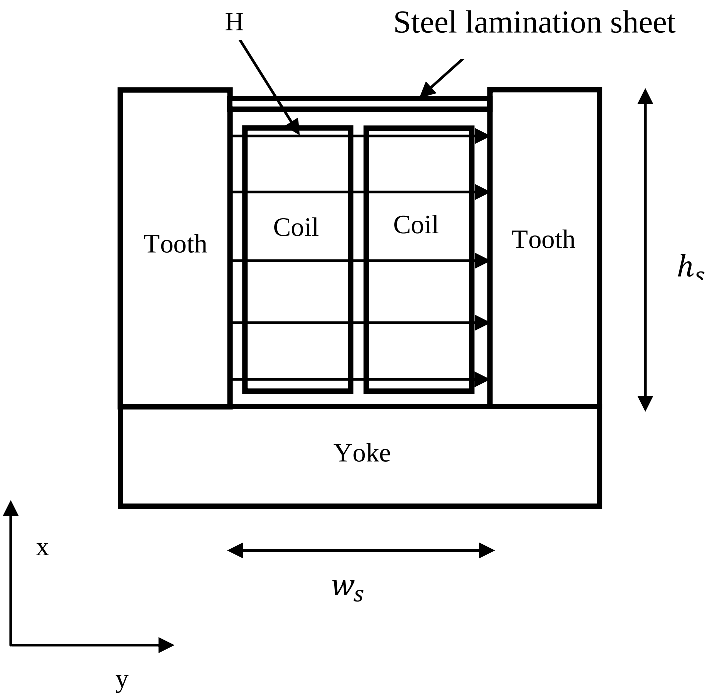

Figure 6-3: Slot leakage inductance with steel lamination sheet for shielding.

The slot leakage inductance L_{sl} can be obtained based on the inductance, co-energy and steel lamination sheet dimension using equation (6.3) as stated in [122]. This inductance is relatively small due to the number of turns in the slot.

$$L_{sl} = N^2 \left[\frac{2\mu_o h_s l_a}{3w_s} + \frac{\mu_o \mu_{r_{Lamination}} l_t l_a}{w_s}\right] \tag{6.3}$$

where I_a is axial length, l_t is lamination thickness, w_s is slot width of slot, h_s is slot height and N is number of turns.

The $\mu_{r_{Lamination}}$ given in (6.3) is relative magnetic permeability of the wedge of different steel lamination sheet as stated early. The first term given in the equation considers the effective permeance of the coil is two–third of the normal permeance of the slot due to winding occupation.

The second terms take the lamination sheet permeability into account. With the steel lamination sheet wedge design, the AC winding loss reduction was possible as the machine slot leakage inductance can be altered by using different type of steel lamination sheet wedge dimensions: l_t and w_s for the given axial length l_a.

6.4 3D Finite Element Analysis

This section presents the 3D finite element analysis to examine the airgap magnetic fields, losses in the machine and this approach is highly attractive due to its accuracy and nature of the machine. But for speed and simplicity one-tooth of the machine was utilised in the analysis.

The current density contour plots and the magnetic flux density contour plots of the proposed segmented steel lamination sheet design are obtained. Figure 6-4 shows the current density contour plots on the steel lamination sheet with rotor motion. It can be seen that, the steel lamination sheet tends to saturate at the tooth edges due to increased flux penetration. The maximum and minimum value of current density is 82.7 MA/mm^2 and 7.8 kA/mm^2 respectively.

This analysis treats the steel lamination sheet in the tangential direction rather than in the axial direction and assumes that the magnetic flux entering the coils from the magnet will see the steel lamination sheet first before the coils and then the core-back, flux will tend to move towards the region of lowest reluctance path by travelling in the lamination surface facing the airgap.

This sets up eddy current in the steel lamination sheet which is not circulating as a result of breaks on the lamination (segmented design). When the lamination surface becomes saturated the flux is forced into the other surface of the lamination and reaches the coils. This process also occurs near the edges of the tooth where stray flux tends to penetrate the coils from the axial direction.

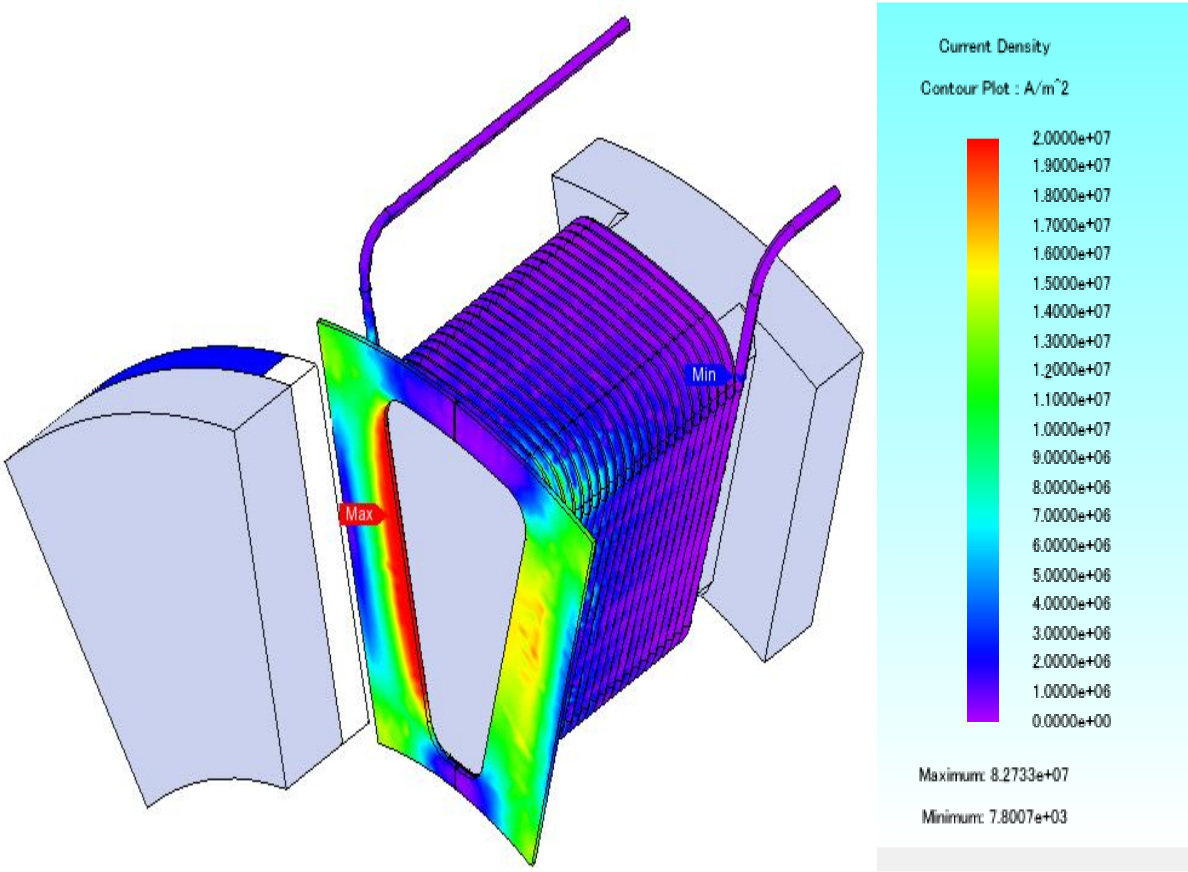

Figure 6-4: Current density contour plots for steel lamination sheet.

This analysis tends to underestimate the saturation level in the steel lamination sheet and any flux entering the coils from the lamination will set up eddy current in lamination that is not present in the coils. This process tends to shield the coils from the high flux densities from the magnet due to open-slot stator winding construction in a way that is not available to the coils, which try to increase the level of saturation on the lamination surface at the edge of the tooth as shown in Figure 6-4.

Figure 6-5 shows a visual illustration of the magnetic flux density contour plots with rotor motion in which the steel lamination sheet tends to saturate at the surface due to increased flux penetration and shielding effect. The steel lamination sheet has the maximum and minimum value of magnetic flux density of 2.1 T and 0.0001 T respectively.

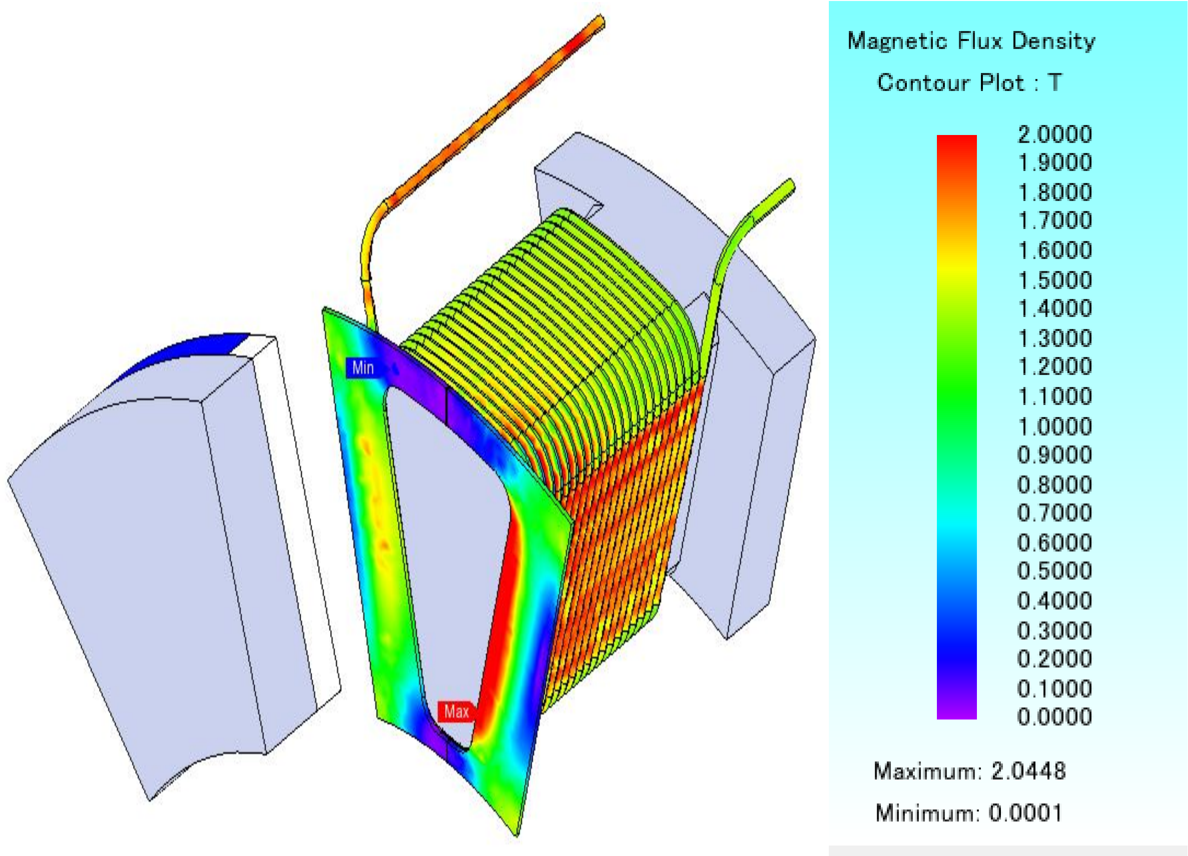

Figure 6-5: Magnetic flux density contour plots for steel lamination sheet

The above two figures capture the current density and magnetic flux density contour plots in the steel lamination sheet and in both cases the fields are from the movement of the rotor. The steel lamination sheets are more saturated in the magnetic flux density contour plot.

For the latter, a non-magnetic conductive material is utilized as a slot wedge in the slot opening of a machine to generate eddy currents within the material to oppose the main field from the rotation of permanent magnet rotor assembly.

This mechanism has additional loss generated within the material which may result in poor overall performance of the machine and extracting the heat generated is another challenge. Therefore, this technique of shielding is not necessary when compared to the former in this type of machine topology. The first approach proved to be more effective especially when higher efficiency and torque density are required.

6.5 FEA Loss Comparison

3D Finite element analysis of the AFM was conducted to investigate the performance of the machine without and with steel lamination sheet placed on top of the coils to shield it from stray fields. The mesh size on the steel lamination sheet is equal to one-third of the skin depth to accurately model the AC winding loss.

The diameter of conductor (3.2 mm) used in this analysis is larger than the skin depth at the operating frequency. For effectiveness of this method, it must work within the saturation limit of the steel lamination sheet as reported in [144].The bar chart of Figure 6-6 presented the 3D FEA comparison of machine without and with steel lamination sheet.

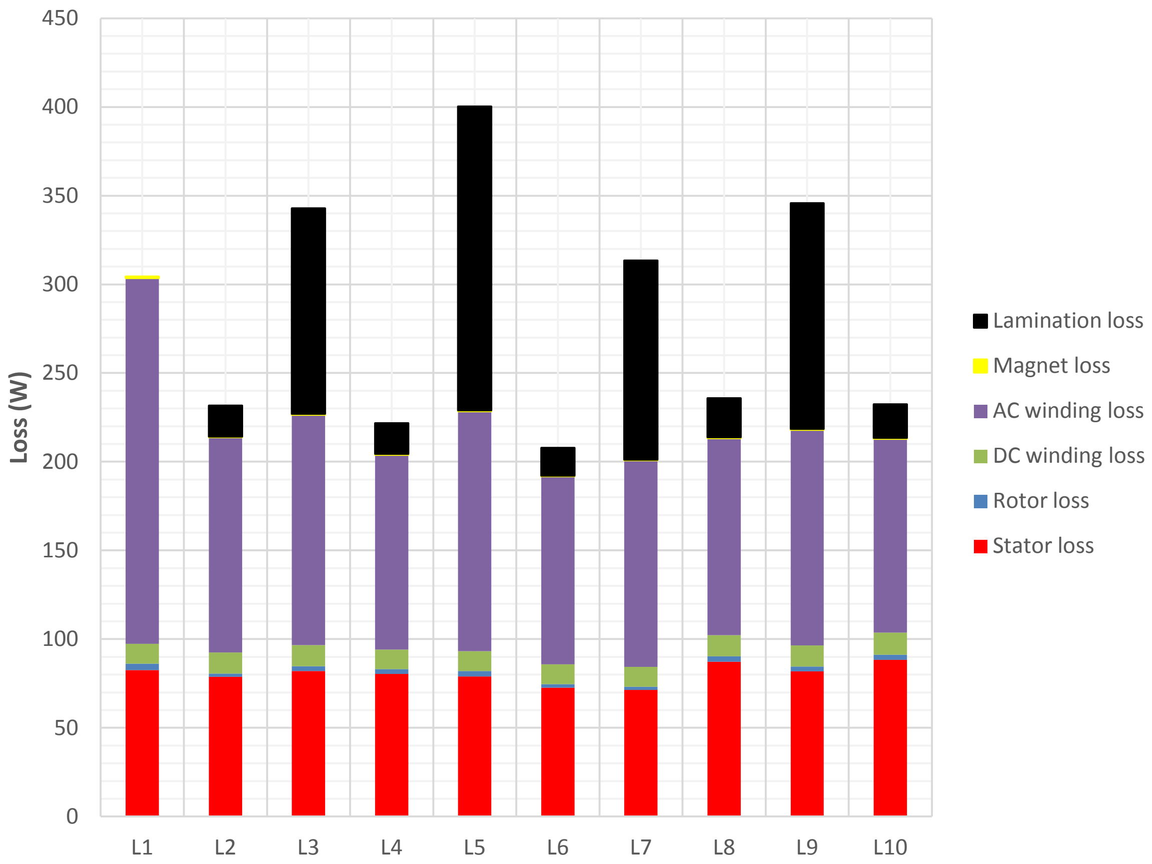

Figure 6-6: 3D FEA loss comparison at 700Hz.

The initial 3D FEA study shows that, the AC winding loss is reduced for machines with segmented design and increased for machines with non-segmented design steel lamination sheet. L2, L4, L6 and L8 reduced the AC winding loss as compared to L1 by 41.2%, 46.8%, 48.7% and 46.2% respectively. Introducing the steel lamination sheet has a minor reduction on induced EMF. Likewise, the cost of AC winding loss reduction is a commensurate minor reduction in torque due to the slight increase in slot leakage inductance due to the present of a steel lamination sheet.

In the case of L10, the current was increased by 3.5% to compensate the reduction in torque and the analysis was conducted only on L4 and found that AC winding loss reduced by 47.1% as shown in Figure 6-6. The non-segmented design in which eddy current is allowed to circulate in the steel lamination sheet, the AC winding loss reduced by 33.0%, 34.4%, 38.6% and 37.1% for L3, L5, L7 and L9 respectively. This is due to the extra losses in the steel lamination as a result of eddy current circulation.

The total machine loss decreases by 23.9%, 27.1%, 31.7% and 22.5% for L2, L4, L6 and L8 respectively. Similarly, for L10, the total loss reduced by 23.7%. But the total loss as compared to L1 increased by 12.7%, 31.5%, 3.0% and 13.6% for L3, L5, L7 and L9 respectively.

It is evident that L3, L5, L7 and L9 have the higher total loss as compared to L1, L2, L4, L6, L8 and L10. Furthermore, L5 has the highest total loss as a result of more losses on the lamination sheet, and L6 with the lowest total loss in the machine. This is evident again that the higher the conductivity of the steel lamination sheets the more power loss on the steel lamination sheet and less AC winding loss in the machine.

The L3, L5, L7 and L9 have additional losses from the steel lamination sheet due to eddy current circulation. The result from the 3D FEA shows that L5 have more additional losses as compared to L3, L7 and L9.

Open-slot stator winding influence AC winding loss in a machine due to field from the rotating permanent magnets on the rotor assembly as stated in [8]. Figure 6-7 presents the predicted 3D FEA of winding loss component at full-load current and different speed operations. In this case only L1, L2, L4, L6, L8 and L10 are compared.

Figure 6-8 shows the bar chart comparison of the predicted 3D FEA of winding loss at full-load current and at different speed of operation. In this case both the AC winding loss and DC winding loss are presented. It is clear that AC winding losses are dominant at AC operation frequency.

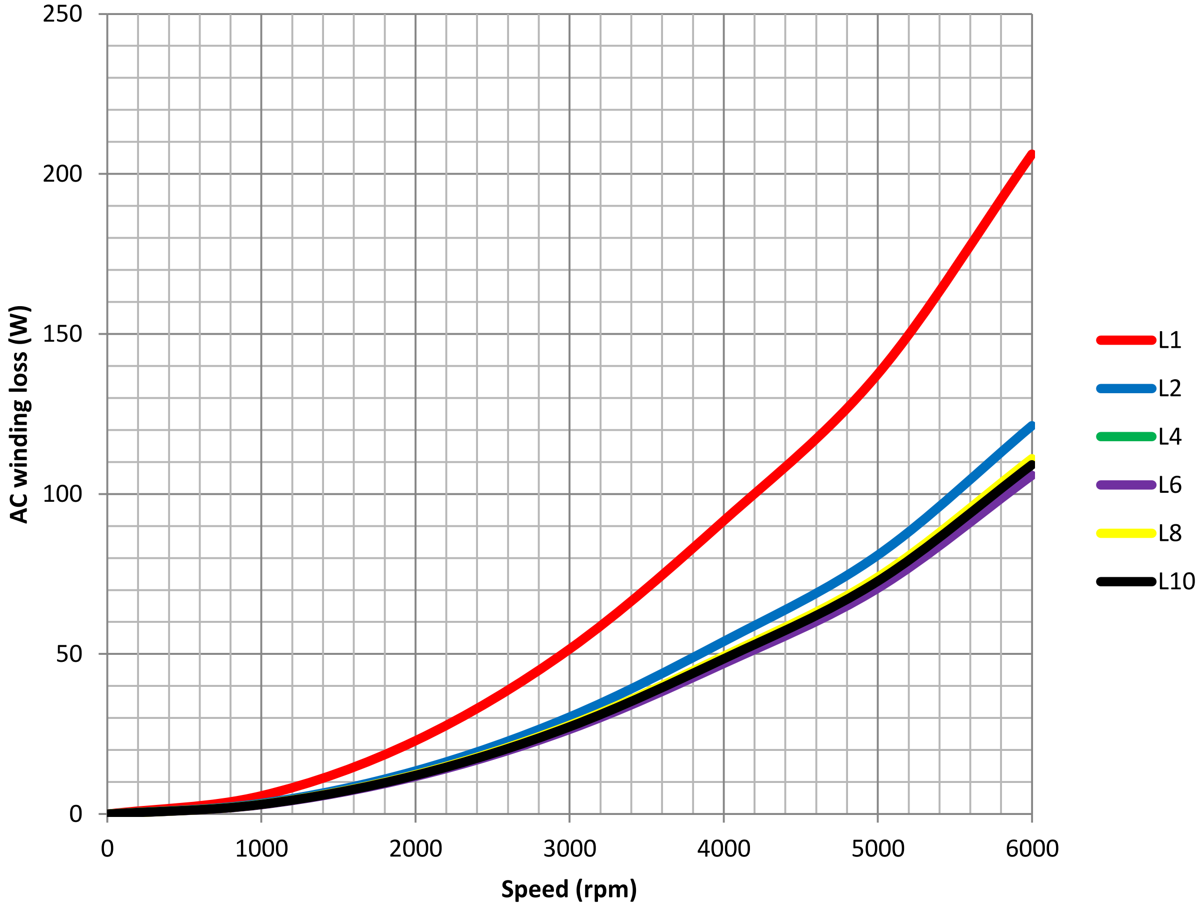

Figure 6-7: 3D FEA AC winding loss at different speed.

It can be seen that, at lower speed up to 2000 rpm DC winding loss are the dominant in the machine as compared to AC winding loss, as the frequency of operation increases the AC winding loss become significant. This is due to the higher frequency of operation resulting in skin-depths of the same order of size as the typical conductor diameters and the effect of time-changing field from the rotation of the permanent magnet rotor assembly which is caused by open-slot stator winding configuration as reported in [8].

At 1000 rpm the AC winding loss represents 20.8%, 13.0%, 12.3%, 11.9%, 12.0% and 11.5% for L1, L2, L4, L6, L8 and L10 respectively. Similarly, at rated speed AC winding loss represents 90.4%, 84.4%, 83.4%, 82.9%, 83.1 and 82.4% for L1, L2, L4, L6, L8 and L10 respectively.

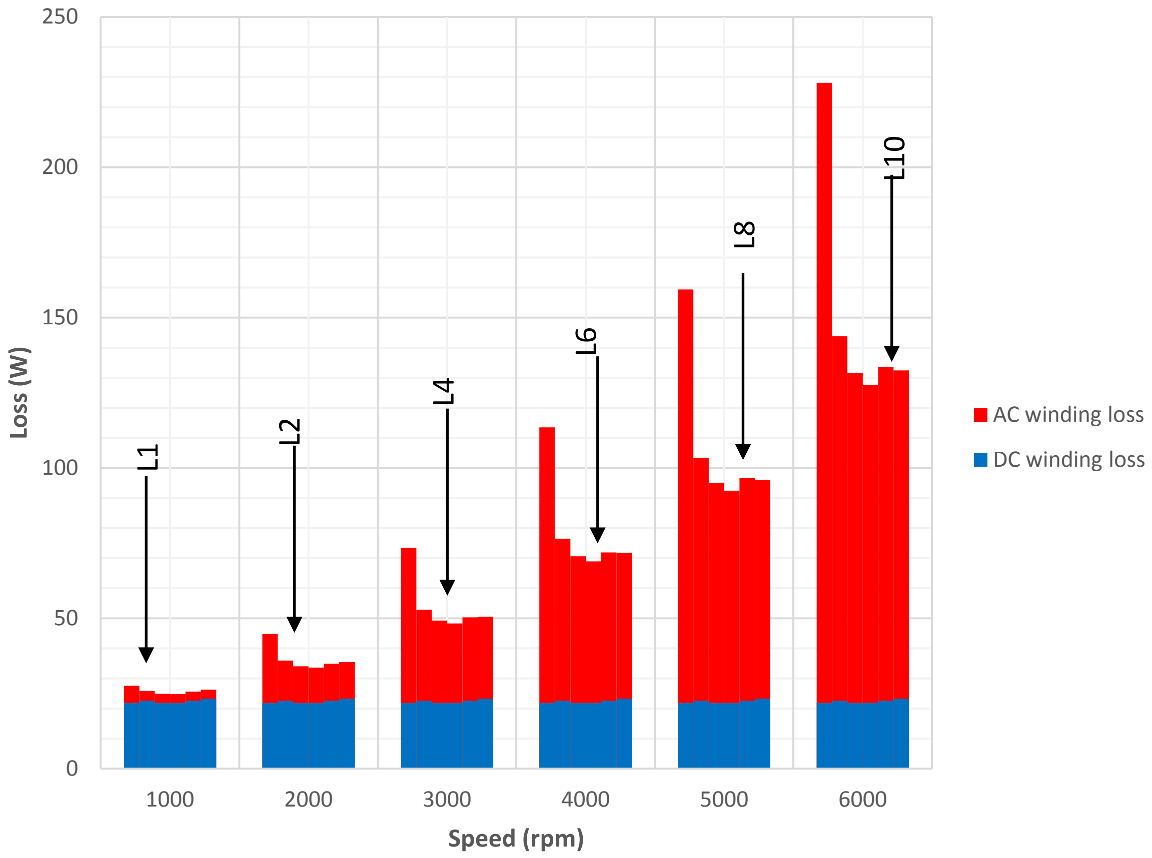

Figure 6-8: 3D FEA winding loss component at different speed.

6.5.1 Airgap Flux Density

Figure 6-9 shows the airgap flux density profile comparison without and with steel lamination sheet using 3D FEA in the z-direction B_Z at midpoint of airgap and average radius. In this case only the segmented designs were compared and the airgap flux densities were presented with variation to mechanical angle.

The L1 has the peak value of 0.8 T. This peak value increased by 30.4%, 23.1%, 31.0% and 25.9% for L2, L4, L6 and L8 respectively, in L10 the peak value of airgap density increased by 33.0%. Apart from the L10, L6 has the highest peak value as compared to L1, L2, L4 and L8.

The analysis were carried out on-load condition and it can be seen that the flux density of all machines with steel lamination sheet has increased due to the effect of shielding as a results of flux divert on lamination sheet.

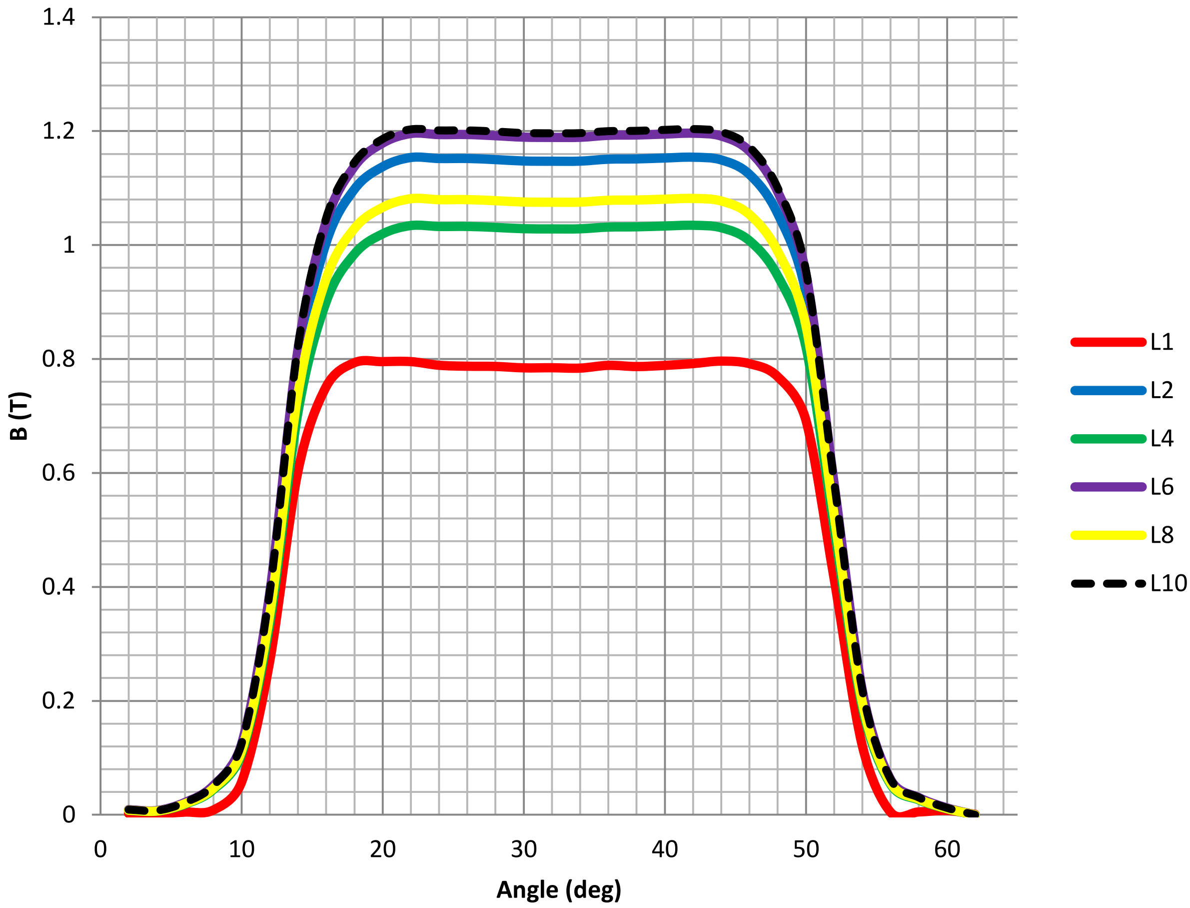

Figure 6-9: 3D FEA airgap flux density B_Z comparison at mean radius at 700Hz.

6.5.2 Cogging Torque and Axial Force

The influence of steel lamination sheet on cogging torque has been investigated in this section; it has been shown that placing it on top of the coils for shielding it from stray fields can help to reduce the cogging torque in the machine. Cogging torque is produced when the winding of the machine is open circuit and as a result of the rotor's tendency to align with stator poles to reduce reluctance.

Cogging torque can be investigated by focusing on the magnetic interaction between the coil and the magnets which means that cogging torque can be determined by airgap flux in the magnetic circuit with the rotating displacement as stated in [28].

It was observed in Figure 6-10 that the 0.168 Nm peak-to-peak cogging torque of L1 decreased by 58.9%, 57.7%, 55.4%, 60.1% and 60.1% for machine design with L2, L4, L6, L8 and L10 respectively due to reluctance of saliency. This shows that the open-slot stator winding construction and placing a steel lamination sheet for flux shielding works well and fulfils the purpose for which it was designed.

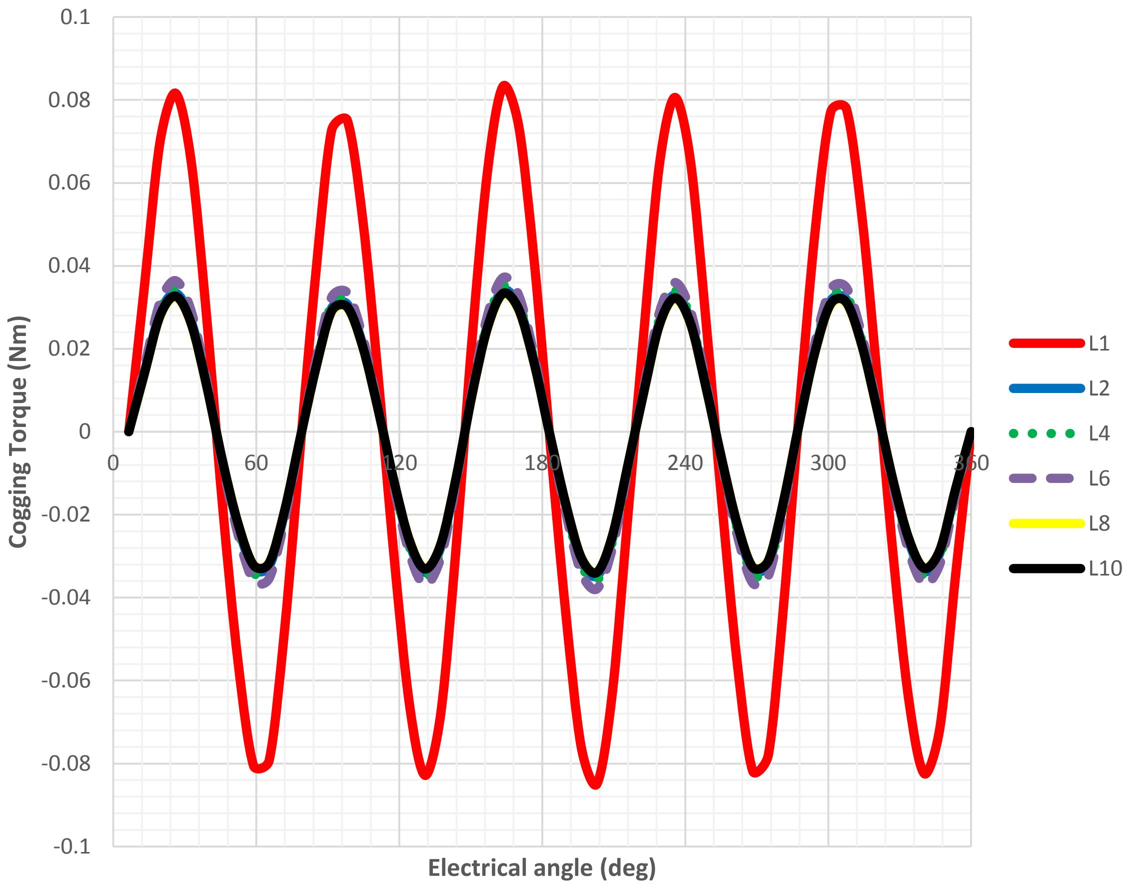

Figure 6-10: 3D FEA comparison of cogging torque waveform at 700Hz.

Figure 6-11 presented the axial force 3D FEA comparison among the segmented steel lamination sheet. It is observed in designs with steel lamination sheet that, L6 has the lowest axial force of attraction between stator disc and rotor disc and L10 with the highest axial force.

From the bar chart, it is clear that L1 provides the highest axial force of attraction of 792 N. The axial force of L2, L4, L6 and L8 decreased by 2.2%, 2.2%, 2.5% and 2.4% respectively as compared to L1 and L10 reduced by 0.2% when compared to L1.

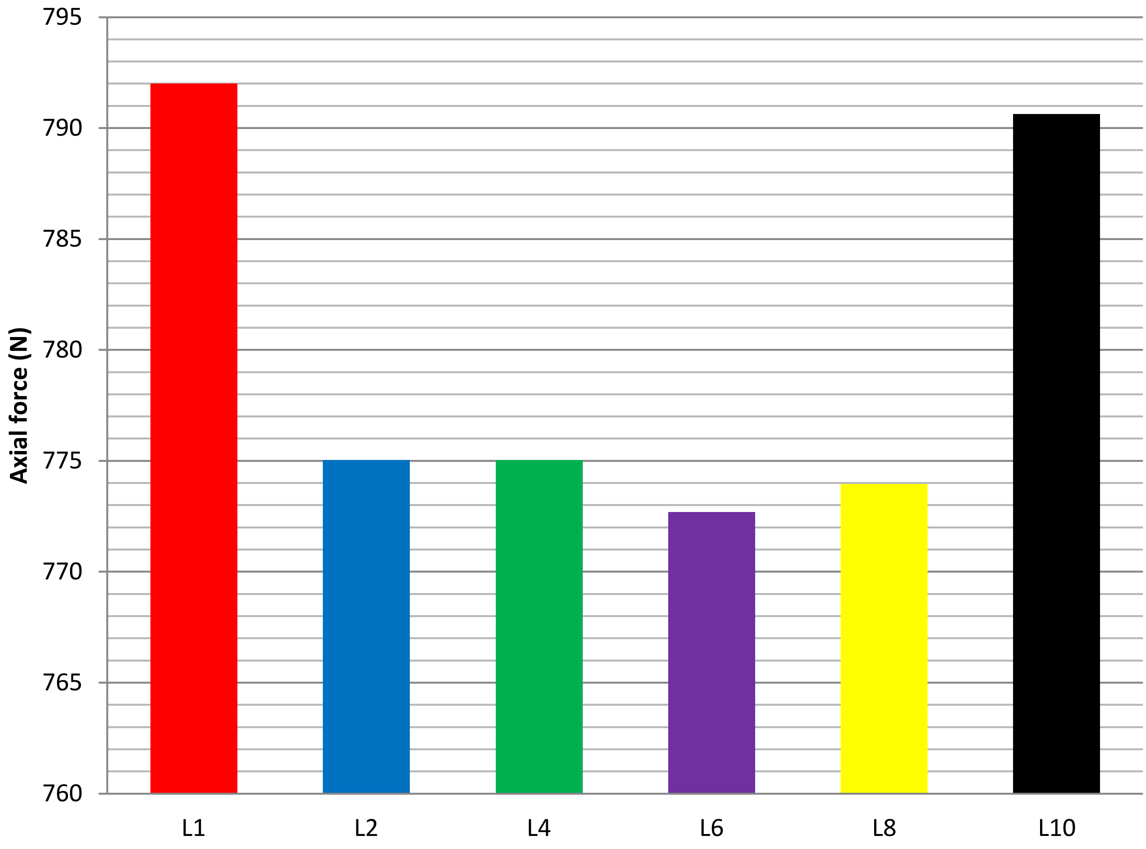

Figure 6-11: 3D FEA comparison of axial force at 700Hz.

6.5.3 Efficiency

Efficiency is a major factor in the usefulness of a machine and is the fraction or percentage of the output divided by the input, which according to the conservation of energy law, the total output energy or work must be equal to the total input energy [28].

The efficiency was derived based on the output power and the total loss in the machine. Figure 6-12 presented the bar chart 3D FEA efficiency comparison of the machine design without and with steel lamination sheet for AC winding loss reduction, in this case only the segmented designs were compared.

The efficiency of L1 was 80.5%, this improved by using a flux shielding technique in the machine. As compared to L1, the efficiency increased by 11.3%, 11.2%, 11.8%, and 10.6% for L2, L4, L6 and L8 respectively. Meanwhile, for matched torque L10 the efficiency has increased by 3.9%.

This is a low cost efficiency improvement in the machine and it can be scaled up and applied to many machines of the same topology as AFM.

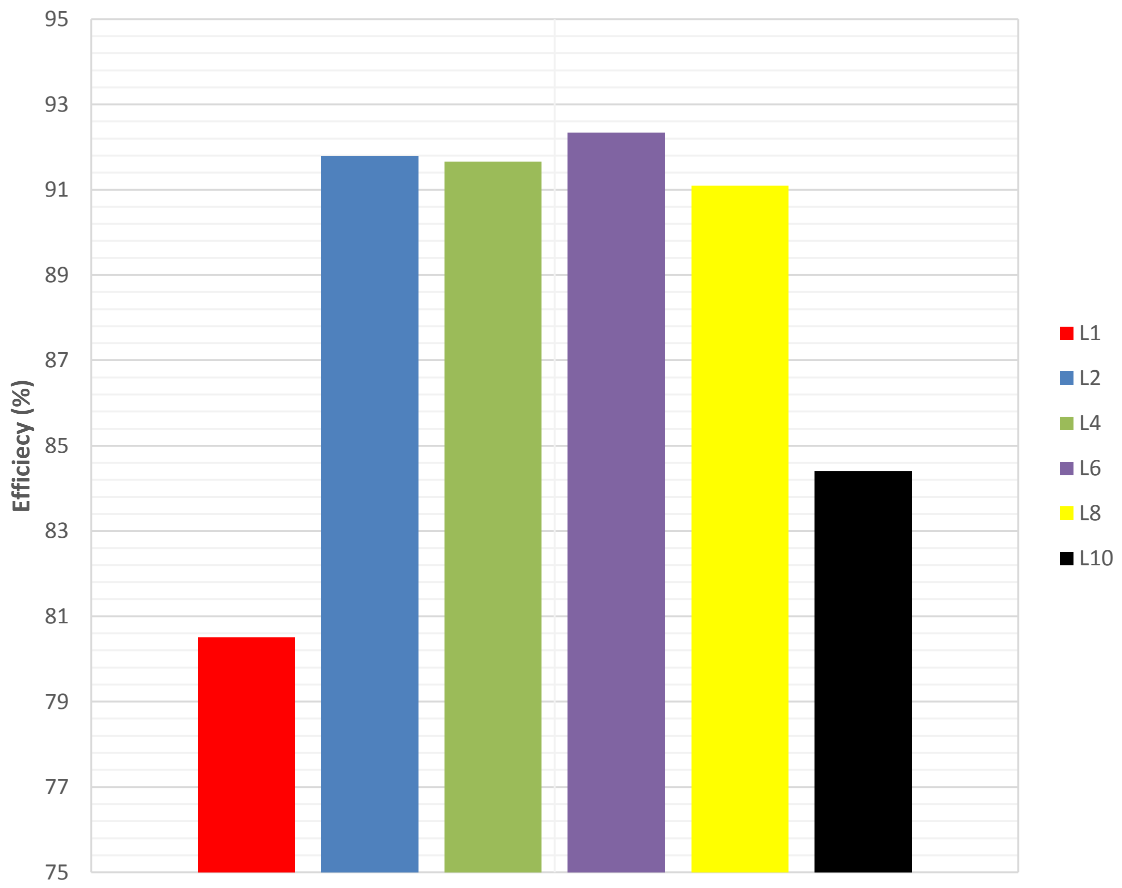

Figure 6-12: 3D FEA Efficiency comparison at 700Hz.

Introducing the steel lamination sheet as a technique for AC winding loss reduction as stated earlier has a minor reduction on torque and induced back EMF due to the slight increase in slot leakage inductance.

There is a slight decrease in the back EMF as shown in Figure 6-13, this decrease is as a result of changes in the slot leakage inductance of the machine. It can be seen from Figure 6-13, the positive peak of the L4 has some distortions which might be due to saturation at a particular point on steel lamination sheet.

L1 has the peak phase back EMF of 22.7V, this peak phase back EMF decreased by 3.5%, 1.2%, 3.6%, 2.4% and 3.5% for L2, L4, L6, L8 and L10 respectively.

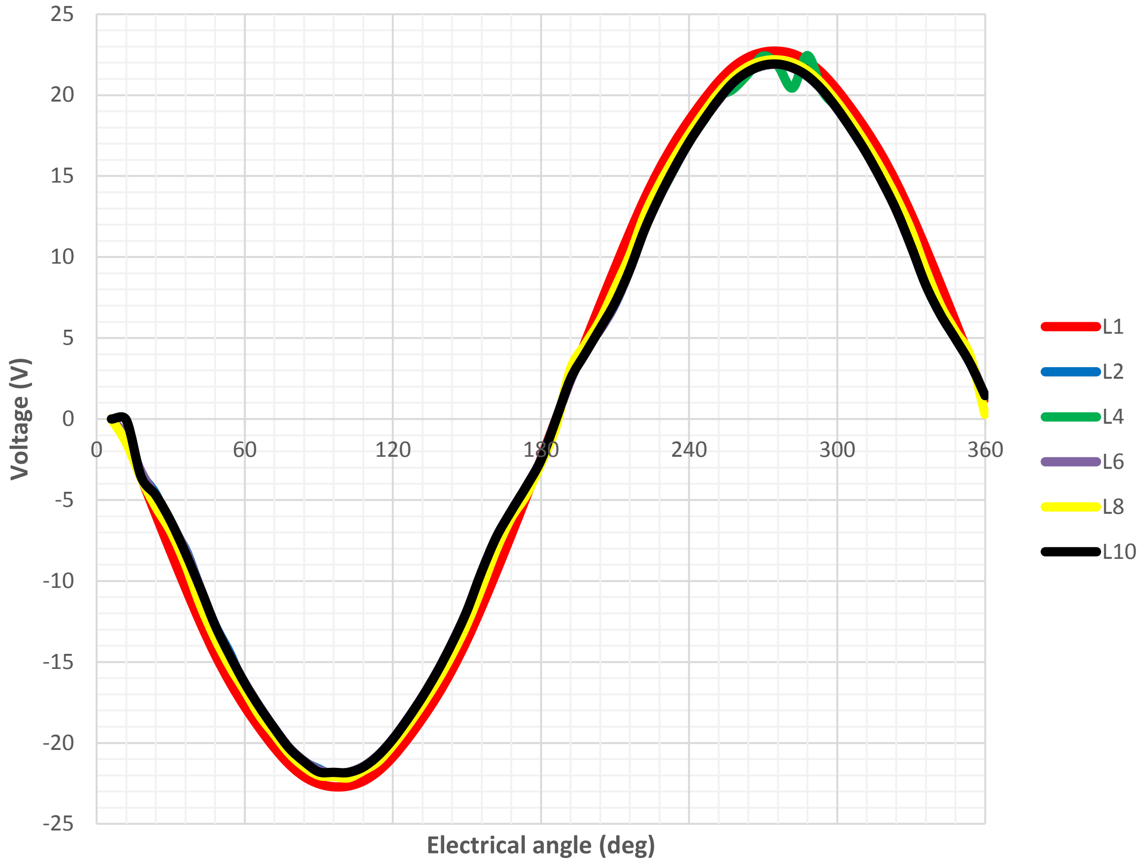

Figure 6-13: 3D FEA back EMF comparison at 700Hz.

Figure 6-14 presented the harmonic analysis of the back EMF and it uses 60 data point sample in the analysis and found the only significant harmonic beyond the fundamental is the 3rd harmonic as shown in the enlarge graph inside Figure 6-14, which represents 4.4%, 4.3%, 4.5%, 2.4% and 4.5% of the fundamental harmonic for L2, L4, L6, L8 and L10 respectively. The 5th, 9th and 11th harmonics are less than 2% of the fundamental harmonic, while the remaining harmonics that is the 2nd, 4th, 6th, 7th, 8th and 10th are less than 1% when compared to the fundamental harmonic.

The decrease in the back EMF due to changes in the slot leakage inductance also leads to reduction in the machine on-load torque as shown in Figure 6-15. It can be seen that the 3D finite element analysis torque of L1 is 2.08 Nm and this torque reduced by 5.3% 5.8%, 5.8 and 2.4% for L2, L4, L6 and L8 respectively.

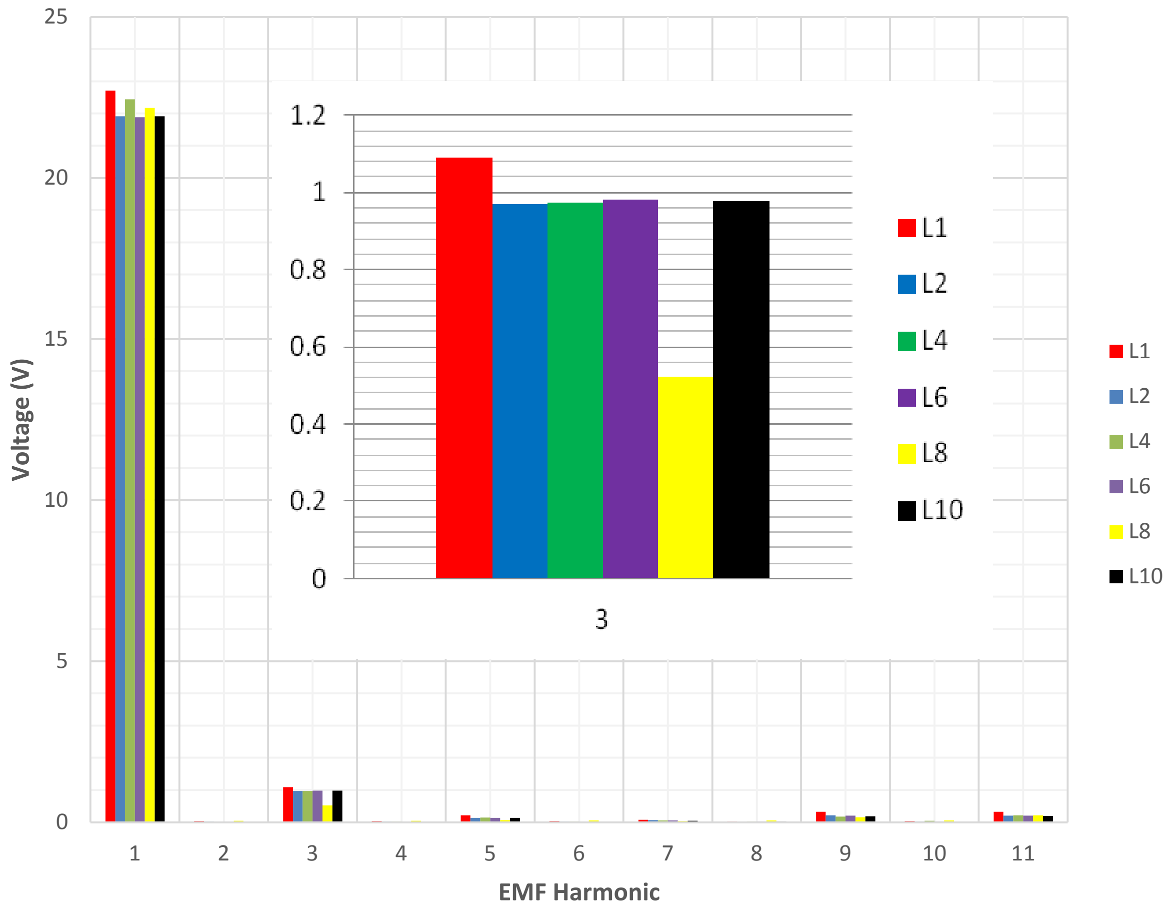

Figure 6-14: Harmonics of the back EMF.

Looking at the conductivity improvement of the performance of each steel lamination sheet used verses the reduction in torque of the machine, it is clear that the higher the value of material conductivity the more the reduction in the torque of the machine as shown in Figure 6-15.

Moreover, the smaller the thickness of the material used as magnetic shielding the lesser the reduction in the torque of the machine. It can be seen that L8 with 0.2 mm thickness has the lowest torque reduction when compared to L2, L4 and L6. The material thickness of those steel lamination sheets is 0.35 mm.

To obtain a best performance machine balance need to be reached on selecting the material conductivity and thickness together with the mechanical minimum to avoid fixing issues during the prototype machine final assembly.

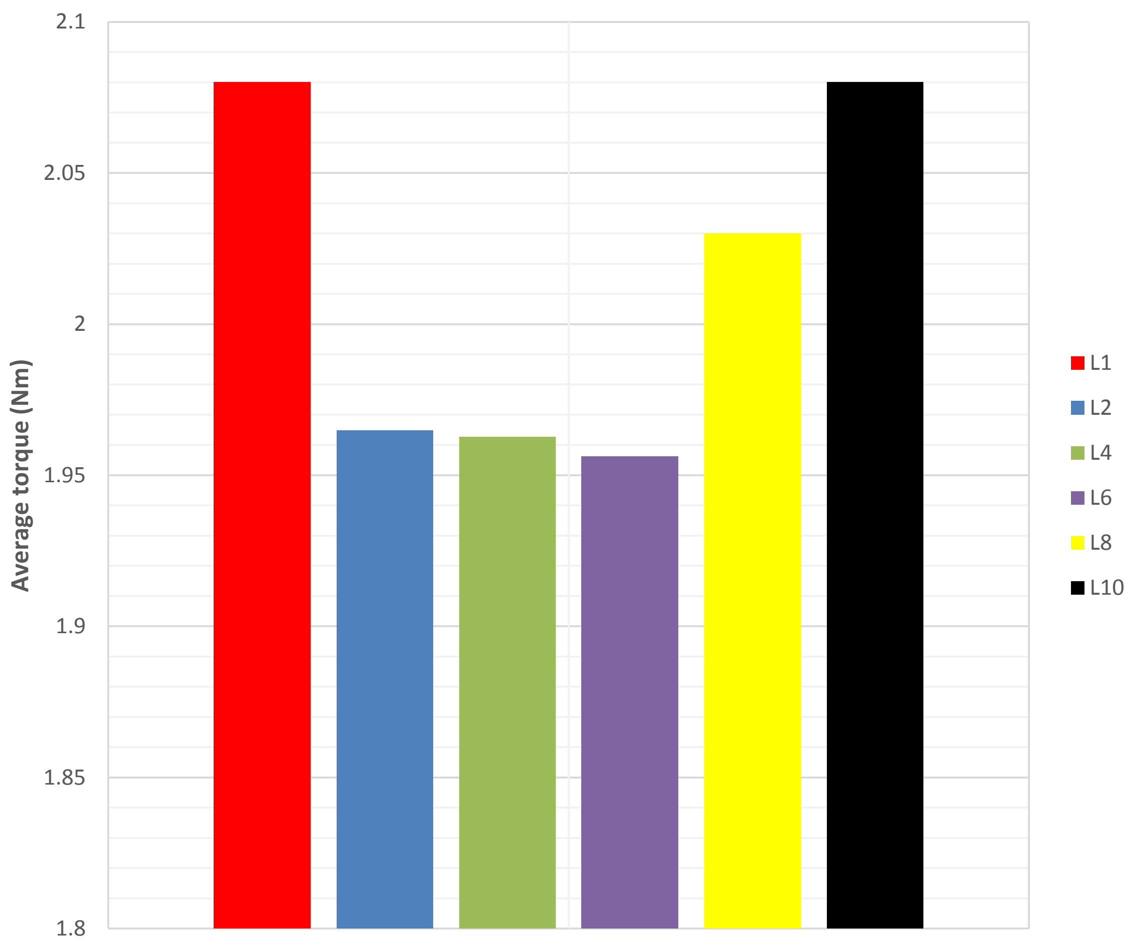

Figure 6-15: 3D FEA Torque comparison at 700Hz.

6.6 Performance Summary

In this section, various steel lamination sheet and designs were presented and the segmented designs were selected based on a good compromise between the AC winding loss reduction and reduction in the back EMF and torque of the machine. Table 6-2 summarized the performance comparison of the machine without and with steel lamination sheet.

The efficiency increased by 11.3%, 11.2%, 11.8%, 10.6% and 3.9% for L2, L4, L6, L8 and L10 respectively. But the average torque decreased by 5.3% 5.8%, 5.8 and 2.4% for L2, L4, L6 and L8 respectively. From the above analysis it can be seen that L6 has the best overall performance as compared to other type of steel lamination sheet.

Table 6-2: Performance Summary

Outputs	L1	L2	L4	L6	L8	L10	Units
Speed	6000	6000	6000	6000	6000	6000	rpm
Torque	2.08	1.97	1.96	1.96	2.03	2.08	Nm
Power	1256.64	1234.54	1231.50	1229.14	1275.49	1256.64	W
Efficiency	80.50	91.79	91.66	92.34	91.09	84.40	%

6.7 Conclusion

Various steel lamination sheets were investigated in this chapter and it was shown that this technique of placing a single steel lamination sheet on top of coils for shielding stray field can be used to reduce the AC winding loss for this particular machine topology by a significant amount. This method of AC winding loss reduction using slot wedges is novel for AFM and does not require conductor alteration as in twisted wires.

The efficiency increased by 11.3%, 11.2%, 11.8%, 10.6% and 3.9% for L2, L4, L6, L8 and L10 respectively as compared to L1. But the average torque compared to L1 decreased by 5.3% 5.8%, 5.8 and 2.4% for L2, L4, L6 and L8 respectively. Similarly, the peak phase back EMF decreased by 3.5%, 1.2%, 3.6%, 2.4% and 3.5% for L2, L4, L6, L8 and L10 respectively when compared to L1. The only significant harmonic beyond the fundamental is the 3rd harmonic, which represents 4.4%, 4.3%, 4.5%, 2.4% and 4.5% of the fundamental harmonic for L2, L4, L6, L8 and L10 respectively.

It is seen from the 3D FE studies that the combination of this technique with conductor diameter larger than the skin depth at operating frequency can be used to reduce AC winding loss greatly, especially when the single steel lamination sheet has high conductivity. From the performance summary, it was observed that the machine with L6 has better overall performance as compared to other types of steel lamination sheet.

Lastly, these techniques have shown the possibility of using a magnetic material to reduce AC winding loss due to open-slot stator winding configuration as a results of the eddy-current losses induced in the stator winding by the time-changing field from the rotation of the PM rotor assembly and the effect of higher frequency of operation resulting in skin-depths of the same order of size as the typical conductor diameters, while keeping the back EMF and torque within acceptable value and keeping the number of components to be made and assembled the same. These techniques were made, and prototype machines were built. The construction of various components of these machines is shown in Chapter 8, while the measured test results are presented in Chapter 9.

This low cost efficiency improvement can be scaled and applied to many machines of the same topologies.

7. Academic Study on Winding Loss Reduction

This chapter presents the academic investigation into the mechanism of loss reduction by examining the separate effects using idealised materials (high reluctance / zero conductivity and vice versa). Basically, there are two mechanisms for shielding – guiding the field way from the coils (magnetically permeable) or generating eddy currents which oppose field (electrically resistive).

7.1 Shielding Mechanisms

In an open-slot stator machine, the slot harmonics can be put down using manufacturing adjustments like skewing the slots, expanding the airgap, reducing the pitch of the winding and either using magnetically or electrically conducting slot wedges. Most of these adjustments are unsteady with other need of the machine especially high efficiency and torque. Consequently, the slot harmonic and AC winding loss cannot be removed completely.

In AFM the possible way to minimise those effects is by the used of steel lamination sheet to shield or to suppress the leakage flux from reaching the windings. Recognising the stator slot opening and the parameters of steel lamination sheet is very important to increasing the overall performance of the machine. This method of using magnetic shielding to redirect the excess leakage flux from entering the open-slot stator winding of AFM proved to be more efficient and reliable.

In [158] the impact of the stator slot opening onto the behaviour of the magnetic flux density in the airgap, changes in the torque and harmonic components of the magnetic flux density identification were investigated. It is found that 3.5 mm stator slot opening presented the best results and the torque increased by about 4.9% when compared with the baseline machine design.

3D FEA was used to examine the circumferential, axial and comprehensive grooves in high speed permanent magnet brushless machines as reported in [159] and found that both circumferential and axial grooves on the metal retaining sleeve, and so the rotor energy loss can be reduced. They concluded that the circumferential grooving proved to be the most effective and simple to implement to reduce the rotor eddy current loss with disadvantage of little negative influence on the sleeve mechanical strength or rotor dynamic balance. These techniques are limited to the rotor of a radial flux machine.

The two mechanisms for shielding are magnetically permeable by guiding the field way from the coils and electrically resistive by generating eddy currents which oppose the field. In the former a magnetic material is used for shielding the leakage flux reaching the coils thereby preventing the coils exposure to more alternating flux from the permanent magnet rotor assembly. Moreover, it has the disadvantage of altering the slot leakage inductance in a machine.

In the latter a non-magnetic conductive material (copper) is usually utilized generating eddy currents which oppose the main magnetic field, this type of shielding is not necessary because of additional loss generated by the non-magnetic material moreover it is very difficult to analysis the magnetic filed in the machine airgap, also it is very difficult to produced a highly efficient machine using the electrically resistive technique due to its excess eddy current generation.

Even though shielding is essential for the normal operation of electrical machines and to avoid the local heating within the machine. Investigations of the parameters effects such as permeability, conductivity and thickness of shielding material would be carried out on flux linkages in the coils, back EMF and harmonic, no-load and on-load total loss, cogging torque and axial force of attraction between the stator disc and rotor disc, on-load torque and two different types of slot design (rectangular and trapezoidal) in this chapter. Figure 7-1 shows a simple diagram to demonstrate the effect of magnetically permeable and electrically resistive shielding.

To examine the shielding effect due to magnetically permeable and electrically resistive, the machine is represented in 2D as shown in Figure 7-1 which tends to ignore the machine curvature to obtain the vector potential and magnetic linear current density distribution from the magnet and the surface of the steel lamination sheet placed in the airgap as presented in Chapter 6.

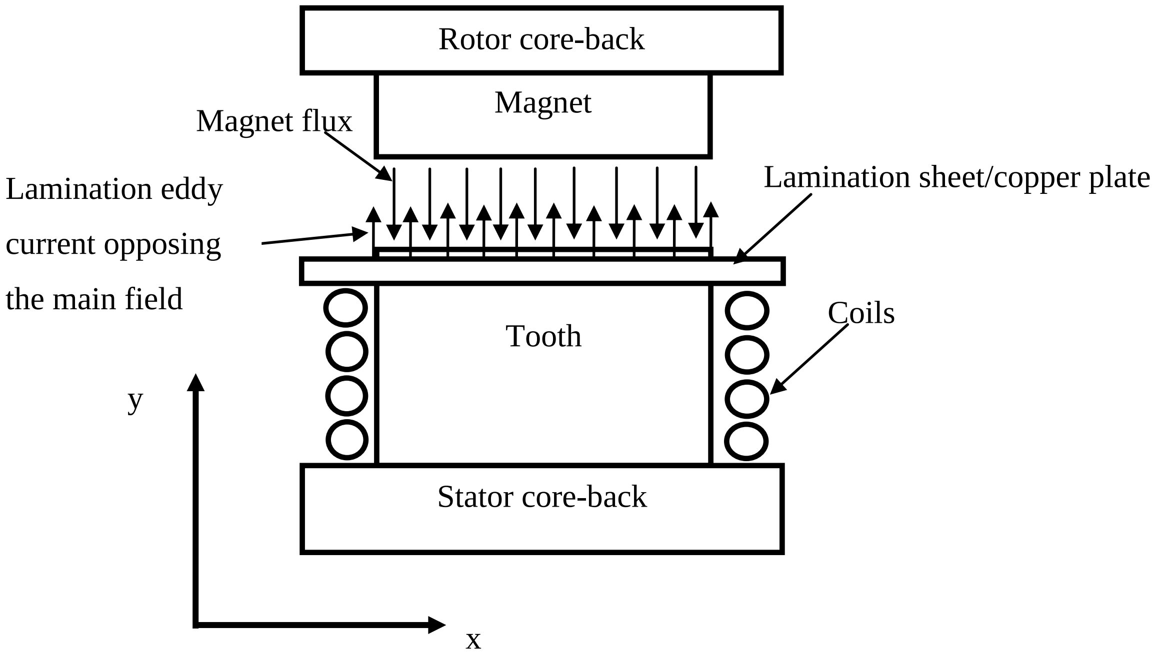

Figure 7-1: The effect of magnetically permeable and electrically resistive shielding.

The x-axis and y-axis represent the peripheral and axial direction respectively. It also assumed that the radial direction of the machine has infinite permeability with stator and rotor having infinitely permeable boundaries to reduce the magnetic energy loss and enhance the flux density in the airgap. In addition to that, it provides the principals of slot leakage inductance of the machine as discussed in Chapter 6.

In this mechanism, the analysis assumes that the lamination sheet has a harmonic distribution in the format as stated in [15] in the airgap. Since the magnetic vector potential in AFM has z-component in the airgap, the lamination sheet have vector potential at any point in the airgap and magnetic flux density as stated in [15] and [122]. The derivation of this vector potential above the steel lamination sheet is shown in the appendix B by solving Laplace's equation at both the steel lamination sheet surface and the current sheet and is used in getting the airgap potential. The current density contour plots and the magnetic flux density contour plots of the proposed segmented steel lamination sheet design are obtained as shown in Figure 6-4 and Figure 6-5 respectively in Chapter 6 above.

It is clear from those figures that the shielding sheets are not saturated assuming that the magnetic characteristic of the material are linear. In the case of magnetic shielding eddy current is not considered while in electrically resistive shielding eddy current is considered and the mesh size on shielding material is equal to one-third of the skin depth in order to accurately analyse the eddy current in the region. It also indicates that at frequency of operation the magnetic shielding is more effectual than the electrically resistive shielding which produces the eddy current to oppose the main magnetic field.

Figure 7-2 and Figure 7-3 illustrate the typical permeability and conductivity consequences on the shielding coefficient S at any point within the shielding steel lamination sheet and is defined by as stated in [94].

$$S = B_{z0}/B_z \tag{7.1}$$

where B_{z0} and B_z are the maximum flux densities at any point without shielding steel lamination sheet and with shielding steel lamination sheet respectively.

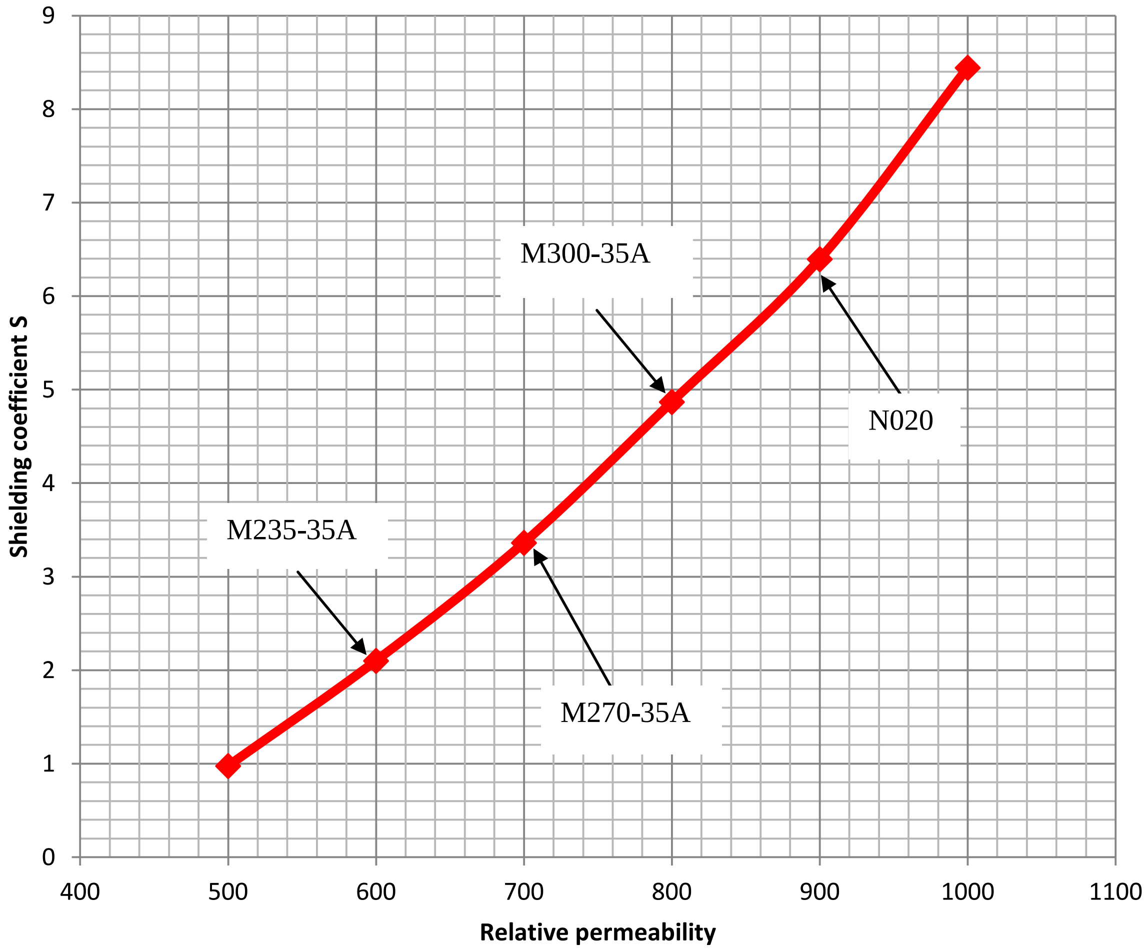

Figure 7-2: Effect of permeability on shielding properties.

It can be seen from Figure 7-2 that as the relative permeability of shielding material increases the shielding coefficient also becomes larger. This is due to the facts that the free space permeability is extremely low in the machine. M235-35A, M270-35A, M300-35A and N020 have shielding coefficient of 2.2, 3.4, 4.8 and 6.4 respectively.

It can hence be concluded that a shielding magnetic material with low relative permeability will most likely has a low shielding coefficient and those with high relative permeability have high shielding coefficient. In this case M235-35A has the lowest relative permeability and shielding coefficient however N020 with highest relative permeability present the highest shielding coefficient.

The effect of conductivity on shielding characteristics of a magnetic material was presented in Figure 7-3. It is clear from the graph that the lower the conductivity of a magnetic material used the higher the shielding coefficient. M235-35A, M270-35A, M300-35A and N020 have shielding coefficient of 5.3, 4.7, 2.5 and 1.3 respectively due to the effect of conductivity on shielding characteristics of a magnetic material.

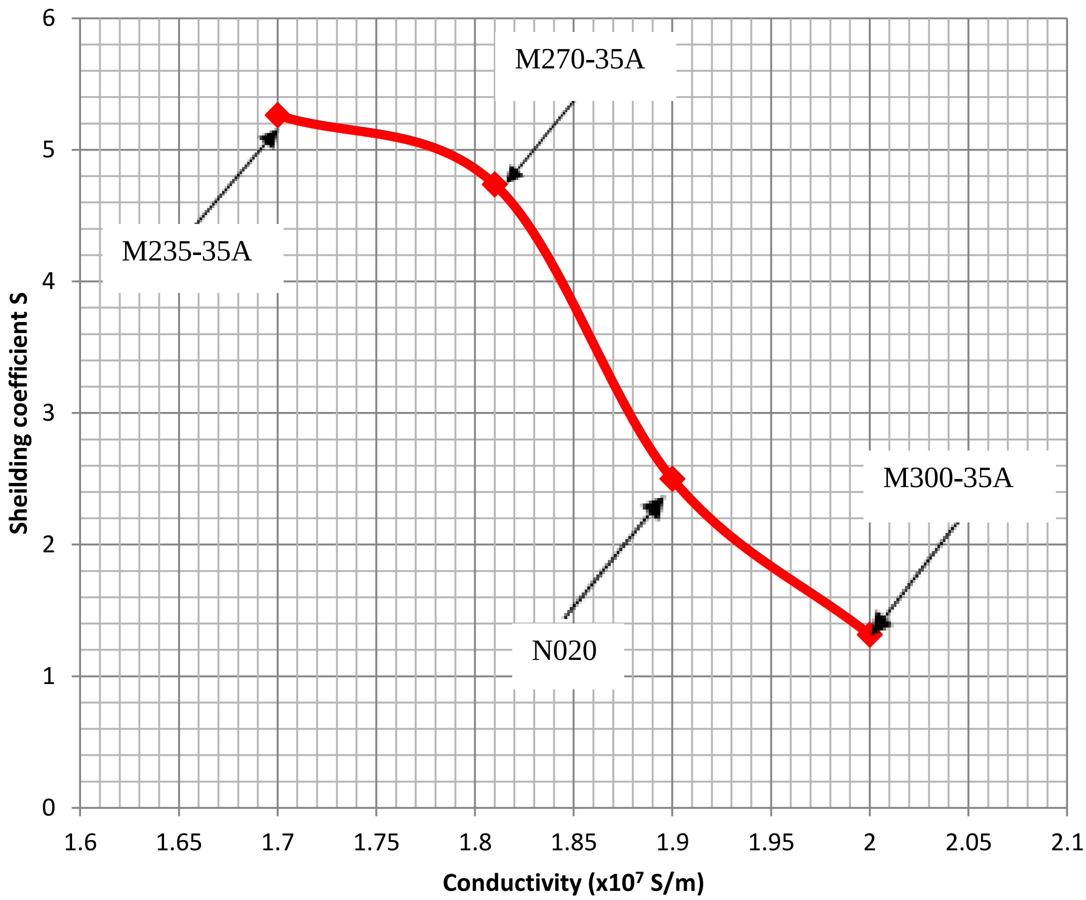

Figure 7-3: Effect of conductivity on shielding properties.

.

The shielding feature of the flux in an electrically shielding becomes undesirable when the conductivity of the material is big as shown in Figure 7-3. Due to the opposing magnetic flux produced by the eddy currents the main flux try not to pass through the magnetic material and reaches the coils using the outermost path.

When the thickness of the shielding material is increased, the quality of shielding is better and worsens when the thickness is decreased, however decreased with conductivity becomes excessively huge. It can be seen from Figure 7-2 and 7-3 above that the shielding characteristic is influenced by the permeability, conductivity and even the thickness of the magnetic material utilised.

7.2 Material Conductivity and Thickness

The analysis and comparison presented in Chapter 6 assumed the material have a value for the conductivity and resistivity. These enforced limitation without considering whether it would be optimal for the final machine design.

It is therefore advised that an examination be carried out into the mechanism of AC winding loss reduction by investigation of the separate effects using idealised materials (with conductivity and resistivity and vice versa), along with deliberation of the correct design for optimal overall performance.

To show the effect of material conductivity and steel lamination thickness on loss reduction for different lamination sheet, Figure 7-4 shows the comparison of conductivities and thicknesses for the different steel lamination sheet used in the analysis.

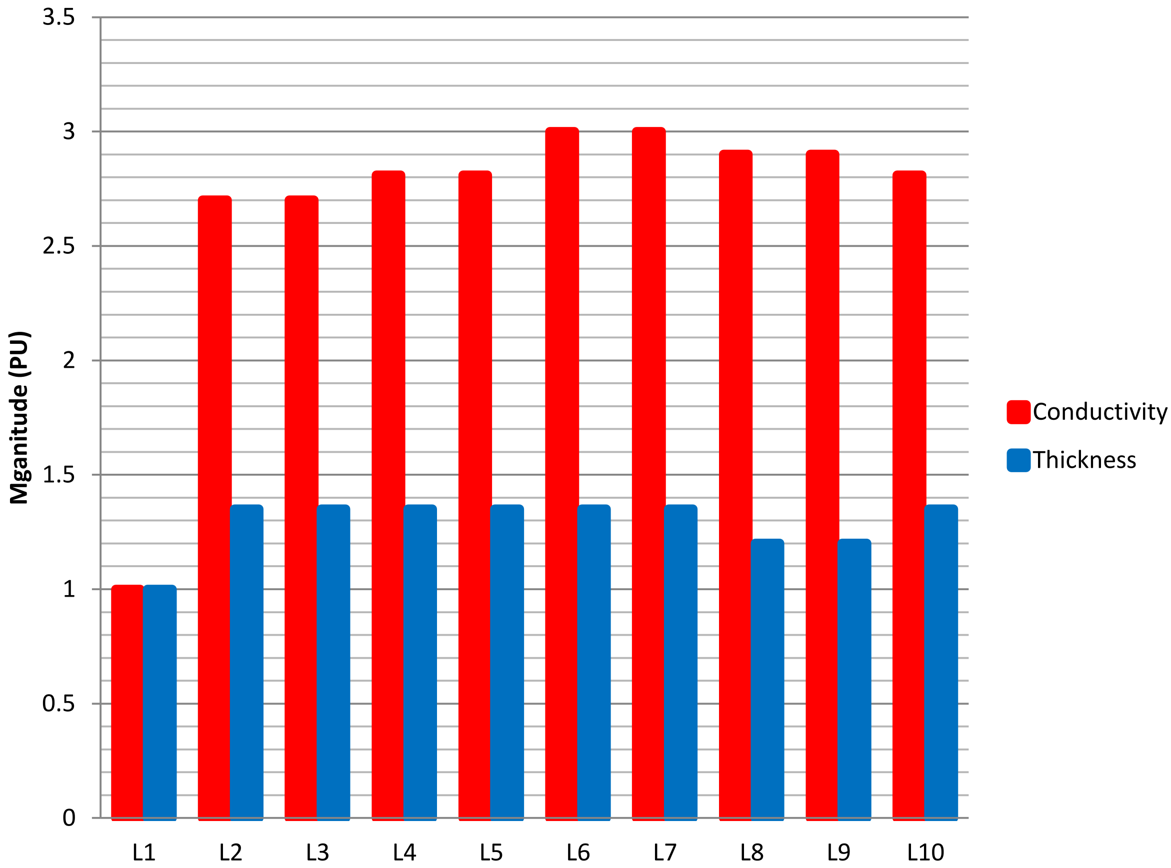

Figure 7-4: Material conductivity and thickness.

The choice to use a steel lamination sheet (M235-35A, M270-35A, M300-35A and N020) for loss reduction in the machine is due to its cost-effectiveness and availability in the market, and they could easily be machined as a single steel lamination sheet in the workshop. The use of a single steel lamination sheet for shielding leakage flux can be seen as an efficient and reliable way to improve the performance of this type of machine topology.

7.3 Flux Linkage

This section presents the comparison of the coils peak flux linkage per phase without and with conductivity on the magnetic material. The design without steel lamination sheet L1 has the highest peak no-load flux linkage per phase when compared to others design with segmented and non-segmented steel lamination sheet. The segmented designs have much better flux linkage per phase than the non-segmented designs counterparts as shown in Figure 7-5. The segmented L8 has the highest peak flux per phase of 2.51 mWb and L3, L5 and L7 have the lowest peak flux pr phase of 0.4 mWb.

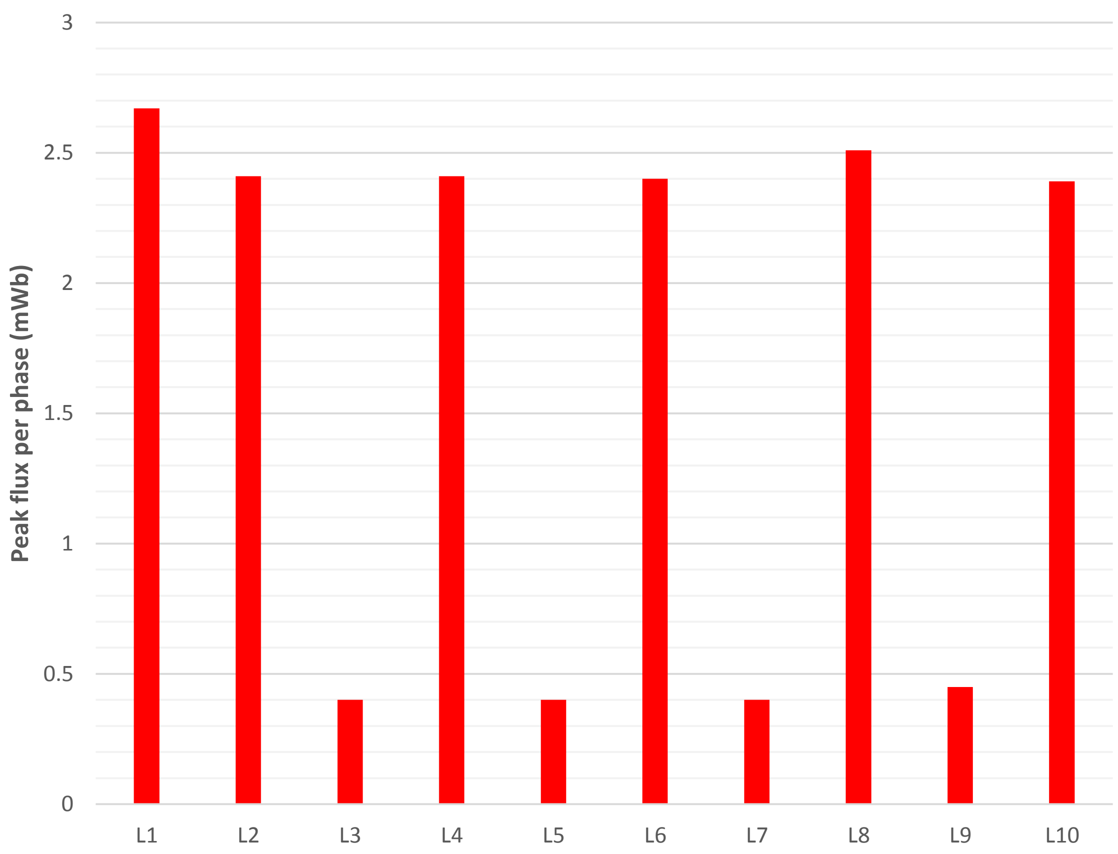

Figure 7-5: Peak flux linkage per phase without conductivity.

The analysis of peak flux per phase with conductivity shows that L1, L2, L4, L6, L8 and L10 have the highest peak value of approximately 0.80 mWb, however L3, L5, L7 and L9 have the lowest peak value of 0.79 mWb per each phase as shown in Figure 7-6.

This shows that the steel lamination sheet must have conductivity to enable proper flux linkage from the field generated due to rotation of rotor assembly to stator winding located at slot.

It is also clear from the graph that all non-segmented steel lamination sheet designs have lower peak flux linkage per phase when compared to L1 and segmented steel lamination sheet, this may be as a result of eddy current circulation within the steel lamination which affect the amount of flux linkages.

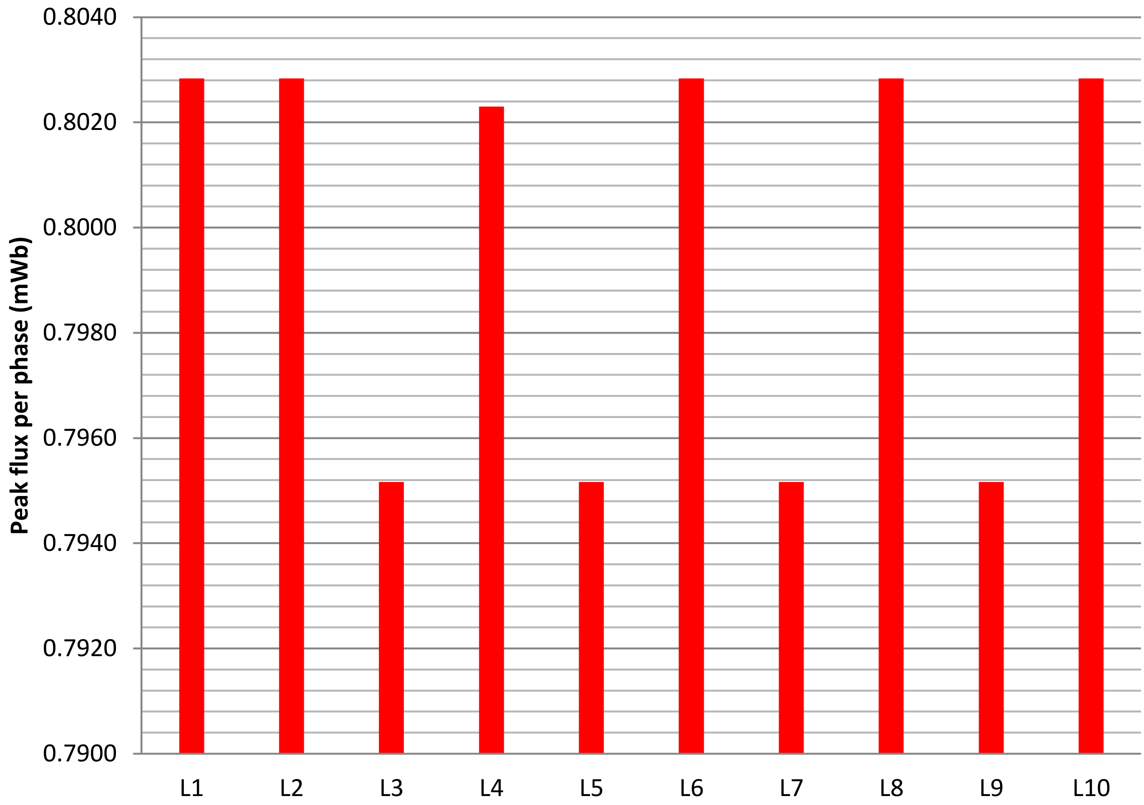

Figure 7-6: Peak flux linkage per phase with conductivity.

7.4 Back EMF and Harmonic Analysis

Figure 7-7 shows the comparison of the peak Back EMF for machine without steel lamination sheet and those with steel lamination sheet, in this analysis all the lamination sheet have zero conductivity. The results from the analysis shows that L1 and L10 have the highest peak back EMF per phase of 1.0 V and 0.999 V respectively, follow by L3, L5 and L7 with peak value of approximately 0.978 V. L6 has the lowest peak back EMF per phase of 0.976 V.

The peak back EMF per phase in L3, L5 and L7 decrease by 1% as compared to L1 and L10. Similarly, when compared to L1 and L10, L6 reduced by 2% and 1% when compared to L3, L5 and L7.

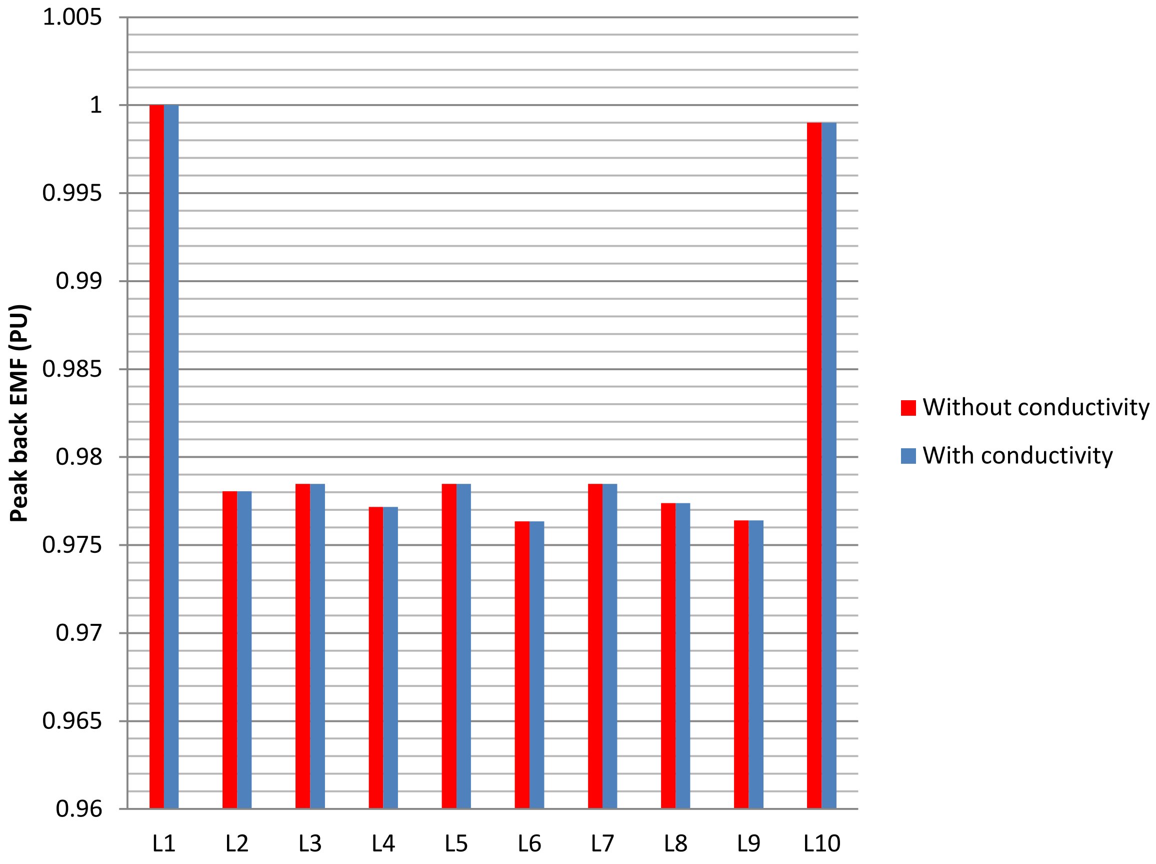

Figure 7-7: Peak back EMF.

The peak back EMF comparison with a value of conductivity on steel lamination sheet shows some similarities in terms of peak back EMF to those with zero conductivity, this indicates that conductivity on steel lamination sheet used as a magnetic shielding has no effect on the back EMF of the machines.

The harmonic analysis shows that the method of using steel lamination sheet is the best way to minimised the back EMF harmonic. Apart from the fundamental harmonic only the 3rd harmonic is up to 4% of the fundamental as presented in the enlarge graph of Figure 7-8.

The 5th, 9th, and 11th are less than 2% of the fundamental harmonic while the 2nd, 4th, 6th, 7th, 8th and 10th harmonics are less than 1% when compared with the fundamental harmonic.

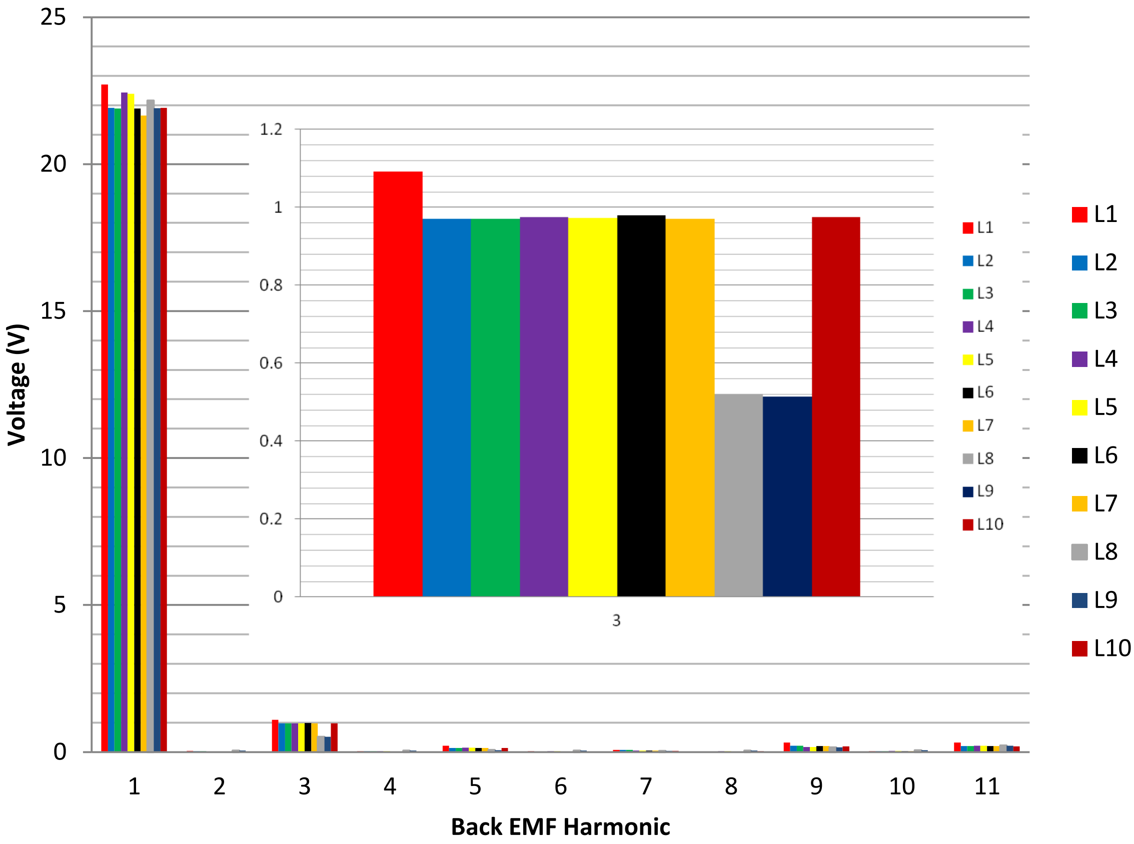

Figure 7-8: Harmonics of the back EMF.

7.5 No-Load and On-Load Total Loss

Loss in the machine is another thing to consider, the flux from the magnets reaches the coils through a steel lamination sheet which shield the stray flux. The flux sees the lamination plane first before reaching the coils and eddy current is induced in the lamination, for segmented design in which there is a cut to stop the eddy current circulation or limited it within a shorter path, while the non-segmented design allows eddy current circulation in it.

The eddy current induced in the lamination has a vital role in the total loss of the steel lamination and the overall performance of the machine. Figure 7-9 shows the comparison of the total no-load loss in each of the machine without steel lamination and with steel lamination.

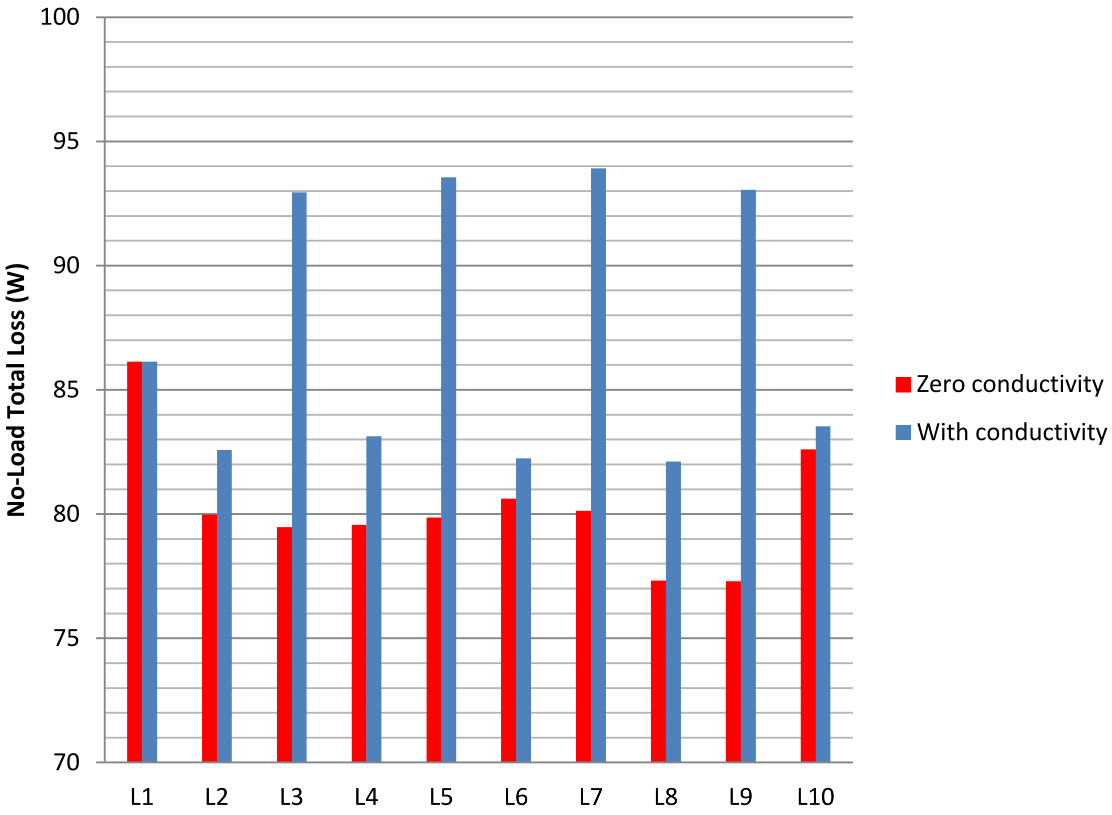

Figure 7-9: No-Load total loss.

As seen in the bar chart of Figure 7-9, the total loss with zero conductivity on steel lamination sheet decreases by 6.3% to 10.5% for L2 to L9 as compared to L1 and decreases by 4% for L10 when compared to L1. The non-segmented designs L3, L5, L7 and L9 with conductivity on steel lamination sheet have the highest no-load loss which increased by 8.0% to 9.2% as compared to L1, but for the segmented designs L2, L4, L6, L8 and L10 the no-load loss decreases by 2.9% to 4.5% when compared to L1.

Figure 7-10 shows the comparison of the on-load total loss in each of the machine without steel lamination and with steel lamination. The main reasons for the reduction of total loss in machine with segmented steel lamination as compared to non-segmented steel lamination and that without steel lamination are shielding effect of the stray flux on the lamination plane as well as the effect of cut to disallow eddy current circulations.

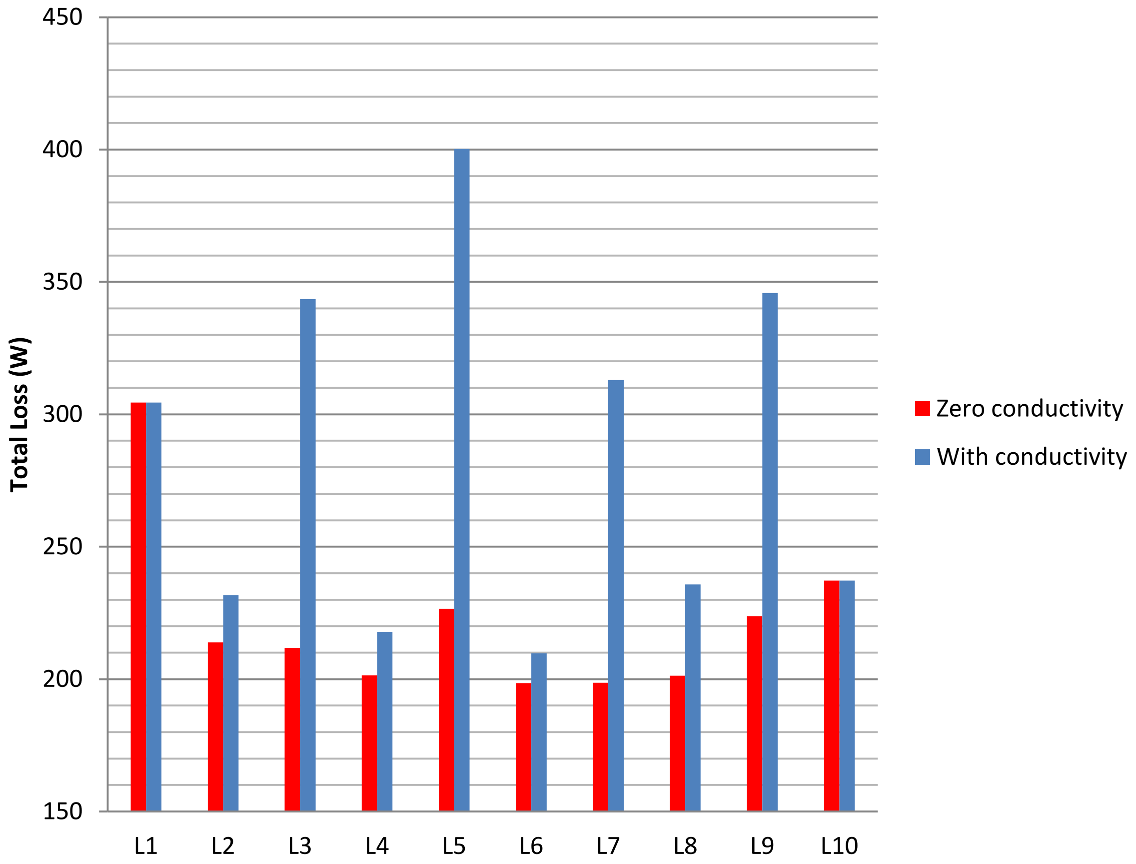

Figure 7-10: On-Load total loss.

The effect of the steel lamination thickness was considered and shows that by changing thickness of the steel lamination, the flux carrying capability was changed and also the resistivity or conductivity of the material is affected, however the total loss of material slightly increased by reducing the thickness of the magnetic material as shown in Figure 7-10 above. It's clear from the bar chart that L6 provides the lowest total loss with and without conductivity on steel lamination sheet.

Figure 7-11 presented the 3D FEA comparison of AC winding loss and the investigation shows that, depending on the type of lamination sheet and for all the designs, the AC winding loss increased by 6.3% to 18% between magnetic material without conductivity and that with conductivity.

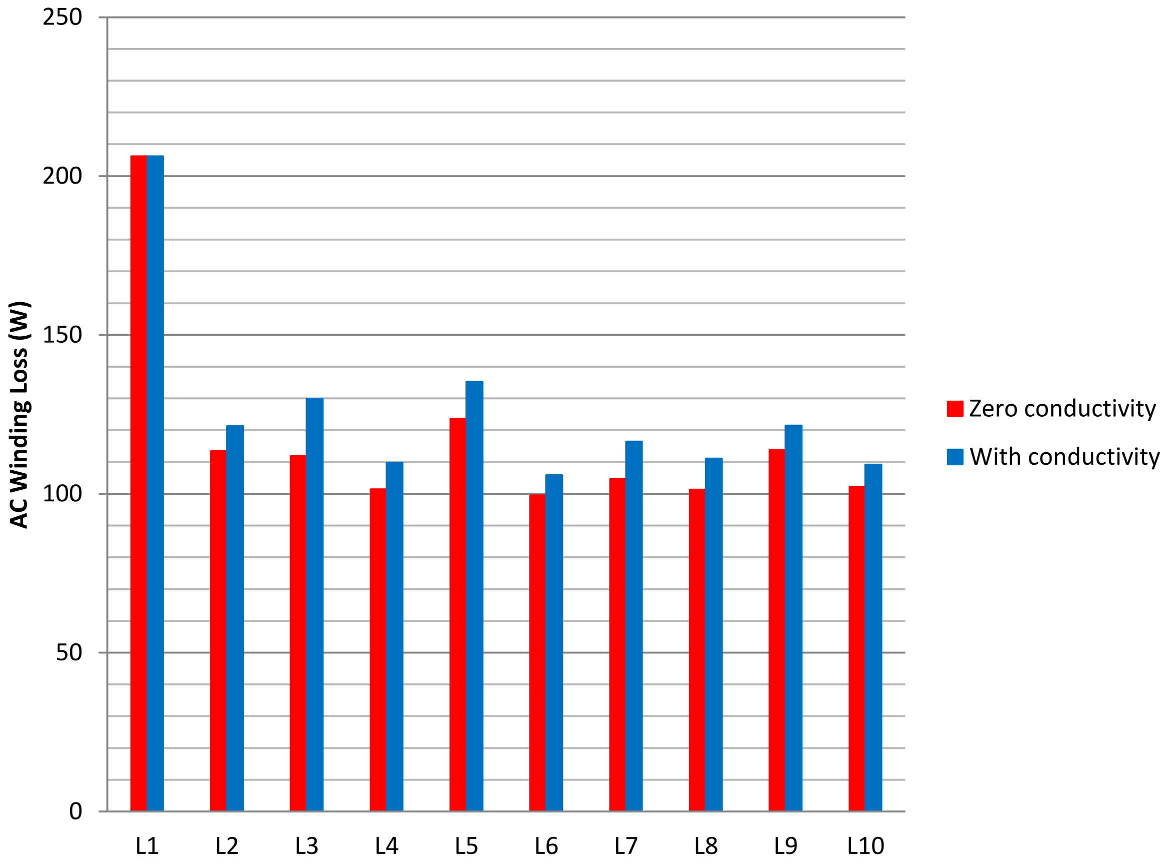

Figure 7-11: AC winding loss.

7.6 Cogging Torque and Axial Force

The change in cogging torque with the steel lamination having conductivity and without (zero) conductivity is something very important to study since cogging torque is produced as a result of rotor's tendency to align with stator poles in order to minimise reluctance even when no current is applied in the winding coils.

Figure 7-12 presents the peak-to-peak cogging torque in various machines without and with steel lamination sheet, together with and without conductivity on steel lamination sheet. It can be seen that L3, L5, L7 and L9 provides the lowest peak-to-peak cogging torque for both machines with and without conductivity on steel lamination. Moreover, L6 provides the lowest peak-to-peak cogging torque among designs with segmented steel lamination sheet.

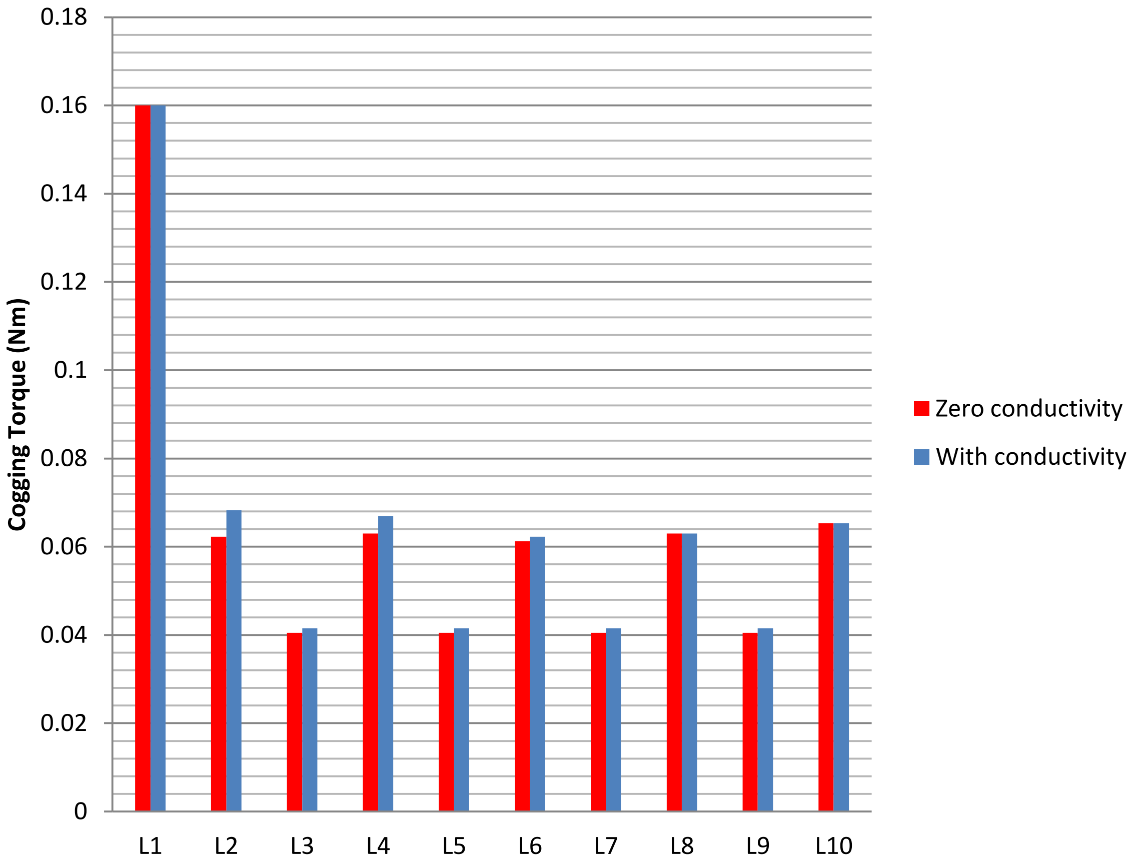

Figure 7-12: Cogging torque.

For L2, L3, L4, L5, L6, L7 and L9, there is little difference in magnitude of peak-to-peak cogging torque between machines without and with conductivity as show in Figure 7-12. These might be as a result of the rate at which heat or magnetic flux passes through the steel lamination sheet.

The non-segmented L3, L5, L7 and L9 provides the lowest peak-to-peak cogging torque of 0.04 Nm for both designs without and with conductivity steel lamination sheet as compare to approximately 0.06 Nm for segmented L2, L4, L6, L8 and L10; a 33.33% reduction. When compared to L1, the non-segmented and segmented peak-to-peak cogging torque reduces by 75% and 62.5% respectively.

The effect of material conductivity on axial force of attraction between stator and rotor was investigated. This is a huge advantage in using such steel lamination sheet as not only the total losses, back EMF and peak-to-peak cogging torque reduced. The axial force also reduced significantly as shown in Figure 7-13. It clear from the graph that, L6 design with conductivity has the lowest axial force of attraction between stator and rotor and L10 with the highest axial force.

From the analysis, it is also clear that L1 provides the highest axial force of attraction of 792 N while L9 provides the lowest axial force; however there is disparity between designs without and with conductivity for L6 and L7 which may be as a result of high conductivity on this particular type of steel lamination sheet.

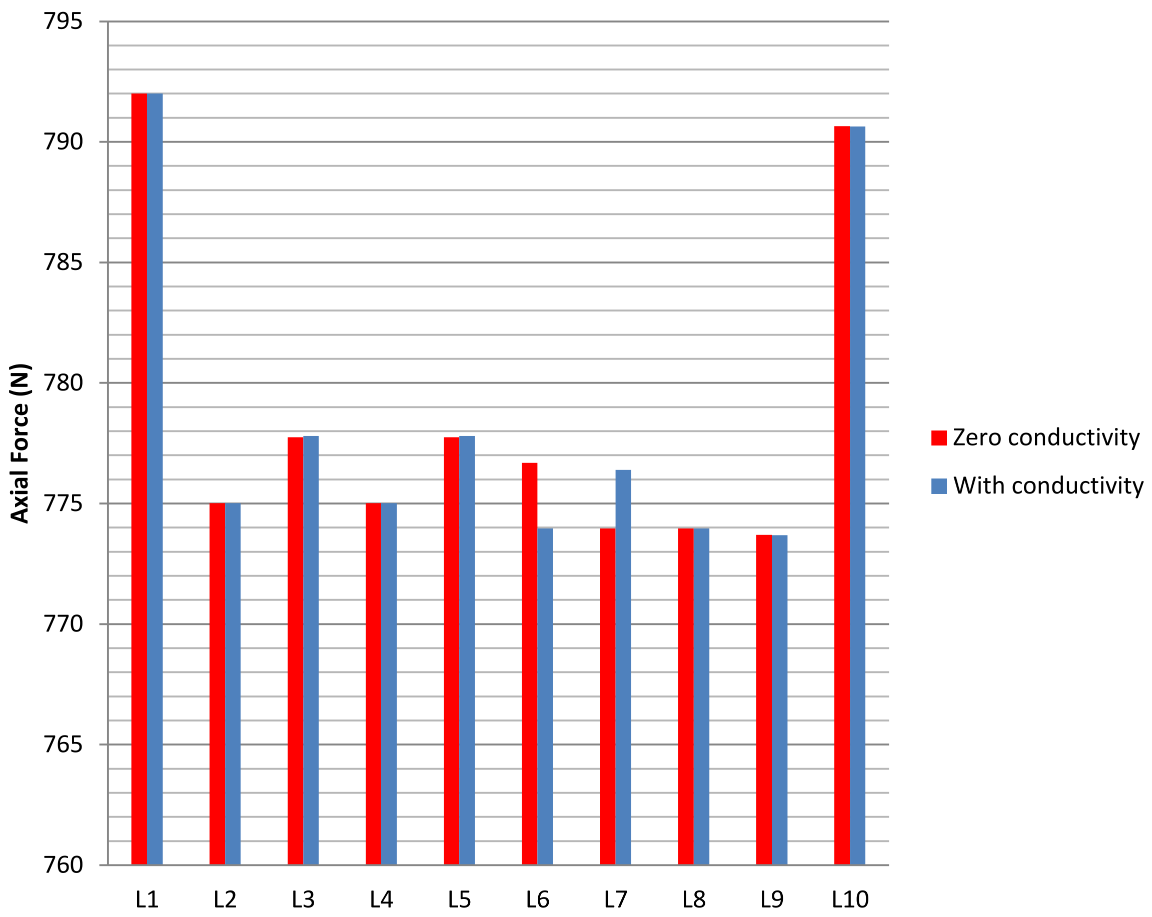

Figure 7-13: Axial force of attraction between stator and rotor disc.

7.7 On-Load Torque

The peak torques for these machines design without and with conductivity on steel lamination sheet is compared and is displayed in Figure 7-14. For all designs the peak torque with conductivity are slightly higher when compared to those without material conductivity. It is clear from the bar chart that to achieved maximum peak torque the steel lamination sheet material for loss reduction must have a higher conductivity to allow more magnetic flux passing through it.

Moreover, the reduction on torque is due to the material conductivity, L6 has the highest material conductivity and the highest torque reduction when compare with the rest of design. From the analysis it is indeed however clear that material with higher conductivity result in more torque reduction compared to material with lower conductivity.

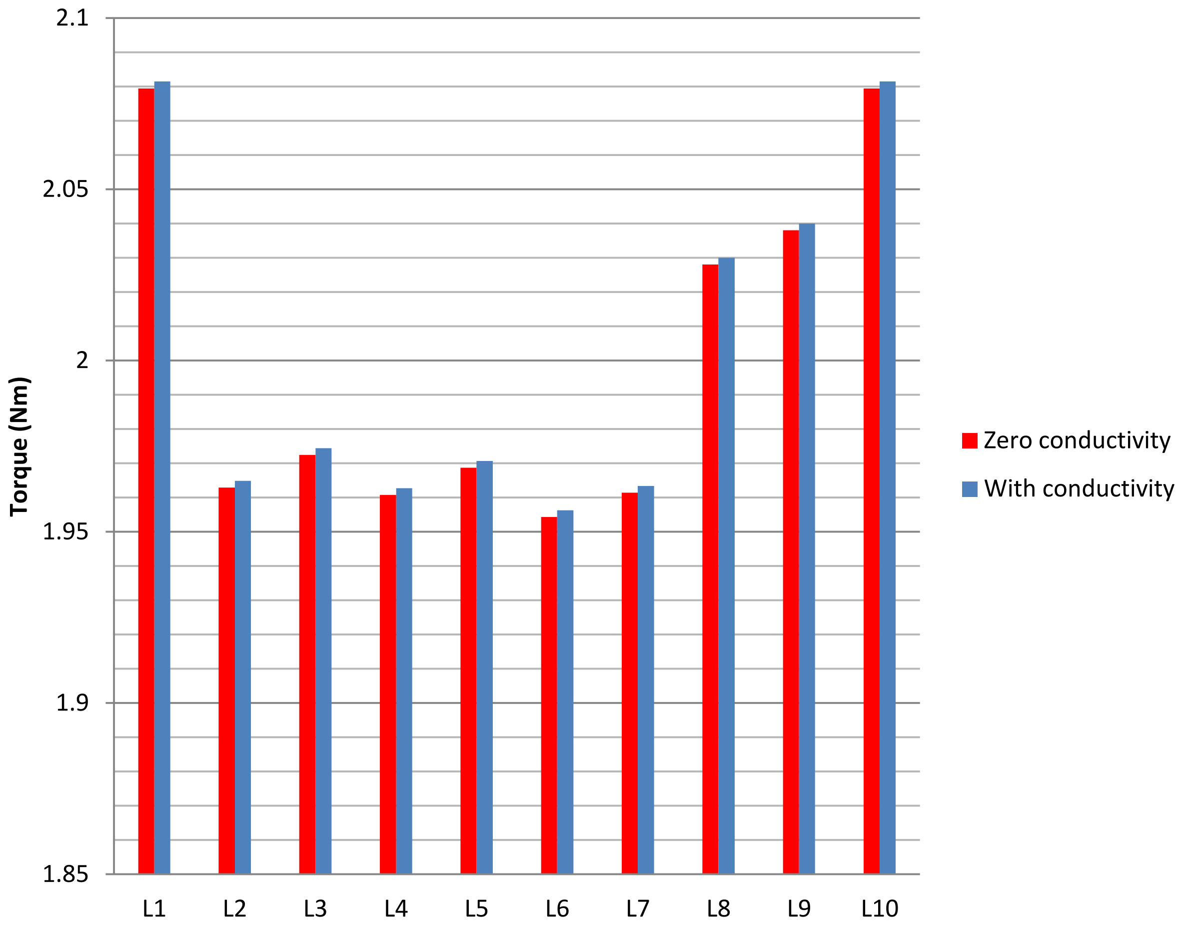

Figure 7-14: On-load Torque comparison.

Figure 7-15 and Figure 7-16 shows the percentage comparison without and with material conductivity of flux linkage, back EMF, no-load loss and on-load loss, peak cogging torque, axial force and on-load torque for L2 to L10 with respect to percentage of L1.

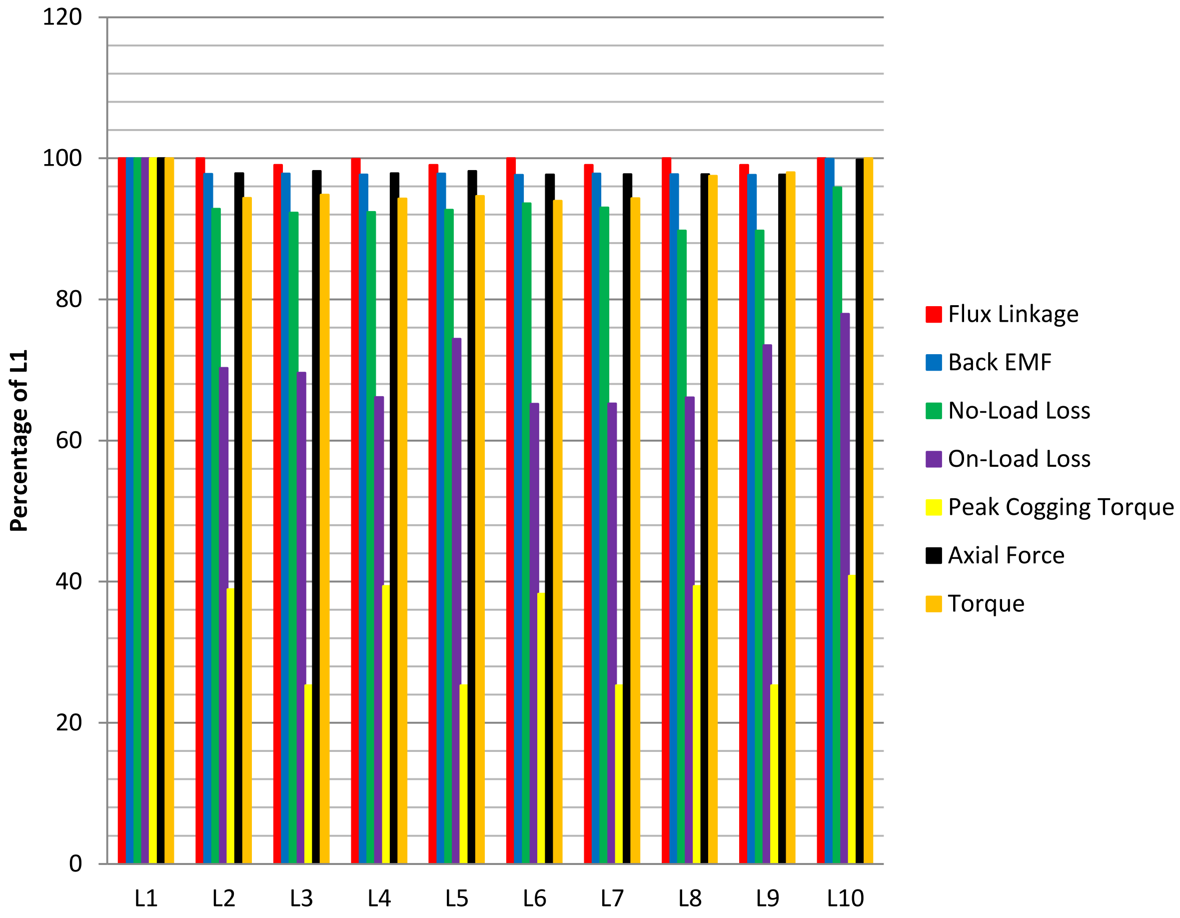

Figure 7-15: Percentage comparison of different parameters without conductivity.

It can be seen from the FEA studies that using steel lamination without conductivity on it can reduce the on-load loss and peak-to-peak cogging torque as shown in Figure 7-15 greatly, when non-segmented lamination were utilised. The peak cogging torque of L3, L5, L7 and L9 reduced to 25% of the L1. Moreover, the axial force, no-load loss and torque also reduced slightly for L2 to L10 as compared to L1.

Segmented design also depict a low cogging torque, but slightly higher when compared to non-segmented design steel lamination sheet. The peak flux linkages in the entire machines are approximately the same however the back EMF of L2 to L9 reduces by less than 3% of L1 and L10.

The analysis in which the steel lamination sheet conductivity is applied, the peak flux linkage of L2, L4, L6, L8 and L10 are the same as L1 however slightly decreases by less than 1% for L3, L5, L7 and L9 as compared to L1.

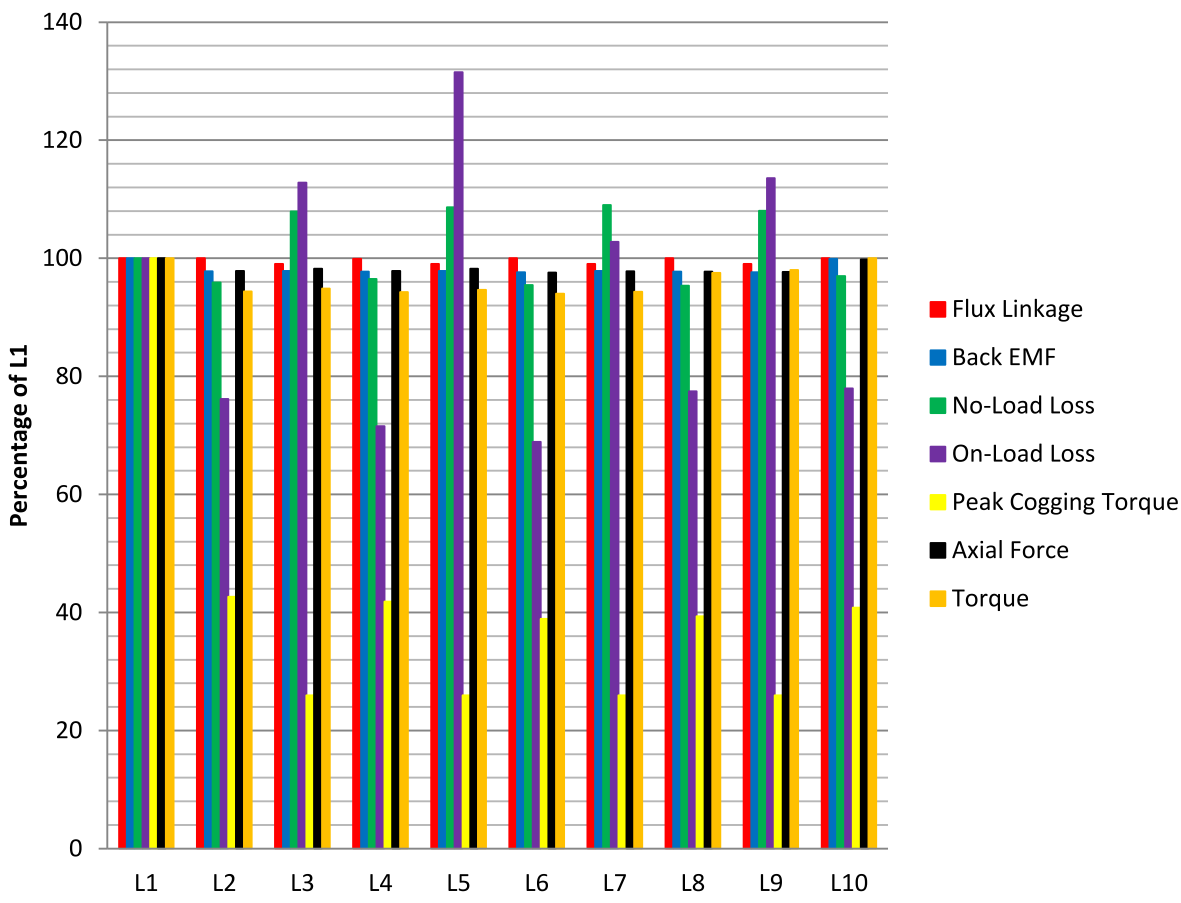

Figure 7-16: Percentage comparison of different parameters with conductivity.

The peak back EMF and axial force of attraction between the stator and rotor disc in all machines seems quite consistent, the no-load loss when compared to L1 increased for L3, L5, L7 and L9 by up to 9% and decreased by up to 29% for L2, L4, L6, L8 and L10.

The on-load loss on segmented design L2, L4, L6, L8 and L10 decreased by up to 32% depending on the type of steel lamination sheet used and increased by up to 32% on non-segmented design L3, L5, L7 and L9. The peak cogging torque of L3, L5, L7 and L9 reduced to 25% of the L1 however they are slightly higher when compared to non-segmented design and torque reduced slightly for L2 to L9 as compared to L1. In this case the cogging torque has similar pattern to those shown in Figure 7-15 above.

7.8 Slot Design

The slot design used in the analysis of the final machines in Chapter 6 is rectangular in shape, for optimal slot shape design there is a need to look at other types of slot shape. In this section comparison between the rectangular and trapezoidal slot shape will be presented in terms of the total losses in the machine.

As reported in Chapter 4 changing the slot area shape from rectangular to trapezoidal, the effective total length of the conductors in the slot increased and the total loss in the machine is higher. Figure 7-17 shows the no-load total loss comparison with zero conductivity on steel lamination sheet.

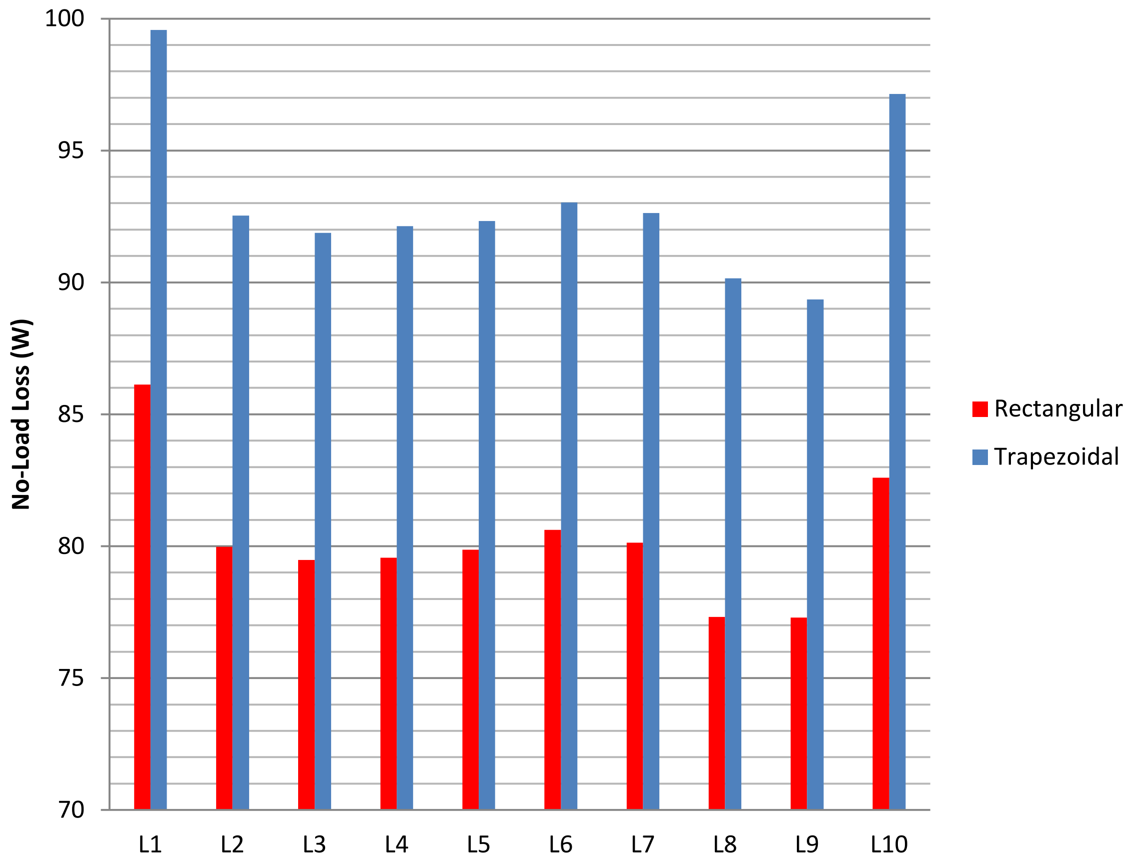

Figure 7-17: No-Load total loss without conductivity.

It is clear from the analysis that at no-load and with high reluctance on steel lamination sheet the total loss in trapezoidal slot increases from 15.7% to 17.6% depending on the type of steel lamination. In L1 the increased is 15.6%.

Figure 7-18 shows the total loss comparison at no-load but with low reluctance on the steel lamination sheet, in this case L10 with trapezoidal slot has the highest total loss and increases by 17.8% as compared to that with rectangular slot, moreover L6 has the lowest total loss which increases by of 16.5%.

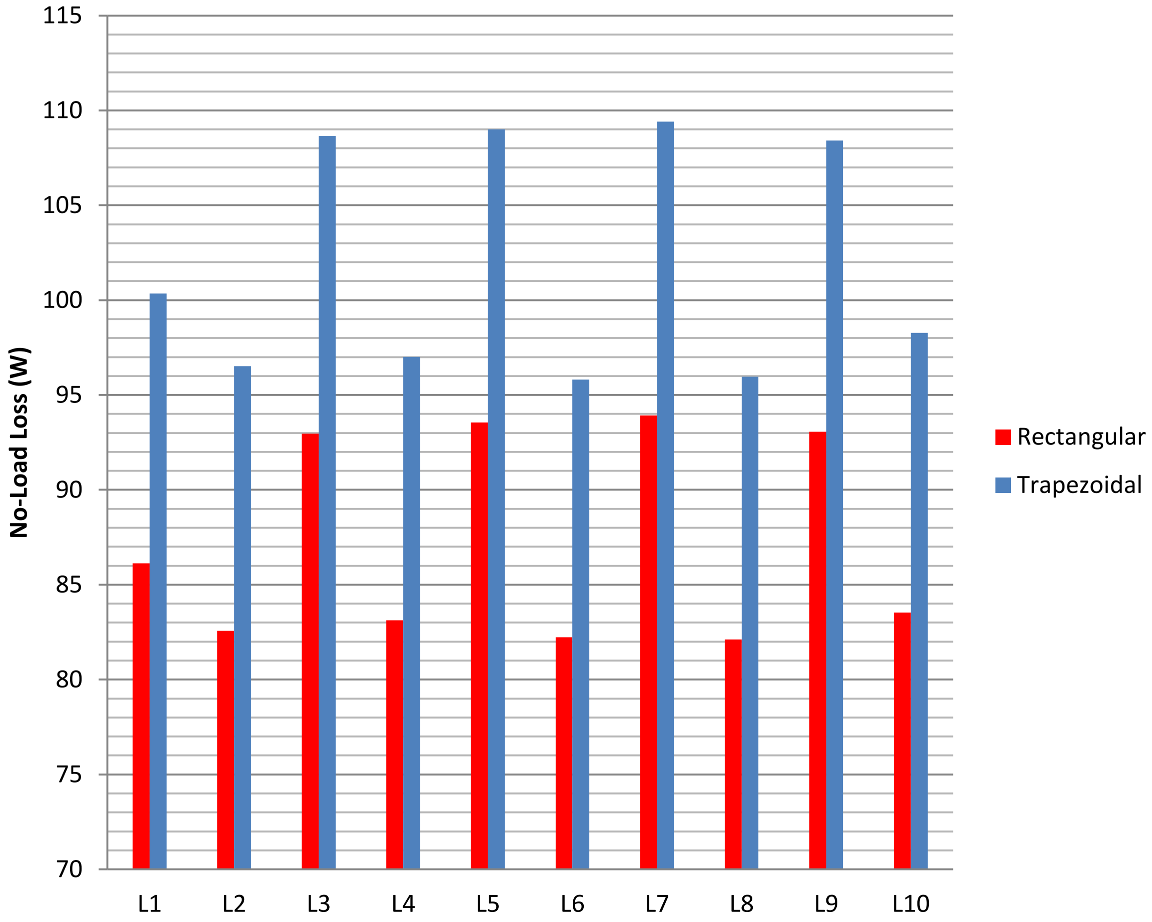

Figure 7-18: No-Load total loss with conductivity

The on-load comparison of the total loss with zero conductivity on steel lamination sheet is shown in Figure 7-19. The bar chart shows that for L1, L2, L4, L6, L8 and L10, the trapezoidal slot increased by 17.6% as compared to rectangular slot, similarly for L3, L5, L7 and L9 the increased is 17.9%.

These show that the machine without steel lamination sheet and those with segmented design have alike increase in the total loss. In addition to that, the percentage of increase in total loss is also the same for the non-segmented design steel lamination sheet.

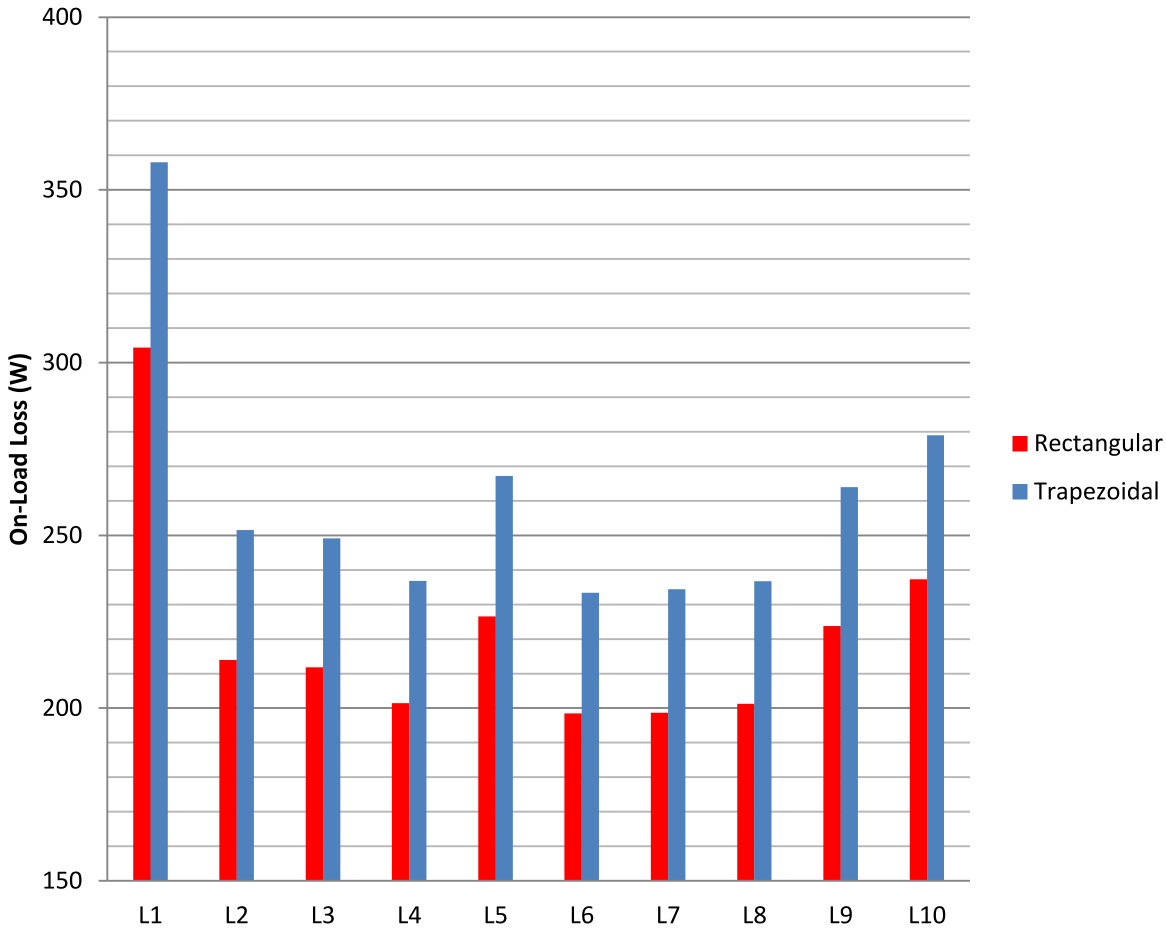

Figure 7-19: On-Load total loss without conductivity.

With steel lamination sheet having conductivity, the increase in total loss varies from L1 to L10 as shown in Figure 7-20. For L1 the total loss increased by 26% when the slot changes from rectangular to trapezoidal and the on-load total loss of trapezoidal slot reduces by 26.5%, 26.8%, 26.6%, 26.9%, 25.7 and 26.1% for L2, L3, L4, L5, L6 and L7 respectively when compared to rectangular slot.

The segmented design L8 has a total on-load loss increase of 26.2% and for the non-segmented design L9, the increase was 26.3%. For the segmented design steel lamination sheet L10 the total on-load loss increase is unalike the remaining machine with steel lamination sheet as it has the same percentage as the machine without steel lamination sheet L1.

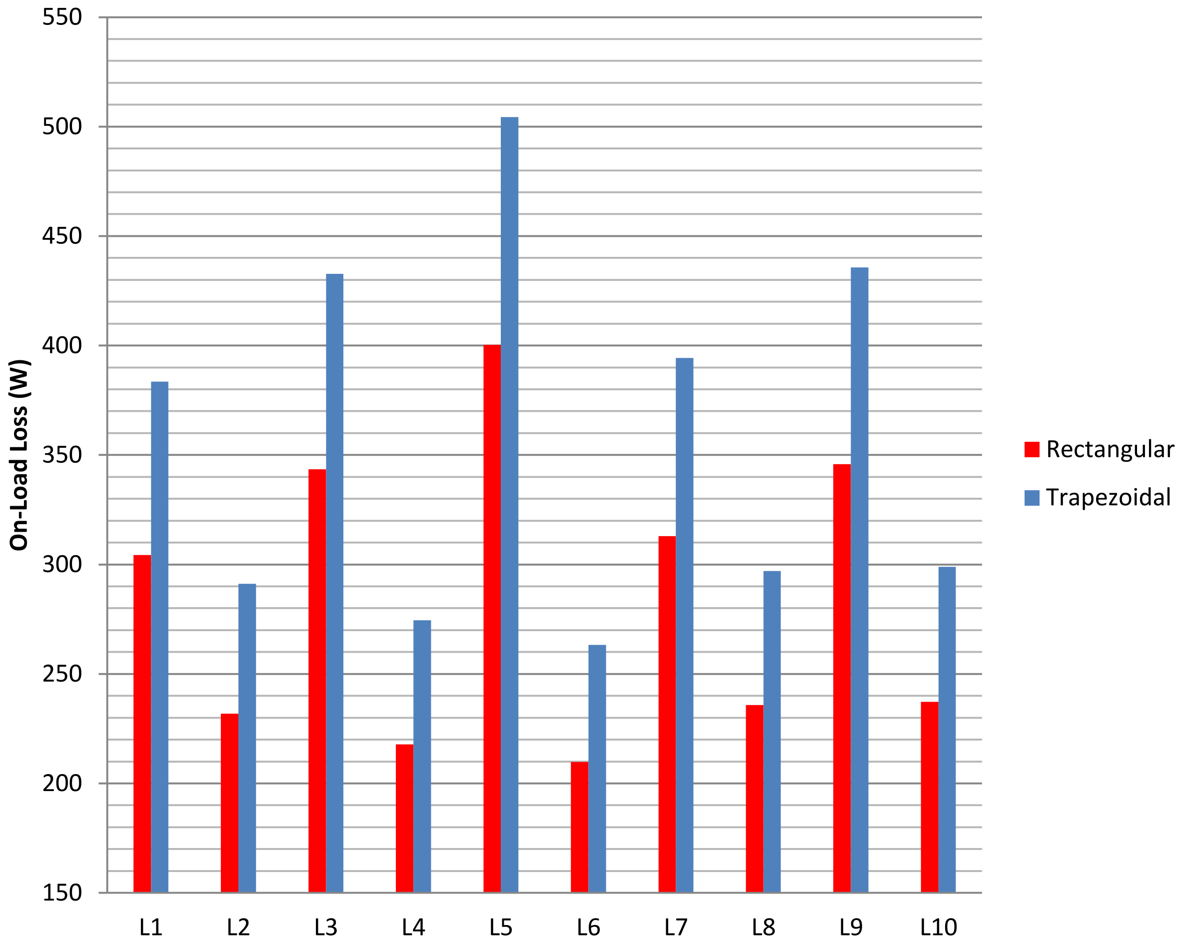

Figure 7-20: On-Load total loss with conductivity.

7.9 Conclusion

In this chapter, academic investigation into the mechanism of loss reduction by investigation of the separate effects using idealised materials (high reluctance / zero resistivity and vice versa) were presented. Various analyses were presented on the effect of steel lamination sheet without and with conductivity and thickness on flux linkage, back EMF and harmonic, no-load loss and on-load loss, cogging torque and axial force, on-load torque and on two different slot design (rectangular/trapezoidal).

It is seen from the FEA studies that using magnetic material like steel lamination sheet with conductivity and low reluctance together with rectangular slot shape can reduce the total loss of the machine, it is also found that the higher the conductivity of that material the more the AC loss reduction. Segmented steel lamination sheet L6 provide the highest loss reduction as compared to others type of lamination sheet utilised in the analysis.

It is clear from the analysis carried out on this chapter that the characteristic of magnetic permeable shielding is superior to that of electrically resistive shielding, moreover the shielding property is determine by the permeability, conductivity and thickness of the magnetic material used for the shielding of AC fields.

Finally, these techniques have shown us the possibilities of reducing the overall loss of an AFM by a reasonable amount while maintaining the back EMF and torque within a reasonable value. The selections of the steel lamination sheet together with thicknesses are all novel methods used in this thesis however the non-segmented steel lamination sheet would be discarded as they produced more lamination losses compared to segmented steel lamination sheet. Chapter 8 presents the prototype construction of segmented designs.

8. Prototype Construction

8.1 Introduction

This chapter details the mechanical design, production and assembling of the prototype machine. The machine is constructed from a prototyping SMC to take into account the 3D flux movement through the core-backs of AFM and can be machine in the workshop directly without losing most of its properties. A single machine with four different steel lamination sheets was manufactured and each lamination sheet was used to suppress the AC winding loss. In total six different machine designs were tested and described as following:

Table 8-1: Steel lamination sheet description.

Label	Description
L1	Machine without steel lamination sheet
L2	Machine with segmented M235-35A steel lamination sheet
L4	Machine with segmented M270-35A steel lamination sheet
L6	Machine with segmented M300-35A steel lamination sheet
L8	Machine with segmented N020 steel lamination sheet
L10	Machine with segmented M270-35A steel lamination sheet in which MMF adjusted to get the same torque as L1

The inner radius, outer radius and thickness dimension of each steel lamination and all other components within the machine are kept constant except N020 that has 0.2 mm thickness so that the comparison is valid. The non-segmented designs were discarded due to the high loss in the steel lamination sheet as results of eddy current circulation as stated in Chapter 6 and Chapter 7. The stator block of the machine is made up of the tooth and core-back from the pressed SMC and has 12 stator teeth. The coils are pre-wound on a former and slide onto the tooth. The rotor is made from pressed SMC and consists of 14 pole magnets from Neodymium grade N35SH and the idea of using solid steel at the back of rotor SMC is to fix the shaft using screws, which is not possible to use screws on SMC. In total three SMC Somaloy blocks were used in manufacturing the prototype machine. The various components of the machine are enclosed within the aluminium casing. Figure 8-1 presented the completed machine assembly without the aluminium hub case and Figure 8-2 shows one of the segmented steel lamination sheets used during the prototype assembly.

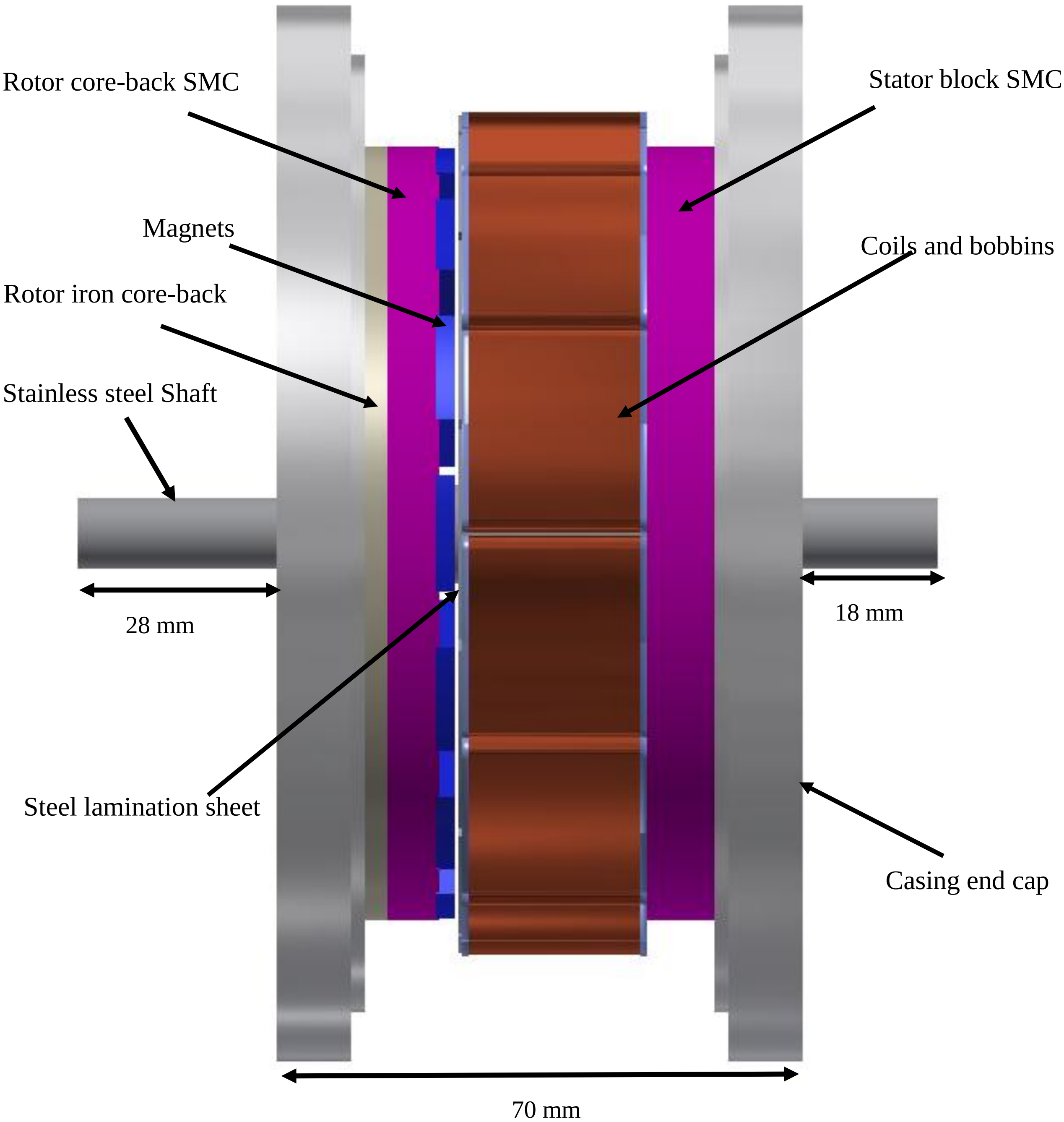

Figure 8-1: CAD model of the prototype machine assembled

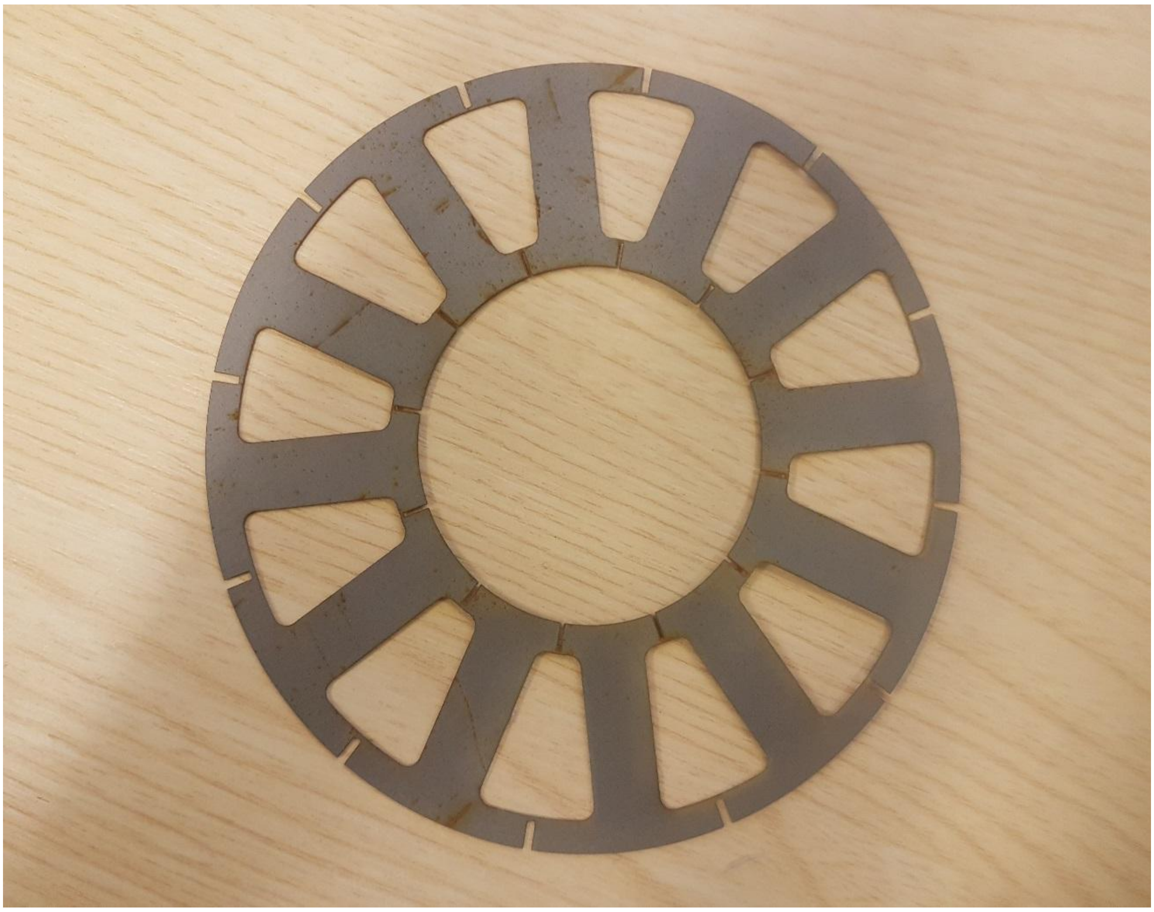

Figure 8-2: Segmented steel lamination sheet

8.2 Stator Block Construction

The stator tooth and core-back were design as a single block by using the available prototype material, which has a diameter of 120 mm and thickness of 20 mm. The outer and inner diameters of the stator are 110 mm and 64 mm respectively. Figure 8-3 shows a sample of SMC prototype material with 120 mm outer diameter and 20 mm thickness. The data sheet of SMC prototype material Somaloy is presented in Appendix C.

The thickness of the stator core is 10 mm and the tooth height and width are 25 mm and 5 mm respectively, which enables more Ampere turns in the machine. To get it as a single block two prototype SMC were heated and merged together in the mechanical workshop to have the thickness of 40 mm, which allows for machining and a 30 degrees tooth span was used to have a 12 tooth in the machine. The two SMC prototype materials were join together using Permabond adhesive ES 562 (heat cure) and machined to obtain the stator block using the CNC milling machine and the lathe machine.

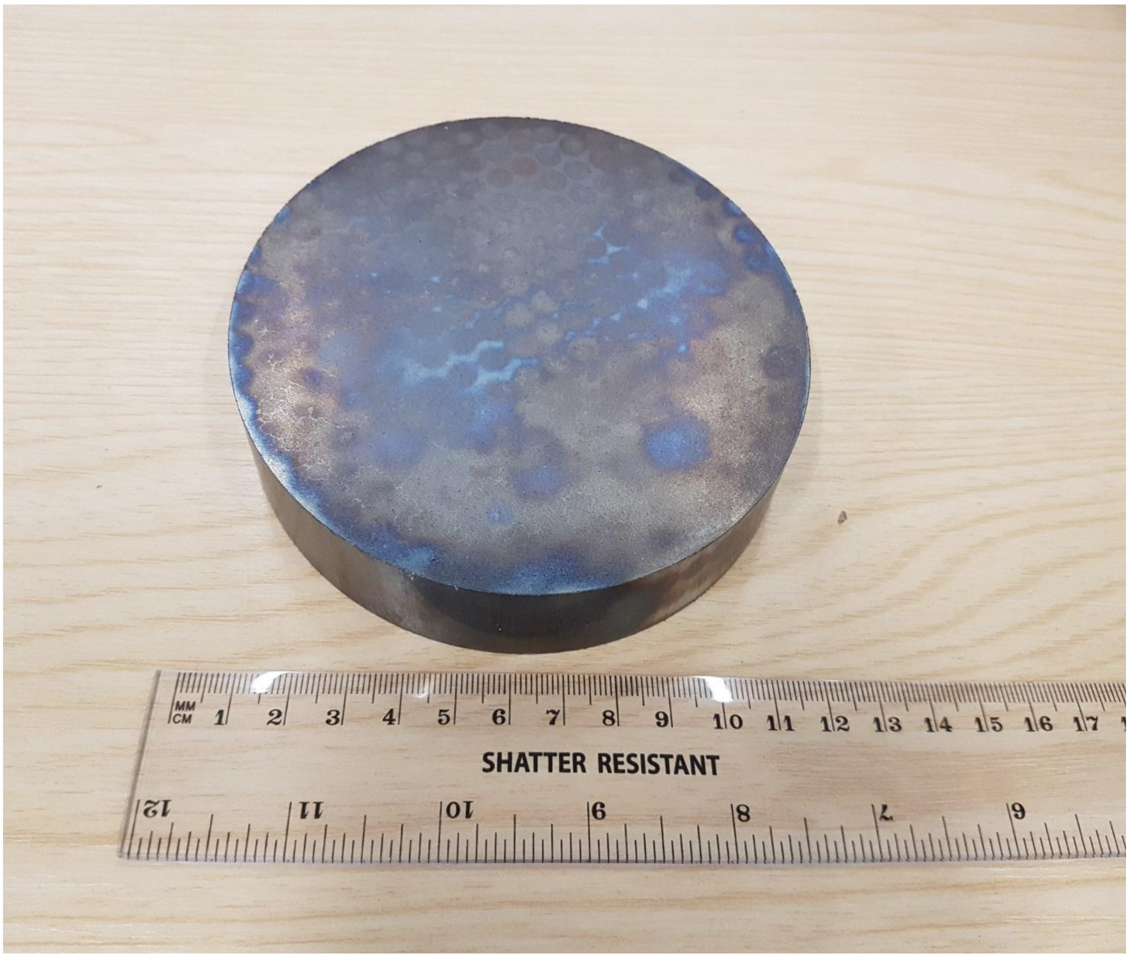

Figure 8-3: A sample of SMC prototype material.

After machining the stator block with the above dimension, a stator block was produced, this consist the stator teeth and stator core-back. Figure 8-4 presented the complete stator block of the machine made from the prototype material.

All the machine components except the plastic bobbin were manufactured using CNC and lathe machines in the mechanical workshop to avoid temperature rise which may affect and damage some properties of the SMC Somaloy, 3D printer was not used in the manufacturing of these components, but it is good for prototyping of machine component provided temperature is kept low.

The casing were manufactured from aluminium and in one of the aluminium case side cover, a 2 mm depth groove was made with the same dimension as the stator core to enable the stator block fix into it. To make the joint rigidity Permabond adhesive ES 562 was used to enable heat transfer from the stator block in to the outside surroundings environment. This adhesive can withstand higher temperatures (130˚C to 160˚C) for brief periods (such as for paint baking and wave soldering processes) providing the joint is not unduly stressed. The minimum temperature the cured adhesive can be exposed to was - 40°C depending on the materials being bonded as stated in the data sheet in Appendix E.

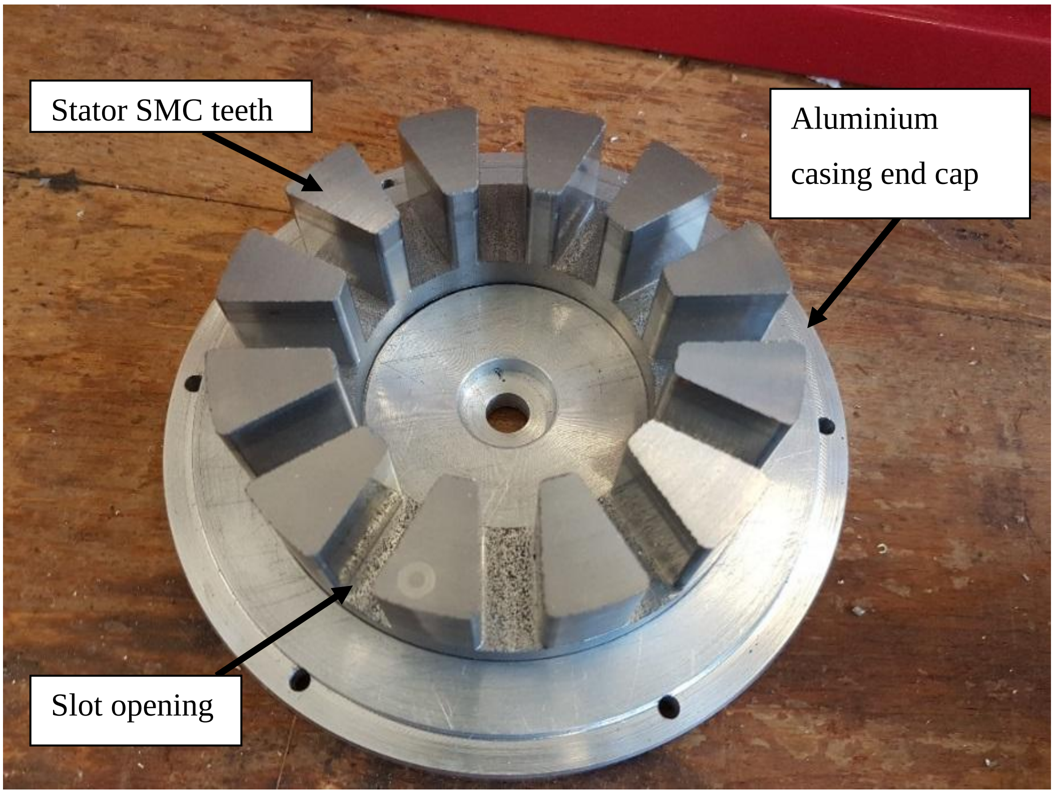

Figure 8-4: Complete stator block with one end cap.

8.3 Stator Winding

Three different diameter conductors were used in the 3D FEA design of the machine namely; 0.85 mm, 1.4 mm and 3.2 mm. The 1.4mm diameter conductor was used for the optimised design and the remaining two together with 1.4 mm diameter conductor were used for AC winding loss analysis. The reason for using different windings is to ascertain the effect of conductor diameter on AC winding loss. Concentrated windings were used in the design.

The windings were pre-wound on a plastic bobbin to achieve high fill factor and slide onto the SMC tooth of the machine, except the 3.2 mm conductor in which a Nomax thermal insulation paper 304 mm x 200 mm x 0.13 mm was used instead of plastic bobbin to achieve high fill factor. This material offers a high dielectric strength, mechanical toughness, flexibility and resilience. In addition, it can withstand a maximum operating temperature of greater than 300˚C. The data sheet of thermal insulation paper is presented in Appendix F.

The bobbins were made using F123 series 3D printers from stratasys as presented in Appendix I. It has the tensile strength ultimate and compressive strength ultimate of 20.7 MPa and 2.6 MPa in XZ orientation respectively as shown in appendix I. Moreover, the material offers the capacity to quickly produce complex shapes and parts.

The duration to produce a bobbin is one and the half hours and the thermal performance of each bobbin range from -42˚C to 176˚C. Lastly, an insulation tape was used to cover the coils on the bobbin. Figure 8-5 presents the 1.4 mm diameter conductor wound on plastic bobbin and Figure 8-6 gives the 3.2 mm diameter conductor wound on thermal insulation paper.

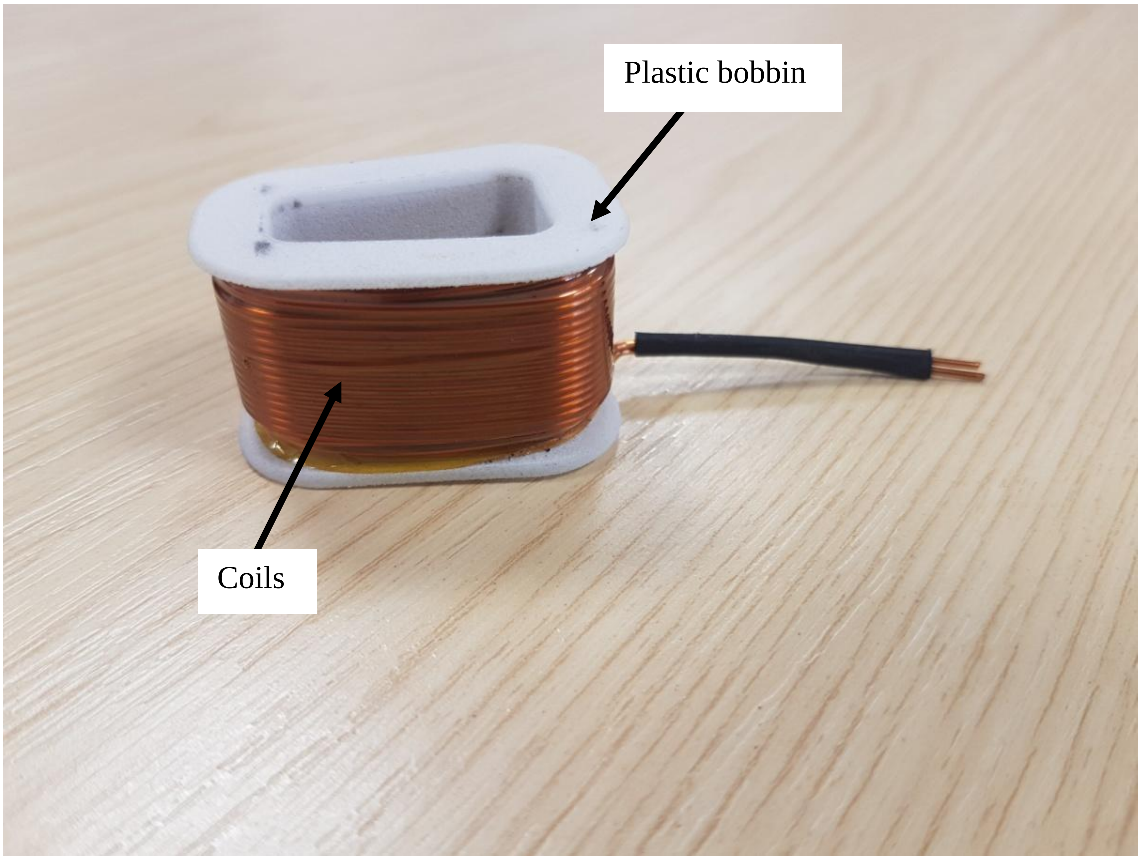

Figure 8-5: 1.4 mm conductor wound on plastic bobbin.

8.4 Shaft Design and Construction

The shaft of the machine was made from the AMINOX ASI; Proprietary (1.4404 ASTM A479 316L) stainless steel rod. The shaft has a length of 116 mm as shown in Figure 8-7 and it presents the final non-magnetic shaft for the AFM machine. The data sheet is presented in Appendix G and the lathe machine was used in the manufacturing of the prototype shaft.

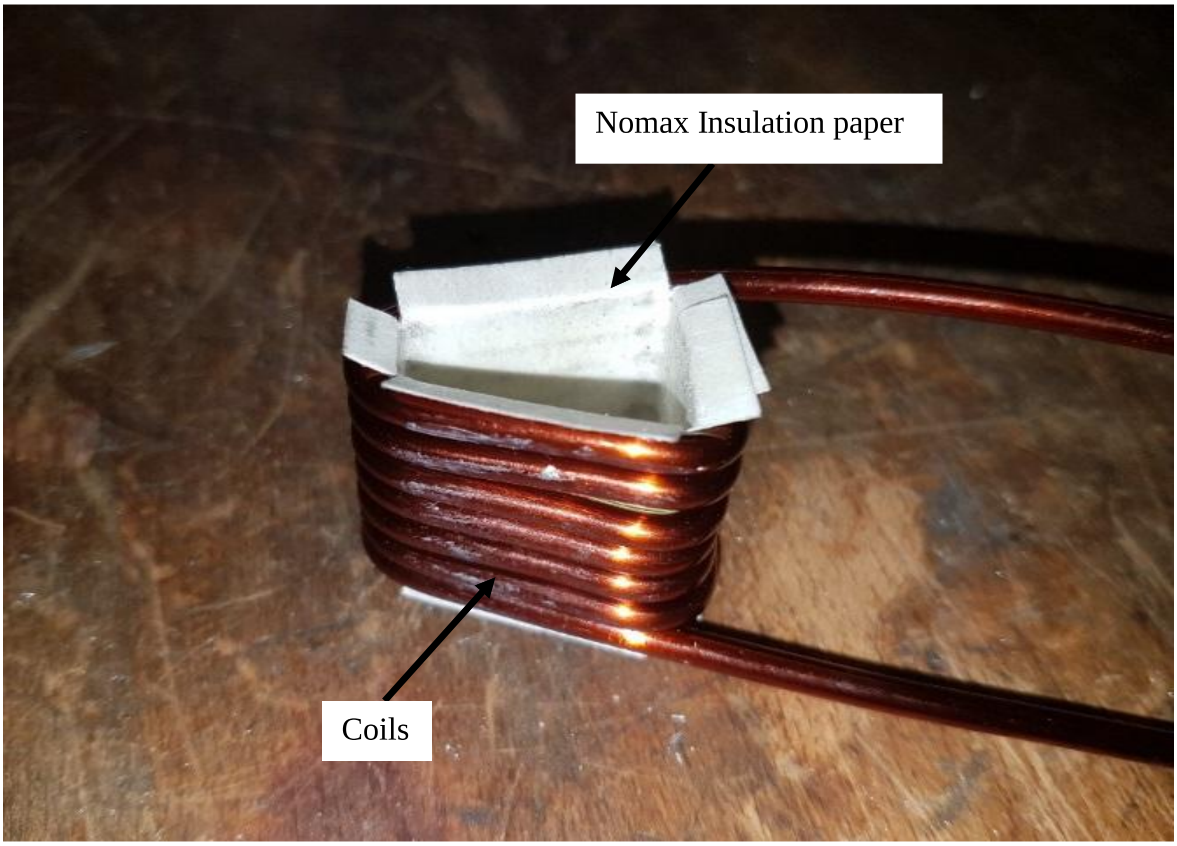

Figure 8-6: 3.2 mm conductor wound on thermal insulation paper.

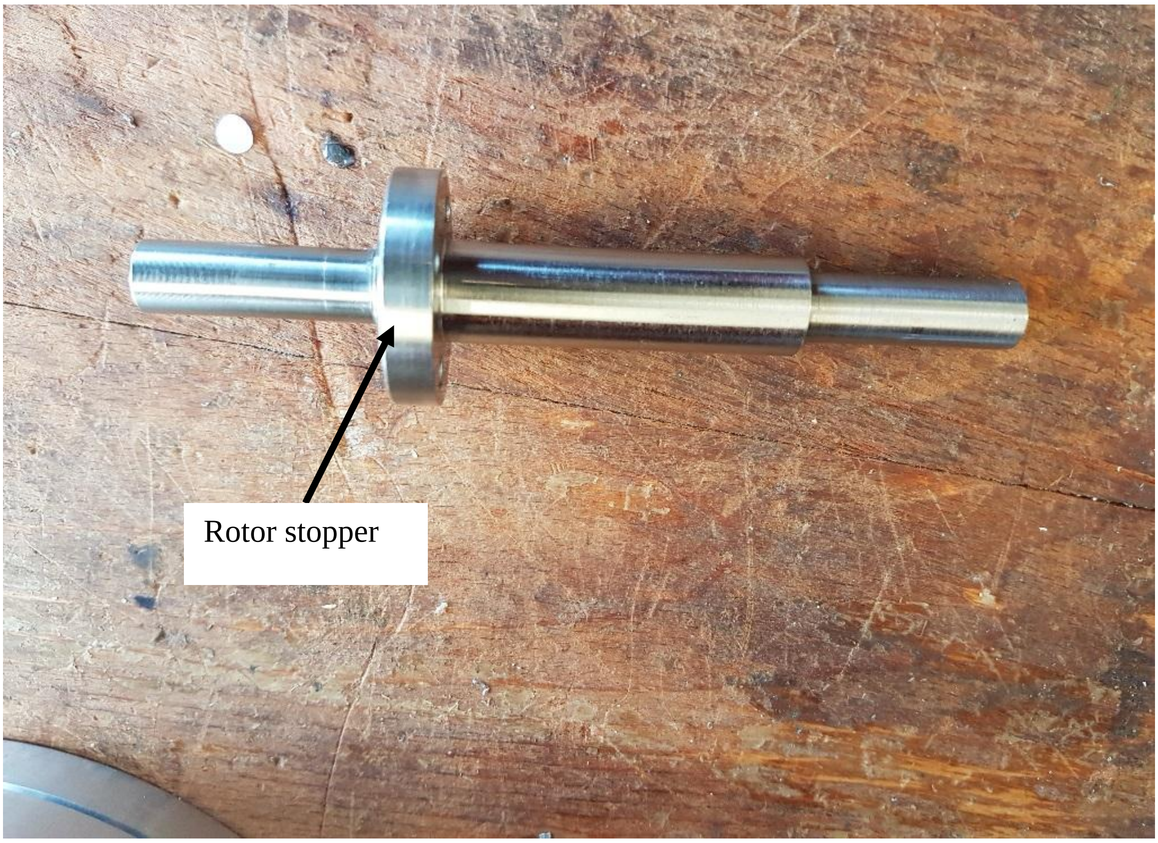

Figure 8-7: The final non-magnetic shaft of the prototype machine.

8.5 The Permanent Magnets

The magnets used in the design were NdFeB N35SH arc magnet, dimensions as per drawing shown in Figure 8-8, Nickel coated and magnetised in axial direction. To minimise the flux leakage at the ends of magnets, the magnet span of 120 degree electrical was used for maximum performance and cost effective. 3D FEA simulation was used to ascertain different magnet span and thickness under the operating conditions as presented in Chapter 4.

The magnets are surface mounted with 0.5 mm inserted on the rotor SMC plate to make them rigidly fitted and to avoid shaking during operation. Moreover, during the fixing of the magnets so many issues were encountered and a solution was proposed. Appendix D presented the data sheet of N35SH magnets from Arnold magnetic. The magnets are mounted on surface of rotor core-back and a Permabond adhesive ES 562 (heat cure) was used to fix the magnets onto rotor SMC core-back surface and heated for about one hour at 150˚C. It is a single-part epoxy adhesive which flows like solder when heated during curing with excellent adhesion to metal surfaces and composites and high bond strength allows it to replace mechanical fastening, soldering or brazing, its low viscosity is such that it self-levels [160].

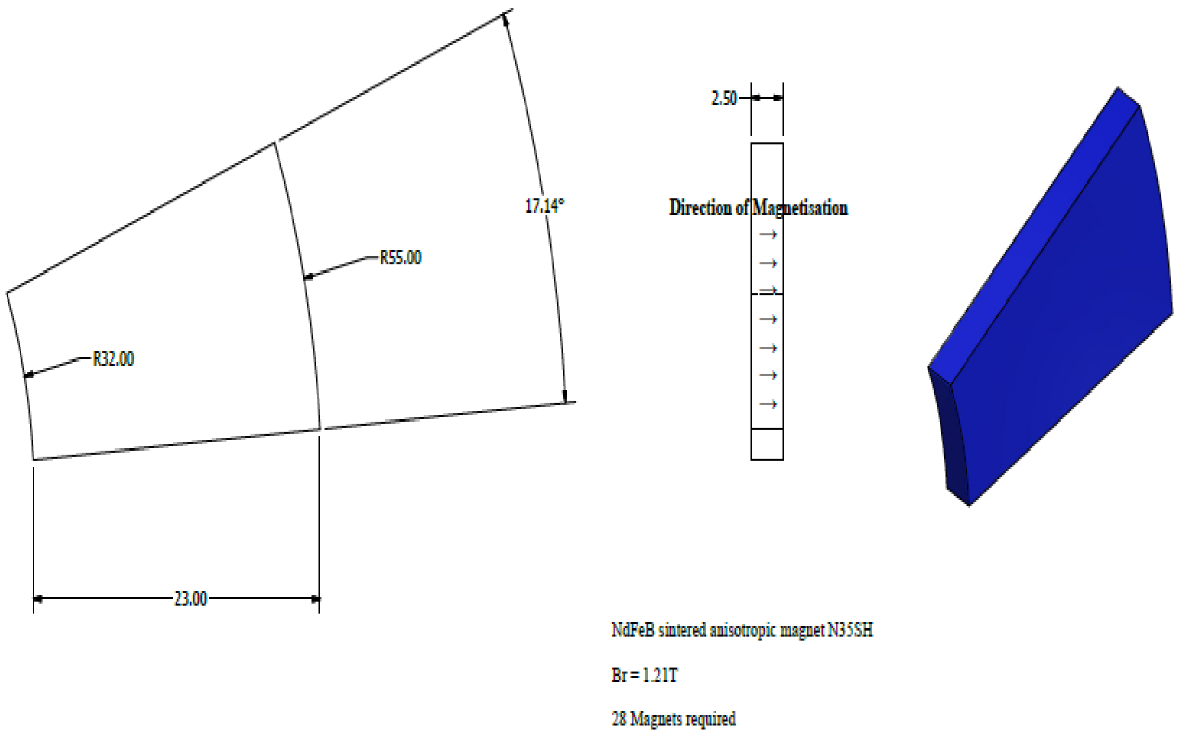

Figure 8-8: CAD diagram of N35SH magnet

It should be noted that before using the adhesive the surfaces need to be clean, dry and grease-free. In this case since the magnets are fixed on soft magnetic composite, emery cloth was used to clean the surface to remove any oxide layer formed during machining process.

The flux pattern in the machine is from the N - pole of the magnet through the airgap to stator core-back to the opposing S - pole magnet before turning 51.43 degrees mechanical, circumferentially within the rotor disc by one pole pitch and completes the path as shown in Figure 8-9, it also presents the 14 poles magnets on the surface of the rotor plate and the non-magnetic stainless steel shaft together with rotor iron core-backs.

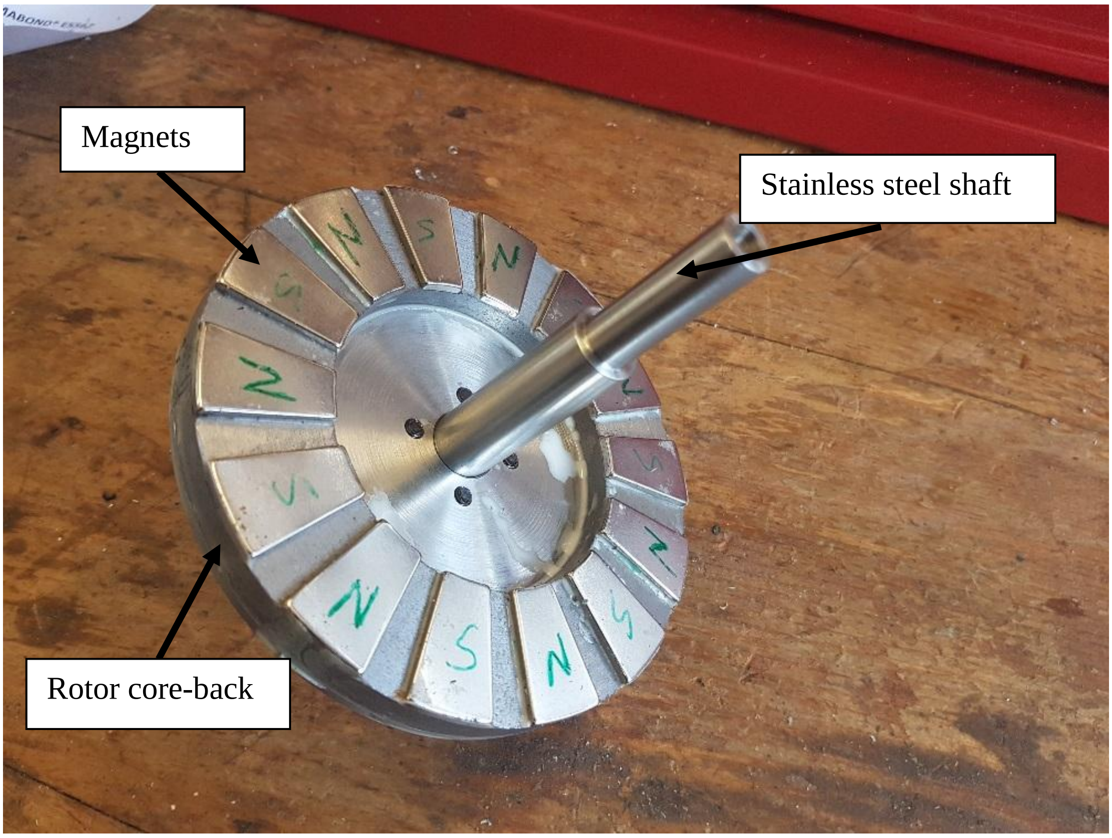

Figure 8-9: Flux pattern concept in the machine

One of the disadvantages of axial flux machine is the large force of attraction between the stator and rotor; care should be taken in fixing the magnets on the rotor surface to avoid damage. As a result of that a groove of 0.5 mm were formed on the SMC rotor disc with the same dimension as the magnets with two holes not through of 2 mm diameter and depth to allow the adhesive there to rigidly hold the magnets.

The North and South poles of the magnets were identified using a pole detector. The detector has a pointer head and screen to display the result. The pointer head was brought close to both sides of the magnets to identify the North and South pole of each magnet used. After putting the adhesive on the channels created the seven North Pole magnets were first fixed and held for some time, later the same procedure is followed for the remaining seven South Pole magnets and finally heated in the cure speed oven for 60 minutes at 150˚C. A similar process was done in the fixing of SMC rotor core-back and stainless steel rotor core-back together.

8.6 Rotor Construction

This section will present the design and construction of SMC rotor core-back and the stainless-steel rotor core-back for the final 110 mm machine. In addition, it describes the bearings used in the machine at the end cap of the aluminium case to hold the rotors and stainless steel shaft and to maintain 1 mm magnetic airgap between the stator and rotor.

8.6.1 Rotor Core-back

The rotor core-back was made of soft magnetic composite material as in the stator block design. The SMC rotor core-back has an outer and inner diameter of 110 mm and 64 mm respectively as shown in Figure 8-9. The rotor core-backs were fixed with the shaft as one component since both of them form part of the rotation in the machine.

A 4 mm thickness AMINOX AS1 (1.4404 ASTM A479 316L) round bar stainless steel was used at the back of the rotor core-back SMC, since it is not advisable to use screw on SMC material. The stainless steel rotor core-back with outer diameter of 110 mm and the same inner diameter as the stainless steel shaft as shown in Figure 8-9 was cut with 1 mm groove base for the SMC rotor core-back to be fitted into as shown in the CAD drawing in Appendix K.

8.6.2 Bearings

Two “off the shelf” W619002Z Stainless Steel Metal Shielded Thin bearings as shown in Figure 8-10 were used at the end cap of the aluminium case to hold the rotor and shaft and to allow for smooth rotation of the rotating part and to maintain a constant magnetic airgap of 1 mm between the stator part and rotating rotor part.

Figure 8-10: “Off the shelf” stainless steel metal shielded bearing.

8.7 Case Construction

This section described the process of making the case of the machine. The case is made from AW6082-T6511; BS EN755 (H30TF) Aluminium alloy 200 mm diameter round bar and 150 mm thickness. The overall weight of the machine has reduced by the use of aluminium casing. Appendix H presented the data sheet of aluminium AW6082-T6511 alloy.

8.7.1 Aluminium End Cap

This sub-section described the design and construction of the two aluminium end caps for the casing of the machine. It has the outer diameter of 146 mm and thickness of 10 mm as shown in Figure 8-11. In this case two were produced with the same dimension.

8.7.2 Aluminium Main Casing

The main aluminium case for the final prototype design as shown in Figure 8-11 was produced to case the machine. It has the outer diameter as the end cap of 146 mm and 55 mm thickness. In this case the final main aluminium case together with one of the end caps is presented as shown in the Figure 8-11.

Figure 8-11: Final aluminium case hub with one end cap

The final machine assembly with a single steel lamination sheet on top of the coils for AC winding loss reduction is shown in Figure 8-12, in which four different types of steel lamination were manufactured and used in the prototype machine for experimental measurements.

The steel lamination sheets were mounting on top of the coils with Nomax insulation paper in between them and a mixture of Permabond ES562 and normal glue with ratio of 10% to 90% was used in placing and holding each of the steel laminations sheets above the winding coils.

The main problem encountered during fixing the steel lamination sheets for AC winding loss reduction was how to make it very rigidly and the used of the this mixture of Permabond ES562 (10%) and normal glue (90%) proved to be strong enough to hold different steel lamination sheets up to 6000 rpm. The overall prototype manufacturing and assembly was simple and cost-effective and this shows that an AFM can be constructed using what are possibly to be mass production method.

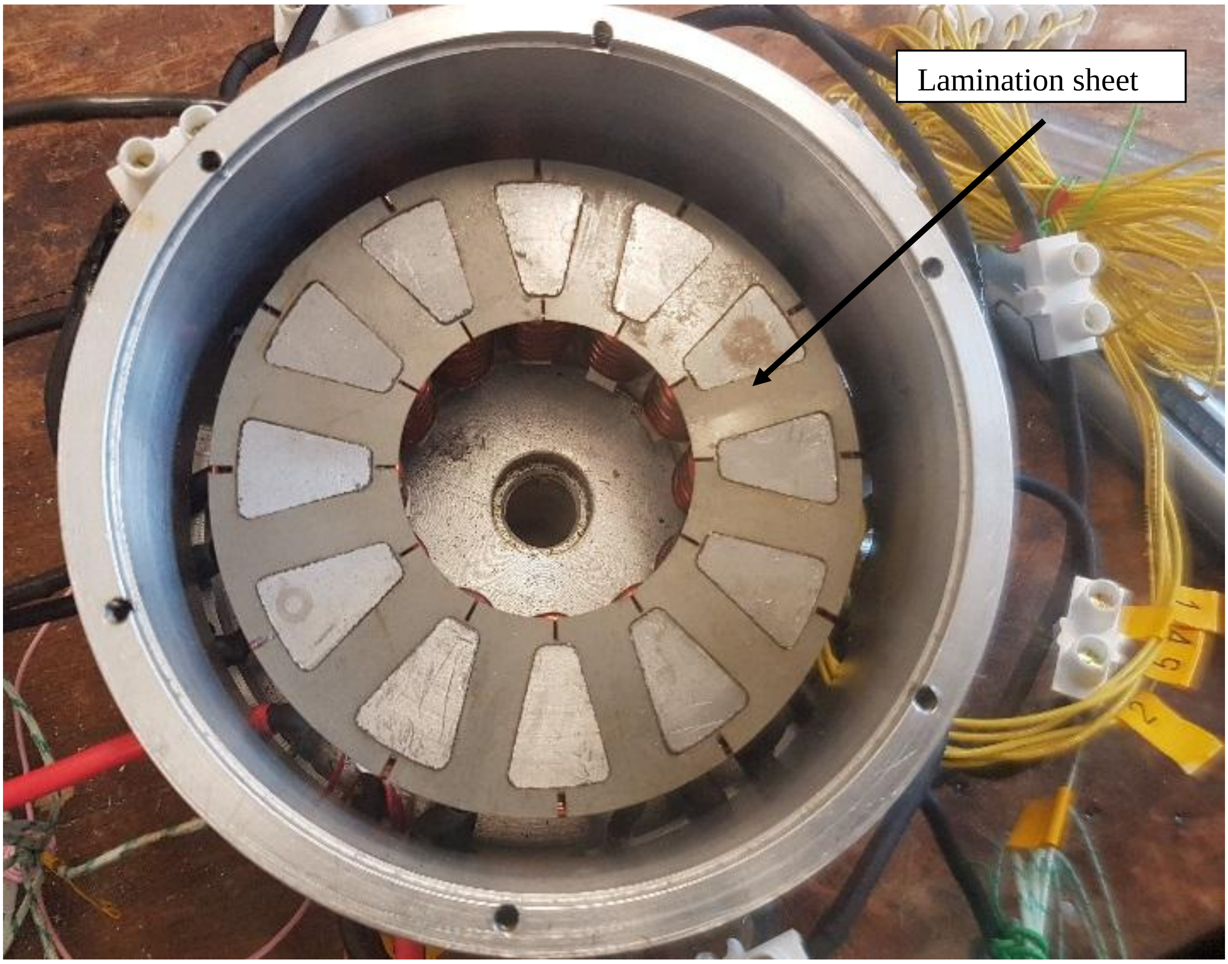

Figure 8-12: Steel lamination sheet placed on top of the coils.

8.8 Mega Ohm Test

The Mega Ohm test was carried out to measure electrical resistance of the coil insulation by supplying high voltage across the coil. SKF static motor analyser (Baker AWAIV-4kV) was used as shown in Figure 8-13. The following procedures were used to carry out the test. Test lead 1 is connected to one terminal of the coil, Test lead 2 is connected to the other terminal of the coil and the Ground lead is connected to the SMC core. The tests were run based on lead 1 and lead 2.

For the 12 slot 14 pole AFM with 1.4 mm diameter conductor, the phase voltage in the stator winding is 113.4 V less than 1000 V. For 3.2 mm diameter conductor with 6 turns, the phase voltage in the stator winding is 22.7 V less than 1000 V. The Mega Ohm test was carried out at 500 V and the Mega Ohm status was overall pass with 500V, the Resistance is 114784 MΩ.

Surge test was also carried out on the coils to diagnose failing or damaged insulation as an integral part of the comprehensive maintenance for machines. This testing is done to detect the burn out of machine as a result of phase to phase shorting. Scientifically, surge testing is done to discharging a capacitor of high voltage into coil. The outcomes are generally a pulse at lower frequencies.

If a rapidly increasing current is applied to a coil, a voltage will be generated across the coil by principle of induction. The voltage across the coil is given by

$$V = L\frac{d_i}{d_t} \tag{7.1}$$

where V is the terminal voltage across the coil, L is the coil's inductance and the rate of change of current pulse is $\frac{d_i}{d_t}$.

In this case the surge test was conducted on each coil with 1010 peak voltage and the overall status is passed.

Figure 8-13: SKF static motor analyser (Baker AWAIV-4kV).

8.9 Final Assembly

This section gives the final assembly of the machine without the case. Figure 8-14 shows an exploded view of unmounted machine assembly. The stator block which contain the coils and rotor block that carry the magnets are separately assemble and aligned in the lathe machine as shown in Figure 8-15.

The rotor is slowly inserted into the stator which is held in the jaws of a lathe and the rotor is held in a tailstock and gradually moved into the stator. The rotor finally aligns itself into the stator and the shaft fits in the two ends bearing and rotated to fit the screw holes in the stator main hub. Appendix K presented the CAD drawing for each part of the machine and final assembly.

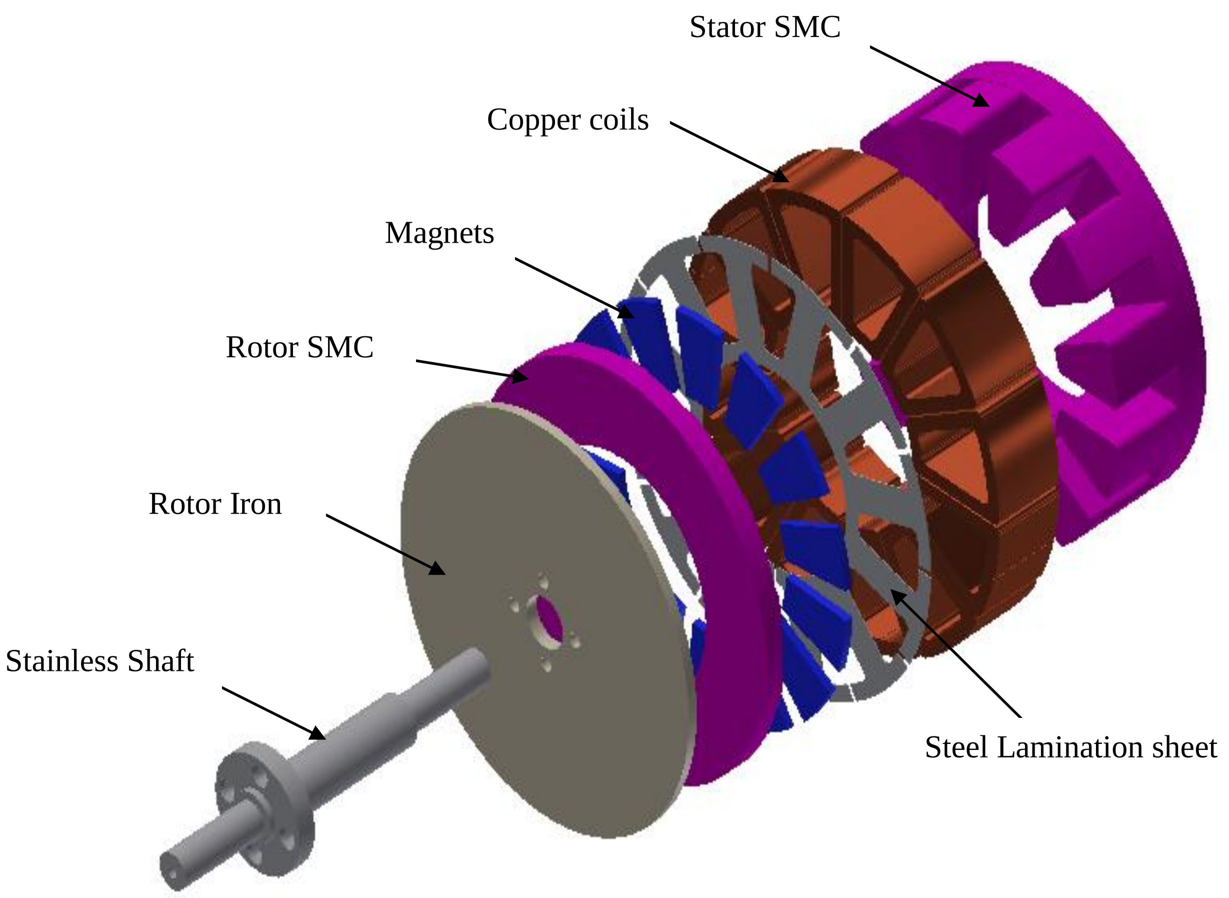

Figure 8-14: CAD version of machine assembly showing an exploded view of components

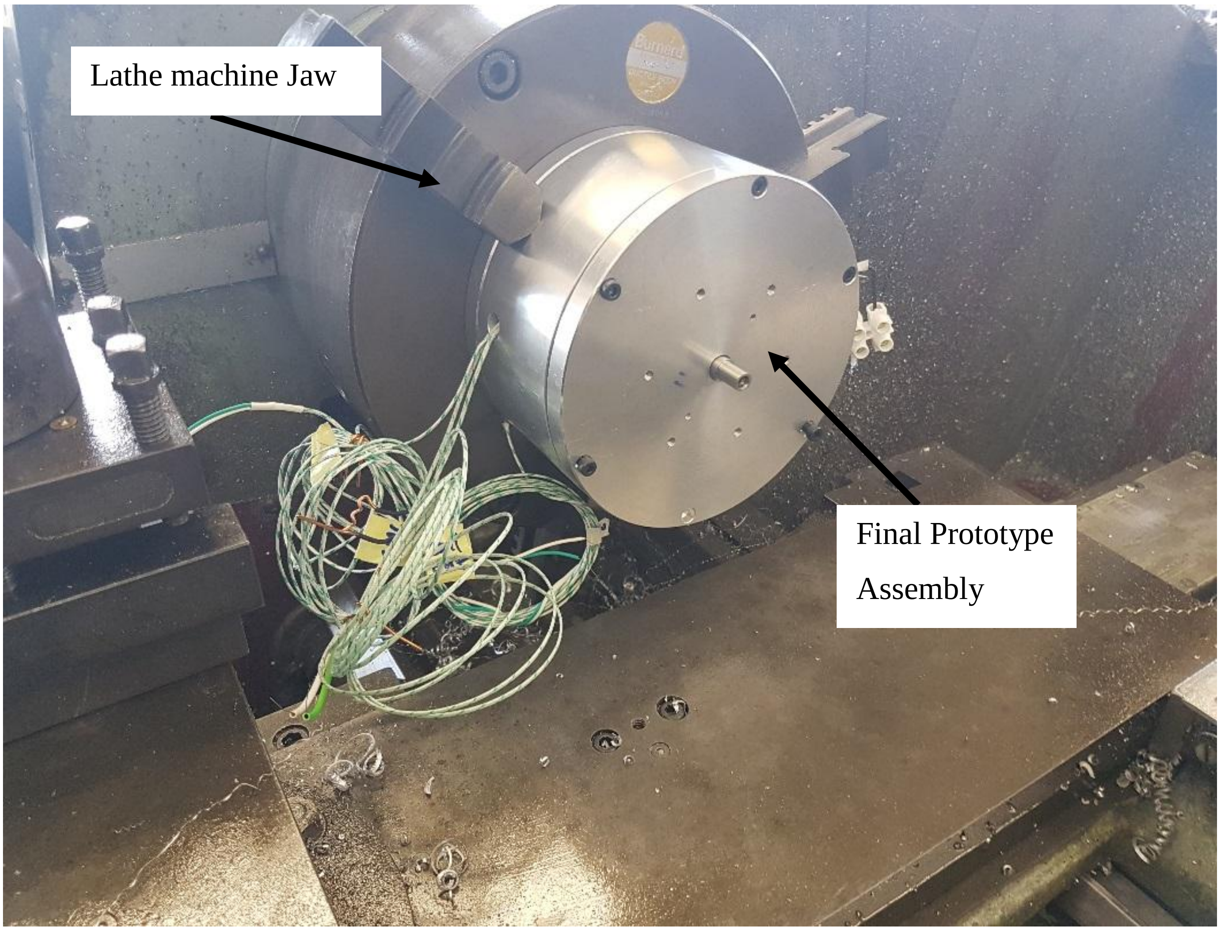

Figure 8-15: Final assembly of the prototype machine

8.10 Block Diagram of the Experimental Test Setup

Figure 8-16 presented the experimental tests measurement setup used in the laboratory. The torque and speed control drive are connected to the prototype machine via torque and speed transducer and the three-phase output of the machine is connected directly to a three-phase resistive load and power analyser. This is to minimise the loss in the cables during testing and to obtain all the reading at the terminal of the machine by displaying on the digital oscilloscope which is connected to the power analyser, however there is a link between the torque and speed transducer and the power analyser for reading the torque and speed at any particular point during the tests. Lastly, the temperature reading unit is connected directly to the coils of the machine.

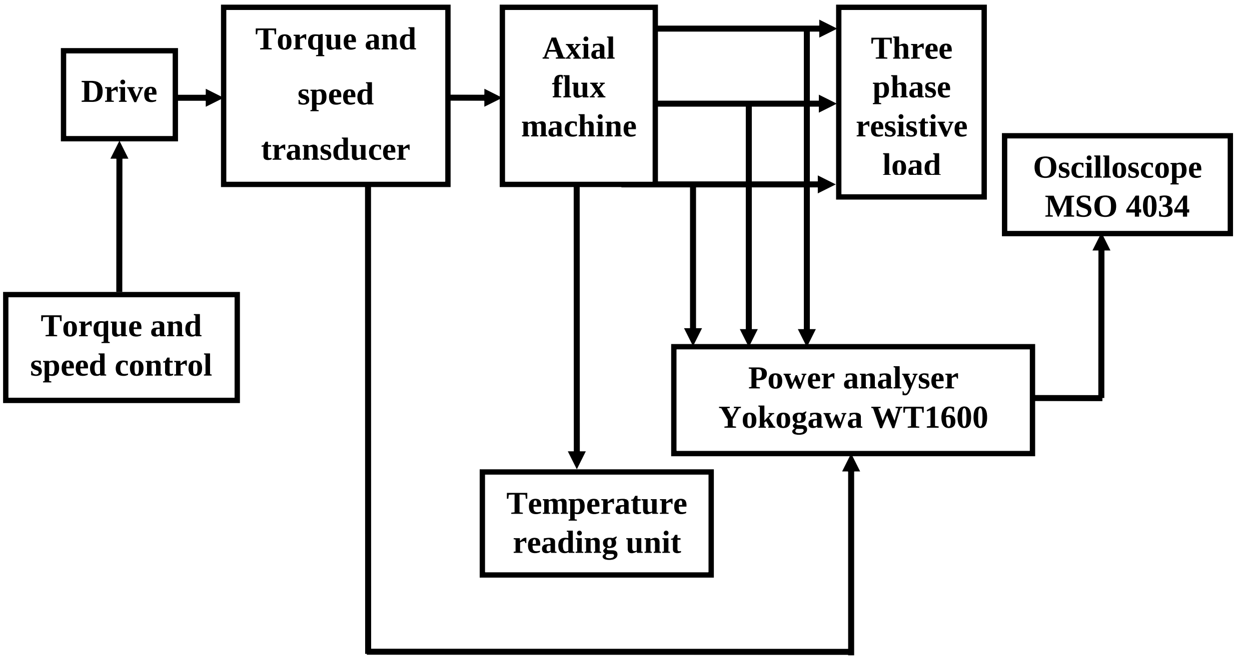

Figure 8-16: Block diagram of the experimental tests set up.

8.11 Conclusion

This chapter described the mechanical design, Mega Ohms and surge tests of coils, individual prototype component construction and assembly of the machine together with the block diagram of the equipment set up for the experimental tests.

Diverse levels of achievement were accomplished in the construction of the different parts of this prototype machine. The construction process of the stator block and rotor core-back using SMC Somaloy prototype material was found to be successful. The stator block was manufacture and machined as a single block, which avoid the difficulties involved in steel lamination stamped.

An ordinary process which could be used for mass production was utilised to manufacture the rotor stainless steel shaft using the lathe machine. The winding of the copper coils on a plastic bobbin and Nomax insulation paper were also successful, the process uses a former and the coils were slide onto stator teeth and a fill factor of 70% was achieved.

The magnets were simply fixed to the SMC rotor core-back using a Permabond ES562 heat cure however the steel lamination sheets were fixed on top of the coil with insulation paper in between using a mixture of the adhesive ES 562 and normal glue. The main problem encountered during the prototype assembly was fixing the steel lamination sheets for AC winding loss reduction.

The overall prototype manufacturing was simple and cost-effective and this chapter has shown that an AFM can be constructed using what are possibly to be mass production method.

9. Experimental Results

This chapter describes the testing of the AFM discussed in Chapters 4-8 and validating the idea of introducing a single steel lamination sheet for AC winding loss reduction due to open-slot stator winding construction. A range of measurements were taken using the high speed dynamic test rig under no-load and loaded conditions. This testing can be divided into; winding resistance, back EMF, on-load torque, output power, terminal voltage, total loss, AC winding loss, efficiency and temperature rise. Four different steel lamination sheets were used with segmented design for testing due to availability and commonly used and table 9-1 presented their description.

Table 9-1: Steel lamination sheet description.

Label	Description
L1	Machine without steel lamination sheet
L2	Machine with segmented M235-35A steel lamination sheet
L4	Machine with segmented M270-35A steel lamination sheet
L6	Machine with segmented M300-35A steel lamination sheet
L8	Machine with segmented N020 steel lamination sheet
L10	Machine with segmented M270-35A steel lamination sheet in which MMF adjusted to get the same torque as L1

One prototype machine was built and two different conductor diameters (1.4 mm and 3.2 mm) were used. The idea of using the two is that at operating frequency the skin depth is 3.03 mm, which is greater than 1.4 mm and less than 3.2 mm. The first measurements were carried out using the 1.4 mm conductor diameter, in which the coils were pre-wound on a plastic bobbin and slid onto the tooth. Moreover, for the second measurements the machine was disconnected and disassembled in the mechanical workshop by separating the stator block and the rotor disc containing the magnets. The plastic bobbin in which the coils were wound were removed using a lathe machine and the 3.2 mm conductor diameter wound on a thermal insulation material Nomax paper 304 mm x 200 mm x 0.13 mm were slid onto the stator tooth with insulation tape covering the coils. The machine was assembled again and mounted on the experimental tests rig for the second stage of experimental tests to be carried out.

9.1 Test Rig

The test rig is shown in Figure 9-1 and equipped with high precision instruments for accurate data reading as shown in Figure 9-2. The machine is connected to the dynamic drive via a torque transducer and the three phases of the machine are connected in star. The drive used was three phase control techniques with rated voltage of 400V and tolerance of ±10%.The maximum rated current is 25A with ambient temperature of less than 30˚C.

The test rig uses a drive motor (prime mover) to rotate the test machine at a precise speed. The torque measurement is with torque transducer TM HS 306/111 with rated torque of 5 Nm and maximum speed of 50000 rpm. The power signals are acquired using the high precise digital power meter WT1600 Yokogawa, with power accuracy of ±0.02% and high precise Tektronix digital oscilloscope DPO 3014.

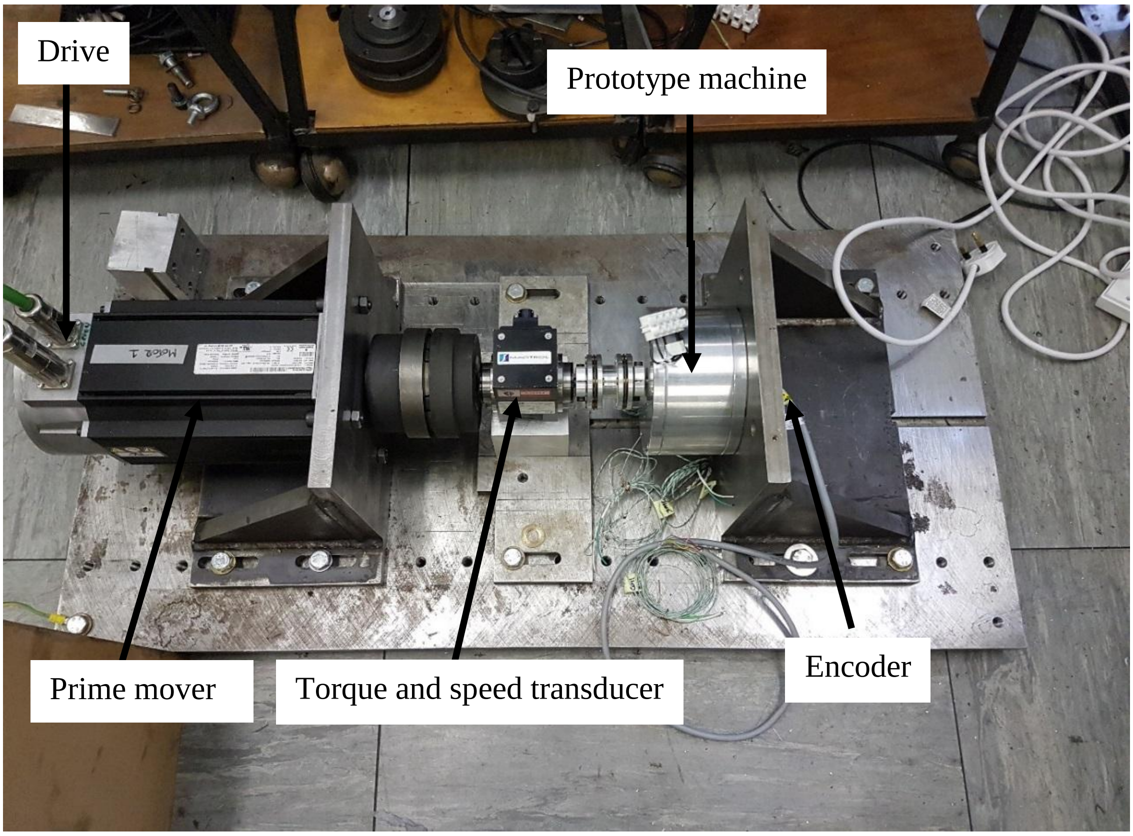

Figure 9-1: Dynamic test rig

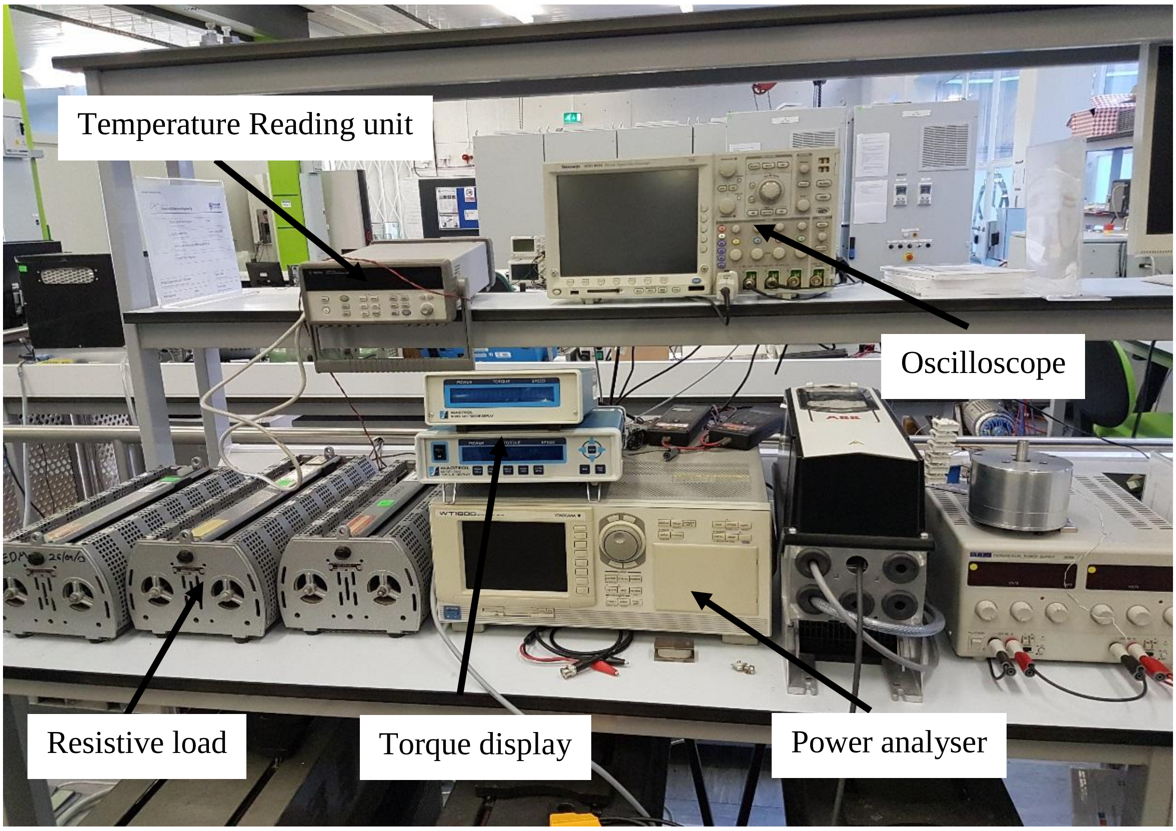

Figure 9-2: Equipment set up

9.2 Winding Resistance

The phase winding resistance was measured using two different methods to evaluate the quality of joints after soldering. The first method was using RLC meter to measure the resistance directly across the terminal of each phase of the machine. While in the second method, a constant DC current was passed through a phase and the voltage measured as close as possible to the machine terminals.

Table 9-2 compared the calculated and measured winding resistance. The measured resistance of 1.4 mm conductor diameter increased by 1.7% and 3.4% for method 1 and method 2 respectively as compare to calculated resistance, while for the 3.2 mm conductor diameter an increment of 0.002 Ω for method 2. This may be as a result of additional resistance of the soldered joints and winding the coil on a separate plastic bobbin and insulation paper with extra length before sliding onto the tooth manually.

Table 9-2: **Measured phase resistance verses projected phase resistance**

Phase resistance (Ω)	Calculated	Measured method 1	Measured method 2	% change
1.4 mm wire	0.1789	0.1820	0.1849	1.6%
3.2 mm wire	0.0066	0.0066	0.0086	3.0%

9.3 Back EMF Measurement and Harmonic Analysis

This section will present the Back EMF measurement of the prototype machine to verify the performance of the magnets and the stator magnetic circuit. In this case, the machine is tested under no-load condition. Both the digital oscilloscope and power analyser are connected directly to the terminals of the machine to avoid voltage drop via the power analyser.

9.3.1 Prototype Machine with 1.4 mm Conductor Diameter

The back EMF was measured at open circuit, with the electrical load disconnected. The actual three phase voltage waveform is sinusoidal in shape as shown in Figure 9-3 and are captured using the oscilloscope described above, with all harmonic distortion of less than 0.5% of the fundamental. Appendix J presented the screenshot from the oscilloscope of the measured back EMF. These tests were performed to verify the 3D FEA prediction presented in Chapter 4. The results showed agreement giving confidence in the use of the prototype machine to carry out AC winding loss with conductor diameter greater than skin depth at the operating frequency.

It is clear from Figure 9-3 that the three phase voltage waveforms are equally distributed and are separated by 120˚electrical; this shows that the phases of the machine are balanced. The experiment was performed at different speeds stepping up to the full load speed and measurements were taken and recorded.

The measured peak back EMF in all the three phase of the prototype machine was 114V and the 3D FEA peak back EMF was 113.4V. There is an increment of 0.5% between the 3D FEA and the measured which may be as a result of slight decrease in the airgap due to final mechanical assembly of the component of the prototype machine.

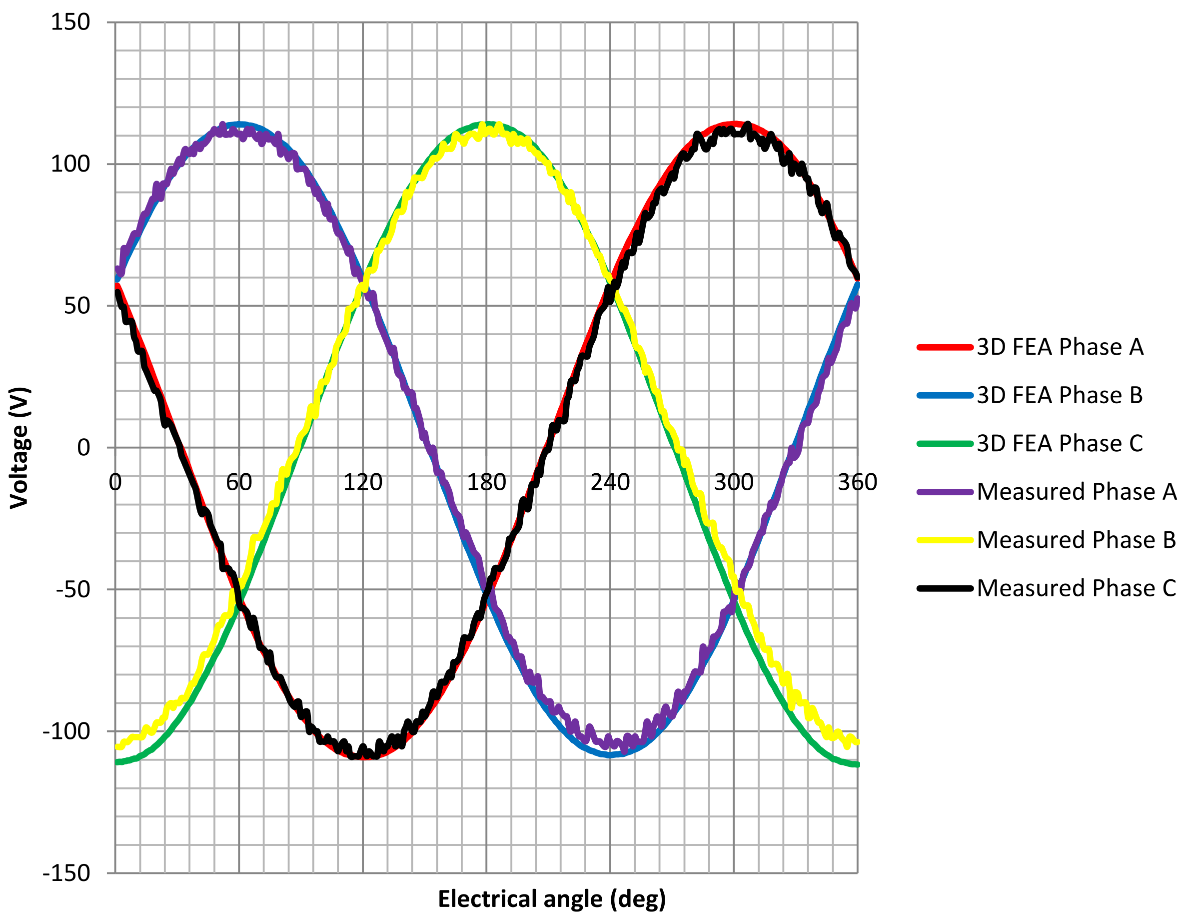

Figure 9-3: Measured back EMF for 1.4 mm conductor diameter at 700Hz.

The back EMF test was carried out three times to confirm the accuracy of the measurement and Figure 9-4 presents the back EMF harmonic analysis. The slot and pole number combination and rounded tooth has minimised most of the harmonics present in the baseline machine reported in Chapter 3.

The significant harmonics besides the fundamental harmonic are the third, fifth, seventh, ninth and eleventh harmonic, with almost all the remaining harmonics are less than 0.5% of the fundamental harmonic and the fundamental measured harmonic is 114V as shown in the spectrum.

The measured third, fifth, seven, ninth and eleventh harmonic are 86.5%, 75%, 66.7%, 87.6% and 87.7% lower than the 3D FEA harmonic. This shows that there is a reduction of 66.7% to 87.7% in these harmonics between the measured and 3D FEA.

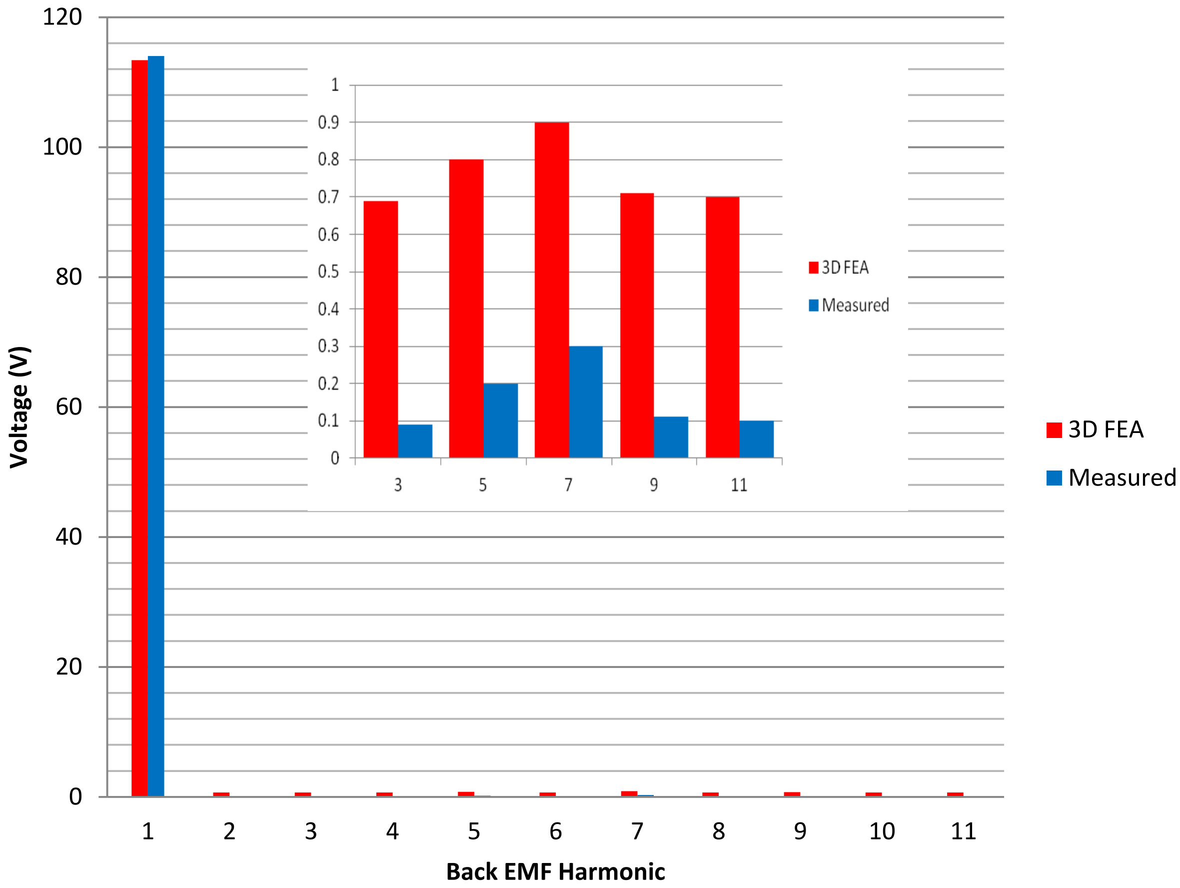

Figure 9-4: Harmonics of the back EMF with 1.4 mm conductor diameter.

However, this reduces the cogging torque of the machine by 55.6%. The measured back EMF is 0.5% higher than the projected 3D FEA. These differences in the magnitude are most likely being the errors in machining and assembly of the final prototype machine components which leads to a slight decreased in the airgap of less than 2%.

The shape of waveforms of the measured back EMF is similar when compare with the projected 3D FEA. The back EMF recorded at different speed has a linear relationship as shown in Figure 9-5. The gradient of the graph shows that an open circuit back EMF of 19V per phase per 1000 rpm.

This also proved that the back EMF of an electrical machine is proportional to the speed and increasing the speed of the machine leads to an increment in the back EMF. Likewise, decreasing the machine speed would results in reduction of the peak value of back EMF.

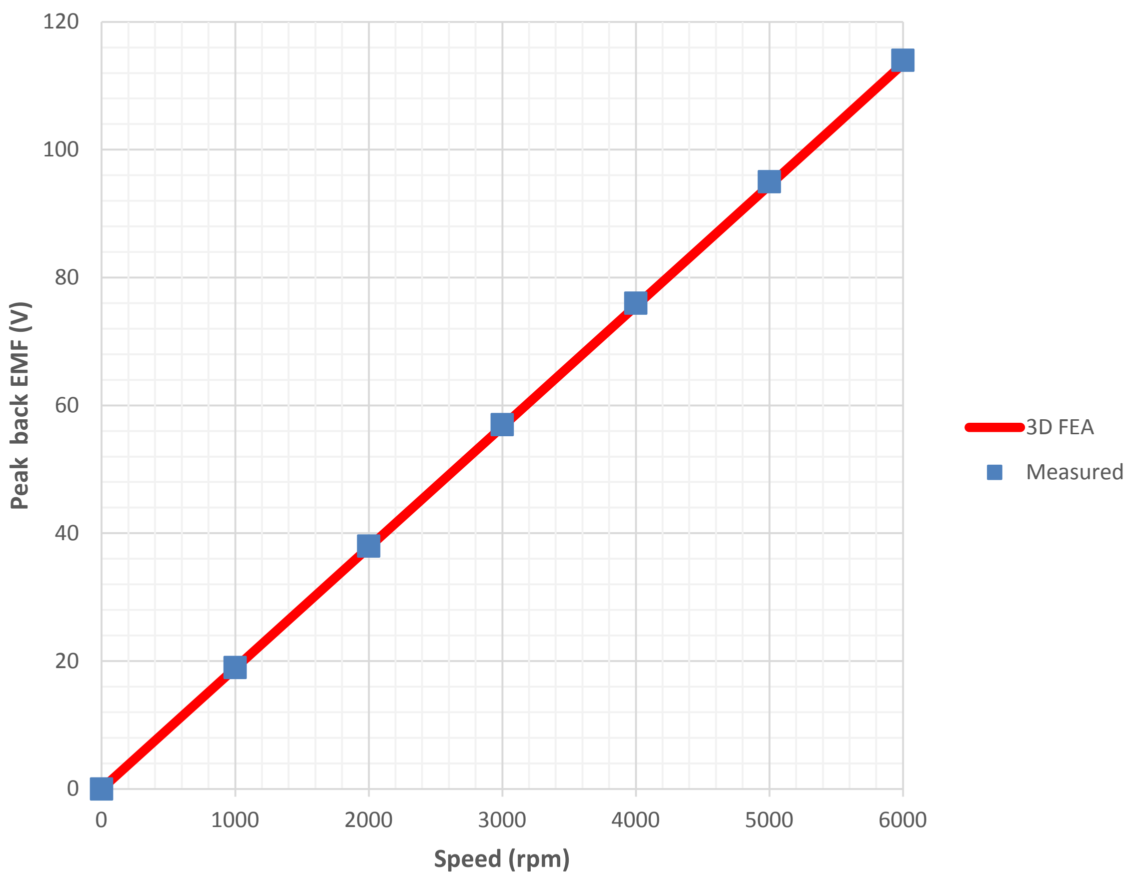

Figure 9-5: Measured and projected peak EMF.

9.3.2 Prototype Machine with 3.2 mm Conductor Diameter

It was observed from the 3D FEA that increasing the size of conductor diameter decreases the number of turns in the machine. This section presented the back EMF measurements for 3.2 mm conductor diameter as shown in Figure 9-6. The phase voltages are sinusoidal in shape with harmonic distortion of less than 1% of the fundamental harmonic. The reason for that is the slot and poles number combination of 12 slot and 14 pole number, these percentage reductions in the harmonics are big enough to reduce the machine vibrations and give a very smooth overall performance.

The decrease in the peak value of voltage per phase is as a result of the decrease in the number of turns in machine slot due to an increase in the conductor diameter. This reduction on the number of turns commensurate the cost of 80.1% reduction in the induced back EMF in the machine as well as increasing the electrical loading in the slot.

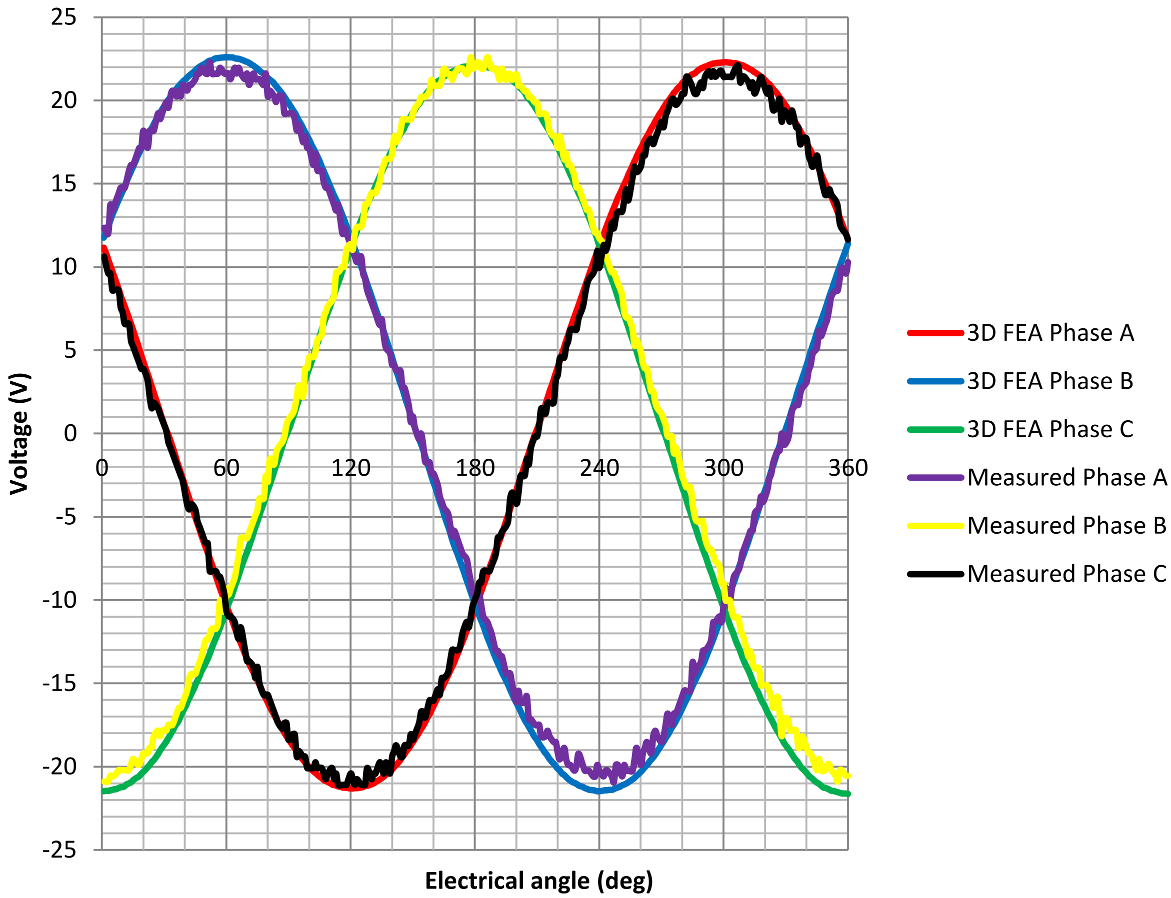

Figure 9-6: Measured back EMF for 3.2 mm conductor diameter at 700Hz.

The idea of using a bigger conductor is to carry out the AC winding loss analysis and measurements and for winding the coil on a former before manual insertion onto the tooth in addition to see the effect of open-slot stator winding construction. In the previous section 9.3.1 and at operating frequency, the conductor diameter is less than the skin depth and the effect of AC winding loss was not included. This leads to the choice of conductor diameter greater than the skin depth to ascertain the skin effect.

Figure 9-7 presents the comparison of the harmonic analysis of 3D FEA and measured back EMF. The analysis shows that the third harmonic is most significant and the measured third harmonic is 11% lower than the 3D FEA, similarly the measured fifth, seventh, ninth and eleventh harmonics are 36%, 12%, 33% and 37% lower than the 3D FEA harmonics respectively.

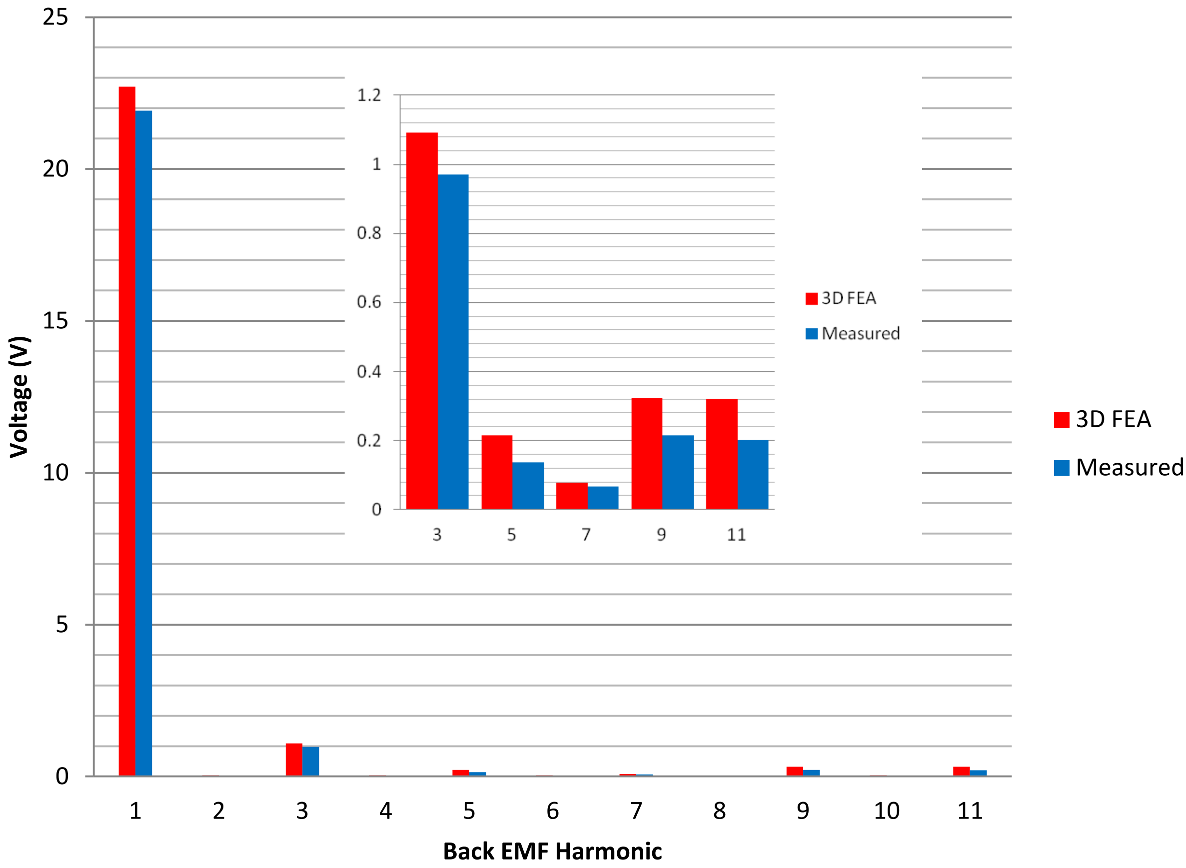

Figure 9-7: Harmonics of the back EMF with 3.2 mm conductor diameter.

9.3.3 Back EMF and Harmonic Analysis with Steel Lamination Sheet

A set of tests similar to those performed in section 9.3.2 on prototype machine with 3.2 mm conductor diameter were repeated. But in this case a single steel lamination sheet is placed on top of the stator block to cover both the coils and end windings as shown in Figure 8-12.

The main idea of doing that is to minimize AC winding loss by using shielding effect. The experimental measurements were conducted using load current and for each experiment we varied the load resistors to get the maximum power require and this is what we mean by load current.

Figure 9-8 compares the phase peak induced back EMF for the 3.2 mm conductor diameter with a single steel lamination sheet for AC winding loss reduction. In this case only the segmented designs were compared, since the non-segmented designs were discarded due to extra losses on lamination sheets. The back EMF was measured at operating point of 700Hz.

It shows that, peak back EMF reduces by 5.5%, 1.0%, 3.5% and 2.5% for L2, L4, L6 and L8 respectively as compared to L1. Similarly, it reduces by 3.4% for L10 as compared to L1; in this case we deliberately increase the MMF which in turns increases the torque to be the same as L1 in order to demonstrate the AC winding loss reduction technique.

Moreover, in these measurements the back EMF waveform are similar to those in section 9.3.2 above and thicker as compared to that in L1, this is as a result of saturation and flux shielding on the surface of steel lamination sheet.

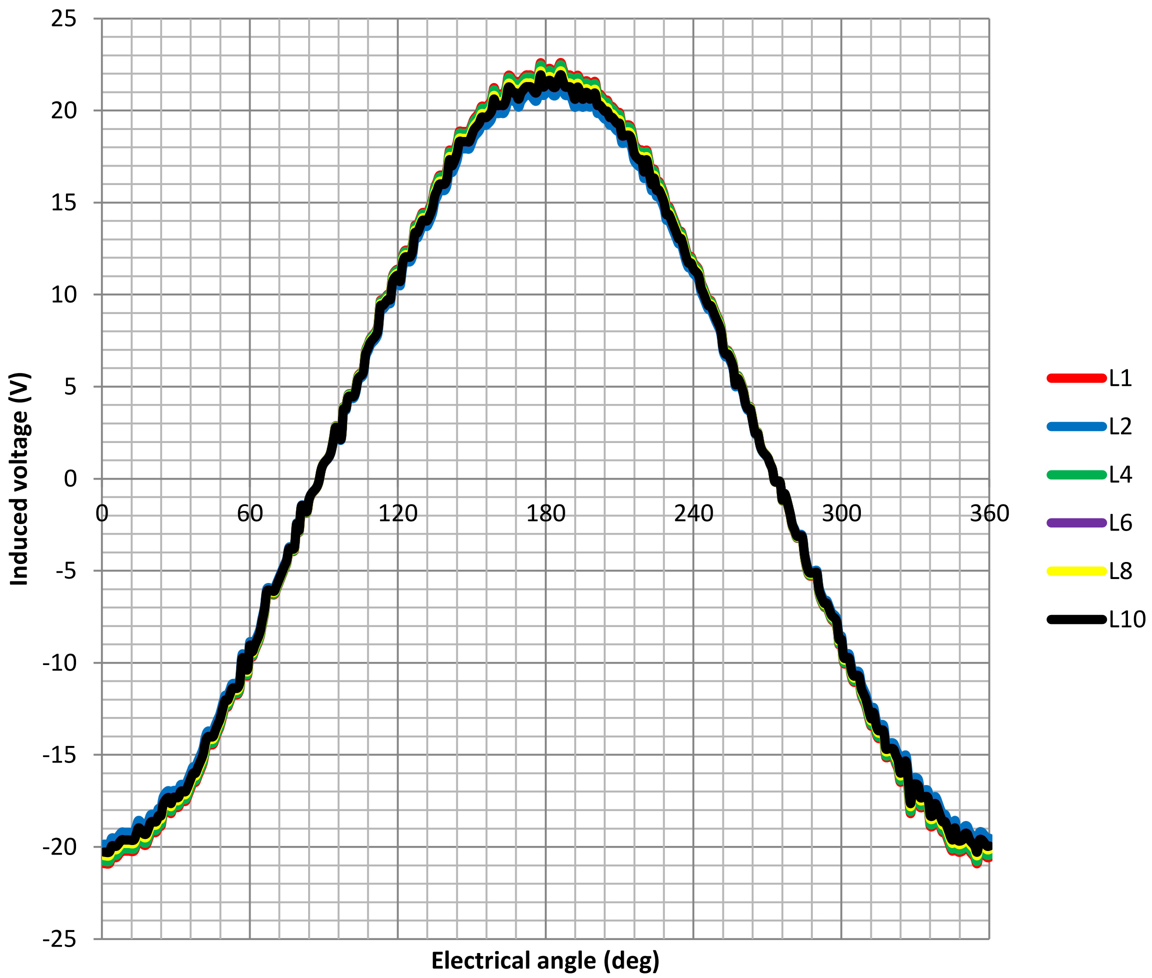

Figure 9-8: Measured back EMF with Lamination sheets at 700Hz.

The peak back EMF of all the prototype machines tested and 3D FEA without and with a single steel lamination sheet are summarized in Figure 9-9. They are all presented as per unit of the 3D FEA L1 machine. It is clear that L2 produced the lowest measured back EMF, a 7% decrease while the highest measured back EMF is produced by L4, an increment of 2.3% compared to L1.

A broad observation can be made from the analysis that putting the a single steel lamination sheet on top of coils affect the induced back EMF and these depends on the material conductivity and thickness.

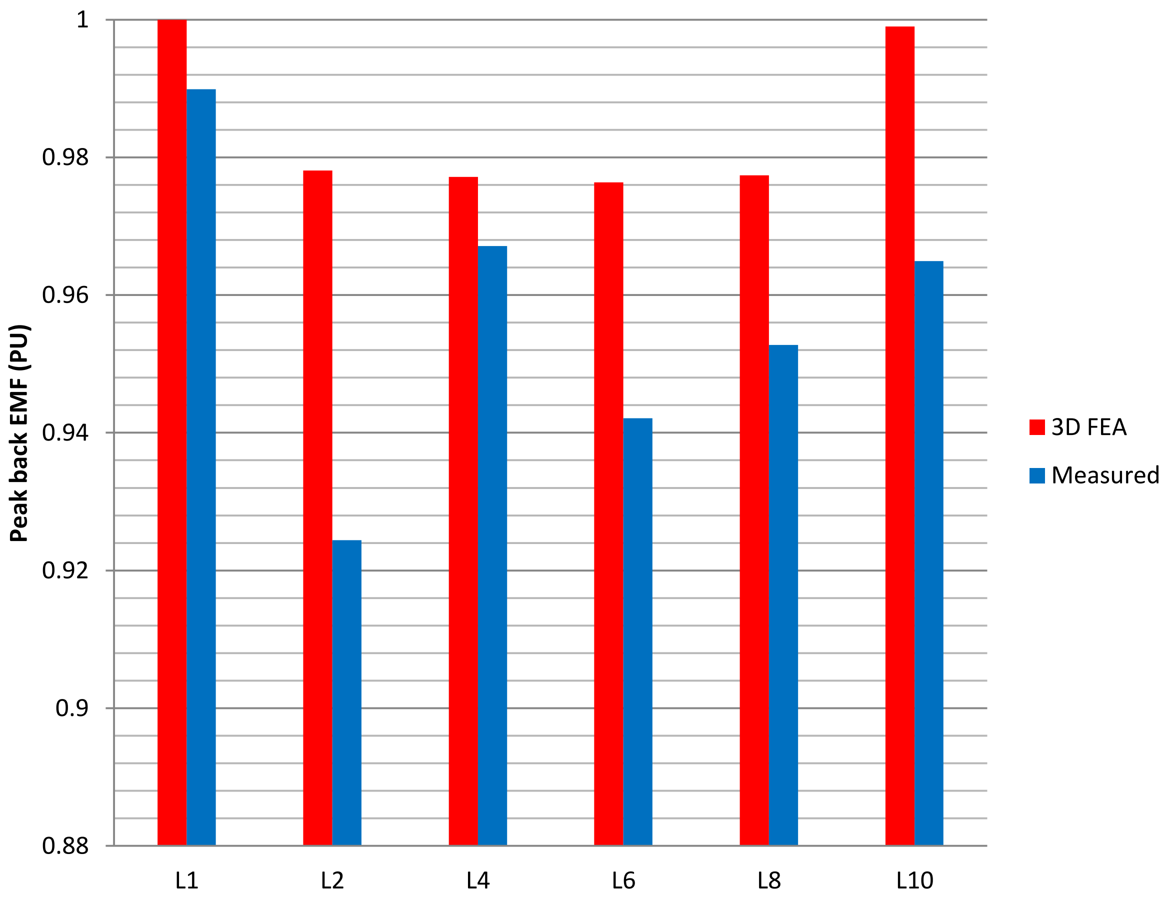

Figure 9-9: Peak back EMF with and without steel lamination sheet comparison at 700Hz.

Figure 9-10 presented the harmonic analysis of the back EMF of the machine with a single steel lamination sheets and the result shows that the only considerable harmonic besides the fundamental is the third harmonic.

The third harmonic of L1, L2, L4, L6, L8 and L10 drop by 95.2%, 95.6%, 95.7%, 95.5%, 97.5% and 95.6% when compared with the fundamental harmonic respectively and all others harmonic are less than 0.5% of the fundamental harmonic.

It is also clear from the analysis that, introduction of a single steel lamination sheet on top of the AFM coils for AC winding loss reduction using shielding effect has minimised the fifth, seventh, ninth and eleventh harmonics to approximately less than 0.5% of the fundamental harmonic of the prototype machine as shown in Figure 9-10.

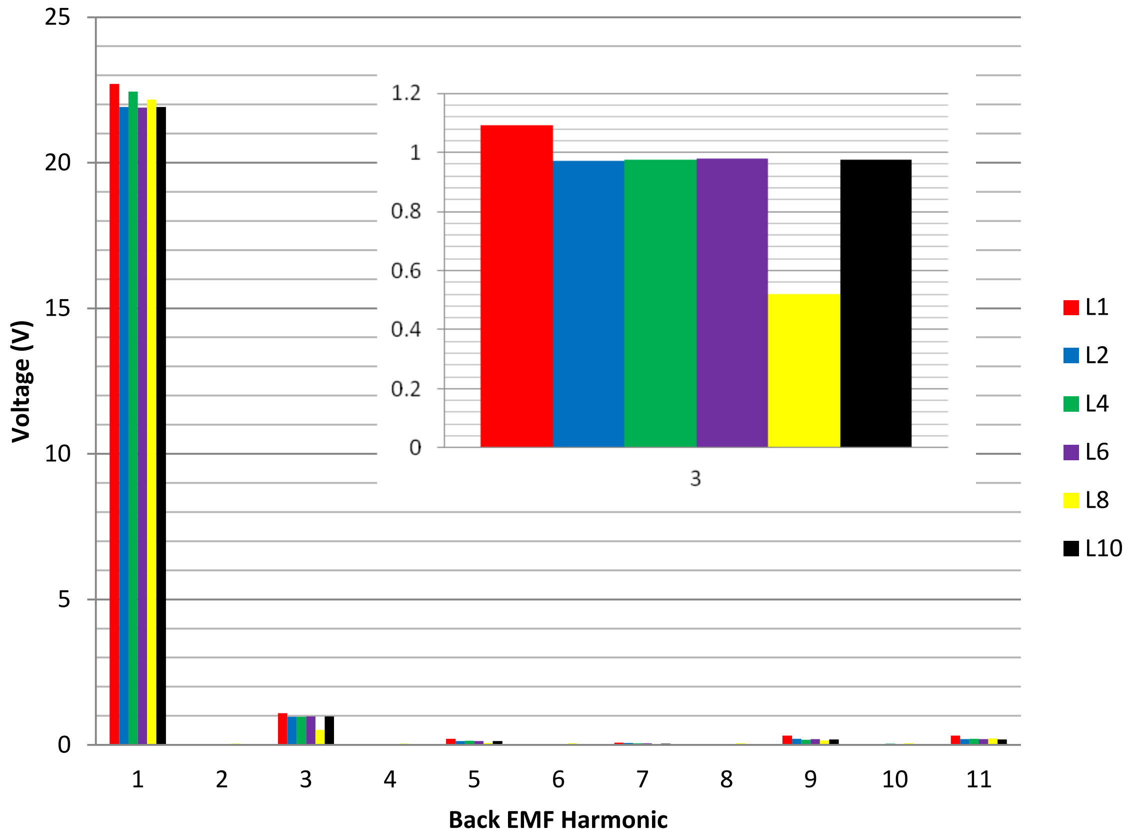

Figure 9-10: Harmonics of the back EMF with and without steel lamination sheet.

9.4 On-Load Torque

The on-load torque of the prototype machine on tests was measured at operating frequency of 700 Hz. Three phase resistive loads were connected to the prototype machine terminal and the resistance was adjusted to attain the maximum current in the circuit and maximum power, this is what is also called load current.

During the testing there was no noticeable temperature rise on the machine case. Readings were taking at step of 1A to the full load current. Figure 9-11 gives the comparison of the 3D FEA and measured average torque against the applied rms current of the machine at operating point of 700 Hz with 1.4 mm conductor diameter and without steel lamination sheet.

It can be seen that the average torque of the machine rises as the applied rms current is increased, at current less than 4A the relationship of the of graph is approximately linear, but as the current exceed 4A the graph behave as non-linear.

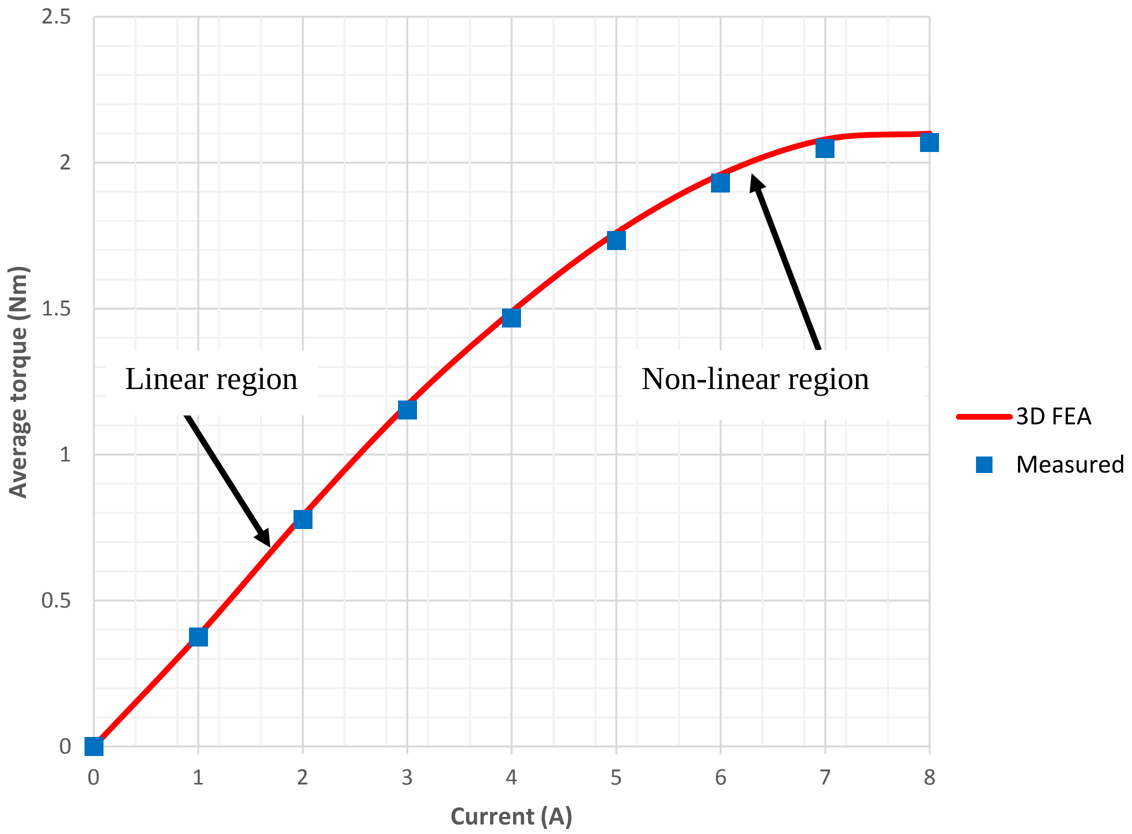

Figure 9-11: Measured average torque variation with rms current.

Figure 9-12 compared the on-load torque of the machine without and with steel lamination sheet. The results from the 3D FEA allowed cogging torque to be subtracted from the total torque of the prototype machine; the remaining torque is the net torque of the machine due to the current excitation only. But, in the case of measured torque, the net torque is the combination of both excitation and non-excitation of current due to the facts that measurements are not necessarily taken in the same position.

The measured on-load torque was found to be 2.08 Nm for L1 which reduce by 5.3%, 5.8%, 5.8% and 2.4% for L2, L4, L6 and L8 respectively. Similarly, for L10 the electrical current was gradually increased to obtain the same torque as L1. During the process, the casing temperature is normal but after the required torque was attained, it was noticed the casing temperature began to rise and the experiment was stopped to avoid damage to the coils of the prototype machine.

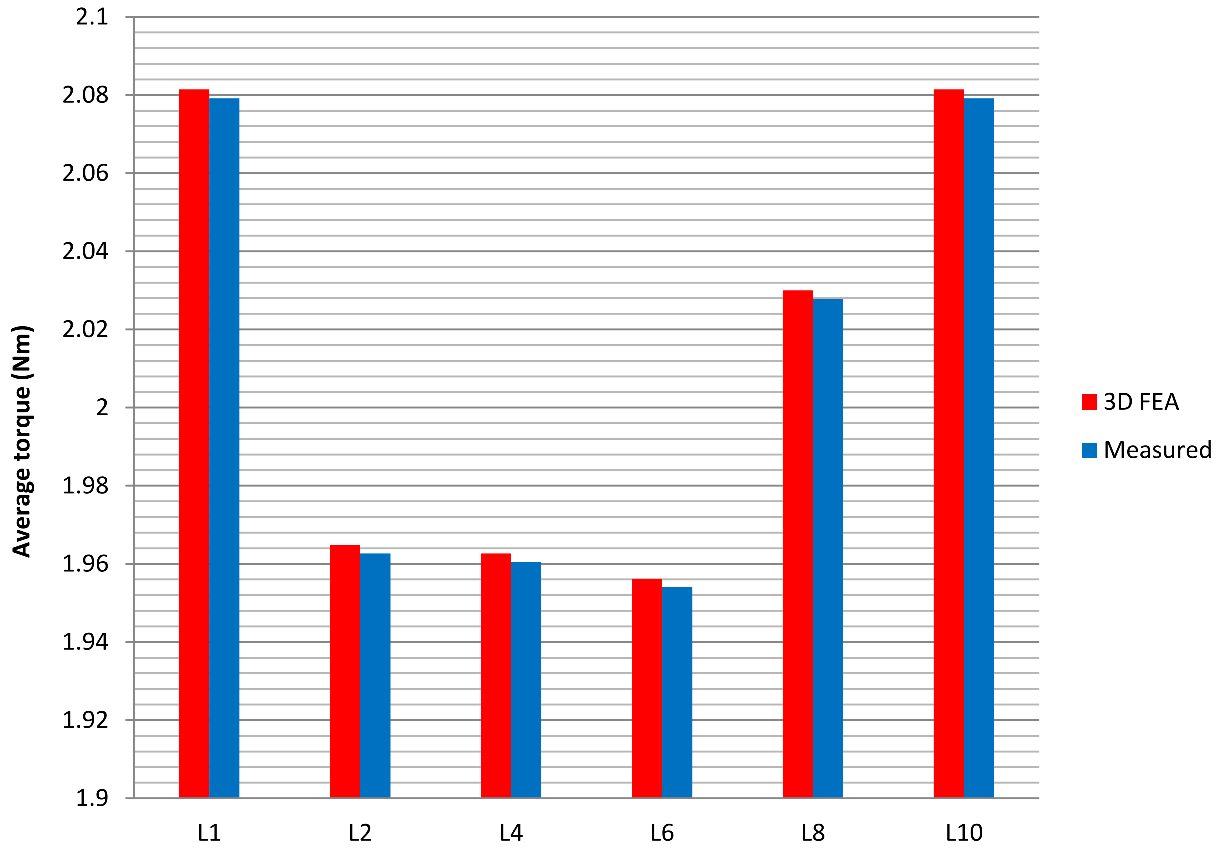

Figure 9-12: On-Load torque comparison at 700Hz.

9.5 Output Power and Terminal Voltage Measurements

This section presents the performance measurement (power and terminal voltage of the prototype machine). The experimental set up is the same as the previous and all tests were carried out at operating point of 700Hz.

The resistance of the three phase resistive loads connected to the prototype machine terminal were adjusted to get the maximum current and maximum power; this is what is also called load current. Moreover, this also dictates the electrical output power, while the mechanical input power is kept constant.

From the phasor diagram in Figure 4-33, assuming unity power factor, the performance of a machine with resistive load for any defined current can be determined using Pythagoras theorem. For a three-phase machine the terminal power is given by equation (9.1).

$$P_{out} = 3IV \tag{9.1}$$

where '3' in equation (9.1) account for the three phase of the machine and the applied mechanical power which is held constant is given by equation (9.2).

$$P_{in} = T\omega \qquad (9.2)$$

Similarly, the terminal voltage can be obtained from equation (9.1), for the design without steel lamination sheet; the input power is given as in equation (9.3).

$$P_{in} = 1319.64\ W \qquad (9.3)$$

Figure 9-13 compared the projected 3D FEA and measured terminal voltage of prototype machine with 1.4 mm conductor diameter wire. The terminal voltage is maximum when the current is zero and is equal to the back EMF, as the current is increasing the terminal voltage of the machine decreases due to the resistance of the coils and that of the resistive load. The measured terminal voltage is 0.99% less than the projected voltage at open circuit (zero current). However, at full load current it is 1% less than the projected value.

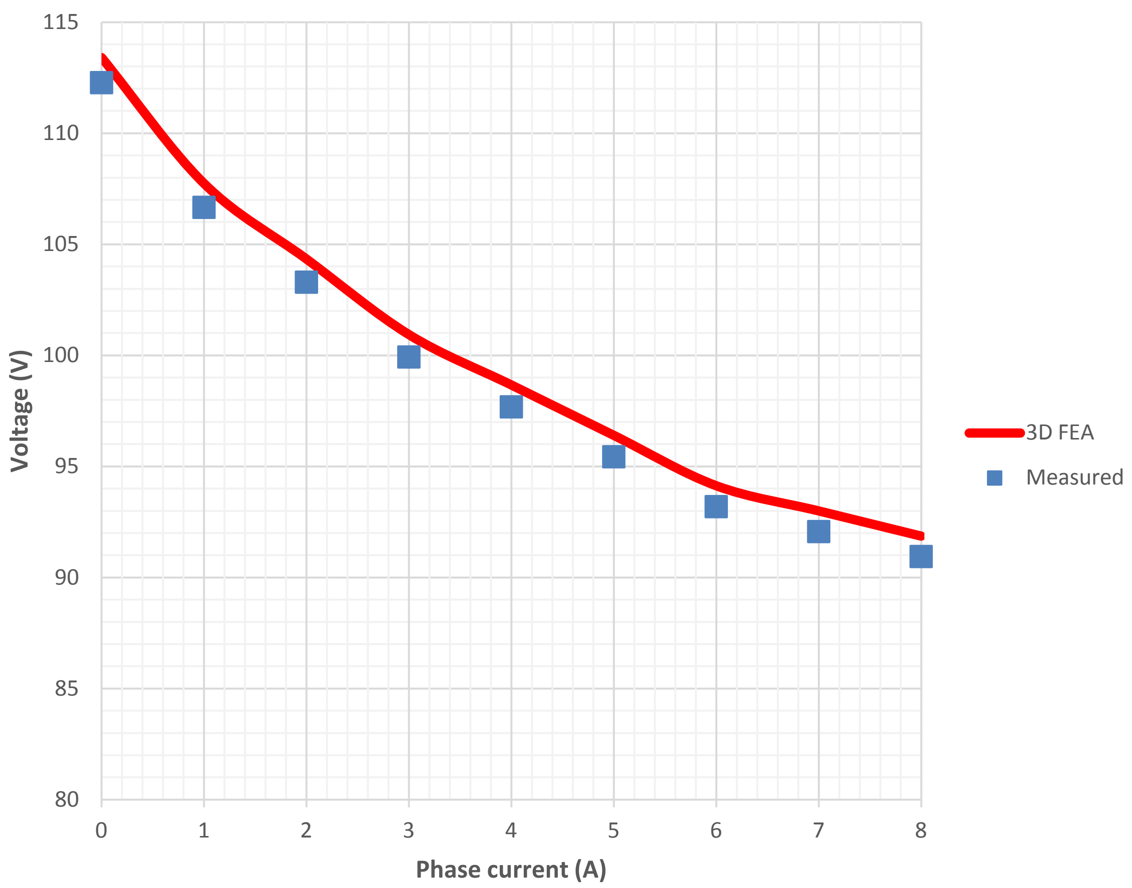

Figure 9-13: Terminal voltage for 1.4 mm conductor diameter.

Figure 9-14 presented the comparison of the output power against the phase current for the same machine with 1.4 mm conductor diameter wire. It is clear from the graph that the output power of the machine increases as the current is increases up to the maximum value of current.

The measured output power of the prototype machine is zero when the phase current is zero. However, as the three phase resistive loads were varied, current started to flow and the maximum current were attained when the value of load resistance is low. The value of the measured output power at full load current is 2.8% less than the projected value. This is due to the fact that projected 3D FEA does not include windage and bearing losses.

Moreover, the output power variation with current from 1A to 4A is uniform. But, as the current increases above 4A the variation is not uniform (non-linear) this may be as a result of changes in the speed and the slot leakage inductance of the machine.

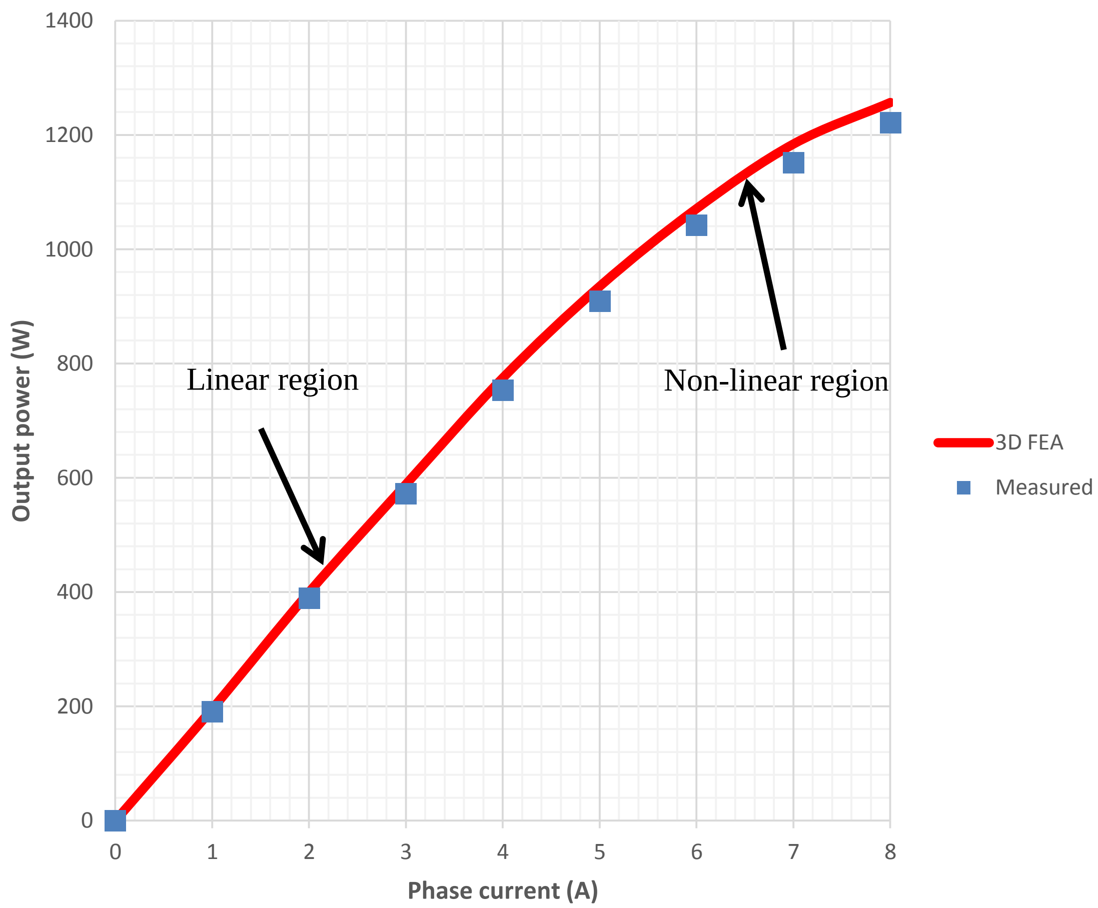

Figure 9-14: Output power verses phase current.

Figure 9-15 compared the projected 3D FEA and measured output power of the prototype machine with 3.2 mm conductor diameter, for L1 and designs with segmented steel lamination sheet for AC winding loss reduction in the machine.

In this case the output power was measured at full load current for L1 and recorded. Furthermore, the same measurement procedure was repeated for each steel lamination sheet and the output powers were recorded. For L2 the measured power is 2.8% less than the 3D FEA power. Moreover, it is 2.8% less than the 3D FEA for L4 and L6.

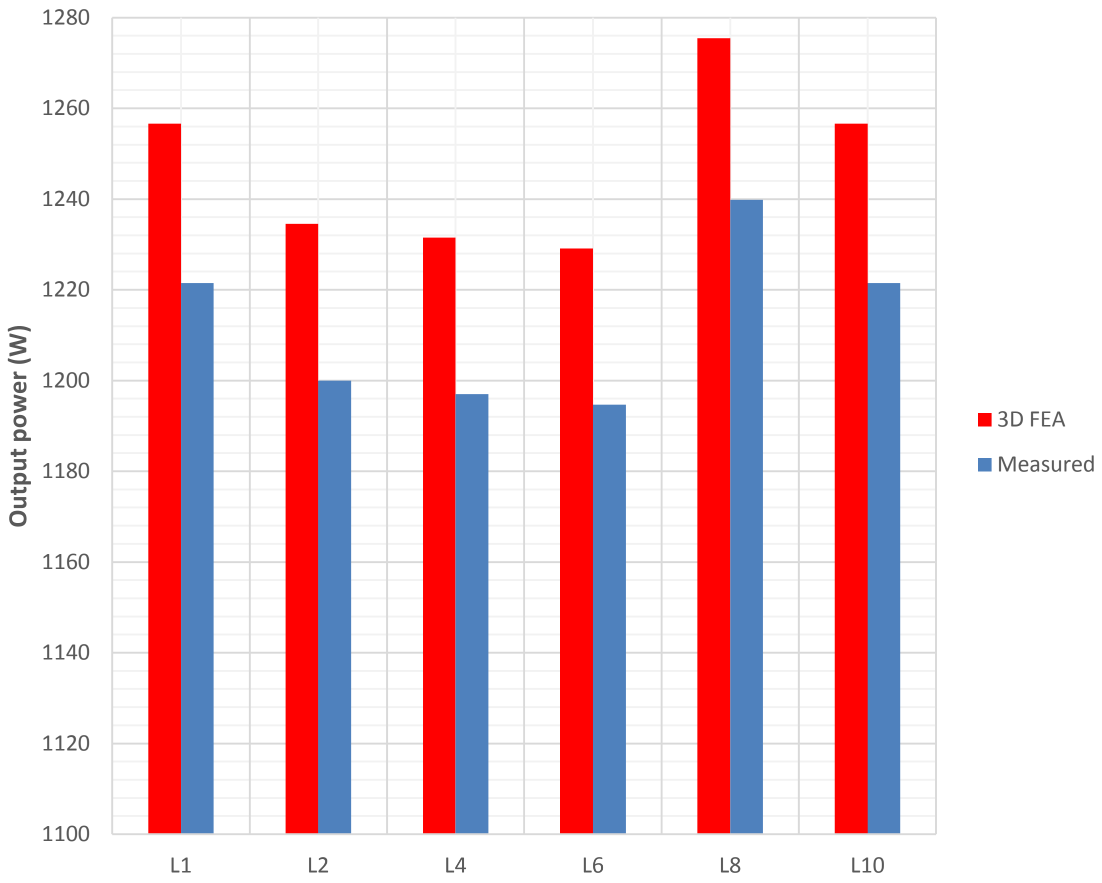

Figure 9-15: Output power comparison at 700Hz.

9.6 Total Loss Measurements

The main aim behind designing the machine were not only to increase the torque and minimized the harmonic content in the back EMF, but also to improve the overall machine performance. This can be done through reducing the total loss of the machine by keeping the AC winding loss as low as possible. The total loss in the machine was measured. This includes the no-load loss and on-load loss.

The no-load losses are usually generated whenever a machine is running at open circuit; the losses comprise of the following losses:

1. The stator and rotor hysteresis loss.
2. The copper (skin and proximity) and magnet eddy current loss.
3. Friction and windage loss.

In some machines, the winding losses may be part of the no-load loss and are in fact the proximity loss in the conductors. But in this case the loss can be ignored, with the introduction of a single steel lamination sheet as a slot and end winding wedge the no-load winding loss reaching the coils is expected to decrease due to flux diversion on the surface of steel lamination sheet.

Figure 9-16 shows the no-load comparison of projected 3D FEA and measured loss. From the bar chart it is clear that the measured no-load loss in all the prototype machines are higher to 3D FEA, in addition to that the measured no-load loss and 3D FEA loss have similar correlation. At operating point of 700 Hz the measured no-load loss increased by approximately 14.2% for all the designs when compared to 3D FEA.

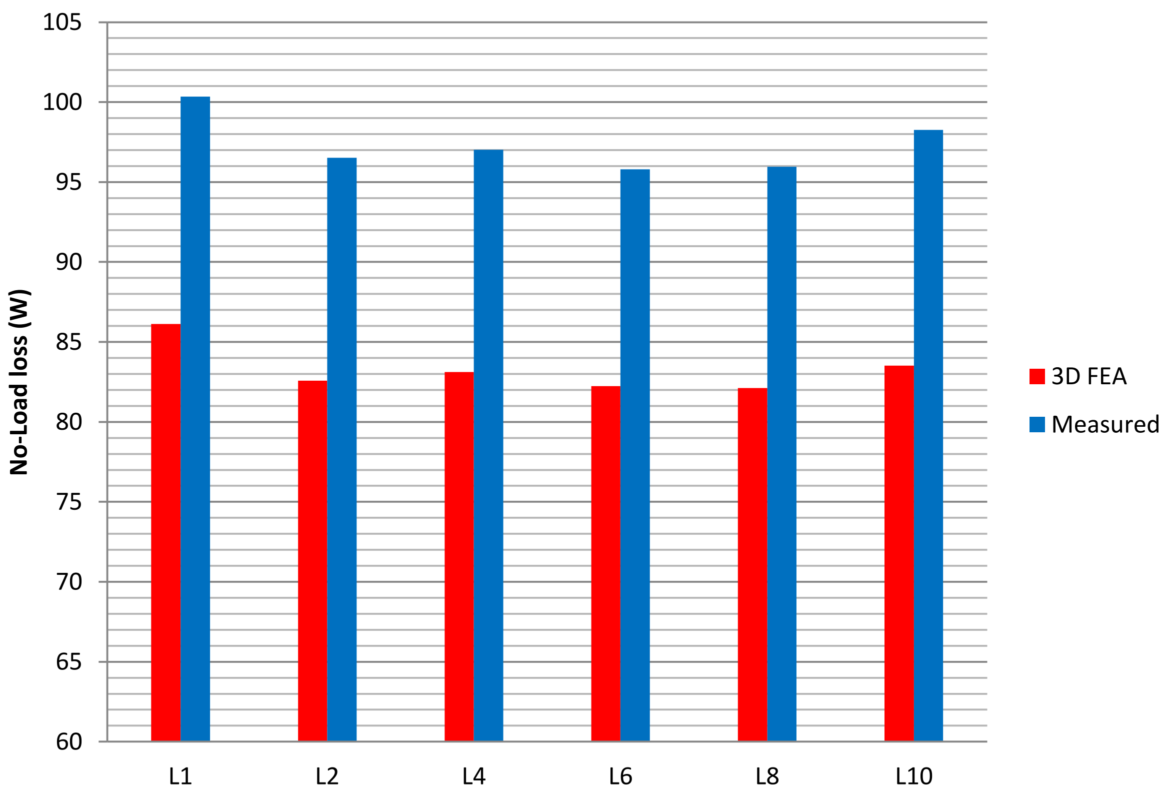

Figure 9-16: No-Load Loss at 700Hz.

The on-load loss of a machine comprises of the following losses:

1. No-load losses.
2. Joule loss.
3. AC winding loss.

In this case, a resistive load is connected to the three-phase terminal of the prototype machine to enable current flow when the machine is driven as a generator as it is done in section 9.5 above. Moreover, the applied mechanical power is given by equation (9.2) and (9.3) above, while the output power is given by equation (9.1) above.

This implies that the total loss in the machine for 1.4 mm conductor diameter can be obtained by equation (9.4).

$$P_{in} = P_{out} + total\ loss \tag{9.4}$$

For 3.2 mm conductor diameter the effect of AC winding loss was taken into consideration and the measured total loss of the machine at 700Hz is given by equation (9.5).

$$Total\ loss = 313.52\ W \tag{9.5}$$

Also, from the 3D FEA the total DC loss is obtained as shown in equation (9.6).

$$Total\ DC\ loss = 98.18\ W \tag{9.6}$$

Therefore, the total loss of the machine with different steel lamination sheet were also measured and found that L1 increased by 3% when compared with the 3D FEA and L8, produces the highest total loss. L2 decreased by 23.9% compared to L1. Similarly, L4 and L6 increase by 27.1% and 31.7% respectively as compared to L1, and L10 increase by 23.7%.

A small conclusion can be derived from the above analysis that L6 seem to reduce the total loss more by 31.7% as a result of higher loss/kg on the steel lamination sheet as shown in Figure 9-17. It is clear from the bar chart that, there is close correlation between the 3D FEA loss and measured loss for the entire different steel lamination sheet used, and that get up to 3% difference at the operating point of 700 Hz. This may be as a result of accuracy deficit in the part of FE model in projecting the losses in a machine.

This increase in the measured total loss of the machine has led to a decrease in the output power as presented in Figure 9-15. It is clear in Figure 9-17 that magnetic materials (single steel lamination sheet) can be implemented to control the airgap magnetic flux in a machine to minimize AC winding loss. Moreover, it was found that L6 with single steel lamination sheet M300-35A has the overall better performance as compared to L1, L2, L4, L8 and L10.

It is clear from the above analysis that the measured total loss in the entire prototype machines tested was higher than the 3D FEA total loss this is due to the fact that 3D FEA total loss does not take into account the windage and bearing losses.

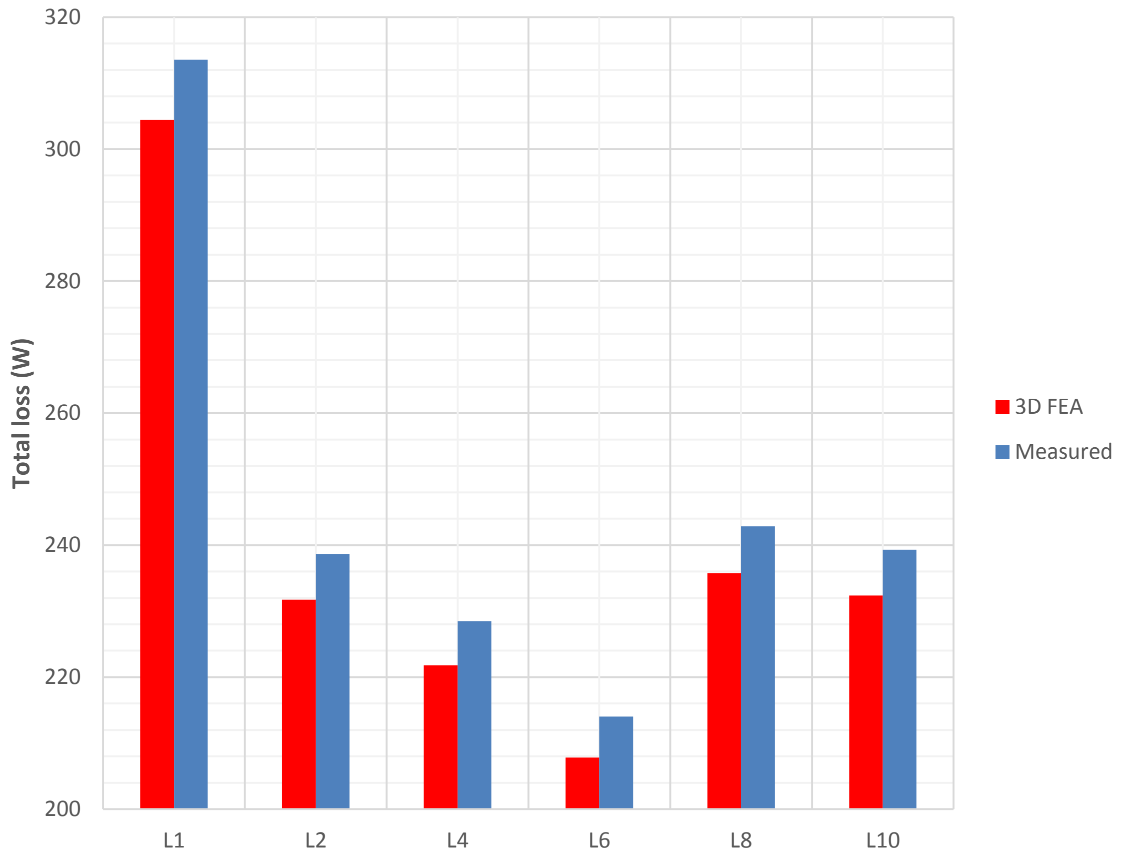

Figure 9-17: 3D FEA and Measured total loss comparison at 700Hz.

9.7 AC Winding Loss for 3.2 mm Conductor Diameter

The measured total loss comprises both the AC winding loss and the iron loss. 3D FEA was carried out and iron loss has been found. As stated in [24], the total AC winding loss of machine is obtained from the total measured loss by subtracting the FEA DC iron loss as expressed by equation (9.7).

$$AC\ winding\ loss = Total\ loss - Total\ DC\ loss \qquad (9.7)$$

Figure 9-18 shows the comparison of the 3D FEA and measured AC winding loss of the machine without and with different steel lamination sheet for 3.2 mm conductor diameter. This also shows the maximum AC winding loss produced by each design of the prototype machine.

L2 produces the highest AC winding loss; a 40.1% decrease compared to L1 and L6 produces the lowest AC winding loss a 48.0% decrease as compared to L1. It can be seen from Figure 9-18 that L6 with the lowest AC winding loss and total loss as presented above achieved best performance as compared to others designs with single steel lamination sheet.

This is because of the higher loss/kg on the steel lamination sheet and the isotropic and thermal properties of SMC, and the ability to produce the 3D flux paths that are ideal for this machine topology.

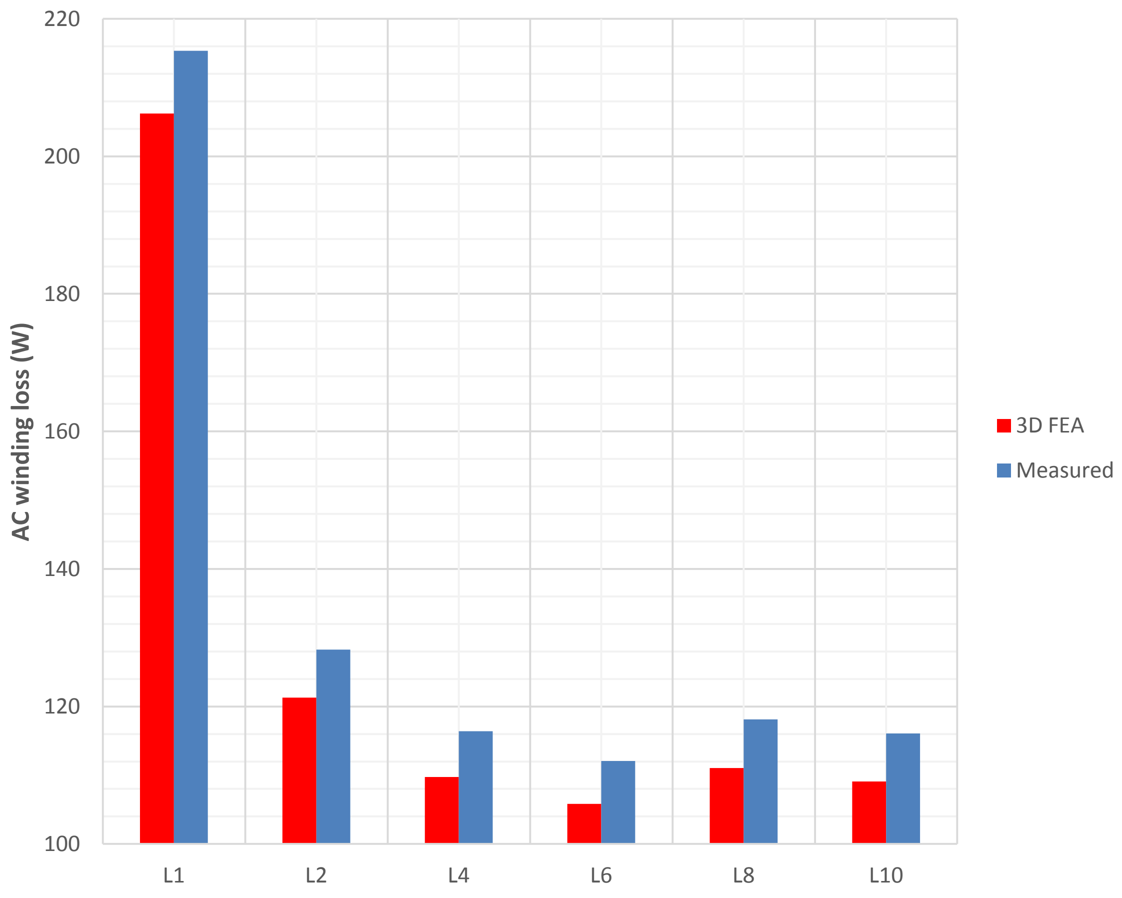

Figure 9-18: AC winding loss comparison at 700Hz.

9.8 Efficiency of the Machine

This section presents the efficiency analysis of the prototype machine; attention would be given to all sources of loss in the machine. The efficiency of a machine can be obtained based on the previous measurement of total loss and derived power of machine carried out at the operating point of 700Hz.

A good cost-effective machine design must take advantages of the inherent performance properties of the material used in the design and construction. In this case soft magnetic composite was utilised together with a single steel lamination sheet for AC winding loss reduction.

The efficiency of a machine is inversely proportional to the total power losses. These losses have been categorised in the previous section 9.6 and 9.7 above.

The electrical efficiency of the machine can be measured using the relationship in equation (9.8).

$$\eta_{measured} = \frac{P_{out}}{P_{in}} \times 100 \qquad (9.8)$$

Figure 9-19 presents the efficiency variation with speed for L1 machine; in this case AC winding loss was take into consideration, while Figure 9-20 compared the 3D FEA and measured efficiency of the machine for different design without and with steel lamination sheet. It is clear from Figure 9-19 that the efficiency keeps changing before 2000 rpm and almost constant for the remaining speed.

The efficiency of L1 with AC winding loss included decreases by 2.4% as compared to 3D FEA value. However, the efficiency for L2, L4, L6, L8 and L10 were found to be 89.1%, 88.9%, 89.6%, 88.4% and 81.8% respectively.

The result shows that the highest loss reduction occurs with L6 due to higher conductivity in that steel lamination sheet, moreover the more power loss on the steel lamination sheet the less total AC winding loss in the machine and better overall performance. The smaller the thickness of the steel lamination sheet used the smaller the power loss per kg on it and result in the efficiency of the machine to be lower, similarly the larger the thickness of a single lamination sheet slot wedge the bigger the loss/kg in the lamination sheet and the better the efficiency of the machine.

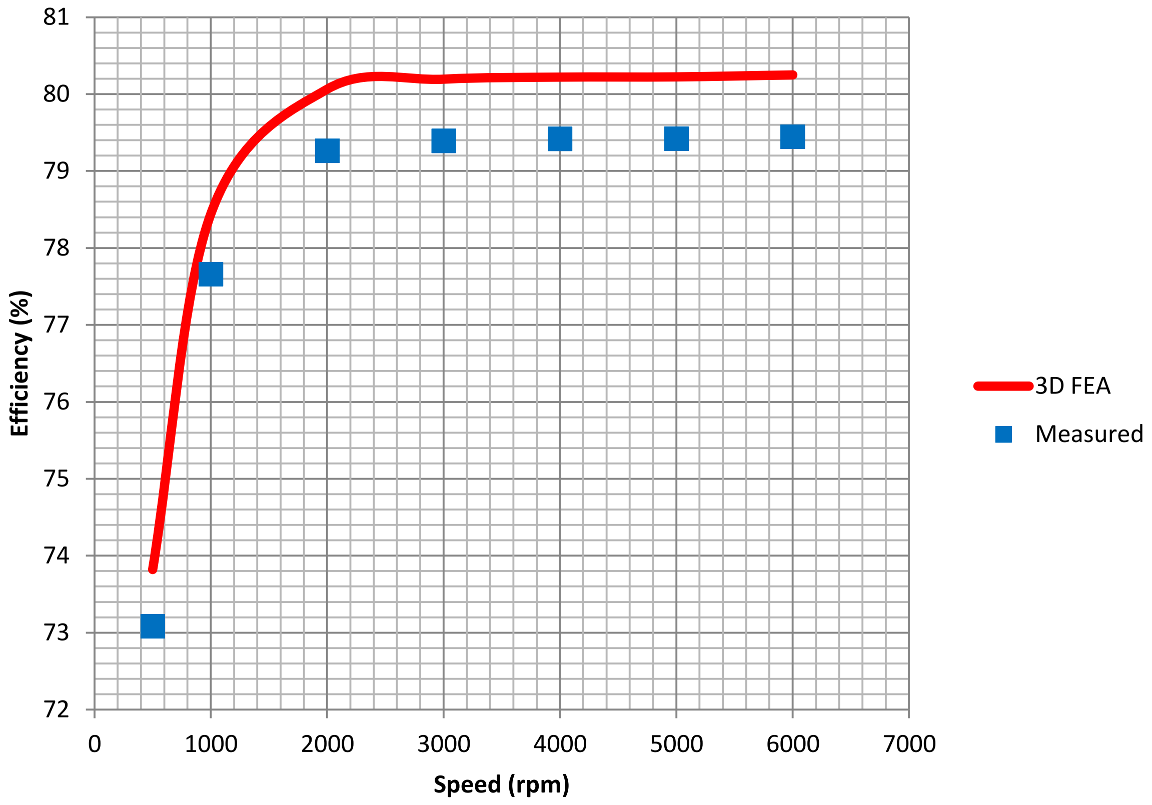

Figure 9-19: Efficiency variation of L1 with speed.

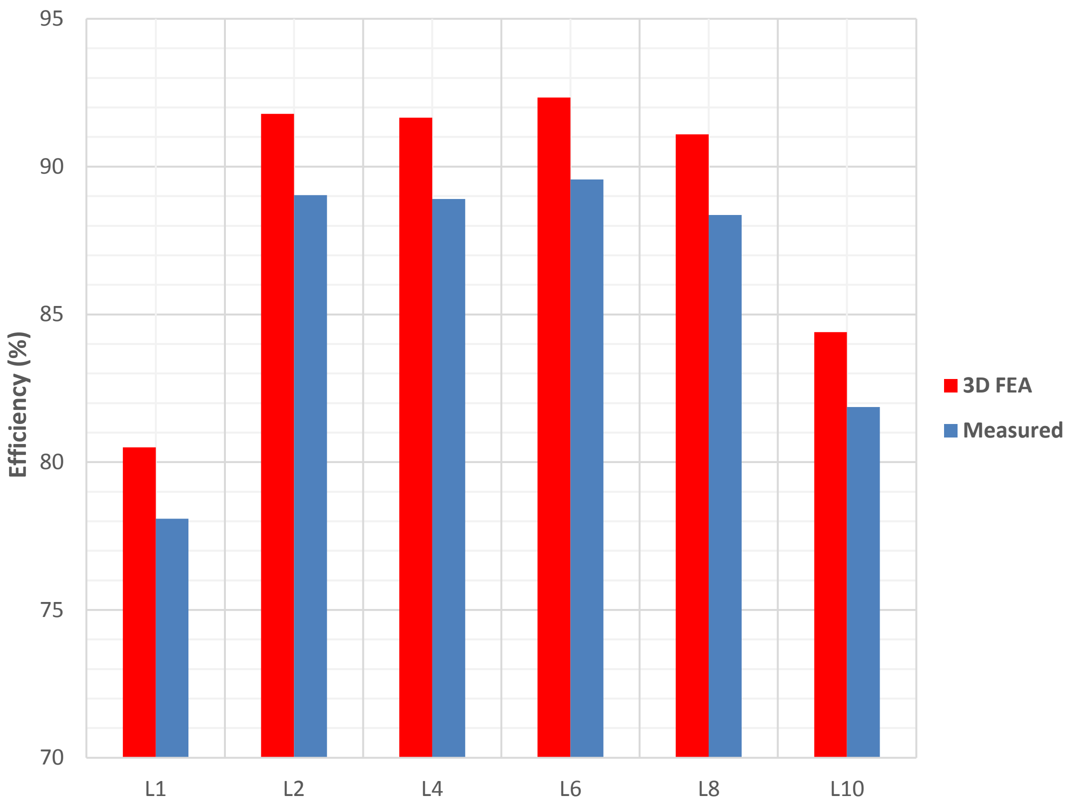

Figure 9-20: Efficiency comparison for 3D FEA and measured at 700Hz.

Figure 9-21 presents the percentage comparison of different parameters at operating point of 700 Hz with respect to L1.The parameters are back EMF, on-load torque, output power, no-load loss, on-load loss, AC winding loss and efficiency. It can be seen from the bar chart that using a single steel lamination sheet with conductivity on it have effect on those parameters in some cases their value drop greatly while others increase.

The peak back EMF of L2, L4, L6, L8 and L10 reduced by 2.2%, 2.3%, 2.4%, 2.3% and 0.1% respectively as compared to L1. On-load torque drops by 5.6% for L2, 5.7% for L4, 6.0% for L6 and 2.5% for L8. Similarly the output power reduces by 1.8% for L2, 2.0% for L4, 2.2% for L6, but increased by 1.5% for L8. The no-load loss decreases by 4.1%, 3.5%, 4.5%, 4.7% and 3.0% for L2, L4, L6, L8 and L10. The on-load loss reduces by 23.8%, 28.4%, 31.1%, 22.6 and 22.1% for L2, L4, L6, L8 and L10 respectively.

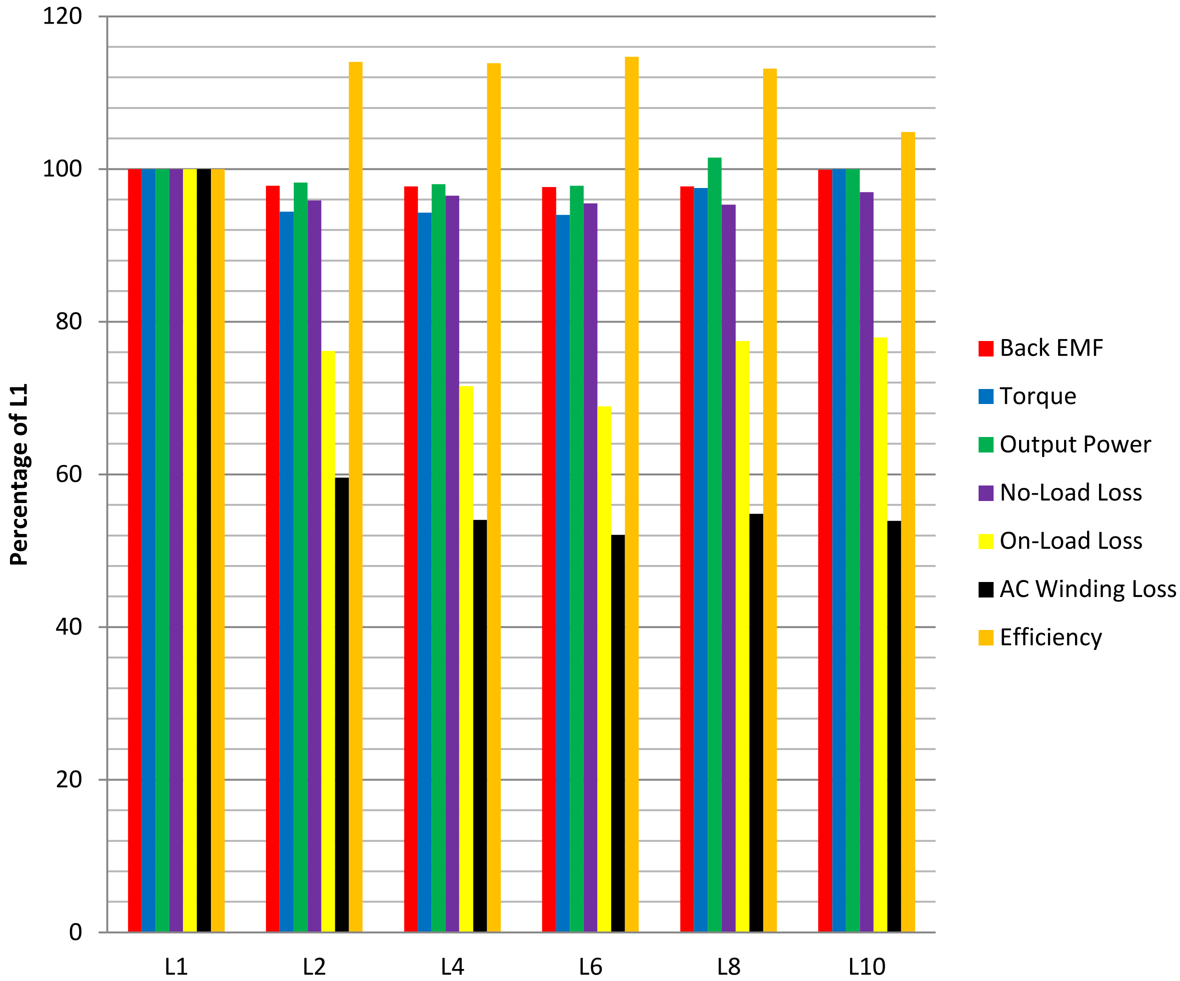

Figure 9-21: Percentage comparison of different parameters at 700Hz.

All segmented design tested also depict a very low AC winding loss, L6 produced the highest AC winding loss reduction of 48.0% and L2 produced the lowest reduction of 40.4% as compared to L1. These greatly drop in AC winding loss improve the overall performance of prototype machines. It is clear from bar chart in Figure 9-21 that L6 produced the highest efficiency, an increase of 14.7% as compared to L1 and the efficiency of L2 increase by 14.0%, L4 by 13.9% and L8 by 13.2%. L10 has the lowest efficiency of 4.8% when compared to L1.

From all the tests and analysis above, it is clear that L6 with a single steel lamination sheet M300-35A presents the best overall performance compared to others.

9.9 Temperature Rise in Coils

To obtain an economic utilization of the materials and safe operation of an electrical machine, it is necessary to predict with reasonable accuracy the temperature rise of the internal parts, especially the coils and magnets. The steady state temperature of the machine was obtained giving the typical behaviour of the winding with air as natural cooler and Figure 9-22 presented the temperature rise in the prototype machine loaded coils.

The temperature rise in the machine was monitored using thermocouple K type located in the winding, since from the FEA simulation the rise in temperature with 1.4 mm conductor diameter is approximately 53˚C and that of 3.2 mm conductor diameters is approximately 49˚C.

To get the temperature rise in the winding, a DC current of 10A was applied to a phase of the machine for 5000 seconds. The winding temperature rise was monitored at 30 second intervals and the peak rise in temperatures are plotted as shown in Figure 9-22 for the two different windings, the 1.4 mm conductor diameter and 3.2 mm conductor diameter.

It is shown from the graph that the temperature is constant from 0-200 seconds, after that the temperature starts to rise gradually until almost 2500 seconds and 2600 seconds for 1.4 mm and 3.2 mm conductor diameter respectively. Then the temperature rises stabilised and become constant for the remaining duration.

The maximum measured rise in temperature is 52.6˚C and 48.8˚C for 1.4 mm and 3.2 mm conductor diameters respectively. The measured temperature rises in the machine with 1.4 mm conductor diameter decreased by 0.4˚C as compared to 3D FEA. Similarly, the temperature rises reduced by 0.2˚C for the machine with 3.2 mm conductor diameter. Moreover, during experiment testing no noticeable temperature rise was felt on the outer case.

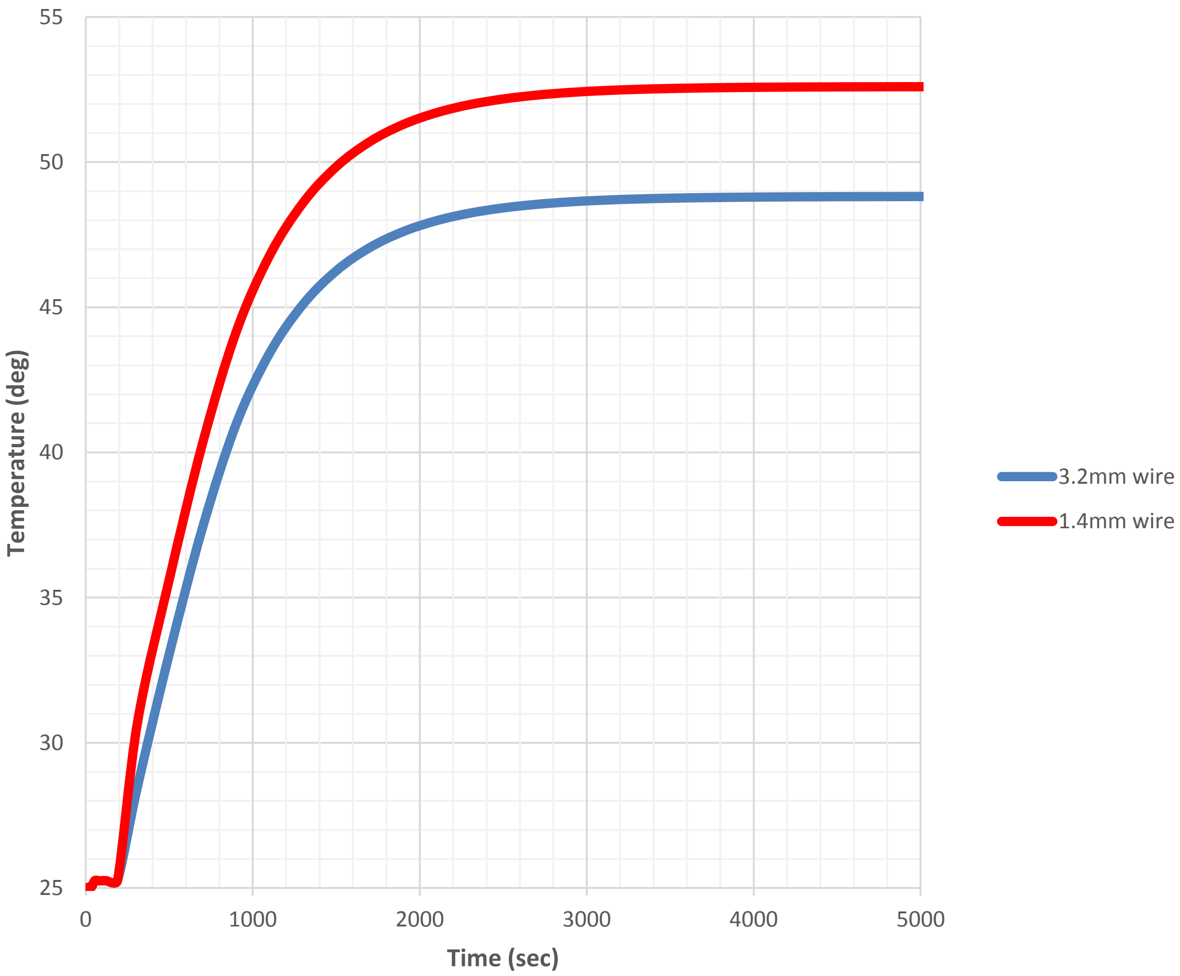

Figure 9-22: Measured temperature rise in the loaded coil.

9.10 Conclusion

This chapter evaluated the electromagnetic characteristics of the prototype machines using 1.4 mm and 3.2 mm conductor diameter, in which the same dynamic high speed test rig was used for no-load and loaded condition experimental tests. These included resistance measurements, back EMF, cogging torque and on-load torque, temperature rise in coils, total loss and AC winding loss for 3.2 mm conductor diameter.

Derived performance was also carried out to include the output power and efficiency of the machine. Back EMF and torque are the main two aspects of evaluating the performance of a machine. The former is associated the performance of permanent magnet with relation to rotating speed, and the torque is related to the current applied.

Eddy current losses in a machine are directly proportional to the squared of frequency and to achieve a high efficiency in the machine, it is very important to reduce the higher frequency content within the machine to obtain lower losses.

The initial 3D FEA described in Chapter 3 showed that the machine had significant harmonics content in the back EMF. Adjusting the dimension of machine describe in Chapter 3 by using rounded tooth, modifying the rotor design lead to the design of machine in chapter 4 and 5. The 3D FEA showed that most of the harmonic present in L1 disappears due to slot and pole number combination, moreover the machine had higher AC winding loss due to open-slot stator winding configuration which affect the overall performance, causing the efficiency to be relatively lower than expected.

Introduction of a single steel lamination sheet for AC winding loss reduction using shielding effect as described in Chapter 6 and 7 were techniques tested in this chapter. It is evident that the novelty of this research work is that a shield techniques made from a single steel lamination sheet can be used to reduce the AC winding loss of an AFM, which is hard to imagine a single lamination sheet making all the slot wedges in a radial flux machine. In the other hand reduces the total loss thereby improving the overall performance of the machine, while having a minor reduction on the peak back EMF and torque.

It was seen from the above experimental tests and analysis that, the best machine is the L6; in which the AC winding loss reduced by 48.0%, back EMF by 3.5%, torque by 5.8%, total loss by 31.7%, output power by 2.8% and efficiency has increased by 10.3%.

10. Conclusions and Further Work

10.1 Introduction

This thesis has proposed and demonstrated a cheap and simple flux shield capable of delivering a 48.0% reduction in AC winding losses and 31.7% reduction in the machine total loss. Moreover, the main aim of this thesis was to develop a highly efficient AFM by enhancing the existing AFM to reduce the back EMF harmonics and AC winding loss. Techniques such as combination of slot and pole number, rounded tooth and modifying the rotor design and introduction of a single steel lamination sheet were applied to reduce the back EMF harmonic and excess AC winding loss in the machine due to open-slot stator winding construction, which encourages an elevated winding loss from the rotation of PM rotor assembly.

3D FEA investigations were carried out to find out the best and optimal design which was then developed and manufactured using soft magnetic composite and tested. The prototype machines were tested to confirm the above techniques. A single steel lamination sheet was used to shield the coils from stray fields which is easy to implement for this type of machine topology and does not require the use of more complex twisted and Litz type conductors has reduce the AC winding loss significantly.

It was shown that this technique improves the overall machine performance through 3D FEA and experimental tests to minimize both copper windings AC loss and steel lamination eddy current losses. It has been shown that L6 with segmented steel lamination sheet M300-35A has the best efficiency and overall performance.

The results from the projected 3D FEA and experimental tests shows that this approach has answer the research question stated in Chapter 1 by reducing the AC winding loss in the machine through harnessing the shielding effect of the steel lamination sheet and the overall performance of the machine has increased.

10.2 Research Conclusions

The three phase AFM is composed of a stator block and a rotor disc. The stator block consists of the tooth and stator core-back, while the rotor disc has magnets fixed to it. The windings on the stator are separated by 120º electrical to complete the phase arrangement.

The thesis begins with the research background information, challenges of open-slot stator winding configuration, objective of the thesis, research contributions to knowledge furtherance and thesis outline were presented together with the list of published work from the research work.

Literature and technology reviews of the research work done so far relating to this thesis were carried out. It has three main objectives which include; ensuring that the research work carried out in this project is new and not being done before. Secondly, to give a summary of the work done by other researchers in these field of study and finally, the evaluation of the previous work and see away to further knowledge in the course of this research work.

It also reviewed the effect of utilising SMC in electrical machines design and using magnetic slot wedge for AC winding loss reduction which proved to be efficient for radial flux machine together with loss mechanisms in electrical machines. In a radial machine it is hard to imagine a single steel lamination sheet making all the slot wedges. This partially results from wanting to slip the coils onto the tooth. Lastly, it reviewed the AFM topologies

A prototype machine that was built with SMC and tested in Newcastle University was used as a baseline, the main aim was to investigate the benefit of using SMC as a core material and evaluate the performance of the machine, including; back EMF, cogging torque, axial force, losses and on-load torque using 3D FEA. The initial 3D FEA showed that the slot and pole number combination resulted in significant third, fifth and seventh harmonics in the back EMF and low efficiency of 65%. Trapezium teeth were used which lead to low fill factor in the machine.

In order to validate the 3D FEA, the prototype machine is tested, and its performance compared with these predictions at no-load and loaded condition. The experimental tests conducted shows that the machine exhibits 4% less torque than the 3D FEA target torque. Furthermore, there is a need to improve the machine overall performance.

To improve the performance of the baseline machine to meet or exceed the target torque, a new machine was designed by altering the dimension of the baseline machine. The slot number of the baseline machine was kept and the pole number was changed.

3D FEA was conducted on the improved machine and the available SMC prototype material was utilised which showed that there is a reduction in the amount of magnet used by 25% as compared to the baseline machine, this lead to decrease in the machine total loss and temperature in the magnets moreover the machine was extended to Chapter 5 to assess the AC winding loss. This calculation is very important in determining the efficiency and overall performance of the machine.

A simple technique of AC winding loss reduction were explored and these method relies on a single steel lamination sheet placed on top of the coils to cover both the slots and end windings by shielding flux reaching the coils and altering the slot leakage inductance of the machine. Different steel lamination sheets and two designs (segmented and non-segmented) were used and found that segmented design L6 with steel lamination sheet M300-35A provides the best performance that reduced the total loss of the machine by approximately 32% of the original value and AC winding loss by 48.0%.

This method exhibits some disadvantages which include; additional Ohmic loss on the steel lamination sheet, decreased in the torque, output power and back EMF of the machine. This technique of AC winding loss reduction can be implemented in this type of machine topology; hence prototype was constructed and assembled as described in Chapter 8.

The analysis in Chapter 6, consider only a magnetic material with conductivity and the results from the study may not be the optimal performance however these leads to academic investigation into the two mechanisms (magnetically permeable, guiding the field way from the coils and electrically resistive, by generating eddy currents to oppose the main field) of loss reduction using magnetic shielding (a single steel lamination sheet) by examining the separate effects of using idealised materials (high reluctance / zero conductivity and vice versa) as demonstrated in Chapter 7.

The different single steel lamination dimensions were all identical and based on the stator and rotor dimension. This ensured that the technique to reduce AC winding loss and improve the performance was compared fairly. From the 3D FEA study, it was found that the machines design with segmented steel lamination sheet have less total loss due to non-circulation of eddy current and therefore only the segmented designs were produced for prototype testing. The prototypes were tested for their back EMF, torque on-loaded condition, total loss and derived AC winding loss and efficiency. These results for each machine L2, L4, L6, L8 and L10 were compared against the L1 and using a single laminated shield of 0.35 mm thickness has been shown to reduce AC winding loss in the machine by 48.0% for a 5.8% reduction in torque.

Lastly, the thesis provides the results for the electromagnetic characteristics testing carried out on the prototype machine without steel lamination sheet and with different steel lamination sheet. A total of six machines were tested, it was concluded that the machine L6 with a single steel lamination sheet M300-35A provided the base design and better overall performance.

The AC winding loss reduced by 48.0%, back EMF by 3.5%, torque by 5.8%, total loss by 31.7%, output power by 2.8% and efficiency has increased by 10.3%. The temperature in the coils of the machine were monitored and recorded for almost 5000 seconds. The rises in temperature were 52.6˚C and 48.8˚C for 1.4 mm and 3.2 mm conductor diameter respectively. These tested were carried out without steel lamination sheet and during experiment test no noticeable temperature rise was felt with hand on the outer case of the machine at full load speed and current.

This PhD work produced AFM using SMC and a single steel lamination sheet to reduce the AC winding loss due to open-slot stator winding construction and the higher frequency of operation, various steel lamination sheet and two design techniques (segmented and non-segmented) were utilised to improve the performance. A prototype machine was built which ultimately stemmed in 6 machines being tested without and with steel lamination sheet to confirm these techniques and finally one optimum design reduced the AC winding loss by 48.0%, total loss in the machine by 31.7% and increased the efficiency by 10.3%.

10.3 Further Work

The research work covered in thesis concentrated on design techniques only on single-sided AFM to reduce the AC winding loss due to the open-slot stator construction which encourage an elevated AC loss at AC operation however the research work could be extended in five main areas.

1. Extending the single-sided design to double-sided configuration, with either two rotors and one stator or two stators and one rotor for more output power and torque density. In addition to that, multistage configuration could be used for fault tolerant application and to see the effectiveness of this simple novel technique for AC winding loss reduction using a single steel lamination sheet for shielding effect.
2. Structural analysis of the AFM needs to be carryout to have a good prediction of the rotor plate deflections which may be caused by the magnet forces, the deformation that occurred during assembly is not well understood and should be the subject of further modelling work.
3. Investigating the use of other design features cut into the single steel lamination sheet to further reduce losses induced in the lamination sheet.
4. Investigation on the use of different speed (changing frequency) together with power factor and load current to ascertain the effect of magnetic shielding on AC winding loss and machine total loss.
5. Investigation on the potential effect of this shield in terms of annual energy consumption if it is adopted in a domestic household item.

Appendix A – Main Dimensions and Specification

Stator outer diameter	110 mm
Stator inner diameter	64 mm
Axial length	48 mm
Slot depth	25 mm
Slot width	5 mm
Magnet thickness	2.5 mm
Airgap length	1 mm
Magnet span	120 degrees electrical
Stator core-back thickness	10 mm
Rotor core-back thickness	12 mm
Operating speed	6000 rpm
Fill factor	70 %
Core material	SOMALOY 1000_5P
Diameter of copper wire	1.4 mm and 3.2 mm
Number of turns	32
Permanent Magnets	N35SH

Appendix B – Mathematical Derivations

Derivation of the vector potential from a current sheet

Figure B-1 is used demonstrate the 2D mathematical model of the machine model to obtain the magnetic field in the airgap.

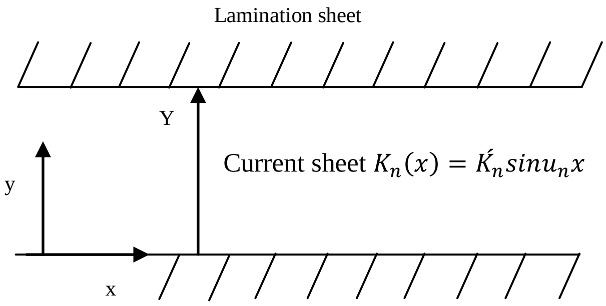

Figure B-1: Current sheet model.

Y represents the region in which air, lamination sheet and magnet are placed. Based on the assumption stated in Chapter 7 and the magnetic property of the region is given by the relationship between the magnetic field intensity, H(in A/m), and flux density, B(in Tesla), as

$$B = \mu_0 \mu_r H + \mu_0 M \qquad \text{(B.1)}$$

where μ_0 is the permeability of free space with a value of $4\pi \times 10^{-7}$ H/m, $\mu_r$the relative permeability of Permanent magnets, $M = B_{rem}/\mu_0$the residual magnetization vector in A/m, and $B_{rem}$the remanence.

The governing equations of magnetic field are the Laplace's equation. These are used to obtain the general solution of magnetic field using current sheet model.

$$\nabla \cdot B = 0 \qquad \text{(B.2)}$$

It can be proved that for any vector, the divergence of its curl is always equal to zero. Thus, we can have a magnetic vector potential, so that

$$B = \nabla \times A \qquad \text{(B.3)}$$

But

$$\nabla \times A = 0$$

This implies that,

$$\nabla \times B = -\nabla^2 A \tag{B.4}$$

The Laplace's equation is given by

$$\nabla \times B = \nabla \times \mu_0 H = \mu_0 J \tag{B.5}$$

Substituting equation (B.4) into equation (B.5)

$$\nabla^2 A = -\mu_0 J \tag{B.6}$$

where J(A/m^2) is current density in the field and assume to be zero. Therefore, the Laplace's equation is obtained as

$$\nabla^2 A = 0 \tag{B.7}$$

But, to obtain the relationship with current density, the combination of Maxwell's equation and equation (B.2) was used

$$\nabla \times B = \mu_0 \mu_r J + \mu_0 \nabla \times M \tag{B.8}$$

$$\nabla^2 A = -\mu_0 \nabla \times M \tag{B.9}$$

General solution to Laplace's equation

In AFM the magnetic vector potential has z-component only, that is to say it is infinite in that direction, the vector potential and magnetic field at the surface of the lamination are found by solving the Laplace's equation above. This implies that $\frac{\partial^2 A}{\partial y^2} = 0$ becomes

$$\frac{\partial^2 A}{\partial x^2} + \frac{\partial^2 A}{\partial y^2} = 0 \tag{B.10}$$

Using separation of variables, we assume that

$$A = X(x)\, Y(y) \tag{B.11}$$

Substituting in the Laplace equation it gives

$$X^{\parallel}(x)Y(y) + X(x)Y^{\parallel}(y) = 0 \quad \text{(B.12)}$$

Equation (B.13) can be written as

$$\frac{X^{\parallel}}{X(x)} = -\frac{Y^{\parallel}}{Y(y)} = \alpha \quad \text{(B.13)}$$

$$X^{\parallel}(x) + \alpha X(x) = 0 \quad \text{(B.14)}$$

$$Y^{\parallel}(y) - \alpha Y(y) = 0 \quad \text{(B.15)}$$

For $\alpha > 0, \alpha = u^2$

$$X^{\parallel}(x) + u^2 X(x) = 0 \quad \text{(B.16)}$$

Introducing trial solution satisfy the above equation

$$X(x) = K_1 \cos(\propto x) + K_2 sin(\propto x) \quad \text{(B.17)}$$

For $A(0, y) = 0$

$$X(0) = 0 = K_1 \quad \text{(B.18)}$$

Similarly, for $A(\lambda, y) = 0$

$$X(\lambda) = 0 = K_2 sin(u\lambda) \quad \text{(B.19)}$$

This implies

$u = \frac{2n\pi}{\lambda}$ where λ, the wavelength is two times the pole pitch.

$$X_n(x) = g_n sinu_n x \quad \text{(B.20)}$$

$$Y^{\parallel}(y) - \alpha Y(y) = 0 \quad \text{(B.21)}$$

Implies that

$$Y(y) = K_1 coshu_n Y + K_1 sinhu_n Y \quad \text{(B.22)}$$

$$Y_n(y) = K_n sinhu_n Y \quad \text{(B.23)}$$

$$A(x, y) = \sum_{n=1}^{\infty} K_n \, sinu_n x sinhu_n y \quad \text{(B.24)}$$

$$A_n = \sum_{n=1}^{\infty} K_n \, sinu_n x sinhu_n y \tag{B.25}$$

$$\int_0^a A_n sinu_n dx = \sum_{n=1}^{\infty} K_n \, sinhu_n a \int_0^y sinu_n x sinu_n x dx \tag{B.26}$$

But

$K_n(x) = \widehat{K}_n sinu_n x$ and $\int_0^{u_n} sinu_n sinu_n dx = \begin{cases} 0, \\ \frac{u_n}{2}, \end{cases}$

$$u_n \int_0^a A_n sinu_n dx = K_n sinh\, u_n a \int_0^y sin^2 u_n x dx \tag{B.27}$$

$$K_n(x) = \begin{cases} \dfrac{\widehat{K}_n \mu_0}{u_n sinhu_n}, \\ 0, \end{cases}$$

$$A_{zn} = -\frac{\widehat{K}_n \mu_0}{u_n} \sum_{n=1}^{\infty} \frac{coshu_n a}{sinhu_n a} coshu_n a \times sinu_n x \tag{B.28}$$

Based on the boundary conditions the airgap magnetic potential in which the steel lamination sheet is placed has a general solution in form of equation (B.28).

Appendix C – Somaloy Typical Data

Somaloy® typical data

General	
Base material: Somaloy Prototyping Material	Somaloy Prototyping Material blanks exhibit stable mechanical properties up to 150°C

Mechanical properties			Standards
Transverse rupture strength/150°C	[MPa]	60/60	SS-ISO 3325
Tensile strength	[MPa]	15*	SS-EN 10002-1, ISO
Yield strength	[MPa]	5*	SS-EN 10002-1, ISO
Young's modulus	[GPa]	100*	ASTM E 1876-99
Poisson's ratio	–	0.23	ASTM E 1876-99
Impact Energy	[J]	1.3	SS-EN 10045, SS-EN

* The machining quality may influence the expected mechanical strength.

Physical properties			Standards
Density	[g/cm³]	7.3	SS-ISO 2738
Thermal expansion	[K⁻¹]	11 e-06	ASTM E 228/MPIF 35
Resistivity	[μΩm]	300	Four point measurements on nominal size OD 55mm ID 45mm Height 5mm

Magnetic properties			Standards
B@4000A/m	[T]	1.19	IEC 60404-4
B@10000A/m	[T]	1.46	IEC 60404-4
H_c	[A/m]	210	IEC 60404-4
μ_r-max	–	430	IEC 60404-4

Available blanks	Size
Cylindrical	OD 80/H20 mm
Cylindrical	OD 80/H40 mm
Cylindrical	OD 120/H20 mm
Ring	OD155/ID105/H20 mm

Magnetising curve

Data adjusted for use in Finite Element Modeling.

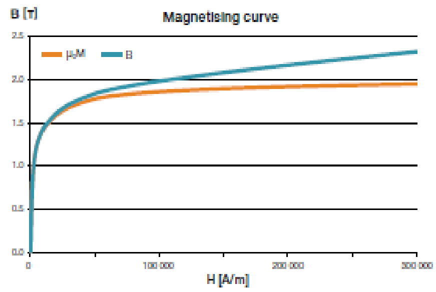

H[A/m]	μ_0M[T]	B[T]	H[A/m]	μ_0M[T]	B[T]
0	0.00	0.00	12904	1.47	1.49
93	0.03	0.03	26799	1.65	1.68
165	0.06	0.06	49770	1.77	1.83
284	0.13	0.12	74770	1.82	1.92
399	0.19	0.19	99770	1.85	1.98
457	0.23	0.23	124770	1.87	2.03
1104	0.58	0.58	149770	1.89	2.08
1594	0.77	0.77	189770	1.91	2.15
2306	0.94	0.95	229770	1.92	2.21
3606	1.12	1.13	279770	1.93	2.29
6468	1.30	1.31	304770	1.94	2.33

Core loss

[W/kg]	50/60 Hz	100 Hz	200 Hz	300 Hz	400 Hz	500 Hz	600 Hz	700 Hz	800 Hz	900 Hz	1000 Hz	2000 Hz
0.5T	1.6 / 1.9	3.1	6	10	14	17	21	26	30	34	39	95
1.0T	5.2 / 6.3	11	22	34	47	60	74	88	104	120	136	339
1.5T	11 / 13	22	45	70	96	123	153	183	216	249	284	719

Measured according to CEI/IEC 60404-6:2003 on ring sample (OD55 ID45 H5 mm).

Loss model

K_h	0.103	K_{ep}	0.000027

Model is verified up to 1.5 T and 5000 Hz.

$$P_{tot} = K_h \cdot f \cdot B^{1.75} + K_{ep} \cdot f^2 \cdot B^2 + \frac{B^2 \cdot f^2 \cdot d^2}{1.8 \cdot \rho \cdot resistivity \cdot 1000} \text{ [W/kg]}$$

K_h	Hysterisis loss coefficient	f	Frequency	[Hz]
K_{ep}	In particle eddy current coefficient	B	Field strength	[T]
d	Smallest cross section of component [mm]	ρ	Density	[g/cm³]
		resistivity		[μΩm]

Find out more

Contact your local sales representative or visit www.hoganas.com/somaloy

Appendix D – Arnold Magnetic N35SH Data Sheet

ARNOLD MAGNETIC TECHNOLOGIES

Neodymium-Iron-Boron Magnet Grades

Summary Product List & Reference Guide

Basic Grades

Properties	B_r		H_{cB}		H_{cJ}		$(BH)_{max}$		Temp. Coef.		T_w
Grade**	Typical mT	Typical gauss	min kA/m	min oersteds	min kA/m	min oersteds	Typical kJ/m^3	Typical MGOe	$\alpha(B_r)$ %/°C	$\alpha(H_{cJ})$ %/°C	max °C
N30	1105	11050	796	100000	955	12000	235	30	-0.12	-0.750	80
N33	1150	11500	836	10500	955	12000	259	33	-0.12	-0.750	80
N35	1210	12100	860	10800	955	12000	0	0	-0.12	-0.618	80
N38	1260	12600	860	10800	955	12000	306	38	-0.12	-0.618	80
N40	1285	12850	923	11600	955	12000	318	40	-0.12	-0.618	80
N42	1315	13150	860	10800	955	12000	334	42	-0.12	-0.618	80
N45	1350	13500	860	10800	955	12000	350	44	-0.12	-0.618	80
N48	1400	14000	836	10500	875	11000	374	47	-0.12	-0.618	80
N50	1425	14250	836	10500	875	11000	390	49	-0.12	-0.618	80
N52	1450	14500	836	10500	875	11000	406	51	-0.12	-0.618	60
N55	1490	14900	716	9000	876	11000	430	54	-0.15	-0.618	60
N33M	1175	11750	836	10500	1114	14000	267	34	-0.12	-0.595	100
N35M	1210	12100	868	10900	1114	14000	283	35	-0.12	-0.595	100
N38M	1260	12600	899	11300	1114	14000	307	39	-0.12	-0.595	100
N40M	1285	12850	923	11600	1114	14000	322	40	-0.12	-0.595	100
N42M	1315	13150	955	12000	1114	14000	338	42	-0.12	-0.595	100
N45M	1350	13500	971	12200	1114	14000	354	44	-0.12	-0.595	100
N48M	1395	13950	995	12500	1114	14000	0	0	-0.12	-0.595	100
N50M	1415	14150	1035	13000	1114	14000	390	49	-0.12	-0.675	100
N52M	1445	14450	995	12500	1035	13000	406	51	-0.12	-0.675	1000
N30H	1105	11050	796	10000	1353	17000	235	30	-0.12	-0.572	120
N33H	1175	11750	836	10500	1353	17000	267	34	-0.12	-0.572	120
N35H	1210	12100	868	10900	1353	17000	283	35	-0.12	-0.572	120
N38H	1260	12600	899	11300	1353	17000	307	39	-0.12	-0.572	120
N40H	1285	12850	923	11600	1353	17000	322	40	-0.12	-0.572	120
N42H	1300	13000	955	12000	1353	17000	330	41	-0.12	-0.572	120
N45H	1350	13500	971	12200	1353	17000	354	44	-0.12	-0.572	120
N48H	1390	13900	1011	12700	1273	16000	378	48	-0.12	-0.572	120
N50H	1415	14150	1035	13000	1274	16000	390	49	-0.12	-0.605	120
N30SH	1125	11250	811	10200	1592	20000	243	31	-0.12	-0.549	150
N33SH	1175	11750	844	10600	1592	20000	267	34	-0.12	-0.549	150
N35SH	1210	12100	876	11000	1592	20000	283	35	-0.12	-0.549	150
N38SH	1260	12600	907	11400	1592	20000	307	39	-0.12	-0.549	150
N40SH	1285	12850	939	11800	1592	20000	322	40	-0.12	-0.549	150
N42SH	1310	13100	955	12000	1592	20000	330	41	-0.12	-0.549	150

Rev. 181031

770 Linden Avenue, Rochester, NY 14625
Ph: (+1) 585-385-9010
E-mail: info@arnoldmagnetics.com
www.arnoldmagnetics.com

ARNOLD MAGNETIC TECHNOLOGIES

N35SH

Sintered Neodymium-Iron-Boron Magnets

These are also referred to as "Neo" or NdFeB magnets. They offer a combination of high magnetic output at moderate cost. Please contact Arnold for additional grade information and recommendations for protective coating. Assemblies using these magnets can also be provided.

	Characteristic	Units	min.	nominal	max.
Magnetic Properties	**Br**, Residual Induction	Gauss	11,700	12,100	12,500
		mT	1170	1210	1250
	H_{cB}, Coercivity	Oersteds	11,000	11,500	12,000
		kA/m	876	915	955
	H_{cJ}, Intrinsic Coercivity	Oersteds	20,000		
		kA/m	1,592		
	BHmax, Maximum Energy Product	MGOe	33	36	38
		kJ/m^3	263	283	302

	Characteristic	Units	C //	C ⊥
Thermal Properties	Reversible Temperature Coefficients [1]			
	of Induction, α(Br)	%/°C	-0.120	
	of Coercivity, α(Hcj)	%/°C	-0.535	
	Coefficient of Thermal Expansion [2]	ΔL/L per °C x 10^{-6}	7.5	-0.1
	Thermal Conductivity	W / (m • K)	7.6	
	Specific Heat [3]	J / (kg • K)	460	
	Curie Temperature, Tc	°C	310	
Other Properties	Flexural Strength	psi	41,300	
		MPa	285	
	Density	g/cm^3	7.5	
	Hardness, Vickers	Hv	620	
	Electrical Resistivity, ρ	μΩ • cm	180	

Notes: (1) Coefficients measured between 20 and 150 °C
(2) Between 20 and 200 °C (3) Between 20 and 140 °C

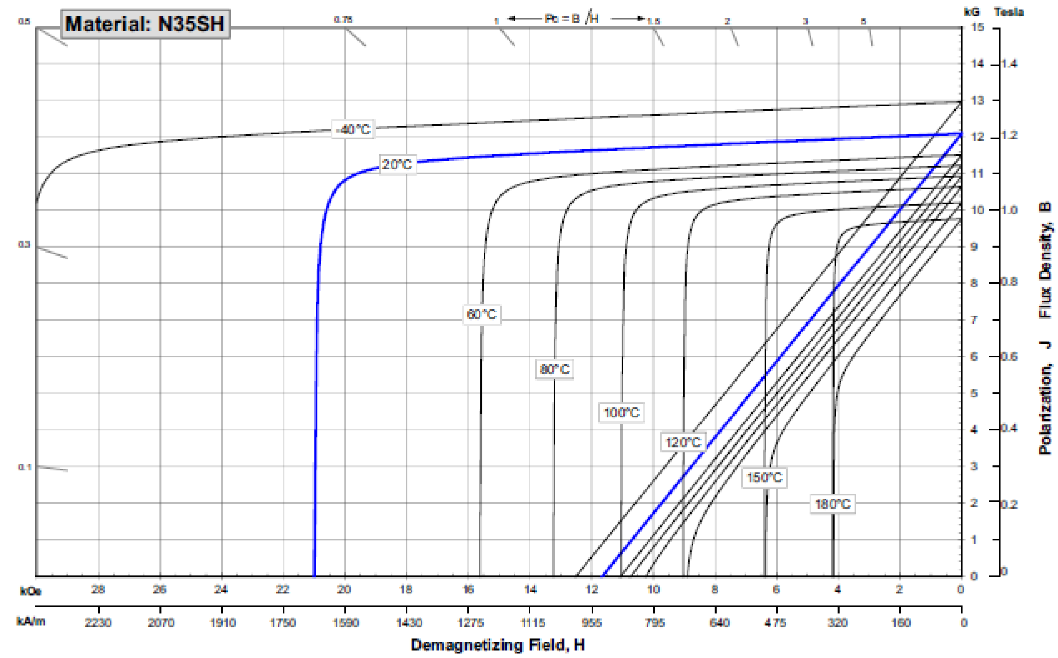

1 kA/m = 12.566 Oe 1 kOe = 79.577 kA/m

Notes The material data and demagnetization curves shown above represent typical properties that may vary due to product shape and size.
Magnets can be supplied thermally stabilized or magnetically calibrated to customer specifications.
Additional grades are available. Please contact the factory for information.

770 Linden Avenue, Rochester, NY 14625
Ph: (+1) 585-385-9010
E-mail info@arnoldmagnetics.com
www.arnoldmagnetics.com
Rev. 151021a

Appendix E – Permabond ES 562 Data Sheet

Permabond®
Engineering Adhesives

PERMABOND® ES562
Single-part, heat-cure Epoxy
Technical Datasheet

Features & Benefits

- Excellent adhesive strength
- Excellent resistance to vibration
- Easy to use – no mixing required
- High shear strength
- Low viscosity, self levelling
- Good resistance to chemicals

Description

PERMABOND® ES562 is a single-part epoxy adhesive which flows like solder when heated during curing. The adhesive has excellent adhesion to metal surfaces and composites. The high bond strength of this adhesive allows it to replace mechanical fastening, soldering or brazing. The adhesive's low viscosity is such that it self-levels.

Physical Properties of Uncured Adhesive

Chemical composition	Epoxy Resin
Appearance	White
Viscosity @ 25°C	15,000 – 30,000 mPa.s *(cP)*
Specific gravity	1.2

Typical Curing Properties

Flow at high temperature	Free flow
Maximum gap fill	0.25 mm *0.01 in*
Cure speed (oven) *	130° C *(266°F)*: 60 minutes 150°C *(300°F)*: 45 minutes 160°C *(320°F)*: 20 minutes
Cure speed (induction)	<3 minutes

**Actual cure times will depend on the time it takes for the adhesive to reach this temperature - for example, large assemblies or a crowded oven will require longer to reach full cure. Alternative, quicker methods of curing include induction, hotplates, infrared lamps and hot-air guns.*

Typical Performance of Cured Adhesive

Shear strength* (ISO4587)	Steel 20 - 35 MPa *(3000 – 5000 psi)* Aluminium 14 - 27 MPa *(2000 – 4000 psi)* Zinc 14 - 27 MPa *(2000 – 4000 psi)*
Tensile strength (DIN53504)	40 N/mm² *(5800 psi)*
Hardness (ISO868)	80-85 Shore D
E-modulus	2.1 GPa
Elongation at break (DIN53504)	<3%
Coefficient of thermal expansion	50 x 10^{-6} mm/mm/°C (below Tg) 165 x 10^{-6} mm/mm/°C (above Tg)
Thermal conductivity	0.30 W/(m.K)
Glass transition temperature (Tg – DSC)	115°C *(240°F)*
Water absorption (ISO62)	<0.5% (at room temperature)

**Strength results will vary depending on the level of surface preparation and gap.*

Hot Strength

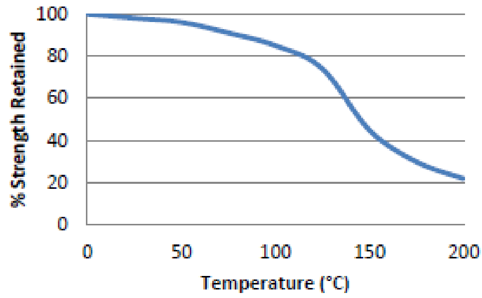

"Hot strength" shear strength tests performed on mild steel. Fully cured then conditioned to pull temperature for 30 minutes before testing.

ES5562 can withstand higher temperatures for brief periods (such as for paint baking and wave soldering processes) providing the joint is not unduly stressed. The minimum temperature the cured adhesive can be exposed to is -40°C (-40°F) depending on the materials being bonded.

Chemical Resistance

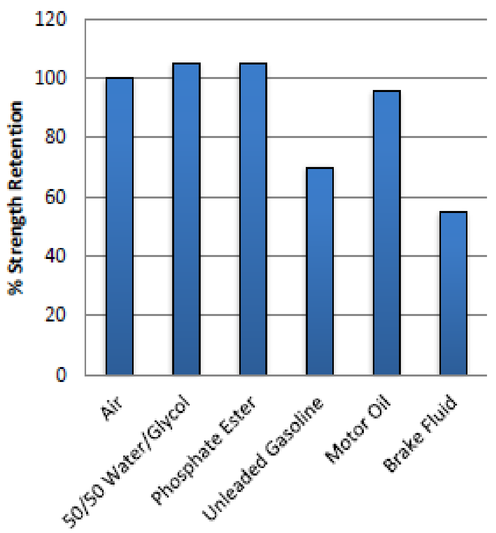

Specimens were immersed for 30 days at 85ºC and tested at room temperature.

Surface Preparation

Surfaces should be clean, dry and grease-free before applying the adhesive. Use a suitable solvent (such as acetone or isopropanol) for the degreasing of surfaces. Some metals such as aluminium, copper and its alloys will benefit from light abrasion with emery cloth (or similar), to remove the oxide layer.

Directions for Use

1) The adhesive should be dispensed from the bottle via the nozzle supplied (this can be cut to give the appropriate sized bead to cover the bond area).
2) Apply the adhesive to one surface and avoid entrapping air.
3) Assemble parts applying sufficient pressure to ensure the adhesive spreads to cover the entire bond area.
4) Use a jig / clamp to prevent parts moving during cure.
5) It is advisable not to disturb the joint until the adhesive is fully cured.
6) Cure with heat – see page one for cure schedule.

Video Links

Surface preparation:
https://youtu.be/8CMOMP7hXjU

Single-part epoxy directions for use:
https://youtu.be/_KupaieuuZw

Additional Information

This product is not recommended for use in contact with strong oxidizing materials.
Information regarding the safe handling of this material may be obtained from the safety data sheet (SDS).
Users are reminded that all materials, whether innocuous or not, should be handled in accordance with the principles of good industrial hygiene.

This Technical Datasheet (TDS) offers guideline information and does not constitute a specification.

Storage & Handling

Storage Temperature	2 to 7°C *(35 to 45°F)*

www.permabond.com
• *UK: 0800 975 9800*
• *General Enquiries: +44 (0)1962 711661*
• *US: 732-868-1372*
• *Asia: + 86 21 5773 4913*
info.europe@permabond.com
info.americas@permabond.com
info.asia@permabond.com

Appendix F – Thermal Insulating Data Sheet

ENGLISH

Datasheet

RS Pro Nomex Thermal Insulating Sheet, 304mm x 200mm x 0.25mm

RS Stock No: **775-7469**

Product Details

RS Pro nomex thermal insulating sheet measures 304 x 200 x 0.25 mm and is a calendared insulation paper. It is perfect for the majority of electrical equipment applications. It offers a high dielectric strength, mechanical toughness, flexibility and resilience.

Features and Benefits

- 0.8 g/cc density
- Thermal Conductivity 0.1/0.16 W/m·K
- Flame retardant
- High chemical and solvent resistant

RS, Professionally Approved Products, gives you professional quality parts across all products categories. Our range has been testified by engineers as giving comparable quality to that of the leading brands without paying a premium price.

ENGLISH

Specifications:

Material	Nomex
Density	0.96 g/cm³
Length	304 mm
Maximum Operating Temperature	+300°C
Thickness	0.25 mm
Width	200 mm
Application	Electrical Equipment

Appendix G – 316 Stainless Steel Data Sheet

316 / 316L Stainless

Technical Datasheet

SMITHS

Austenitic Stainless Steel with added Molybdenum

Service. Quality. Value.

Typical Applications

- Heat exchangers
- Pressure vessels
- Chemical containers
- Food preparation equipment
- Furnace parts
- Valves & pumps

Product Description

Type 316 is an austenitic stainless steel with added molybdenum which gives the alloy improved corrosion resistance. It is commercially almost as popular as 304. The mechanical properties of the alloy are similar to Type 304 except that this grade is stronger at elevated temperatures. Type 316L is a low carbon version of Type 316 which minimizes carbide precipitation due to welding.

Weldability of 316 alloys is excellent and machinability is good. Corrosion resistance is good - excellent pitting resistance and good resistance to most chemicals involved in such industries as paper, photographic and textiles.

Key features

- Austenitic stainless steel with added molybdenum
- Improved corrosion resistance (better than 304) particularly in chloride environments.
- Use 316L for welding applications.

Machinability

Good machinability.

Weldability

Weldable by common fusion and resistance techniques.

Availability

Round bar, flat bar, plate, sheet, wire, hexagon and tube

Corrosion resistance

Excellent pitting resistance and good resistance to most chemicals.

Chemical Composition (weight %)

	C	Cr	Mo	Si	P	S	Ni	Mn	Fe
min		16.5	2.00				10.0		Bal
max	0.08	18.5	2.50	1.00	0.05	0.02	13.0	2.00	Bal

Mechanical Properties

Tensile strength	520 - 680	MPa
Proof Stress	220 min	MPa
Elongation A5	40 min	%

Physical Properties

Density	8.00	kg/m^3
Melting Point	1400	°C
Modulus of Elasticity	193	GPa
Electrical Resistivity	0.074	$x10^{-6}$ Ω.m
Thermal Conductivity	16.3	W/m.K
Thermal Expansion	15.9	$x10^{-6}$ /K

Technical Assistance

Our knowledgeable staff backed up by our resident team of qualified metallurgists and engineers, will be pleased to assist further on any technical topic.

www.smithmetal.com sales@smithmetal.com

Biggleswade	Birmingham	Bristol	Chelmsford	Gateshead	Horsham	Leeds
01767 604604	0121 7284940	0117 9712800	01245 466664	0191 4695428	01403 261981	0113 3075167
London	Manchester	Nottingham	Norwich	Redruth	Verwood	General
020 72412430	0161 7948650	0115 9254801	01603 789878	01209 315512	01202 824347	0845 5273331

Appendix H – Aluminium Alloy 6082 Data Sheet

Aluminium Alloy 6082 - T6 Extrusions

aalco®

SPECIFICATIONS

Commercial	6082
EN	6082

Aluminium alloy 6082 is a medium strength alloy with excellent corrosion resistance. It has the highest strength of the 6000 series alloys. Alloy 6082 is known as a structural alloy. In plate form, 6082 is the alloy most commonly used for machining. As a relatively new alloy, the higher strength of 6082 has seen it replace 6061 in many applications. The addition of a large amount of manganese controls the grain structure which in turn results in a stronger alloy. It is difficult to produce thin walled, complicated extrusion shapes in alloy 6082. The extruded surface finish is not as smooth as other similar strength alloys in the 6000 series.
In the T6 and T651 temper, alloy 6082 machines well and produces tight coils of swarf when chip breakers are used.

Applications
6082 is typically used in:
~ Highly stressed applications
~ Trusses
~ Bridges
~ Cranes
~ Transport applications
~ Ore skips
~ Beer barrels
~ Milk churns

CHEMICAL COMPOSITION

BS EN 573-3:2009
Alloy 6082

Element	% Present
Silicon (Si)	0.70 - 1.30
Magnesium (Mg)	0.60 - 1.20
Manganese (Mn)	0.40 - 1.00
Iron (Fe)	0.0 - 0.50
Chromium (Cr)	0.0 - 0.25
Zinc (Zn)	0.0 - 0.20
Others (Total)	0.0 - 0.15
Titanium (Ti)	0.0 - 0.10
Copper (Cu)	0.0 - 0.10
Other (Each)	0.0 - 0.05
Aluminium (Al)	Balance

ALLOY DESIGNATIONS

Aluminium alloy 6082 also corresponds to the following standard designations and specifications but may not be a direct equivalent:
AA6082
HE30
DIN 3.2315
EN AW-6082
ISO: Al Si1MgMn
A96082

TEMPER TYPES

The most common tempers for 6082 aluminium are:

- T6 - Solution heat treated and artificially aged
- O - Soft
- T4 - Solution heat treated and naturally aged to a substantially stable condition
- T651 - Solution heat treated, stress relieved by stretching then artificially aged

SUPPLIED FORMS

Alloy 6082 is typically supplied as Channel, Angle, Tee, Square bar, Square box section, Rectangular box section, Flat bar and Tube.

- Extrusions
- Bar
- Tube

GENERIC PHYSICAL PROPERTIES

Property	Value
Density	2.70 g/cm³
Melting Point	555 °C
Thermal Expansion	24 x10^{-6} /K
Modulus of Elasticity	70 GPa
Thermal Conductivity	180 W/m.K
Electrical Resistivity	0.038 x10^{-6} Ω .m

[1 OF 3] CONTINUED

Aluminium Alloy 6082 - T6 Extrusions

aalco®

MECHANICAL PROPERTIES

BS EN 755-2:2008 Rod & Bar Up to 20mm Dia. & A/F	
Property	Value
Proof Stress	250 Min MPa
Tensile Strength	295 Min MPa
Elongation A50 mm	6 Min %
Hardness Brinell	95 HB
Elongation A	8 Min %

Properties above are for material in the T6 condition

BS EN 755-2:2008 Rod & Bar 20mm to 150mm Dia. & A/F	
Property	Value
Proof Stress	260 Min MPa
Tensile Strength	310 Min MPa
Hardness Brinell	95 HB
Elongation A	8 Min %

Properties above are for material in the T6 condition

BS EN 755-2:2008 Bar 150mm to 200mm Dia. & A/F	
Property	Value
Proof Stress	240 Min MPa
Tensile Strength	280 Min MPa
Hardness Brinell	95 HB
Elongation A	6 Min %

Properties above are for material in the T6 condition

BS EN 755-2:2008 Bar 200mm to 250mm Dia. & A/F	
Property	Value
Proof Stress	200 Min MPa
Tensile Strength	270 Min MPa
Hardness Brinell	95 HB
Elongation A	6 Min %

Properties above are for material in the T6 condition

BS EN 755-2:2008 Tube Up to 5mm Wall Thickness	
Property	Value
Proof Stress	250 Min MPa
Tensile Strength	290 Min MPa
Elongation A50 mm	6 Min %
Hardness Brinell	95 HB
Elongation A	8 Min %

Properties above are for material in the T6 condition

BS EN 755-2:2008 Tube 5mm to 25mm Wall Thickness	
Property	Value
Proof Stress	260 Min MPa
Tensile Strength	310 Min MPa
Elongation A50 mm	8 Min %
Hardness Brinell	95 HB
Elongation A	10 Min %

Properties above are for material in the T6 condition

BS EN 755-2:2008 Open & Hollow Profile Up To 5mm Wall Thickness	
Property	Value
Proof Stress	250 Min MPa
Tensile Strength	290 Min MPa
Elongation A50 mm	6 Min %
Hardness Brinell	95 HB
Elongation A	8 Min %

Properties above are for material in the T6 condition

BS EN 755-2:2008 Open & Hollow Profile 5mm to 25mm Wall Thickness	
Property	Value
Proof Stress	260 Min MPa
Tensile Strength	310 Min MPa
Elongation A50 mm	8 Min %
Hardness Brinell	95 HB
Elongation A	10 Min %

Properties above are for material in the T6 condition

[2 OF 3] CONTINUED

Aluminium Alloy 6082 - T6 Extrusions

WELDABILITY

6082 has very good weldability but strength is lowered in the weld zone. When welded to itself, alloy 4043 wire is recommended. If welding 6082 to 7005, then the wire used should be alloy 5356.

Weldability – Gas: Good
Weldability – Arc: Good
Weldability – Resistance: Good
Brazability: Good
Solderability: Good

FABRICATION

Workability - Cold: Good
Machinability: Good

CONTACT

Address:	Please make contact directly with your local service centre, which can be found via the Locations page of our web site
Web:	www.aalco.co.uk

REVISION HISTORY

Datasheet Updated	13 November 2018

DISCLAIMER

This Data is indicative only and as such is not to be relied upon in place of the full specification. In particular, mechanical property requirements vary widely with temper, product and product dimensions. All information is based on our present knowledge and is given in good faith. No liability will be accepted by the Company in respect of any action taken by any third party in reliance thereon.

Please note that the 'Datasheet Update' date shown above is no guarantee of accuracy or whether the datasheet is up to date.

The information provided in this datasheet has been drawn from various recognised sources, including EN Standards, recognised industry references (printed & online) and manufacturers' data. No guarantee is given that the information is from the latest issue of those sources or about the accuracy of those sources.

Material supplied by the Company may vary significantly from this data, but will conform to all relevant and applicable standards.

As the products detailed may be used for a wide variety of purposes and as the Company has no control over their use; the Company specifically excludes all conditions or warranties expressed or implied by statute or otherwise as to dimensions, properties and/or fitness for any particular purpose, whether expressed or implied.

Advice given by the Company to any third party is given for that party's assistance only and without liability on the part of the Company. All transactions are subject to the Company's current Conditions of Sale. The extent of the Company's liabilities to any customer is clearly set out in those Conditions; a copy of which is available on request.

Appendix I – FDM TPU 92A Data Sheet

FDM TPU 92A

FDM® TPU 92A is a thermoplastic polyurethane with a Shore A value of 92. The material exhibits high elongation, superior toughness, durability and abrasion resistance.

FDM TPU 92A brings the benefits of elastomers to FDM 3D printing and offers the capability to quickly produce large and complex elastomer parts. Typical applications include flexible hoses, tubes, air ducts, seals, protective covers and vibration dampeners.

FDM TPU 92A is available on the F123™ Series 3D Printers and is compatible with QSR™ soluble support material.

Mechanical Properties	Test Method	Value	
		XY Orientation	XZ Orientation
Shore Hardness (molded)	ASTM D2240	92 Shore A	92 Shore A
Tensile Strength, Yield (Type 1, 0.125", 0.2"/min)	ASTM D412	15.6 MPa (2,265 psi)	16.1 MPa (2,332 psi)
Tensile Strength, Ultimate (Type 1, 0.125", 0.2"/min)	ASTM D412	16.8 MPa (2,432 psi)	17.4 MPa (2,519 psi)
Tensile Modulus (Type 1, 0.125", 0.2"/min)	ASTM D412	15.3 MPa (2,212 psi)	20.7 MPa (3,000 psi)
Elongation at Break (Type 1, 0.125", 0.2"/min)	ASTM D412	552%	482%
Elongation at Yield (Type 1, 0.125", 0.2"/min)	ASTM D412	466%	385%
Tensile Stress at 100% Elongation (PSI)	ASTM D412	6.9 MPa (999 psi)	7.6 MPa (1,096 psi)
Tensile Stress at 300% Elongation (PSI)	ASTM D412	11.0 MPa (1,598 psi)	11.9 MPa (1,722 psi)
Flexural Strength (Method 1, 0.05"/min)	ASTM D790	1.8 MPa (255 psi)	2.4 MPa (351 psi)
Flexural Modulus (Method 1, 0.05"/min)	ASTM D790	25.6 MPa (3,719 psi)	36.9 MPa (5,349 psi)
Flexural Strain at Break (Method 1, 0.05"/min)	ASTM D790	No break	No break
Tear Strength - Stamped	ASTM D624-C	84.6 N/mm (483 lbF/in)	NA
Compressive Strength, Yield (Method 1, 0.05"/min)	ASTM D695	2.6 MPa (384 psi)	2.6 MPa (384 psi)
Compressive Strength, Ultimate (Method 1, 0.05"/min)	ASTM D695	2.6 MPa (384 psi)	2.6 MPa (384 psi)
Compressive Modulus (Method 1, 0.05"/min)	ASTM D695	16.9 MPa (2,457 psi)	16.9 MPa (2,457 psi)
Compression Set at 22 Hours @ 23 °C	ASTM D395	21%	NA
Compression Set at 22 Hours @ 70 °C	ASTM D395	44%	NA

stratasys

FDM TPU 92A

Thermal Properties	Test Method	Value
Heat Deflection (HDT) @ 66 psi	ASTM D648	38 °C (100.4 °F)
Heat Deflection (HDT) @ 15 psi	NA	56 °C (132.8 °F)
Vicat Softening Temperature (Rate B/50)	ASTM D1525	95 °C (203 °F)
Glass Transition Temperature (Tg)	DMA (SSYS)	-42 °C (-43.6 °F)
Coefficient of Thermal Expansion (x-direction)	ASTM E831	139 μm/(m·°C) (7.72E-05 in/(in·°F))
Coefficient of Thermal Expansion (y-direction)	ASTM E831	159 μm/(m·°C) (8.83E-05 in/(in·°F))
Coefficient of Thermal Expansion (z-direction)	ASTM E831	176 μm/(m·°C) (9.78E-05 in/(in·°F))

Electrical Properties	Test Method	Value	
		XY Orientation	XZ Orientation
Volume Resistivity	ASTM D257	6.09E+10 ohm-cm	7.17E+13 ohm-cm

Other	Test Method	Value
Specific Gravity	ASTM D792	1.13502

Stratasys Headquarters

7665 Commerce Way,
Eden Prairie, MN 55344
+1 800 801 6491 (US Toll Free)
+1 952 937-3000 (Intl)
+1 952 937-0070 (Fax)

1 Holtzman St., Science Park,
PO Box 2496
Rehovot 76124, Israel
+972 74 745 4000
+972 74 745 5000 (Fax)

stratasys.com
ISO 9001:2008 Certified

Appendix J – Back EMF Screenshots from Oscilloscope.

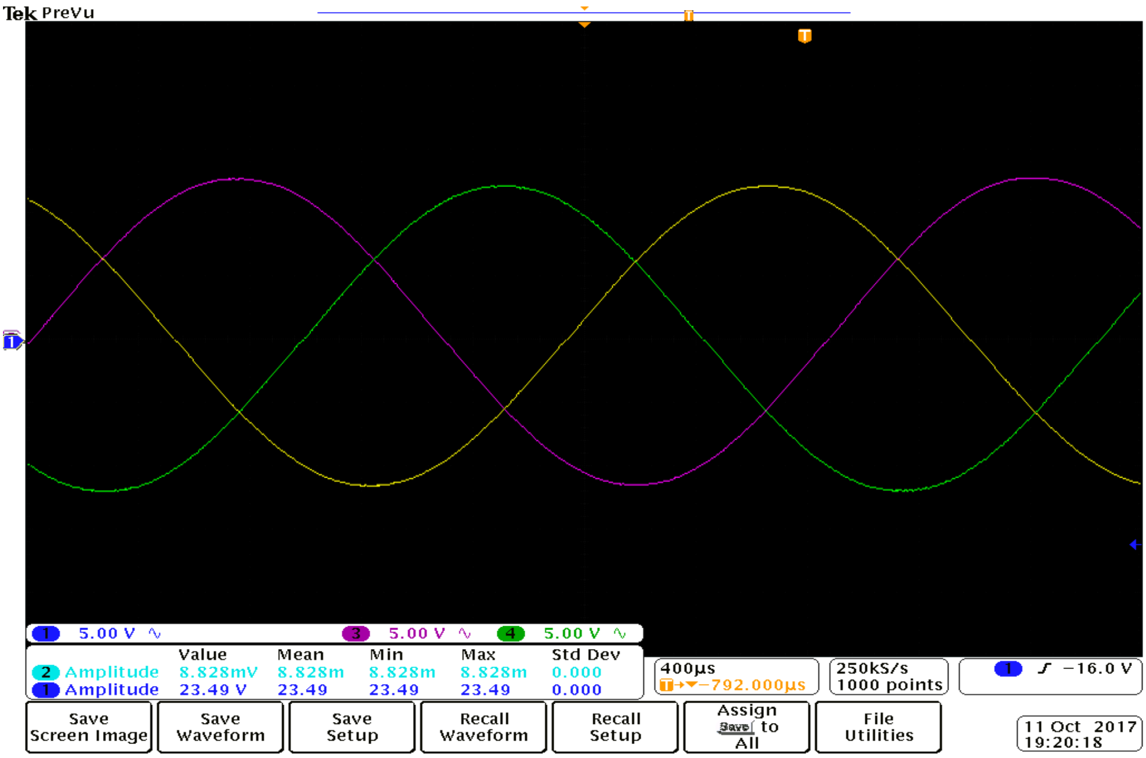

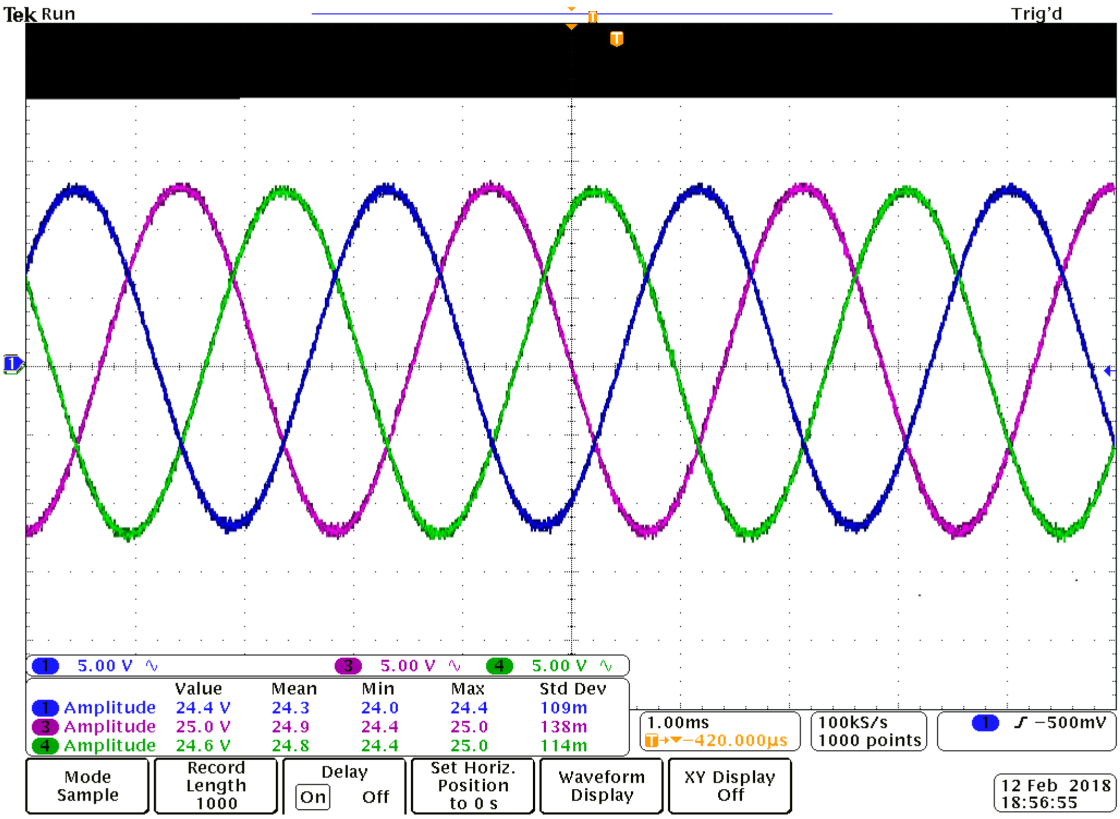

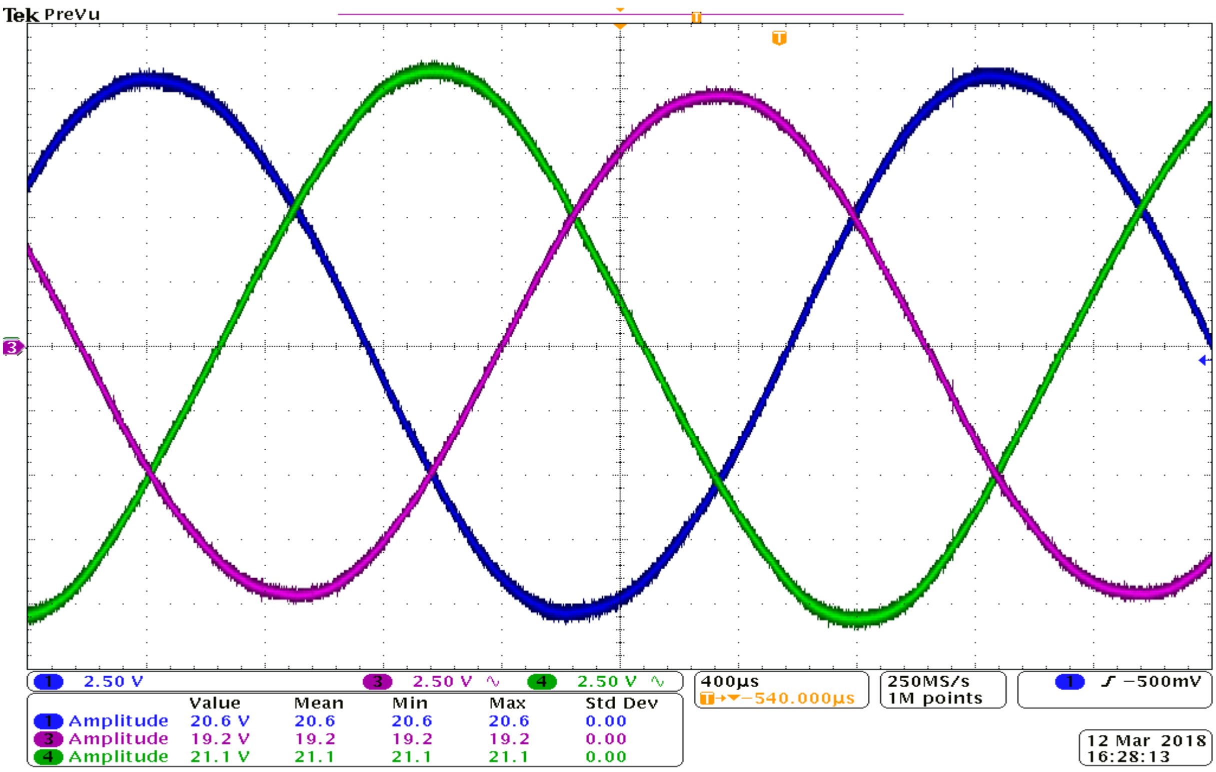
Tek PreVu
1 2.50 V
3 2.50 V
4 2.50 V
400µs
−540.000µs
250MS/s
1M points
1 −500mV
Value Mean Min Max Std Dev
1 Amplitude 20.6 V 20.6 20.6 20.6 0.00
3 Amplitude 19.2 V 19.2 19.2 19.2 0.00
4 Amplitude 21.1 V 21.1 21.1 21.1 0.00
12 Mar 2018
16:28:13

Appendix K – Final 110 mm Machine Design

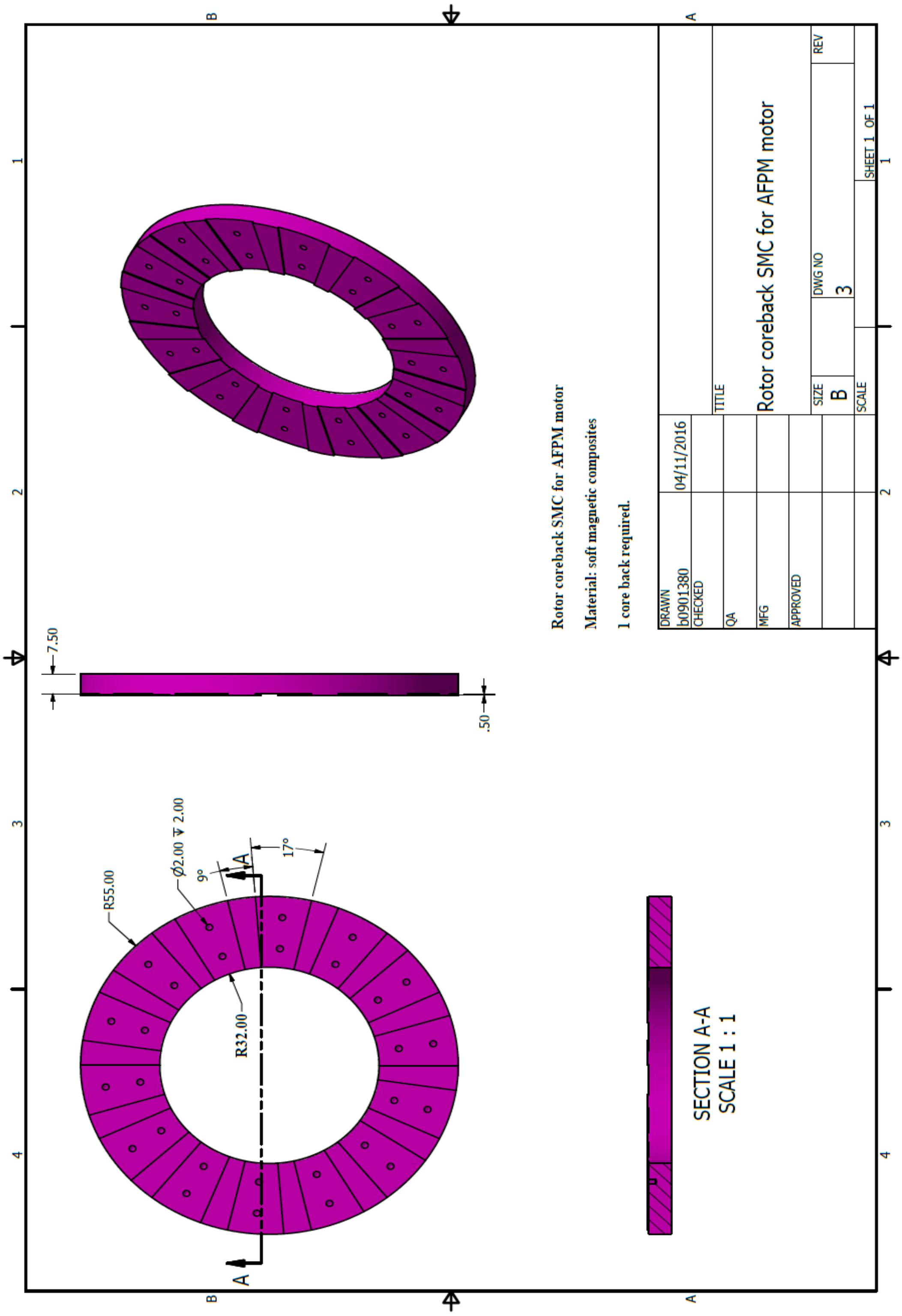

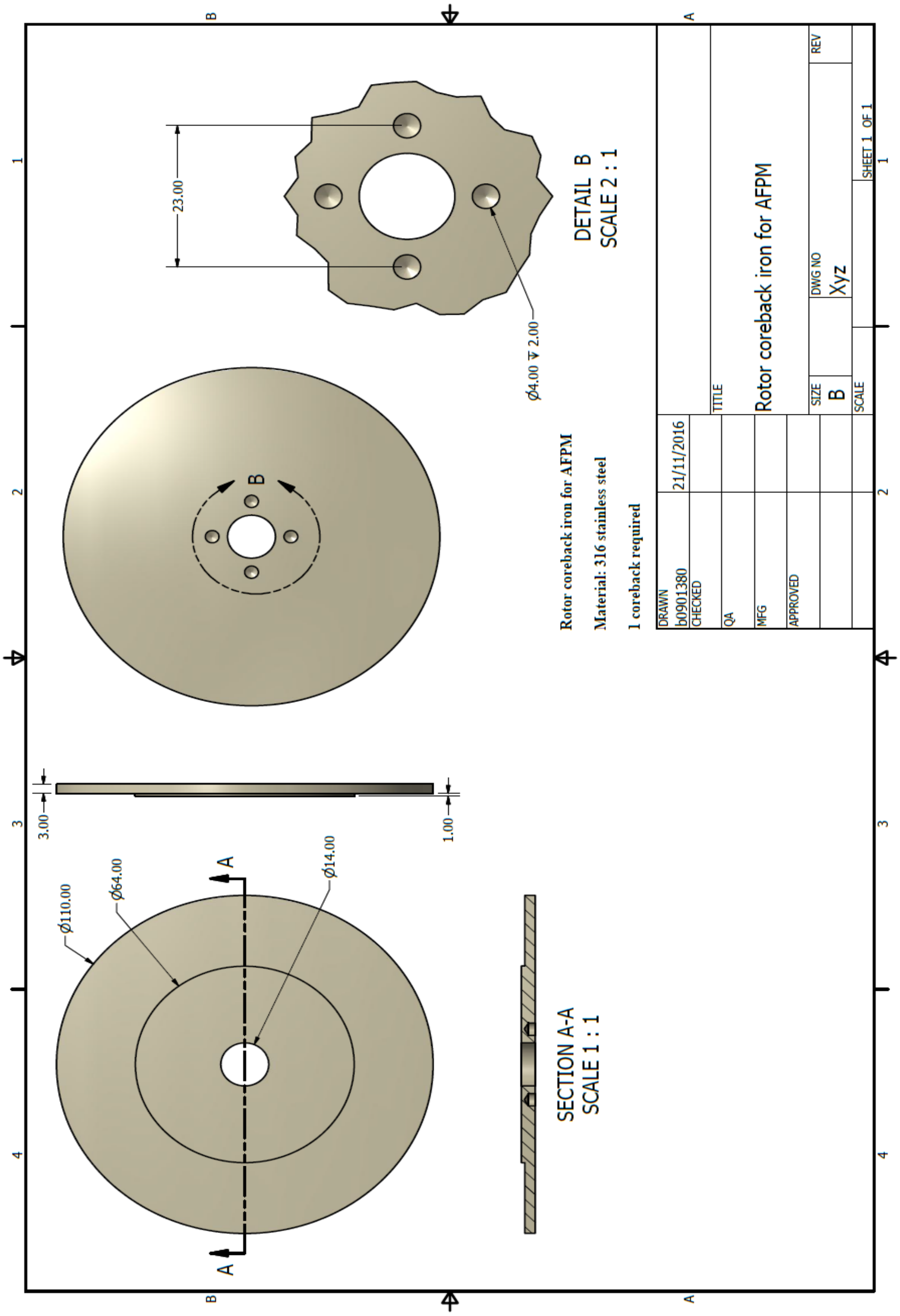

DETAIL B
SCALE 2 : 1
23.00
Ø4.00 ↧ 2.00
Rotor coreback iron for AFPM
Material: 316 stainless steel
1 coreback required
DRAWN
b0901380
21/11/2016
CHECKED
QA
MFG
APPROVED
TITLE
Rotor coreback iron for AFPM
SIZE
B
DWG NO
Xyz
REV
SCALE
SHEET 1 OF 1
3.00
1.00
Ø110.00
Ø64.00
Ø14.00
A
SECTION A-A
SCALE 1 : 1

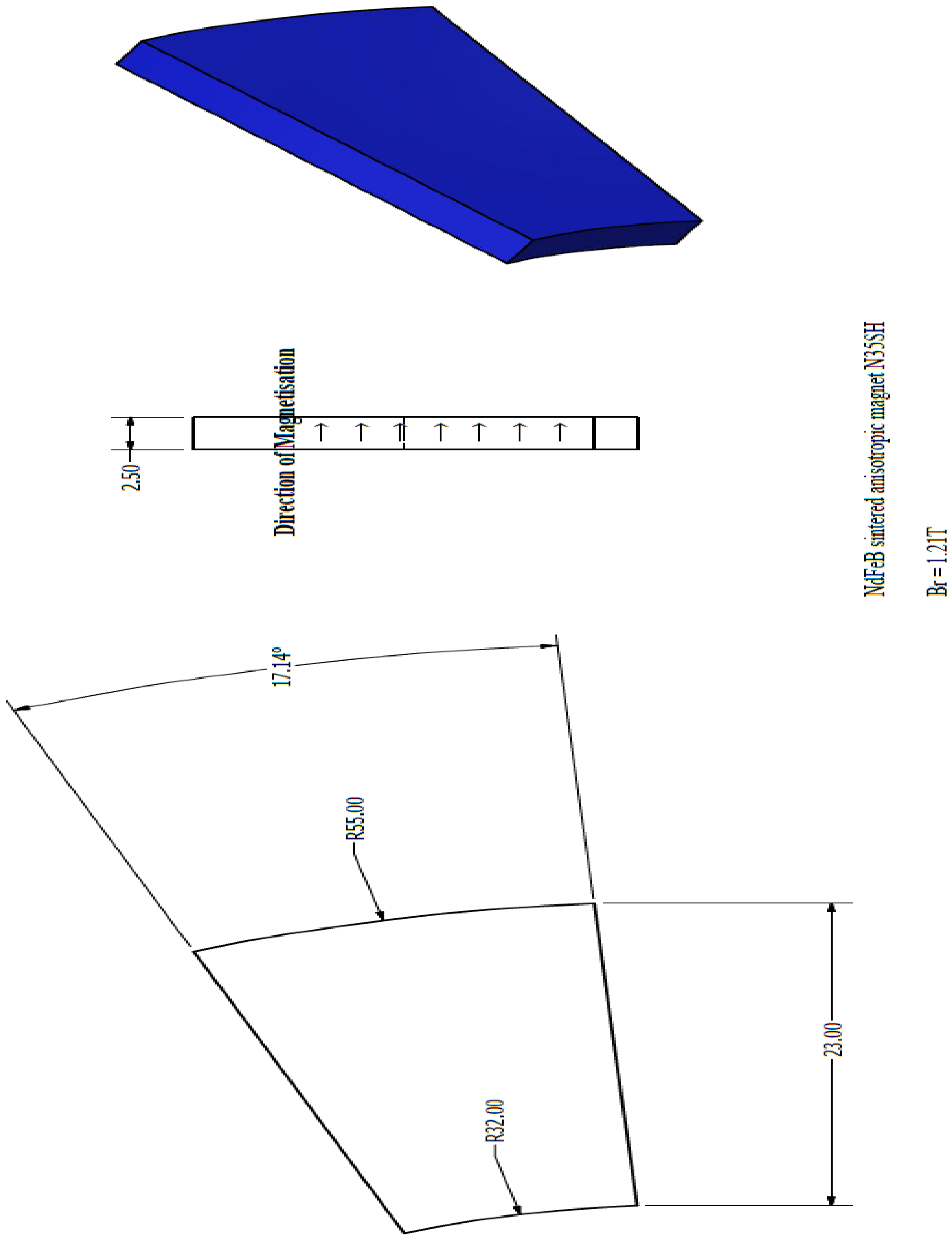
Direction of Magnetisation
2.50
NdFeB sintered anisotropic magnet N35SH
Br = 1.21T
17.14°
R55.00
R32.00
23.00

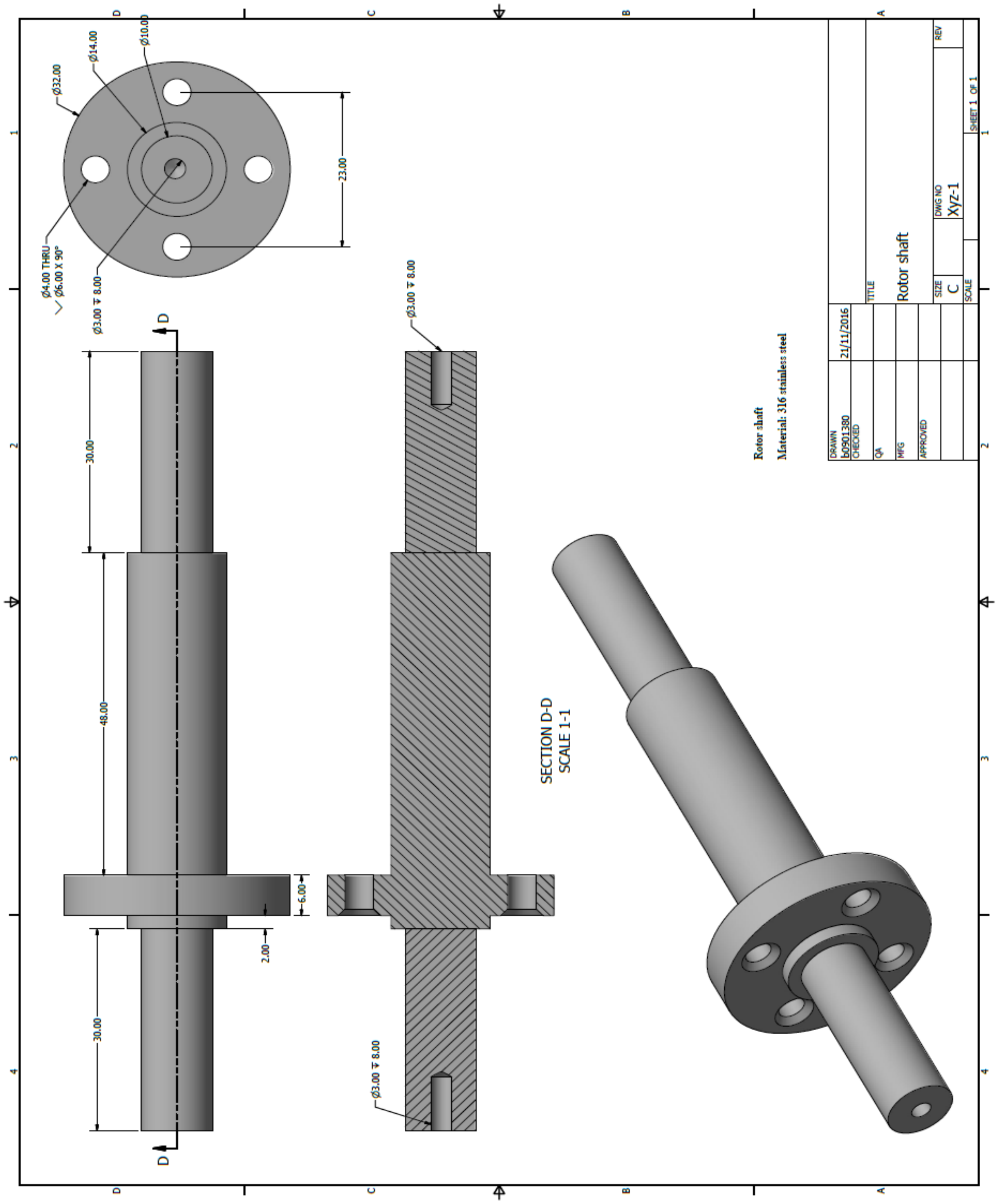
Ø32.00
Ø14.00
Ø10.00
Ø4.00 THRU
Ø6.00 X 90°
Ø3.00 ↧ 8.00
23.00
30.00
48.00
6.00
2.00
SECTION D-D
SCALE 1-1
Rotor shaft
Material: 316 stainless steel
DRAWN
b0901380
21/11/2016
CHECKED
QA
MFG
APPROVED
TITLE
Rotor shaft
SIZE
C
DWG NO
Xyz-1
REV
SCALE
SHEET 1 OF 1

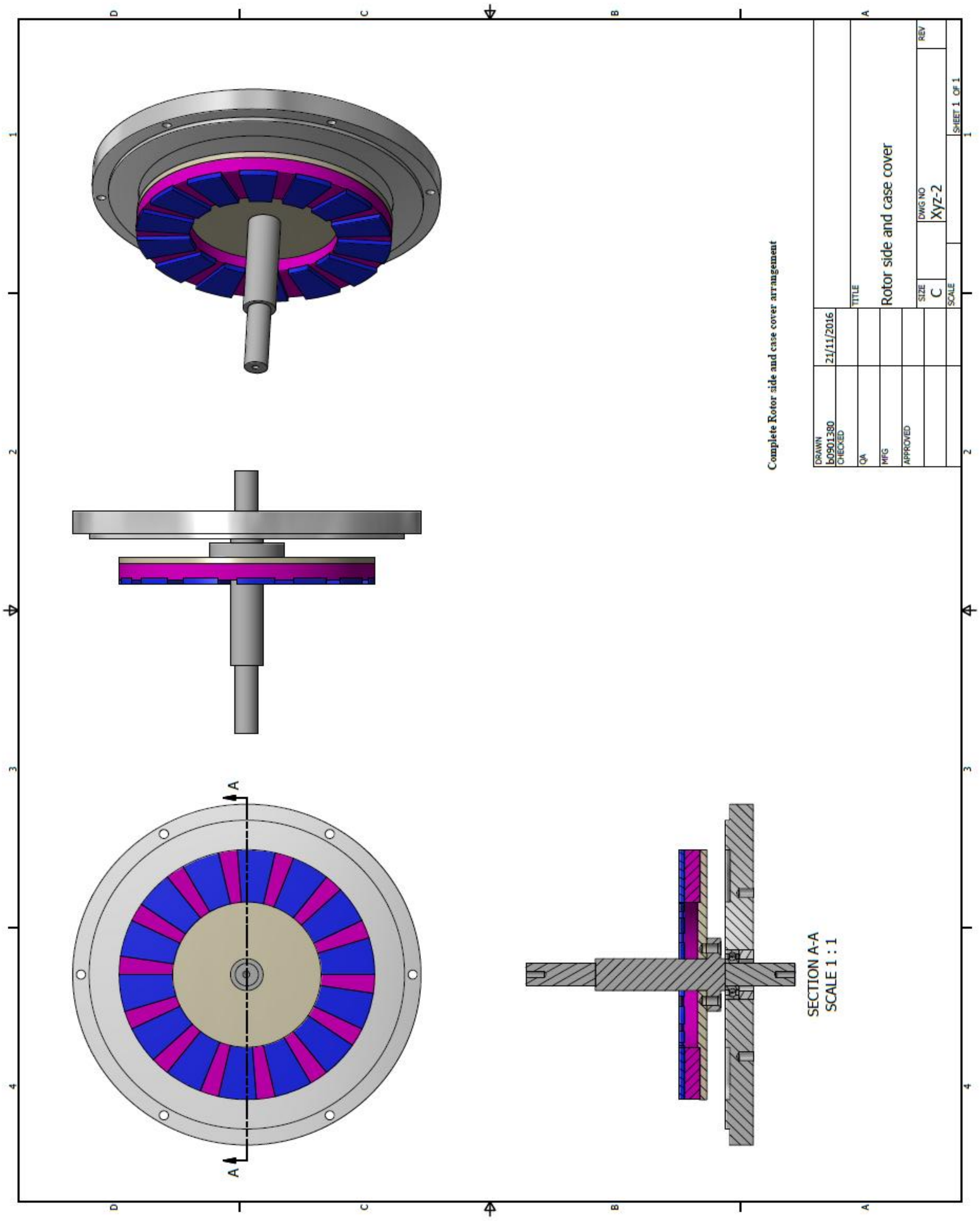
Complete Rotor side and case cover arrangement
DRAWN
b0901380
21/11/2016
CHECKED
QA
MFG
APPROVED
TITLE
Rotor side and case cover
SIZE
C
DWG NO
Xyz-2
REV
SCALE
SHEET 1 OF 1
SECTION A-A
SCALE 1 : 1

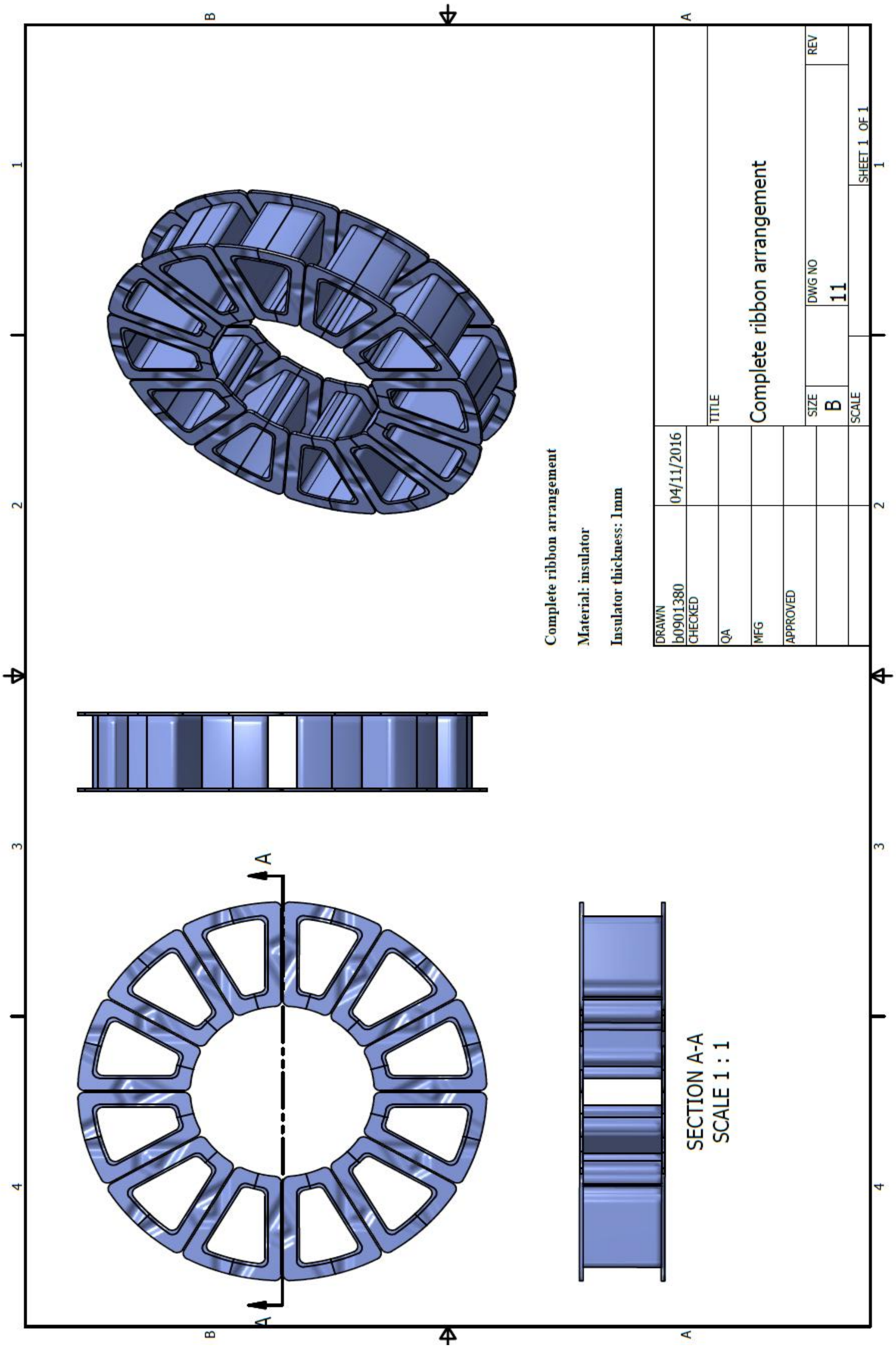
Complete ribbon arrangement
Material: insulator
Insulator thickness: 1mm
DRAWN
b0901380
04/11/2016
CHECKED
QA
MFG
APPROVED
TITLE
Complete ribbon arrangement
SIZE
B
DWG NO
11
REV
SCALE
SHEET 1 OF 1
SECTION A-A
SCALE 1 : 1
A
A

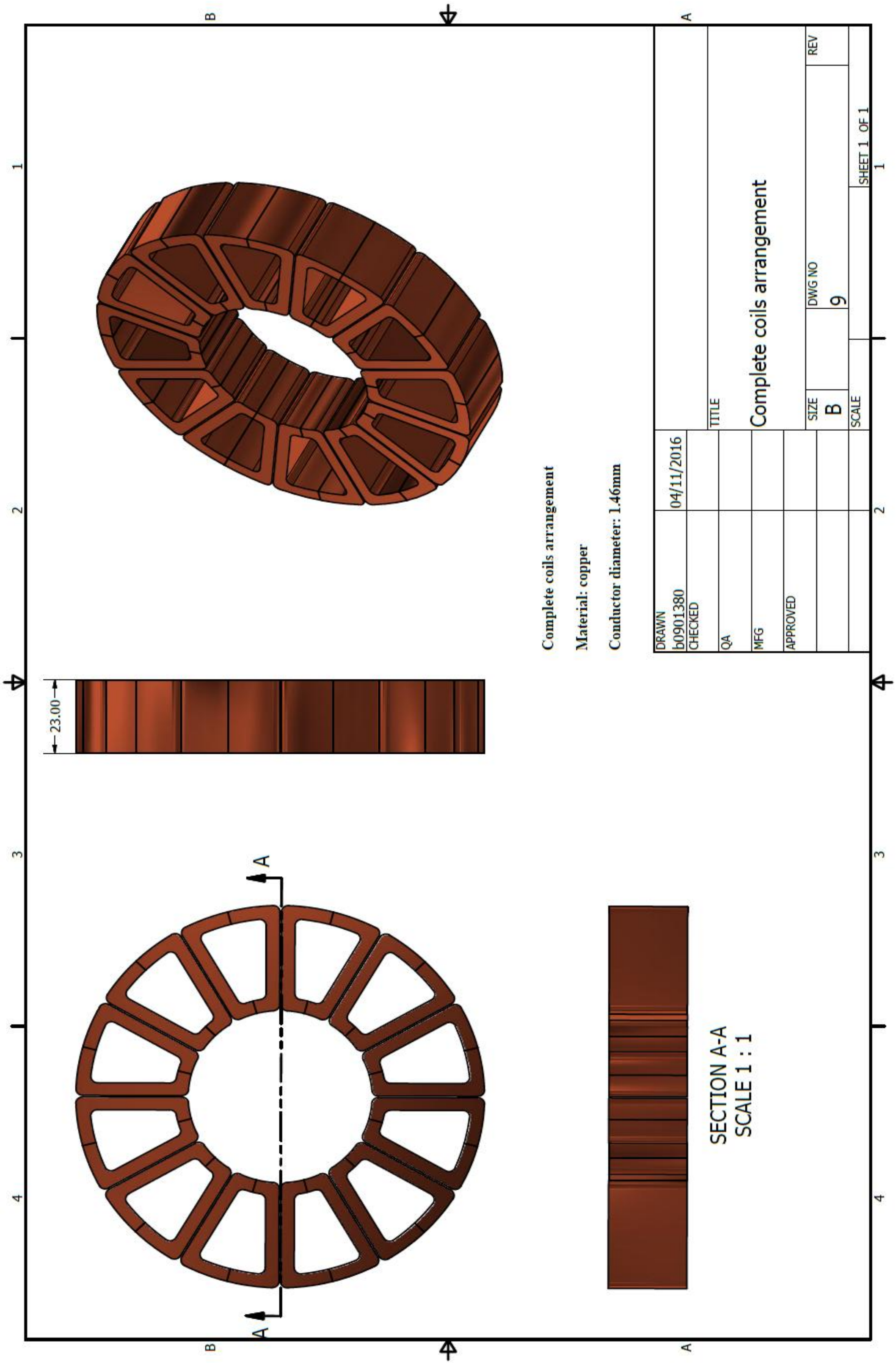
Complete coils arrangement
Material: copper
Conductor diameter: 1.46mm
23.00
SECTION A-A
SCALE 1 : 1
DRAWN
b0901380
04/11/2016
CHECKED
QA
MFG
APPROVED
TITLE
Complete coils arrangement
SIZE
B
DWG NO
9
REV
SCALE
SHEET 1 OF 1

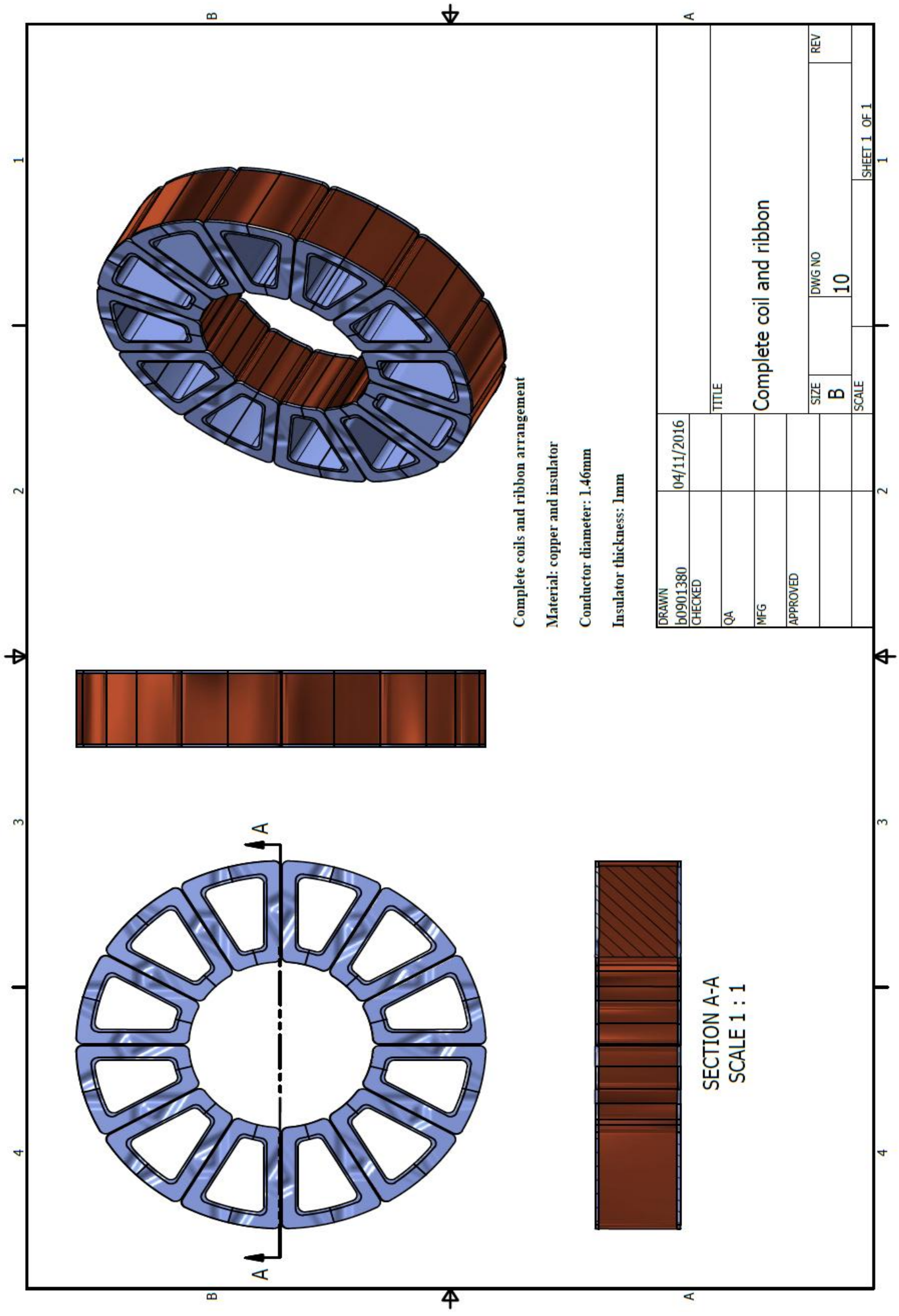
Complete coils and ribbon arrangement
Material: copper and insulator
Conductor diameter: 1.46mm
Insulator thickness: 1mm
DRAWN
b0901380
04/11/2016
CHECKED
QA
MFG
APPROVED
TITLE
Complete coil and ribbon
SIZE
B
DWG NO
10
REV
SCALE
SHEET 1 OF 1
SECTION A-A
SCALE 1 : 1
A
B
1
2
3
4

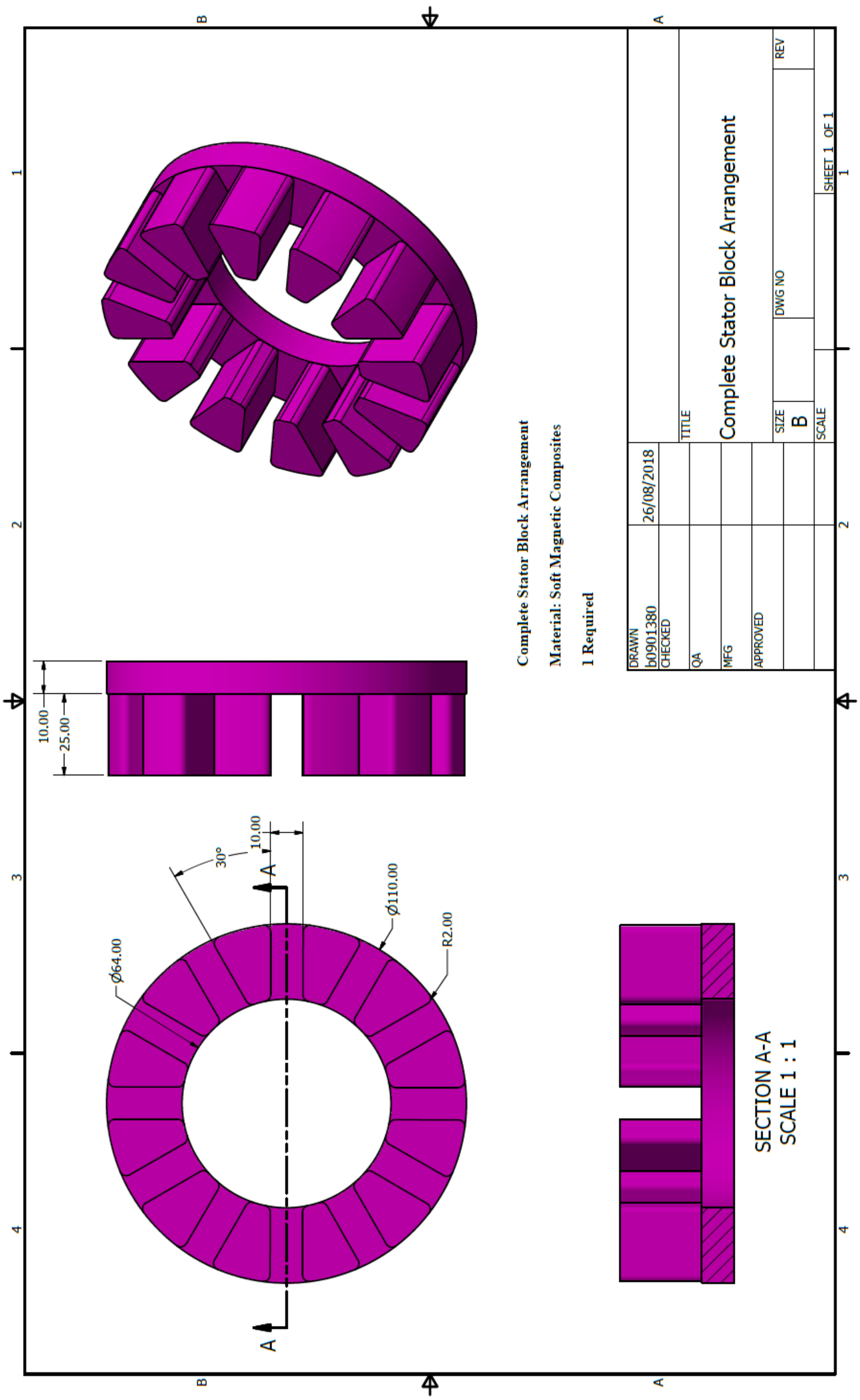
Complete Stator Block Arrangement
Material: Soft Magnetic Composites
1 Required
DRAWN
b0901380
26/08/2018
CHECKED
QA
MFG
APPROVED
TITLE
Complete Stator Block Arrangement
SIZE
B
DWG NO
REV
SCALE
SHEET 1 OF 1
10.00
25.00
30°
10.00
Ø110.00
R2.00
Ø64.00
A
A
SECTION A-A
SCALE 1 : 1

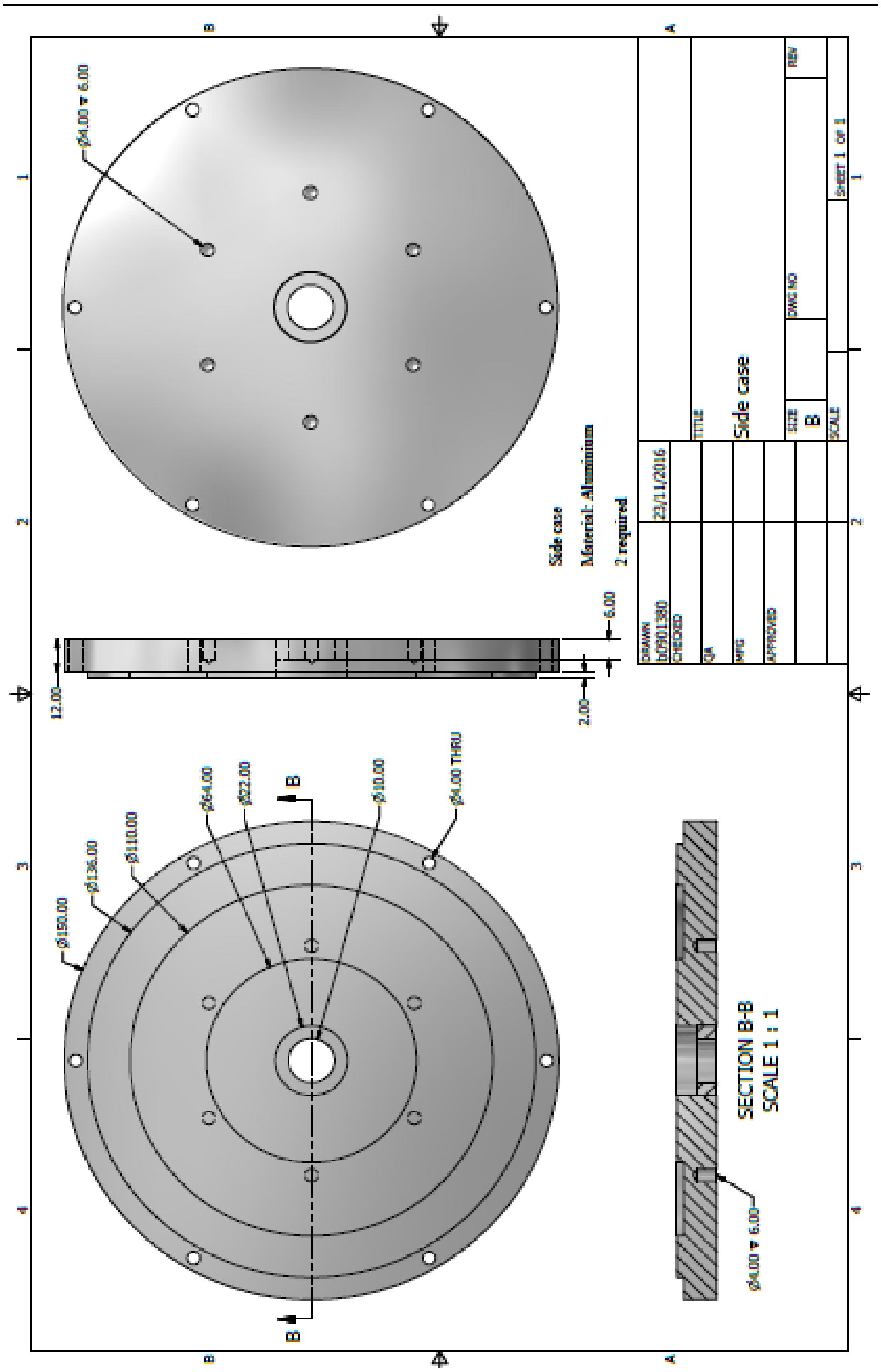
Side case
Material: Aluminium
2 required
Side case
23/11/2016
b0901380
SECTION B-B
SCALE 1 : 1
Ø4.00 ▾ 6.00
Ø150.00
Ø136.00
Ø110.00
Ø64.00
Ø22.00
Ø10.00
Ø4.00 THRU
12.00
2.00
6.00

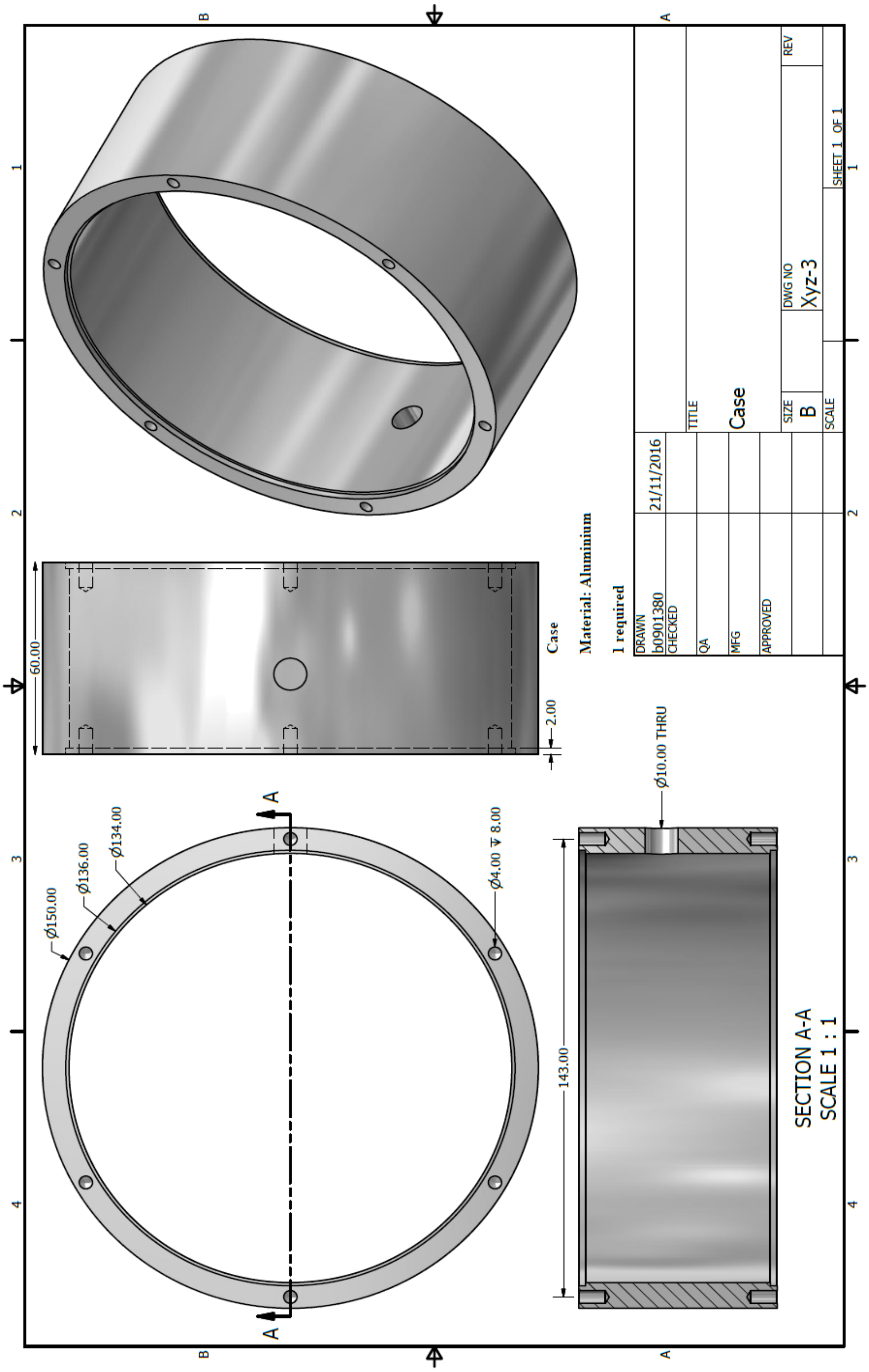
Case
Material: Aluminium
1 required
60.00
2.00
Ø10.00 THRU
Ø150.00
Ø136.00
Ø134.00
Ø4.00 ↧ 8.00
143.00
SECTION A-A
SCALE 1 : 1
DRAWN
b0901380
21/11/2016
CHECKED
QA
MFG
APPROVED
TITLE
Case
SIZE
B
DWG NO
Xyz-3
REV
SCALE
SHEET 1 OF 1

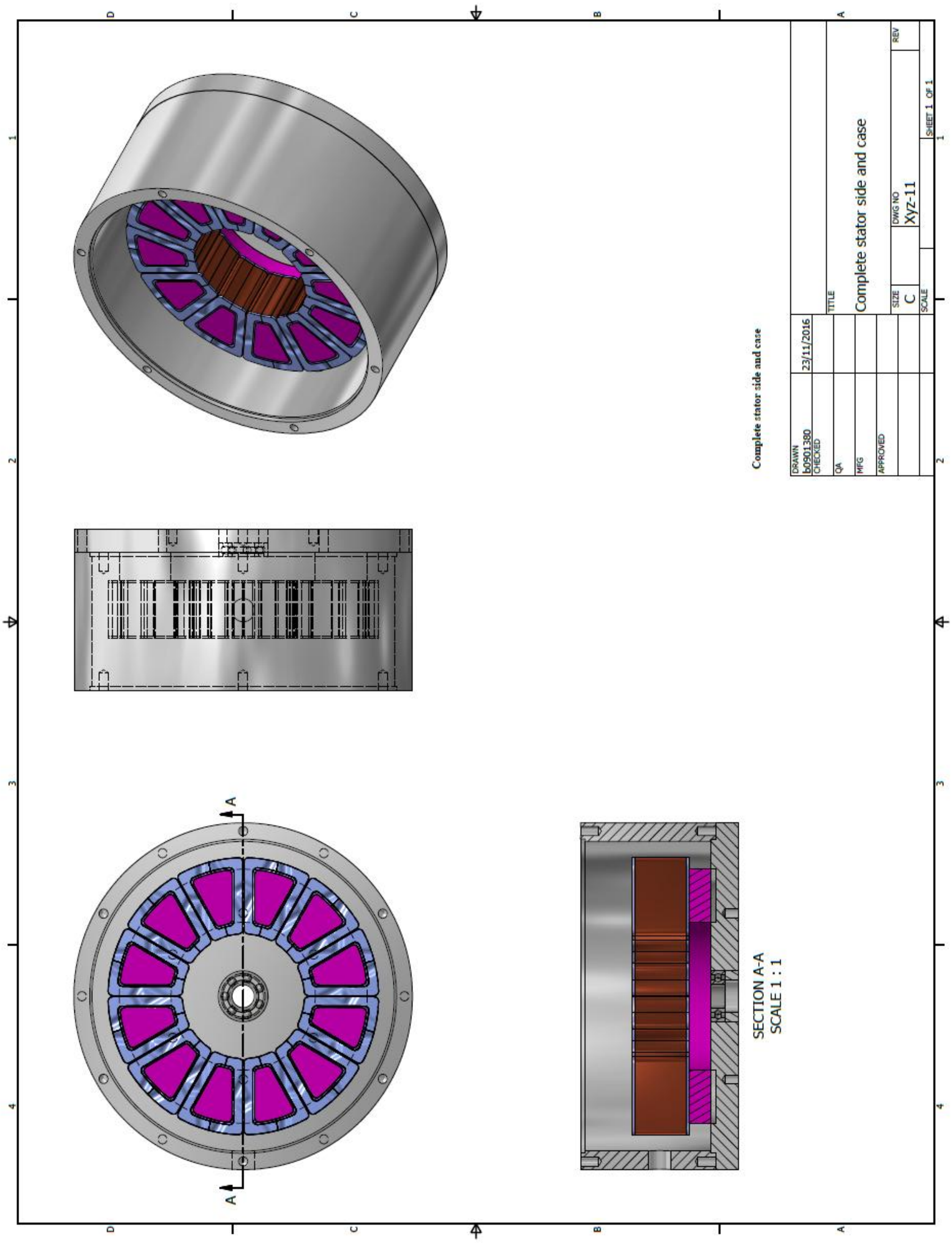
Complete stator side and case
DRAWN
b0901380
23/11/2016
CHECKED
QA
MFG
APPROVED
TITLE
Complete stator side and case
SIZE
C
DWG NO
Xyz-11
REV
SCALE
SHEET 1 OF 1
SECTION A-A
SCALE 1 : 1

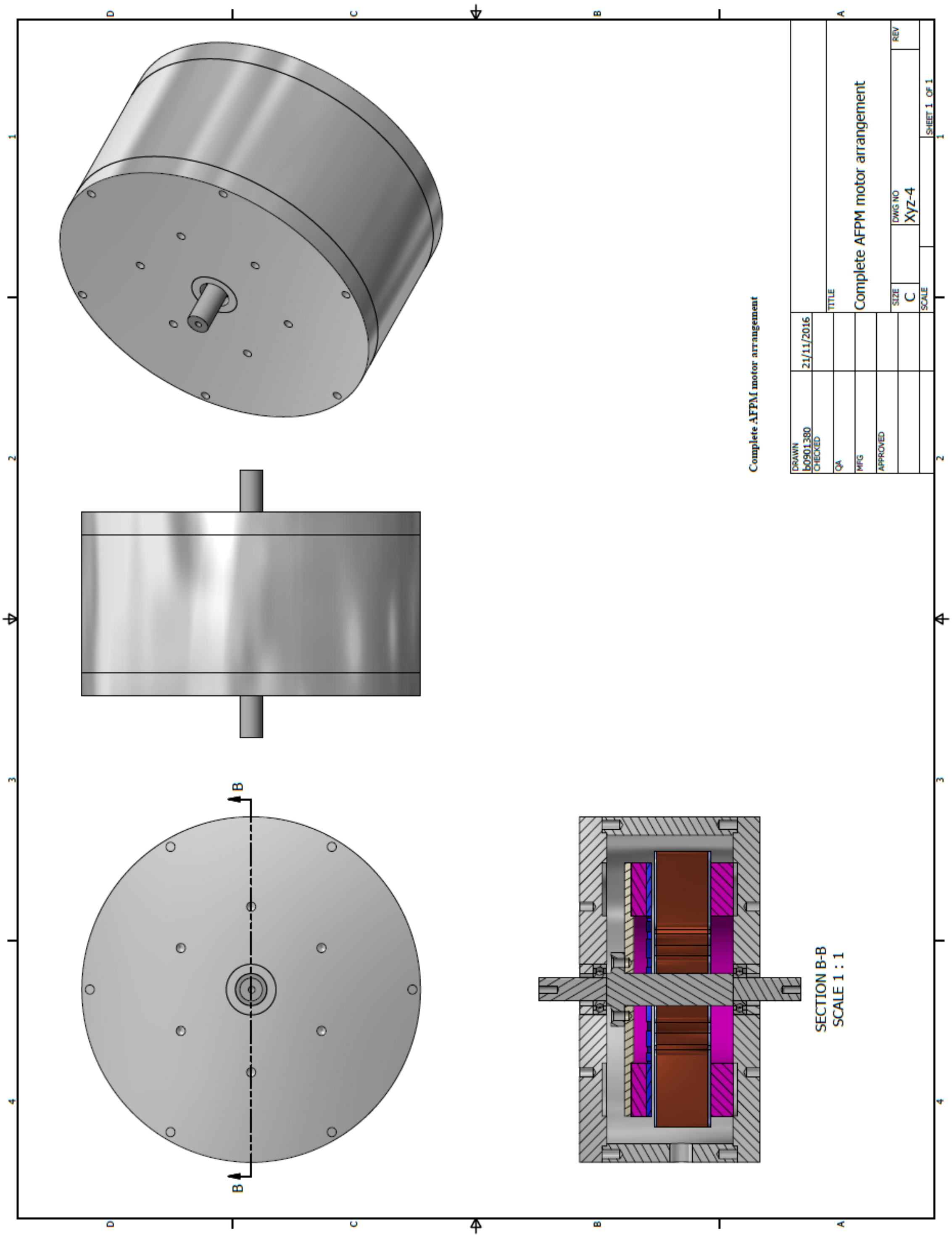
Complete AFPM motor arrangement
DRAWN
b0901380
21/11/2016
CHECKED
QA
MFG
APPROVED
TITLE
Complete AFPM motor arrangement
SIZE
C
DWG NO
Xyz-4
REV
SCALE
SHEET 1 OF 1
SECTION B-B
SCALE 1 : 1
B
B

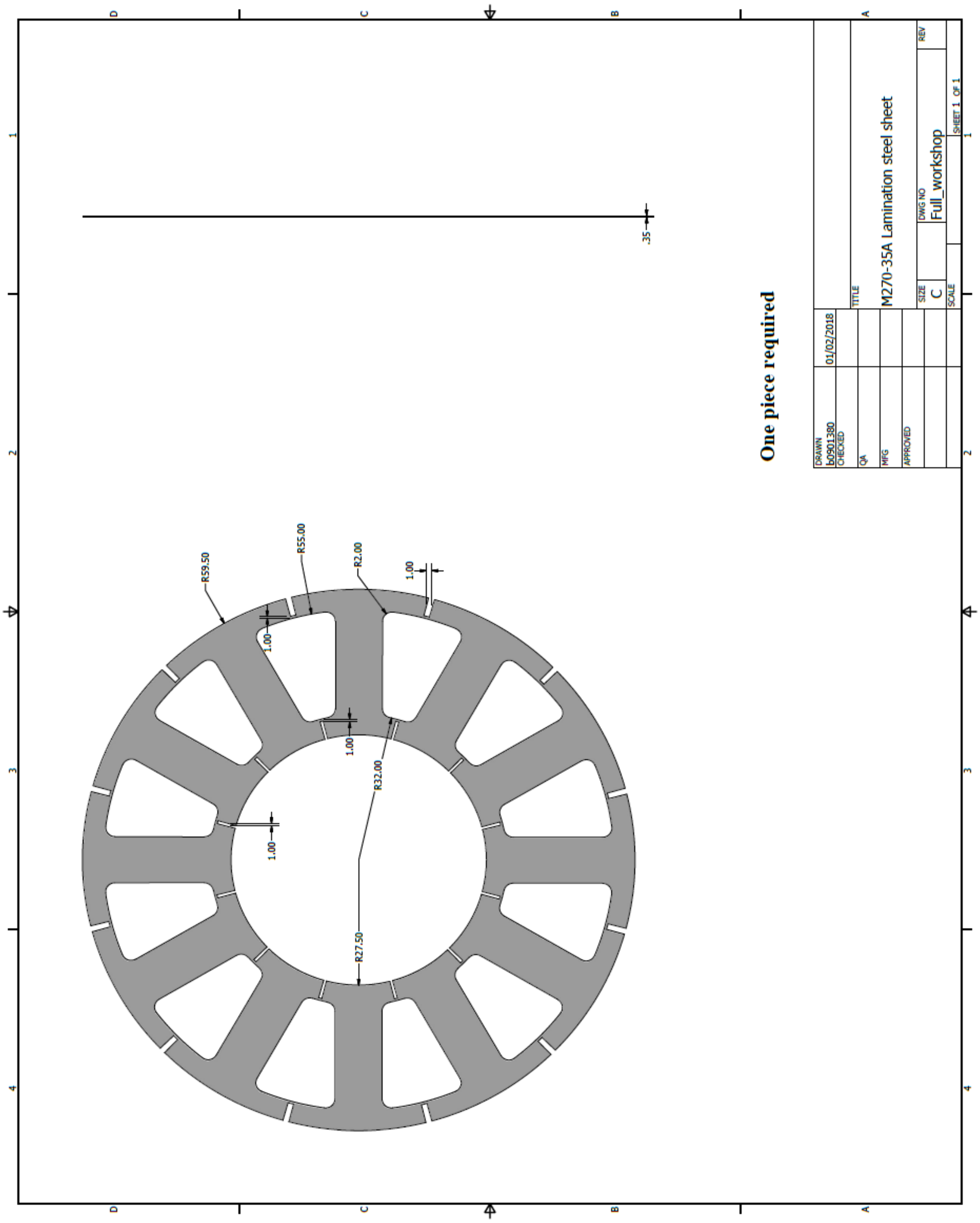
One piece required
DRAWN
b0901380
01/02/2018
CHECKED
QA
MFG
APPROVED
TITLE
M270-35A Lamination steel sheet
SIZE
C
DWG NO
Full_workshop
REV
SCALE
SHEET 1 OF 1
R59.50
R55.00
R2.00
1.00
R32.00
R27.50
.35

References

[1] W. A. Pluta “Some Properties of Factors of Specific Total Loss Components in Electrical Steel” IEEE Transactions on Magnetics, Vol. 46, No. 2, February 2010.

[2] P. G. Dickinson, “Application of Soft Magnetic Composites in Electrical Machines,” PhD Thesis, School of Electrical, Electronic and Computer Engineering, Newcastle University, United Kingdom, 2002. Unpublished.

[3] AB, Höganäs "Brochures and datasheets all documents for soft magnetic composites—SOMALOY-5p material data" in *Höganäs Catalogue SMC,* Höganäs AB Sweden: June 2018. Online at https://www.hoganas.com/globalassets/download-media/sharepoint/brochures-and-datasheets---all-documents/somaloy-5p_material-data_june_2018_2274hog.pdf

[4] M. Aydin, S. Huang, and T. A. Lipo, "Axial flux permanent magnet disc machines: A review," Proceedings of the 2004 SPEEDAM, 2004.

[5] K. Liu, X. Fu, M. Lin, and L. Tai “AC Copper Losses Analysis of the Ironless Brushless DC Motor used in a Flywheel Energy Storage System” IEEE Transactions on applied super conductivity, VOL. 26, NO. 7, October 2016.

[6] F. G. Capponi, G. De Donato, and F. Caricchi, "Recent advances in axial-flux permanent-magnet machine technology," *IEEE Transactions on Industry Applications*, vol. 6, pp. 2190-2205, 2012.

[7] A. Parviainen, "Design of axial-flux permanent-magnet low-speed machines and performance comparison between radial-flux and axial-flux machines," Ph.D thesis *Acta Universitatis Lappeenrantaensis*, 2005.

[8] R. Wrobel, D. Staton, R. Lock, J. Booker, and D. Drury “Winding Design for Minimum Power Loss and Low-Cost Manufacture in Application to Fixed-Speed PM Generator” IEEE Transactions on Industry Applications, VOL. 51, NO. 5, September/October 2015

[9] M. Gheorghe, M. Moţ, M. Greconici, M. Biriescu, and D. Vesa. "Performances analysis of an induction motor with stator slot magnetic wedges." In *2016 International Conference on Applied and Theoretical Electricity (ICATE)*, pp. 1-7. IEEE, 2016.

[10] M. Watanabe, K. Ide, R. Takahashi and N. Takahashi “Magnetically Anisotropic Slot Wedges for Rotating Machines” IEEE Transactions on Magnetics, pp. 407-410. VOL. 26, No. 2, March 1990

[11] M. Gheorghe, M. Greconici, M. Biriescu, and M. Moţ. "Effects of stator slot magnetic wedges on the induction motor performances." In *2012 13th International Conference on Optimization of Electrical and Electronic Equipment (OPTIM)*, pp. 489-492. IEEE, 2012.

[12] M. Dems, K. Komeza, and J. K. Sykulski. "Analysis of effects of magnetic slot wedges on characteristics of large induction motor." *Przeglad Elektrotechniczny* 88, No. 7b (2012): 73-77.

[13] M. Lavanya, P. Selvakumar, S. Vijayshankar, and C. Easwarlal. "Performance analysis of three phase induction motor using different magnetic slot wedges." In *2014 IEEE 2nd International Conference on Electrical Energy Systems (ICEES)*, pp. 164-167. IEEE, 2014.

[14] A. Cavagnino, M. Lazzari, F. Profumo, and A. Tenconi, "A comparison between the axial flux and the radial flux structures for PM synchronous motors," in Industry Applications Conference, 2001. Thirty-Sixth IAS Annual Meeting. Conference Record of the 2001 IEEE, 2001, pp. 1611-1618.

[15] J. R. Bumby, R. Martin, M. A. Mueller, E. Spooner, N. L. Brown, and B. J. Chalmers, "Electromagnetic design of axial-flux permanent magnet machines," in Electric Power Applications, IEE Proceedings-, 2004, pp. 151-160.

[16] A. Egea. (2013) "Design of Electrical Machines: Axial Flux Machines." *Electric Energy Magazine*.*Faculty of engineering-Electric Energy Group, mondragon university*.

[17] J. F. Gieras, R. J. Wang, and M. J. Kamper, Axial flux permanent magnet brushless machines: Springer Science & Business Media, 2008.

[18] L. A. Kilgore, "*Low-loss dynamo-electric machine*". Westinghouse Electric Co LLC, 1937. U.S. Patent 2,078,668.

[19] G. S. Liew, "Analysis and Design of Sinsle-Sided Slotted AMM Axial-Field Permanent Magnet Machies" Ph.D thesis University of Adelaide, Australia. E-Theses Online at http://hdl.handle.net/2440/60062

[20] D. J. Patterson, J. L. Colton, B. Mularcik, B. J. Kennedy, S. Camilleri, and R. Rohoza, "A comparison of radial and axial flux structures in electrical machines." In *2009 IEEE International Electric Machines and Drives Conference*, 2009, pp. 1029-1035.

[21] S. Huang, M. Aydin, T. A. Lipo, "TORUS Concept Machines: PrePrototyping Design Assessment for Two Major Topologies, Proceedings, Industry Application Society Annual Meeting 2001, IAS '01, Chicago, USA.

[22] K. Sitapati, K. Krishnan, "Performance Comparisons of Radial and Axial Field, Permanent Magnet, Brushless Machines", IEEE Transactions on Industry Applications, Vol. 37, No. 5, Sept./Oct. 2001.

[23] A. Cavignino, M. Lazzari, F. Profumo, A. Tenconi, "A Comparison Between the Axial Flux and the Radial Flux Structures for PM Synchronous Motors", IEEE Transactions on Industry Applications, vol 38, No. 6, November/December 2002.

[24] A. Parviainen, M. Niemela, J. Pyrhonen, J. Mantere, "Performance comparison between low-speed axial-flux and radial-flux permanent magnet machines including mechanical constraints," IEEE International Conference on Electric Machines and Drives, May 2005, pages 1695-1702.

[25] A. G. Jack, B. C. Mecrow, G. Nord, and P. G. Dickinson, "Axial flux motors using compacted insulated iron powder and laminations-design and test results," in *Electric Machines and Drives, 2005 IEEE International Conference on*, 2005, pp. 378-385.

[26] Y. Guo, J. G. Zhu, Z. W. Lin, and J. J. Zhong, "Measurement and modeling of core losses of soft magnetic composites under 3-D magnetic excitations in rotating motors," *IEEE transactions on magnetics*, vol. 41, pp. 3925-3927, 2005.

[27] J. Washington, G. J. Atkinson, N. J. Baker, A. G. Jack, B. C. Mecrow, B. B. Jensen, L. Pennander, G. L. Nord, and L. Sjöberg. "Three-phase modulated pole machine topologies utilizing mutual flux paths." *IEEE Transactions on Energy Conversion* 27, No. 2, 2012: 507-515.

[28] N. Ahmed, J. G. Washington, G. J. Atkinson, N. J. Baker, and L. Sjoberg. "Reduction of cogging torque and back EMF harmonics in modulated pole machine by variations in tooth span." In *2015 IEEE International Electric Machines & Drives Conference (IEMDC)*, pp. 482-488. IEEE, 2015.

[29] Y. Guo, J. G. Zhu, P. A. Watterson, and W. Wu, "Development of a PM transverse flux motor with soft magnetic composite core," *Energy Conversion, IEEE Transactions on*, vol. 21, pp. 426-434, 2006.

[30] J. Wang and D. Howe, "Influence of soft magnetic materials on the design and performance of tubular permanent magnet machines," *Magnetics, IEEE Transactions on*, vol. 41, pp. 4057-4059, 2005.

[31] Y. Enomoto, M. Ito, H. Koharagi, R. Masaki, S. Ohiwa, C. Ishihara, *et al.*, "Evaluation of experimental permanent-magnet brushless motor utilizing new magnetic material for stator core teeth," *Magnetics, IEEE Transactions on*, vol. 41, pp. 4304-4308, 2005.

[32] Y. Chen and P. Pillay, "Axial-flux PM wind generator with a soft magnetic composite core," in *Industry Applications Conference, 2005. Fourtieth IAS Annual Meeting. Conference Record of the 2005*, 2005, pp. 231-237.

[33] Y. Guo, J. G. Zhu, P. A. Watterson and W. Wu "Comparative study of 3-D flux electrical machines with soft magnetic composite core" *IEEE transactions on Industry Applications.* 39(6), pp. 1696-1703. (2003)

[34] A. G. Jack, B. C. Mecrow and S. A. Evans “Low cost SMC brushless DC motors for high volume application in the automotive sector” *IEE Conference Publication* (Vol, 1 pp. 356-360). London; Institute of Electrical, Engineers; 1999.

[35] G. Nord, P. Jansseon, C. C. Petersen, T. Yamada “Vertical electrical motor using soft magnetic composites” *In Electric Machines and Drives, IEEE International Conference*, pp. 373-377. May 2005.

[36] W. Ouyang, S. Huang, A. Good, T. A. Lipo “Modular permanent magnet machine based on soft magnetic composite” *Electrical Machine and Systems, 2005. ICEMS 2005. Proceedings of the Eighth International Conference (Vol. 1. Pp. 235-239). IEEE.*

[37] M. A. Khan, P. Pillay, R. Guan, N. R. Batane, D. J. Morrison “Performance assessment of a PM wind generator with machined SMC cores” *In Electric Machines and Drive Conference, 2007. IEMDC’07. IEEE International (Vol. 2, pp. 1049-1053). IEEE.*

[38] K. Vijayakumar, R. Karthikeyan, S. Kannan, G. P. Suuder, R. Arumugam, “Dynamic analysis of Switched Reluctance Motor using Soft Magnetic Composite material” In *Power Electronics, Drives and Energy systems (PEDES) & 2010 Power India, 2010 Joint International Conference on* (pp. 1-6). IEEE.

[39] B. Jankowski, C. Jedryczka, D. Kapelski, W. Szelag, B. Ślusarek, R. M. Wojciechowski “High sped permanent magnet motor with powder magnetic core” *In Power Electronics, Electrical Drives, Automation and Motion (SPEEDAM), 2012 International Symposium on* (pp. 1230-1234). IEEE.

[40] A. Mahmoudi, N. A. Rahim and W. P. Hew, "Axial-flux permanent-magnet machine modeling, design, simulation, and analysis," Scientific Research and Essays, vol. 6, pp. 2525-2549, 2011.

[41] A. Muetze, A. G. Jack, and B. C. Mecrow, "Brushless DC Motor using Soft Magnetic Composites as a Direct Drive in an Electric Bicycle," in 9th European Conference on Power Electronics and Applications (EPE 2001), Graz, 2001, pp. 27-29.

[42] A. G. Jack, B. C. Mecrow, and C. P. Maddison, "Combined radial and axial permanent magnet motors using soft magnetic composites," in Electrical Machines and Drives, 1999. Ninth International Conference on (Conf. Publ. No. 468), 1999, pp. 25-29.

[43] F. Caricchi, F. Crescimbini, and E. Santini, "Basic principle and design criteria of axial-flux PM machines having counterrotating rotors," Industry Applications, IEEE Transactions on, vol. 31, pp. 1062-1068, 1995.

[44] F. Caricchi, F. Crescimbini, and O. Honorati, "Low-cost compact PM machine for adjustable-speed pump application," in Industry Applications Conference, 1996. Thirty-First IAS Annual Meeting, IAS'96., Conference Record of the 1996 IEEE, 1996, pp. 464-470.

[45] E. Spooner and B. J. Chalmers, "'TORUS': a slotless, toroidal-stator, permanent-magnet generator," Electric Power Applications, IEE Proceedings B, vol. 139, pp. 497-506, 1992.

[46] F. Caricchi, F. Crescimbini, O. Honorati, A. D. Napoli, and E. Santini, "Compact wheel direct drive for EVs," Industry Applications Magazine, IEEE, vol. 2, pp. 25-32, 1996.

[47] P. P. Acarnley, B. C. Mecrow, J. S. Burdess, J. N. Fawcett, J. G. Kelly, and P. G. Dickinson, "Design principles for a flywheel energy store for road vehicles," Industry Applications, IEEE Transactions on, vol. 32, pp. 1402-1408, 1996.

[48] K. R. Pullen, M. R. Etemad, and A. Fenocchi, "The high speed axial flux disc generator-unlocking the potential of the automotive gas turbine," 1996.

[49] M. Van Dessel, R. Belmans, R. Hanitsch, and E. A. Hemead, "Design of a small, axial-flux permanent-magnet motor," European transactions on electrical power, vol. 6, pp. 81-90, 1996.

[50] R. Wrobel, D. E. Salt, A. Griffo, N. Simpson and P. H. Mellor, “Derivation and scaling of AC copper loss in thermal modeling of electrical machines.” IEEE Transactions on Industrial Electronics, 61(8), pp.4412-4420, 2014.

[51] T. S. Kwon, S. K. Sul, L. Alberti, and N. Bianchi, "Design and control of an axial-flux machine for a wide flux-weakening operation region," *Industry Applications, IEEE Transactions on*, vol. 45, pp. 1258-1266, 2009.

[52] F. Marignetti, G. Tomassi, P. Cancelliere, V. D. Colli, R. D. Stefano, and M. Scarano, "Electromagnetic and mechanical design of a fractional-slot-windings axial-flux PM synchronous machine with soft magnetic compound stator," in *Industry Applications Conference, 2006. 41st IAS Annual Meeting. Conference Record of the 2006 IEEE*, 2006, pp. 62-69.

[53] D. Ishak, Z. Q. Zhu, and D. Howe, "Eddy-current loss in the rotor magnets of permanent-magnet brushless machines having a fractional number of slots per pole," *Magnetics, IEEE Transactions on*, vol. 41, pp. 2462-2469, 2005.

[54] J. Pyrhönen, T. Jokinen, and V. Hrabovcová, “Design of rotating electrical machines” Wiley Online Library, 2008.

[55] S. Huang, J. Luo, F. Leonardi, and T. A. Lipo, "A comparison of power density for axial flux machines based on general purpose sizing equations," *Energy Conversion, IEEE Transactions on*, vol. 14, pp. 185-192, 1999.

[56] A. Di Gerlando, G. Foglia, M. F. Iacchetti, and R. Perini, "Axial flux PM machines with concentrated armature windings: Design analysis and test validation of wind energy generators," *Industrial Electronics, IEEE Transactions on*, vol. 58, pp. 3795-3805, 2011.

[57] J. Azzouzi, G. Barakat, and B. Dakyo, "Quasi-3-D analytical modeling of the magnetic field of an axial flux permanent-magnet synchronous machine," *Energy Conversion, IEEE Transactions on*, vol. 20, pp. 746-752, 2005.

[58] T. F. Chan, L. L. Lai, and S. Xie, "Field computation for an axial flux permanent-magnet synchronous generator," *Energy Conversion, IEEE Transactions on*, vol. 24, pp. 1-11, 2009.

[59] A. Parviainen, M. Niemelä, and J. Pyrhönen, "Modeling of axial flux permanent-magnet machines," *Industry Applications, IEEE Transactions on*, vol. 40, pp. 1333-1340, 2004.

[60] Y. N. Zhilichev, "Three-dimensional analytic model of permanent magnet axial flux machine," *IEEE transactions on magnetics,* vol. 34, 1998.

[61] R. E. Gilman, “Eddy current losses in armature conductors” Presented at the 36th Annual Convention of the American Institute of Electrical Engineers, White Sulphur Springs, W. Va., June 29-July 2, 1920.Westinghouse Electric Mfg. Co.

[62] C. R. Sullivan, “Computationally efficient winding loss calculation with multiple windings, arbitrary waveforms, and two-dimensional or three-dimensional field geometry." *IEEE transactions on power electronics* 16, no. 1 (2001): 142-150.

[63] P. Silvester, Skin effect in multiple and polyphase conductors." *IEEE Transactions on Power Apparatus and Systems* 3 (1969): 231-238.

[64] L. J. Long, H. B. Hamilton, “Simplified approach to radial flux loss calculation in cylindrical rotor generators” IEEE transactions on power apparatus and system, vol. PAS-94, no. 5, September/October 1975.

[65] I. A. Tsukerman, A. Konrad and J. D. Lavers, “A method for circuit connections in time-dependent eddy current problems” *IEEE Transactions on Magnetics*, Volume 28, Issue 2, March 1992, pp. 1299–1302.

[66] J. Gyselinck, and F. Robert, “Frequency-and time-domain homogenization of windings in two-dimensional finite-element models.” In *2005 European Conference on Power Electronics and Applications*, 11-14 September 2005, (pp. 10). IEEE.

[67] J. Fouladgar and E. Chauveau, “The influence of the harmonics on the temperature of electrical machines.” *IEEE transactions on magnetics,* Volume 41, Issue 5, May 2005, pp. 1644–1647.

[68] F. Marignetti, V. D. Colli, and Y. Coia, "Design of axial flux PM synchronous machines through 3-D coupled electromagnetic thermal and fluid-dynamical finite-element analysis," *Industrial Electronics, IEEE Transactions on,* vol. 55, pp. 3591-3601, 2008.

[69] J. L. Colton, D. J. Patterson, and J. Hudgins, "Rotor losses in axial-flux permanent-magnet machines with non-overlapped windings," in *Power Electronics, Machines and Drives (PEMD 2010), 5th IET International Conference on*, 2010, pp. 1-6.

[70] C. H. Lim, J. R. Bumby, R. G. Dominy, G. I. Ingram, K. Mahkamov, N. L. Brown, *et al.*, "2-D lumped-parameter thermal modelling of axial flux permanent magnet generators," in *Electrical Machines, 2008. ICEM 2008. 18th International Conference on*, 2008, pp. 1-6.

[71] D. A. Howey, A. S. Holmes, and K. R. Pullen, "Measurement and CFD prediction of heat transfer in air-cooled disc-type electrical machines," *Industry Applications, IEEE Transactions on,* vol. 47, pp. 1716-1723, 2011.

[72] M. Aydin, R. Qu, and T. A. Lipo, "Cogging torque minimization technique for multiple-rotor, axial-flux, surface-mounted-PM motors: alternating magnet pole-arcs in facing rotors," in *Industry Applications Conference, 2003. 38th IAS Annual Meeting. Conference Record of the*, 2003, pp. 555-561.

[73] M. Aydin, S. Huang, and T. A. Lipo, "Torque quality and comparison of internal and external rotor axial flux surface-magnet disc machines," *Industrial Electronics, IEEE Transactions on,* vol. 53, pp. 822-830, 2006.

[74] M. Aydin, Z. Q. Zhu, T. A. Lipo, and D. Howe, "Minimization of cogging torque in axial-flux permanent-magnet machines: Design concepts," *Magnetics, IEEE Transactions on,* vol. 43, pp. 3614-3622, 2007.

[75] D. A. González, J. A. Tapia, and A. L. Bettancourt, "Design consideration to reduce cogging torque in axial flux permanent-magnet machines," *Magnetics, IEEE Transactions on,* vol. 43, pp. 3435-3440, 2007.

[76] L. Del Ferraro, F. Caricchi, and F. G. Capponi, "Analysis and comparison of a speed-dependant and a torque-dependant mechanical device for wide constant power speed range in AFPM starter/alternators," *Power Electronics, IEEE Transactions on,* vol. 21, pp. 720-729, 2006.

[77] F. G. Capponi, R. Terrigi, F. Caricchi, and L. Del Ferraro, "Active output voltage regulation for an ironless axial-flux PM automotive alternator with electromechanical

flux weakening," *Industry Applications, IEEE Transactions on,* vol. 45, pp. 1785-1793, 2009.

[78] M. A. Khan, P. Pillay, N. R. Batane, and D. J. Morrison, "Prototyping a composite SMC/steel axial-flux PM wind generator," in *Industry Applications Conference, 2006. 41st IAS Annual Meeting. Conference Record of the 2006 IEEE,* 2006, pp. 2374-2381.

[79] T. J. Woolmer and M. D. McCulloch, "Analysis of the yokeless and segmented armature machine," in *Electric Machines & Drives Conference*, 2007, pp. 3-5.

[80] W. Fei, P. Luk, and K. Jinupun, "A new axial flux permanent magnet Segmented-Armature-Torus machine for in-wheel direct drive applications," in *Power Electronics Specialists Conference, 2008. PESC 2008. IEEE*, 2008, pp. 2197-2202.

[81] H. Vansompel, P. Sergeant, and L. Dupré, "Optimized design considering the mass influence of an axial flux permanent-magnet synchronous generator with concentrated pole windings," *Magnetics, IEEE Transactions on,* vol. 46, pp. 4101-4107, 2010.

[82] J. G. Wanjiku, H. Jagau, M. A. Khan, and P. Barendse, "A simple core structure for small axial-flux PMSGs," in *Electric Machines & Drives Conference (IEMDC), 2011 IEEE International*, 2011, pp. 1510-1515.

[83] C. T. Liu, T. S. Chiang, J. F. D. Zamora, and S. C. Lin, "Field-oriented control evaluations of a single-sided permanent magnet axial-flux motor for an electric vehicle," *Magnetics, IEEE Transactions on,* vol. 39, pp. 3280-3282, 2003.

[84] H. Kierstead, R. J. Wang, and M. J. Kamper, "Design Optimization of a Single Sided Axial Flux Permanent Magnet In-Wheel Motor with Non-Overlap Concentrated Winding," *Proc. SAUPEC,* pp. 36-40, 2009.

[85] M. J. Kamper, R. J. Wang, and F. G. Rossouw, "Analysis and performance of axial flux permanent-magnet machine with air-cored nonoverlapping concentrated stator windings," *IEEE Trans. Ind. Appl,* vol. 44, pp. 1495-1504, 2008.

[86] N. L. Brown and L. Haydock, "New brushless synchronous alternator," in *Electric Power Applications, IEE Proceedings-*, 2003, pp. 629-635.

[87] M. A. Mueller, A. S. McDonald, and D. E. Macpherson, "Structural analysis of low-speed axial-flux permanent-magnet machines," in *Electric Power Applications, IEE Proceedings-*, 2005, pp. 1417-1426.

[88] S. Kahourzade, A. Mahmoudi, H. W. Ping and M. N. Uddin, “A comprehensive review of axial-flux permanent-magnet machines.” *Canadian journal of electrical and computer engineering*, 2014, vol *37, no.* 1, pp.19-33.

[89] A. G. Jack, "Experience with the use of soft magnetic composites in electrical machines," in *International Conference on Electrical Machines*, 1998, pp. 1441-1448.

[90] L.-O. Pennander and A. G. Jack, "Magnetic Materials: Soft Magnetic Iron Powder Materials AC Properties and their Application in Electrical Machines," in *European Congress and Exhibition on Powder Metallurgy. European PM Conference Proceedings*, 2003, p. 1.

[91] N. Ahmed, “Improving the torque quality of a modulated pole machine,”Engineering Doctorate (EngD) Thesis, School of Electrical, Electronic and ComputerEngineering, Newcastle University, United Kingdom, 2016. Available at Newcastle university E-Theses Online http://theses.ncl.ac.uk/jspui/handle/10443/3684

[92] H. Shokrollahi and K. Janghorban, "Soft magnetic composite materials (SMCs)," *Journal of Materials Processing Technology*, vol. 189, pp. 1-12, 2007.

[93] D. H. Kim, J. K. Sykulski, and D. A. Lowther, “The Implications of the Use of Composite Materials in Electromagnetic Device Topology and Shape Optimization” IEEE TRANSACTIONS ON MAGNETICS, VOL. 45, NO. 3, MARCH 2009

[94] N. Takahashi, K. Fujiwara and J. Takehara “Basic study on characteristics of magnetic shielding and electromagnetic shielding” Transactions on Engineering Sciences vol 31, © 2001 WIT Press, www.witpress.com, ISSN 1743-3533

[95] J. Kappatou, C. Gyftakis, A. Safacas, “A study of the effects of the stator slots wedges material on the behavior of an induction machine.” Proceedings of the 2008 International Conference on Electrical Machines. Paper ID 949.

[96] H. Mikami, K. Ide, K. Arai, M. Takahashi and K. Kajiwara, “Dynamic Harmonic Field analysis of a cage type induction motor when magnetic slot wedges are applied” IEEE Transactions on Energy Conversion, Vol. 12, No. 4, December 1997

[97] K. Delaere, R. Belmans and K. Hameyer, “Influence of rotor slot wedges on stator currents and stator vibration spectrum of induction machines: A Transient Finite-Element Analysis” IEEE Transactions on magnetics, Vol. 39, No. 3, May 2003.

[98] S. Salon, D. Burow, M. DeBortoli, C. Slavik, “Effects of slot closure and magnetic saturation on induction machine behaviour” IEEE Transactions on magnetics Vol. 30, No. 5, September 1994.

[99] S. Wang, Z. Zhao, L. Yuan and B. Wang, “Investigation and analysis of the influence of magnetic wedges on high voltage motors performance” IEEE Vehicle Power and Propulsion Conference (VPPC), September 3-5, 2008, Harbin, China.

[100] M. G. Pantelyat, O. Bíró, A. Stermecki, “Electromagnetic Forces in Synchronous Turbogenerator Rotor Slot Wedges” In *Proceedings of the Joint INDS'11 & ISTET'11*, pp. 1-4. IEEE, 2011.

[101] M. Belhadi, G. Krebs, C. Marchand, H. Hannoun and X. Mininger, “Evaluation of a switched reluctance motor with magnetic slot wedges” *International Conference on Electrical Machines (ICEM)*, pp. 150-155. IEEE, 2014.

[102] R. Curiac, H. L. PE “Improvements in energy efficiency of induction motors by the use of magnetic wedges." *Record of Conference Papers Industry Applications Society 58th Annual IEEE Petroleum and Chemical Industry Conference (PCIC)*, pp. 1-6. IEEE, 2011.

[103] T. R. Gaerke and D. C. Hernandez, “The Temperature Impact of Magnetic Wedges on TEFC Induction Motors” IEEE transactions on industry applications, vol. 49, no. 3, May/June 2013.

[104] Y. Anazawa, A. Kaga, H. Akagami, S. Watabe and M. Makino “Prevention of harmonic torques in squirrel cage induction motors by means of soft ferrite magnetic wedges” IEEE Transactions on magnetic, Vol. MAG-18, No. *6,* November 1982.

[105] K. N. Gyftakis, P. A. Panagiotou, J. Kappatou, “The influence of semi-magnetic wedges on the electromagnetic variables and the harmonic content in induction motors." *XXth International Conference on Electrical Machines*, pp. 1469-1474. IEEE, 2012.

[106] S. A. Evans “Salient pole shoe shapes of interior permanent magnet synchronous machines." *The XIX International Conference on Electrical Machines-ICEM 2010*, pp. 1-6. IEEE, 2010.

[107] V. Venegas, R. Escarela, R. Mota, E. Melgoza and J. L. Guardado, "Calculation of electrical parameters for transient overvoltage studies on electrical machines," IEEE International Electric Machines and Drives Conference, 2003. IEMDC'03., Madison, WI, USA, 2003, pp. 1978-1982 vol.3, doi: 10.1109/IEMDC.2003.1210722.

[108] R. Wrobel, P. Mellor, M. Popescu & D. Staton “Power Loss Analysis in Thermal Design of Permanent Magnet Machines: A Review” IEEE Transaction on Industry Applications, 52(2), 1359-1368, 2016

[109] W. Choi, S. Li, and B. Sarlioglu, “Core loss estimation of high speed electric machines: An assessment,” *in Industrial Electronics Society, IECON 2013 - 39th AnnualConference of the IEEE*, 2013, pp. 2691–2696.

[110] Z. Gmyrek, A. Boglietti, and A. Cavagnino, “Iron loss prediction with PWM supply using low-and high-frequency measurements: Analysis and results comparison,” Industrial Electronics, IEEE Transactions on, vol. 55, no. 4, pp. 1722–1728, 2008.

[111] L. Hsing-Pang, M. Werst, J. H. Jonathan and D. Bogard. "Prediction of windage losses of an enclosed high speed composite rotor in low air pressure environments." In *Heat Transfer Summer Conference*, vol. 36932, pp. 15-23. 2003.

[112] G. De Donato, F. G. Capponi, and F. Caricchi, "Influence of magnetic wedges on the load performance of axial flux permanent magnet machines," in *IECON 2010-36th Annual Conference on IEEE Industrial Electronics Society*, 2010, pp. 876-882

[113] M. Aydin, S. Huang, and T. A. Lipo, "Optimum design and 3D finite element analysis of non-slotted and slotted internal rotor type axial flux PM disc machines," in Power Engineering Society Summer Meeting, 2001, 2001, pp. 1409-1416.

[114] N. Aliyu, G. Atkinson, and N. Stannard. "Concentrated winding permanent magnet axial flux motor with soft magnetic composite core for domestic application." In *2017 IEEE 3rd International Conference on Electro-Technology for National Development (NIGERCON)*, pp. 1156-1159. IEEE, 2017.

[115] J. Holtz. "On the spatial propagation of transient magnetic fields in AC machines." *IEEE Transactions on industry applications* 32, no. 4 (1996): 927-937.

[116] J. R. Bumby and R. Martin, "Axial-flux permanent-magnet air-cored generator for small-scale wind turbines," in *Electric Power Applications, IEE Proceedings-*, 2005, pp. 1065-1075.

[117] F. Magnussen and C. Sadarangani, "Winding factors and Joule losses of permanent magnet machines with concentrated windings," in *Electric Machines and Drives Conference, 2003. IEMDC'03. IEEE International*, 2003, pp. 333-339.

[118] N. Bianchi and M. D. Pré, "Use of the star of slots in designing fractional-slot single-layer synchronous motors," in *Electric Power Applications, IEE Proceedings-*, 2006, pp. 459-466.

[119] M. Lin, L. Hao, X. Li, X. Zhao, and Z. Q. Zhu, “A Novel Axial Field Flux-Switching Permanent Magnet Wind Power Generator” IEEE TRANSACTIONS ON MAGNETICS, VOL. 47, NO. 10, OCTOBER 2011.

[120] J. R. Hendershot and T. J. E. Miller, *Design of brushless permanent-magnet motors*: Magna Physics Pub., 1994.

[121] D. J. Griffiths and C. Reed, *Introduction to electrodynamics* vol. 3: prentice Hall Upper Saddle River, NJ, 1999.

[122] D. C. Hanselman, “Brushless permanent magnet motor design” The Writers' Collective, 2003.

[123] M. K. Kazimierczuk, “High Frequency Magnetic Components” John Wiley & Sons, Ltd. 2nd Edition, 2014.

[124] K. Atallah, D. Howe, P. H. Mellor, and D. A. Stone, "Rotor loss in permanent-magnet brushless AC machines," *Industry Applications, IEEE Transactions on*, vol. 36, pp. 1612-1618, 2000.

[125] N. Stannard, “Generator design for, and modelling of, small-scale wind turbines”, Durham theses, 2008 Durham University. Available at Durham E-Theses Online: http://etheses.dur.ac.uk/1846/[Accessed: 10- October- 2016].

[126] P. H.Mellor, R. Wrobel, and N.McNeill, “Investigation of proximity losses in a high speed brushless permanent magnet motor,” in Conf. Rec. 2006 IEEE Ind. Appl. Conf. 41st IAS Annu. Meet. Nov. 2006, pp. 1514–1518.

[127] A. Lehikoinen, N. Chiodetto, E. Lantto, A. Arkkio, A. Belahcen “Monte Carlo Analysis of Circulating Currents in Random-Wound Electrical Machines” IEEE TRANSACTIONS ON MAGNETICS, VOL. 52, NO. 8, AUGUST 2016.

[128] F. Gomory, M. Vojenciak, E. Pardo, M. Solovyov, and J. Souc, “AC losses in coated conductors,” Supercond. Sci. Technol., vol. 23, no. 034012, 2010.

[129] E. Pardo, J. Souc, and M. Vojenciak, “AC loss measurement and simulation of a coated conductor pancake coil with ferromagnetic parts,” Supercond. Sci. Technol., vol. 22, no. 075007, 2009.

[130] M. D. Ainslie, T. J. Flack, Z. Hong, and T. A. Coombs, “Comparison of first- and second-order 2D finite element models for calculating AC loss in high temperature superconductor coated conductors,” Int. J. Comput. Math. Elect. Electron. Eng., vol. 30, no. 2, pp. 744–762, 2011.

[131] M. D. Ainslie, V. M. Rodriguez-Zermeno, Z. Hong, W. Yuan, T. J. Flack, and T. A. Coombs, “An improved FEM model for computing transport AC loss in coils made of RABiTS YBCO coated conductors for electric machines,” Supercond. Sci. Technol., vol. 24, no. 045005, 2011.

[132] N. Amemiya, K. Yoda, S. Kasai, Z. Jiang, G. A. Levin, P. N. Barnes, and C. E. Oberly, “AC loss characteristics of multifilamentary YBCO coated conductors,” IEEE Trans. Appl. Supercond., vol. 15, no. 2, pp. 1637–1642, Jun. 2005.

[133] M. Majoros, B. A. Glowacki, and A. M. Campbell, “Transport ac losses and screening properties of Bi-2223 multifilamentary tapes covered with magnetic materials,” Phys. C, vol. 338, pp. 251–262, 2000.

[134] M. Majoros, B. A. Glowacki, and A. M. Campbell, “Modelling of the influence of magnetic screening on minimisation of transport AC losses in multifilamentary superconductors,” IEEE Trans. Appl. Supercond., vol. 11, no. 1, pp. 2780–2783, 2001.

[135] M. Majoros, M. D. Sumption, and E. W. Collings, “Transport AC loss reduction in striated YBCO coated conductors by magnetic screening,” IEEE Trans. Appl. Supercond., vol. 19, no. 3, pt. 3, pp. 3352–3355, Jun. 2009.

[136] M. D. Ainslie, T. J. Flack and A. M. Campbell, “Calculating transport AC losses in stacks of high temperature superconductor coated conductors with magnetic substrates using FEM,” Phys. C, vol. 472, pp. 50–56, 2012.

[137] M. D. Ainslie, W. Yuan, Z. Hong, R. Pei, T. J. Flack and T. A. Coombs, “Modeling and electrical measurement of transport AC loss in HTSbased superconducting coils for electric machines,” IEEE Trans. Appl. Supercond., vol. 21, no. 3, pt. 3, pp. 3265–3268, Jun. 2011.

[138] A. D. Podoltsev, I. N. Kucheryavaya, and B. B. Lebedev, “Analysis of effective resistance and eddy-current losses in multi turn winding of high frequency magnetic components,” IEEE Trans. Magn., vol. 39, no. 1, pp. 539–548, Jan. 2003.

[139] R. J. Wang and M. J. Kamper, “Calculation of Eddy Current Loss in Axial Field Permanent-Magnet Machine with Coreless Stator” IEEE TRANSACTIONS ON ENERGY CONVERSION, VOL. 19, NO. 3, SEPTEMBER 2004

[140] F. Caricchi, F. Crescimbini, O. Honorati, G. L. Bianco, and E. Santini, “Performance of core-less winding axial-flux PM generator with power output at 400 Hz—3000 rev/min,” IEEE Trans. Ind. Applicat., vol. 34, pp. 1263–1269, Nov./Dec. 1998.

[141] G. W. Carter, “The Electromagnetic field in its engineering aspect”, Longman, 2nd Edition, 1967.

[142] D. C. Hanselman, W.H. Peake 'Eddy current effects in slot-bound conductors' by, IEE Proc. –Electrical Power Applications. Vol 142, No.2, March 1995.

[143] N. Xi and C. R. Sullivan "Simplified high-accuracy calculation of eddy-current loss in round-wire windings." In 2004 IEEE 35th Annual Power Electronics Specialists Conference (IEEE Cat. No. 04CH37551), vol.2, pp. 873-879. IEEE 2004.

[144] M. D. Ainslie, W. Yuan and T. J. Flack, "Numerical Analysis of AC Loss Reduction in HTS Superconducting Coils Using Magnetic Materials to Divert Flux" IEEE TRANSACTIONS ON APPLIED SUPERCONDUCTIVITY, VOL. 23, NO. 3, JUNE 2013.

[145] C. E. Oberly, B. Razidlo and F. Rodriguez, "Conceptual approach to the ultimate low AC loss YBCO superconductor," IEEE Trans. Appl. Supercond., vol. 15, no. 2, pt. 2, pp. 1643–1646, Jun. 2005.

[146] F. Gomory, M. Vojenciak, E. Pardo and J. Souc, "Magnetic flux penetration and AC loss in a composite superconducting wire with ferromagnetic parts," Supercond. Sci. Technol., vol. 22, no. 034017, 2009.

[147] S. Safran, F. Gomory and A. Gencer, "AC loss in stacks of Bi-2223/Ag tapes modified with ferromagnetic covers at the edges," Supercond. Sci. Technol., vol. 23, no. 105003, 2010.

[148] M. Vojenciak, J. Souc and F. Gomory, "Critical current and AC loss analysis of a superconducting power transmission cable with ferromagnetic diverters," Supercond. Sci. Technol., vol. 24, no. 075001, 2011.

[149] H. C. Lovatt, V. S. Ramdenand and B. C. Mecrow, " Design an in-wheel motor for a solar-powered electric vehicle," IEE Proceedings B, vol.145, no. 5, pp. 402-408, 1998.

[150] P. B. Reddy and T. M. Jahns "Scalability investigation of proximity losses in fractional-slot concentrated winding surface PM machines during high-speed operation." In *2011 IEEE Energy Conversion Congress and Exposition*, pp. 1670-1675. IEEE, 2011.

[151] M. Van Der Geest, H. Polinder, J. A. Ferreira and D. Zeilstra. "Stator winding proximity loss reduction techniques in high speed electrical machines." In *2013 International Electric Machines & Drives Conference*, pp. 340-346. IEEE, 2013.

[152] A. Mlot, M. Lukaniszyn and M. Korkosz. "Influence of an end-winding size on proximity losses in a high-speed PM synchronous motor." In *2015 Selected Problems of Electrical Engineering and Electronics (WZEE)*, pp. 1-6. IEEE, 2015.

[153] M. Vetuschi and F. Cupertino. "Minimization of proximity losses in electrical machines with tooth-wound coils." *IEEE Transactions on Industry Applications* 51, no. 4 (July/August 2015): 3068-3076.

[154] P. Sergeant and A. P. M. Van den Bossche,"Influence of the Amount of Permanent-Magnet Material in Fractional-Slot Permanent-Magnet Synchronous Machines" IEEE TRANSACTIONS ON INDUSTRIAL ELECTRONICS, VOL. 61, NO. 9, SEPTEMBER 2014.

[155] M. Centner, R. Hanitsch and U. Schäfer, "Comparison of high-speed induction motors employing cobalt-iron and silicon electrical steel" Proceedings of the 2008 International Conference on Electrical Machines. Paper ID 1386.

[156] Cogent by SIR-Gruppen Sweden "Electrical Steel Thin Non Oriented" data sheet 2003-2004. [Online]. Available:https://perso.uclouvain.be/ernest.matagne/ELEC2311/T2006/ThinNOFP.pdf. [Accessed: 10- May- 2017].

[157] P. Ponomarev, P. Lindh and J. Pyrhönen, "Effect of Slot-and-Pole Combination on the Leakage Inductance and the Performance of Tooth-Coil Permanent-Magnet Synchronous Machines" IEEE TRANSACTIONS ON INDUSTRIAL ELECTRONICS, VOL. 60, NO. 10, OCTOBER 2013.

[158] M. Skalka, C. Ondrusek, J. Kurfurst and R. Cipin "Harmonic Reduction in Induction Machine using Slot Wedges Optimization" International Symposium on Power Electronics, Electrical Drives, Automation and Motion 2012

[159] S. Jian-Xin, H. Hao, J. Meng-Jia and C. Yuan "Reduction of Rotor Eddy Current Loss in High Speed PM Brushless Machines by Grooving Retaining Sleeve" IEEE transactions on magnetics, Vol. 49, No. 7, July 2013.

[160] Permabond Engineering Adhesive "Permabond ES562 Single-part heat-cure Epoxy Technical Datasheet" 28 October 2016 [Online]. Available: https://www.permabond.com/wp-content/uploads/2016/04/ES562_TDS.pdf [Accessed: 10- October- 2017].